AD NUMBER
AD384856

CLASSIFICATION CHANGES	
TO:	unclassified
FROM:	confidential

LIMITATION CHANGES

TO:

Approved for public release, distribution unlimited

FROM:

No foreign distribution

AUTHORITY

AFRPL ltr., 15 Mar 1971; AFRPL ltr., 5 Feb 1986

AFRPL-TR-67-246-Vol II

(Unclassified Title)

FINAL REPORT, ADVANCED AERODYNAMIC SPIKE CONFIGURATIONS

Volume II

Hot-Firing Investigations:
1. Basic Performance vs Altitude and Secondary Flow;
2. Performance in Slipstream;
3. Liquid (N_2O_4) Side Injection TVC

Rocketdyne Advanced Projects, Large Engines

Rocketdyne
A Division of North American Aviation, Inc.,

TECHNICAL REPORT AFRPL-TR-67-246-Vol II

September 1967

Air Force Rocket Propulsion Laboratory
Research and Technology Division
Edwards, California 93523
Air Force Systems Command
United States Air Force

UNCLASSIFIED

AFRPL-TR-67-246-VOL II

(Unclassified Title)

FINAL REPORT, ADVANCED AERODYNAMIC SPIKE CONFIGURATIONS

Volume II

Hot-Firing Investigations:

1. Basic Performance vs Altitude and Secondary Flow;
2. Performance in Slipstream;
3. Liquid (N_2O_4) Side Injection TVC

Rockstdyne Advanced Projects, Large Engines

Group 4
Downgraded at 3-Year Intervals
Declassified After 12 Years

THIS MATERIAL CONTAINS INFORMATION AFFECTING THE NATIONAL DEFENSE OF THE UNITED STATES WITHIN THE MEANING OF THE ESPIONAGE LAWS, TITLE 18 U. S. C., SECTIONS 793 AND 794, ITS TRANSMISSION OR THE REVELATION OF ITS CONTENTS IN ANY MANNER TO AN UNAUTHORIZED PERSON IS PROHIBITED BY LAW.

In addition to security requirements which must be met, this document is subject to special export controls and each transmittal to foreign governments or foreign nationals may be made only with prior approval of AFRPL(RPPR-STINFO), Edwards, California 93523.

UNCLASSIFIED

UNCLASSIFIED

FOREWORD

(U) This report was prepared in compliance with Contract AF04(611)-9948 covering the period 1 July 1964 through 28 February 1967. This study was conducted for the Air Force Rocket Propulsion Laboratory, Edwards, California. The program structure number is 750G and the project number is 3058. The Rocketdyne internal report number is R6959. Classified information (Confidential, Group 4) has been extracted from (asterisked) documents listed under References.

(U) This technical report has been reviewed and is approved.

Roy Silver
Project Engineer
Air Force Rocket Propulsion Laboratory
Edwards, California

UNCLASSIFIED

ABSTRACT (VOLUME II)

(C) Three hot-firing aerodynamic spike nozzle programs are described. One program had as its objective to obtain a large background of parametric hot-firing aerospike performance data. Performance data were obtained over a range of pressure ratio from approximately 350 down to 22. Thirty 8-second each duration firings, 10 at near sea level conditions and 20 over a range of high pressure ratio, were conducted. Secondary flowrate was varied from zero to 5 percent of primary flowrate and supplied by a gas generator utilizing N_2O_4 / UDMH-N_2H_4(50-50) propellants. G.G. mixture ratio was varied from approximately 0.10 to 0.18 at 3 percent secondary flowrate to determine the effect of secondary gas energy level. The 12 percent length aerospike thrust chamber had an area ratio of 26 and generated approximately 7400 pounds of thrust at design altitude and 300 psia chamber pressure. Gains in nozzle efficiency were noted with the use of up to 3 percent secondary flowrate. A high degree of altitude compensation was noted with this engine down to a pressure ratio equal to approximately 12 percent of design pressure ratio (approximately 300). A complete tabulation of performance is given. For the second program, the nozzle section of the above engine was lengthened to 25 percent (of an equivalent 15 degree conical nozzle) and modified to incorporate liquid (N_2O_4) side injection TVC capability. Thirty-three firings of 6 seconds each duration were conducted at altitude to determine liquid injection TVC performance trends with variations in injection parameters. Results are compared with theory and applied to typical applications. LITVC performance with N_2O_4 was generally low and other injection fluids and techniques are recommended. A third hot-firing test program was conducted to determine the influence of external flow on in-flight nozzle performance. An aerospike thrust chamber using H_2O_2 propellants was enclosed by a simulated vehicle body. The engine generated 400 pounds of thrust at a chamber pressure of 200 psia. The 20 percent length aerospike nozzle had an area ratio of 25 and was tested over a range of pressure ratio from 30 to 470 and at slipstream Mach numbers of 0, 0.55, 0.90, 1.20, 1.40, 1.80 and 2.2. Fifty-seven firings of 1 minute each duration were accomplished. Still air nozzle efficiency was very high and significant performance improvement was obtained with the addition of secondary flow. Nozzle performance was relatively unaffected by slipstream in the nozzle operating region of practical interest for booster engine application.

(CONFIDENTIAL ABSTRACT)

UNCLASSIFIED

ABSTRACT (VOLUME I)

(U) Investigations of the aerodynamic spike nozzle concept are discussed in this report. These investigations include experimental cold-flow testing of high-area ratio aerospikes, aerospike nozzles with various combustor configurations and various size segments of aerospike nozzles and parametric analytical application studies for the nozzle concept. One cold-flow test series investigated the performance of very high area ratio ($\epsilon = 150$) short length aerospike nozzles using helium as the test fluid. A ten percent length contoured nozzle and a six percent length conical nozzle were tested. Theoretical and experimental performance results are presented. The second cold-flow test series determined the performance of a series of aerospike nozzles having various combustor configurations. The effect of nozzle base bleed and intermodule bleed on performance was investigated. Combustor configurations consisted of shrouded and unshrouded continuous annular (toroidal) combustors and multichamber configurations with eight and sixteen discrete conventional combustors clustered around a common spike. Spacing between chambers, spike length, and engine shrouding were varied for the multichamber configurations. All nozzles had an area ratio of 50. Theoretical and experimental performance results are presented. A third cold-flow test series investigated the relative nozzle wall and base pressures for 45, 90, and 180 degree segments of an aerospike nozzle compared to a full annular aerospike. Experimental results are presented. Analytical and design studies were made to determine effective methods of utilizing toroidal and multichamber constructions for aerodynamic spike configurations over a wide range of thrust level, chamber pressure, and nozzle area ratio. Design layouts at several thrust levels of interest are presented. Heat transfer studies establishing cooling feasibility and parametric weight studies are described. Combustor effects on nozzle performance are discussed.

(UNCLASSIFIED ABSTRACT)

UNCLASSIFIED
This page is Unclassified

TABLE OF CONTENTS

ILLUSTRATIONS

UNCLASSIFIED

Page

UNCLASSIFIED

Page

		Page
170.	Porous Base Plate Configuration	309
171.	TVC Nozzle Ring Configuration Number 1	311
172.	TVC Nozzle Ring Configuration Number 2	312
173.	Typical TVC Flow Ring Assembly	313
174.	Main Engine Chamber Instrumentation	315
175.	Aerospike Engine, Outer Throat Instrumentation	316
176.	Engine Inner Nozzle Instrumentation	317
177.	Gas Generator Instrumentation	318
178.	Six-Component Thrust Stand	319
179.	Test Installation at AEDC	320
180.	Test Sequence	322
181.	Facility Propellant and Cooling Water Supply System Instrumentation	323
182.	TVC Propellant Supply System	324
183.	Hardware Damage Incurred During Test BE32	332
184.	Critical Parameters for a Reference Test (No TVC) with Secondary Flow	333
185.	Time Variation of Critical SITVC Parameters	336
186.	Side Force Ratio vs Flowrate Ratio for Liquid Injection at $\alpha/\ell = 0.25$	337
187.	Side Force Ratio vs Flowrate Ratio for Liquid Injection at $\alpha/\ell = 0.4, 0.7$	338
188.	Off Center Force Ratio vs Flowrate Ratio for Liquid Injection at $\alpha/\ell = 0.25$	339
189.	Off Center Force Ratio vs Flowrate Ratio for Liquid Injection at $\alpha/\ell = 0.4, 0.7$	340
190.	Relative Change in Axial Thrust vs Flowrate Ratio for Liquid Injection at $\alpha/\ell = 0.25$	341

TABLES

NOMENCLATURE FOR TVC AND TWELVE PERCENT LENGTH NOZZLE DISCUSSION

A	Area, in^2
A_p	Geometric Throat Area, in^2
A_B	Nozzle Base Area, in^2
A^*	Effective Throat Area, $A^* = (\dot{W}_p/\dot{W}_{pid})A_t$, in^2
A_H	Total Porous Plate Flow Orifice Area, in^2
C^*	Characteristic Velocity, ft/sec^2
C_D	Flow Discharge Coefficient, $C_D = \dot{W}/\dot{W}_{id}$
C_T	Nozzle Thrust Efficiency
$C_{T_{top}}$	Topping Cycle Thrust Efficiency
C_p	Specific Heat at Constant Pressure, BTU/lb °F
C_v	Specific Heat at Constant Volume, BTU/lb °F
C_F	Thrust Coefficient, $C_F = F/P_c A^*$
d	Distance from the Nozzle Throat Plane to the Yaw Force Load Cells, in.
d_e	Nozzle Exit Diameter, in.
d_t	Nozzle Equivalent Throat Diameter, $d_t = 2\sqrt{A_t/\pi}$, in.
F	Thrust, Measured Adiabatic Engine Thrust, lbs.
F_v	Reference (no TVC) Vacuum Thrust Uncorrected for Heat Loss, lbs.
F_A	Measured Axial Thrust, lbs.
ΔF_A	Change in Axial Thrust During LITVC, lbs.
F_s	Side Thrust, lbs.
F_{oc}	Off Center Thrust, lbs.
f	Induced Thrust per Port, lbs.

G	Empirical Spreading Coefficient (Fig. 152)
g	Gravitational Constant, $lb_f.ft/lb_m.sec^2$; throat gap width, in.
h	Distance from the Engine Gimbal (Throat) Plane to the Vehicle Center of Gravity, in.; Heat Transfer Coefficient, Btu/in^2, sec, ^oF
H	Enthalpy (per unit mass), BTU/lb
I_s	Specific Impulse, $I_s = F/\dot{w}$, sec
J_o	Blast Wave Constant (function of γ)
K_s	Side Thrust Amplification Factor (Appendix 4)
K_M	Off Center Thrust Amplification Factor (Appendix 4)
$\bar{K}$	Control Moment Amplification Factor (Appendix 4)
k_1	Integral of the First Order Blast Wave Theory Pressure Distribution Function (function of γ)
k	Summation Index ; Thermal conductivity, Btu/in,sec, ^oF
ℓ	Axial Length of the Nozzle Measured from the Throat Plane to the End of the Nozzle, in.
M_{∞}	Free Stream Mach Number
$\dot{m}$	Mass Flow Rate, lb_m/sec
$\mathcal{M}$	Molecular Weight, lb_m/mole
MR	Oxidizer-to-Fuel Mixture Ratio (by weight)
M	Moment, in.lbs.
M_T	Moment About the Throat Reference Plane, in.lbs.
n	Number of Injection Ports
P	Pressure, psia
PR	Chamber-to-Ambient Pressure Ratio, P_c/P_a
Q	Primary Stream Heat Loss, BTU/ lb; Heat Absorbed by Baffles, Btu

r_e	Nozzle Exit Radius, in.
s	Wetted Contour Length from the Injection Port to the End of the Nozzle, in.
T	Temperature, ^{o}F (or ^{o}R)
t	Flight time; time, sec.
t_b	Flight Time for Stage Burnout, sec.
u_{∞}	Free Stream Velocity, ft/sec.
v_j	Injectant Velocity, ft/sec
$\dot{W}$, $\dot{w}$	Weight Flowrate, lb/sec
x	Length; Axial Distance Measured from Nozzle Ref. Plane (Fig. 218), in.
y	Radial Distance Measured from the Engine Centerline (Fig. 218), in.

Greek

α	Contour Wall Angle, degrees (Fig. 218), Also thermal diffusivity
β	Injection Angle with Respect to a Normal to the Engine Centerline (Fig. 218), degrees
γ	Specific Heat Ratio, $\gamma = C_p/C_v$
ϵ	Nozzle Area Ratio, $\epsilon = A_e/A^*_p$
η_{c^*}	Characteristic Velocity Efficiency
η_{I_s}	Specific Impulse Efficiency
θ	Radial Injection Angle (Fig. 218, $\theta = 0$ Implies Radial Stream Injection, $\theta = \parallel$ Implies Parallel Stream Injection, $\theta = \Delta$ Implies Convergent Stream Injection), degrees ; also time, sec.
λ	Axial Injection Angle with Respect to a Tangent to the Nozzle Wall at the Point of Injection (Fig. 218), degrees

$\mathcal{V}$	Function of γ and Mach Number, $\mathcal{V} = 1 + \frac{\gamma - 1}{2} M_{oo}^2$
ρ	Density, lb_m/ft^3
φ	Equivalent Gimbal Angle (Appendix 4), degrees
ψ	Total Radial Arc Included by the TVC Injection Ports (Fig. 218), degrees
$\Delta\psi$	Radial Arc Between Injection Ports (Fig. 218), degrees
ω	Charge Energy Per Unit Mass of Charge Normalized in Terms of the Square of the Free Stream Velocity, u_{oo}

Subscripts

a	Refers to ambinet conditions
A	Denotes an axial force component
A	Denotes an aft load cell (Fig. 178)
B	Refers to nozzle base
c	Refers to chamber; Cold wall conditions
D	Denotes friction performance loss
e	Refers nozzle exit
e	Refers to total engine flowrate (primary plus secondary) exclusive of the TVC flow
F	Denotes a forward load cell (Fig. 178)
g	Gas, gas side conditions
H	Hot wall conditions
id	Ideal Quantity
i	Induced Force Component; Initial value at time = 0
int.	Refers to intrinsic thrust exclusive of ambient pressure drag
j	Refers to TVC injectant
k	Denotes kinetics performance loss

m	Denotes a measured quantity
N	Refers to the nozzle
opt	Denotes optimum thrust (one dimensional ideal value corresponding to P_c/P_a)
p	Refers to primary stream
P	Denotes pitch load cells (Fig.178)
R	Denotes roll load cells (Fig. 178)
r	Denotes a jet momentum force component
s	Refers to the secondary stream
s	Denotes a side force component
th	Refers to theoretical value
top	Topping cycle efficiency or specific impulse
TVC	Refers to the TVC system or flowrate
v,vac	Refers to vacuum conditions
w	Refers to the nozzle
x	Refers to length location
Y	Denotes yaw load cells (Fig. 178)

Superscripts

–	Average quantity (obtained through area integration if the quantity is pressure)

NOMENCLATURE FOR SLIPSTREAM DISCUSSION

A	Area, in^2
A_T	H_2O_2 Engine Area (refer to Fig. 108), in^2
C_F	Thrust Coefficient, $C_F = F/(P_c A_t)$
C^*	Characteristic Velocity, $C^* = (P_c A_t g)/\dot{W}$, ft/sec
C_T	Nozzle Thrust Efficiency (refer to Appendix 2)
D	Diameter, in.
F	Thrust, lbs_f
g	Gravitational Constant, ft. $lb_f/lb_m \cdot sec^2$
I_s	Specific Impulse, sec.
M	Mach Number
P	Pressure, lbs/in^2
P_{B_V}	Missile Base Pressure, lbs/in^2
P_B	Nozzle Base Pressure, lbs/in^2
PR	Chamber to Free-Stream Static Pressure Ratio, P_c/P_∞
$PR)_{des}$	Nozzle Design Pressure Ratio
$\%\ell$	Nozzle Axial Length in Percent of the Length of a 15-degree Conical Nozzle with the Same Area Ratio and Throat Area
T	Temperature, degrees Rankine (unless otherwise noted)
W	Weight, lbs.
$\dot{W}$	Weight flow rate, lbs/sec
x	Axial Contour Coordinate (Fig. 104), inches
y	Radial Contour Coordinate (Fig. 104), inches
R_t	Equivalent Throat Radius, $R_t = \sqrt{A_t/\pi}$, inches

Greek

η_{I_s}	Nozzle Specific Impulse Efficiency (refer to Appendix 2)
η_{c^*}	Nozzle Characteristic Velocity Efficiency (refer to Appendix 2)
ϵ	Nozzle Area Ratio, $\epsilon = A_e/A_t$
Φ	Missile Base Pressure Correlating Parameter (refer to Appendix 2)
Φ'	Missile Base Pressure Correlating Parameter (refer to Appendix 2)
γ	Specific Heat Ratio

Subscripts

t	throat
w	nozzle wall
c	chamber
v	vacuum
e	exit
a	ambient
∞	free stream
B	nozzle base
i	ideal
opt	optimum expansion through P_c/P
p	primary flow
s	secondary flow

SECTION I

INTRODUCTION

(U) As discussed in Volume I of this report, the aerospike nozzle represents a departure from conventional conical or bell nozzles. There are many advantages over conventional nozzles inherent in the aerospike nozzle concept. The results of contract AF04(611)-9948, presented in Volume I and II of this report, represent effort designed to verify and quantify such advantages.

(U) The overall approach included theoretical studies, cold-flow experiments, and hot-flow experiments. Specific goals of the study were:

1) to evaluate aerospike nozzle performance characteristics at high area ratios,
2) to compare methods of applying the concept to advanced vehicle configurations,
3) to demonstrate basic nozzle performance by means of hot-firing tests,
4) to evaluate the hot-firing thrust vector control characteristics of an aerospike nozzle using liquid side injection,
5) to evaluate hot-firing aerospike nozzle performance in a typical flight environment (slipstream)
6) to analytically investigate nozzle base bleed configurations, and perform a hot-firing demonstration of a promising configuration, and
7) to perform a cold-flow investigation of aerospike nozzle segment performance.

(U) Volume I of this report presents the results of the cold-flow test programs and the analytical and design studies. This volume, Volume II, presents the results of the hot-firing test programs.

(U) The aerodynamic spike nozzle performance characteristics investigated in the hot-firing tasks (i.e., basic still air performance vs altitude and secondary flow parameters, fluid side injection TVC performance, and performance in slipstream had previously been studied in cold-flow programs under this (Volume I) and other contracts, and internal research and development funding. Correlation of hot- and cold-flow test results serve to substantiate theoretical methods and enables the prediction of hot-firing nozzle performance from relatively inexpensive cold-flow test data. Therefore, the hot firing test results from this program are compared to applicable previous cold-flow test results.

(U) Although the results of the tests are presented, interpreted and applied to some practical cases in this report, the principal value to be derived from this report will come from the detailed documentation of test results. It is expected that these data shall be referred to frequently in future studies of aerodynamic spike nozzles.

SECTION II

SUMMARY

(C) Three hot-firing aerodynamic spike nozzle programs were conducted under Air Force contract AF04(611)-0048. Each program investigated a different area of interest in characterizing aerodynamic spike nozzle performance. A 12-percent length aerospike thrust chamber generating approximately 7400 pounds altitude thrust with N_2O_4/UDMH-N_2H_4 (50-50) propellants was tested over a pressure ratio range from approximately 22 to 350. The objective of this program was to obtain a large background of basic aerospike hot-firing performance data. The nozzle portion of the above engine was lengthened to 25 percent and modified to incorporate liquid (N_2O_4) side injection TVC capability. An extensive series of tests was conducted at altitude to determine liquid injection performance trends with variations in injection parameters. A third hot-firing program investigated the effect of external flow (slipstream) on aerospike nozzle performance. A 400-pound thrust aerospike thrust chamber utilizing H_2O_2 propellants was enclosed in a simulated missile body and fired over a range of altitude and Mach number conditions. A schedule showing the time periods during which the actual testing for the three programs was accomplished is shown in Fig. 1.

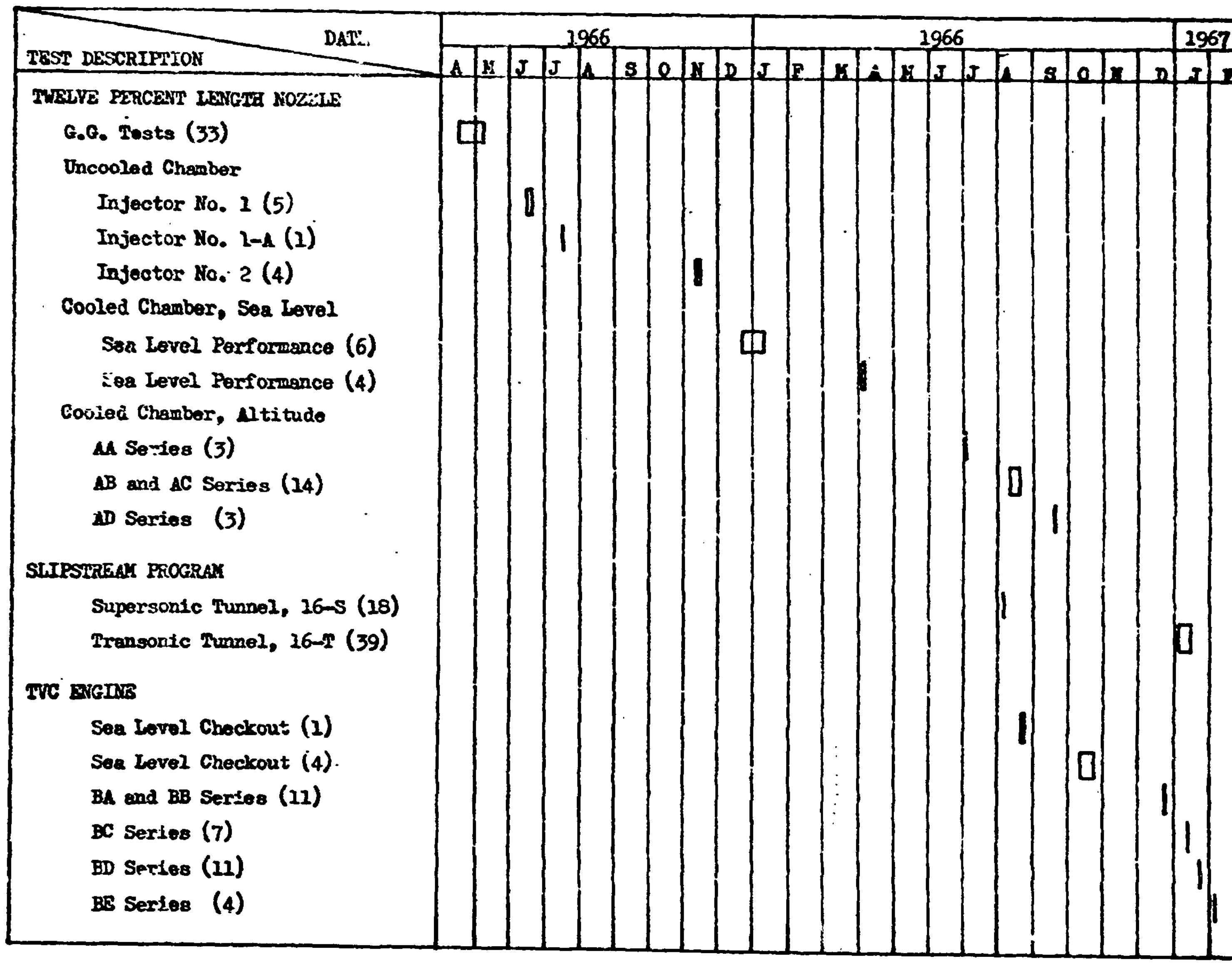

Note: Numbers in parentheses designate the number of tests accomplished.

Figure 1. Hot-Firing Program Test Schedule

TWELVE PERCENT LENGTH NOZZLE PROGRAM

(U) In July 1964, a program was initiated to demonstrate the aerodynamic spike nozzle concept with a hot-firing model and to obtain an extensive compilation of basic parametric performance data. At that time essentially no hot-firing performance data existed for this new nozzle concept and performance for proposed new aerospike rocket engines was estimated from cold-flow data. The objective of this program was successfully accomplished with the achievement of valid test data from 26 thrust chamber firings of approximately 8 seconds each duration.

Scope

(U) Two water cooled and one uncooled aerospike thrust chambers were fabricated. The combustion chamber and nozzle geometries were identical for the two thrust chamber types except the water cooled version had a 12 percent length nozzle and the uncooled version had an 8 percent length nozzle. The same injector was used in both versions. The uncooled chamber was used for injector checkout tests (at Rocketdyne facility) of 0.5 to 0.8 seconds duration (Fig. 2). The water cooled thrust chamber assembly (Fig. 3) was used for relatively long duration (to 8 seconds) data firings at sea level (Rocketdyne) and at altitude (Arnold Engineering Development Center).

(C) The thrust chambers utilized N_2O_4/UDMH-N_2H_4 (50-50) propellants in both the primary chamber and in a gas generator which supplied secondary bleed gas into the nozzle base region. The uncooled chamber was tested at chamber pressures from 300 to 500 psia, and the water cooled chamber was nominally operated at 300 psia (approximately 7400-pound thrust at design altitude), after three initial firings (to 5 seconds duration) at 400 psia.

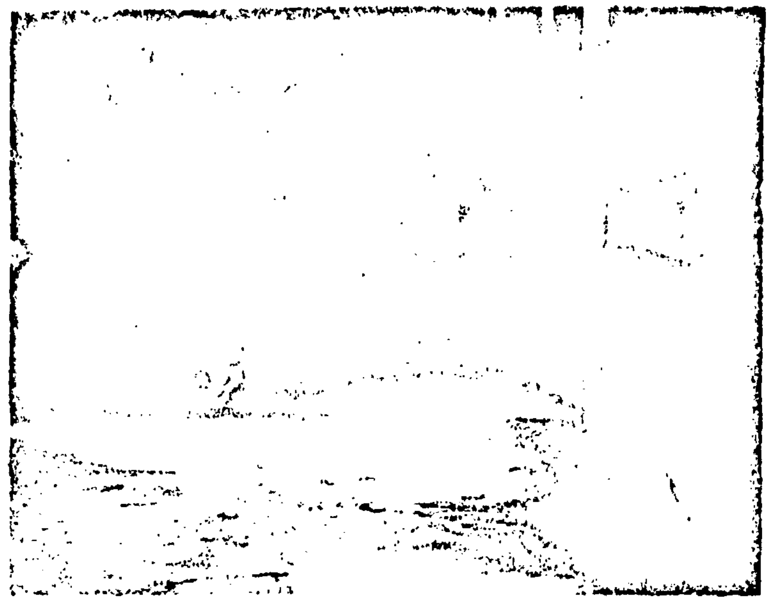

b. Injector Checkout Firing

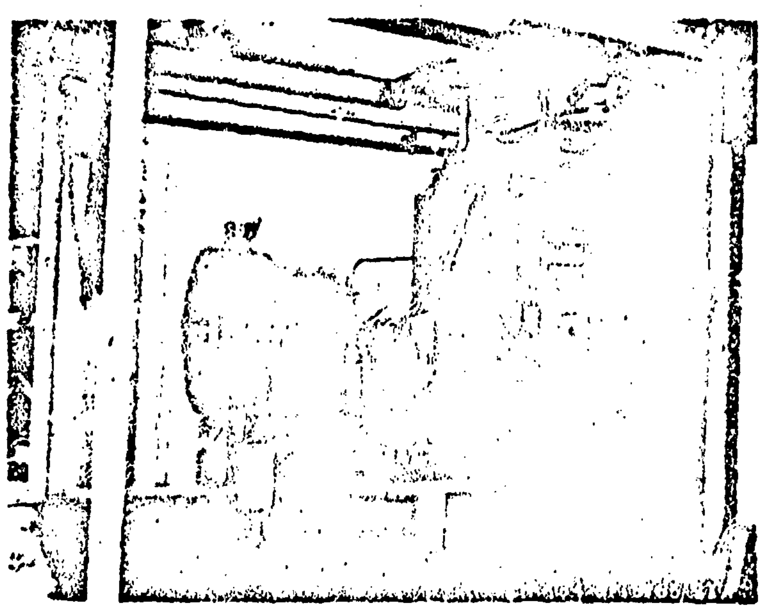

a. Installation, Sugar Stand, Propulsion Research Area, Santa Susana Field Laboratory

Figure 2, Uncooled Aerospike Thrust Chamber

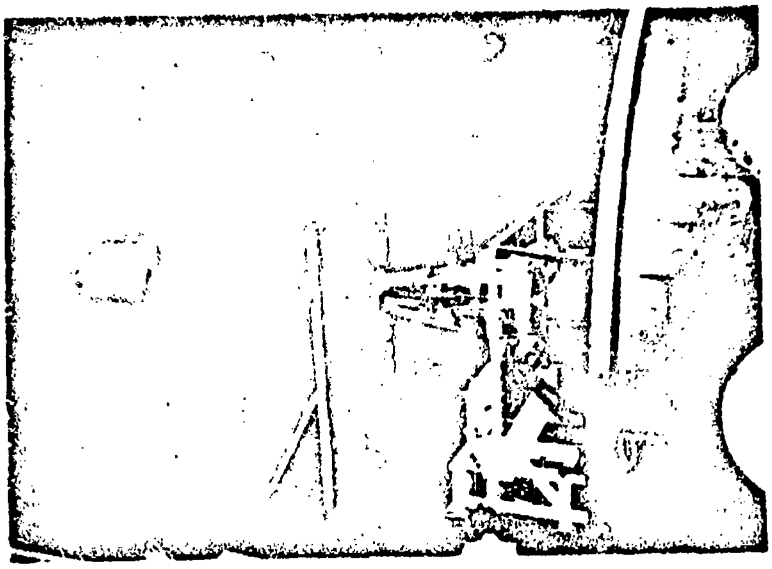

b. AEDC Installation, Rocket Test Facility, J-2 Cell

a. Rocketdyne Installation, Sugar Stand

Figure 3 . Water Cooled Twelve Percent Length Aerospike

(U) The test program was conducted in the following five phases: (1) A series of 33 gas generator tests (with a high flowrate and a low flowrate gas generator) was conducted to establish operating characteristics over a range of flowrates and propellant mixture ratio; (2) Ten uncooled thrust chamber firings with three injector configurations were conducted at sea level to obtain an injector suitable for use in the water cooled hardware; (3) Ten sea level firings with the water cooled TCA[1] were conducted to establish hardware integrity and operating characteristics and to obtain low pressure (PR = 22 to 29) ratio performance data over a range of secondary flowrates (0 to 5 percent); (4) Seventeen TCA firings were achieved over a range of high pressure ratios (PR = 35 to 350), secondary flowrates (0 to 5 percent), and gas generator mixture ratios (0.09 to 0.18) to obtain parametric performance data; (5) Three constant altitude firings were conducted with a perforated nozzle base configuration to evaluate the effect of secondary flow injection configuration on performance.

Results

(U) The 33 gas generator tests successfully characterized the combustion efficiency over a range of mixture ratios from .05 to .185 and flowrates from 0.5 lbs/sec to 2.8 lbs/sec.

(C) Five uncooled thrust chamber firings of 0.5 second duration were made with the first injector configuration at chamber pressures from 300 to 500 psia. All tests showed high frequency (2300 cps) chamber pressure oscillations with a peak to peak amplitude of approximately 50 percent of chamber pressure. This injector was modified slightly by tapering and shortening the injector baffles and by plugging fuel orifices adjacent to the baffles. One test was made with this configuration at 410 psia chamber pressure. A low frequency (530 cps) frequency instability with a peak to peak amplitude approximately 75 percent of chamber pressure was experienced.

1. Thrust Chamber Assembly (TCA)

(C) A redesigned injector configuration was constructed and four uncooled thrust chamber tests were conducted at chamber pressures from 300 to 450 psia. No measurable chamber pressure oscillations were experienced in any of these tests and the injector was found suitable for use in the water cooled hardware.

(C) Nine sea level tests and seventeen altitude tests were accomplished with the water cooled thrust chamber to evaluate the effect of secondary flowrate and secondary gas energy level on nozzle performance. A nozzle efficiency, C_T, of 96.0 percent was achieved with no secondary flow at design pressure ratio ($\sim$300). The addition of from 1 to 3 percent secondary flow increased nozzle efficiency at design pressure ratio to approximately 96.5 percent. Maximum efficiency gains of about 1.5 percent were achieved at intermediate pressure ratios ($\sim$120) with the addition of from 1 to 3 percent secondary flow. Over the low pressure ratio range, from 35 to 22, performance with and without 1 to 3 percent secondary flowrate was about the same.

(C) No significant difference in performance was found among the different energy level secondary flows. A high degree of altitude compensation was obtained over a pressure ratio range from 300 to 35. Nozzle efficiency decreased from 96.0 to 93.8 over this pressure ratio range.

(C) Three 8-second duration tests were made with a perforated base plate mounted at the nozzle exit plane. Operational difficulties with the gas generator prevented determination of the secondary flowrate for all three tests. Low frequency (487 cps) combustion instability in the primary thrust chamber was experienced during the second test. Hardware damage was sufficient to preclude further testing to evaluate base configurations.

LIQUID (N_2O_4) SIDE INJECTION TVC PROGRAM

(C) Recent advances in rocket engine technology have resulted in a need for increased study of means for providing directional thrust control for future generation rocket engines. Secondary injection of fluids into the engine exhaust streams has proven to be an effective and efficient method of thrust vector control (TVC) in several present applications; and cold-flow testing, complemented by analytical system studies, has shown that this is also a competitive TVC technique for advanced aerospike engines. The objective of this investigation was to supplement current aerospike TVC technology by providing sufficient hot-flow liquid (N_2O_4) injection TVC test data to establish design criteria and enable quantitative performance evaluations for future high-thrust aerospike engines. The objective was successfully accomplished.

Scope

(U) A test program was formulated so that the liquid injection TVC technique could be studied using a modified version of the 12 percent length, N_2O_4/UDMH-N_2H_4(50-50) aerospike thrust chamber. All thrust chamber assembly components except for the inner nozzle were identical. Performance testing was conducted at altitude at the Rocket Test Facility (J-2 Cell) at Arnold Engineering Development Center after sea level checkout testing at Rocketdyne (Fig. 4).

(C) Chamber pressure selected for the TVC testing was 200 psia with an attendant vacuum thrust level of 5600 pounds. Area ratio of the aerospike nozzle was 25 and the axial length was 25 percent of an equivalent 15-degree conical nozzle. Injection of the TVC flow was effected through orifices located in uncooled contoured flow rings which comprised the aft section of the nozzle.

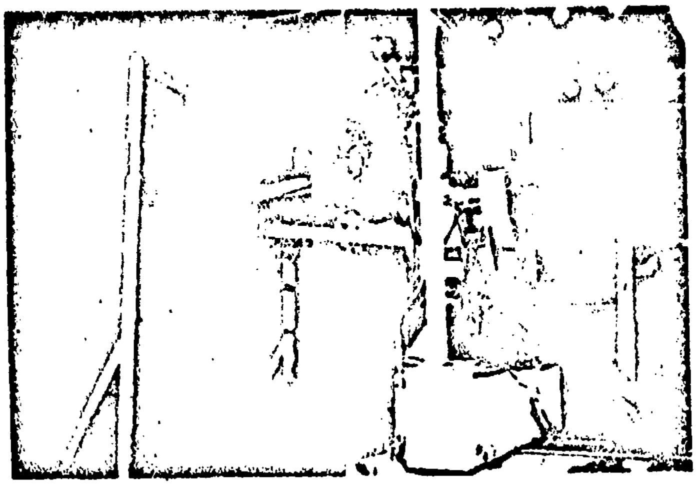

b. AEDC Installation, J-2 Cell

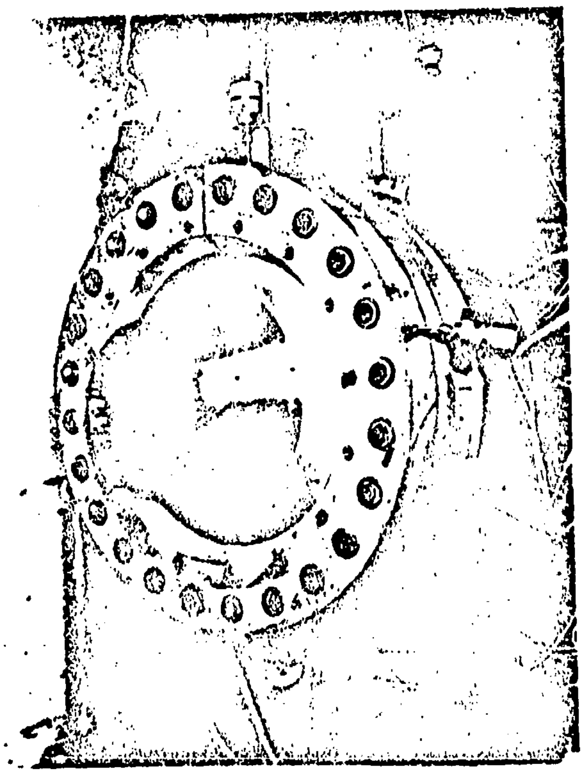

a. Rocketdyne Checkout Installation, Sugar Stand

Figure 4 . Aerospike Engine with Side Injection TVC Capability

(U) Four uncooled flow rings incorporating 29 different injection patterns were fabricated to investigate injection parameters which could influence TVC performance. These configurations enabled the experimental evaluation of (1) constant-velocity injection flowrate variation, (2) axial location of the point of injection, (3) angle of injection with respect to the nozzle contour, (4) one, three, and five-port injection patterns, (5) spacing between holes in an injection pattern, (6) angle of impingement of adjacent holes in an injection pattern and (7) injection velocity variation at constant flowrate.

Results

(C) Thirty-three firings of 6 seconds each duration were conducted at altitude to establish engine performance without TVC, and to determine LITVC performance trends with variations in the injection parameters. Five sea level checkout tests of from 1/2 to 5 seconds durations were conducted at Rocketdyne prior to the altitude testing. The thrust efficiency of the engine was 95.1 percent for $\dot{W}_s/\dot{W}_p = 0$ and 95.2 percent for $\dot{W}_s/\dot{W}_p = 0.017$. Combustion efficiency (η_{C*}) was nominally 89 percent throughout the program.

(C) A semi-empirical blast-wave theory was utilized in conjunction with experimental data from various sources to provide a basis for selection of SITVC test configurations. Testing of these configurations established that measured LITVC side-force efficiency trends with an aerospike are similar to those expected on the basis of preliminary analysis: injection near the throat provides higher side-force efficiency than injection near the nozzle exit, multiple-port inclination has no influence on LITVC performance in the range tested near the nozzle exit, and parallel stream injection affords higher performance than radial stream injection at both locations

studied. Control moment and nozzle specific impulse efficiency trends were found to be dependent upon the engine-vehicle geometric relationship. These efficiencies followed trends established by the side-force efficiency for boost vehicles ($r_e/h = 0.25$), but in some cases optimized differently for upper-stage configurations ($r_e/h = 1.0$).

(C) Comparison of the side-thrust efficiency TVC data obtained in this program with that obtained from other nozzles revealed that LITVC performance with an aerospike is equal to or less than with other nozzles, because of the relatively short length of the aerospike. The level of side thrust efficiency for N_2O_4 injection established through this testing was also found to be lower than that estimated using the blast wave analysis in conjunction with an empirical coefficient obtained for gas injection into flow over a flat plate. It was necessary to revise this coefficient to obtain quantitative agreement between theory and experiment for the configuration tested. Application of the test data to full-scale engine systems showed that liquid injection may be competitive with gas injection under certain conditions. In general, fuel injection provides higher in-flight engine specific impulse efficiency but lower density impulse than oxidizer injection if vaporization and reaction do not occur within the nozzle.

(C) On the basis of these results, it is recommended that the relative merits of liquid injection TVC be investigated through comparative systems analysis using the conservative performance estimates presented herein for full-scale engines. It is also recommended that improved LITVC designs such as a bipropellant injection technique be studied, and that the performance and operating characteristics of attractive systems be evaluated through large-scale environmental hot-flow testing.

SLIPSTREAM PROGRAM

(C) Because of interaction which occurs between external and nozzle flows, vehicle base flow characteristics encountered in missile flight differ from those prevalent in quiescent air nozzle performance investigations. These base flow characteristics are of little consequence with conventional nozzles since the expansion process is internal in this case; that is, the exhaust gases within the nozzle are shielded from the external flow by the physical expansion surface provided by the nozzle. However, with an aerospike nozzle, the external expansion boundary is formed by a gas-gas interface, and is influenced by flow interference effects. Since the position of this outer boundary in the flow affects aerospike nozzle performance at low pressure ratios where the base pressure follows changes in ambient pressure ("open wake"), the presence of an external flow can affect aerospike performance under certain conditions. Previous cold-flow testing conducted under contract NAS 8-2654 (Ref. 21) established that the effect of external flow is small and is confined to a narrow range of in-flight operating conditions. Experimental study of these effects was continued under contract AF04(611)-9948. The primary objective of this program was to confirm and extend, through hot-flow testing, the results obtained in the cold-flow slipstream study. A secondary objective was to evaluate the effect of base bleed flowrate on nozzle still air performance.

Scope

(C) A hot-flow test program was conducted to determine the influence of external flow on in-flight aerospike nozzle performance. A hot-firing aerospike engine using hydrogen peroxide propellants was enclosed by an aerodynamic fairing constructed in the shape of a missile body to simulate an actual flight configuration. The engine generated 400 pounds of altitude thrust

at a chamber pressure of 200 psia. An aerospike nozzle with an area ratio of 25 and a length equal to 20 percent of an equivalent 15 degree conical nozzle was utilized to control the expansion of engine exhaust gases. The secondary flowrate was 0.8 percent of the primary flowrate for all tests with external flow. Testing was conducted in the 16-foot transonic and supersonic propulsion wind tunnels at Arnold Engineering Development Center (AEDC). Installation of the model in these facilities is shown in Fig. 5 .

Results

(C) Fifty-two tests of approximately 1 minute each duration were conducted to obtain still air and slipstream performance trends in the transonic and supersonic wind tunnels. Valid data was obtained from only forty of these, however, because of a seal failure and excessive model leakage. In addition, five tests were conducted in the transonic facility to demonstrate engine performance trends with secondary flowrate. Results of these tests confirmed that high quiescent air performance (approximately 98 percent of ideal at design pressure ratio) can be obtained throughout a representative range of pressure ratios with a properly designed aerospike nozzle. The addition of secondary flow proved beneficial at all pressure ratios. It was found that the correct experimental performance level and trend with pressure ratio could be estimated above pressure ratios at which nozzle recompression occurs using previously developed semi-empirical base pressure relationships in conjunction with a potential primary flow analysis and viscous drag computations.

(C) Nozzle performance was found to be unaffected by external flow in the "closed wake" pressure ratio region (pressure ratios at which nozzle base pressure is constant in still air). At low pressure ratios ("open wake") performance of the model tested decreased at a rate which was dependent

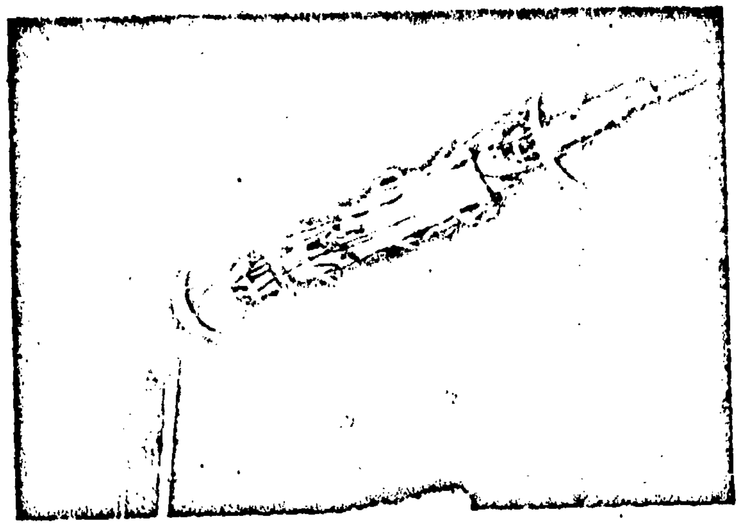

b. Partial Installation, Supersonic Wind Tunnel (16-S), PWT, AEDC

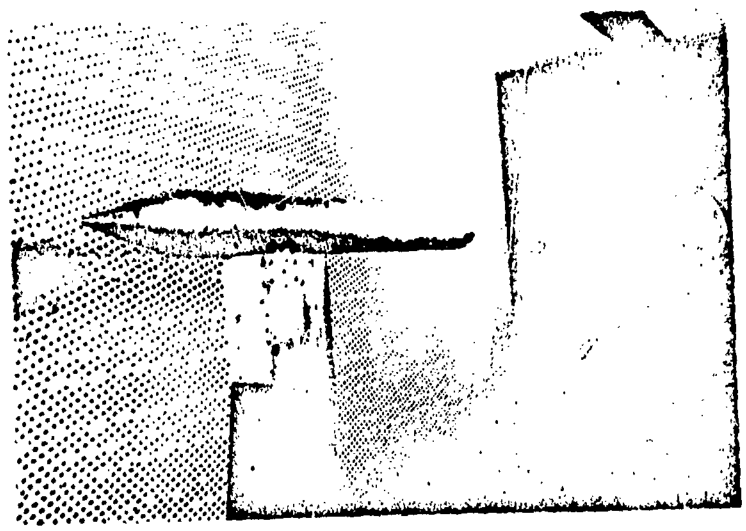

a. Completed Installation, Transonic Wind Tunnel (16-T), PWT, AEDC

Figure 5 . Slipstream Model

on free stream Mach number and chamber pressure ratio. When strong flow interaction effects occurred, they were found to result in relatively high nozzle base pressure, which was also shown by previous cold-flow data. When flow interaction did not influence nozzle base pressure, both hot- and cold-flow nozzle performance data correlated with the "effective" chamber pressure ratio, $P_c/\overline{P}_{B_V}$. On the basis of this result, it was concluded that: (1) missile base pressure approaching ambient pressure will result in nozzle efficiency in slipstream nearly identical to that obtained in still air, and (2) strong slipstream-primary flow interaction results in relatively high in-flight nozzle performance.

(c) In-flight performance estimates generated under severe assumptions demonstrated that the time-integrated external flow effects over a typical mission result in a change in average specific impulse ($\overline{I}_s$) of less than 0.2 percent. Boat-tailing, mass addition to the missile wake flow, and reduction in missile base area are shown to be effective methods of reducing these effects still further.

SECTION III

PERFORMANCE EVALUATION OF A HOT-FIRING AEROSPIKE NOZZLE

INTRODUCTION AND SUMMARY

(U) In July 1964, work was initiated on the design and fabrication of a hot-firing aerodynamic spike nozzle. At that time, essentially no hot-firing performance data existed for this new nozzle concept. Basic performance for proposed new rocket engines utilizing this new nozzle concept was based upon data obtained from cold-flow tests. This program was initiated to provide a substantial background of parametric hot-firing performance data with an aerodynamic spike nozzle configuration and to correlate these data with cold-flow data. The specific objectives were to determine the performance of an aerodynamic spike nozzle as a function of nozzle pressure ratio, secondary gas flowrate, and secondary gas energy level. A secondary objective was the determination of nozzle base thermal environment.

(C) A 12 percent length truncated ideal spike nozzle thrust chamber with an area ratio of 25 was constructed and tested at Rocketdyne Propulsion Field Laboratory at near sea level conditions and at varying altitude conditions at the Rocket Test Facility (J-2 cell) of Arnold Engineering Development Center. The thrust chamber utilized N_2O_4/UDMH-N_2H_4(50-50) propellants and generated approximately 7400 pounds thrust at design pressure ratio. A gas generator utilizing the same propellants supplied secondary flowrates from 0 to 5 percent of the primary flowrate to the nozzle base region.

(U) Ten sea level firings and 20 altitude firings were accomplished. The basic program objective of supplying a large quantity of aerospike nozzle parametric data was successfully accomplished.

HARDWARE DESCRIPTION

(U) Two water cooled thrust chambers and one uncooled thrust chamber were constructed for this test program. The water cooled chambers were used for obtaining aerospike performance data in relatively long (to 8 seconds) duration firings. A geometrically identical (except for a shorter nozzle length) uncooled thrust chamber with a firing duration of approximately 0.8 seconds was used for injector evaluation and establishment of test procedures. Both chamber types are of nonflightweight construction.

Water Cooled Thrust Chamber Assembly

(U) The water cooled thrust chamber assembly (TCA) is shown in Figs. 6, 7 and 8. It is equipped with an aerospike nozzle having a geometric area ratio of approximately 25 (defined as the ratio of the area enclosed by d_e in Fig. 6 to the measured throat area). The nozzle length from the throat to the exit plane is 12 percent of the length of a 15 degree conical nozzle having the same area ratio and throat. Base area (defined by d_b in Fig. 6) and design throat area of the nozzle are 167.5 $in.^2$ and 14.9 $in.^2$, respectively.

(U) The TCA is composed of an annular injector, inner and outer combustion chamber casing sections, inner and outer nozzle throat sections, and a nozzle base plate (Fig. 6) which attaches to the inner throat section to enclose the nozzle base region. A gas generator (GG) for introducing secondary gas flow into the base region is attached to the upstream side of the base plate. Overall length, diameter, and weight of the TCA (with GG attached) are approximately 17 in., 34 in., and 2500 lb_m, respectively. Thrust of the TCA at the design nozzle pressure ratio (PR) of 300 is 7400 lb_f. Nominal test duration and combustion chamber pressure are 7 to 8 seconds and 300 psia, respectively.

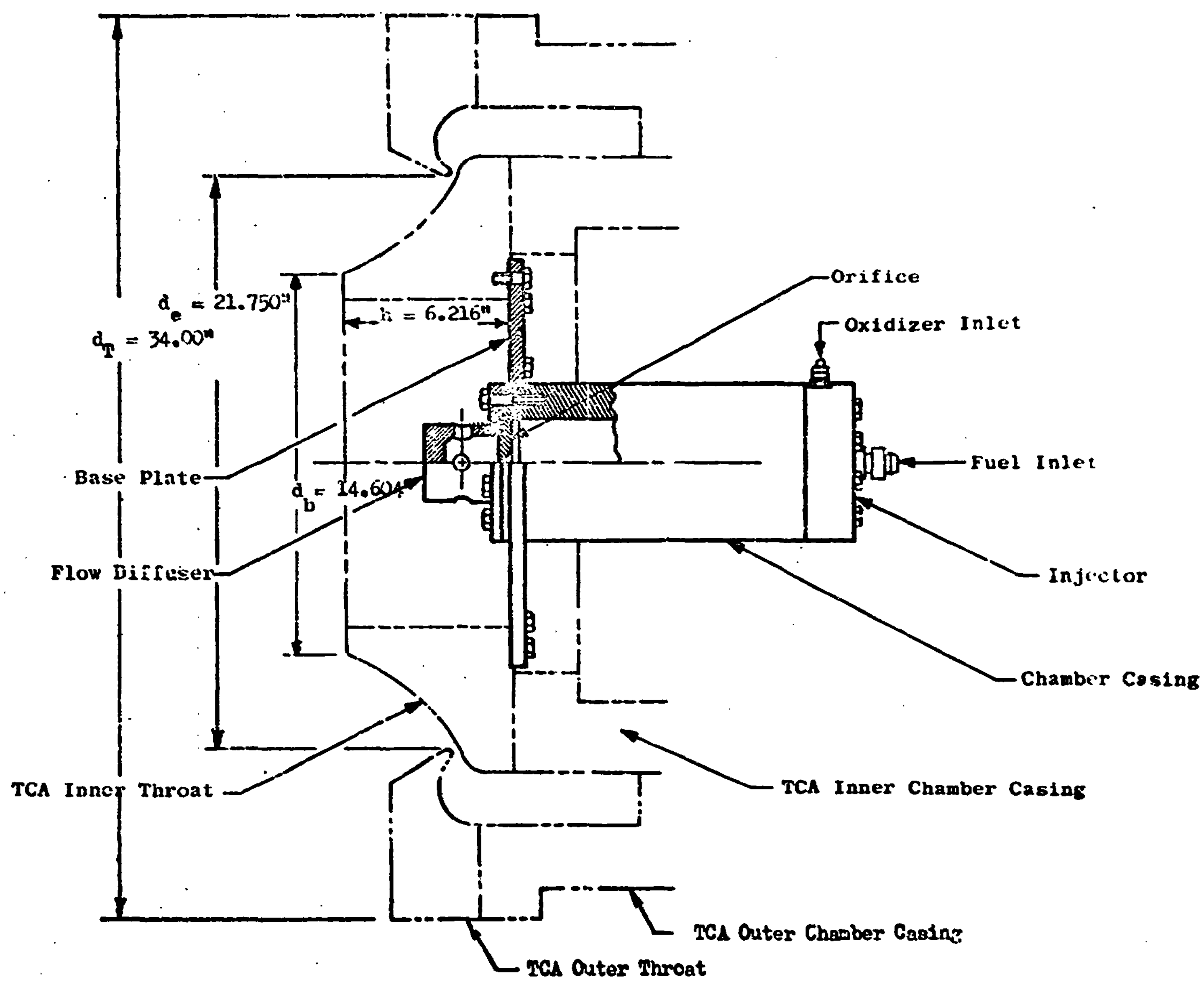

c. Nozzle Base Plate and Gas Generator Assembly

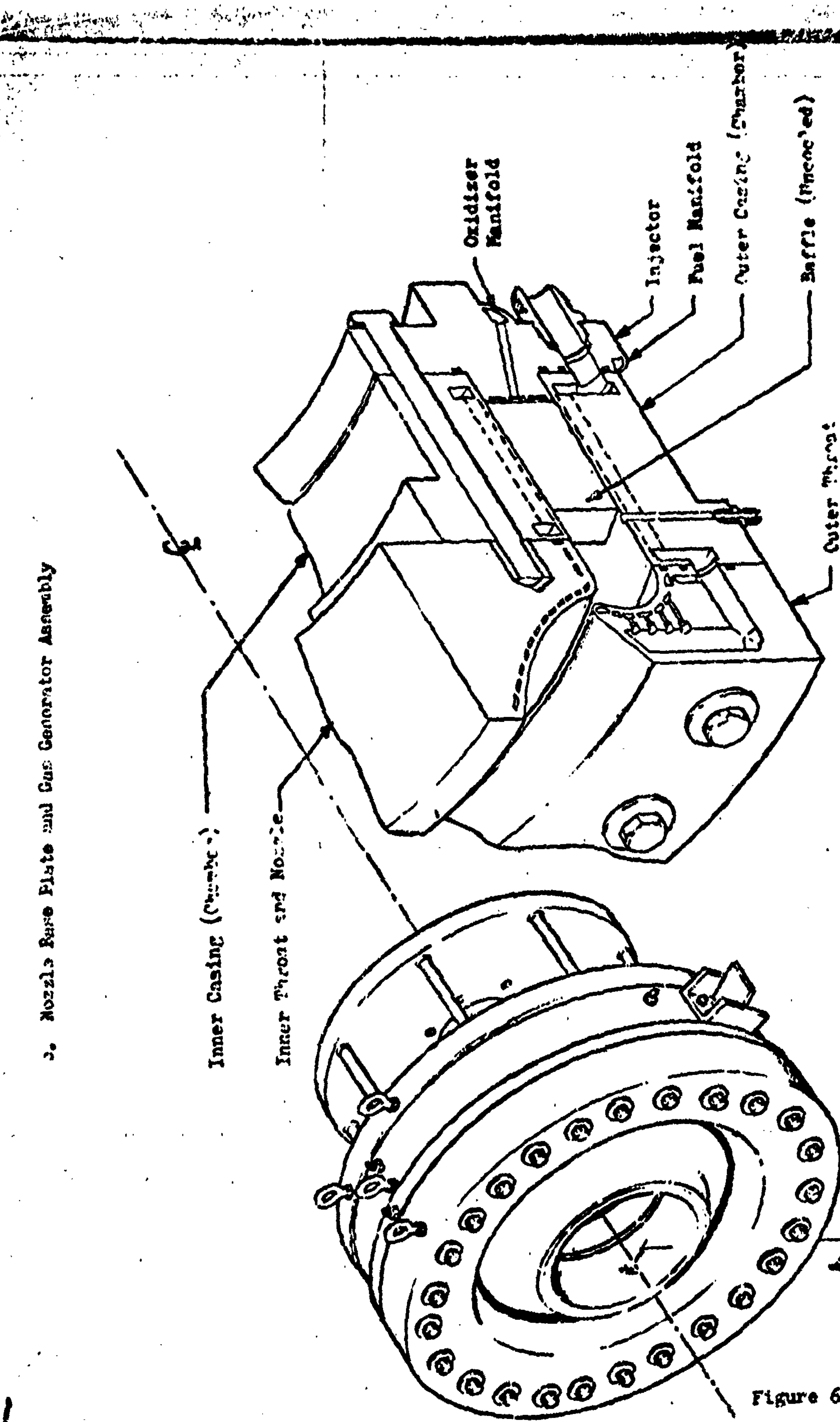

Figure 6. Water Cooled Aerospike Thrust Chamber

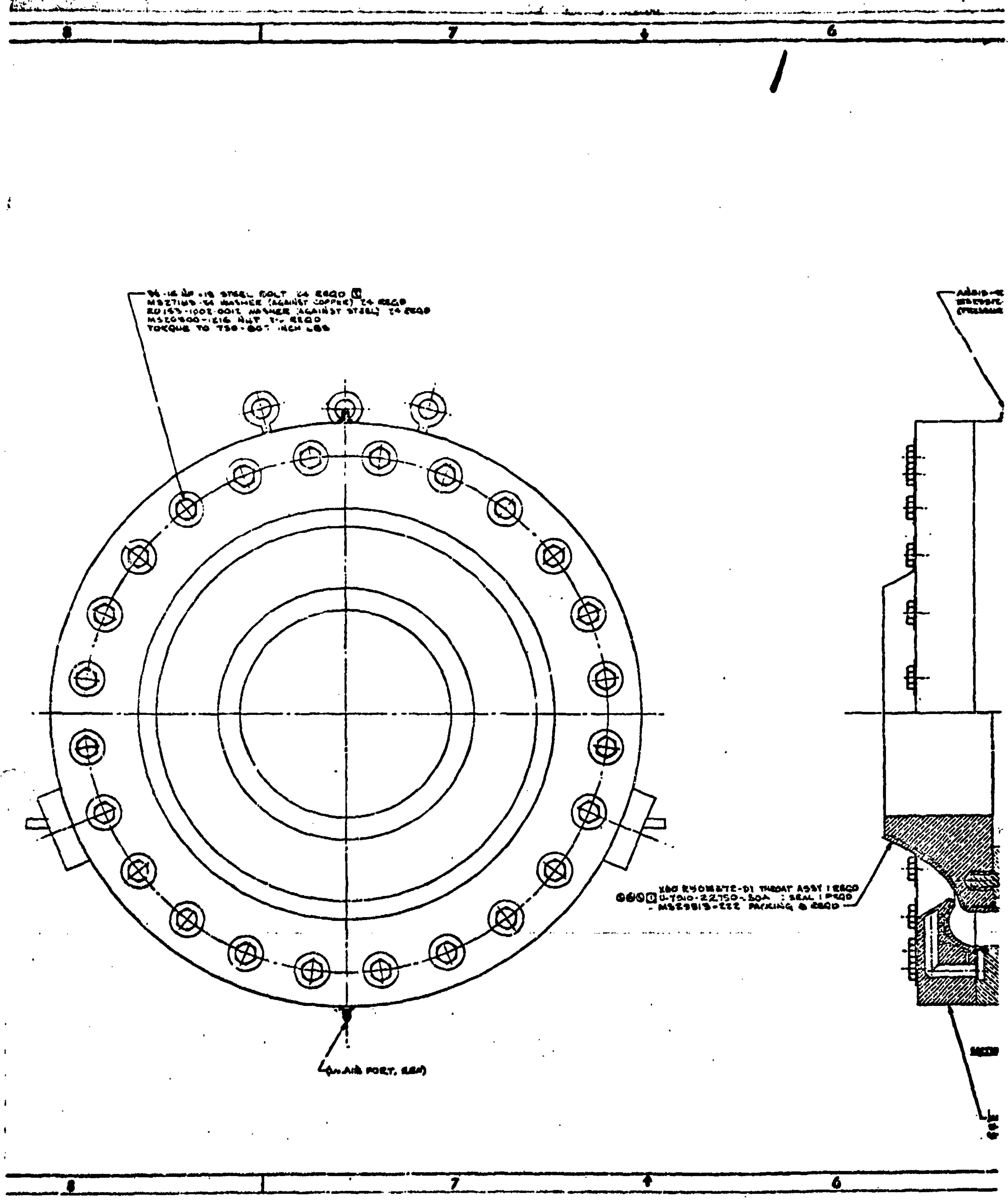
8
7
6
MS20900-1216 NUT 24 REQD
U-7310-22750-30A : SEAL 1 REQD
PACKING
AIR PORT, REF

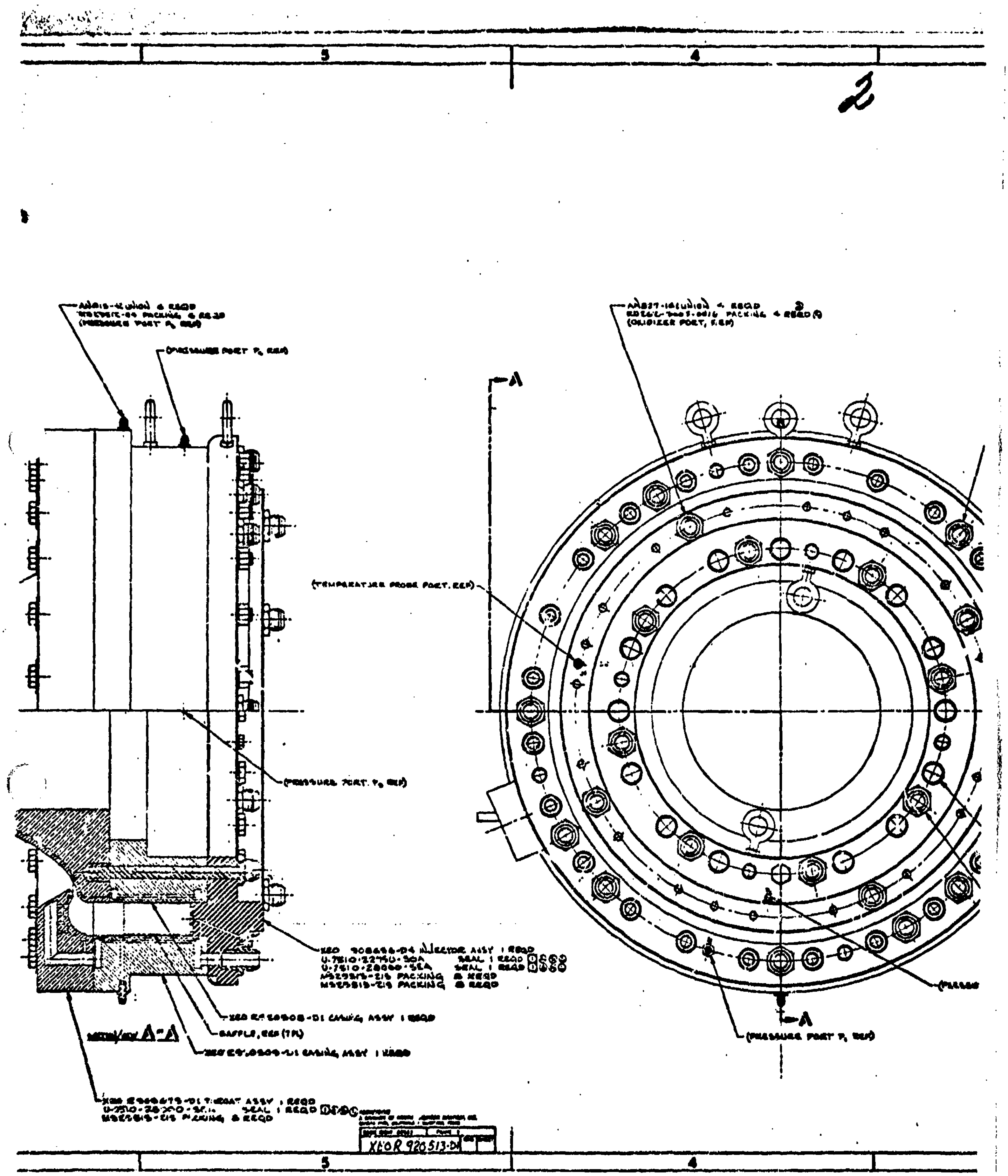
5
4
2
(TEMPERATURE PROBE PORT, REF)
XLOR 920513-D4
5
4

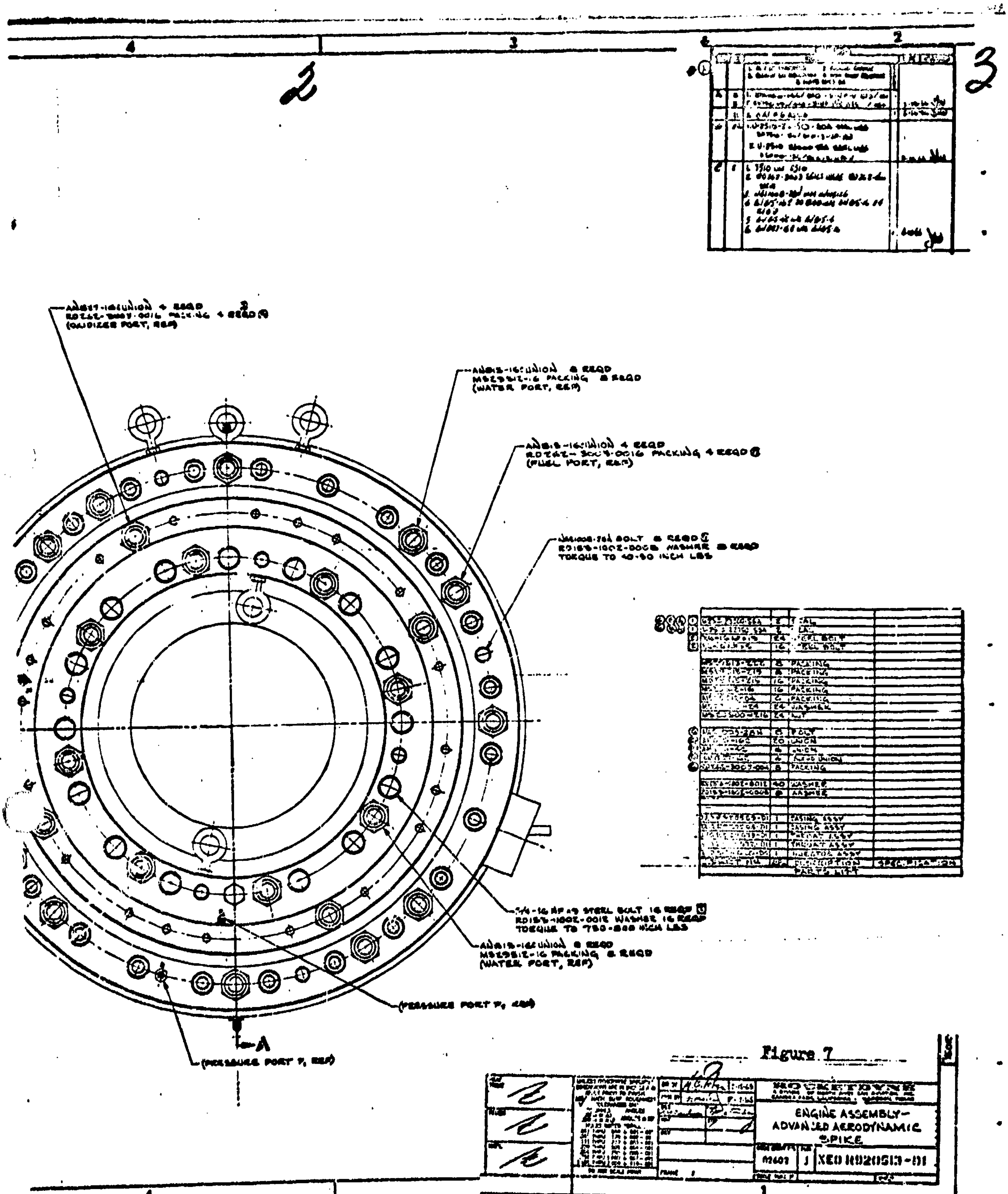

(WATER PORT, REF)
(FUEL PORT, REF)
TORQUE TO 40-50 INCH LBS
(PRESSURE PORT P, REF)
A
DESCRIPTION
PARTS LIST
ENGINE ASSEMBLY—
ADVANCED AERODYNAMIC
SPIKE

Figure 7

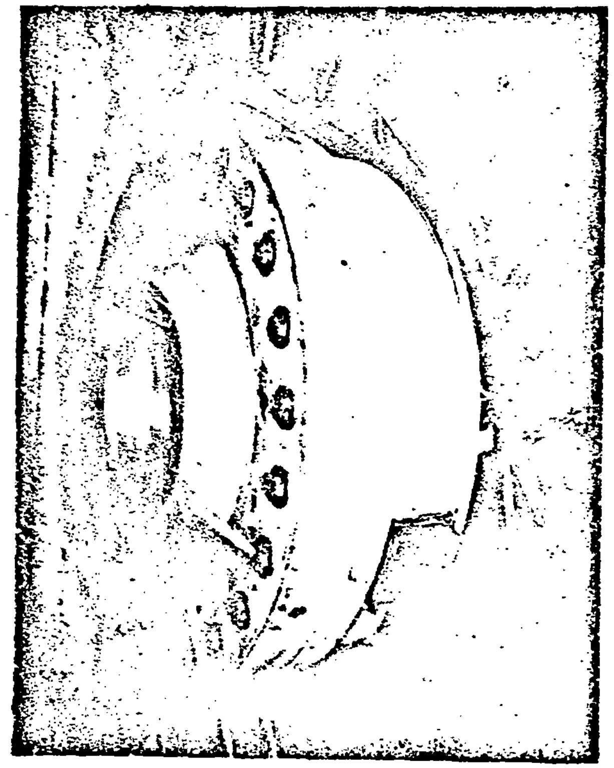

a. Closeup View

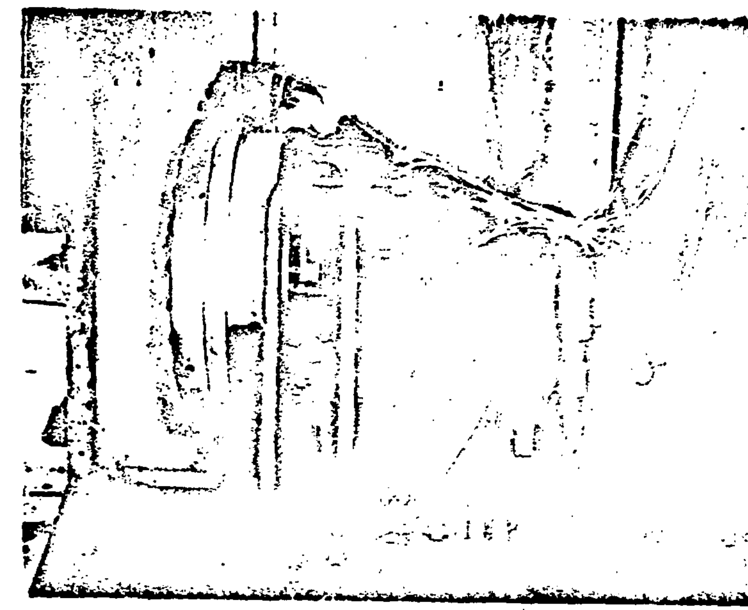

b. Side View

Figure 6 . Water Cooled Thrust Chamber Installation at Rocketdyne
(Sugar Stand, Propulsion Research Area)

(C) The TCA utilized the two hypergolic propellants, nitrogen tetroxide (N_2O_4) and an equal gravimetric mixture of hydrazine (N_2H_4) and unsymmetrical dimethylhydrazine ($N_2H_2\,[CH_3]_2$). Required total propellant flow rate is approximately 27 lb_m/sec at a nominal mixture ratio (O/F) of 1.8. Design total flow rate range of the GG is from 1 to 5 percent of the TCA flow rate. Operating pressure of the GG, using the same propellants as the TCA at a nominal mixture ratio of 0.1, is from 100 to 400 psia, depending on the flowrate.

Injector

(U) The TCA injector is constructed from type 347 stainless steel with stainless steel oxidizer and copper fuel ring inserts brazed into slots in the injector face. Three injector configurations were tested before satisfactory combustion stability was achieved.

(U) Injector No. 1 (Fig. 9a) had an annular three ring self-impinging doublet injection pattern. The outer and inner rings were for fuel injection and each contained 119 elements with orifice diameters of 0.025 in. All fuel fans were oriented in a position parallel to the adjacent chamber or baffle walls were thus oriented parallel to a radial line. Each fuel element was offset from the fuel rings centerline radius a distance of ± 0.025 in. in an alternating plus or minus manner. This prevented fan edge interference of adjacent fuel elements.

(U) The oxidizer ring (center ring) consisted of 210 elements with orifice diameters of 0.031 in. All fans were oriented at a 75 degree angle with a radial line to prevent fan interference of adjacent oxidizer elements. The spacing between rings was nominally 0.544 in. The injector was divided into seven equal peripheral segments by two-inch thick baffles brazed to its face. A section of the injector face near a baffle is shown in Fig. 9c. A detailed drawing of the injector is shown in Fig. 10.

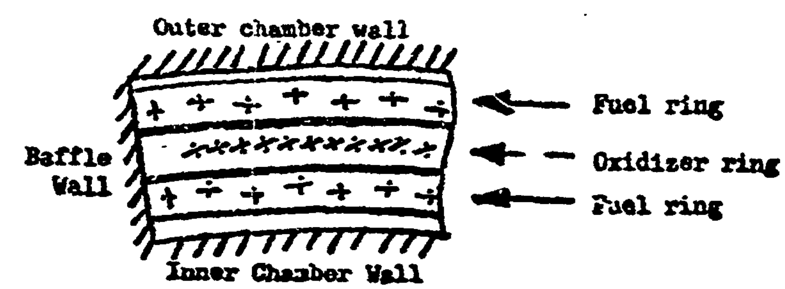

c. Hole Pattern

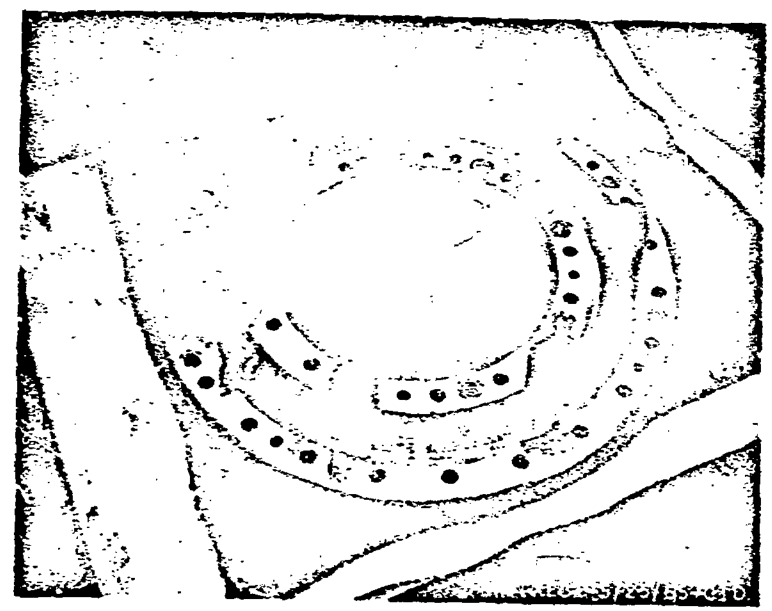

a. Injector Number 1

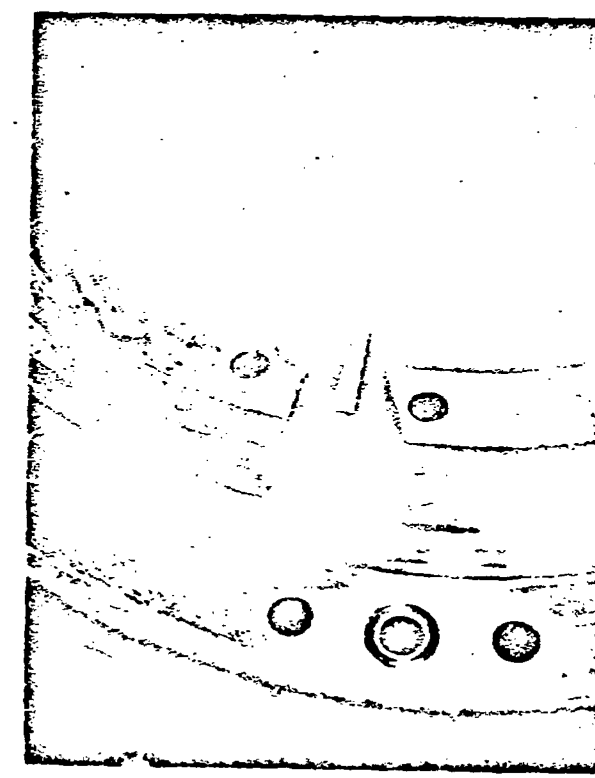

b. Injector Number 1A

Figure 9 Injector Configuration

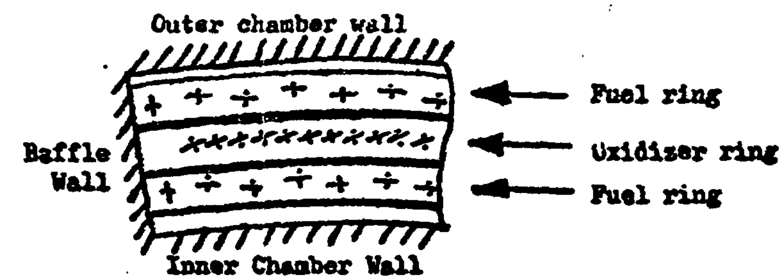

c. Hole Pattern

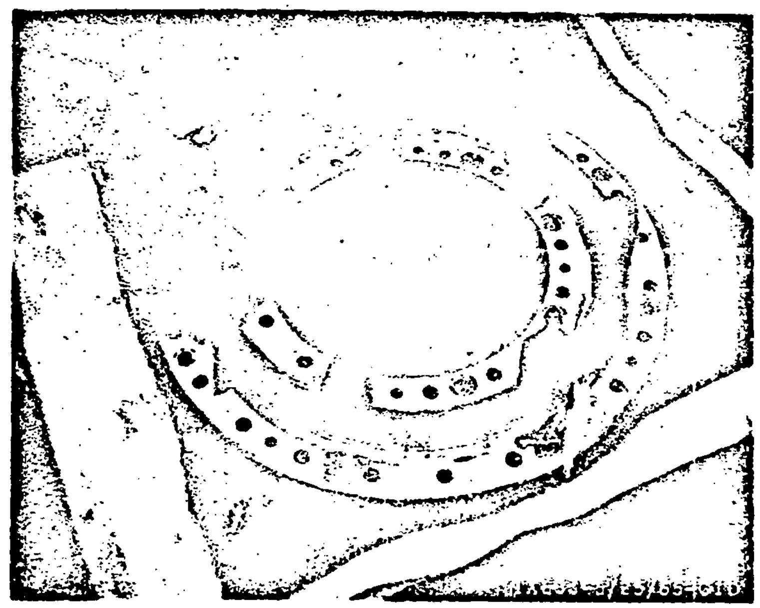

a. Injector Number 1

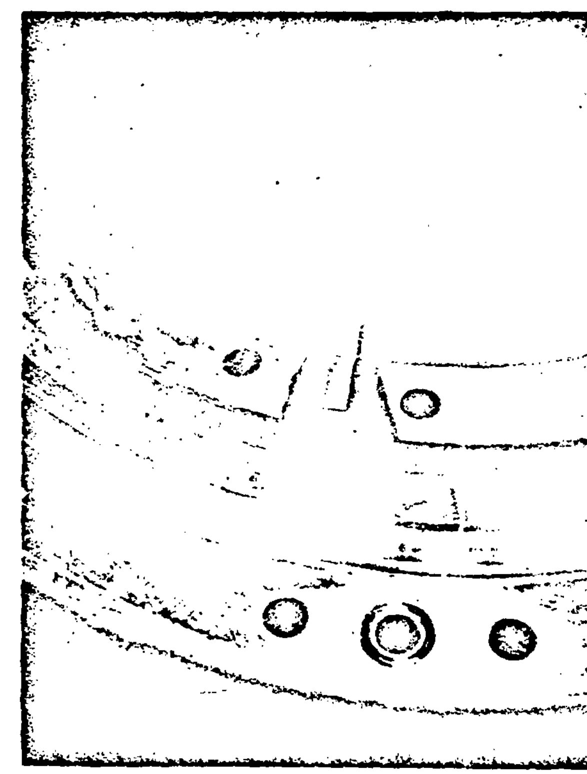

b. Injector Number 1A

Figure 9 Injector Configuration

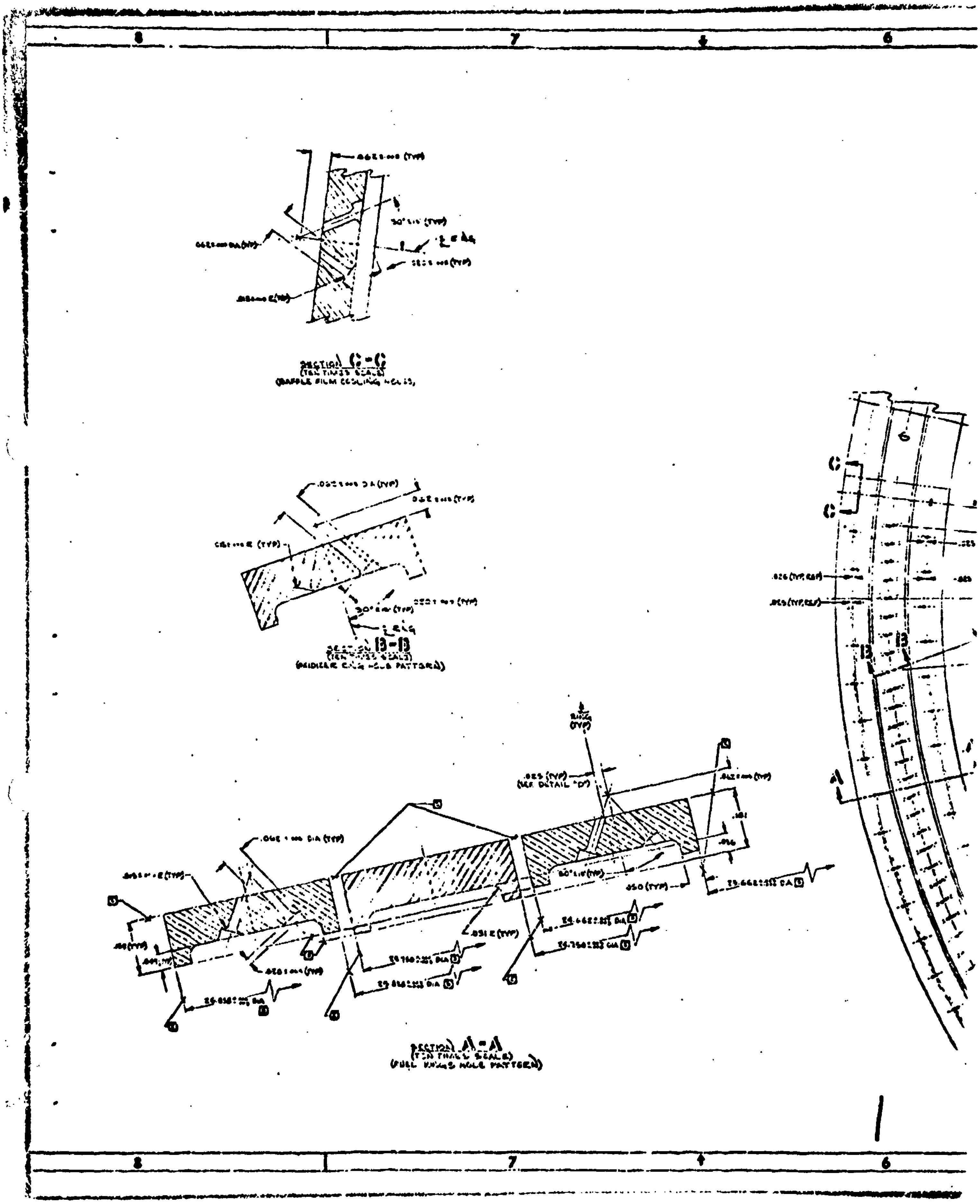
8
7
6
SECTION C-C
(TEN TIMES SCALE)
(BAFFLE FILM COOLING HOLES)
SECTION B-B
(TEN TIMES SCALE)
SECTION A-A
(TEN TIMES SCALE)
30° (TYP)
.050 (TYP)
.031 E (TYP)
.025 (TYP)
(SEE DETAIL "D")
C
B
A

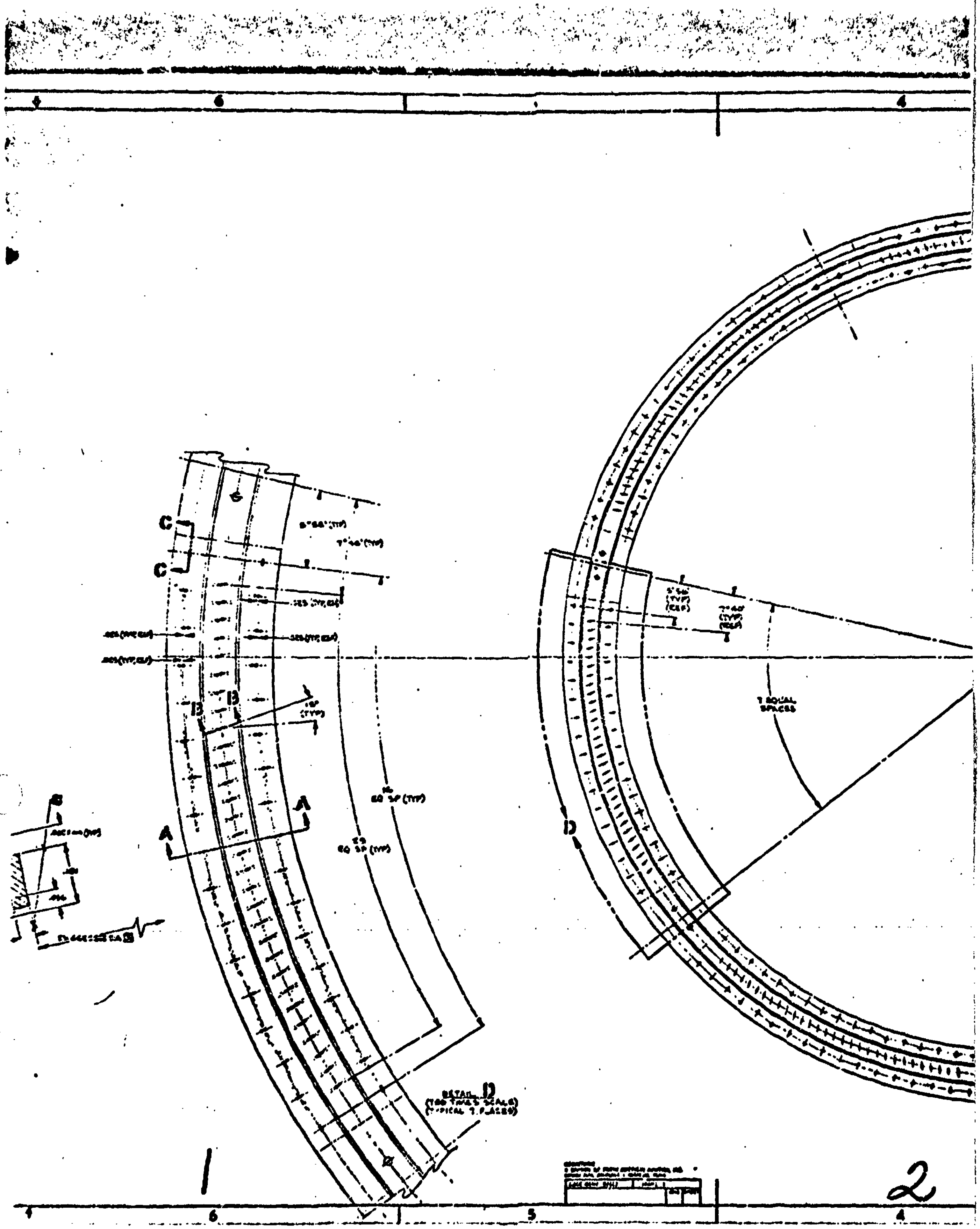
C
C
B
B
A
A
D
7 EQUAL SPACES
DETAIL D
(TWO TIMES SCALE)
(TYPICAL 7 PLACES)
1
2

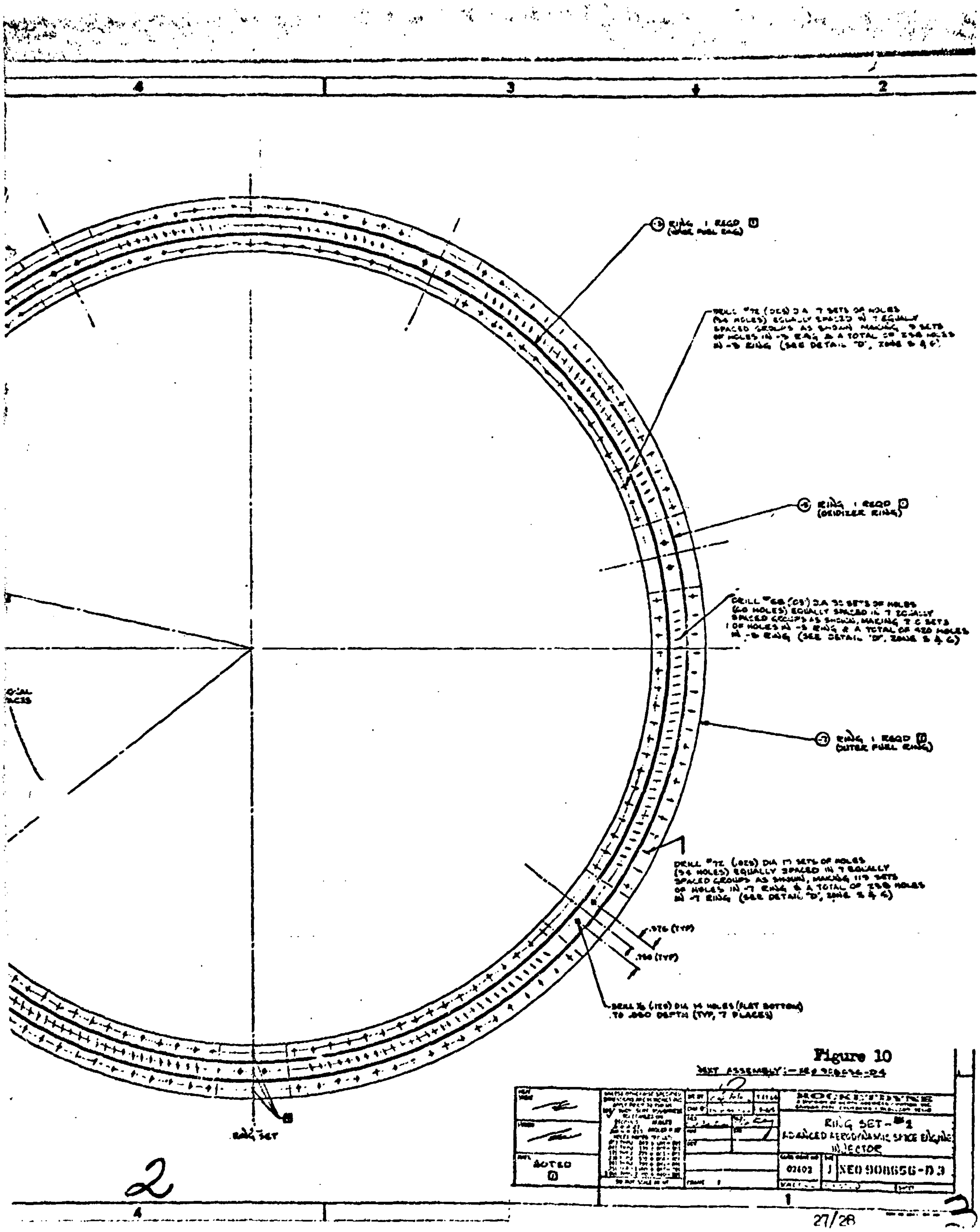

RING 1 REQD
(OXIDIZER RING)
RING 1 REQD
(OUTER FUEL RING)
DRILL #68 (.031) DIA 30 SETS OF HOLES (60 HOLES) EQUALLY SPACED IN 7 EQUALLY SPACED GROUPS AS SHOWN, MAKING 210 SETS OF HOLES IN -5 RING & A TOTAL OF 420 HOLES IN -5 RING (SEE DETAIL "D", ZONE 5 & 6)
DRILL #72 (.025) DIA 17 SETS OF HOLES (34 HOLES) EQUALLY SPACED IN 7 EQUALLY SPACED GROUPS AS SHOWN, MAKING 119 SETS OF HOLES IN -7 RING & A TOTAL OF 238 HOLES IN -7 RING (SEE DETAIL "D", ZONE 5 & 6)
.376 (TYP)
.350 (TYP)
.TO .060 DEPTH (TYP, 7 PLACES)
RING SET
NEXT ASSEMBLY
ROCKETDYNE
RING SET - #1
ADVANCED AERODYNAMIC SPIKE ENGINE INJECTOR
02602
J
XE0 908656-D3
NOTED
4
3
2
1

Figure 10

(U) Injector number 1 was subsequently modified to injector number 1A (Fig. 9b) in an effort to eliminate high frequency combustion instability. The modification consisted of tapering and reducing the length of the baffles from 4 inches to 3 inches. In addition, the fuel elements adjacent to the baffles were brazed shut. This injector exhibited an unsatisfactory low frequency instability.

(U) The injector pattern was redesigned and satisfactory operation was achieved with injector number 2 (Figs. 11 and 12). This injector was used for all water cooled hardware tests. Injector number 2 is divided into thirteen equal compartments by uncooled OFHC copper baffles (4 inches in length by $1\frac{1}{2}$ X 2 inches in cross section) brazed to the injector face. The baffles are the only part of the engine assembly which run uncooled, and thus are the limiting factor on test duration. They were designed for 10 seconds duration at 500 psia chamber pressure.

(U) The injector pattern (Fig. 12) consists of 208 pairs of like-on-like doublet elements. There are 16 element pairs in each of the 13 baffle compartments. Oxidizer and fuel orifices are 0.031 and 0.026 in. diameter, respectively. All fuel elements are canted 20 degrees toward the central oxidizer ring. Each fuel ring contains a single row of eight doublet elements per compartment. Oxidizer elements are directed perpendicular to the injector face and there are two rows of eight doublet elements per compartment in the single ring. The propellant jet impingement point is 0.150 in. from the injector face for all elements. The spacing between fuel and oxidizer fans in an element pair is set at 0.040 in. Injector elements are equally spaced on the inner fuel ring only. However, the pattern is symmetrical about a radial line through the center of the baffled compartment.

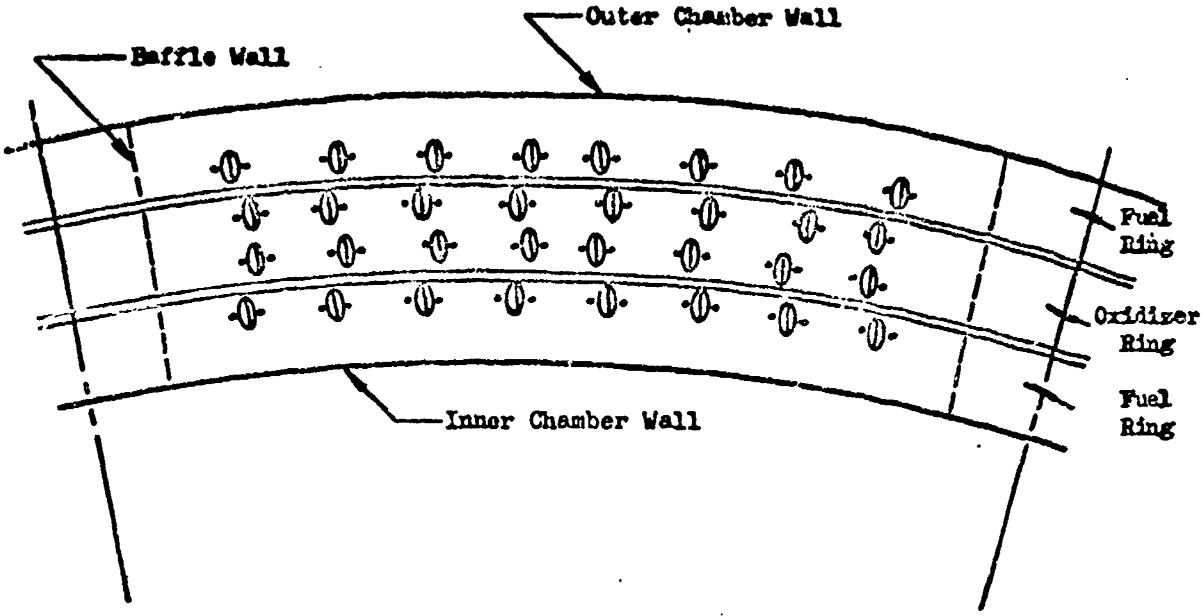

b. Injector Number 2 Pattern

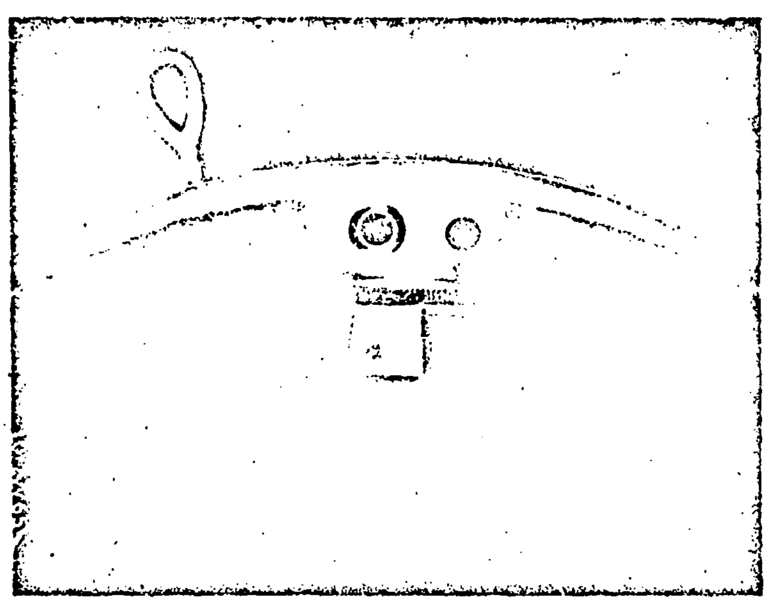

a. Injector Number 2 Assembly

Figure 11. Injector Number 2

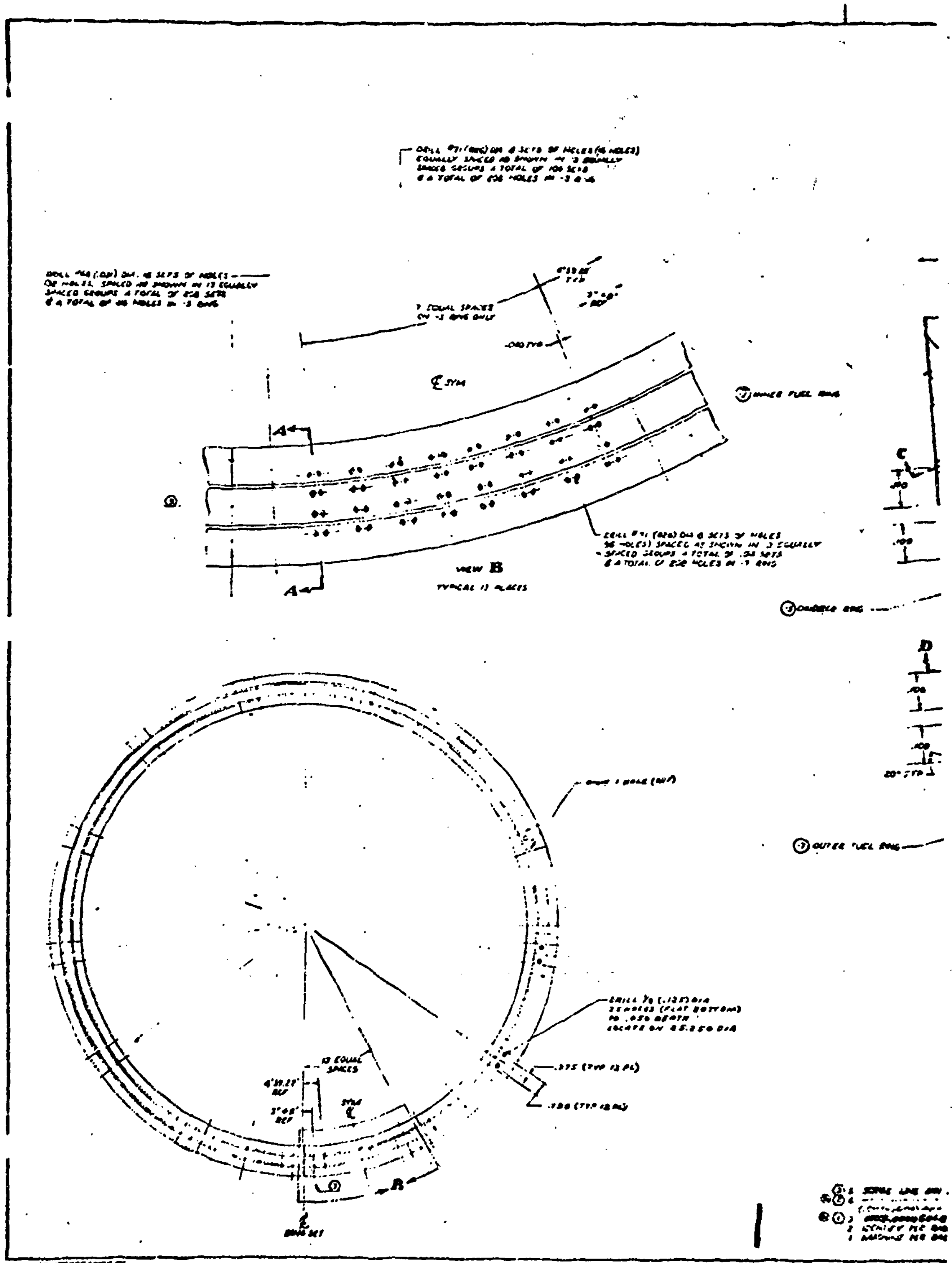

.020 TYP
VIEW B
TYPICAL 12 PLACES
A
A
B
INNER FUEL RING
OUTER FUEL RING
12 EQUAL SPACES

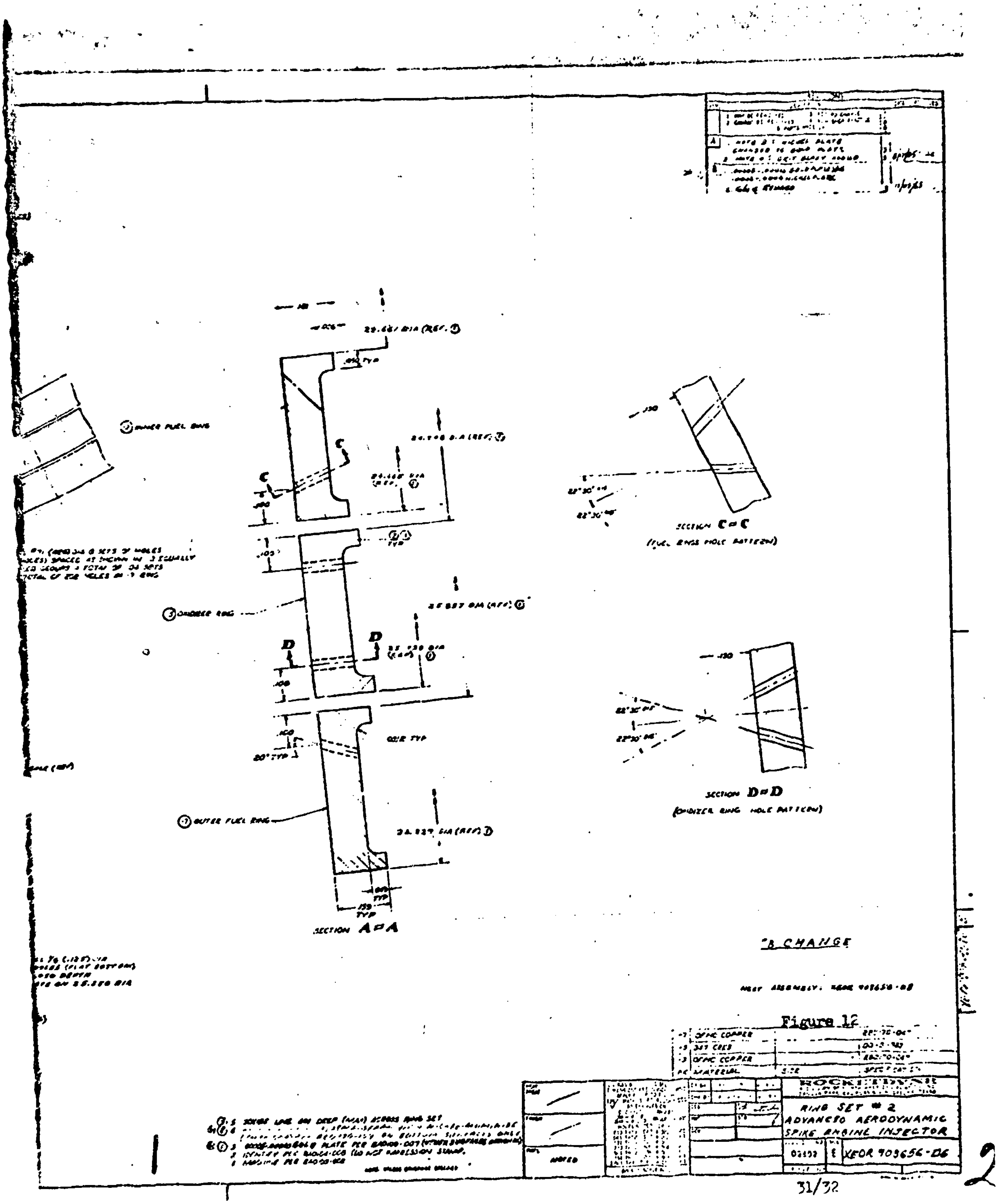
SECTION A-A
SECTION C-C
(FUEL RING HOLE PATTERN)
SECTION D-D
(OXIDIZER RING HOLE PATTERN)
B CHANGE
ROCKETDYNE
RING SET # 2
ADVANCED AERODYNAMIC
SPIKE ENGINE INJECTOR
OFHC COPPER
347 CRES
MATERIAL

Figure 12

Combustion Chamber Assembly

(U) The inner and outer throat and casing sections (Fig. 6) are fabricated from OFHC copper. The sections bolt to the injector to form an annular combustion chamber with an inner diameter of 23.2 in., an outer diameter of 27.3 in., and a length of approximately 7.3 in. Leakage of gas from the chamber is prevented by the use of single O-ring seals at each section-to-section or injector-to-section interface. Cooling of the combustion chamber walls is accomplished by flowing water through 5/16 inch diameter axial water passages (88 and 112 passages in the inner and outer sections, respectively) in the gas side walls. Eight isolated internal manifolds are located fore and aft of each casing. Water is supplied to and returned from the casings through sixteen feed holes in the injector body. The combustion chamber gas side walls are gold-plated to prevent erosion of the copper.

Throat Assembly

(U) The inner and outer throat sections are so constructed (with OFHC copper) that, when these sections are properly attached to the remainder of the TCA, an annular throat, having a mean diameter and nominal gap of 22.1 and 0.215 in., respectively, is formed (Fig.6). The inner side of the outer throat section has a contour immediately downstream of the throat with sufficient divergency (30 degrees) to ensure flow separation and thereby free expansion of the outer exhaust plume boundary at the nominal operating pressure ratio (PR) range of the nozzle.

(U) Cooling of the inner and outer throat sections was accomplished by flowing water through a series of continuous circumferential coolant slots (fourteen and seven slots on the inner and outer throats, respectively) located 0.15 to 0.25 in. from the gas side surface. Water from the casings enters each throat section (inner and outer) through four manifolds. Each

manifold contains a set of drilled holes leading into the circumferential coolant slots. Water flows through the slots in each circumferential direction from the inlet holes over an arc of 45 degrees to the adjacent outlets. The flow returns through four (in each throat section) main throat outlets, the casing, and injector ports. Flow distribution in the throats is accomplished by varying the sizes of holes feeding each slot, directing the majority of the coolant water into the critical areas. The cooling circuit is symmetrical so that the casings and throats may be rotated relative to each other and to the injector without affecting the intended flow distribution. Gas side walls of the inner and outer nozzle throat sections are also gold-plated to minimize hot-gas erosion.

Gas Generator

(C) The gas generator (Fig. 13) was constructed entirely of type 347 stainless steel and consisted of two interchangeable injectors, a single combustion chamber casing, an internal flow mixer and two interchangeable throat orifices. One injector and a matching orifice (low-flow GG) were used for firings requiring secondary flow from 0 to 3 percent of primary flow; the other injector-orifice combination (high-flow GG) was used for firings requiring 3 to 5 percent secondary flow. The injector orifices were sized for these percentages of a primary flowrate of 41.6 lbs/sec (P_c = 500 psia). However, actual primary flowrate was nominally 27 lbs/sec (P_c = 300 psia) for the majority of the tests. The correspondingly derated flow conditions for the gas generator did not noticeably affect combustion efficiency of the high flowrate system. However, the combustion efficiency of the low flowrate gas generator was 10 to 20 percent lower with the reduced flow.

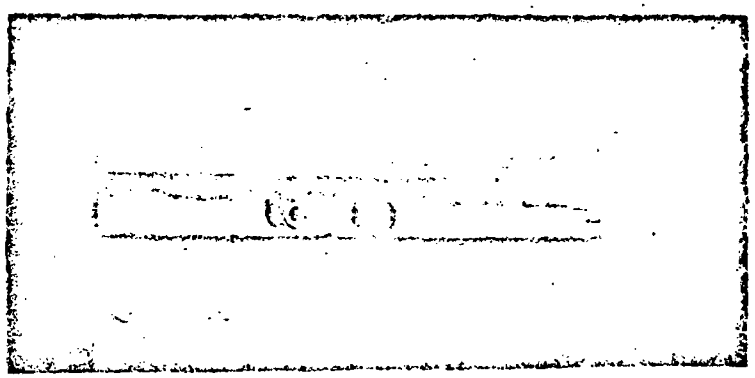

a. Gas Generator Body

b. High Flowrate Injector

Figure 13. Gas Generator Assembly

(U) The injector pattern of both injectors provides four fuel streams impinging on one central oxidizer stream. Both injectors contained five pentad elements. To insure good mixing and combustion a high chamber L* (L* = 150 to 450 inches depending on the flow control orifice used) and an internal flow deflector were used.

(U) The GG sections were bolted to the base plate with the diffuser and orifice downstream side of the plate and the chamber section and injector on the upstream side (Fig. 6). The GG was pressure fed and required oxidizer and fuel supply systems separate from the TCA systems. Operation of the uncooled GG at relatively low mixture ratios (O/F = 0.1) prevented the metal surfaces from exceeding their design temperature of 1800 degrees F.

Base Configurations

(U) Two base configurations were employed for injection of secondary flow. A hat shaped diffuser (Fig. 14) constructed of 347 stainless steel was used for all tests except the last three (AD test series at AEDC). Four ¾ inch holes diffused the GG flow (secondary flow) radially outward into the base cavity.

(U) Prior to the last test series this diffuser was modified by plugging the ¾ inch holes and replacing them with twenty-eight ¼ inch radial holes. The modified diffuser was installed along with the perforated base plate for the AD test series. A perforated base plate was fabricated and bolted to the nozzle exit face for use in the AD test series. The base plate was constructed of ½ inch 347 stainless steel and contained 578 holes of 3/32 inch diameter. An extensive series of steady state tests at AEDC with the perforated plate and the modified flow diffuser were planned. However, operational difficulties and hardware damage prevented the obtaining of satisfactory data with either of the later base configurations.

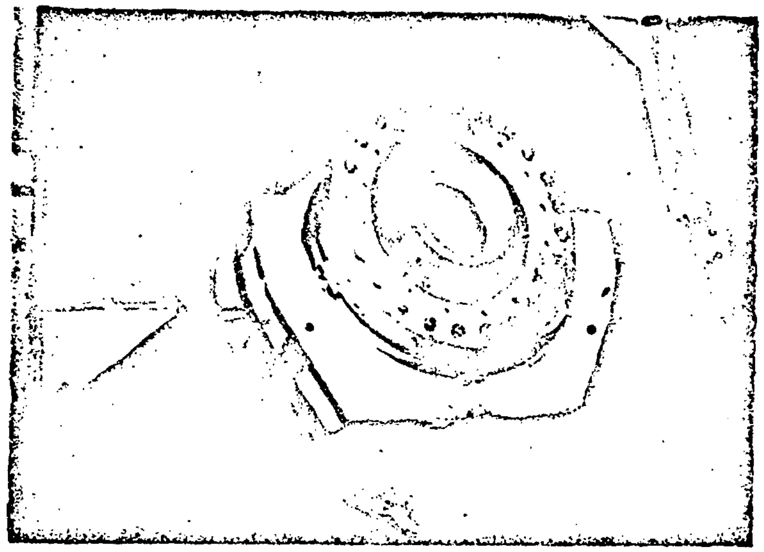

a. Flow Diffuser- Radial Outward

b. Perforated Base Plate Assembly

Figure 14. Base Configurations Installed on the 12 Percent Length Aerospike

Uncooled Thrust Chamber Assembly

(U) A solid wall, uncooled thrust chamber (Fig. 15) was used for evaluation of injector performance and checkout of operational procedures. The uncooled chamber is dimensionally identical to the water cooled configuration with the exception that the nozzle length was eight percent instead of twelve percent and the base diameter was therefore larger (base area of 201 in^2). The chamber casings are constructed of 347 stainless steel and the nozzle sections are constructed of OFHC copper. The inner nozzle was plated with a thin dense chrome coating. The thrust chamber is capable of approximately 0.8 second firing durations at 500 psia chamber pressure. A base plate and gas generator were mounted to the inner nozzle in a manner similar to that employed with the water-cooled thrust chamber.

Fluid Systems

(U) Fluid fittings provided on the thrust chamber assembly consist of four primary fuel inlets, four primary oxidizer inlets, one secondary oxidizer inlet, one secondary fuel inlet, eight water inlets (four for the annulus and four for the outer annulus) and eight water outlets. The fitting locations and the fluid flow paths are illustrated schematically in Fig. 16 .

TEST INSTALLATION

(U) Thirty-three gas generator tests, ten uncooled thrust chamber tests and ten water cooled thrust chamber tests were conducted at Rocketdyne sea level facilities. Twenty water cooled thrust chamber firings were accomplished at the altitude facility (Rocket Test Facility, J-2 Cell) of Arnold Engineering Development Center (AEDC).

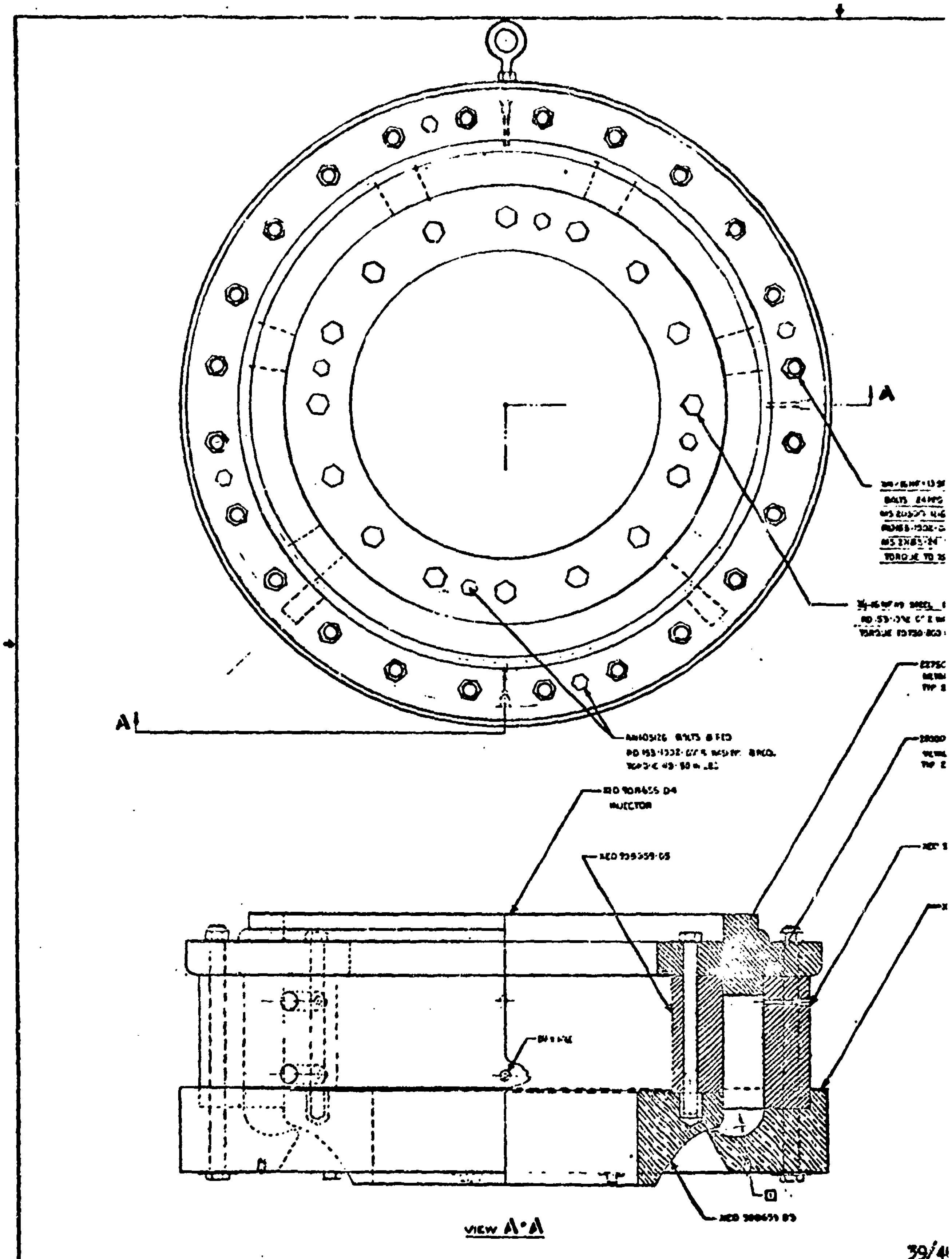
A
A
VIEW A•A

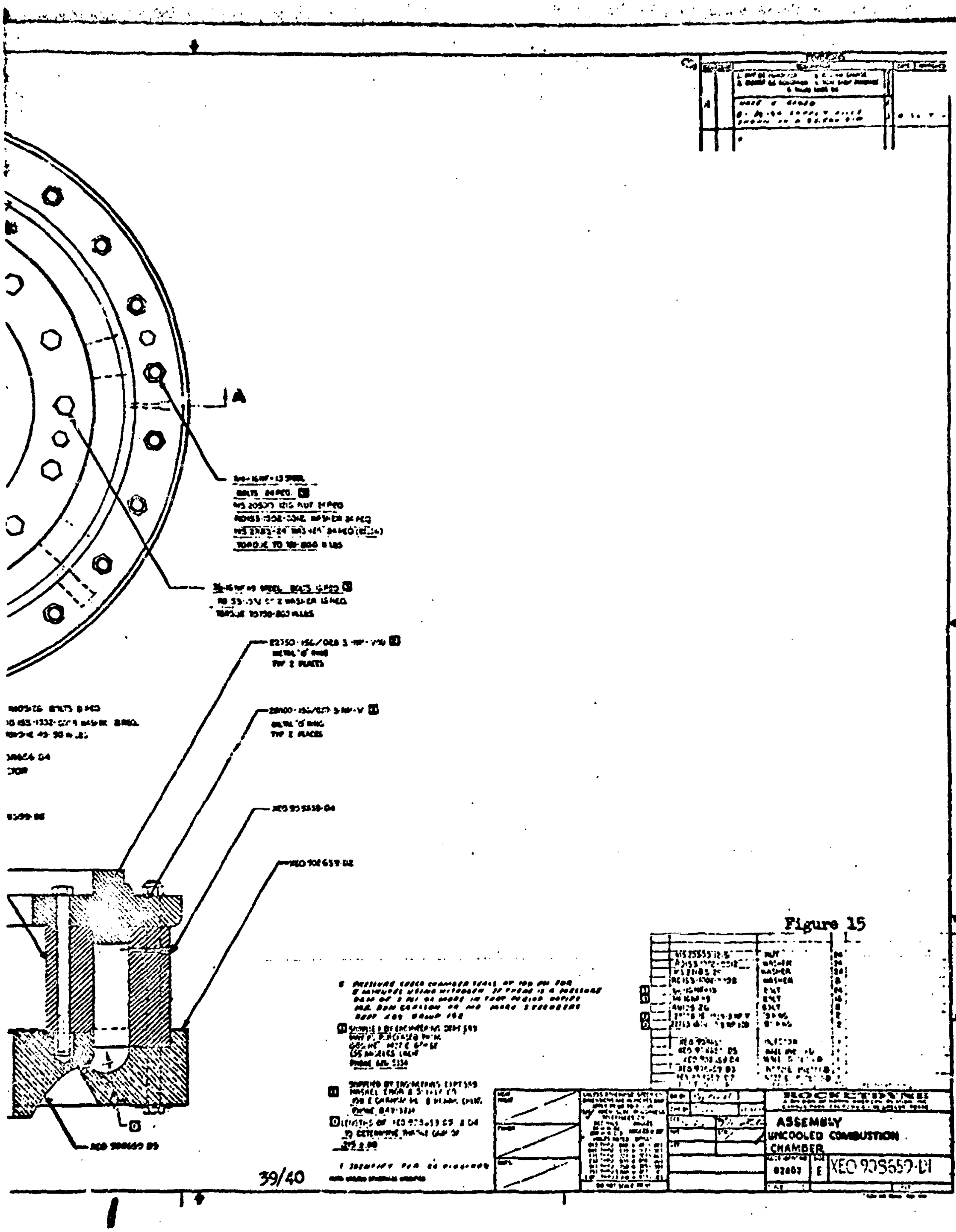

Figure 15

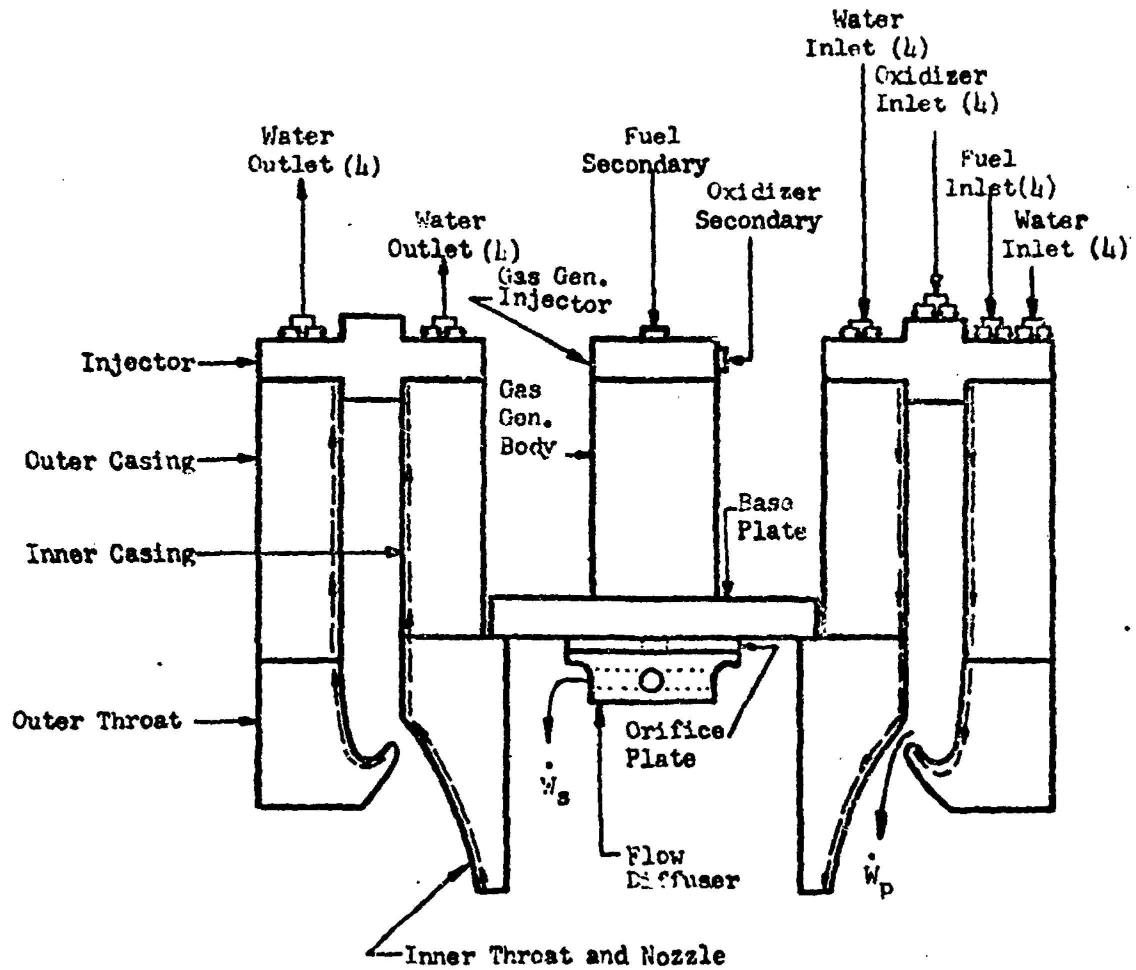

Figure 16. Hot-Firing Aerospike Engine Flows.

Sea Level Test Installation

(U) Sea level tests with the GG and with the uncooled and water cooled TCA's were conducted on Sugar Stand at the Propulsion Research Area of the Santa Susana Field Laboratory. The horizontal firing thrust structure (Fig. 17) was newly constructed for this test program. The engine assembly attaches to the main support pylon which is attached by axial and yaw flexures to the main support stand. The aft section of the engine is supported by structure having only axial flexures.

(U) The propellant system (Fig. 18) included a 300-gal primary fuel tank, a 200-gal primary oxidizer tank, 43-gal secondary fuel and oxidizer tanks, a gaseous nitrogen pressurization system, and the required valves and fittings. Gaseous nitrogen systems were also provided for system purging and secondary propellant and water valve actuation. A hydraulic system was utilized for primary propellant valve actuation. Coolant water was supplied from a nitrogen pressurized 800-gal tank. Control of both propellant and coolant water flow was obtained by the use of automatic preset pressure regulators in the tank pressurization systems.

Altitude Test Installation (AEDC)

(U) Propulsion Engine Test Cell (J-2) (Fig. 19 and 20 and Ref. 25) is a water-jacketed test cell, 20 ft. in diameter, used for captive horizontal testing of propulsion systems at pressure altitude conditions. J-2 is capable of producing constant pressure altitudes in excess of 100,000 ft. by the use of parallel primary and secondary steam ejector-diffusers operating in series with the RTF facility exhausters. However, for this test program, nozzle pressure ratio transients (hence test cell pressure transients) were obtained by essentially isolating the test cell and

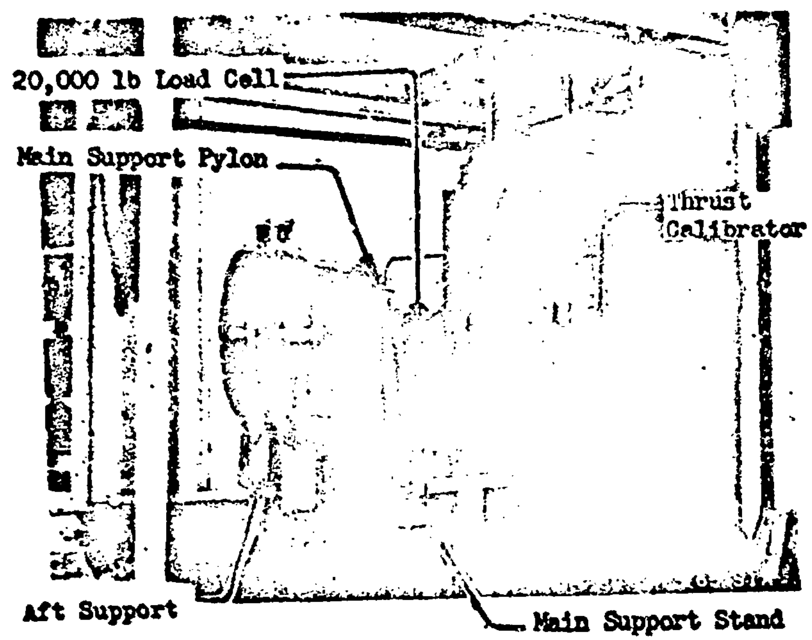

a. Installation

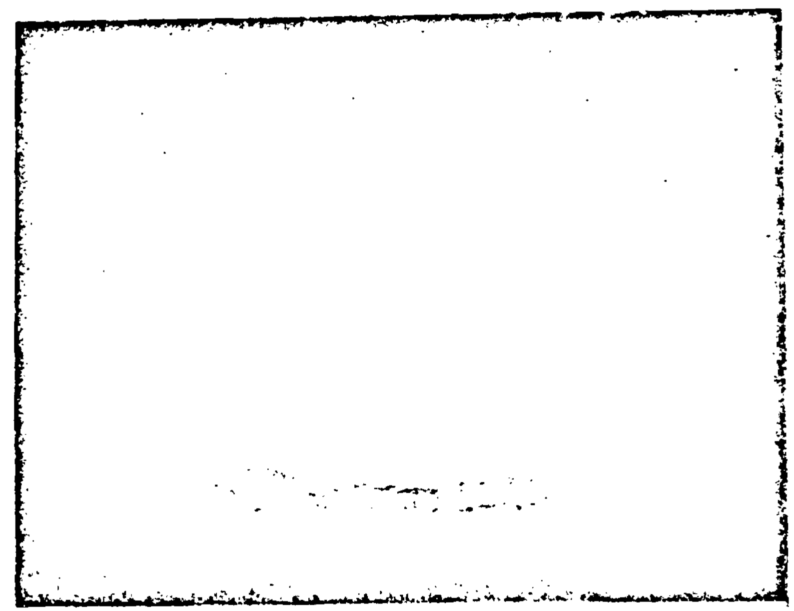

b. Firing

Figure 17. Uncooled Thrust Chamber Installation and Firing on Sugar Stand
(Propulsion Research Area, Santa Susana Field Laboratory)

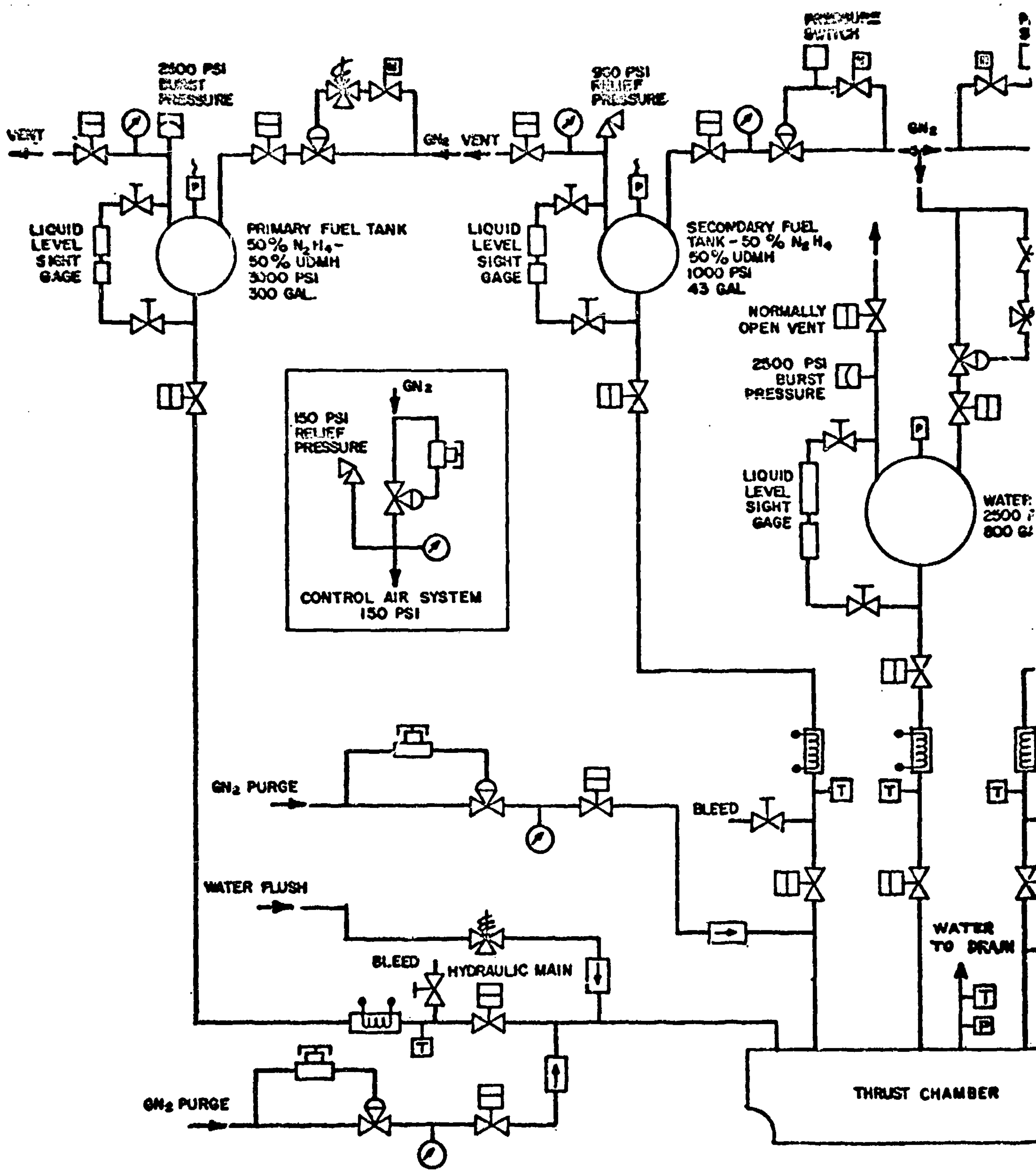

2500 PSI
BURST
PRESSURE
VENT
GN2 VENT
950 PSI
RELIEF
PRESSURE
PRESSURE
SWITCH
GN2
LIQUID
LEVEL
SIGHT
GAGE
PRIMARY FUEL TANK
50% N2H4-
50% UDMH
3000 PSI
300 GAL.
SECONDARY FUEL
TANK - 50 % N2H4
50% UDMH
1000 PSI
43 GAL.
NORMALLY
OPEN VENT
2500 PSI
BURST
PRESSURE
GN2
150 PSI
RELIEF
PRESSURE
CONTROL AIR SYSTEM
150 PSI
LIQUID
LEVEL
SIGHT
GAGE
GN2 PURGE
BLEED
WATER FLUSH
BLEED
HYDRAULIC MAIN
WATER
TO DRAIN
GN2 PURGE
THRUST CHAMBER

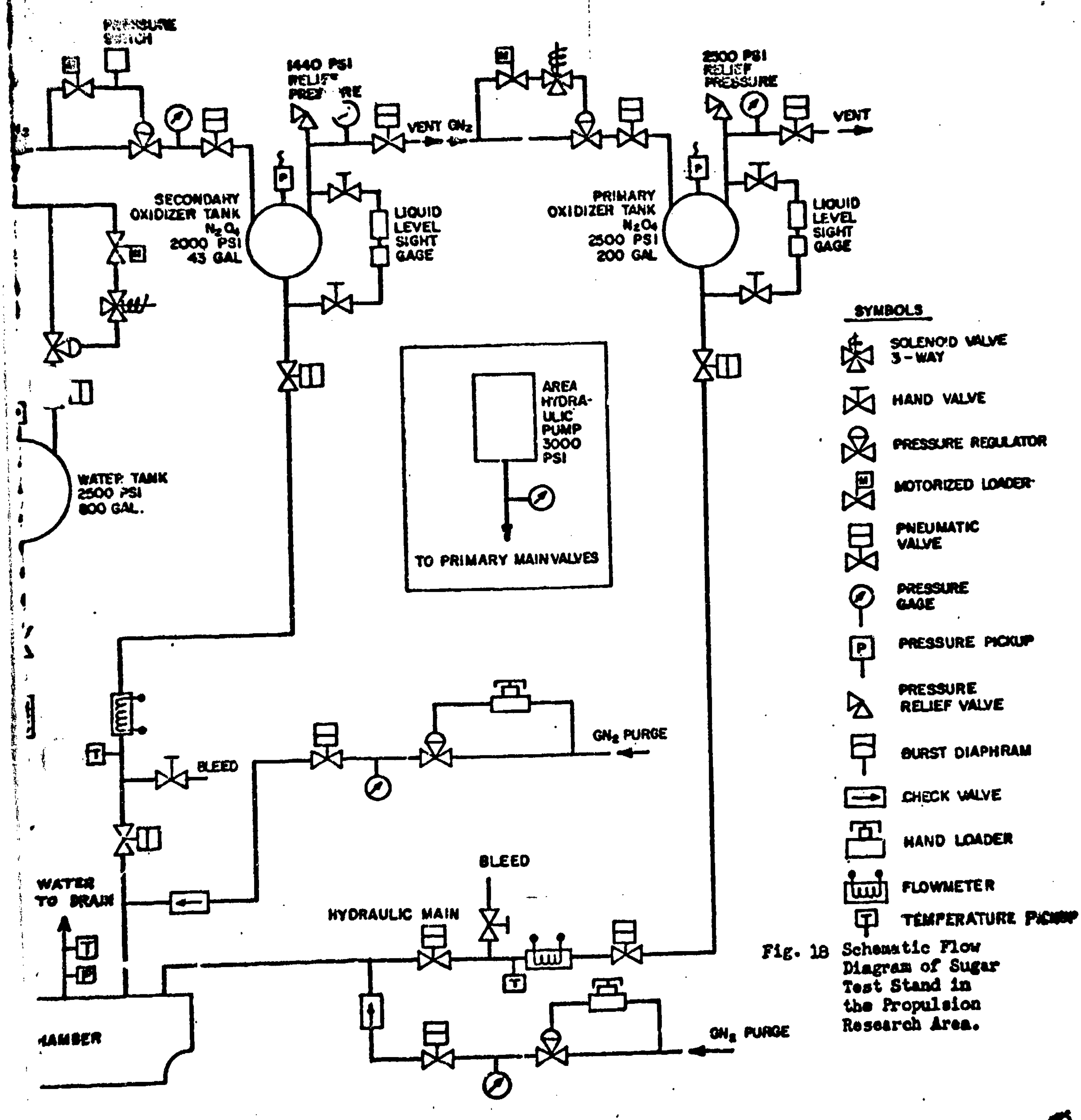

Fig. 18 Schematic Flow Diagram of Sugar Test Stand in the Propulsion Research Area.

2

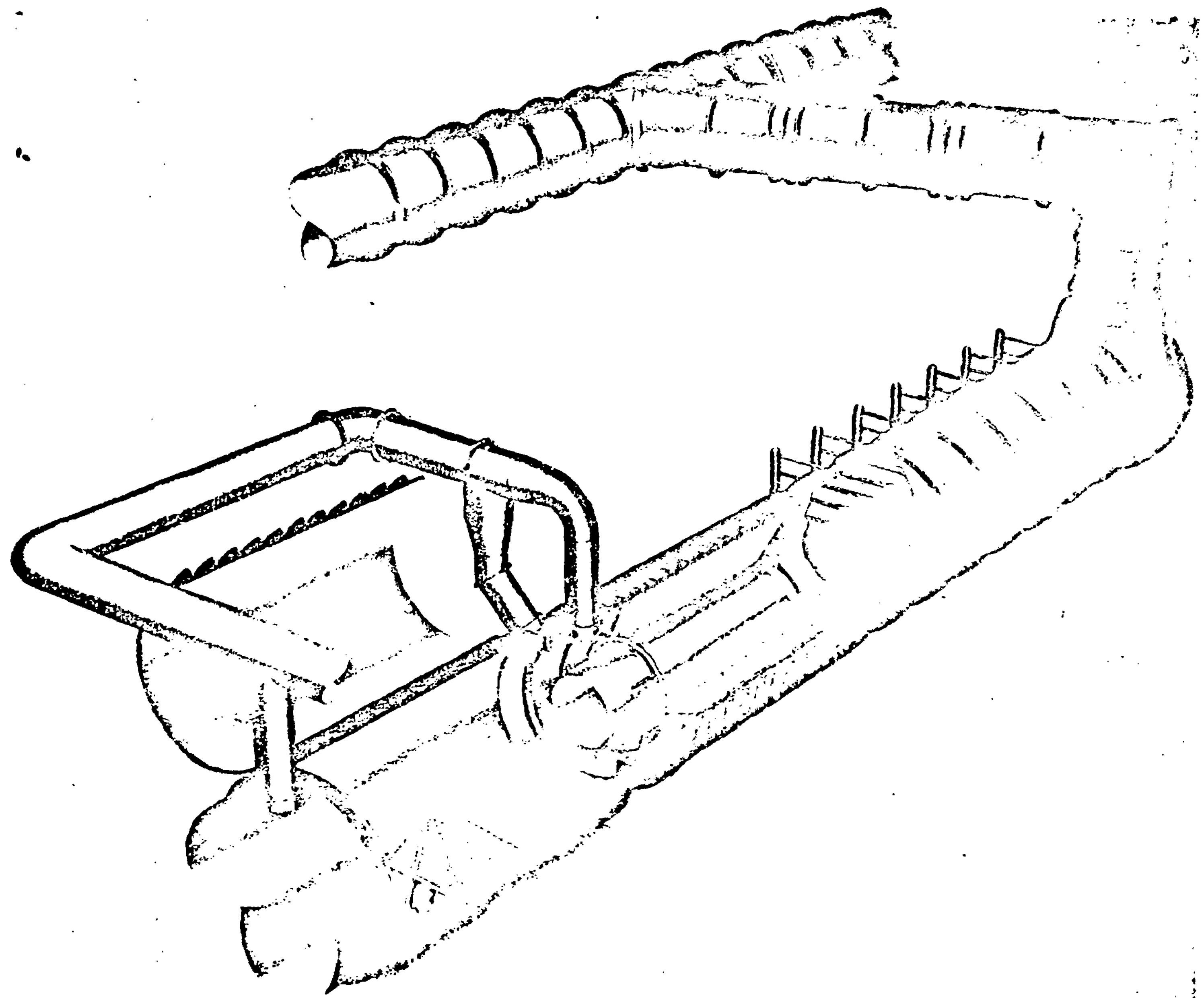

Figure 19 . Propulsion Engine Test Cell (J-2), Pictorial View

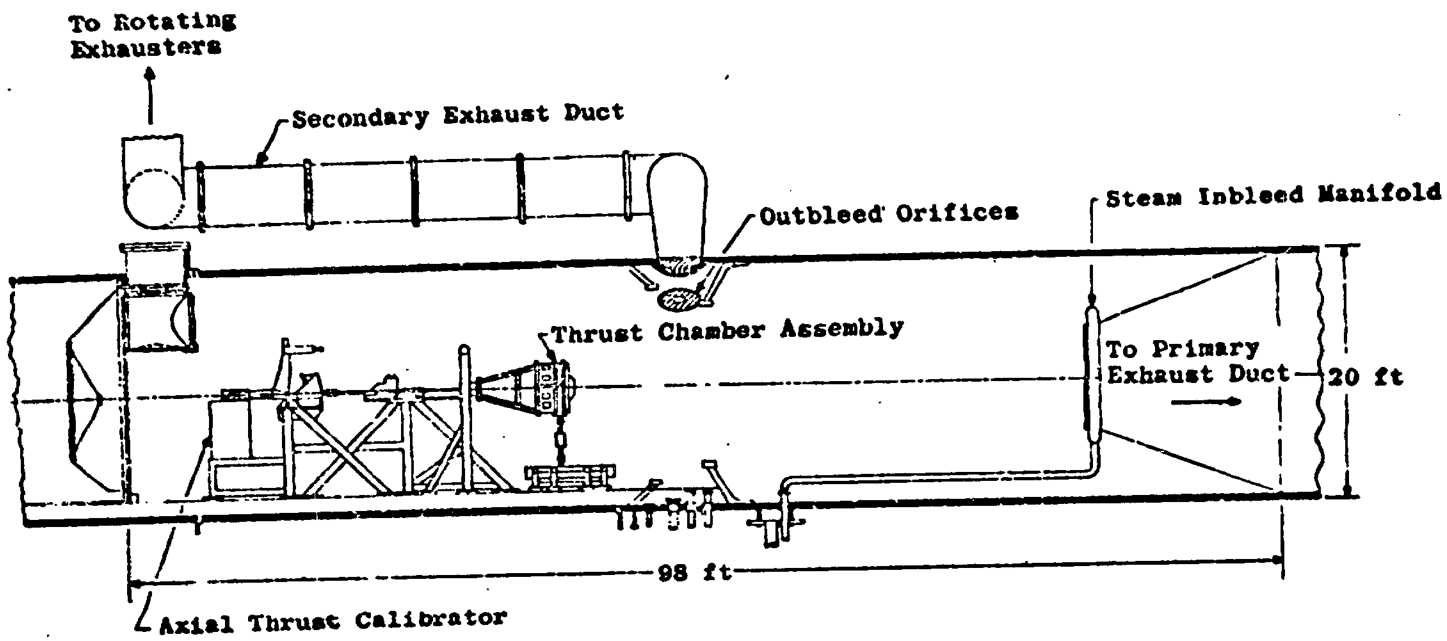

Figure 20. Propulsion Engine Test Cell (J-2), Elevation View (Ref. Reproduced from Ref. 25)

allowing engine exhaust gases to increase test cell pressure during the firings. Test cell isolation was obtained by valving-off the primary exhaust duct and orificing the inlet to the secondary exhaust duct. Both the range and gradient of the transients were controlled by the use of two remotely interchangeable exhaust inlet orifices and the inbleeding of steam into the test cell during the firings. Desired pre-firing test cell pressures were obtained by setting pumping ratios on the facility exhausters.

(U) Firings requiring constant nozzle pressure ratios (constant test cell pressures) were conducted with the primary exhaust ducting open to the facility exhausters and without steam inbleed. By thus creating a sufficiently large test cell outbleed area, test cell pressure remained essentially at pre-firing levels throughout the firings.

(U) The engine was mounted horizontally in an engine support assembly, which consisted of a thrust abutment, an aft support stand, and an engine pylon (Fig. 21). The TCA was mounted rigidly to the engine pylon which was attached to the aft support stand in both the pitch and yaw planes by universal flexures. Axial force was measured by two series-mounted load cells attached to the thrust abutment and the engine pylon by universal flexures which permitted forces to be transmitted only along the longitudinal axis of the load cells.

(U) The propellant system (Fig. 22) utilized for this test program included primary (1500 gal) oxidizer and fuel supply tanks, a gaseous nitrogen pressurization system, and the required valves and fittings. Gaseous nitrogen systems were also provided for both TCA and GG injector purging and propellant valve actuation. Water for TCA cooling was provided by a high-pressure supply system (Fig. 22) utilizing a 1000-gal tank pressurized by gaseous nitrogen. Control of both propellant and cooling water flow to the TCA and GG was obtained by the use of automatic preset pressure regulators in the tank pressurization systems.

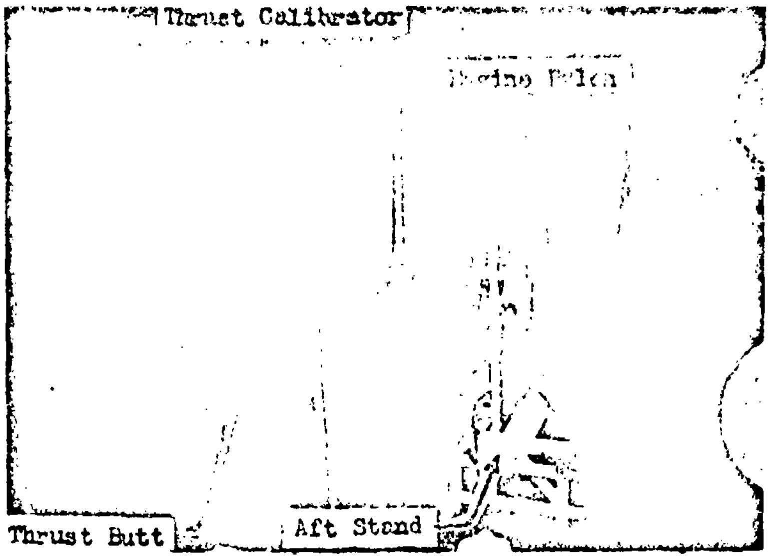

a. Side View

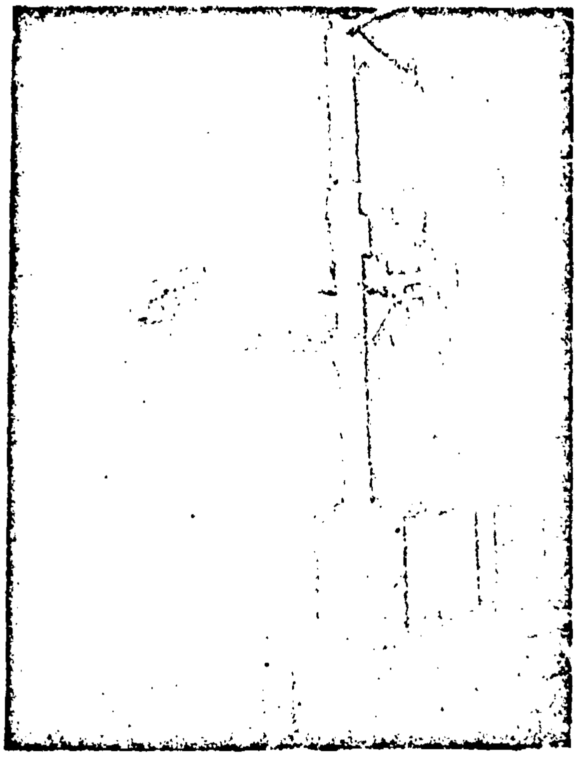

b. Closeup View

Figure 21. Test Cell Installation

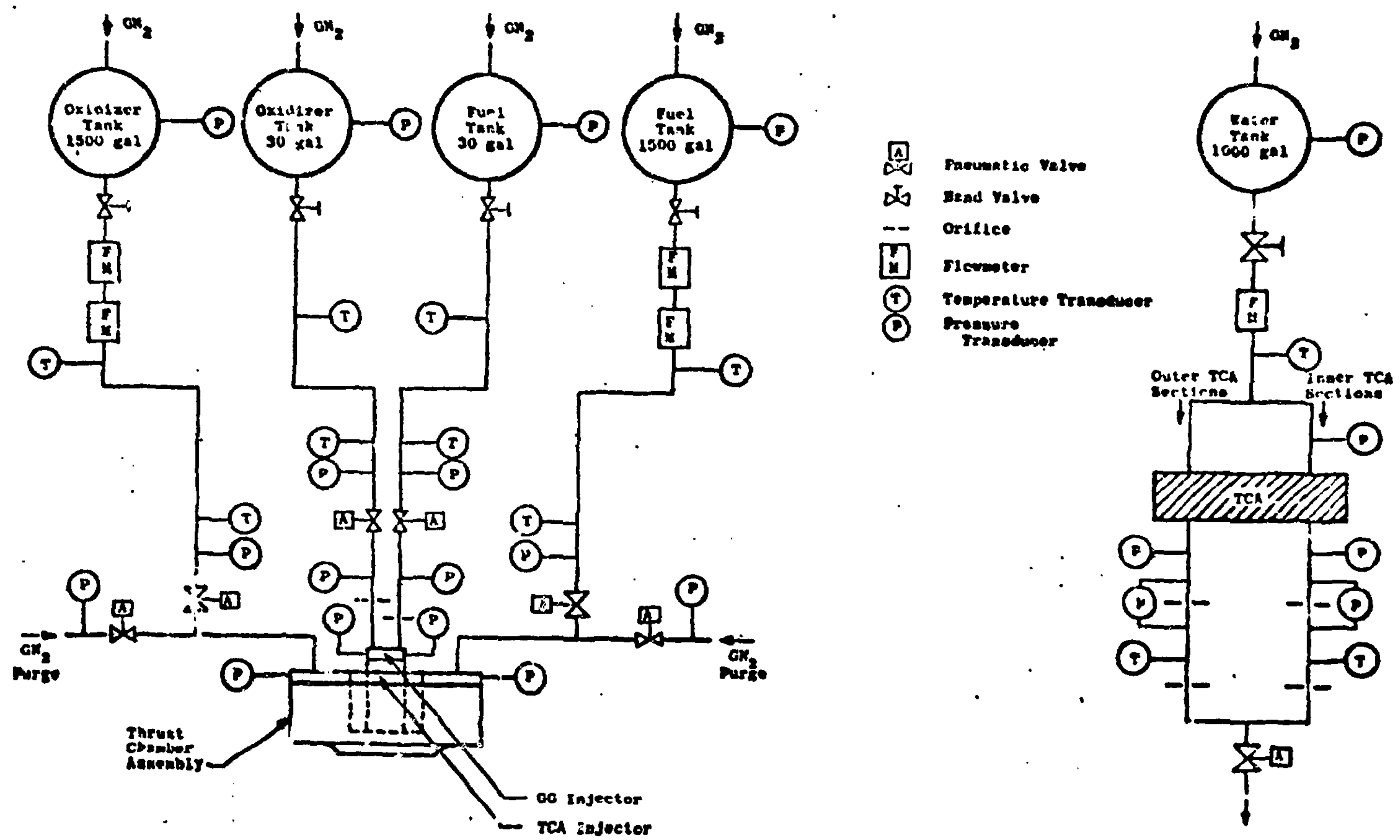

Figure 22. Propellant and Water Supply System Schematics, J-2 Cell, AEDC (Reproduced from Ref. 25)

INSTRUMENTATION

(U) Instrumentation was provided to obtain measurements of axial thrust, TCA and GG combustion chamber and injector pressures, nozzle outer wall and base pressures, test cell pressures, nozzle base plate temperatures, GG combustion temperatures, propellant and cooling water flow rates, and propellant and cooling water system pressures and temperatures. Visual monitoring of the testing was provided by closed-circuit television and motion-picture cameras. Table 1 presents transducer ranges, recording systems used for primary data acquisition, and estimated measurement accuracies for the AEDC test program. For the sea level test program instrumentation ranges and accuracies were similar. However, all performance and base heating parameters (chamber pressures, flow rates, nozzle and base pressures, thrust, and response temperatures were recorded by a Beckman model 210 digital data acquisition system and reduced by computer program. Location of TCA and GG instrumentation is shown in Figs. 23, 24, 25 and 26. Location of water and propellant system instrumentation is shown in Fig. 18 and 22 .

Force Measurement

(U) Altitude Testing. Axial thrust was measured using two dual-output strain-gage-type load cells mounted in series having ranges from 0 to 10,000 lb_f and 0 to 20,000 lb_f, respectively. Primary data recordings of the load cell outputs were in frequency form on magnetic tape. Calibration of the thrust measuring system was accomplished by a remotely controlled deadweight calibrator. The accuracy of the thrust calibrator was determined by comparison to a National Bureau of Standards certified standard to be within 0.2 percent. Overall thrust measurement accuracy is estimated to be within 1.0 percent.

TABLE 1
PRIMARY DATA ACQUISITION SYSTEMS
(Reproduced From Ref. 25)

Parameter	Transducer Range	Data Conditioning	Recorder	Estimated Accuracy
Force, lbf				
Axial	0-[illegible],000	Analog-to-Frequency Converter	Magnetic Tape	±1.0 percent
Pressure, psia				
TCA Combustion Chamber	0-300	Analog-to-Frequency Converter	Magnetic Tape	±0.5 percent
GG Combustion Chamber	0-500			
Test Cell	0-15			
Main Oxidizer Tank	0-750			
Main Fuel Tank				
Secondary Oxidizer Tank				
Secondary Fuel Tank				
Water Tank	0-1500			
TCA Oxidizer Supply Line	0-750	Analog-to-Digital Commutator		
TCA Fuel Supply Line				
GG Oxidizer Supply				
GG Fuel Supply Line				
GG ·xidizer Injector Inlet				
GG Fuel Injector Inlet	0-500			
GG Oxidizer Injector				
GG Fuel Injector				
TCA Oxidizer Injector				
TCA Fuel Injector				
Nozzle Base	0-25			
Nozzle Outer Wall				
TCA Oxidizer Purge	0-300	Direct	Recording Nu.·-Balance Potentiometer	±2.0 percent
TCA Fuel Purge				
GG Oxidizer Purge				
GG Fuel Purge				
TCA Water Inlet	0-1500	Analog-to-Digital Commutator	Magnetic Tape	±0.5 percent
TCA Inner Water Outlet				
TCA Outer Water Outlet				
Flow Sensor Static	0-20			
Pressure Differential, psid				
TCA Water Inner Orifice	0-300	Analog-to-Frequency Converter	Magnetic Tape	±0.5 percent
TCA Water Outer Orifice				
Flow Sensor Upstream	±3	Analog-to-Digital Commutator		
Flow Sensor Downstream	±3	Analog-to-Digital Commutator		
Flow Rate, lb_m/sec				
TCA Oxidizer	5-45	Direct	Magnetic Tape	±1.0 percent
TCA Fuel	3-27			
GG Oxidizer	---	---	Computed from Pressure Data	±3.0 percent
GG Fuel	---	---		
TCA Water	30-170	Direct	Magnetic Tape	±1.0 percent
Temperature, °F				
TCA Oxidizer	0-200	Analog-to-Frequency Converter	Magnetic Tape	±1°F
TCA Fuel				
GG Oxidizer				
GG Fuel				
TCA Water Inlet				
TCA Inner Water Outlet				
TCA Outer Water Outlet				
GG Combustion Gas	0-2000	Analog-to-Digital Commutator		±40°F
Nozzle Base Plate	0-2000	Analog-to-Digital Commutator		±40°F
Valve Position				
TCA Oxidizer	Open-Close	Direct	Light-Beam Oscillograph	---
TCA Fuel				---
GG Oxidizer				---
GG Fuel				---
Time, sec	---	---	Light-Beam Oscillograph	±0.002 sec

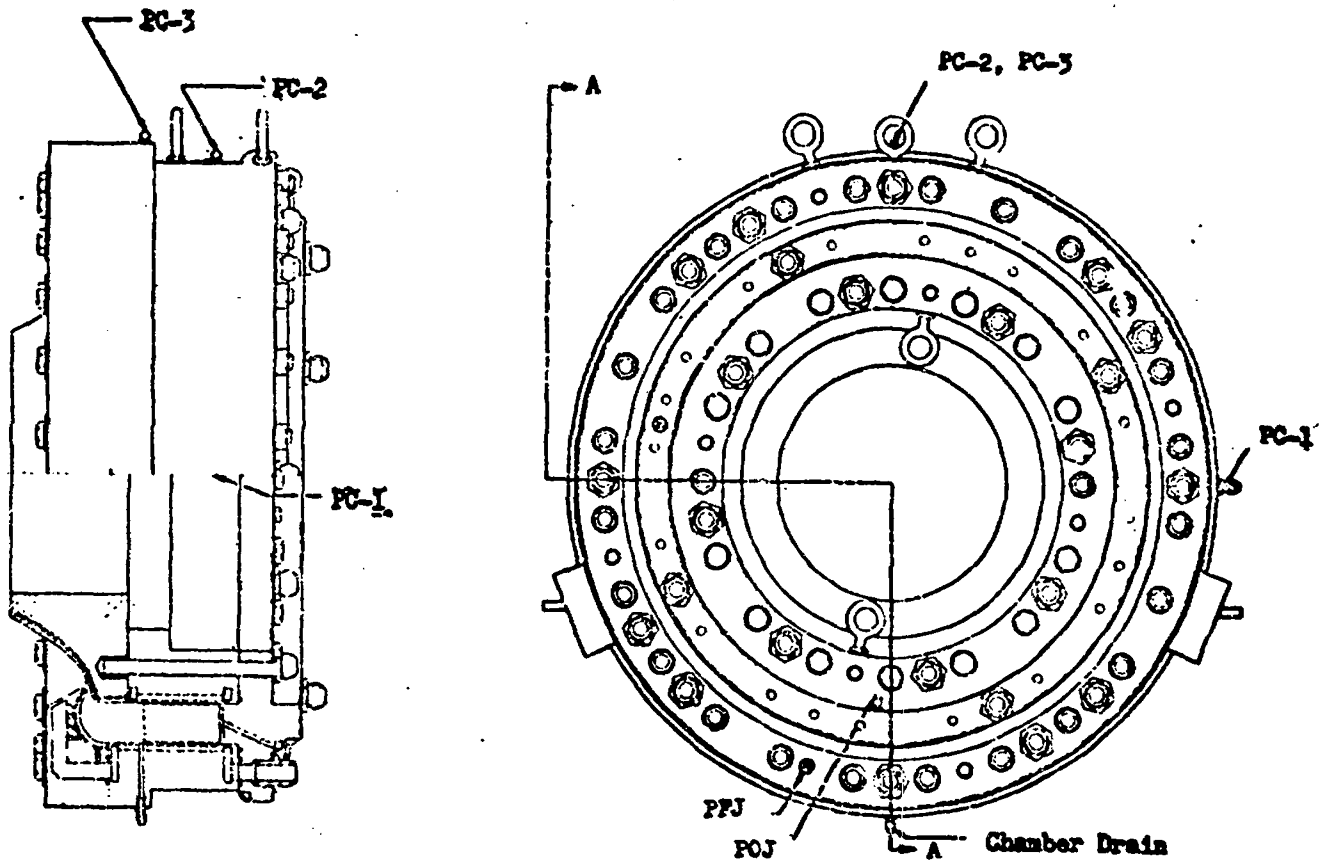

Section A-A

Figure 23. Thrust Chamber Assembly Instrumentation

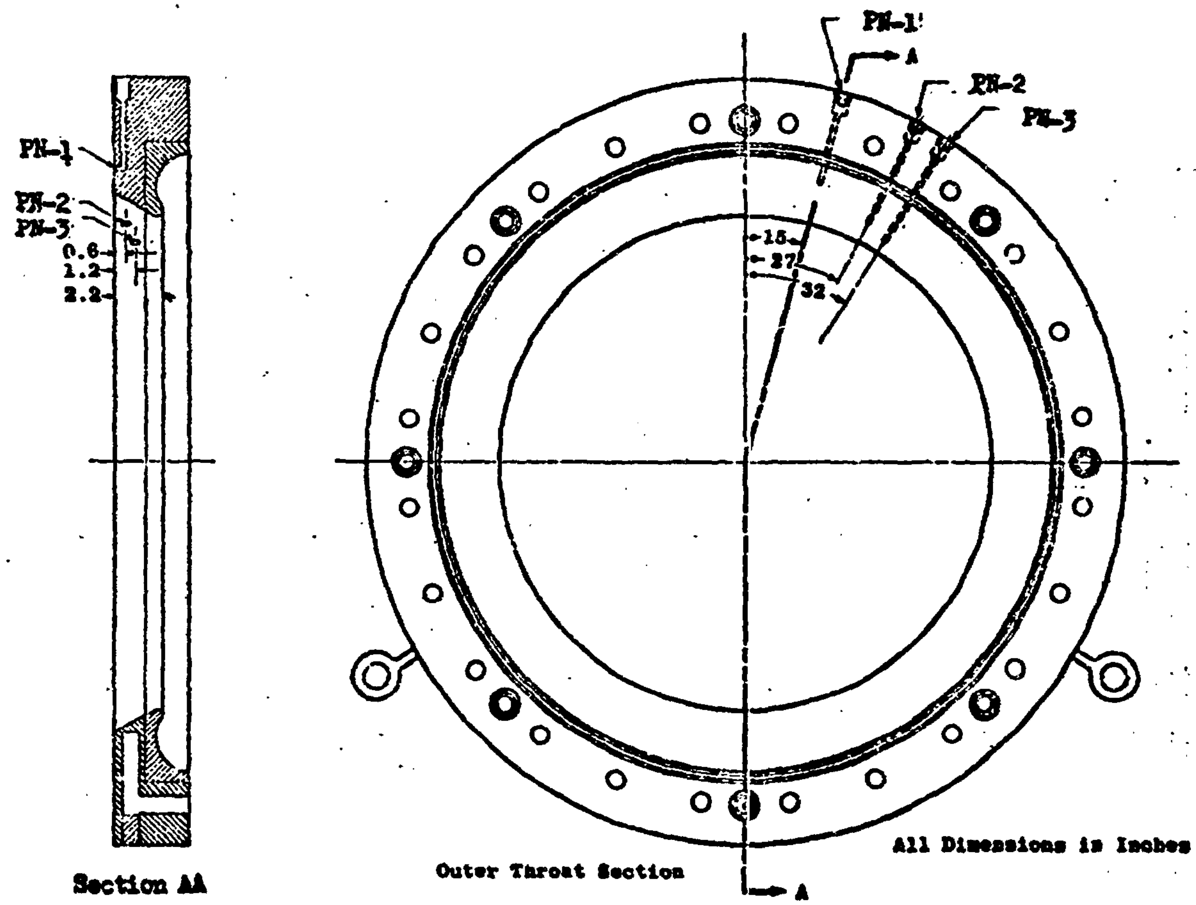

Figure 24 . Outer Nozzle Instrumentation

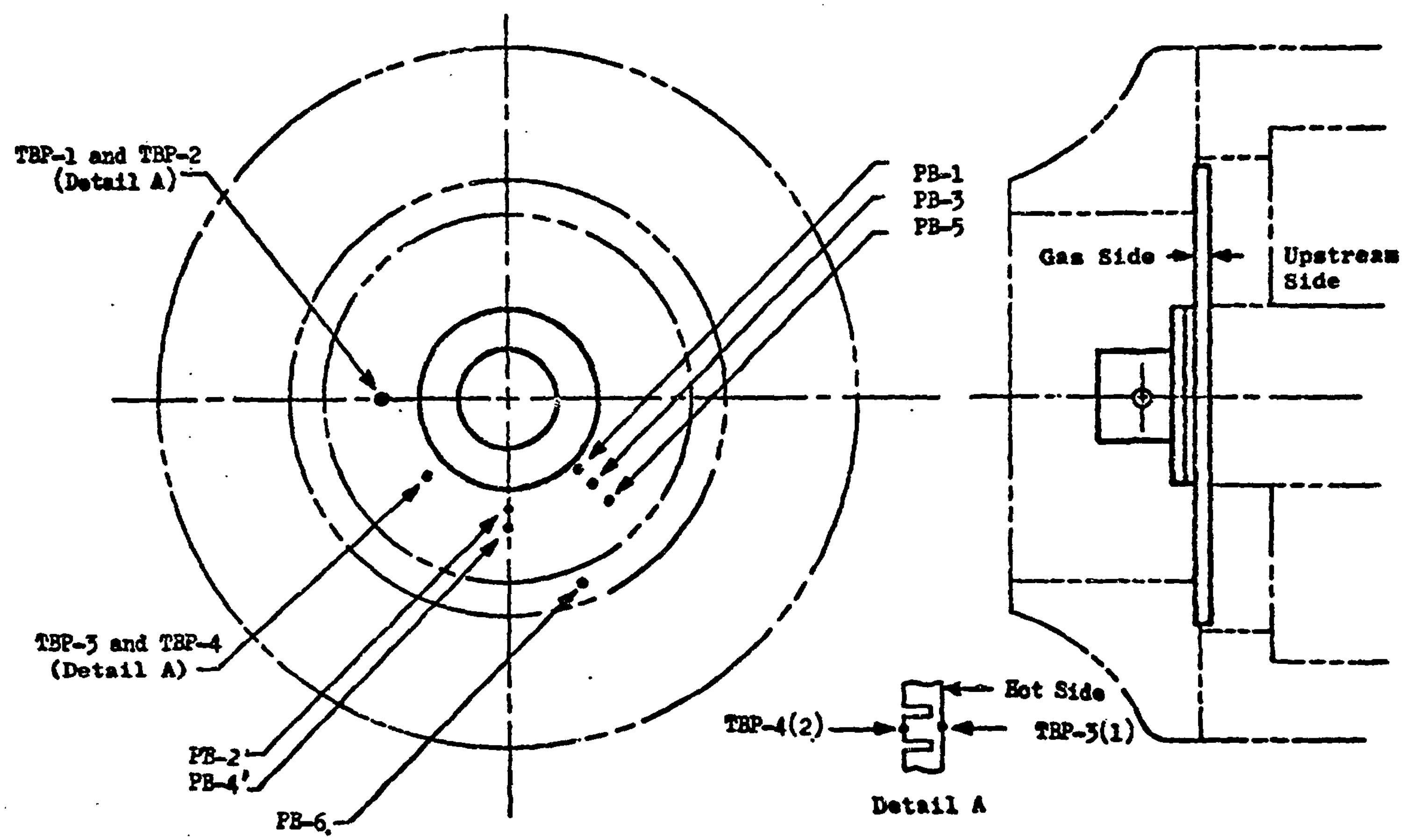

Figure 25. Base Plate Instrumentation

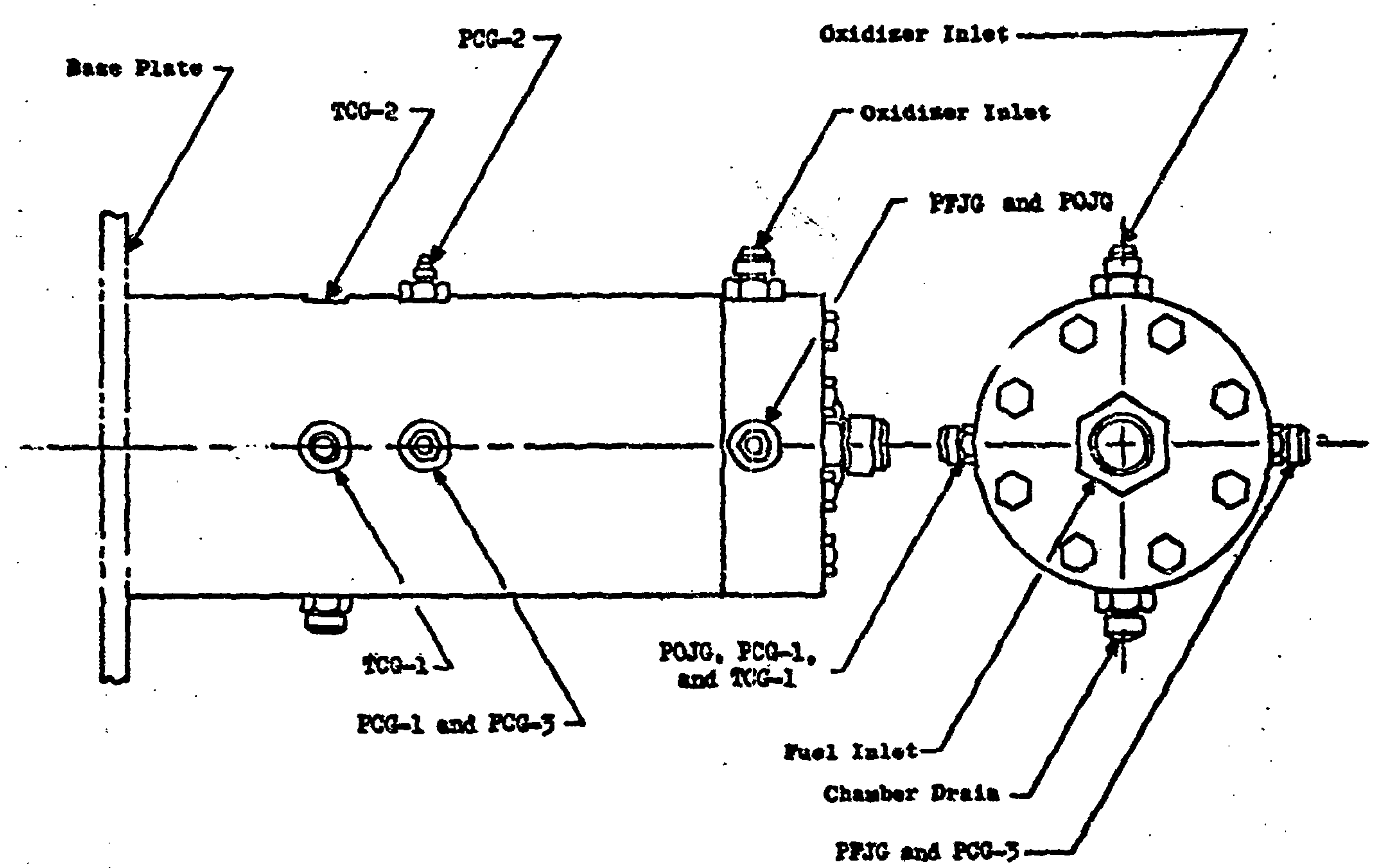

Figure 26. Gas Generator Instrumentation

(U) Sea Level Testing. Thrust was measured using a Baldwin bonded strain gage, load cell rated at 20,000 lb_f. Calibration of the thrust measuring system was accomplished by hydraulically loading the system and comparing measurements with an in-line, strain gage type thrust ring. The thrust ring was calibrated at the NBS and certified to have a precision of ± 0.1 percent. Overall precision of the thrust measurement and recording system was determined from periodic calibrations during the testing to be ± 0.3 percent.

Pressure Measurements, Altitude and Sea Level Testing

(U) TCA and GG combustion chamber pressures were sensed by bonded strain-gage-type transducers having ranges from 0 to 300 and 0 to 500 psia, respectively. Nozzle base (Fig. 23) pressures were sensed by the same type of transducers having ranges from 0 to 25 psia. Test cell pressures were sensed by bonded strain-gage-type transducers with ranges from 0 to 15 and 0 to 20 psia. Propellant and water system pressures were sensed by strain-gage-type transducers having various ranges (Table 1). Sensing of TCA and GG injector pressures was by 0- to 500-psia, strain-gage-type transducers. Primary data recordings of all pressure transducer outputs, with the exception of both TCA and GG purge pressure transducers, were on magnetic tape in either frequency or digital form. Recordings of the purge pressure transducer outputs were on strip charts (recording null-balance potentiometers).

(U) All pressure transducers were calibrated under laboratory conditions by comparison to secondary standards. Preselected precision electrical resistances were used in the transducer circuitry to simulate applied pressures electrically. The pressure values thus simulated were determined by comparing the outputs of the resistance-shunted transducers with outputs obtained during the previous secondary standard calibrations. Prior to an actual firing, these same precision shunt resistances were used to obtain calibrations of each of the pressure data recording systems.

(U) The precision of pressure measurements obtained using electrical resistance calibrations of both the frequency and digital tape recording systems is estimated to be within 0.5 percent.

Flowrate Measurements

(U) Altitude Testing. Propellant flowrates to the thrust chamber assembly were measured by dual-output, turbine-type flowmeters. Two such flowmeters were installed in series in both the oxidizer and fuel supply lines to the TCA. Calibrations of the flowmeters were obtained under laboratory conditions on a flow-calibration bench using water as the working fluid.

(U) A flow calibration using water as the working fluid was made to determine the pressure drop-flowrate relationship for each secondary system. The pressure drop-flowrate functions thus determined were used with tank and GG combustion chamber pressure differentials to determine flowrates to the GG during the test firings.

(U) A single, dual-output, turbine-type flowmeter and two calibrated square-edged orifices were used to determine total cooling water flowrate and flowrates to the inner and outer sections of the TCA, respectively. Calibration of the water flowmeter was obtained in a laboratory flow calibration bench. The two orifices were individually calibrated in place using the flowmeter as a calibration standard. Pressure differentials across the orifices were sensed by 0- to 300-psid, strain-gage-type pressure transducers. Recording systems and calibration methods used with the orifice transducers were identical to those described previously.

(U) The precision of pressure measurements obtained using electrical resistance calibrations of both the frequency and digital tape recording systems is estimated to be within 0.5 percent.

Flowrate Measurements

(U) Altitude Testing. Propellant flowrates to the thrust chamber assembly were measured by dual-output, turbine-type flowmeters. Two such flowmeters were installed in series in both the oxidizer and fuel supply lines to the TCA. Calibrations of the flowmeters were obtained under laboratory conditions on a flow-calibration bench using water as the working fluid.

(U) A flow calibration using water as the working fluid was made to determine the pressure drop-flowrate relationship for each secondary system. The pressure drop-flowrate functions thus determined were used with tank and GG combustion chamber pressure differentials to determine flowrates to the GG during the test firings.

(U) A single, dual-output, turbine-type flowmeter and two calibrated square-edged orifices were used to determine total cooling water flowrate and flowrates to the inner and outer sections of the TCA, respectively. Calibration of the water flowmeter was obtained in a laboratory flow calibration bench. The two orifices were individually calibrated in place using the flowmeter as a calibration standard. Pressure differentials across the orifices were sensed by 0- to 300-psid, strain-gage-type pressure transducers. Recording systems and calibration methods used with the orifice transducers were identical to those described previously.

(U) Primary data recordings of all flowmeter outputs were in frequency form on magnetic tape. The flowmeter data recording systems were calibrated by applying input signals of known frequency. Overall measurement accuracies of the secondary propellant flow data and the orifice water flow data are estimated to be within 3.0 percent.

(U) Sea Level Testing. Primary and secondary propellant and coolant water flowrates were measured with single, Fisher-Porter turbine type flowmeters. Because of the low flowrate in the secondary oxidizer feed system, this meter was calibrated using N_2O_4. All other flowmeters were calibrated with water. The water calibrations were corrected by the viscosity ratio of water to propellant to make the calibrations applicable for the respective propellant.

(U) The precision of the propellant flowmeters was determined from periodic calibration to be ± 0.25 percent. The precision of the water flowmeter is within 2.0 percent (manufacturer's certification).

Temperature Measurements, Altitude and Sea Level Testing

(U) Fuel, oxidizer, and water temperatures were measured by immersion-type resistance temperature transducers (RTT) located as shown in Figs. 18 and 22. Nozzle base plate temperatures were sensed by thermocouples attached to the base plate at locations shown in Fig. 25. GG combustion gas temperatures were measured by thermocouple probes as shown in Fig. 26. Primary recordings of the temperature sensor data were in either frequency or digital form on magnetic tape. Calibration of the RTT recording systems and spanning of the thermocouple recording systems were obtained electrically. Estimated overall measurement accuracies of fluid temperature data are ±1F. Nozzle base, plate and GG gas temperature accuracies are ±40F.

Miscellaneous

(U) Altitude Testing. A pitot-static flow sensor was installed near the TCA to determine direction and magnitude of any external flow field that might influence nozzle performance. This flow sensor used a 0- to 15-psia, strain-gage-type transducer which measured local static pressure and two similar ±3-psid transducers which measured the difference between the static pressure and the total pressure in two directions parallel to the longitudinal axis of the TCA. Data recording and calibrations of the flow sensor instrumentation were identical to those described previously.

(U) Indications of propellant valve functions required for TCA and GG operation were recorded on light-beam oscillographs. Oscillographs were also used for redundant recording of primary data and for time correlation. Strip charts were used to monitor the firings and to provide immediate access data. Events in the test cell during the firings were monitored by a closed-circuit television system and recorded by five 16-mm. motion picture cameras using color film.

(U) Sea Level Testing. The uncooled thrust chamber was instrumented with three photocons for the first five firings and with five photocons for the last five firings (Fig. 27). Photocon output was recorded on light-beam oscillographs and high speed tape with a frequency resolution of approximately 15,000 cps.

(U) Indications of valve functions were recorded on Easterline Angus recorders. Oscillographs and strip charts were used to record primary data for immediate access. Three 16-mm motion picture cameras provided visual records of the firings.

PROCEDURES

Sea Level Testing

(U) Pre-test procedures consisted of system and hardware leak checks, calibration of instrumentation, and measurement of nozzle throat area. Nozzle throat gap measurements were made at six or more locations around the throat circumference with a ball micrometer.

(U) The propellant and water supply tank were pressurized. Coolant water flow was initiated manually and the flowrate observed on a strip chart. When adequate water flow was achieved, the automatic firing sequencer was activated. This sequencer controlled primary purges, all propellant valves, and the recording system. Venting of the water tank, closing the water valve, and post-fire purging of the GG were performed manually. Posttest calibrations, inspection of the hardware and measurement of the throat area were then performed.

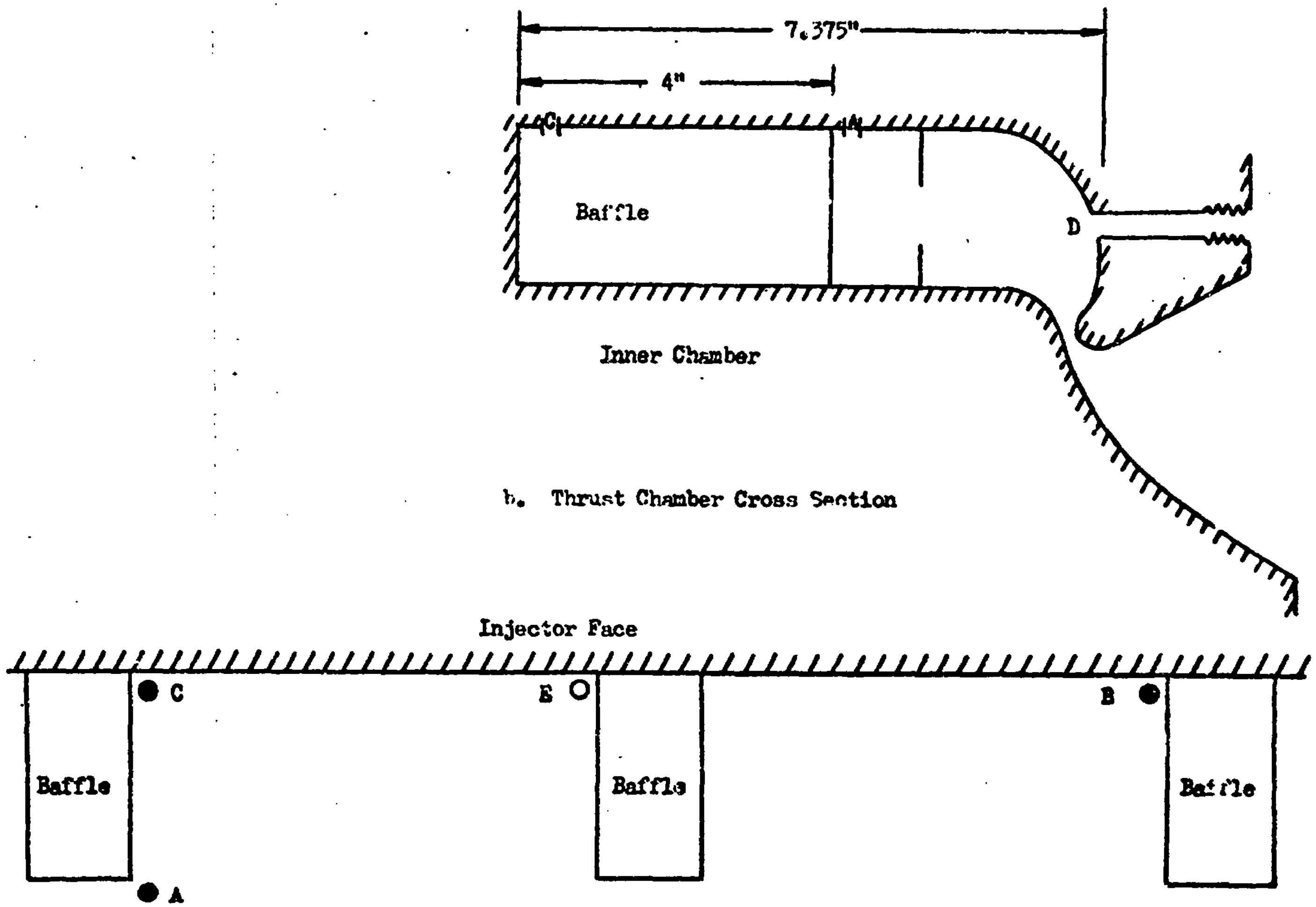

b. Thrust Chamber Cross Section

● Initial Photocon
○ Photocon Added After First Five Firings

a. Plane View of Injector

Figure 27. Photocon Locations on the Uncooled Aerospike Thrust Chamber

Altitude Testing

(U) The test program consisted of four test periods with three to nine TCA firings conducted at either transient or constant pressure altitude conditions during each test period.

(U) Pre-test procedures, including electrical and mechanical checks of all test hardware, measurement of the nozzle throat area and static leakage checks of the propellant and water-supply systems, the thrust chamber assembly, and the gas generator, were conducted prior to each test period. The propellant tanks were loaded, and samples were taken from the primary tanks and analyzed to determine propellant specific gravity variations with temperature and to determine that the propellants met applicable specifications. The test cell hatch was closed, and pre-test instrumentation calibrations were performed at atmospheric pressure. The test cell was then evacuated to a pressure of approximately 0.5 psia by the facility exhausters, and pre-test instrumentation calibrations were repeated. Propellant, water, and steam system bleed-ins were accomplished at pressure altitude conditions.

(U) For each of the firings requiring test cell pressure transients, the primary exhaust duct was valved off, and the proper orifice was positioned at the inlet to the secondary exhaust duct. The steam inbleed system valve controller was positioned so that when the steam inbleed valve was opened at TCA ignition, the required flow rate of steam would enter the test cell. Test cell pressure was set at the required pre-firing level using the facility exhausters. The propellant water, and steam systems were then pressurized.

(U) The final 60 seconds of the firing countdown was performed automatically by an electrical sequencer which activated all firing systems, started the recording instrumentation, initiated cooling water flow to the TCA, initiated nitrogen purges through both the TCA and GG injectors, and sequenced both TCA and GG propellant valves to fire the engine for the prescribed firing duration. A typical sequence of major events is shown in Fig. 28 for a nine second firing with the GG shutdown two seconds before the main engine.

(U) The firings requiring a constant test cell pressure were conducted in the same manner, except that the primary exhaust system was not valved off and steam was not inbled into the test cell.

(U) At the completion of each test period, instrumentation calibrations were again performed at low test cell pressure. The test cell was vented to atmospheric pressure, and posttest atmospheric pressure calibrations were taken. Posttest procedures including measurement of the nozzle throat area were then performed on the test article.

Data Reduction

(U) For the sea level testing all data necessary for determining engine performance (except for propellant temperature and pressure, which were recorded on direct inking graphic recorders) were recorded in digital form on tape using a Beckman 210 system. These data, with the proper calibration adjustments, were reduced to engineering quantities and units by a computer program. The data was printed out in 0.01-second intervals. Approximately fourteen 0.01-second interval data points were used to obtain 0.5 second average data. Flowrates were printed out in cps and reduced to lbs/sec by hand.

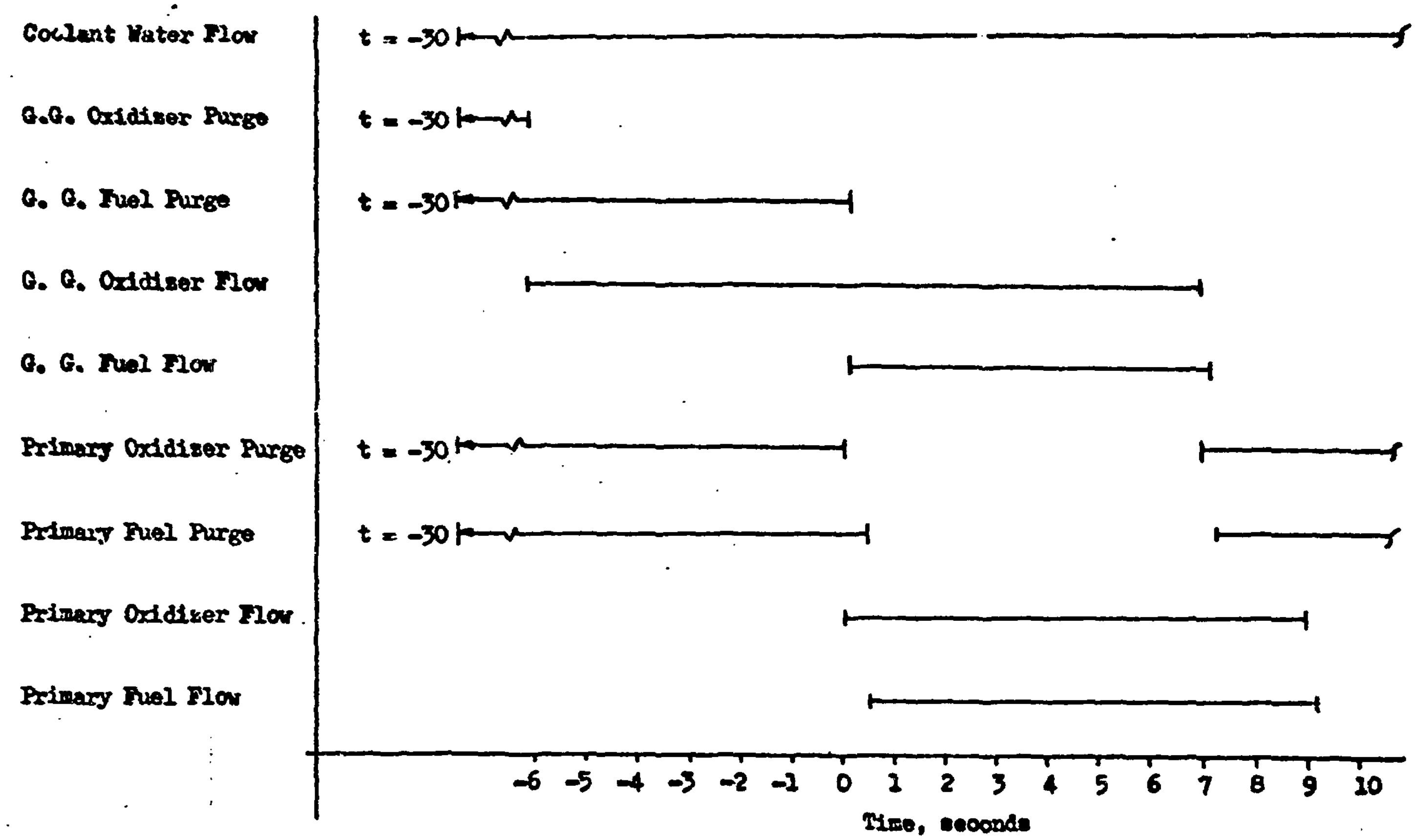

Figure 28 . Aerospike Engine Operating Sequence

(U) For the altitude testing, all data recorded in frequency form on magnetic tape were translated into digital form. The digital-form data thus obtained and the data originally recorded in digital form on magnetic tape were reduced to standard engineering units and tabulated by a digital computer at 0.1-second intervals for each firing. The computer was also programmed to use the measured data to compute average TCA and GG performance parameters over 0.1- and 0.5-second intervals for each firing. The performance parameters computed by this program were not used for the final performance computations, but were used for preliminary interpretation of engine performance and operating characteristics.

(U) Basic engineering data (propellant flows, ambient pressure, chamber and base pressures, temperatures, throat areas, and thrust) from both sea level and altitude test series were supplied to a computer program which computed, tabulated and plotted pertinent performance parameters averaged over 0.5-second intervals.

TESTING SUMMARY

(U) The basic objective of this test program was to demonstrate the performance of an aerospike nozzle over a range of altitude from sea level to design altitude and to determine the influence of secondary flowrate and properties on performance over this same altitude range. In achieving this objective, testing activity was divided into four main areas: (1) a large number of gas generator tests were accomplished to determine operating characteristics over a range of flowrates and mixture ratios, (2) uncooled thrust chamber testing was conducted to evaluate primary injector performance prior to its use in the water cooled hardware and to establish test procedures, (3) sea level testing with water cooled hardware was conducted to establish engine operating characteristics, to uncover and correct engine structural deficiencies and to obtain performance data, and (4) tests were conducted over

a pressure ratio range from approximately 350 to 40 at AEDC to determine nozzle performance. The chronological sequence of the test activity is shown in Fig. 29. A description of the testing accomplished and operational difficulties is presented.

Gas Generator Tests

(U) During April and May 1965, 33 gas generator firings (13 low flowrate and 20 high flowrate) were conducted. The objectives of the gas generator testing program were: (1) establish propellant valve sequencing and special operating procedures, (2) determine injector and overall pressure losses, (3) determine C* efficiencies and combustion gas temperature over a broad range of mixture ratios and propellant flowrates, and (4) demonstrate the feasibility of 10-second duration gas generator firings at a chamber pressure of 400 psia and a gas temperature of approximately 1800°F.

(U) All objectives of the test program were met and the hardware was in good condition after 33 tests. Test results are summarized in Table 2.

Uncooled Thrust Chamber Tests

(U) The objective of the uncooled hardware test program was primarily to conduct short duration (to 0.8 second) sea level tests to obtain a stable injector with reasonable performance for use in obtaining performance data with the longer duration cooled hardware.

(C) Five tests were conducted using Injector No. 1 with the uncooled aerodynamic spike engine. The tests covered a range of chamber pressures from 293 to 507 psia and a mixture ratio range of 1.63 to 1.94. These variations were purposely imposed to insure stability over a wide range of potential operating conditions. High-frequency

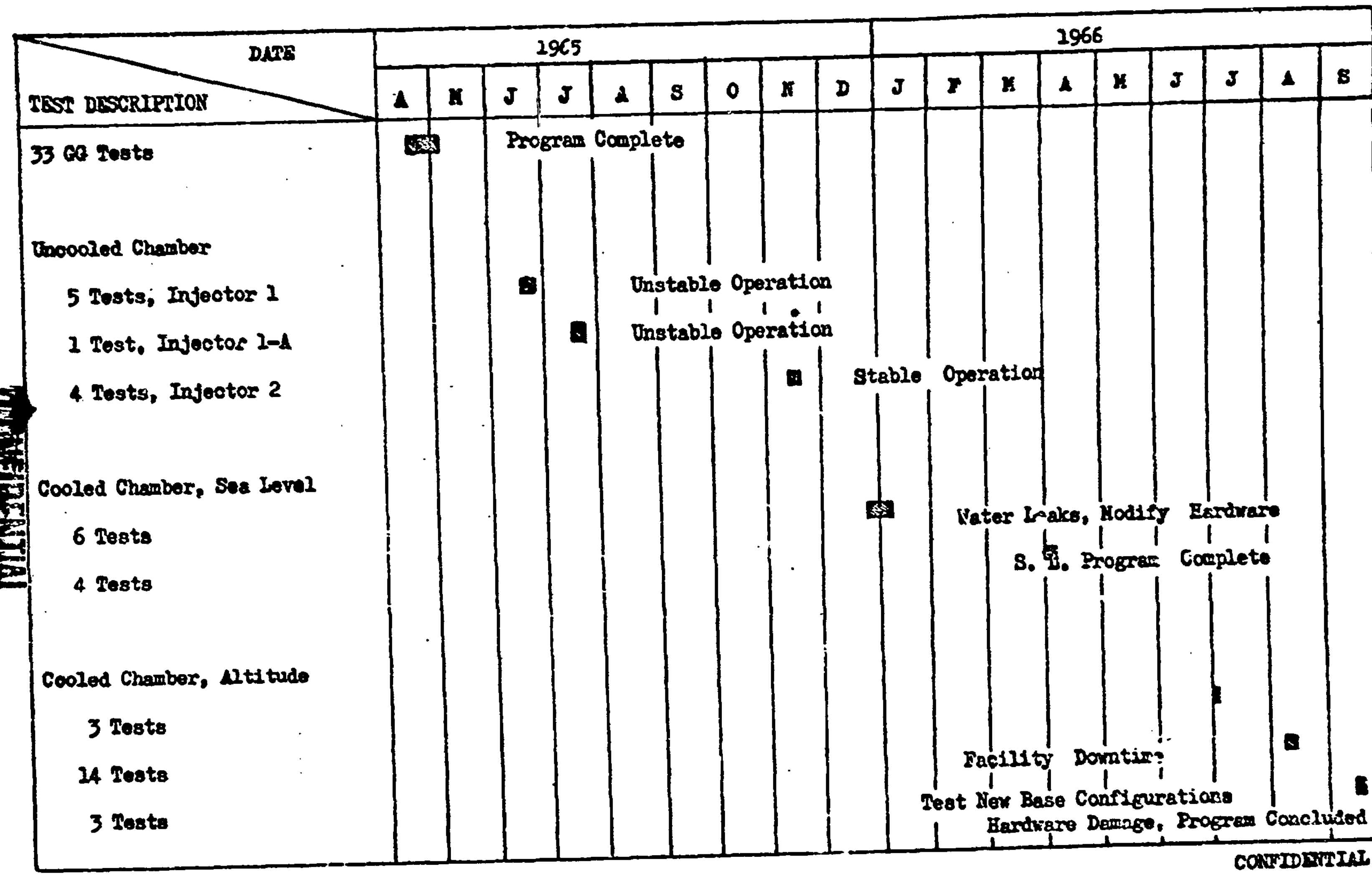

CONFIDENTIAL

Figure 29 . Hot-Firing Test Schedule - 12 Percent Length Aerospike

TABLE 2 GAS GENERATOR TEST SUMMARY

CONFIDENTIAL

Test	P_o psia	Mixture Ratio	η_{c^*} Meas.	*Comb. Temp. 1 deg F	*Comb. Temp. 2 deg F	Duration Seconds	G.G. Type	$\dot{w}$ (lb /sec)
13	- -	- -	- -	- -	- -	- -	LF**	- -
14	444	0.077	- -	- -	- -	- -	LF	0.590
15	489	0.062	- -	- -	- -	2.23	LF	0.616
16	449	0.109	90.9	- -	- -	2.24	LF	0.600
17	417	0.084	89.2	- -	- -	2.23	LF	0.570
18	394	0.068	85.5	- -	- -	3.27	LF	0.570
19	461	0.108	87.9	- -	- -	3.26	LF	0.640
20	450	0.119	89.0	1880	- -	3.27	HF	2.01
21	253	0.105	89.0	1750	- -	3.30	HF	1.15
22	314	0.084	86.5	1620	- -	3.29	HF	1.46
23	357	0.111	89.0	1760	- -	3.31	HF	1.61
24	363	0.076	54.1	- -	- -	3.31	HF	2.72
25	355	0.073	50.5	- -	710	3.09	HF	2.83
26	465	0.059	78.6	- -	- -	2.25	HF	2.40
27	459	0.060	80.5	- -	1265	3.09	HF	2.32
28	218	0.053	35.7	- -	350	3.09	HF	2.51
29	492	0.185	94.1	- -	1640	3.09	HF	2.06
30	469	0.087	89.8	- -	1530	3.09	HF	2.10
31	445	0.104	90.5	1650	1195	3.17	LF	0.601
32	- -	- -	- -	- -	- -	- -	LF	- -
33	459	0.055	82.4	990	1070	3.17	LF	0.691
34	446	0.070	85.8	1175	1075	3.17	LF	0.641
35	312	0.086	80.7	940	850	3.17	LF	0.477
36	294	0.052	69.1	495	530	3.17	LF	0.530
37	431	0.080	68.2	1660	1660	3.17	HF	2.35
38	246	0.085	87.8	1650	1530	3.17	HF	1.36
39	411	0.091	91.0	- -	1690	3.17	HF	2.17
40	211	0.096	89.5	1719	1620	3.17	HF	1.14
41	231	0.052	43.6	375	365	3.27	HF	2.60
42	116	0.057	39.2	- -	320	3.17	HF	1.45
43	221	0.154	94.8	1840	1630	3.08	HF	1.11
44	410	0.096	92.8	1747	1729	3.15	HF	2.12
45	414	0.085	93.0	1736	1749	11.57	HF	2.14

** Low flowrate gas generator - LF
High flowrate gas generator - HF

* Thermocouples 1 and 2 are located approximately 1.25 inches and 0.25 inch from the 3.40 inch ID combustor wall, respectively.

oscillations (predominantly 2300 cps) were experienced during these initial tests. No hardware damage was sustained during any of the tests (Fig. 30). The injector was subsequently modified (designated 1A) and fired in the uncooled thrust chamber at a chamber pressure of 410 psia for 0.75 second. Low frequency (530 cps) pressure oscillations were present over the entire run duration. No hardware damage was sustained from this test.

(U) Since the injector operating characteristics of Injector No. 1 did not meet the standards desired, a different injector pattern (designated Injector No. 2) was fabricated and tested.

(C) Four tests were conducted with Injector No. 2 in the uncooled thrust chamber. All four tests with Injector No. 2 exhibited extremely stable operation over a wide range of chamber pressure and mixture ratio with essentially no chamber pressure oscillations (Fig. 31). The hardware was in excellent condition after the tests. A summary of the uncooled test series conducted during June and November of 1965 is shown in Table 3.

Cooled Thrust Chamber Tests at Sea Level

(U) The objective of the water-cooled thrust chamber test series was to demonstrate the durability of the hardware assembly and obtain sea level data. Ten firings were conducted at Rocketdyne and the results are summarized in Table 4.

(C) The water-cooled thrust chamber was initially designed to operate at a chamber pressure of 500 psia and deliver a sea level thrust of approximately 10,000 pounds. However, during preliminary water blowdowns of the coolant system, it became apparent that the pressure drop required to supply the desired water flowrate was higher than theoretically estimated and above the normal capabilities of both the Rocketdyne and AEDC facilities selected

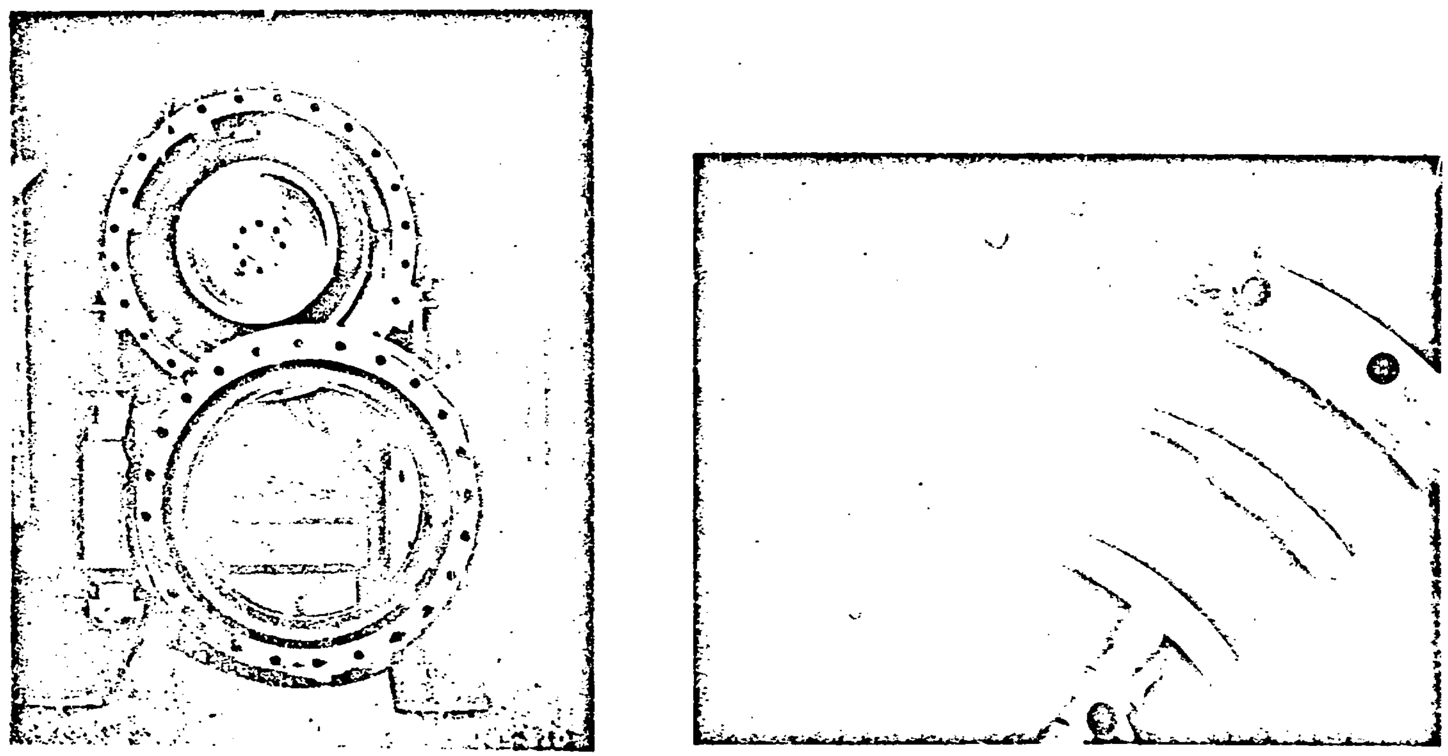

a. Front View

b. Close Up View

Figure 30. Condition of Uncooled Hardware After the Initial Five Firings

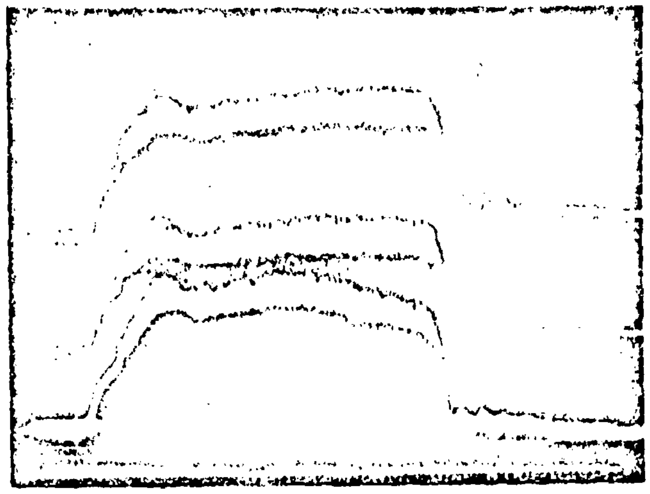

A. Test 48, Injector No. 1

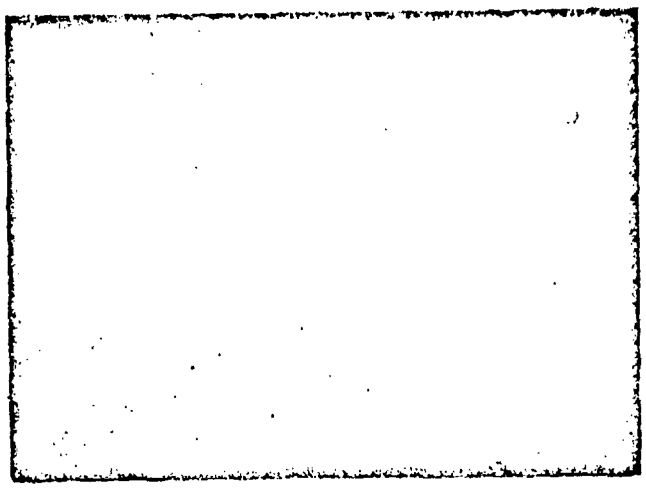

CONFIDENTIAL

B. Test 64, Injector No. 2

Figure 31 Comparison of Photocon Records for Typical Tests with Injectors No. 1 and No. 2.

TABLE 3

SUMMARY OF INJECTOR CHECKOUT TESTS
(Uncooled Thrust Chamber)

CONFIDENTIAL

Injector Configuration	Date	Test Number	Operating Conditions: Chamber Pressure psia	Operating Conditions: Mixture Ratio	Operating Conditions: Duration Seconds	Stability: Frequency cps	Stability: Amplitude psi
No. 1	6/13/65	46	293	1.63	0.51	—	—
1	6/22/65	47	307	1.74	0.55	2300	190
1	6/22/65	48	406	1.87	0.52	2300	190
1	6/23/65	49	414	1.71	0.40	2300	190
1	6/23/65	50	507	1.94	0.47	2300	250
No. 1-A	7/16/65	51	[illegible]	1.85	0.73	530	320
No. 2	11/10/65	64	298	1.43	0.50	Stable Operation	
2	11/10/65	65	390	1.58	0.52	Stable Operation	
2	11/12/65	66	453	1.90	0.58	Stable Operation	
2	11/12/65	67	418	1.89	0.74	Stable Operation	

TABLE 4

WATER COOLED CHAMBER, SEA LEVEL TEST SUMMARY

Run No.	Date	P_{c_p} Psia	Duration Seconds	$\dot{w}_s/\dot{w}_p$ Percent	MR_p	MR_s	PR
RD68	12/20/65	~300	0.5	0	—	—	21.9
RD69	12/22/65	398	1.51	0	1.75	—	29.2
RD71	12/28/65	388	2.92	0	1.82	—	28.4
RD01	1/4/66	396	5.02	0	1.73	—	28.7
RD01	1/4/66	396	5.02	1.63	1.73	0.046	28.7
RD02	1/6/66	299	7.2	0	1.67	—	21.6
RD02	1/6/66	299	7.2	1.10	1.67	0.263	21.6
RD03	1/10/66	302	7.9	0	1.72	—	21.9
RD03	1/10/66	302	7.9	1.96	1.72	0.092	21.9
RD03	1/10/66	302	7.9	0	1.72	—	21.9
RD05	4/1/66	314	1.66	0	1.74	—	23.0
RD06	4/1/66	321	5.16	0	1.84	—	23.5
RD08	4/4/66	311	5.16	3.22	1.90	0.165	22.5
RD08	4/4/66	311	5.16	0	1.90	—	22.5
RD09	4/4/66	314	8.17	5.30	1.87	0.162	22.8
RD09	4/4/66	314	8.17	0	1.87	—	22.8

to conduct the test program. The static water pressure within the hardware would also have been higher than desirable with operation at 500 psia chamber pressure. The first series of hot-firing tests (No's. 68, 69, 71, and 01, Table 4), therefore, was planned to evaluate thrust chamber integrity and performance at a chamber pressure of 400 psia.

(C) The first three firings were conducted with increasing durations up to three seconds. The gas generator was not used for these tests. Inspection of the hardware after the third test showed a slight discoloration above one of the 14 circumferential coolant slots of the inner throat and covering a 45-degree section of the throat. This indicated overheating suggested partial blockage of a 45-degree section of the circumferential coolant slot in the throat region.

(C) The fourth test in the series (RD01) was conducted at a chamber pressure of approximately 400 psia for a duration of 5 seconds. Posttest inspection of the injector and thrust chamber revealed no hardware damage but a discoloration and slight "melting" (~ 0.50-inch diameter area) of the inner throat (Fig. 32). This occurred only on the same 45-degree section of the inner throat where a discoloration had been noted during the previous test. Because of this evidence of overheating and the limitation on increased coolant flow, the chamber pressure was decreased to 300 psia, while maintaining the same coolant flowrate, for succeeding tests. The gas generator was used during test RD01; however, a very low mixture ratio was obtained and the gas generator "flamed out." The fifth and sixth tests (RD02 and RD03) were conducted with increasing duration and the gas generator was employed satisfactorily for these tests. Combustion stability was excellent for all tests.

(C) Prior to conducting further tests, water leakage was noted. Upon disassembly and inspection, leakage was noted from braze joints in the inner and outer throat sections and in the outer casing. Prior to further testing, design

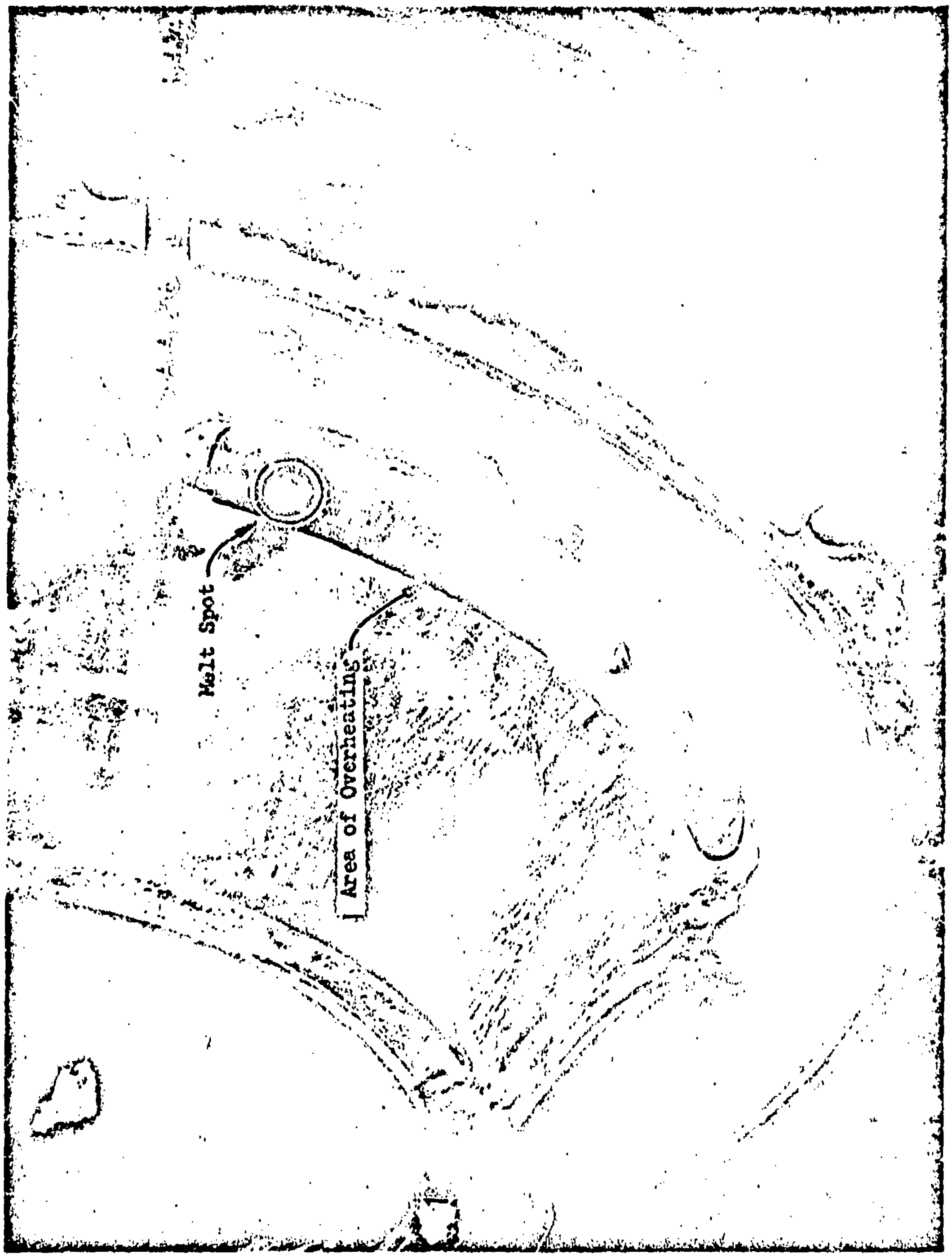

Figure 32. Condition of Inner Throat and Nozzle After Five Second Test at 400 psia. Chamber Pressure.

modifications and hardware rework were accomplished. Testing was resumed in April 1966, and the final four planned tests were conducted successfully without incident. These tests were at a chamber pressure of approximately 315 psia, and with secondary flowrates of 0, 3.2, and 5.3 percent of primary flowrate.

(U) Because of the small changes in efficiency expected with secondary flow, it was desirable to operate with and without secondary flow during a single firing. This allows a comparison of the change in efficiency with the addition of secondary flow during a firing without dependence on knowing the absolute level of efficiency. Therefore, during the sea level testing, the sequencing of secondary flow was varied (Fig. 33) to establish the best method of obtaining data with and without secondary flow for a single test. It was determined that when secondary flow was initiated after several seconds of main engine operation, or was cut off several seconds prior to the completion of main engine operation, an accurate representation of performance changes was achieved. Based on the results achieved in the sea level test program, the test sequence selected for the altitude testing was eight to nine seconds duration primary thrust chamber firings with gas generator operation initiating simultaneously with the primary chamber and terminating 2 seconds before primary cutoff.

Water Cooled Hardware Tests at Altitude

(U) The primary objective of the altitude test program was to determine nozzle performance as a function of pressure ratio (PR), secondary gas flowrate, secondary gas mixture ratio, and secondary gas injection method (base configuration). A secondary objective was the determination of nozzle base thermal environment.

UNCLASSIFIED

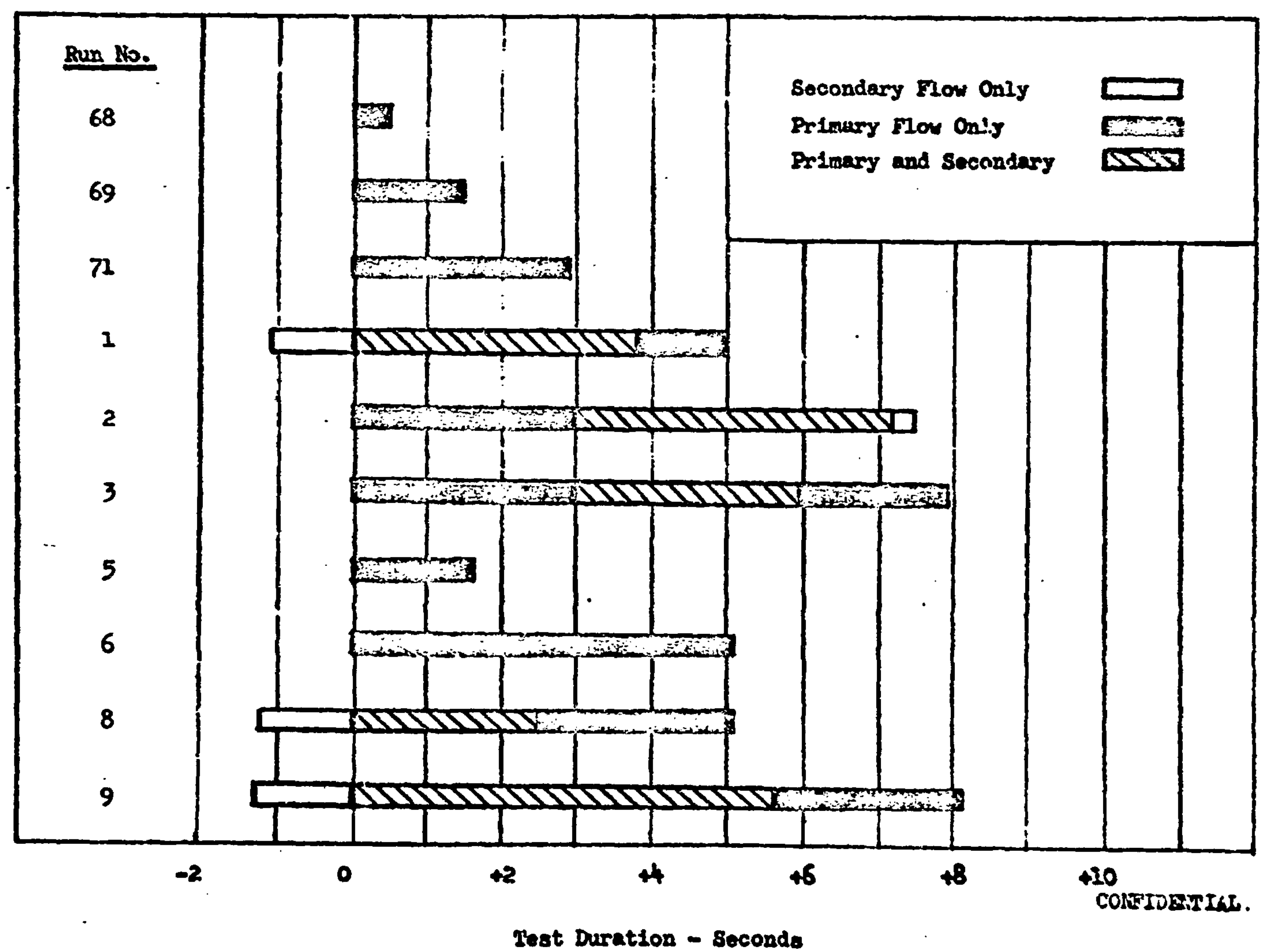

CONFIDENTIAL.

Figure 33. Water Cooled Aerospike Test Sequencing Summary

UNCLASSIFIED

(C) Twenty thrust chamber firings were achieved (Table 5) in four test periods (distinguished by the second letter in the test number). The test cell remained closed and evacuated to altitude conditions during a test period, hence, inspection of the hardware and throat area measurements between firings were not accomplished. The first sixteen thrust chamber firings (AA01 through AC20) were conducted with a varying ambient-to-chamber pressure ratio and the final four firings (AC21 through AD24) were conducted at a constant pressure ratio of approximately 350.

(C) Figure 34 illustrates typical engine operation and the transients obtained for two 8 second mainstage duration firings with constant secondary flowrate (AC13 and 15, $\dot{W}_s/\dot{W}_p$ = 3.0 percent). Typically, two 8 second firings with constant secondary flowrate were used to cover a pressure ratio range from approximately 350 to 40. The GG firing was initiated simultaneously with the primary but was cut 2 seconds prior to primary thrust chamber cutoff.

(C) The high altitude firing started above design pressure ratio and continued through the pressure ratio at which the nozzle base wake opens (PR ≈ 150 to 180 with 0 to 5 percent $\dot{W}_s$, respectively). During the last two seconds, the GG was turned off to obtain zero secondary flow data.

(C) The low altitude firing started with the nozzle operating in the open wake and continued through a pressure ratio of approximately 40. The GG was turned off 2 seconds before primary engine cutoff to obtain nozzle performance with no secondary flow. However, because of the slow decay of secondary chamber pressure after GG cutoff, valid performance data could not be obtained during the final 2 seconds of any altitude test with secondary flow.

TABLE 5
ALTITUDE TEST SUMMARY

Test Period	Date	Firing	Firing Duration, sec [1]	Primary Combustion Chamber P_{cp}, psia	$\dot{W}_p$, lb_m/sec	MR_p (—)	GG Combustion Chamber P_{cs}, psia	$\dot{W}_s$, lb_m/sec	MR_s (—)	Test Col[illegible] Pa_{min} [2] psia	Pa_{max} [2] psia
AA	6/30/66	1	2.9	280	25.3	1.70	-	0	-	0.42	1.8[illegible]
		2	7.5	304	27.3	1.77	-	0	-	0.51	3.46
		3	↓	305	27.4	1.77	-	0	-	2.65	8.74
AB	8/9/66	4	6	-	0	-	-	-	-	-	-
		5		-	0	-	-	-	-	-	-
		6		-	0	-	-	-	-	-	-
		7	↓	-	0	-	-	-	-	-	-
		8	1.0	-	-	-	-	-	-	0.59	1.85
		9	8.2	300	26.6	1.73	270	0.703	0.088	0.64	5.10
		10		295	26.2	1.75	116	0.325	0.109	0.81	5.44
		11		300	26.6	1.76	246	0.624	0.114	2.00	8.77
		12		298	26.4	1.71	116	0.320	0.111	1.98	8.87
AC	8/17/66	13		307	27.1	1.67	147	0.834	0.111	0.46	3.45
		14		304	26.8	1.79	249	1.34	0.118	0.48	3.35
		15		307	26.8	[illegible]	151	0.823	0.114	1.96	8.00
		16		305	26.7	1.71	251	1.33	0.117	2.00	8.26
		17		306	26.8	1.73	145	0.828	0.096	1.96	8.51
		18		305	26.6	1.73	144	0.817	0.097	0.57	3.75
		19		307	26.8	1.75	151	0.792	0.176	0.55	3.36
		20		306	26.8	1.74	154	0.794	0.174	1.98	7.83
		21		306	26.7	1.72	153	0.803	0.113	$P_{a_{avg}}$ =	0.88
AD	9/19/66	22		306	26.8	1.66	-	-	-		0.83
		23		318	25.8	1.66	-	-	-		1.00
		24	↓	318	26.1	1.74	-	-	-		0.96

1. Mainstage operation
2. During firing duration
3. During stabilized TCA and GG opera[illegible]
4. Shutdown caused by spurious signal [illegible] safety circuit designed to initiat[illegible] TCA cooling water outlet pressure

CONFIDENTIAL

TABLE 5
ALTITUDE TEST SUMMARY

...on Chamber	GG Combustion Chamber			Test Cell		Nozzle			
MR_p (—)	P_{cs}, psia	$\dot{W}_s$, lb_m/sec	MR_s (—)	Pa_{min} [2] psia	Pa_{max} [2] psia	PR_{min} [3] (—)	PR_{max} [3] (—)	$\dot{W}_s/\dot{W}_p$ percent	Remarks
1.70	-	0	-	0.42	1.85	150	406	0	TCA Checkout Firing
1.77	-	0	-	0.51	3.46	88	422	0	
1.77	-	0	-	2.65	8.74	35	93	0	
-	-	-	-	-	-	-	-	-	GG Checkout Firing
-	-	-	-	-	-	-	-	-	↓
-	-	-	-	-	-	-	-	-	↓
-	-	-	-	-	-	-	-	-	↓
-	-	-	-	0.59	1.35	200	257	2.60	Premature Shutdown[4]
1.73	270	0.703	0.088	0.64	5.10	65	360	2.64	
1.75	116	0.325	0.109	0.81	5.44	60	284	1.23	
1.76	246	0.624	0.114	2.00	8.77	39	143	2.34	
1.71	116	0.320	0.111	1.98	8.07	39	133	1.22	
1.67	147	0.834	0.111	0.46	3.45	103	532	3.08	
1.79	249	1.34	0.118	0.48	3.39	100	512	5.01	
1.68	151	0.823	0.114	1.96	8.00	44	154	3.05	
1.71	251	1.35	0.117	2.00	8.28	42	146	4.96	
1.73	145	0.828	0.096	1.96	8.51	41	147	3.08	
1.73	144	0.817	0.097	0.57	3.75	97	504	3.06	
1.75	151	0.792	0.176	0.55	3.36	102	526	2.94	
1.74	154	0.794	0.174	1.98	7.83	44	146	2.90	
1.72	153	0.803	0.113	$P_{a_{avg}}$ =	0.88	PR_{avg} =	347	3.00	
1.66	-	-	-		0.83		378	-	GG Oxidizer Inlet Orifice Plugged at Ignition
1.66	-	-	-		1.00		317	-	Unstable TCA Combustion; GG Drain Plug Lost at Ignition
1.74	-	-	-		0.96		340	-	GG Drain Plug Off

3. During stabilized TCA and GG operation
4. Shutdown caused by spurious signal from automatic safety circuit designed to initiate shutdown on low TCA cooling water outlet pressure

2

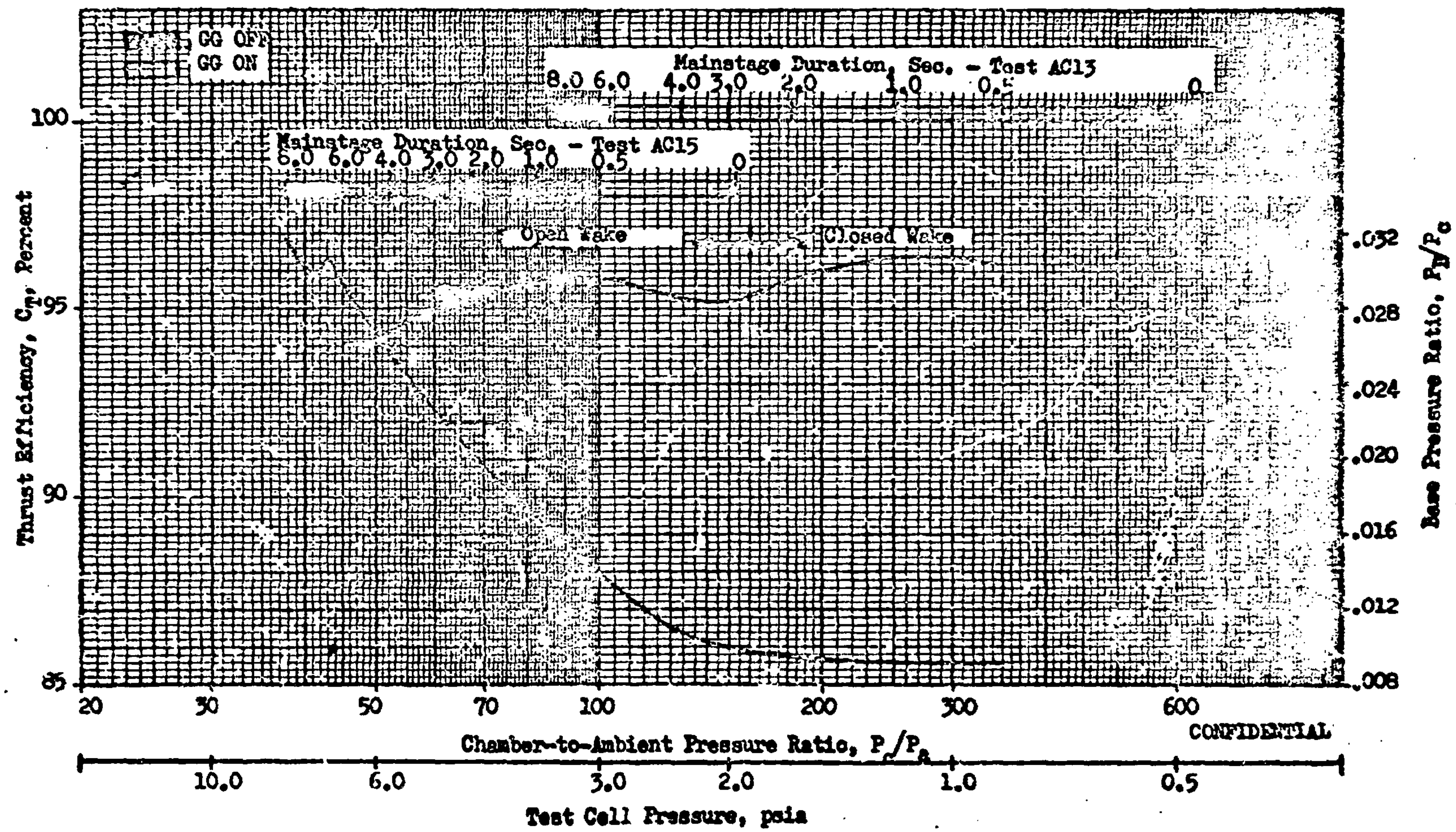

Figure 34. Typical Altitude Transient and Test Duration

(U) The first firing (AA01) was a 3-second checkout test with no secondary flow. Tests AA02 and AA03 were 7.4-second firings with no secondary flow over pressure ratios from 422 to 88 and 93 to 35, respectively. After these tests the engine was disassembled, inspected and reassembled with new seals and with the outer engine bolts reversed from the position shown in Fig. 7 . With the hex nuts located on the aft end of the engine, checking of the bolt torque and tightening of the outer casing and throat were more easily accomplished. Throat area data from the sea level and altitude firings indicated that the outer throat was not adequately tightened when the nuts were torqued on the injector end of the engine. Relatively large (to 3.5 percent) increases in measured throat area were noted after a single engine firing for tests with the engine assembled in this manner, whereas relatively small decreases in throat area were noted for the assembly configuration used for tests AB08 through AD24. This will be discussed again in the presentation of test results.

(U) The AB test series was to evaluate nozzle performance with 1 and 2 percent secondary flow using the low flowrate GG. Tests AB04 through AB07 were GG checkout firings to establish operating procedures. GG performance data was not obtained because of plugging of a ΔP control orifice in the oxidizer supply system. Fill times required for the oxidizer and fuel systems were approximately 7.5 and 0.4 seconds, respectively. Because of the large capacity of the feed system, the GG chamber pressure did not decay rapidly enough to establish zero secondary flow nozzle performance in the two second period between GG cutoff and primary engine cutoff.

(U) Test AB08 was a scheduled 8-second firing with 2.6 percent secondary flow which was prematurely shut down by an erroneous signal to a low coolant water pressure cutoff switch. Tests AB09 and AB10 were 8-second duration tests covering the high altitude transient with approximately 2.6 and 1.2 percent secondary flow, respectively. Tests AB11 and 12 were 8-second tests covering the low altitude transient with 2.35 and 1.2 percent secondary flow.

(U) The AC series of tests investigated nozzle performance with secondary flowrates of 3 and 5 percent. The high flowrate GG injector and orifice were installed for this series. Tests AC13 through AC16 were 8-second transient altitude tests with 3 and 5 percent secondary flow and a GG mixture ratio of .11. These tests completed the series designed to evaluate the effect of secondary flowrate (0 to 5 percent) at constant mixture ratio (≈ 0.1) on nozzle performance.

(U) Tests AC17 through AC20 were transient altitude tests to investigate the effect of GG mixture ratio on performance at a constant secondary flowrate of 3 percent. GG mixture ratios of 0.096 and 0.175 were tested. The low mixture ratio obtained was (0.096) somewhat higher than intended (.08) because of difficulties in precisely controlling the small oxidizer flow.

(U) The last test in the series, AC21, was conducted at a constant pressure ratio of approximately 350. This test was with 3 percent secondary flow and a GG mixture ratio of 0.1, identical to AC13 except for the constant altitude condition. Because the critical closed wake data was obtained over a very short (≈ 2 seconds) portion of mainstage operation, this test at constant altitude was conducted to provide more high altitude performance data. As will be shown later, excellent agreement was obtained between results for this test and the comparable transient altitude tests. The AC test series completed the planned program to evaluate secondary flow effects on performance.

(U) Eighteen constant altitude tests subsequent to the AC series were planned. The tests were to evaluate the effect of base configuration on nozzle performance and to provide additional high altitude data with various secondary flowrates. The first four tests were to evaluate a perforated base configuration (Fig. 14b) with secondary flowrates of 1, 2, and 3 percent. The remaining 14 tests were to be conducted with the open base and the modified (24 hole) flow diffuser (Fig. 14a) at constant pressure ratios of 300, 120 and 70 and secondary flowrates of 0, 1, 2, and 3 percent. However, operational difficulties were encountered during all three tests in the AD series and hardware damage was sustained precluding further testing.

(U) Test AD22 was a constant altitude test (PR = 378) with approximately 1 percent secondary flow. Main thrust chamber operation was satisfactory; however, the GG oxidizer inlet orifice plugged at start causing a reduced and unknown oxidizer flowrate(GG flowrates determined from system pressure drop) and poor combustion ($\eta_{C*} \approx$ 30 percent).

(C) Combustion instability occurred in the primary combustion chamber during firing AD23. Propellant flowrate and mixture ratio for this firing were nominal, and ignition was normal; however, approximately 0.5 seconds after iginition, TCA combustion became unstable (Fig. 35). Measured fundamental frequency and peak-to-peak amplitude of combustion instability pressure fluctuations were 487 cps and 60 psi (Fig. 35b).

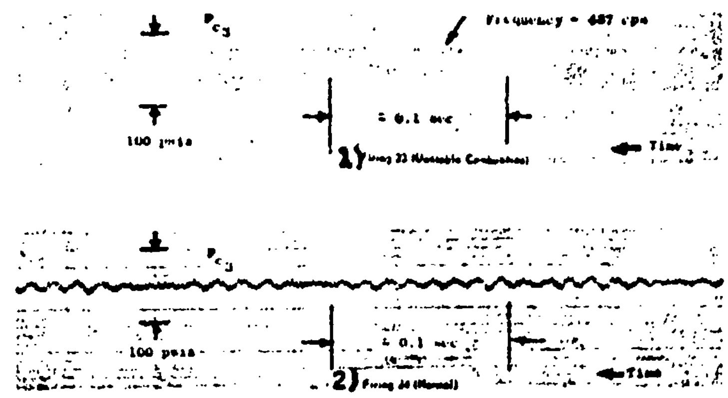

b. Combustion Pressure Waveforms

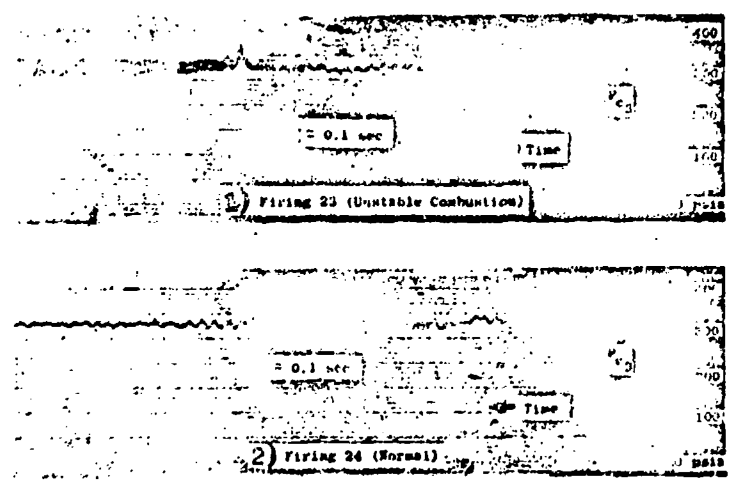

CONFIDENTIAL

a. Ignition Transient

Figure 35 . TCA Chamber Pressure Traces
(Reproduced from Reference 25)

(U) A cap on the GG drain fitting blew off during GG ignition in Test AD23, thereby venting an unknown portion of secondary flow upstream of the mounting plate. Test AD24 was conducted without knowledge of these operational difficulties and, although stable TCA combustion was obtained, the results are of questionable value.

(U) Inspection of the test hardware after firing 24 revealed extensive melting of the combustion chamber baffles, heavy deposits of melted copper from the baffles in the nozzle convergent section, several radial cracks in the injector outer fuel ring and excessive water leakage from a yielded braze joint in the outer throat. The damage, apparently caused by the severe thermal environment within the combustion chamber associated with the instability, was sufficient to preclude further testing (Figs. 36 and 37).

b. Outer Throat

a. Assembly With Outer Throat Removed

Figure 36 . Engine Condition; Post-Fire AD Series

b. Ring Cracking

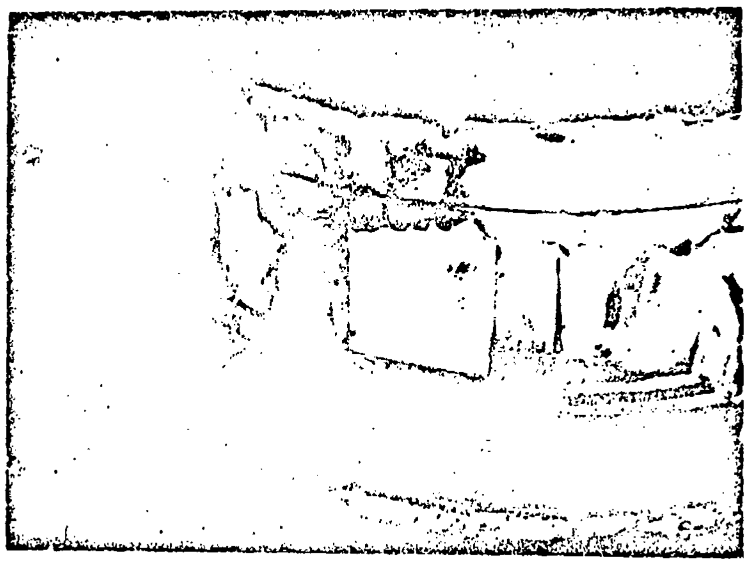

a. Baffle Erosion

Figure 37. Injector Damage; Post-Fire AD Series

DATA ANALYSIS

(U) Several studies were conducted to analyze the performance and determine the influence of operating conditions upon the performance of the cooled thrust chamber. The major studies were determination of the effect of heat loss to the model and cooling water, the effect of propellant impurities, and theoretical determination of nozzle performance. Using the results of these studies, a procedure to calculate performance from hot-firing data was developed and programmed for automatic computation. All measured data were averaged over a 0.5-second interval for input to the program. A discussion of these studies and the computational procedure is presented in the following sub-section.

(U) In addition, base heating information can be determined through analysis of temperature measurements by probes located in the base plate. A method of analysis is presented for determining the adiabatic wall temperature and heat transfer coefficient of the gases adjacent to the nozzle base plate.

Performance Parameters

(U) The basic parameters which were used to appraise the performance of the hot-firing model are the characteristic exhaust velocity efficiency of the primary combustion chamber, specific impulse efficiency of the thrust chamber and thrust efficiency of the nozzle. In addition, the base pressure is of prime concern since the base pressure acting over the base area contributes a significant portion of the thrust. Measured changes in base pressure with secondary flow can also be used to compute changes in nozzle performance independent of an accurate knowledge of engine thrust and flow changes and hence provide a check on these measurements. Base pressure and thrust efficiency are the parameters which are used to correlate aerodynamic spike hot-firing and cold-flow data.

(U) Characteristic velocity (C^*_p) efficiency of the primary flow is defined by

$$\eta_{C^*_p} = \frac{P_c \, A^*_p \, g_c}{C^*_{th} \, \dot{w}_p}$$

(U) Specific impulse efficiency of the aerodynamic spike thrust chamber is defined as the total nozzle thrust compared to the sum of the theoretical thrusts of the primary and secondary flows when optimally expanded to local ambient pressure.

$$\eta_{I_s} = \frac{F}{F_{opt,p} + F_{opt,s}}$$

where $F_{opt,p} = I_{s,opt,p} \, \dot{W}_p$

$F_{opt,s} = I_{s,opt,s} \, \dot{W}_s$

(U) Theoretical optimum specific impulses are based on the respective properties of the primary and secondary flows, however, the reference pressure ratio is the primary chamber pressure ratio for both flows.

(U) An alternate definition of specific impulse efficiency in common use and computed for this engine is

$$\eta_{I_s, top} = \frac{F}{I_{s,opt,p} \, (\dot{W}_p + \dot{W}_s)}$$

This definition references the measured thrust to the total theoretical thrust delivered if both the primary and secondary flows are considered to have a theoretical optimum I_s based on the primary flow properties. This is commonly referred to as a topping cycle efficiency.

(U) Nozzle thrust efficiency, C_T, is a measure of the nozzle expansion process including the base region and does not include combustion chamber effects or inefficiencies. It is defined in a similar manner to specific impulse efficiency with the exception that the reference thrusts are based upon actual characteristic velocities.

$$C_T = \frac{F}{F_{opt,p}\,\eta_{C^*_p} + F_{opt,s}\,\eta_{C^*_s}}$$

(U) When a theoretical primary reference only is used, a topping cycle nozzle thrust efficiency is defined by

$$C_{T,\,top} = \frac{F}{\eta_{C^*_p}\, I_{s,opt,p}\,(W_p + W_s)} = \frac{F}{\eta_{C^*_p}\, F_{opt,p}(1 + W_s/W_p)}$$

with no secondary flow, either definition reduces to

$$C_T = \frac{\eta_{I_s}}{\eta_{C^*}}$$

Theoretical Considerations in Reducing Data

(U) In determining the above parameters from the test data, all of the potential factors which may influence performance were considered. The areas which were considered included nozzle stagnation pressure, aerodynamic throat area, theoretical performance, propellant impurity, heat loss effects, and base pressure. In reducing data, factors whose effect was be[illegible]rved to be less than 0.1 percent were neglected.

(U) Nozzle Stagnation Pressure. Two chamber pressure taps (PC-1 and PC-2) are located near the injector, and one tap (PC-3) is located downstream of the injector near the contraction zone (Fig. 23, page 54). The chamber taps are located at a contraction ratio of approximately 10 where P_{static}/P_{total} = 0.9978 from one-dimensional ideal flow, and therefore, the pressure reading is corrected by 0.22 percent for static to total pressure.

(U) Combustion effects on the nozzle stagnation pressure were considered because there is a loss in total pressure for heat addition to a gas flowing in a constant area duct. Because a pressure tap (PC-3) is located 4 inches downstream of the injector just prior to the contraction zone, the combustion process can be considered to be completed and the combustion effect on P_c downstream of this tap is negligible. A drag (friction) analysis was conducted for this model, and the effect of drag between the pressure tap and throat was negligible. Nozzle total pressure was therefore computed from P_c = PC-3/.9978.

(U) Aerodynamic Throat Area. To accurately distinguish between nozzle efficiency and characteristic velocity efficiency a transonic potential flow analysis and boundary layer analysis of the throat region was conducted. Potential flow and frictional flow discharge coefficients were determined to be .9954 and .9939, respectively, with a resulting actual flow discharge coefficient, C_D equal to 0.9893.

(C) From geometry, the geometric throat area A_p is based upon the average throat gap (g) as determined by pretest and posttest measurements.

$$A_p = \pi(R_1 + R_2)\, g$$

where

R_1 = 11.064 in. (outer throat radius at the throat)

R_2 = 11.048 in. (inner throat radius at the throat)

or A_p = 69.53 g

(C) Applying the discharge coefficients C_D the aerodynamic throat area A^*_p is

$$A^*_p = 69.53\ C_D\ g = 68.79\ g$$

(U) During the sea level test program the throat gap was measured in six locations around the throat circumference. During the altitude test program, the throat gap was measured in sixteen locations and two sets of sixteen readings each were taken. A ball micrometer was used to obtain the measurements.

(U) A stress analysis was performed to determine the deformation of the throat region caused by thermal and pressure stress under hot firing conditions. There was an uncertainty as to the manner and direction of the throat deformations. However, the maximum deflection that could reasonably be expected would give a throat area change of 1 percent. The major effect on throat deflections was found to be a cyclic thermal buckling of the throat coolant slot walls.

(U) Because of the uncertainty as to the manner and exact magnitude of the throat deflection, an analytical stress correction to the throat area was not used in the data analysis. The determination of the throat area during a firing was made by considering both the measured pre- and posttest throat areas and a throat change established by the change in primary thrust during the firing. This method is discussed in detail in the results section.

(U) Theoretical Performance. Theoretical propellant performance was calculated for NTO/UDMH-N_2H_4(50-50) based upon one-dimensional expansion in chemical equilibrium (shifting performance) for mixture ratios of 1.4, 1.6, 1.8 and 2.2 at chamber pressures of 300, 400, and 500 psia. Figure 38 is a sample page of the IBM printout (from Rocketdyne's theoretical propellant performance program) at a mixture ratio of 1.8 and chamber pressure of 300.

TABLE II - EXIT CONDITIONS ** SHIFTING COMPOSITION

DATA TAPE 35 11/24/65 P = 300 PSIA

PROPELLANT	HEAT OF FORMATION	RELATIVE WEIGHT	MASS FRACTION	RELATIVE VOLUME	DENSITY
N2O4, 298K 1.0000	-4.680	1.4000	0.5833	0.9770	1.4330
HUDNH5G 1.0000	29.373	1.0000	0.4167	1.1282	0.8064

	PC/PE	P PSIA	T DEG. K	GAMMA	EPSILON	CF-VAC	I-VAC LB-SEC/LB	B	CF-OPT	I-OPT LB-SEC/LB
	1.00	300.000	3014.5	1.178	0.	0.	0.	0.	0.	0.
THROAT	1.76	170.087	2777.2	1.192	1.00	1.2400	221.0	0.59	0.6730	120.0
	8.49	35.345	2118.2	1.236	2.00	1.4629	260.6	1.19	1.2263	218.6
	20.41	14.696	1784.8	1.250	3.54	1.5770	281.1	2.10	1.4036	250.2
	33.74	8.891	1613.1	1.255	5.00	1.6323	291.0	2.97	1.4841	264.6
	43.76	6.856	1530.0	1.257	6.00	1.6583	295.6	3.57	1.5212	271.2
	54.39	5.516	1463.4	1.258	7.00	1.6788	299.3	4.16	1.5501	276.3
	69.38	3.357	1321.0	1.261	10.00	1.7216	306.9	5.94	1.6097	286.9
	155.83	1.925	1177.3	1.262	15.00	1.7637	314.4	8.91	1.6674	297.2
	192.09	1.562	1127.3	1.262	17.50	1.7781	317.0	10.40	1.6870	300.7
	230.07	1.304	1085.9	1.262	20.00	1.7900	319.1	11.88	1.7030	303.6
	269.60	1.113	1050.8	1.262	22.50	1.8000	320.9	13.37	1.7165	306.0
	310.54	0.966	1020.5	1.261	25.00	1.8086	322.4	14.85	1.7281	308.1
	352.81	0.850	993.8	1.261	27.50	1.8162	323.7	16.34	1.7352	309.9
	396.27	0.757	970.2	1.261	30.00	1.8229	324.9	17.83	1.7472	311.4
	486.54	0.617	929.9	1.261	35.00	1.8342	327.0	20.80	1.7623	314.1
	580.93	0.516	896.4	1.261	40.00	1.8437	328.6	23.77	1.7748	316.4
	780.40	0.384	843.3	1.261	50.00	1.8585	331.3	29.71	1.7944	319.9
	992.59	0.302	802.3	1.262	60.00	1.8698	333.3	35.65	1.8094	322.5
	1215.91	0.247	769.2	1.263	70.00	1.8789	334.9	41.59	1.8214	324.7
	1449.01	0.207	741.8	1.262	80.00	1.8864	336.3	47.54	1.8312	326.4
	1690.49	0.177	718.9	1.258	90.00	1.8928	337.4	53.48	1.8396	327.9
	1938.79	0.155	699.6	1.250	100.00	1.8984	338.4	59.42	1.8468	329.2

Figure 38. Propellant Performance Printout

(U) A summary of theoretical primary performance is presented in Figs. 39 to 42. A summary of the gas generator combustion gas properties is shown in Appendix, 4, Figs. 213 to 216. Theoretical performance, as shown in the figures was used in a data reduction program to determine nozzle reference performance reported in Ref. 25. Although theoretical primary C* were properly accounted for as a function of mixture ratio, primary theoretical $I_{s,opt}$ was programmed as a function of pressure ratio at a constant mixture ratio. Unfortunately this tends to prejudice the results towards those tests at high mixture ratio. As an example, one high altitude test with no secondary flow (AA01) was conducted at a primary mixture ratio of 1.77 whereas one high altitude test with 3 percent secondary flow was conducted at a primary mixture ratio of 1.67, (AC13). At a mixture ratio of 1.67 and a pressure ratio PR of 300, $I_{s,opt} = 311.0$ whereas at the same PR and a mixture ratio of 1.77, $I_{s,opt} = 312.5$. From the expression

$$C_T = \frac{F}{\eta_{C^*_p} I_{s,opt,\,p}\, \dot{w}_p}$$

and with correct value of $\eta_{C^*_p}$

$$\frac{(C_T)_{MR = 1.77}}{(C_T)_{MR = 1.67}} = \frac{312.5}{311.0} = 1.0048$$

(U) A difference of 0.1 unit in mixture ratio results in a difference of 0.48 percent in both the relative C_T and $\eta\, I_s$ for two tests performing equally but at this difference in mixture ratio. For the altitude test program (see Table 5) the no secondary flow tests were "automatically" higher performing

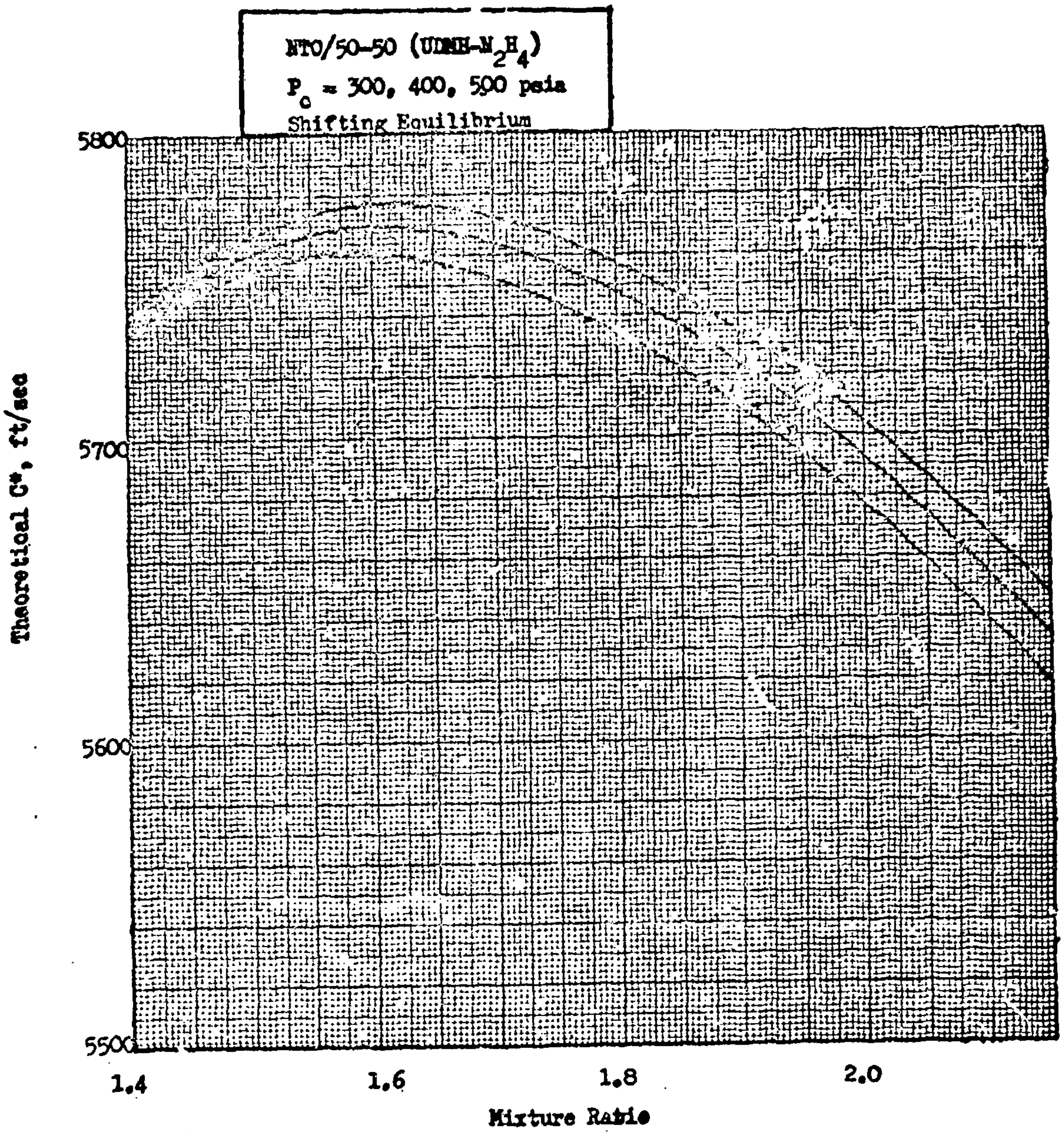

Figure 39. Theoretical C* vs Mixture Ratio

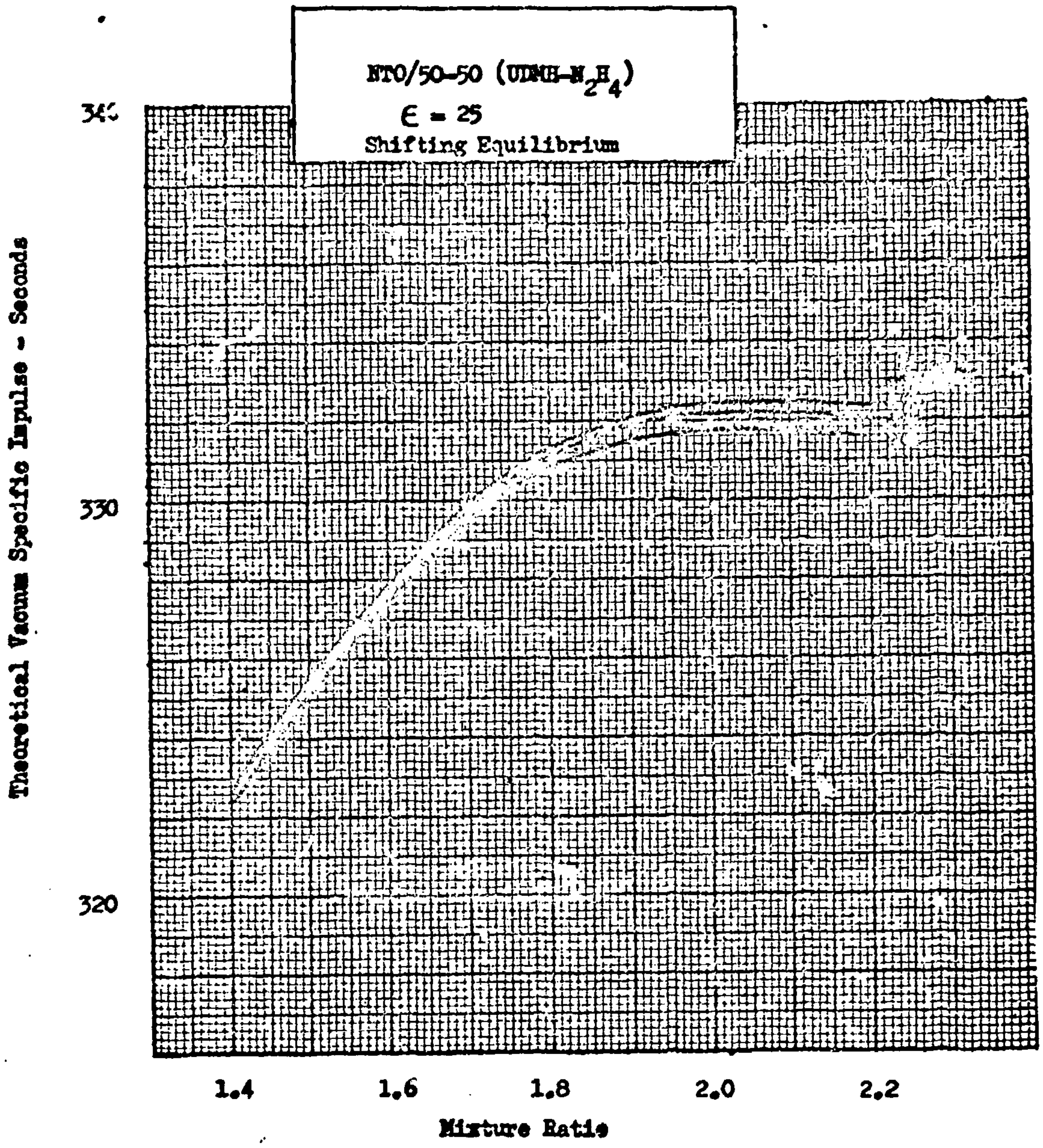

Figure 40 . Vacuum Specific Impulse vs Mixture Ratio

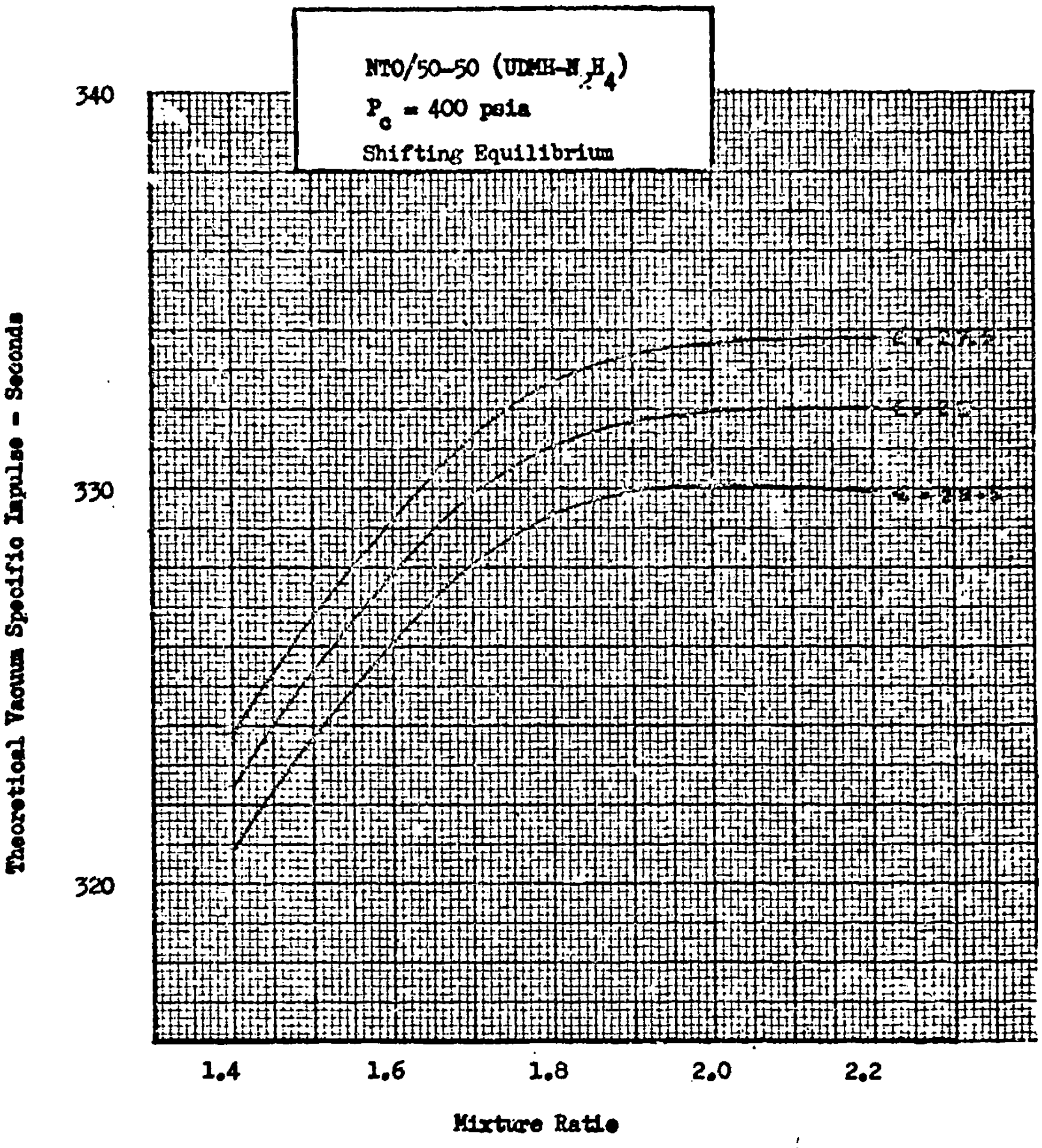

Figure 41. Vacuum Specific Impulse vs Mixture Ratio

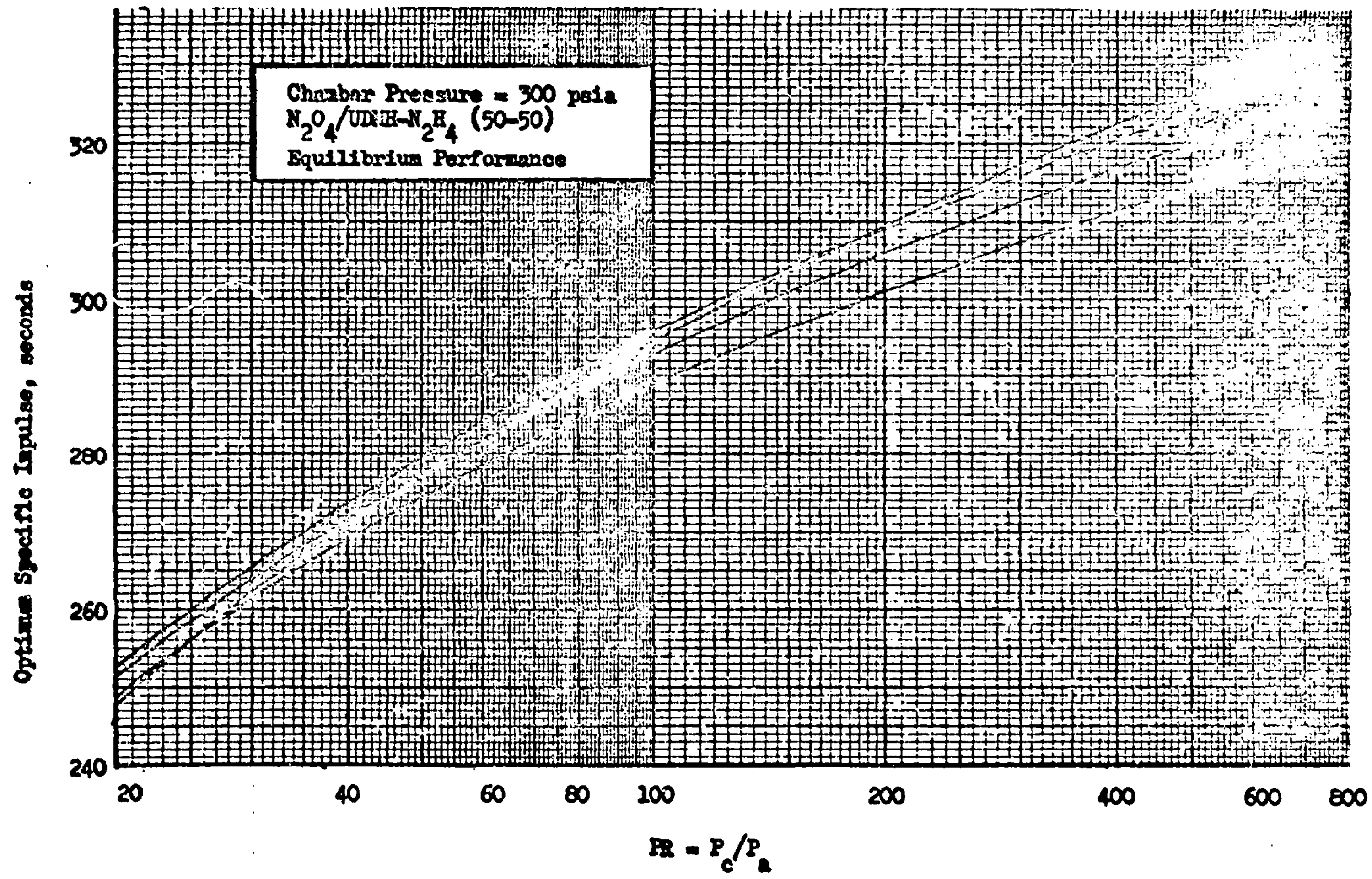

Figure 42 . Optimum Specific Impulse vs. Pressure Ratio

by from 0.2 to 0.5 percent than the tests with secondary flow as reported in Ref. 25 because they were accomplished at a higher mixture ratio. Since these performance differences are in the order of magnitude of the gains expected with secondary flow it is necessary to include the effect of mixture ratio on theoretical reference performance.

(U) A computer program using tabulated theoretical performance data and interpolating mixture ratio, PR, and P_c effects was written at Rocketdyne and used to obtain the final performance data presented in this report. The measured quantities of thrusts, flows, pressures and temperatures obtained from the test sources were used for input.

(U) Propellant Impurity. Because water content in the fuel and oxidizer will change the theoretical performance, theoretical propellant performance was determined for NTO/50-50 with various concentrations of water. In general, water in the propellants increases C_f and decreases C* with a net decrease in I_s. The changes in C* and I_s at a chamber pressure of 400 psia are presented in Fig. 43. These changes are valid for a chamber pressure range of 300 to 500 psia since the change in performance is only slightly dependent upon chamber pressure.

(U) Values of $\eta_{C^*_{H_2O}}(=1-\Delta\eta_{C^*_{H_2O}})$ and $\Delta I_{s_{H_2O}}$ were hand computed for each test and are tabulated in Appendix 1. Maximum values were $\Delta I_{s_{H_2O}}$ = -.30 seconds and $\eta_{C^*_{H_2O}}$ = .9987.

(U) Heat Loss Effects. The effect of heat loss to the cooling water was determined using a computer program. This program calculates one-dimensional theoretical nozzle performance with heat removal or addition at the injector and heat removal in the nozzle. Heat removal in the nozzle is performed in increments by a constant pressure process. The program maintains the propellant in chemical equilibrium through the expansion with heat removal. The magnitude and schedule of the theoretical heat loss per pound of primary propellant, Q_{tn}, for input to the program was determined from a theoretical heat transfer analysis of the actual thrust chamber. At chamber pressures of 300, 400, and 500 psia and a mixture ratio of 1.8, Q_{th} was computed to be 193.1, 184.9, and 177.9 Btu/lb.

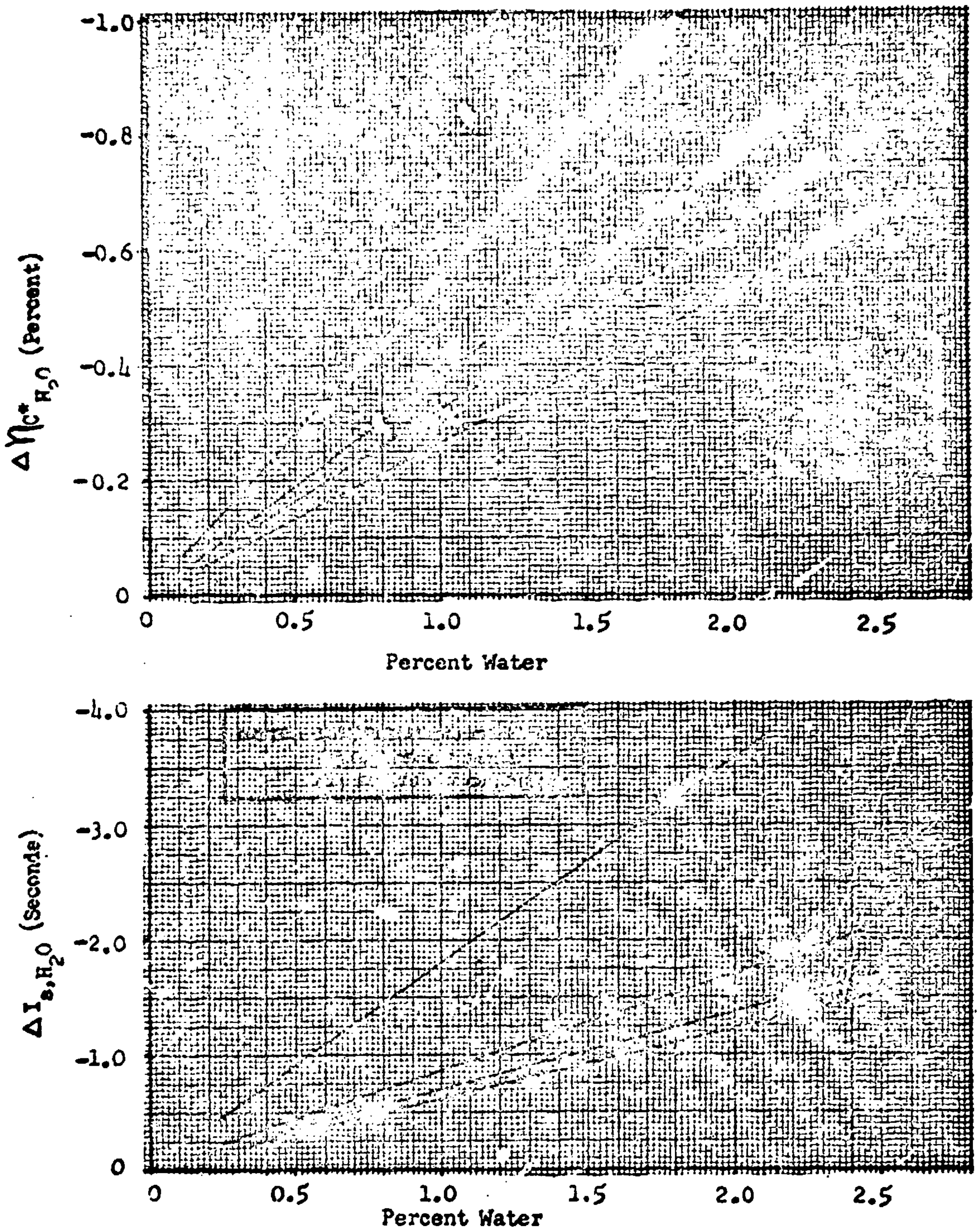

Figure 43. Effect of Water on Theoretical Performance

(U) The decrease of C* efficiency caused by heat removal from the combustion chamber is shown in Fig.44 for P_c of 300 and 400 and MR = 1.8. The ratio of the actual total heat loss per pound of propellant, Q, to the theoretical loss per pound of propellants, Q_{th}, is used as a normalizing parameter. Because the hot-firing tests performed on this nozzle were at various altitudes and because $\eta_{H.L.}$ ($\eta_{H.L.} = I_{s,vac,H.L.}/I_{s,vac,\ adiabatic}$)
where

$I_{s,vac,H.L.}$ = theoretical vacuum specific impulse for a given heat removal rate and schedule

$I_{s,vac,adiabatic}$ = theoretical vacuum specific impulse with no heat removal

can only be directly applied to vacuum specific impulse, a curve of $\Delta I_{s,H.L.}$ (defined as ($I_{s,vac,H.L.} - I_{s,vac,adiabatic}$)) vs heat removed was computed (Fig. 45). The $\Delta I_{s,H.L.}$ was directly applied to the site specific impulse to obtain an adiabatic specific impulse.

(U) The effects of variations in heat loss, chamber pressure and mixture ratio were determined by perturbating each of these parameters over a range of 50 to 200 percent of the heat loss, chamber pressures from 300 to 500 psia and mixture ratios from 1.4 to 2.2. In Fig.46. and 47 are shown the performance variation of $\eta_{C^*_{H.L.}}$ and $\Delta I_{s,H.L.}$ for variations in mixture ratio and chamber pressure.

(U) Total heat transfer to the model includes the heat transfer to the cooling water plus the heat absorbed by the injector baffles in the combustion chamber. For a given test, the actual heat transfer to the cooling water is determined by measuring the bulk temperature rise and water flowrate. The heat absorbed by injector baffles is estimated from a heat transfer analysis rather than test data since the actual heat absorption or baffle temperature at a given point is difficult to measure.

(U) Maximum baffle surface temperatures are shown in Fig. 48 to 50 for chamber pressures of 300, 350, and 400 psia and for C* efficiencies of 100 and 90 percent. Also shown are total heat absorption for the baffles as a function of test duration. These results are based upon the assumption that heating occurs along the surface exposed directly to the gas and to the blunt trailing edge but not to the surfaces immediately adjacent to the chamber walls. These

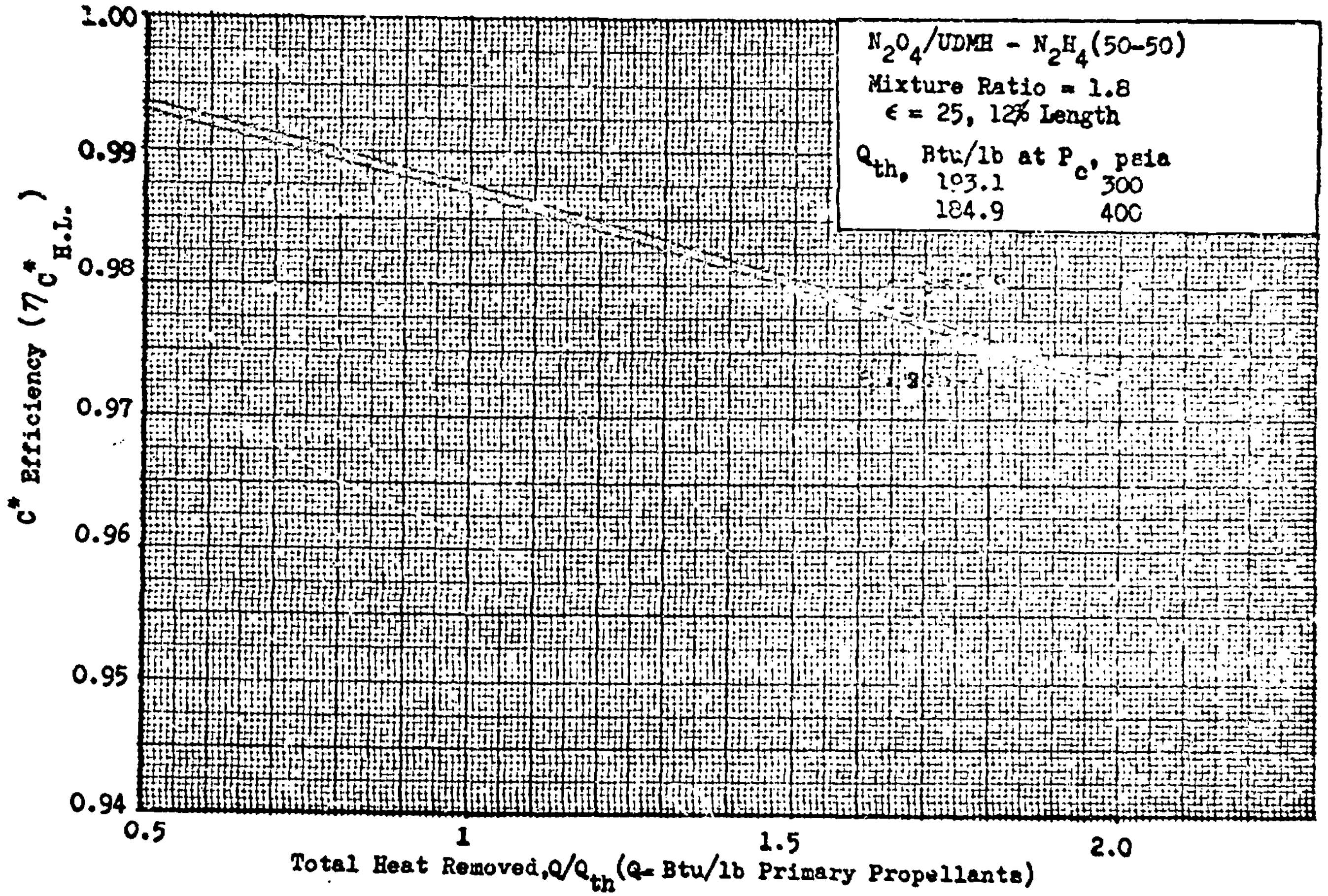

Figure 44 . Effect of Heat Loss on $\eta_{C^*_{H.L.}}$

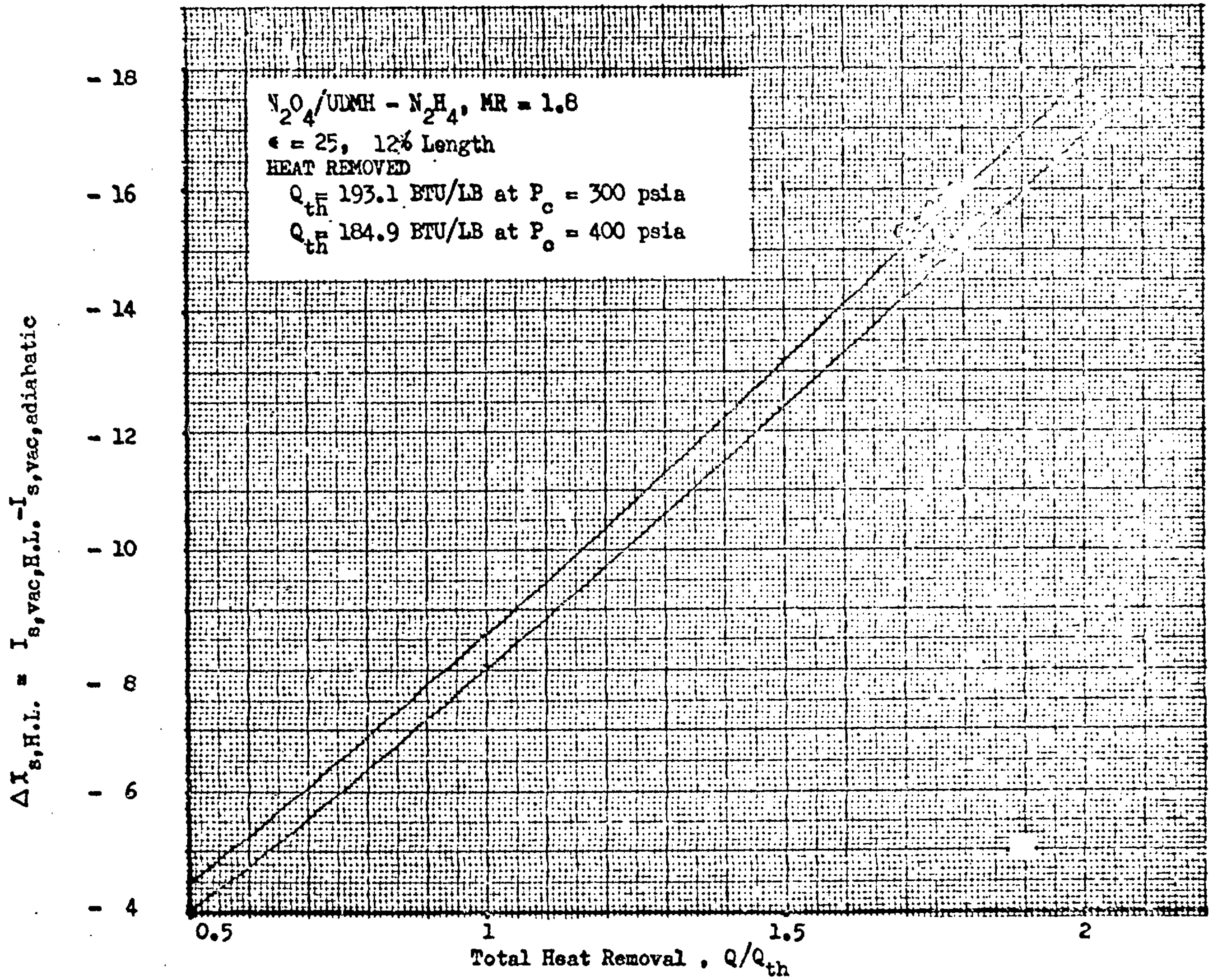

Figure 45. Effect of Heat Loss on Vacuum Specific Impulse

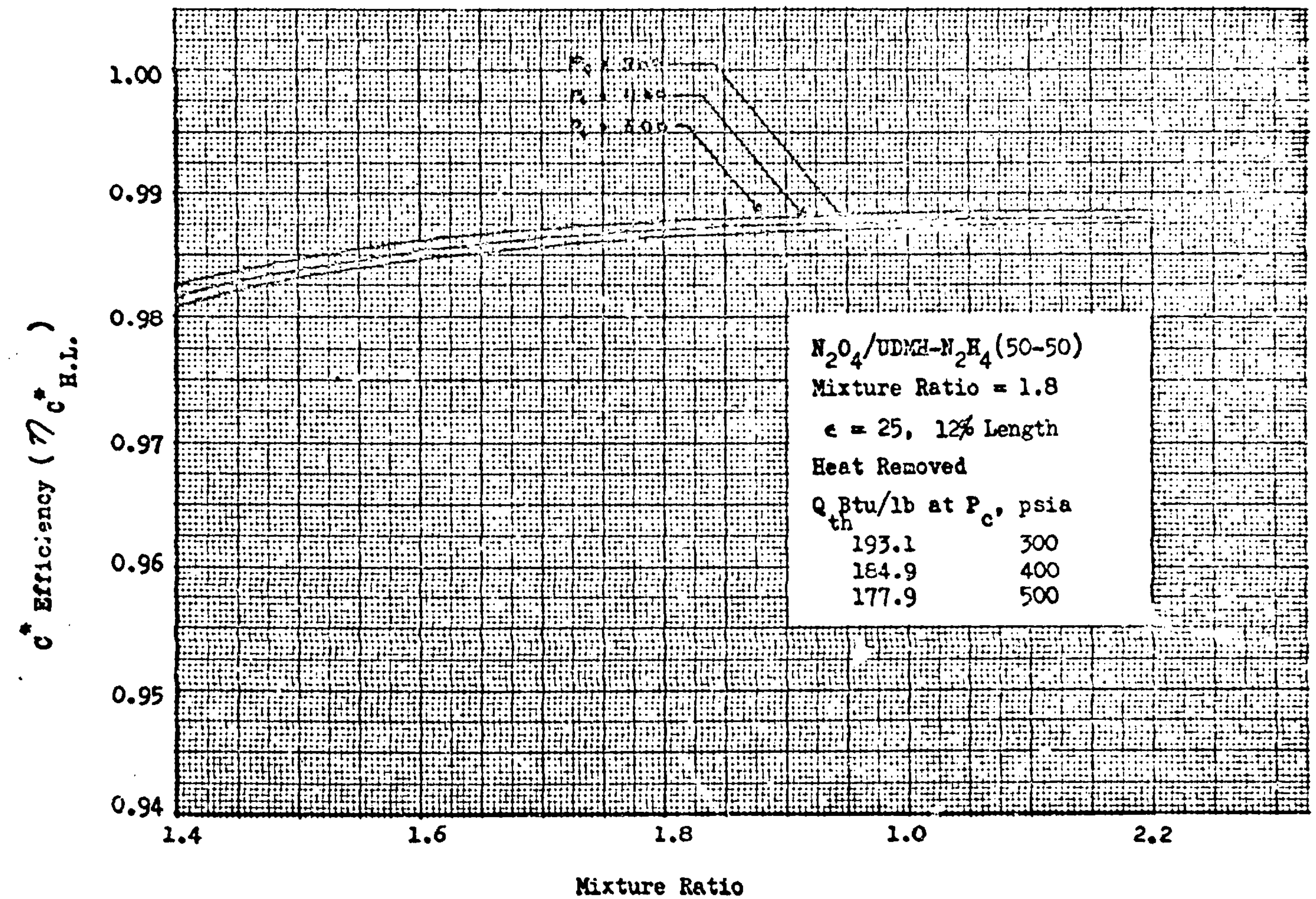

Figure 46. Heat Loss Effects on $\eta_{c^*_{H.L.}}$ vs Mixture Ratio and Chamber Pressure

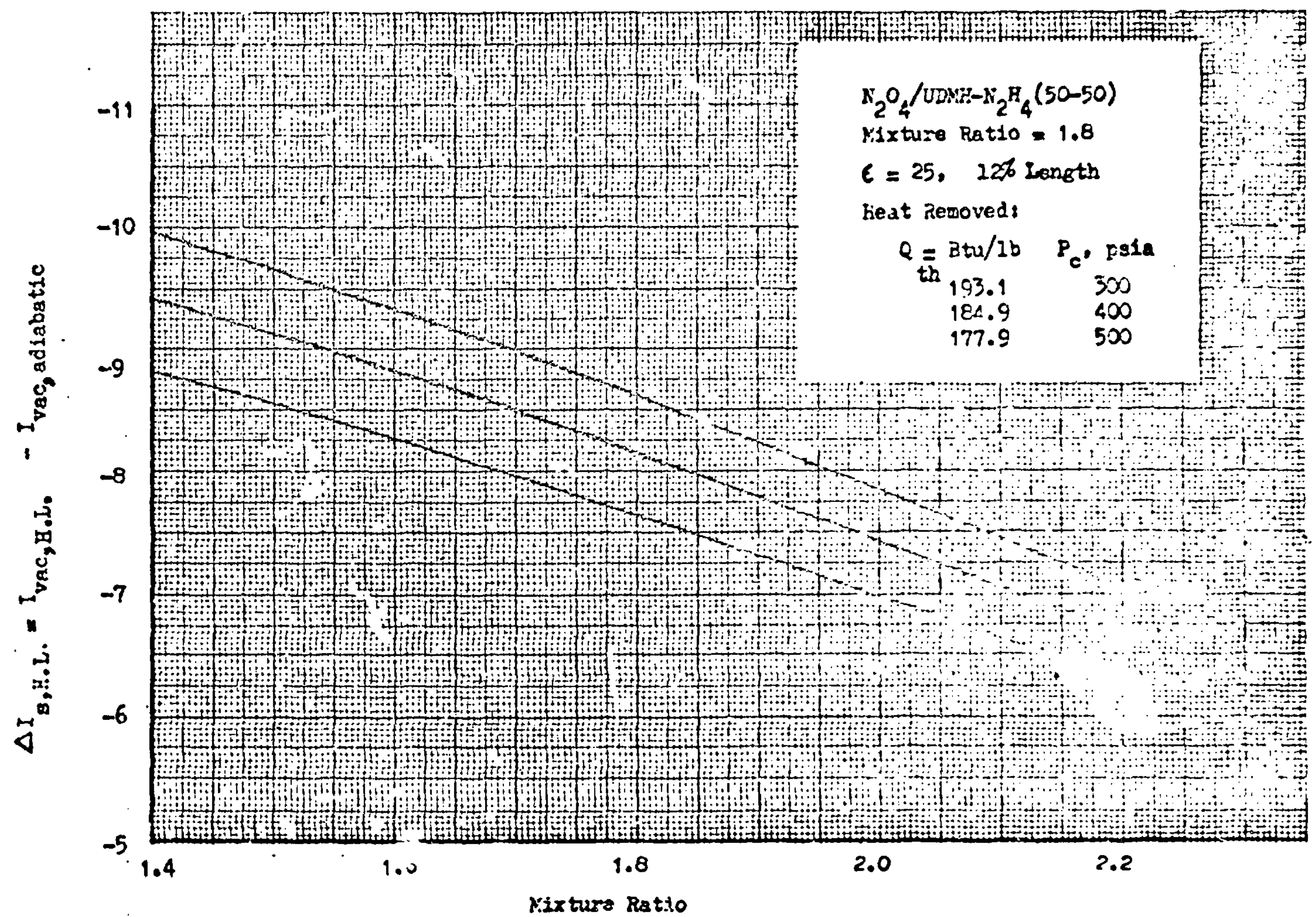

Figure 47. Heat Loss Effects on $I_{s,H.L.}$ vs. Mixture Ratio and Chamber Pressure

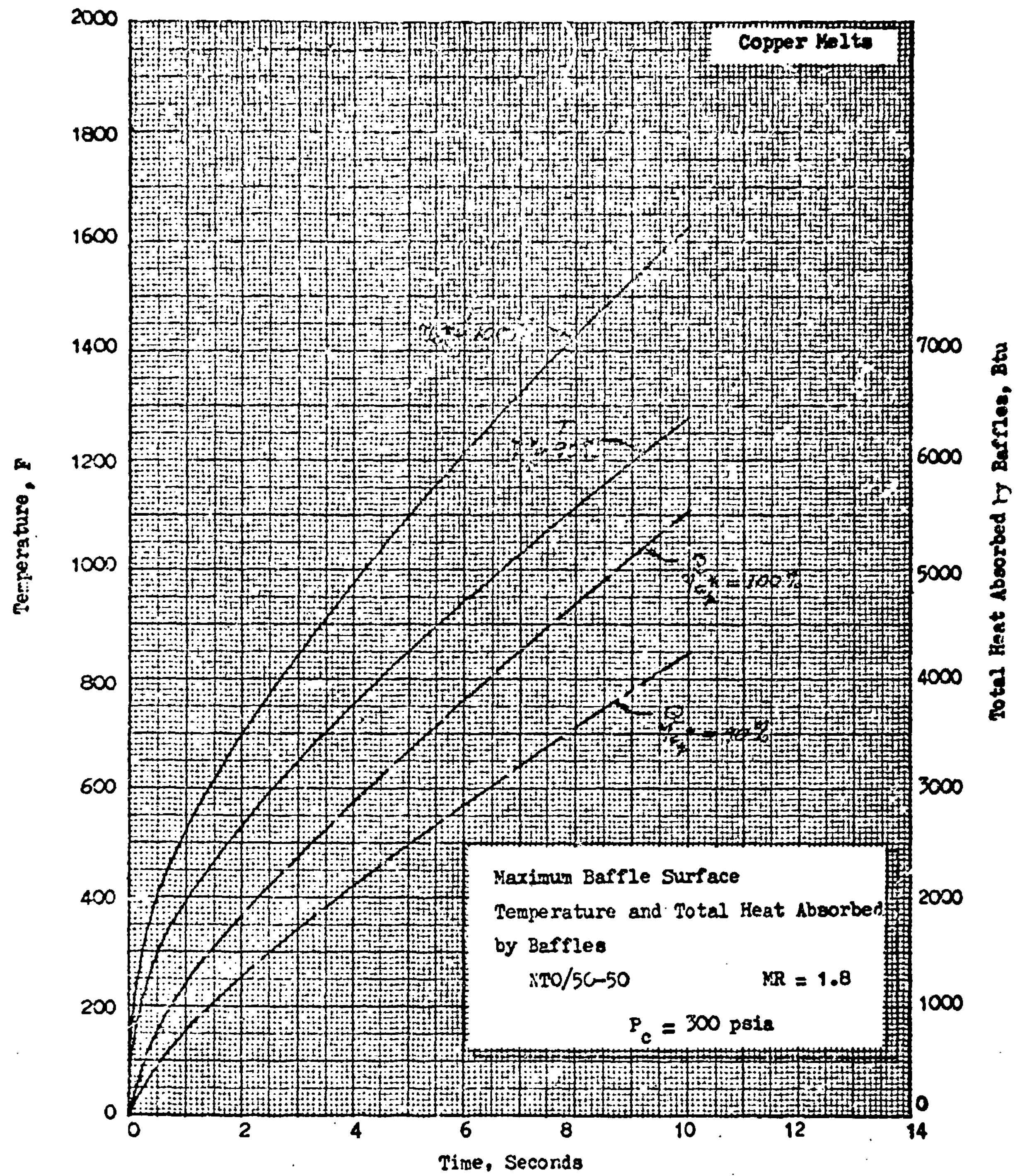

Figure 48. Baffle Surface Temperature and Total Heat Absorbed vs. Time

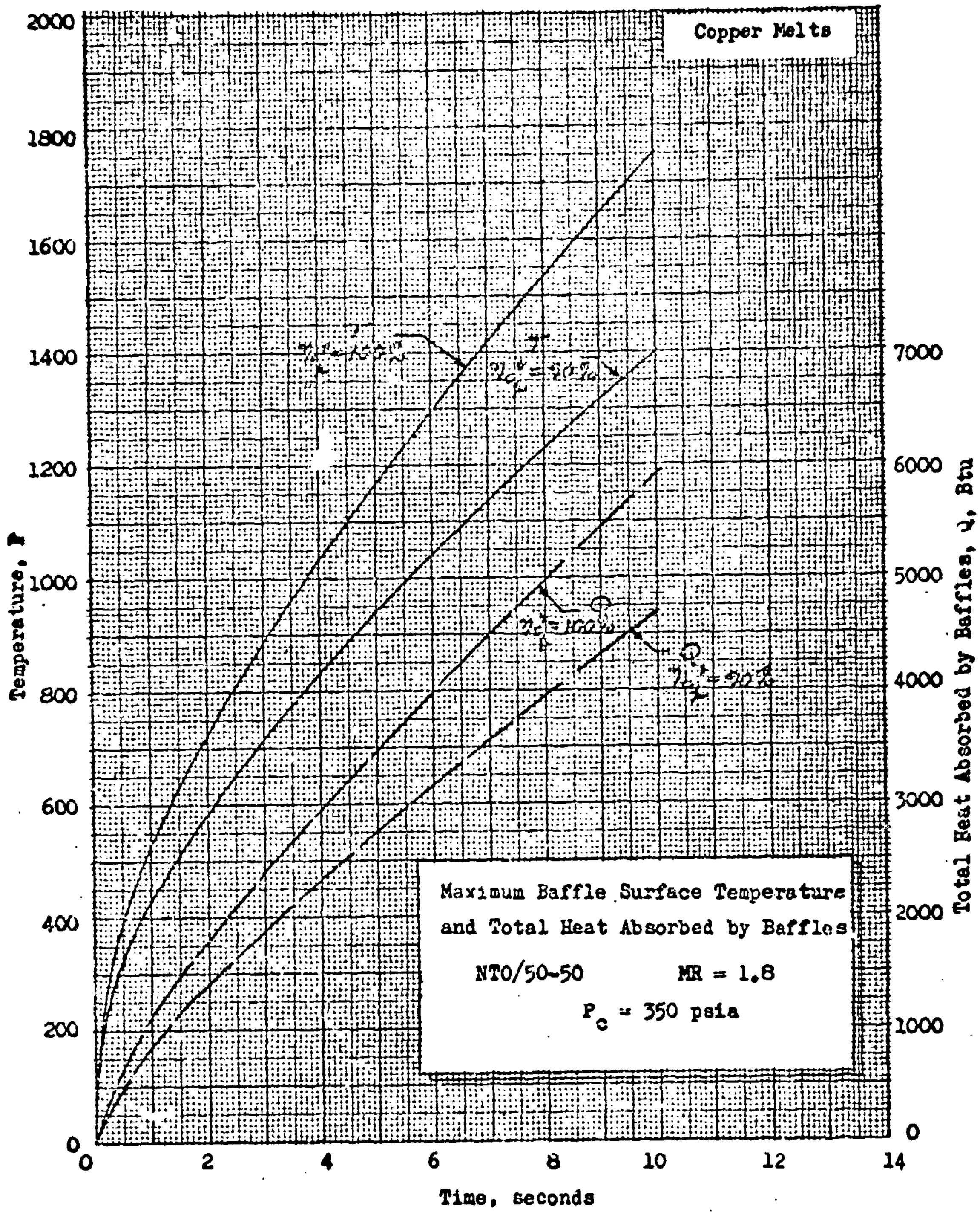

Figure 49. Baffle Surface Temperature and Heat Absorbed vs Time

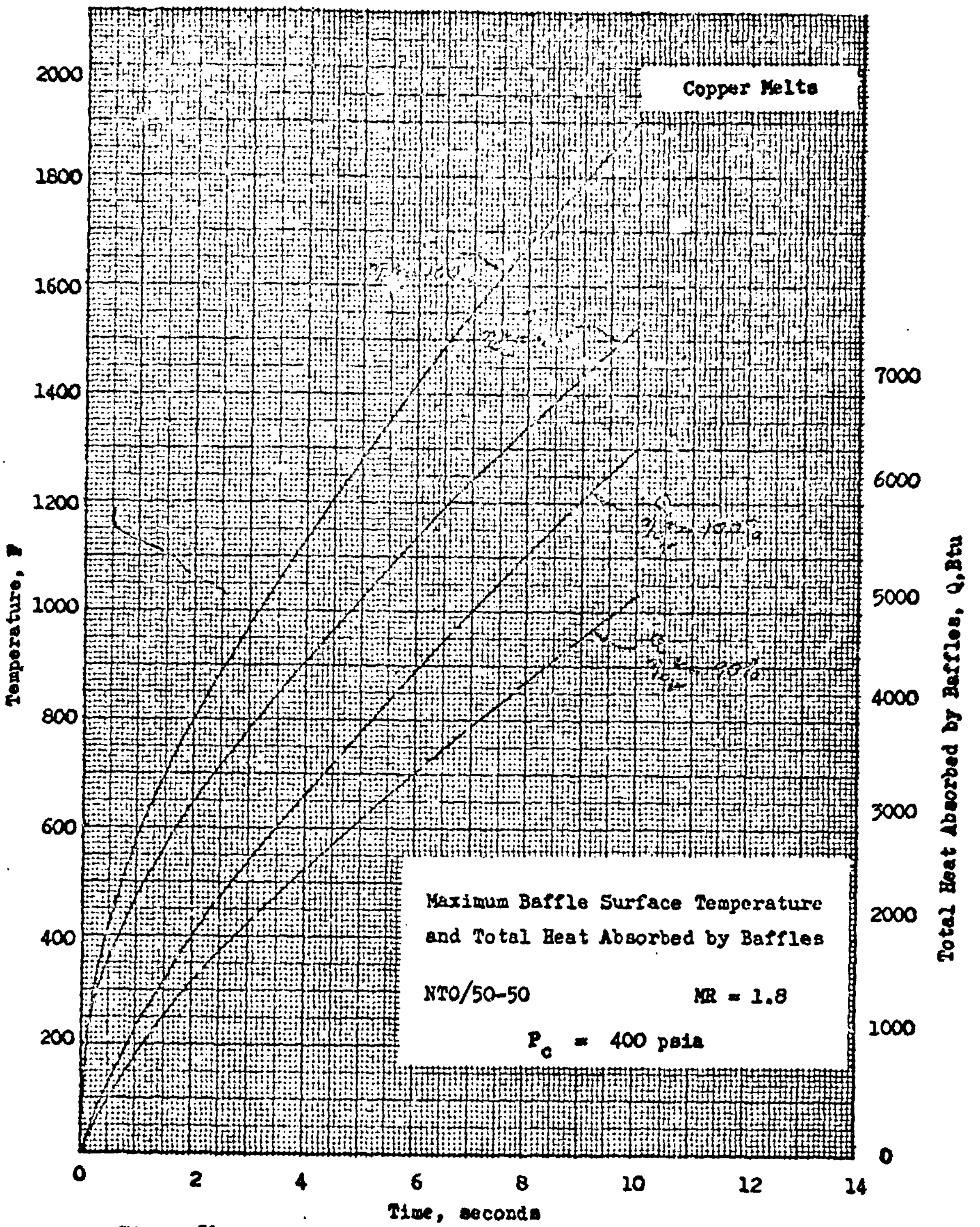

Figure 50. Baffle Surface Temperature and Heat Absorbed vs Time

assumptions are considered to be the most realistic. The rate of absorption is not constant but decreases with increasing duration. Results indicate that the baffle heat absorption rates are approximately one-sixth the coolant absorption rates.

(U) Heat loss effects were hand computed from measured water flowrate and temperature rise data. A typical outlet water temperature profile is shown in Fig. 51 . Since there is a lag in water temperature rise the maximum temperature achieved was used in the heat loss computation. A constant baffle heating rate of 445 BTU/sec was used. The heating rates for all tests were compared at the same firing duration by comparing water temperature rise curves and adjusting for the temperature rise over the difference in mainstage duration. This correction was approximately 1°/sec or less.

(U) The ratio of the "measured" heat loss per pound of propellant, Q, to the theoretical heat loss, Q_{th}, was computed from

$$Q/Q_{th} = \frac{C_{PH_2O}\left[\left(\int \dot{W}_{H_2O}\,\Delta T_{H_2O}\right)_{inner} + \left(\int \dot{W}_{H_2O}\,\Delta T_{H_2O}\right)_{outer}\right]}{193.1\int \dot{W}_p} + \frac{445}{193.1\ \dot{W}_p}$$

for the altitude tests and from

$$Q/Q_{th} = \frac{C_p\ \dot{W}_{H_2O}\ \Delta T_{H_2O}}{193.1\ \dot{W}_p} + \frac{445}{193.1\ \dot{W}_p}$$

for the sea level tests.

(U) For the initial tests at approximately 400 psia chamber pressure, a reference constant of 184.9 was used in place of 193.1.

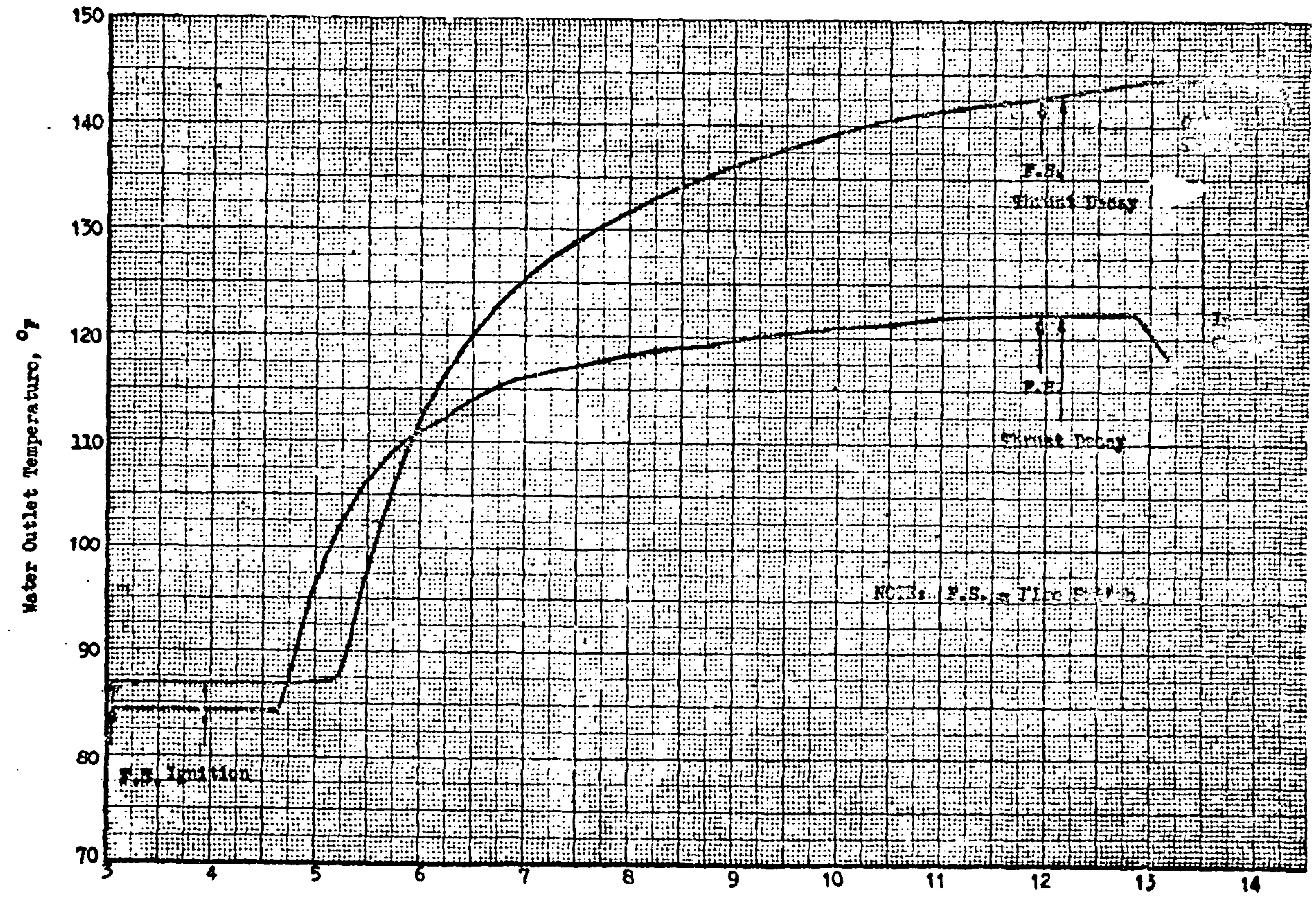

Figure 51. Cooling Water Outlet Temperature, Test AB-11

(U) It should be noted that the heat loss effects are corrected to that of an adiabatic engine. This is slightly conservative when considering the engine in a regeneratively cooled application. The effect of the heat being removed and added to the inlet propellants was investigated for this engine operating at 400 psia chamber pressure using the same computer program. The effect of the overall heat removal and addition cycle as shown in Fig. 52 was to slightly improve engine performance over an adiabatic engine.

(U) Base Pressure. Six pressure taps are located in the nozzle base cavity and exit lip to measure the base pressures as shown in Fig. 53. The resulting average base pressure is determined by taking a weighted average of the six readings by area. Each of the two lines of taps is weighted by one-half the base cavity area, and the lip tap is weighted by the lip area. Based on the geometry of the base region, Fig. 53 presents the areas used to weight the pressure readings.

(U) Change in engine performance with secondary flow relative to performance without secondary flow can be computed from the equations

$$\eta_{I_s,\dot{W}_s} = \eta_{I_s,\dot{W}_s=0} \left[\frac{1 + \left(\frac{\Delta \bar{P}_B}{P_c}\right)\left(\frac{P_c}{\dot{W}_p}\right)\left(\frac{A_B}{I_{s,\dot{W}_s=0}}\right)}{1 + \left(\frac{I_{s,opt,s}}{I_{s,opt,p}}\right)\left(\frac{\dot{W}_s}{\dot{W}_p}\right)} \right]$$

$$C_{T,\dot{W}_s} = C_{T,\dot{W}_s=0} \left[\frac{1 + \left(\frac{\Delta \bar{P}_B}{P_c}\right)\left(\frac{P_c}{\dot{W}_p}\right)\left(\frac{A_B}{I_{s,\dot{W}_s=0}}\right)}{1 + \frac{\eta_{C^*_s}}{\eta_{C^*_p}}\left(\frac{I_{s,opt,s}}{I_{s,opt,p}}\right)\left(\frac{\dot{W}_s}{\dot{W}_p}\right)} \right]$$

Propellant: N_2O_4/UDMH-N_2H_4

Pc = 400 psia

MR = 1.8:1

Nozzle: Advanced Aerospike

ϵ = 25:1 12% Length

Regeneratively Cooled

Heat Removed and Added: Q_{th} = 184.9 Btu/lb.

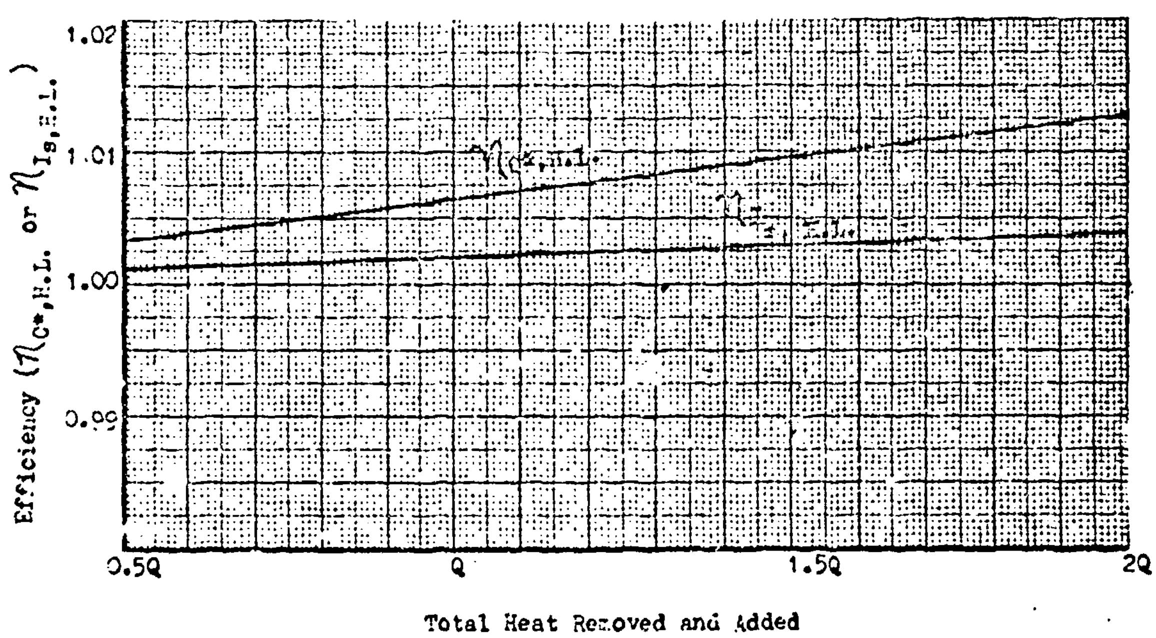

Figure 52. Nozzle Heat Transfer Efficiency Versus Total Heat Transferred-Regeneratively Cooled Nozzle

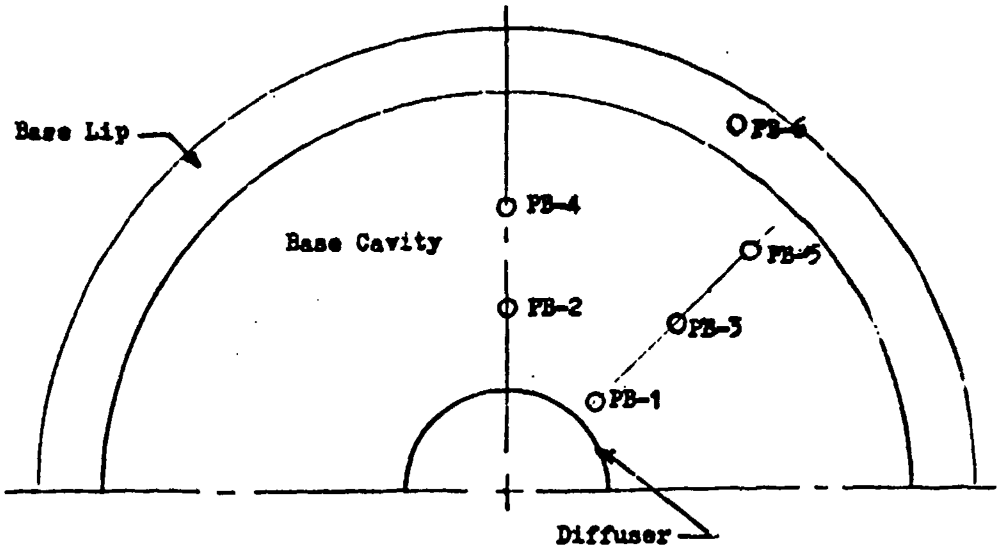

BASE REGION

Base Cavity Area	120.3
Base Lip Area	47.2
	167.5 sq. in.

Integrated Base Pressure = $\sum P_b \times A$ x Factor

P_b Tap I.D.	Area - Sq In.	Area Factor, Percent of Total Area
PB-1	20.1	12.0
PB-2	30.1	17.9
PB-3	20.1	12.0
PB-4	30.1	17.9
PB-5	20.3	12.0
PB-6	47.1	28.2
	167.5	100.0

Figure 53. Integrated Base Pressure

Performance Calculation Procedure

(U) The equations used to determine engine performance are described below. The equations with an asterisk were used in the Rocketdyne data reduction program. Other computed quantities were hand computed or supplied by the Rocketdyne Research and AEDC RTF test organizations.

(U) Measured thrusts, flows (except H_2O), and pressures are 0.5 second averages except for two tests (RDC2 and RDO3) which were 0.5 second Beckman data slices.

1. $P_c = PC\text{-}3/.9978$ (See Fig. 23, page 54 for location of PC-3)
2. $\eta C^*_{H.L.} = f\ (Q,\ MR_p,\ P_c)$ Figs. 44 and 46
3. $\Delta I_{s,H.L.} = f\ (Q,\ MR_p,\ P_c)$ Figs. 45 and 47
4. $\eta C^*_{H_2O} = f$ (percent H_2O, MR_p) Fig. 43
5. $\Delta I_{s,H_2O} = f$ (percent H_2O, MR_p) Fig. 43
6. $\bar{P}_B = .12\ (PB\text{-}1 + PB\text{-}3 + PB\text{-}5) + .179\ (PB\text{-}2 + PB\text{-}4) + .282\ PB\text{-}6$

*7. $\bar{P}_B/P_c = \bar{P}_B/P_c$

*8. $C^*_p = g_o\ P_c\ A^*_p/\dot{W}_p\ \eta C^*_{H.L.}$ $\quad g_o = 32.174\ lb_f\text{-}ft/lb_m\text{-}sec^2$

*9. $C^*_s = g_o\ P_{c,s}\ C_{D,s}\ A_s/\dot{W}_s$ $\quad C_{D,s} = 0.85$ (secondary orifice discharge coefficient)

*10. $C^*_{th,p} = f\ (P_c,\ MR_p)$ (tabulated values programmed)

*11. $C^*_{th,s} = f\ (P_{c,s}\ MR_s)$ (tabulated values programmed)

*12. $I_{s,opt,p} = f\ (P_c,\ MR_p,\ PR_p)$ (tabulated values programmed)

*13. $I_{s,opt,s} = f\ (P_c,\ MR_s,\ PR_s)$ (tabulated values programmed)

*14. $\eta C^*_p = C^*_p/C^*_{th,p}\ \eta C^*_{H_2O}$

*15. $\eta C^*_s = C^*_s/C^*_{th,s}$

16. $\dot{W}_p = \dot{W}_{o,p} + \dot{W}_{f,p}$
17. $\dot{W}_s = \dot{W}_{o,s} + \dot{W}_{f,s}$
18. $\dot{W}_T = \dot{W}_p + \dot{W}_s$
19. $MR_p = \dot{W}_{o,p}/\dot{W}_{f,p}$
20. $MR_s = \dot{W}_{o,s}/\dot{W}_{f,s}$

*21. $F = F_A + \Delta I_{s,H.L.}\ \dot{W}_p$ (F_A is measured axial thrust)

22. $A^*_p = 68.79\ g$ (g is average measured throat gap, in.)
23. $A_s = \pi D_s^2/4$ (D_s is average measured orifice diameter, in.)

*24. $F_{opt,p} = (I_{s,opt,p} + \Delta I_{sH_2O})\,\dot{W}_p$

*25. $F_{opt,s} = I_{s,opt,p}\,\dot{W}_s$

*26. $\eta_{I_s} = F/(F_{opt,p} + F_{opt,s})$

*27. $\eta_{I_{s,opt}} = F/[F_{opt,p}(1 + \dot{W}_s/\dot{W}_p)]$

*28. $C_f = F/(\eta_{C^*_p} F_{opt,p} + \eta_{C^*_s} F_{opt,s})$

*29. $C_{T,opt} = F/[\eta_{C^*_p} F_{opt,p}(1 + \dot{W}_s/\dot{W}_p)]$

*30. $I_s = F/\dot{W}_T$

*31. $(\dot{W}_p/\dot{W}_s)_{eff} = (\dot{W}_p/\dot{W}_s)(C^*_s/C^*_p)$

*32. $\epsilon^* = A_e/A^*_p$ ($A_e = 371.5$ in^2, nozzle exit area)

*33. $PR = P_c/P_a$

Base Heat Transfer Data Reduction

(U) Surface temperature measurements were recorded on the base plate of the aerospike model to gain information on the local heat transfer coefficients and the recirculating gas temperatures. These results will indicate the existance of certain problem areas, such as base cooling requirements. Also, the calculated recirculating gas temperature may indicate the amount of mixing between the secondary and primary flow. The method of analysis and experimental results are presented in the following pages.

(U) Analysis. The experimental method consists of thermoccuples embedded on the gas-side and the insulated surface. A circular slot is formed around the thermoccuples to isolate and to obtain one-dimensional flow as shown in Fig. 54. The actual measurements that are recorded are both surface temperatures vs time. Based on an analytical model, the local heat transfer coefficients and recirculating gas temperatures can be computed.

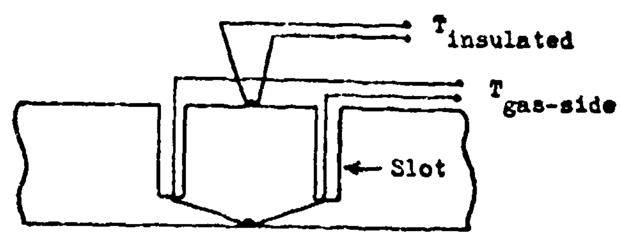

ISOLATION SLOT

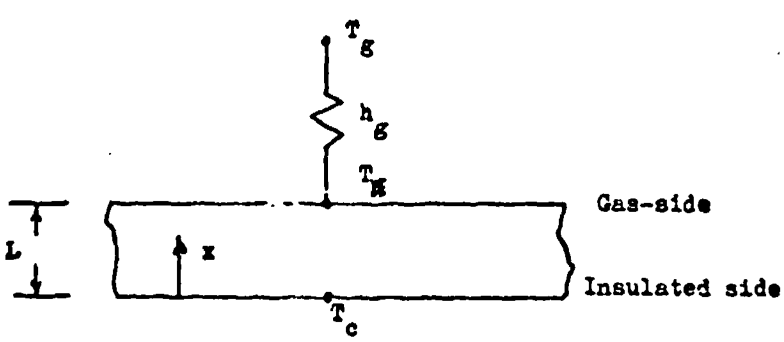

ANALYTICAL MODEL

Figure 54. Base Heat Transfer

(U) The experimental model can be readily analyzed by assuming one-dimensional heat flow, with one side exposed to the hot gas flow and the other insulated. Consider a slab as shown in Fig. 54. To express the temperature distribution in the slab in terms of non-dimensional module, the distribution is written as:

$$\frac{T_g - T_x}{T_g - T_i} = 2\sum_{n=1}^{\infty} \left\{ e^{-\delta_n^2 (\theta\alpha/L^2)} \left[\frac{\sin\delta_n \cos(\delta_n x/L)}{\delta_n + \sin\delta_n \cos\delta_n} \right] \right\}$$

where

$$Fo = \theta\alpha/L^2$$

$$\delta_n \tan\delta_n = \frac{hL}{k} = Bi$$

(U) Thus, the temperature ratio

$$\frac{T_g - T_x}{T_g - T_i}$$

can be expressed in terms of dimensionless terms, Fo, Bi, and x/L.

(U) Another assumption which is required in the data reduction is that the gas-side conditions remain constant from $\theta = 0^+$. This is a basic requirement in the derivation of the one-dimensional heat conduction equation. Since the heat loss from natural convection on the back-side of the base plate is small in comparison to the heat input, the condition that the surface is insulated is valid.

(U) Data Reduction and Test Results Local heat transfer coefficient and gas temperature are the two desired quantities. In order to solve explicitly for the aforementioned values, two degrees of freedoms must exist. By considering a time slice in the two surface temperatures vs time curves and substituting the temperatures and time into the basic conduction equation, two equations are obtained. Solving the equations, simultaneously, the local heat transfer coefficient and gas temperature can be determined. This is the theoretical approach to the data reduction. However, the direct application is almost insurmountable because of the complexity of the one-dimensional conduction equation. In order to converge the equation to an acceptable value, many terms must be solved. Thus, the temperature ratios were predetermined under expected heat transfer conditions and time. Figure 55 and 56 illustrate the temperature ratios for the gas-side surface and back-side surface, respectively. The material is 347 stainless steel with a wall thickness of 0.5 inches.

(U) The more desirable procedure in the data reduction is to obtain the back-side and gas-side surface temperatures for a given time slice. Employing these values in conjunction with Fig. 55 and 56, the local heat transfer coefficient and gas temperature can be obtained from a trial and error solution. However, for early time slices, the back-side temperature will be equal to the initial temperature of the base plate as seen in Fig. 57. Consequently, the above approach cannot be employed for initial time slices. However, two different time slices incorporating two gas-side temperatures can be employed for a trial-and-error solution.

(C) As an example, Fig. 57 depicts a typical surface temperature history for a thermocouple set. Superimposed on the graph is the secondary flow temperature. From the datum slice of five seconds to eight seconds, the recirculating fluid consists of primary flow gases. At the eight-second point, secondary flow was injected. A solution was tried for two time slices, and the following results were obtained.

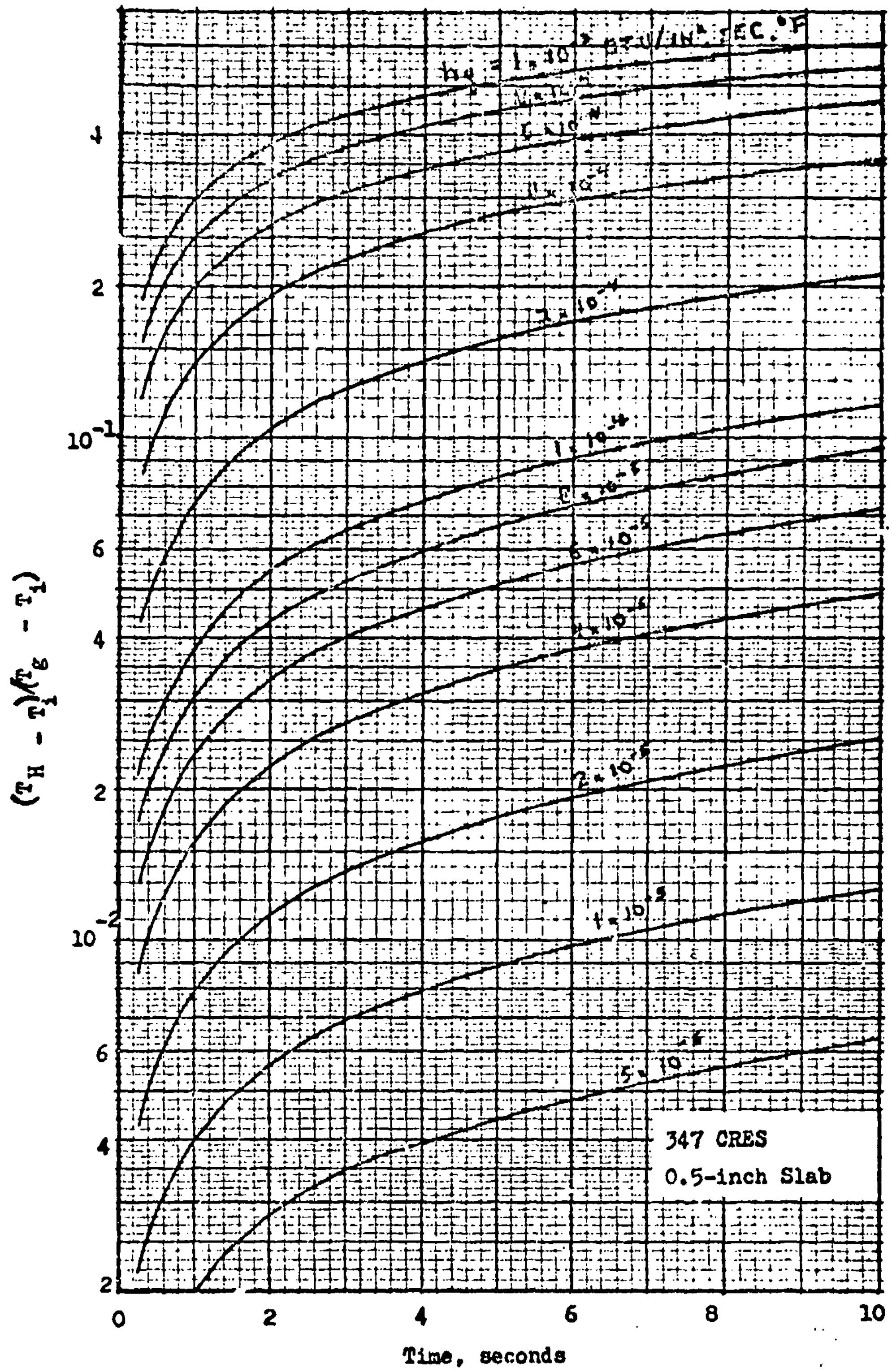

Figure 55. Gas-Side Temperature Ratio vs Time and Heat Transfer Coefficient

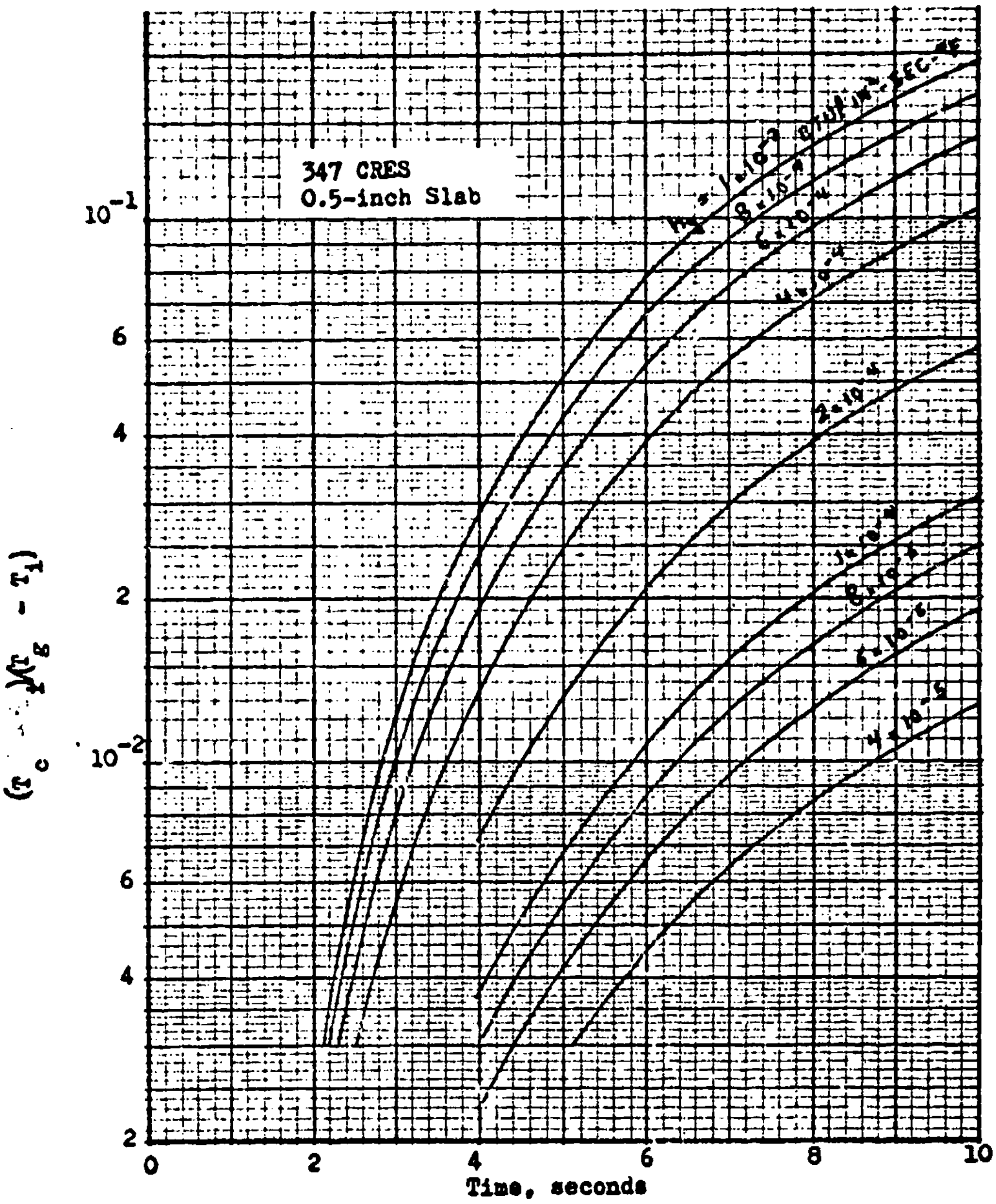

Figure 56. Back-Side Temperature Ratio vs Time and Local Heat Transfer Coefficient

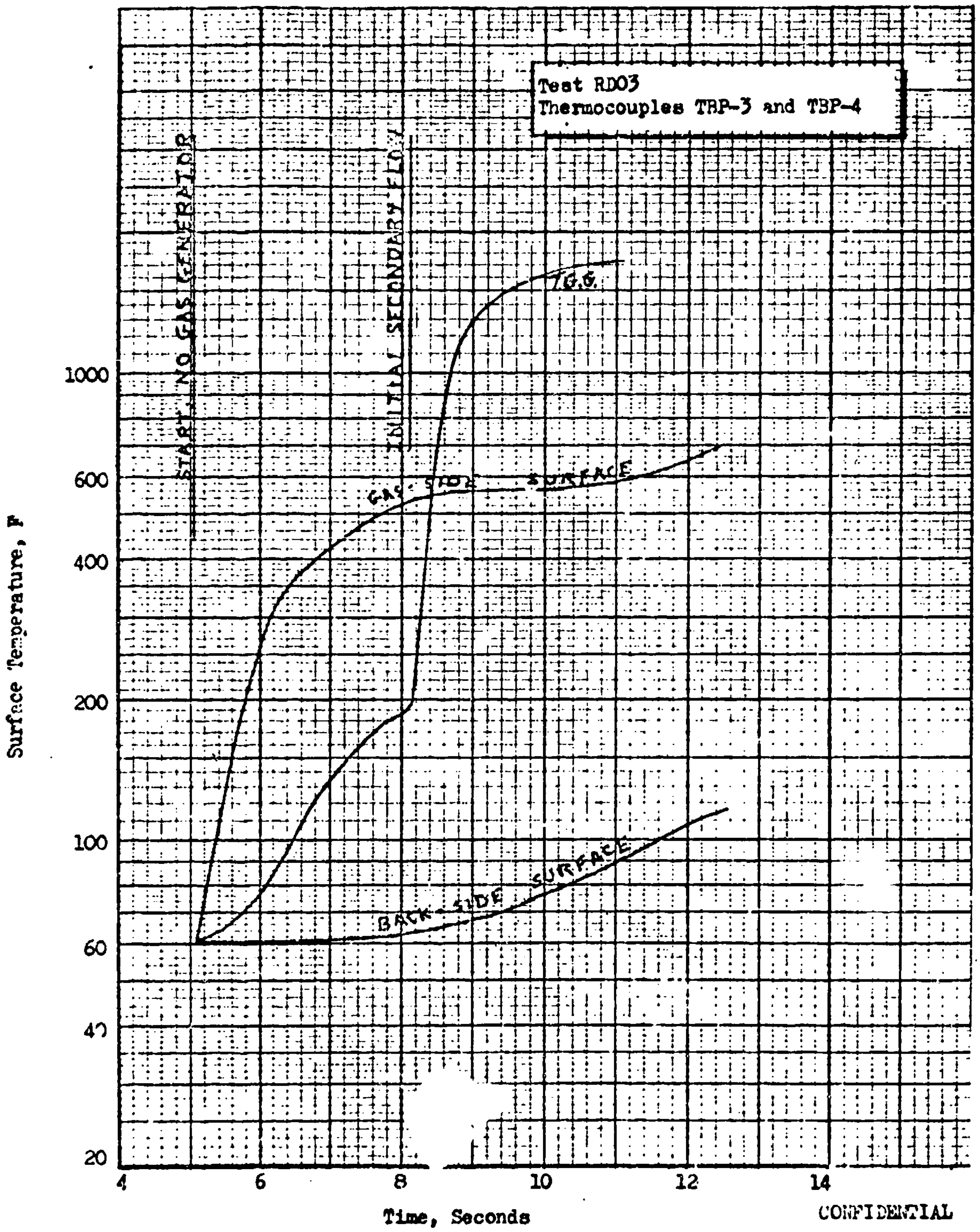

CONFIDENTIAL

Figure 57. Base Plate Temperatures vs. Time, Test No. RD03

θ, sec	T_H, F	T_g, F	h_g, BTU/in^2-sec-F
2	435	5000	1.75×10^{-4}
3	530	5000	1.75×10^{-4}

(C) Typical nozzle base plate temperatures obtained in the altitude test program are shown in Fig. 58. A summary of nozzle base plate temperatures obtained during this test program is presented in Table 6. Maximum gas-side and upstream-side plate temperatures measured were 440 and 180°F, respectively. A general trend of higher gas-side temperatures (TBP-3) during the high test cell pressure transient firings (firings AA03, AB11, AB12, AC15, AC16, AC17 and AC20) was noted. However, this trend was expected, since nozzle base pressure for these firings was proportional to ambient pressure (open wake regime) and the gaseous film heat transfer coefficients are directly proportional to local pressure to the 0.8 power.

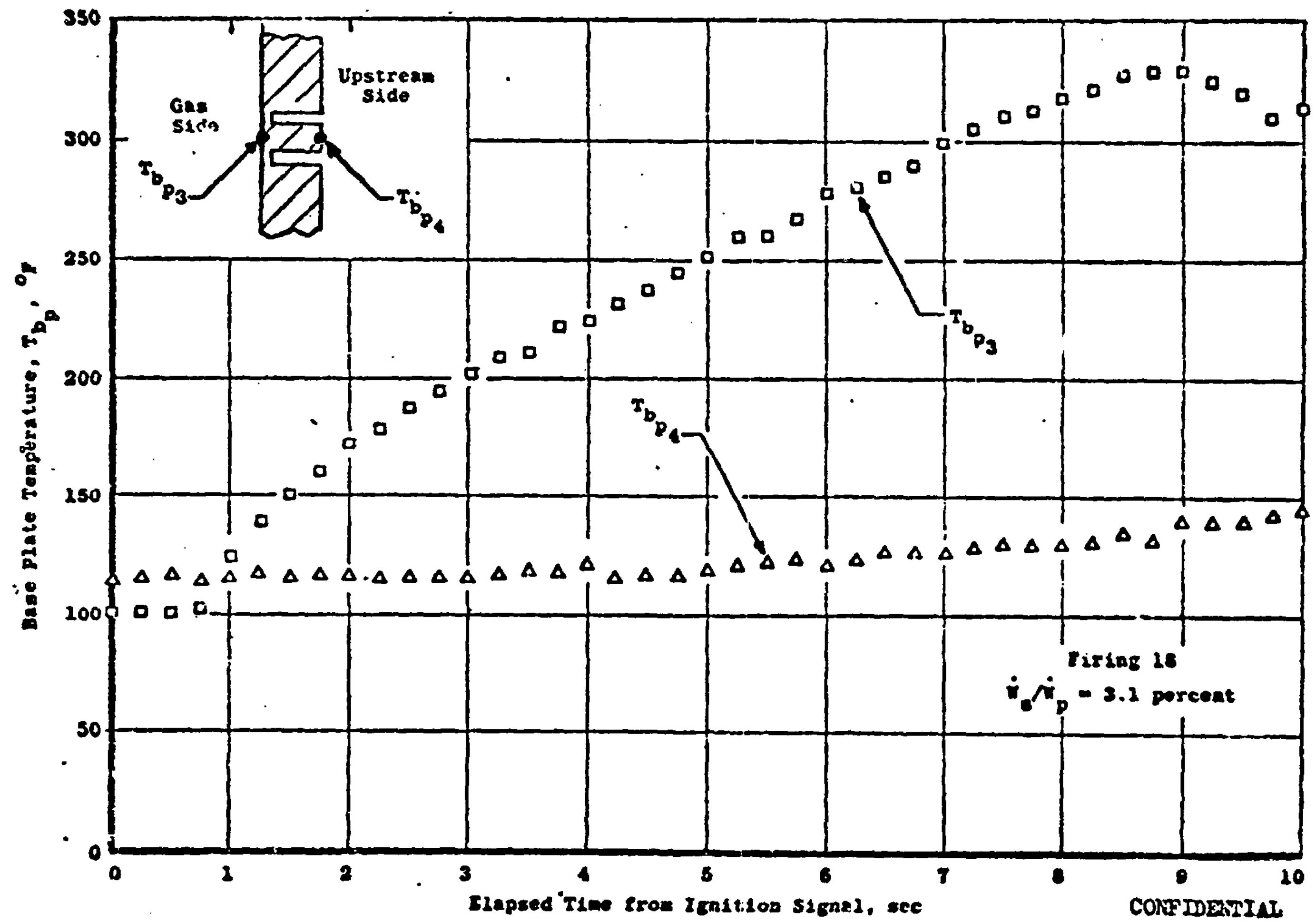

Figure 58. Typical Nozzle Base Plate Temperature (Reproduced from Ref. 25).

Table 6

NOZZLE BASE PLATE TEMPERATURES (ALTITUDE TEST RESULTS)

CONFIDENTIAL

Firing	Thermocouple Number	Nozzle Base Plate Temperature, °F						
		Elapsed Time from Engine Ignition Signal, sec						
		0	1.0	2.0	4.5	7.0	8.0	9.0
AA02	TBP-3	82	90	142	192	253	254	252
	TBP-4	80	82	81	84	95	99	103
AA03	-3	87	96	135	215	323	356	369
	-4	88	88	92	99	101	106	112
AB09	-3	103	110	160	191	269	284	306
	-4	106	106	107	105	109	114	121
AB10	-3	125	126	156	195	243	268	283
	-4	130	135	127	126	130	134	136
AB11	-3	107	114	170	241	311	360	414
	-4	113	118	112	111	121	129	137
AB12	-3	163	162	175	259	319	363	414
	-4	168	170	168	165	168	173	177
AC13	-3	74	88	132	198	259	280	282
	-4	84	80	83	84	95	100	101
AC14	-3	80	102	150	224	286	308	321
	-4	90	88	91	92	99	102	111
AC15	-3	108	127	184	280	345	365	394
	-4	122	126	124	123	131	135	144

Table 6

CONFIDENTIAL

NOZZLE BASE PLATE TEMPERATURES (ALTITUDE TEST RESULTS) (CONT'D)

Firing	Thermocouple Number	Nozzle Base Plate Temperature, °F						
		Elapsed Time from Engine Ignition Signal, sec						
		0	1.0	2.0	4.5	7.0	8.0	9.0
AC16	-3	108	137	197	313	387	407	435
	-4	131	130	128	129	131	143	153
AC17	-3	125	138	178	280	347	367	419
	-4	141	139	138	137	135	144	150
AC18	-3	113	127	162	228	277	295	304
	-4	128	128	129	129	133	133	137
AC19	-3	100	127	174	238	298	315	327
	-4	114	115	115	117	125	130	139
AC20	-3	133	160	217	315	391	413	440
	-4	160	159	158	156	165	172	180
AC21	-3	123	138	182	243	281	298	310
	-4	143	143	139	144	147	154	160
AD22	-3	-	-	-	-	-	-	-
	-4	78	85	85	85	88	88	90
AD23	-3	-	-	-	-	-	-	-
	-4	81	91	99	110	121	131	134
AD24	-3	—	-	-	-	-	-	-
	-4	106	113	121	138	161	169	178

Note: Gas generator was cut off 7 sec after engine ignition signal. (6 sec after ignition)
(Reproduced from Ref. 25)

WATER COOLED HARDWARE TEST RESULTS

(U) Nine sea level test firings and twenty-one altitude test firings were conducted with an experimental, 12 percent length aerodynamic spike thrust chamber. The nozzle had a nominal area ratio of 25 and utilized N_2O_4/UDMH-N_2H_4(50-50) propellants for both primary and secondary propellants.

(U) Sea level testing was conducted over a range of pressure ratios from 22 to 29 (P_c = 300 to 400 psia) and a secondary flowrate range from 0 to 5.3 percent of primary flowrate. Altitude testing was conducted over a pressure ratio range from approximately 40 to 350, a secondary flowrate range from 0 to 5 percent, and a G.G. mixture ratio range from 0.10 to 0.18.

(U) Satisfactory operation of the gas generator was not obtained during firings AD22, AD23, and AD24; therefore, performance data for these firings are not presented.

(U) Determination of the characteristic velocity of the thrust chamber and subsequent nozzle thrust efficiency from the test data required a considerable effort resulting in the development of an aerospike nozzle throat analysis method which should be useful in future testing efforts with this type nozzle. This method is described in detail.

(U) Nozzle performance in terms of C_T, $C_{T_{top}}$ and base pressure are presented as a function of secondary flowrate and gas generator mixture ratio.

Determination of Nozzle Throat Area

(C) Post Test Throat Area Method. Originally it was planned to use the nozzle post test measured throat area (Table 7) for the determination of $\eta_{C_p^*}$ and C_T. However, it became evident that this measurement alone was inadequate because (1) the throat area was obviously increasing in a seemingly repeatable manner during the first 3 or 4 seconds of a test (this conclusion was also reached during testing of the nearly identical TVC engine, Ref. 26) and (2) from 3 to 9 thrust chamber firings were accomplished between throat area measurements in the altitude test program with a likely throat area variation for each test. Characteristic velocity efficiencies (Table 8) showed considerable variation among the altitude firings. Nozzle efficiency trends with altitude did not follow the theoretical trend (Fig. 59) and tests with secondary flow showed gains substantially greater than indicated by base pressure measurements (Fig. 60). This method was therefore considered inadequate for determining nozzle performance.

(C) Constant $\eta_{C_p^*}$ Assumption. Since normally one would expect a close grouping of characteristic velocity efficiency values for repeated tests with the same injector, altitude performance was computed using this method and reported in Ref. 25 . Post test throat area measurements were used to obtain an initial value of average $\eta_{C_p^*}$ over a 2-second interval beginning 4 seconds after ignition (Table 9). An average $\eta_{C_p^*}$ was then computed for each of the three test periods and these averages were in turn averaged to obtain a test program average $\eta_{C_p^*}$. This is an arbitrary weighting and hence the absolute level of performance is also arbitrary. A constant A_p was computed for each test using this $\eta_{C_p^*}$ and 2-second average values of $\dot{W}_p$ and P_c. Using this constant A_p, 0.5-second interval average performance was computed over the duration of each test.

TABLE 7

NOZZLE THROAT AREA MEASUREMENTS CONFIDENTIAL

Test	Pretest $A_{p,m}$ in^2	Post Test $A_{p,m}$ in^2	Percent Change in $A_{p,m}$ (Pre-Post/Pre) x 100
RD 69	14.546	15.067	+ 3.58
RD 71	14.914	15.213	+ 2.00
RD 01	15.311	15.505	+ 1.27
RD 02	15.450	-	-
RD 03	14.970	15.206	+ 1.58
RD 05	-	14.198	-
RD 06	14.198	-	-
RD 08	-	13.892	-
RD 09	13.892	13.989	+ 0.70
AA01-03	13.850	14.347	+ 3.59
[1]AB08-12	14.071	13.828[2]	- 1.73
AC13-21	13.816	13.507	- 2.24

1 Outer throat bolts reversed (torque applied at nozzle end) for tests subsequent to AA test series.

2 This value differs slightly from that reported in Ref. 25.

Table 8

TCA CHARACTERISTIC VELOCITY EFFICIENCY
(ALTITUDE TEST PROGRAM)

CONFIDENTIAL

Firing	Characteristic Velocity Efficiency[1]		
	Pre-Test Period $A_{p,m}$	Post-Test Period $A_{p,m}$	Average $A_{p,m}$
AA02	0.855	0.887	0.871
AA03	0.855	0.888	0.871
AB09	0.878	0.869	0.873
AB10	0.875	0.867	0.871
AB11	0.878	0.870	0.874
AB12	0.878	0.870	0.874
AC13	0.864	0.845	0.854
AC14	0.867	0.848	0.857
AC15	0.871	0.852	0.861
AC16	0.871	0.851	0.861
AC17	0.872	0.852	0.862
AC18	0.873	0.854	0.864
AC19	0.875	0.855	0.865
AC20	0.875	0.855	0.865
AC21	0.880	0.860	0.870

[1] Average of data for 5 to 7 sec after ignition signal. Values are uncorrected for heat loss and water content. (Reproduced from Ref. 25)

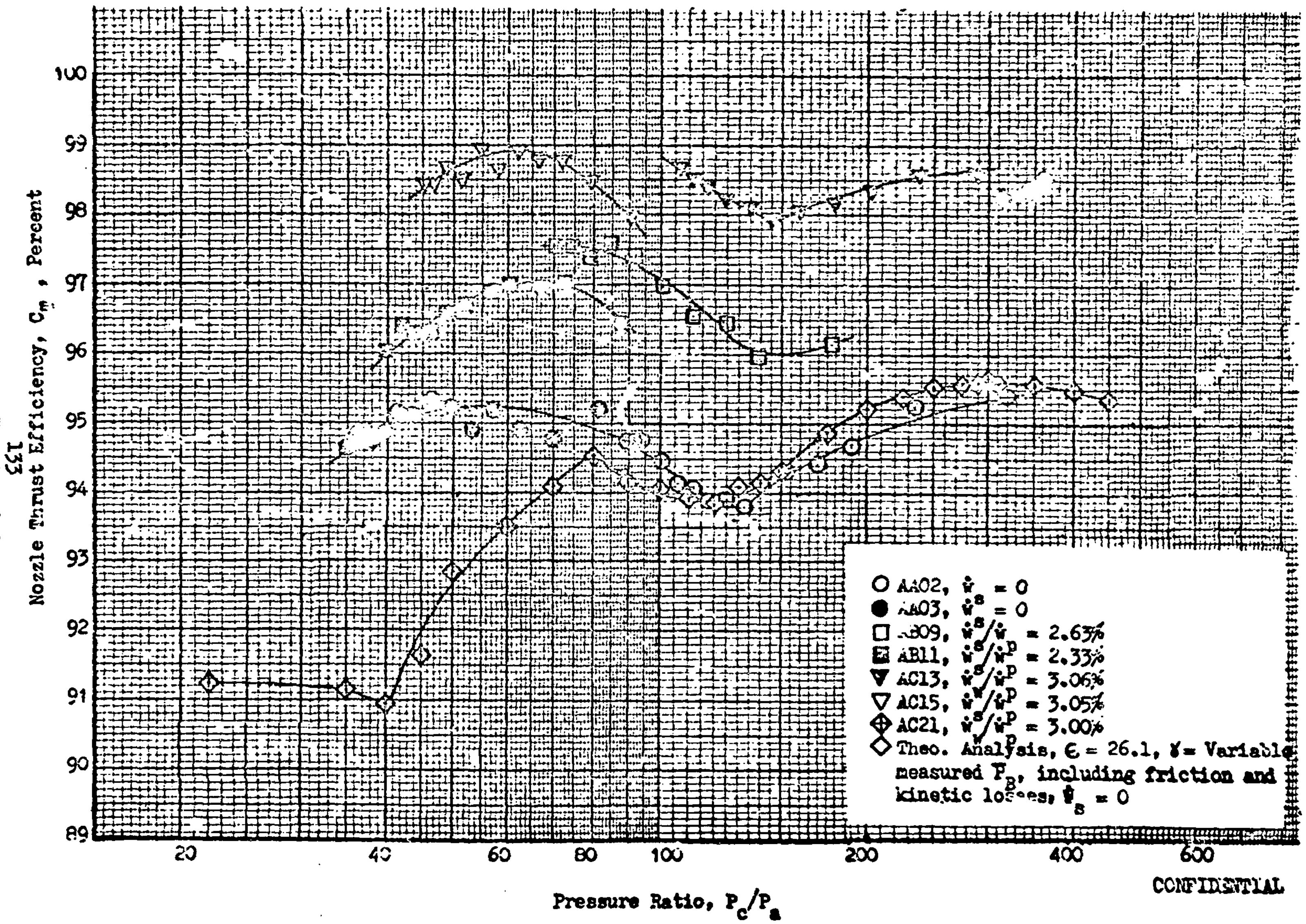

Figure 59. Nozzle Thrust Efficiency Trends Using Post Test Throat Area Measurements

UNCLASSIFIED

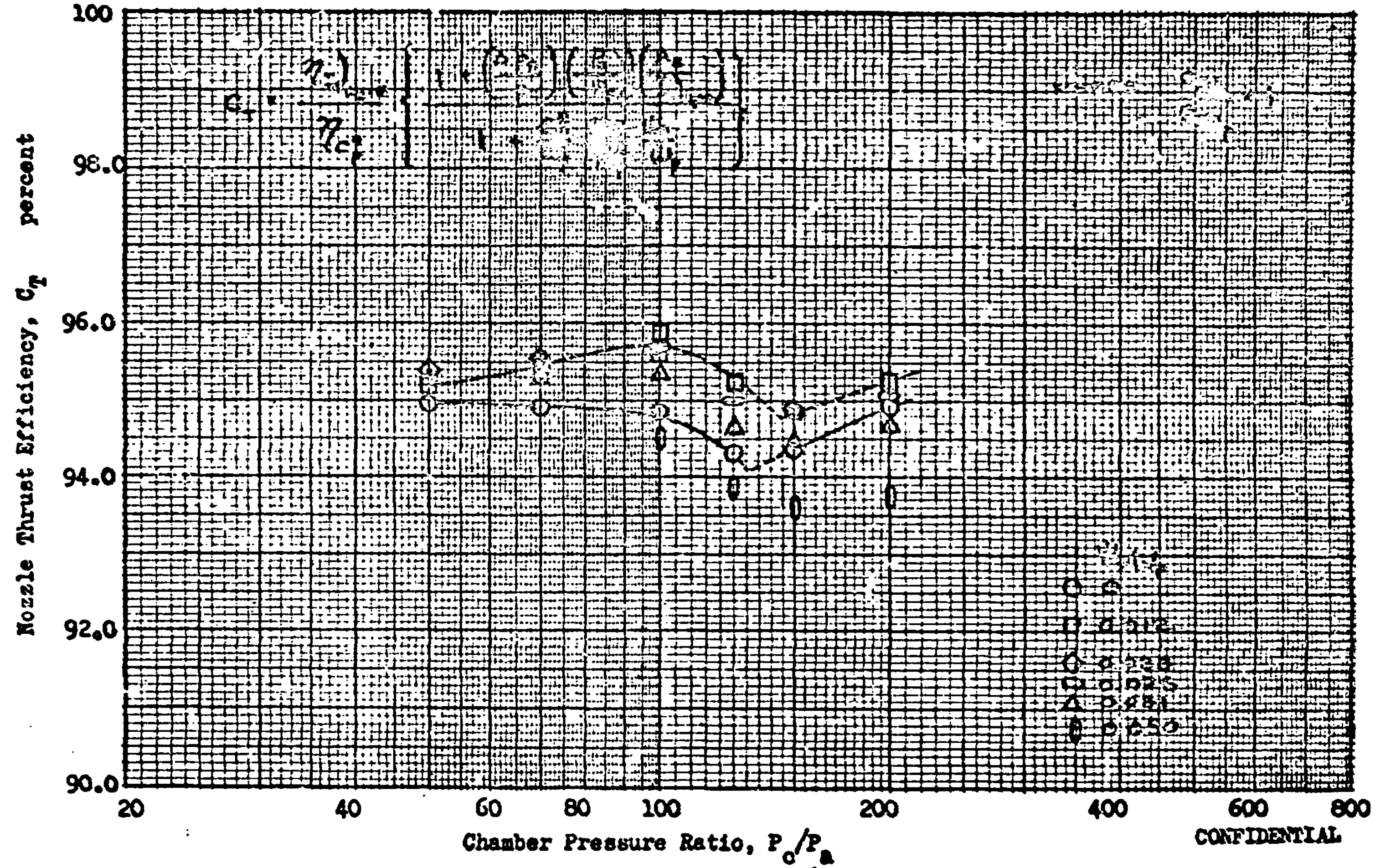

CONFIDENTIAL

Figure 60 Nozzle Thrust Efficiency Change with $\dot{w}_s$ (Determined from Measured Base Pressure)

UNCLASSIFIED

Table 9

NOZZLE THROAT AREA CALCULATIONS

Test Period	Firing	Characteristic Velocity Efficiency[1]			Nozzle Throat Area, A_p Assuming $\eta_{c^*_p} = 0.8694$
		Firing Average	Test Period Average	Test Program Average	
AA	2	0.8872	0.8874	0.8694	14.06
	3	0.8875			14.06
AB	9	0.8694	0.8690		13.94
	10	0.8666			13.99
	11	0.8701			13.93
	12	0.8701			13.93
AC	13	0.8445	0.8519		13.91
	14	0.8477			13.86
	15	0.8516			13.79
	16	0.8510			13.80
	17	0.8522			13.78
	18	0.8538			13.76
	19	0.8553			13.73
	20	0.8549			13.74
	21	0.8599			13.72

[1] Average of data from 4 to 6 sec after ignition, using post-test period throat area measurement. Values uncorrected for heat loss and water content. (Reproduced from Ref. 25)

(C) The time variation of $\eta_{C_p^*}$ (Fig. 61) indicates that $\eta_{C_p^*}$ initially decreases and then increases as the firing progresses. Nozzle thrust efficiency trends (Fig. 62) indicated substantial deviation from theoretical trends with altitude and secondary flowrate. Changing injector flow characteristics (Fig. 63) further indicated that a variation in $\eta_{C_p^*}$ was possible. Based on these results and considerations an alternate method of establishing performance was sought.

(U) Nozzle Primary Thrust Method. Since the nozzle throat area can alternately be deduced from measurements of chamber pressure and the primary thrust of the nozzle and since small variations in $\eta_{C_p^*}$ should likely result in even smaller variations in the primary thrust coefficient C_{F_p}, the use of this quantity in determining throat area was investigated.

(U) The thrust F_p developed by the primary nozzle (Fig. 64) can be expressed in terms of the resultant measured axial thrust F_A and other pressure forces acting over the engine by

$$F_p = F_A + F_{a,e} - F_B + (F_{a,cowl} - F_{N,cowl}) = P_c A_p^* \eta_{C_F} C_{F_{vac}} = P_c A_p^* C_{F_p} \quad (1)$$

(U) The primary nozzle efficiency η_{C_F} is a function of the nozzle design and is essentially unaffected by small changes in nozzle throat area. The theoretical $C_{F_{vac}}$ is a function of nozzle area ratio and propellant mixture ratio (Fig. 65). From Fig. 65 the sensitivity of $C_{F_{vac}}$ to ϵ and mixture ratio variations indicates that two percent changes in ϵ and mixture ratio result in approximately 0.10 and 0.25 percent changes, respectively, in $C_{F_{vac}}$. A potential flow analysis of the nozzle contour (Fig. 66 and 67) indicates that C_{F_p} is unaffected by ambient conditions until a pressure ratio of approximately 50 is reached.

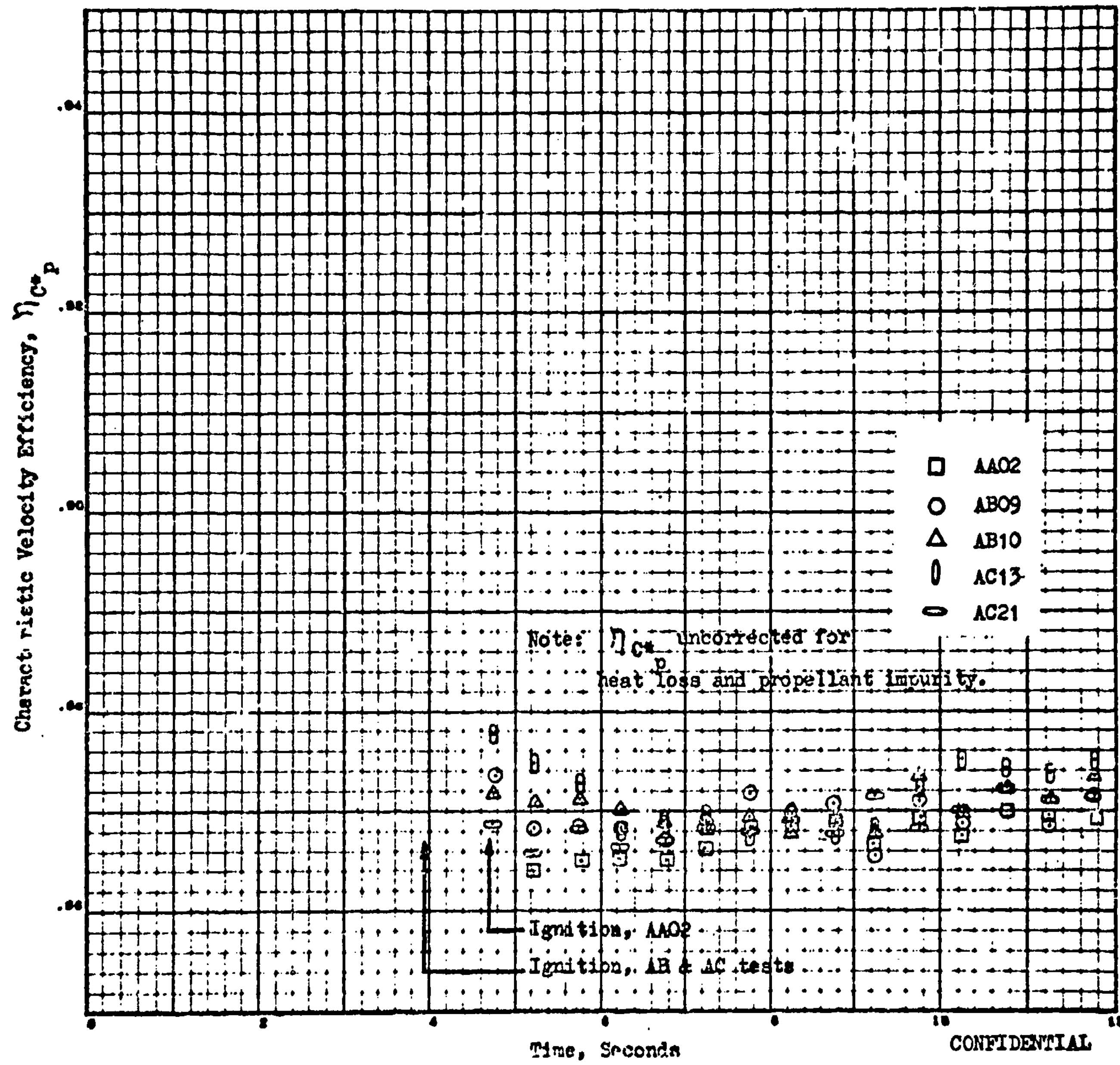

Figure 61. Variation of $\eta_{C^*_p}$ During Firing, Constant η_{C^*} Method

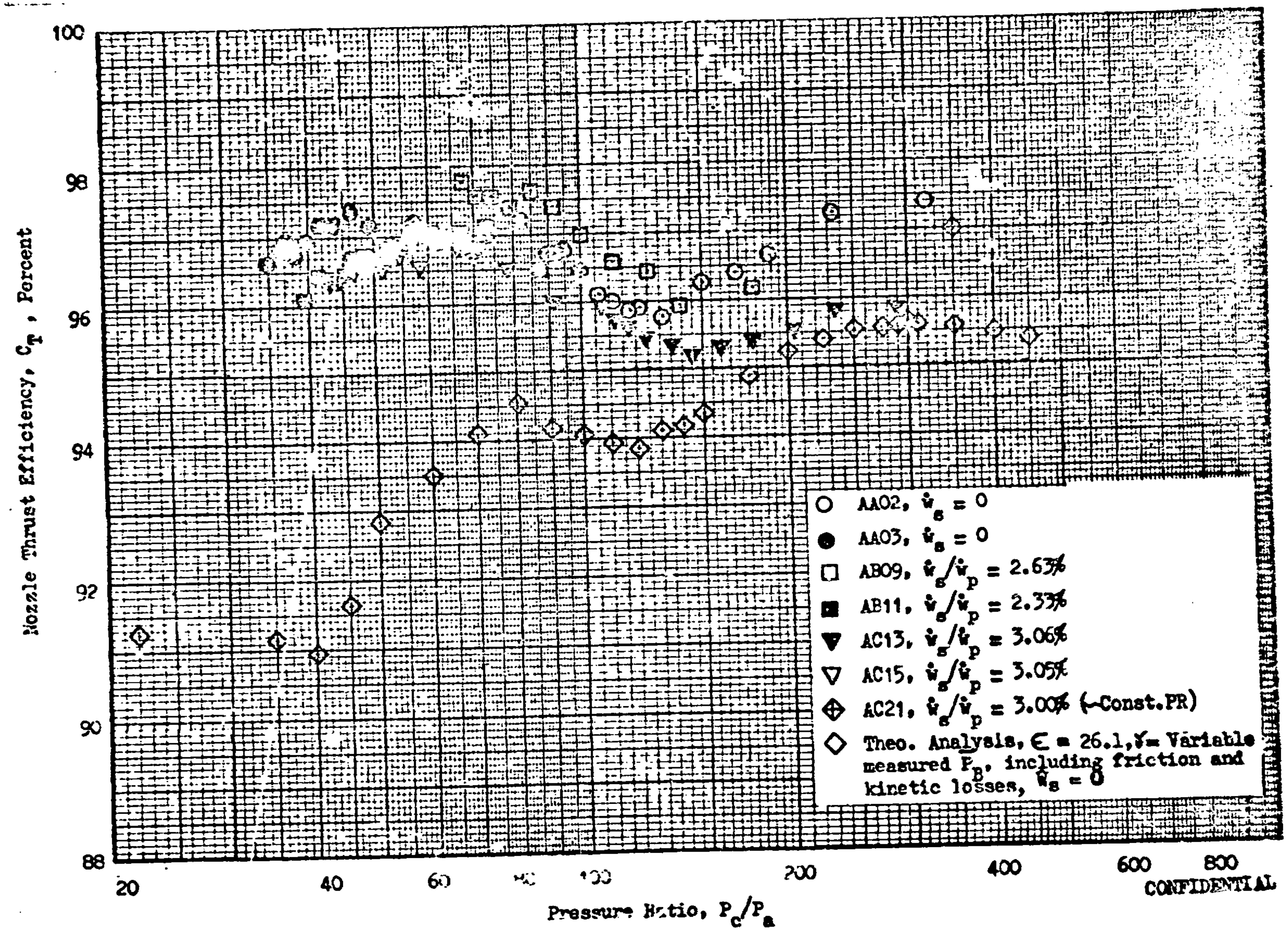

CONFIDENTIAL

Figure 62. Nozzle Thrust Efficiency Trends Based on Constant $\eta_{C^*_p}$

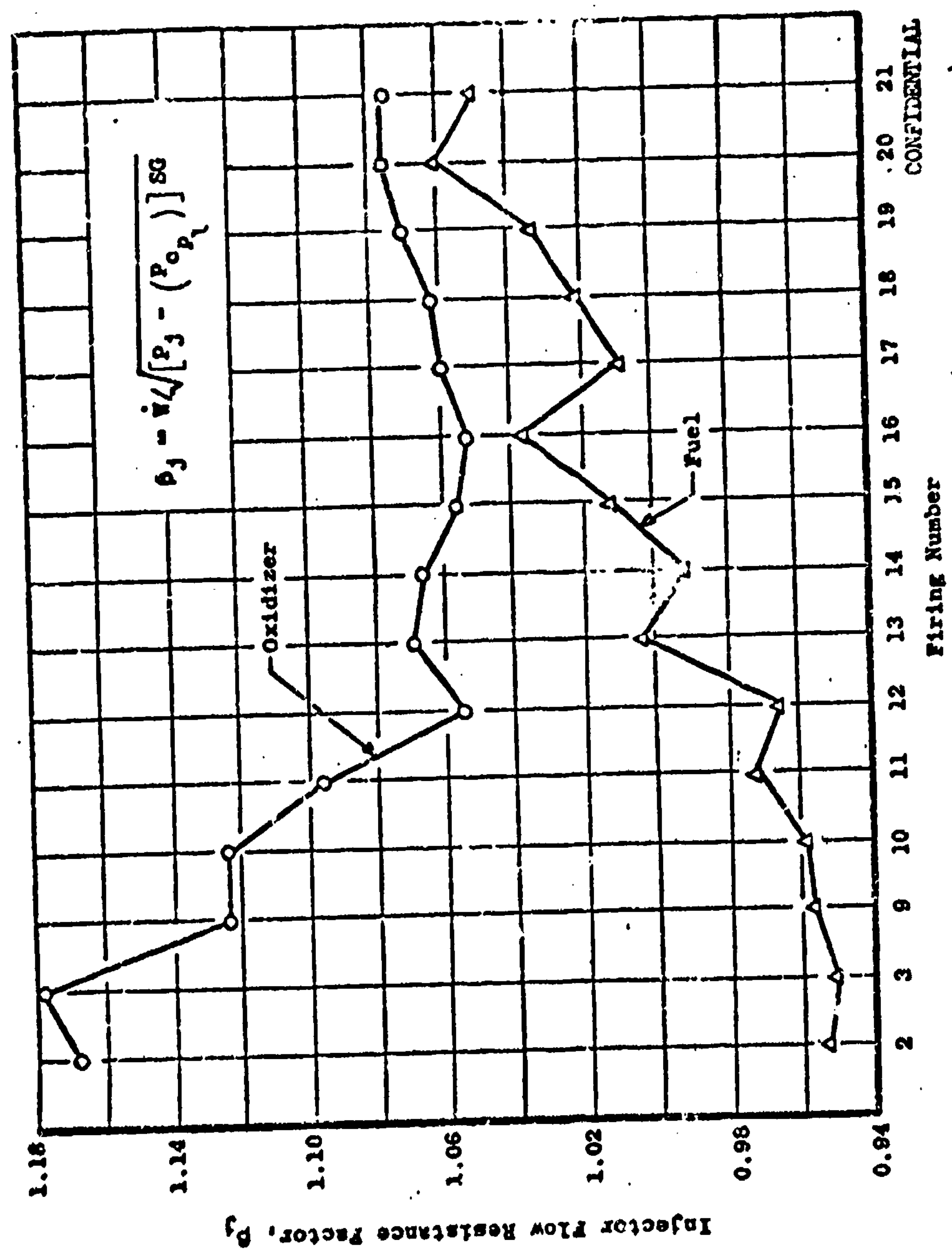

Figure 63. TCA Injector Flow Resistance (Reproduced from Ref. 25)

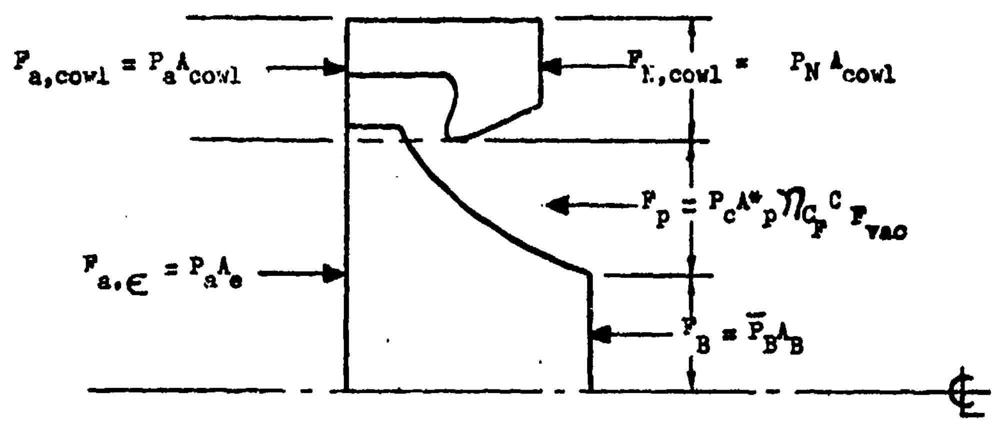

Figure 64. Forces Acting on Aerodynamic Spike Nozzle

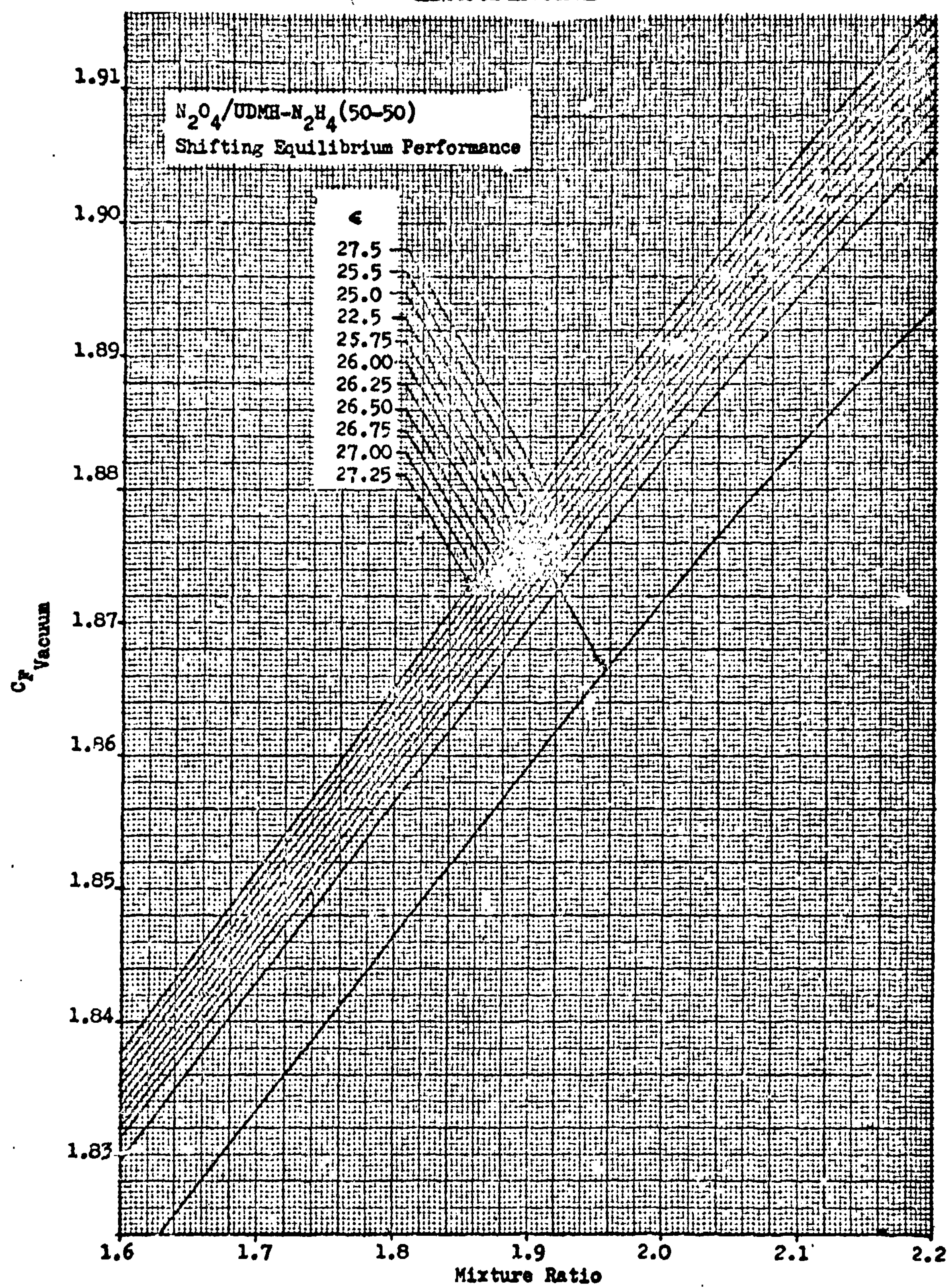

Figure 65. Vacuum C_F vs Mixture Ratio and Area Ratio

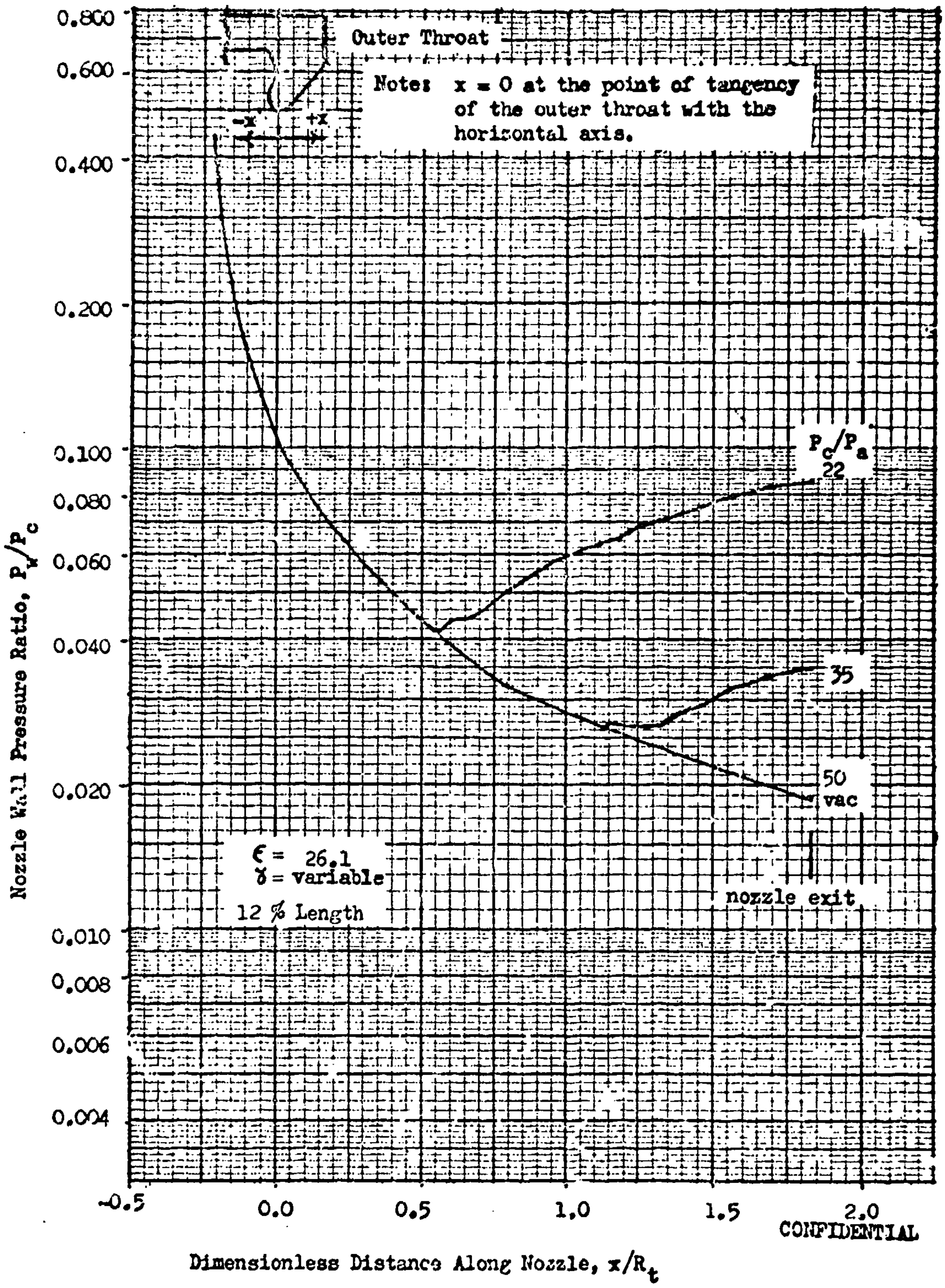

Figure 66. Twelve Percent Length Nozzle Theoretical Pressure Profiles

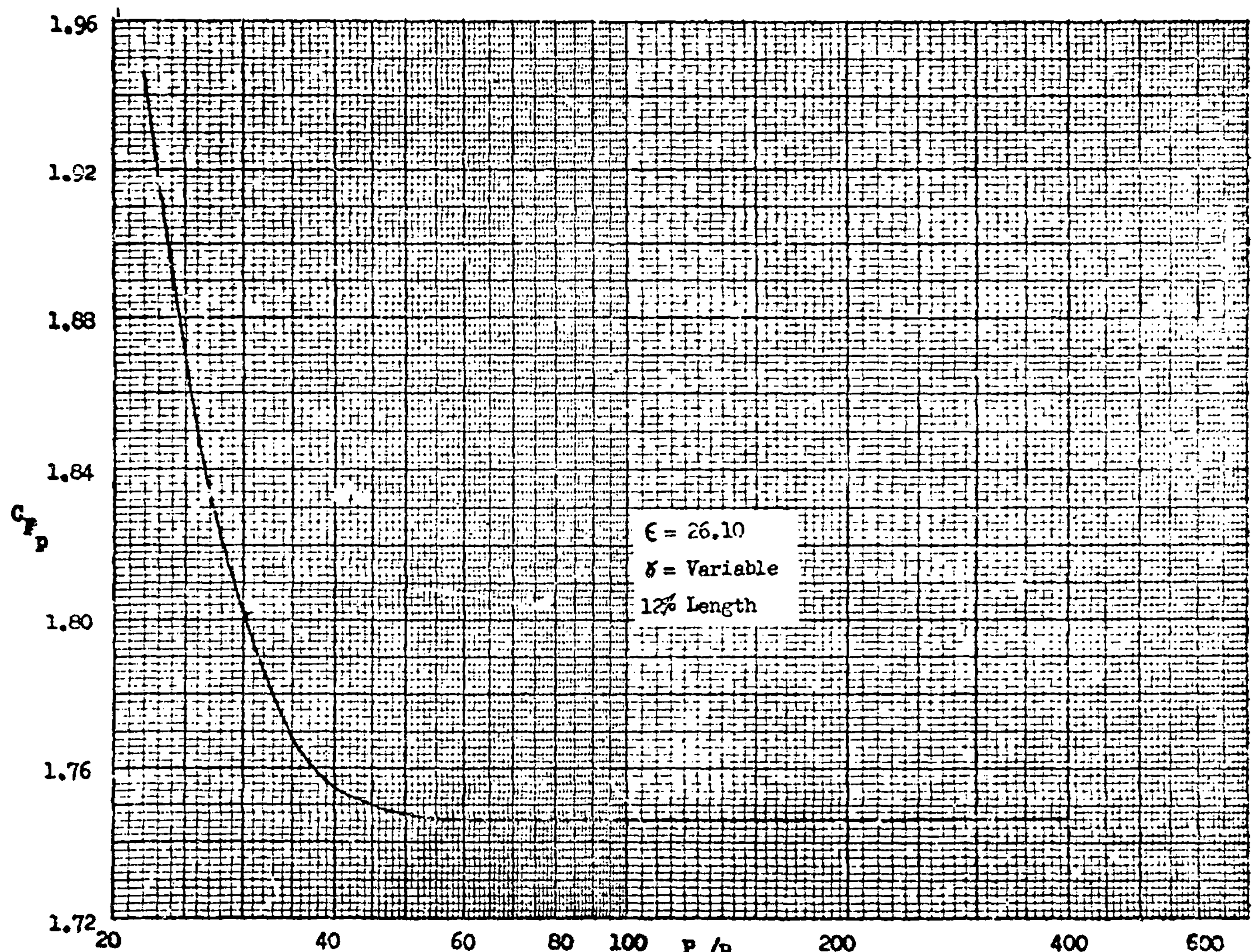

CONFIDENTIAL

Figure 67. Theoretical Primary Thrust Coefficient Variation with Pressure Ratio

(U) The above equation expressed in terms of A_p^* is

$$A_p^* = \frac{F_p}{P_c \eta_{C_F} C_{F_{vac}}}$$

(U) The ratio of the throat area at any time relative to some reference throat area is then

$$\frac{A_p^*}{A_{p,ref}^*} = \frac{(F_p/P_c)\, \eta_{C_{F_{ref}}}\, C_{F_{vac,ref}}}{(F_p/P_c)_{ref}\, \eta_{C_F}\, C_{F_{vac}}}$$

(U) With the assumption that $\eta_{C_{F_{vac,ref}}} = \eta_{C_{F_{vac}}}$

$$A_p^*/A_{p,ref}^* = \frac{(F_p/P_c)\, C_{F_{vac,ref}}}{(F_p/P_c)_{ref} C_{F_{vac}}}$$

where $C_{F_{vac}} = f\,(MR, \epsilon)$

(C) This expression does not establish an absolute throat area but it does establish the throat area change during a firing and the relative throat areas among tests operating above the pressure ratio at which nozzle recompression starts. In the recompression region, η_{C_F} $(C_F/C_{F_{vac}})$ is a strong function of P_c/P_a (Fig. 67) and hence no attempt was made to determine relative throat areas for the altitude tests operating in this region. Fortunately the altitude tests over the low pressure ratio range achieved a stabilized (constant) throat area before recompression occurred. The above expression was not used to compare the sea level throat areas among the different tests because of small differences in P_c and hence P_c/P_a. However, it was felt adequate to determine the change in throat area with time during a given test, since P_c/P_a and η_{C_F} are essentially constant. The steps in the calculation of throat area variation with time for each test and the relative stabilized throat areas among the altitude tests were as follows:

(U) 1. A reference point in the firing (3 to 5 seconds after ignition) was selected. For the altitude firings, a point was selected which avoided the recompression region ($P_c/P_a > 50$).

(C) 2. The primary thrust was computed at 0.5 second intervals from 0.5 second averaged measured test data by

$$F_p = F_A + P_a A_e - \bar{P}_B A_B$$

Since $P_a \approx P_N$, the term $(F_{a,cowl} - F_{N,cowl}) \approx 0$.

(C) Outer nozzle lip pressures PN-1, PN-2, and PN-3 (Fig. 24 , p. 55) were carefully examined for each test. Results presented in Ref. 25 which indicate some aspiration of the outer nozzle are not representative of the actual condition and were caused by a lag in response of pressures PN-2 and PN-3. All constant attitude runs (AC21 and AD series) in this test program and the TVC test program indicate PN-1, PN-2, and PN-3 = P_a.

(C) When computing F_p values it was noted that distinct decreases in F_p of 22 and 31 pounds occurred during G.G. cutoff for the AC series with 3 and 5 percent secondary flow, respectively. This was a definite indication that the base thrust contribution determined from the average base pressures was too low. Primary thrusts computed for the AC test series by equation 1 were therefore reduced by 24 and 31 pounds for 3 (22 pounds for test AC19 and 20: MR_s = 0.18) and 5 percent secondary flow, respectively. No such effect was noted for the AB series of tests with 1.2 and 2.5 percent secondary flow.

(C) Increasing base pressure gradients with increasing secondary flowrate (Fig. 68) may have caused the base pressure averaging technique to be less accurate. During the last two seconds of the tests with secondary flow, the secondary flowrate decreased to less than 0.5 percent. Hence relatively uniform base pressures were achieved and a more accurate base thrust could be computed.

(C) Values of $\bar{P}_B/P_c$ tabulated for the AC test series in Appendix 1 were determined from the measured average base pressures and should be increased by .00048, (.00044 for AC19 and 20) and .00062 for 3 and 5 percent secondary flows to give a more accurate representation of the effective base pressure ratio.

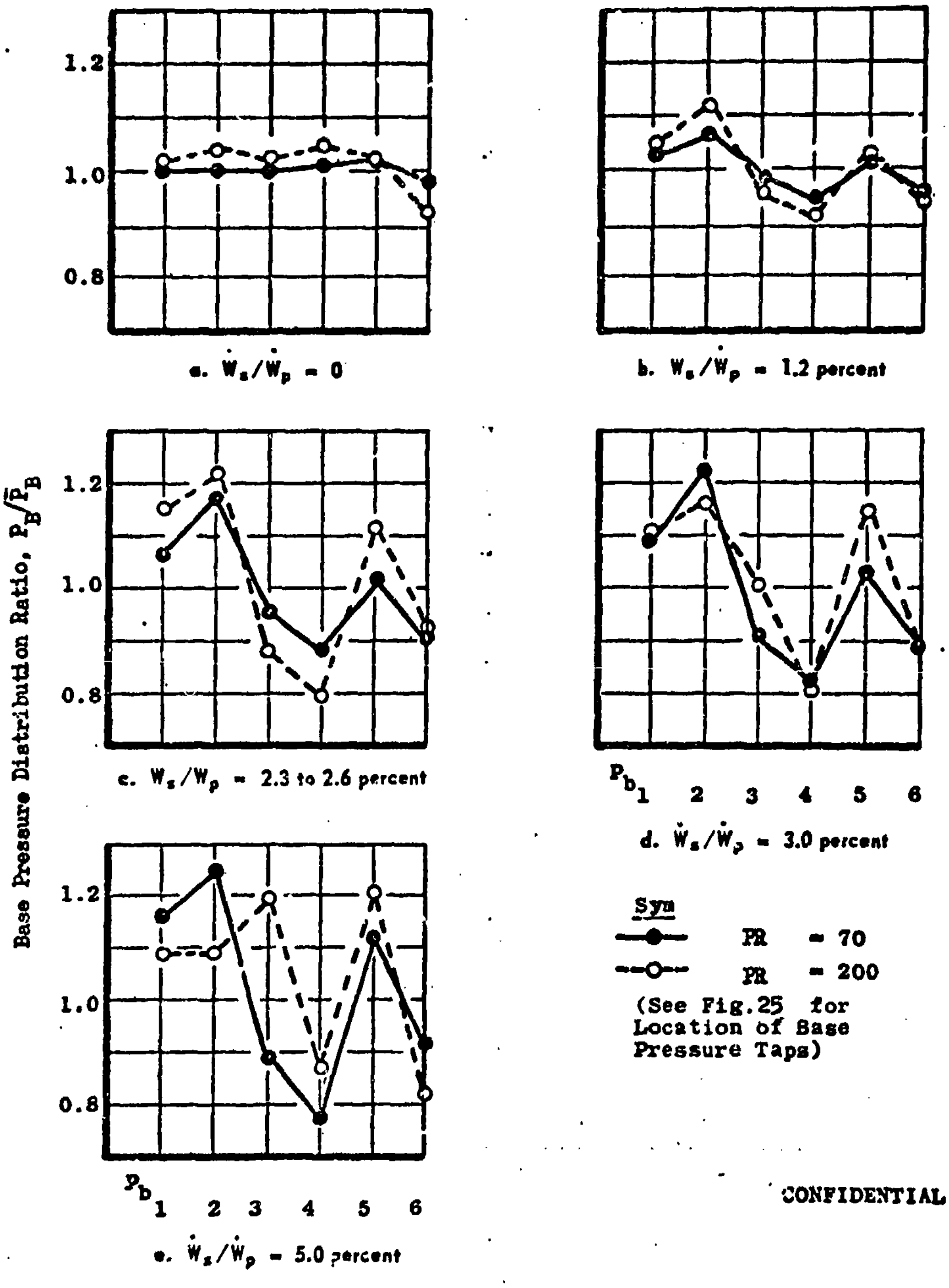

CONFIDENTIAL

Figure 68 . Nozzle Base Pressure Distribution, (Reproduced from Ref. 25)

(U) 3. The primary thrust was normalized to 300 psia. (400 psia for tests RD69, 71, and 01.)

(C) 4. An initial area ratio was selected for each test from available measurements. For the sea level tests, the posttest measurements were used except for RD69 ($\eta_{C^*_{p,RD69}} = \eta_{C^*_{p,RD71}}$) and RD06 (average of pretest RD06 and posttest RD08). For the altitude tests pre- and posttest values were used for the first and last tests in the AB and AC series with a linear throat area variation assumed for intermediate tests (Fig. 69). The test period initial area is adjusted slightly lower than measured because a factor was applied which assumed that the decrease in throat area was caused by a uniform buildup of deposits on the throat. For the AA series the posttest throat area was used for AA03 and throat areas for AA02, and AA01 were extrapolated using an average of the slopes of the AB and AC series. The changes in nozzle throat area indicated in Table 7, page 131 suggested that the method of mounting the outer throat in the sea level test series and in the AA test series was not adequately securing the nozzle assembly. During several disassemblies of the engine it was noted that considerable effort was required to remove the outer throat bolts. This fact and the indicated significant area increases suggested that applying torque to the nuts on the injector end of the engine was not securing the outer throat. Therefore, posttest throat area measurements were considered more reliable for the RD and AA test series. It should be noted that the variation of throat areas in Fig. 69 about the mean value results in a change of only $\pm$ 0.33 percent in theoretical $C_{F_{vac}}$.

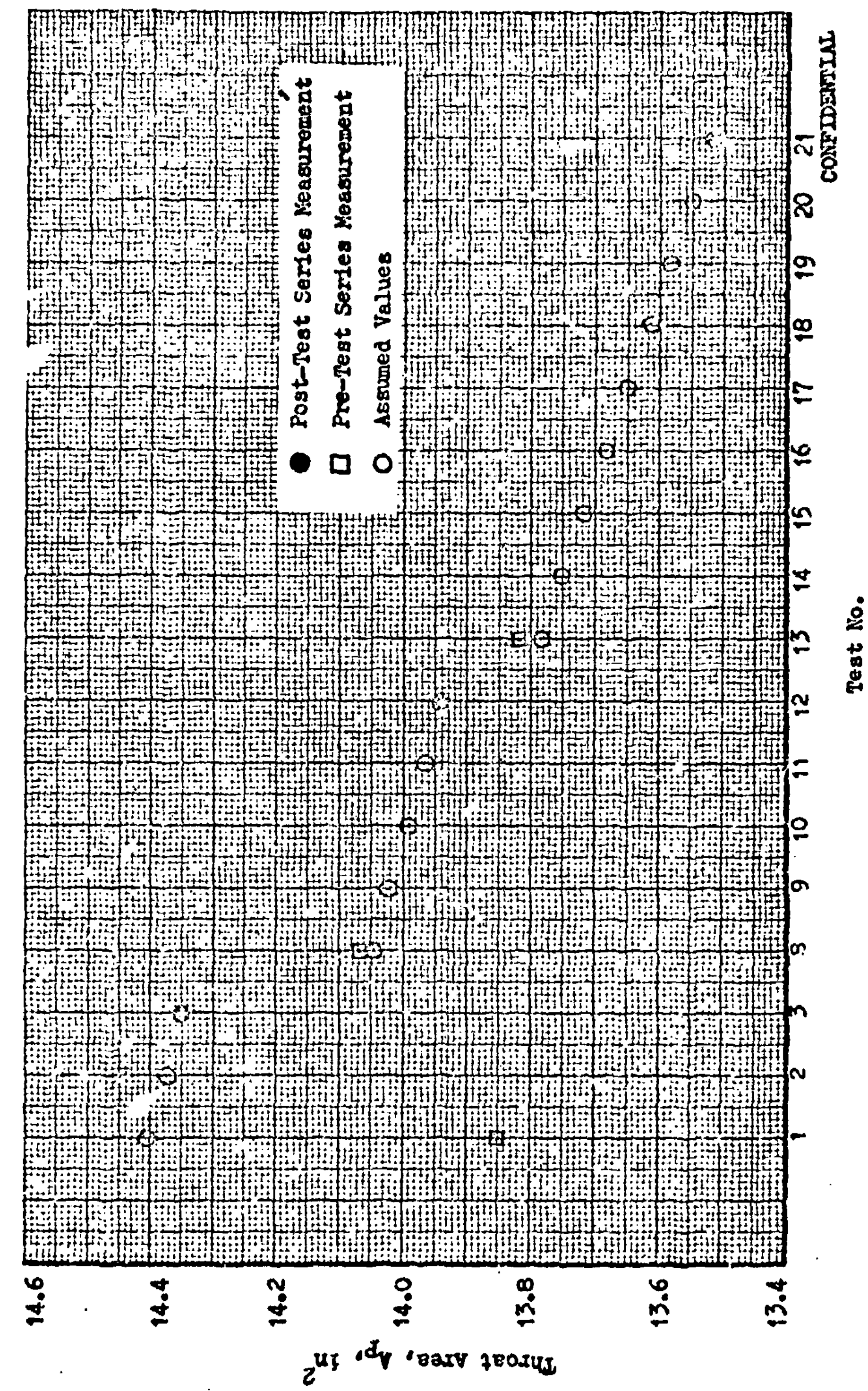

Figure 68. Linear Throat Area Variation (Altitude Test Series)

(U) 5. $C_{F_{vac}}$ was determined as a function of area ratio (const. for a given test) and 0.5-second average mixture ratio.

(C) 6. $A^*_p/A^*_{p_{ref}}$ was computed vs. time for each test. Results (Figs. 70, 71 and 72) indicated that the throat area increased approximately 1.5 to 2.2 percent and reached a constant value within from 3 to 6 seconds after ignition, for the initial tests in a series. As the number of consecutive firings increased, the magnitude of the throat change decreased. Since test AC21 showed very little change, and since it was the only valid test performed at constant altitude, the same technique of analysis was applied to several subsequent tests with a nearly identical TVC engine. The TVC engine tests were all conducted at a constant altitude. Figure 72 shows that tests BA01 and BC12 (each the first test of a series) exhibited similar behavior, i.e., the throat area increased from 1.5 to 2.0 percent during the first 3 to 4 seconds of operation. The throat area change on ignition was noticeably reduced by the eighth firing in the series (BC18). It would appear that some form of slow recovery from thermal cycling in the engine may be occurring.

(C) The scatter in the data between six and seven seconds after ignition is caused by unstable conditions associated with cutoff and rapid chamber pressure decay of the gas generator.

(C) The unusual trend exhibited for tests RD02 and RD03 may have been caused by water leakage into the engine.

(C) 7. For the altitude test series, the stabilized reference throat areas were then compared to the stabilized throat area for test AC13 by the relationship

$$\frac{(A^*_{p,ref})}{(A^*_{p,ref})_{AC13}} = \frac{(F_p/P_c)_{ref}\, C_{F_{vac,ref,\ AC13}}}{(F_p/P_c)_{ref,\ AC13}\, C_{F_{vac,\ ref}}}$$

to establish the relative stabilized throat areas for the altitude test program.

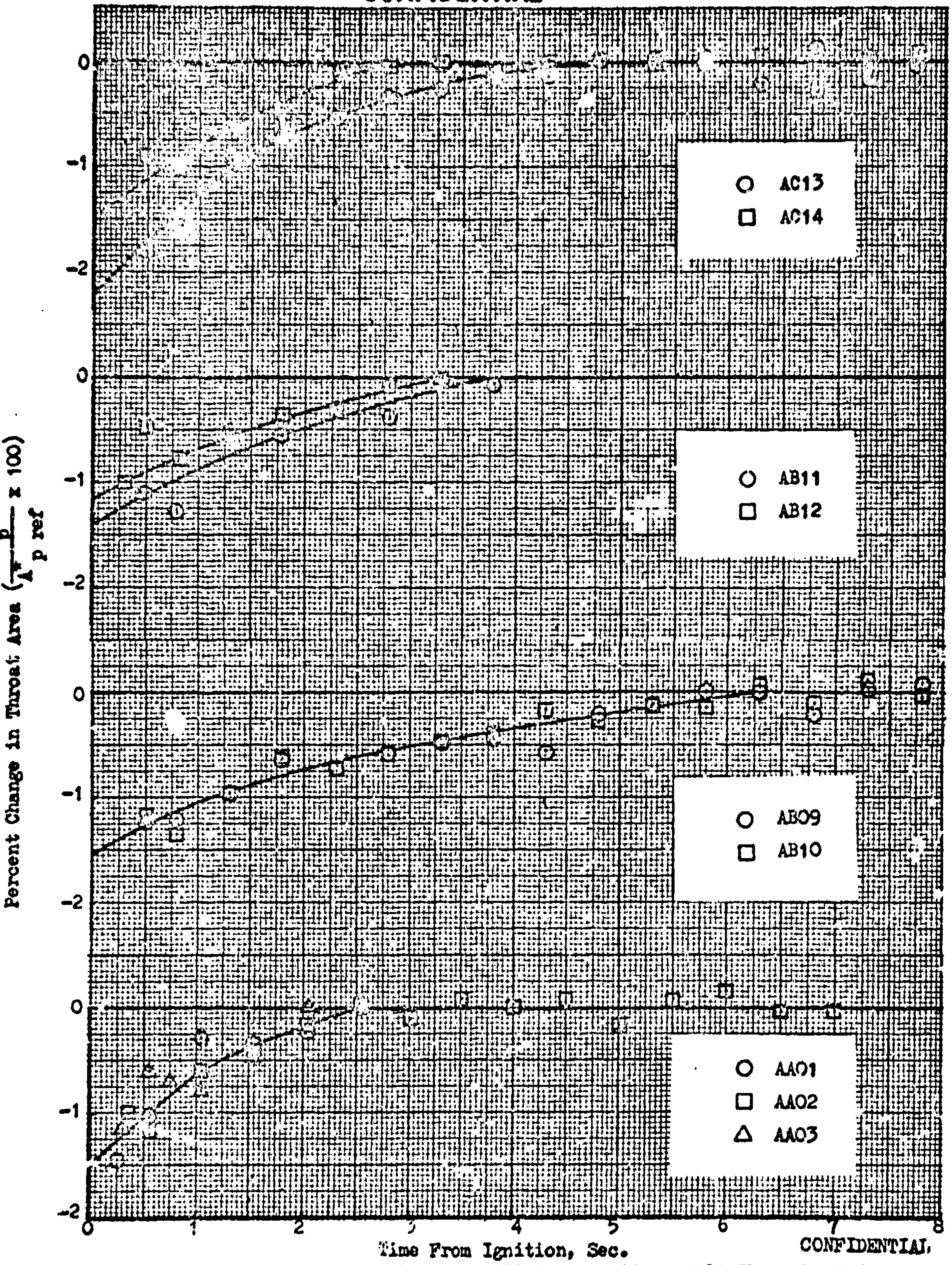

Figure 70. Throat Area Change vs. Firing Duration, AA01 Through AC14

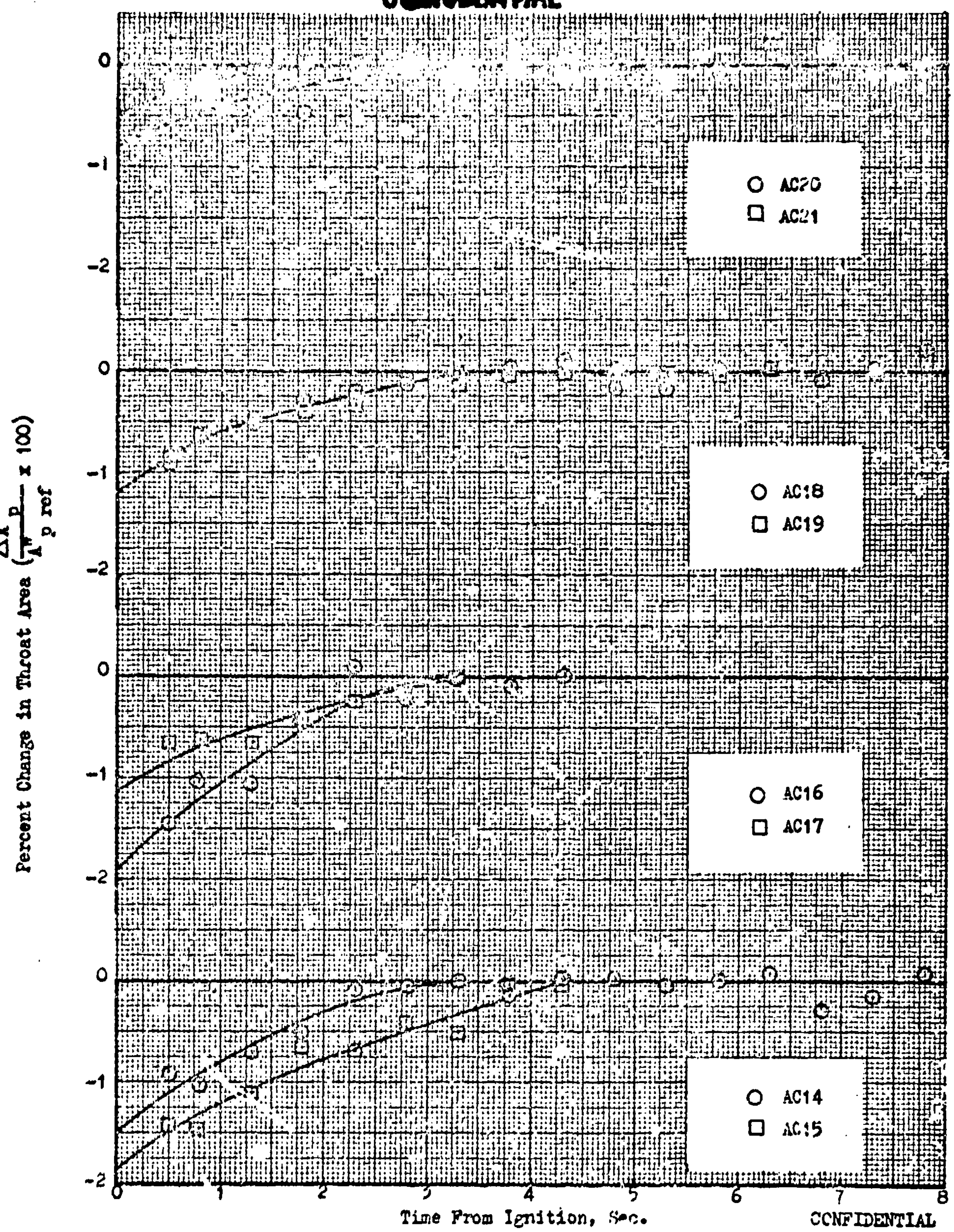

CONFIDENTIAL

Figure 71. Throat Area Change vs. Firing Duration, AC14 Through AC21

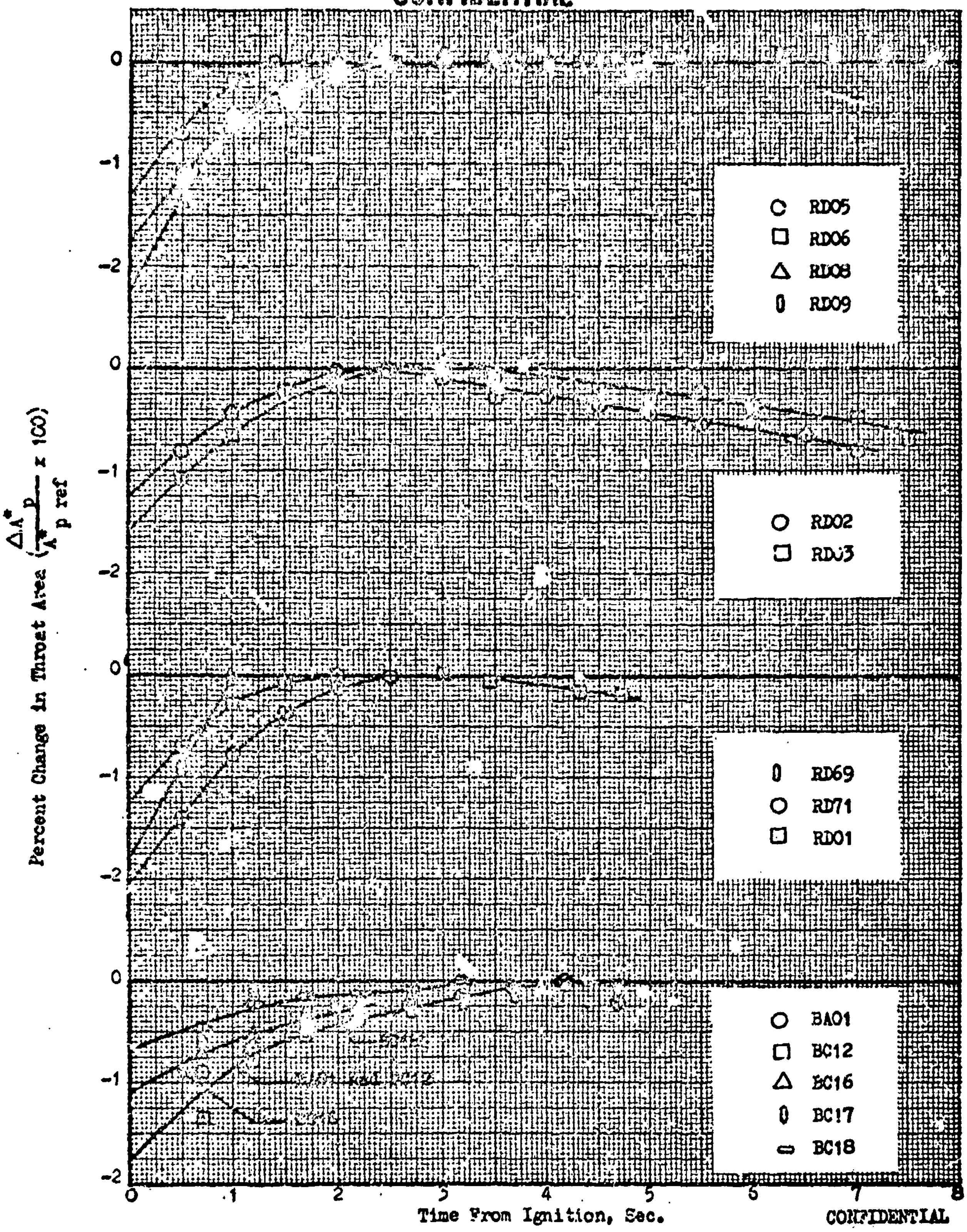

Figure 72. Throat Area Change vs. Firing Duration, TVC Engine Firings and Sea Level Tests

(C) 8. Absolute values of throat areas for the altitude test program were determined by selecting the pretest throat area measurement prior to the AC test series for test AC13 and following the area change curve indicated in Fig. 70. The absolute values of all the throat areas at any time could then be determined by using the $A^*_{p,ref}/A^*_{p,ref,\ AC13}$ equation to establish the hot stabilized throat area for each test and the $A^*_p/A^*_{p,ref}$ equation to establish the time variation of A^*_p during a test. The overall process was repeated for the majority of the tests using the new A^*_p to account for differences between the initially assumed A^*_p (ϵ^*) value and the one calculated on the first iteration. Figures 70, 71, and 72 are the area change curves from the second iteration. The final throat area values (A^*_p) are tabulated in Appendix 1 as a function of time for each test. Sea level throat areas were computed using posttest throat area measurements (except for RD69 and RD06) and the throat area change curves shown in Fig. 69. No posttest area was available for RD05 and an average of pre RD06 and post RD08 values was used. The same C* efficiency was used for test RD69 that was obtained with RD71.

(C) Typical characteristic velocity efficiencies obtained using this method are shown in Figs. 73 and 74 for typical sea level and altitude tests. The values of η_{C*} indicate a gradual upward trend. Some of the curves (AA02 and RD08) appear to have the same initial shape as the throat area change curves. However, test AC13, which has the steepest area change, has the same gradual upward drift of test AC21 which has essentially no throat area change. The fact that η_{C*} is actually varying in the manner indicated is substantiated by identical trends in the vacuum specific impulse of the primary nozzle ($I_{s_p} = F_p/\dot{w}_p$) as shown in Figs. 75 and 76.

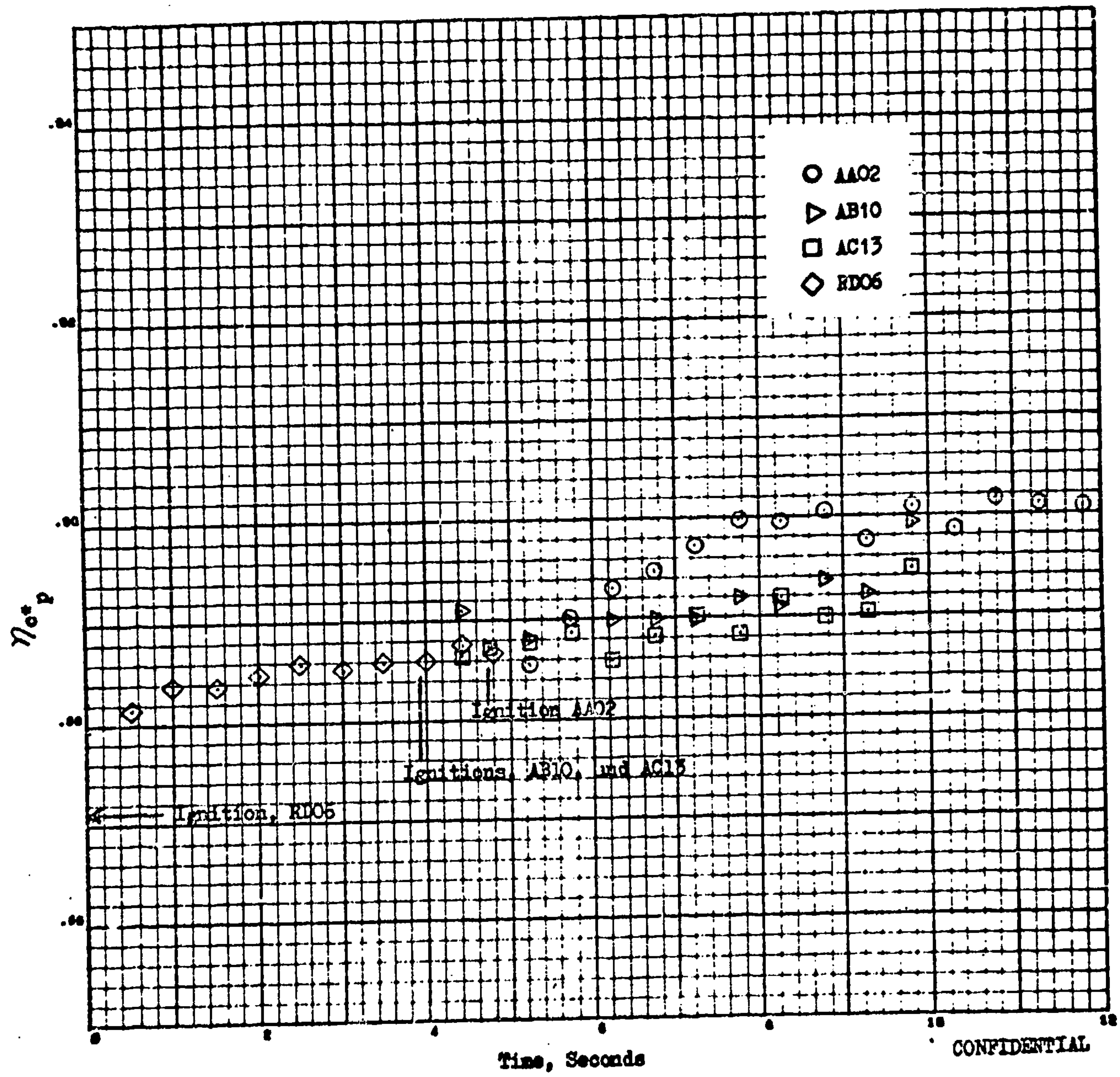

Figure 73. Characteristic Velocity Efficiency vs Time

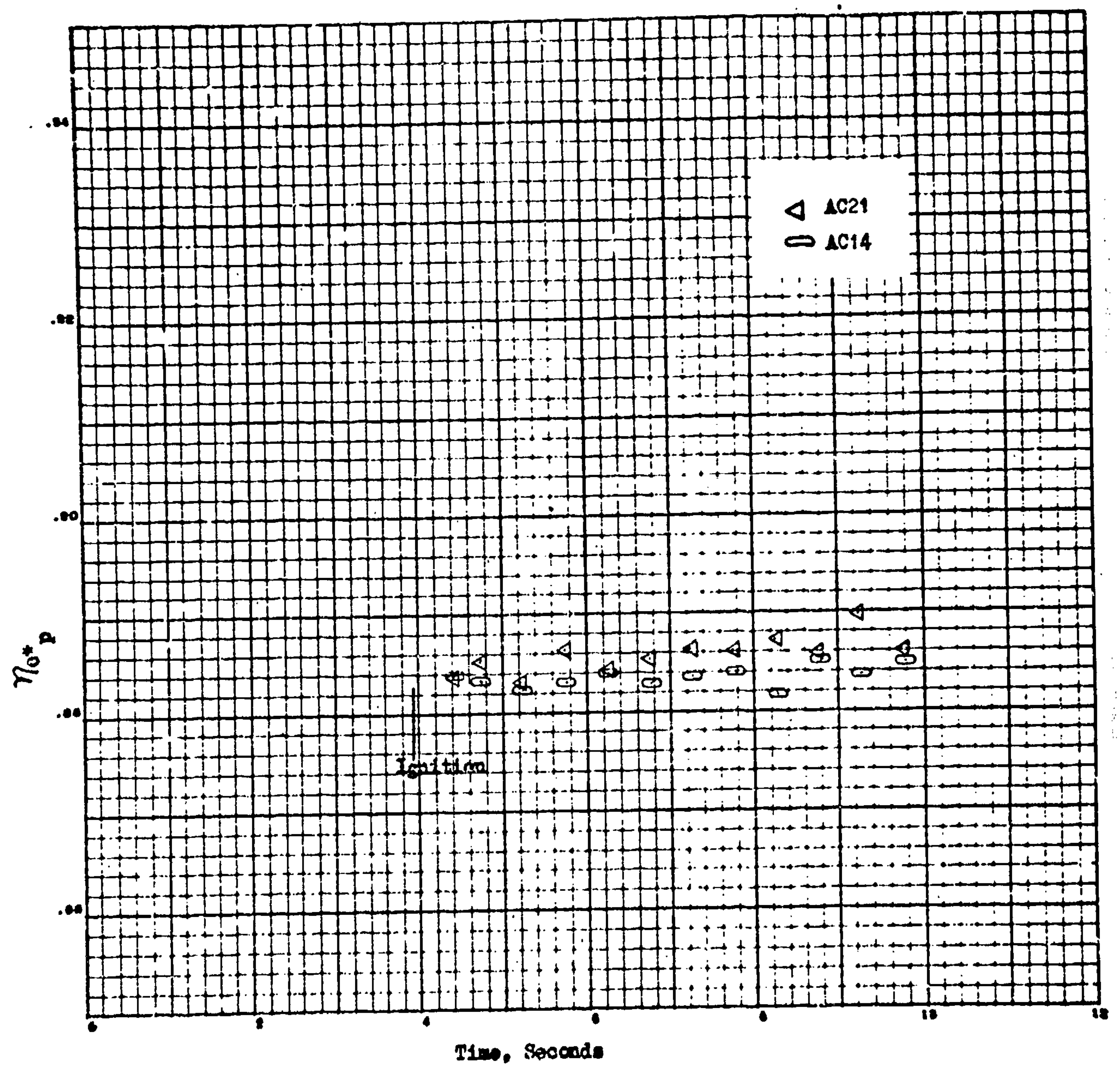

Figure 74. Characteristic Velocity Efficiency vs Time, Tests AC14 and AC21

UNCLASSIFIED

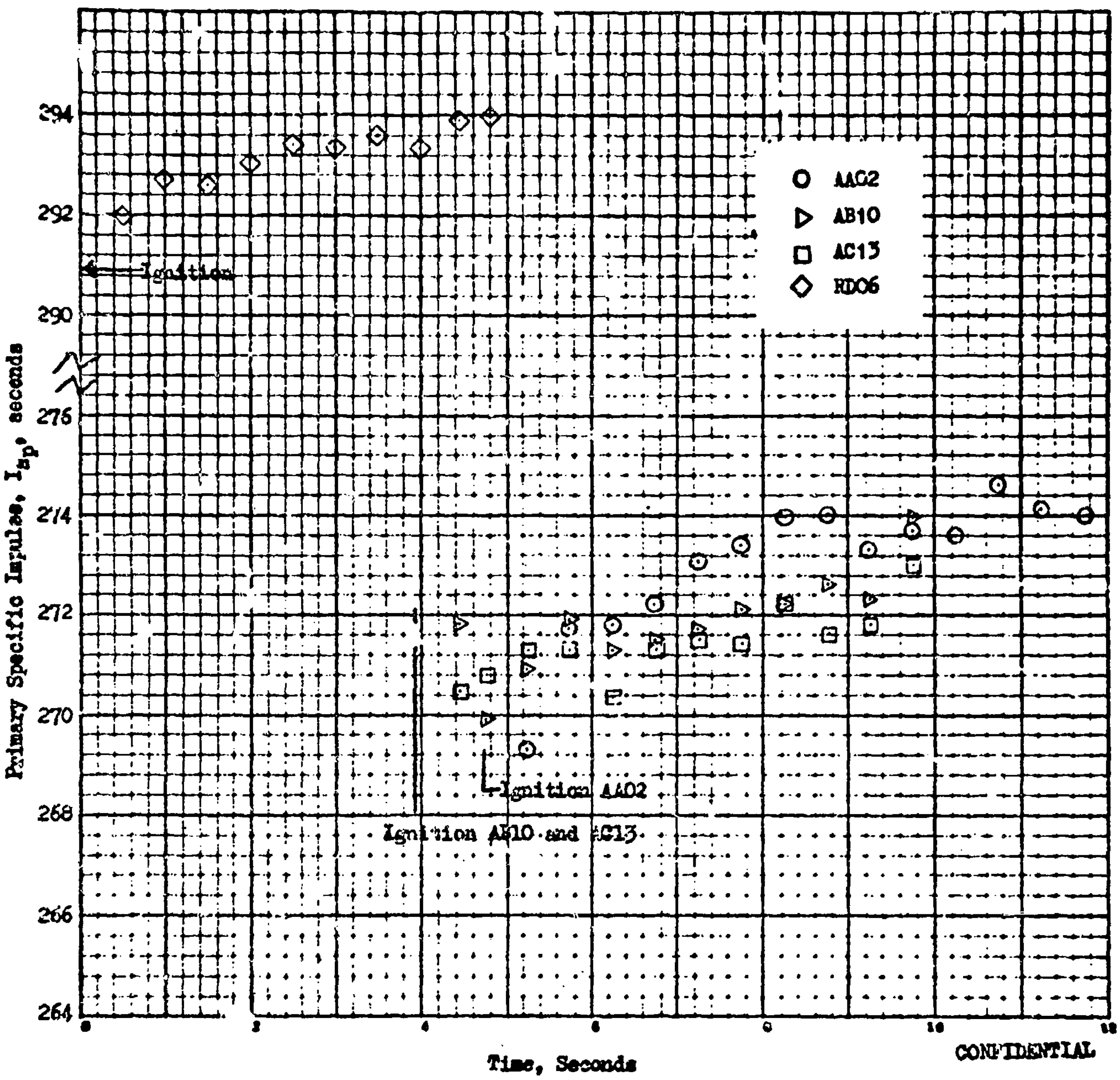

Figure 75. Primary Nozzle Specific Impulse vs Time

UNCLASSIFIED

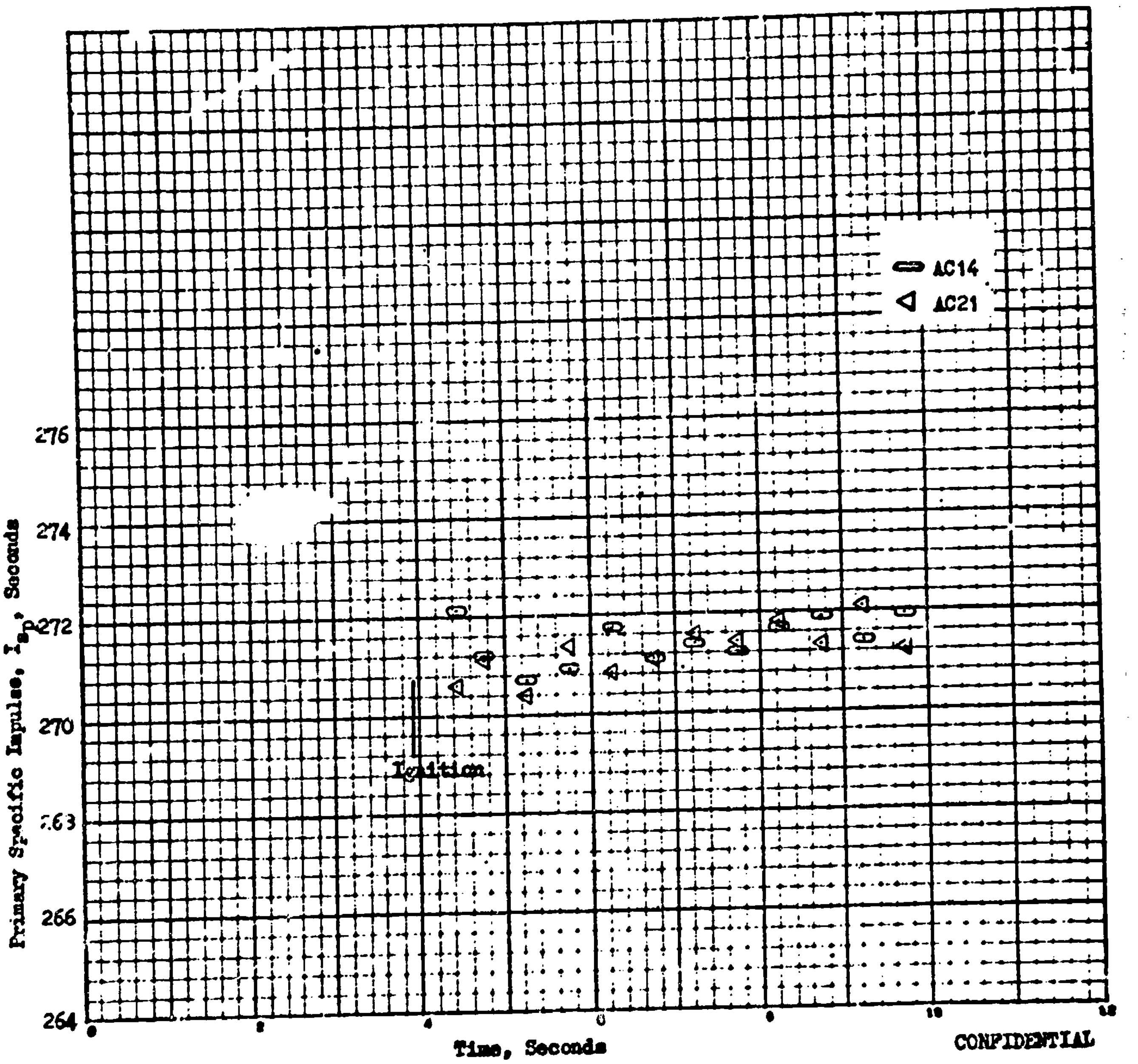

CONFIDENTIAL

Figure 76. Primary Nozzle Specific Impulse vs Time, Tests AC14 and AC21

(U) It is not certain what causes the upward drift in efficiency. One possible reason is that there is a heat sink effect occurring within the chamber. A rough estimate of the difference in heating rate for the engine with cold walls and hot walls (≈ 800°F) indicated that approximately three seconds of specific impulse would be gained during the transition. Reference to the theoretical baffle heating rate curves (Fig. 48, page 109) indicates that relatively constant heating rate occurs after approximately one second of operation. The water-cooled walls should achievé a stabilized surface temperature within even less time. However, in initial sea level tests at 400 psia chamber pressure, melting on a portion of the nozzle surface occured only after five seconds of operation.

(U) Another possible reason for the increase in efficiency is indicated by the injector flow pattern relative to the baffle surface (Fig. 77). One quarter of the orifice pattern is adjacent to the baffle surface. An appreciable portion of flow appears to impinge on the baffle walls. As the baffles heat up, vaporization and more efficient combustion may be promoted.

(C) Nozzle thrust efficiency results obtained with the primary thrust method are illustrated for zero secondary flow in Fig. 73. The altitude tests showed the proper trend with pressure ratio and a very close grouping among the three tests. The results achieved with secondary flow and presented in the next section showed equally consistent agreement with theoretical trends and an exceptionally close grouping of comparable or overlapping tests (high and low pressure ratio) with the same secondary flowrate. The experimental efficiency data obtained with a scaled cold-flow model (See Volume I of this report) are also shown. Except for theoretical friction and kinetic differences, the efficiencies would be virtually the same.

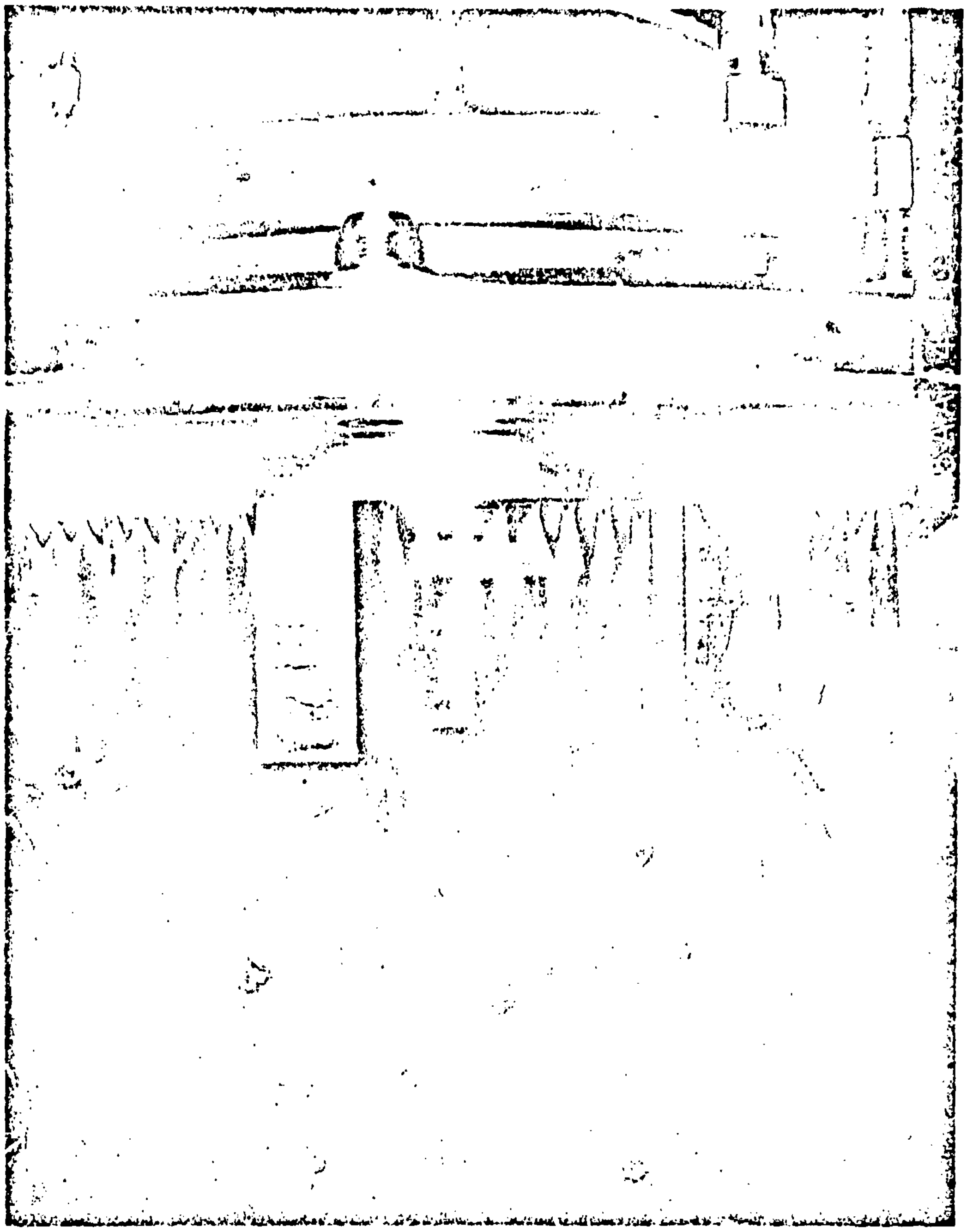

Figure 77. Water Flow Test of Number 2 Injector

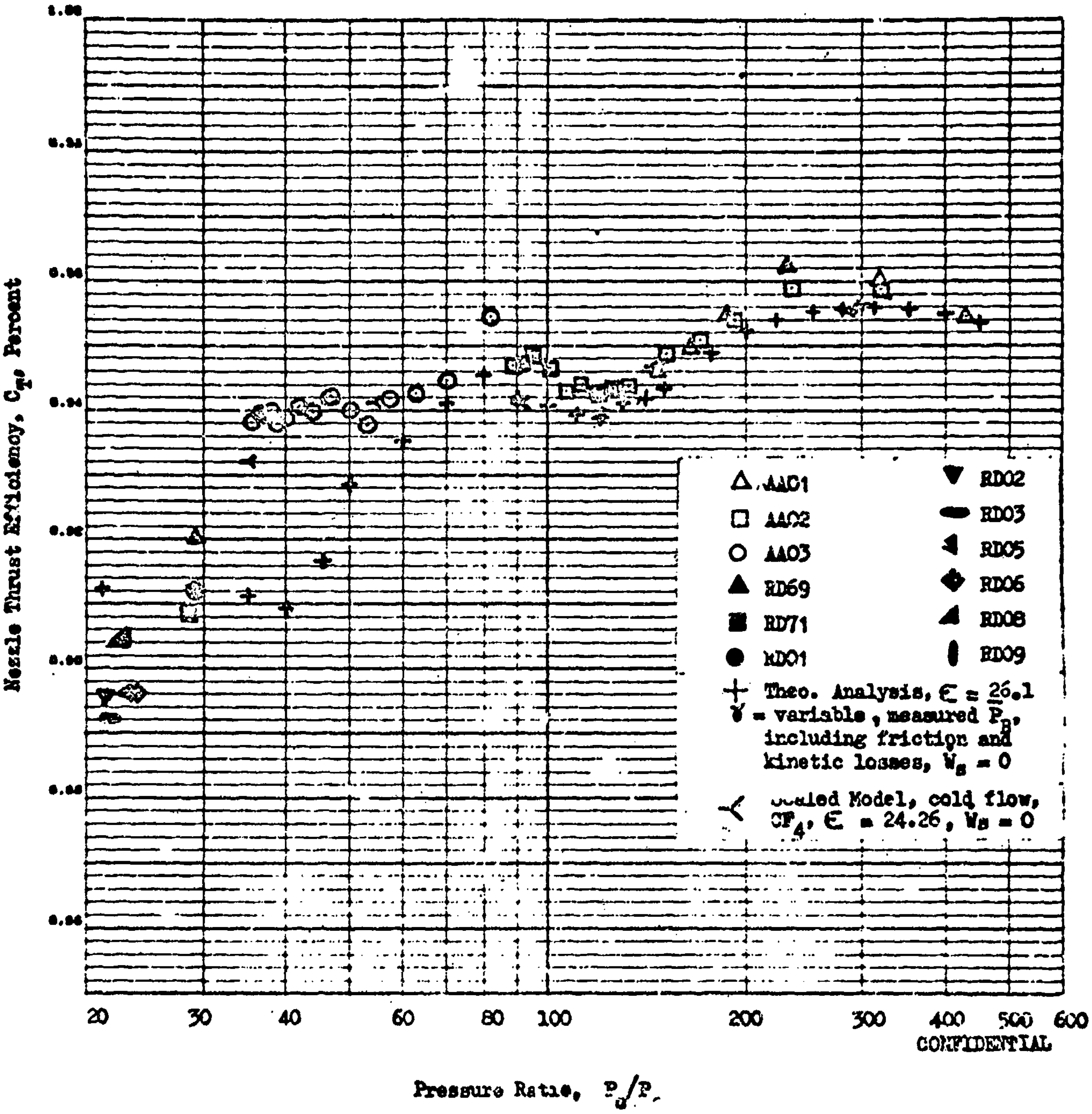

Figure 78. Nozzle Thrust Efficiency vs Pressure Ratio, $\dot{W}_s$ = 0

(C) The theoretical performance estimate for the hot-firing model is comprised of a constant γ ($\gamma = 1.25$) transonic flow analysis of the throat region, a variable γ (corresponding to shifting equilibrium properties during expansion) potential flow analysis of the nozzle, an analysis of theoretical reaction kinetics (using Bray criteria), a viscous flow analysis (drag) and measured base pressures. An area ratio of 26.1 was used for the theoretical computations because this corresponded closely to the actual area ratio during the firings with no secondary flow.

(C) The theoretical efficiency curve shows a peak efficiency of .9565 at a design pressure ratio of 300 compared to an experimental maximum efficiency of 96.0. The experimental data agrees within 1 percent of the theoretical performance from a pressure ratio of 450 to a pressure ratio of 50 where nozzle compression begins. The experimental hot-firing efficiency is approximately 3 percent higher than the theoretical estimates in the pressure ratio range from 35 to 45. The fact that the cold-flow efficiency trend is the same as the hot-firing data suggests that the theoretical trend in the recompression region is in error.

(C) The results achieved using this method were definitely more logical in indicating performance trends than any other method attempted and were adopted for the final interpretation of data presented here. The absolute level of thrust efficiency, however, probably has an uncertainty on the order of $\pm$ 1 percent. If the posttest throat area for AA03 were selected as the reference, the altitude results would be based on 0.9 percent higher throat areas. If either the pre-or posttest A_p for the AB series were selected as the reference, the throat areas would be one percent smaller than the areas actually used. The absolute performance level presented is a mean value and is probably representative of the actual performance level.

Nozzle Performance

(U) Tabulated values of thrust chamber and nozzle performance in terms of $\eta_{C^*_p}$, $\eta_{C^*_s}$, I_s, η_{I_s}, $\eta_{I_{s,top}}$, C_T and $C_{T,top}$ are presented vs time in Appendix 1 along with other pertinent data defining engine performance.

(C) For this discussion nozzle performance is described by nozzle thrust efficiency, C_T and $C_{T_{top}}$. Specific impulse efficiency data is not a good indicator of nozzle performance for this engine because of variations in C* efficiency among the tests and during a test. This is illustrated by Fig. 79 which shows the effect of time (pressure ratio decreases with increasing time) on η_{I_s} for two long duration (7.4 seconds) altitude tests with no secondary flow. It can be seen that for the high pressure ratio test, η_{I_s} at 1/3 of design pressure ratio is equal to η_{I_s} at design pressure ratio. The same trend is shown for test AA03. Except for the first data point, which is in a peak performance region of pressure ratio, the η_{I_s} curve is increasing steadily in a pressure ratio region where it should be decreasing. At approximately 14 percent of design pressure ratio η_{I_s} has decreased only 1/2 percent. Therefore η_{I_s} is not a good indicator of nozzle performance for this particular aerospike engine because its combustion performance is improving with time.

(C) Sea level data is also shown in Fig. 79. There is a difference of 3.8 percent in I_s efficiency between the data. There is, however, a difference of approximately 2.5 percent in $\eta_{C^*_p}$ between the three sea level tests RD69, 71, 01 and the test AA03. However, the average slope of the thrust efficiency curve shown previously (Fig. 78) could readily be extrapolated quite close to the altitude data. Actual differences in η_{C^*} between tests, therefore, can lead to erroneous conclusions about nozzle performance. It can be seen by comparing

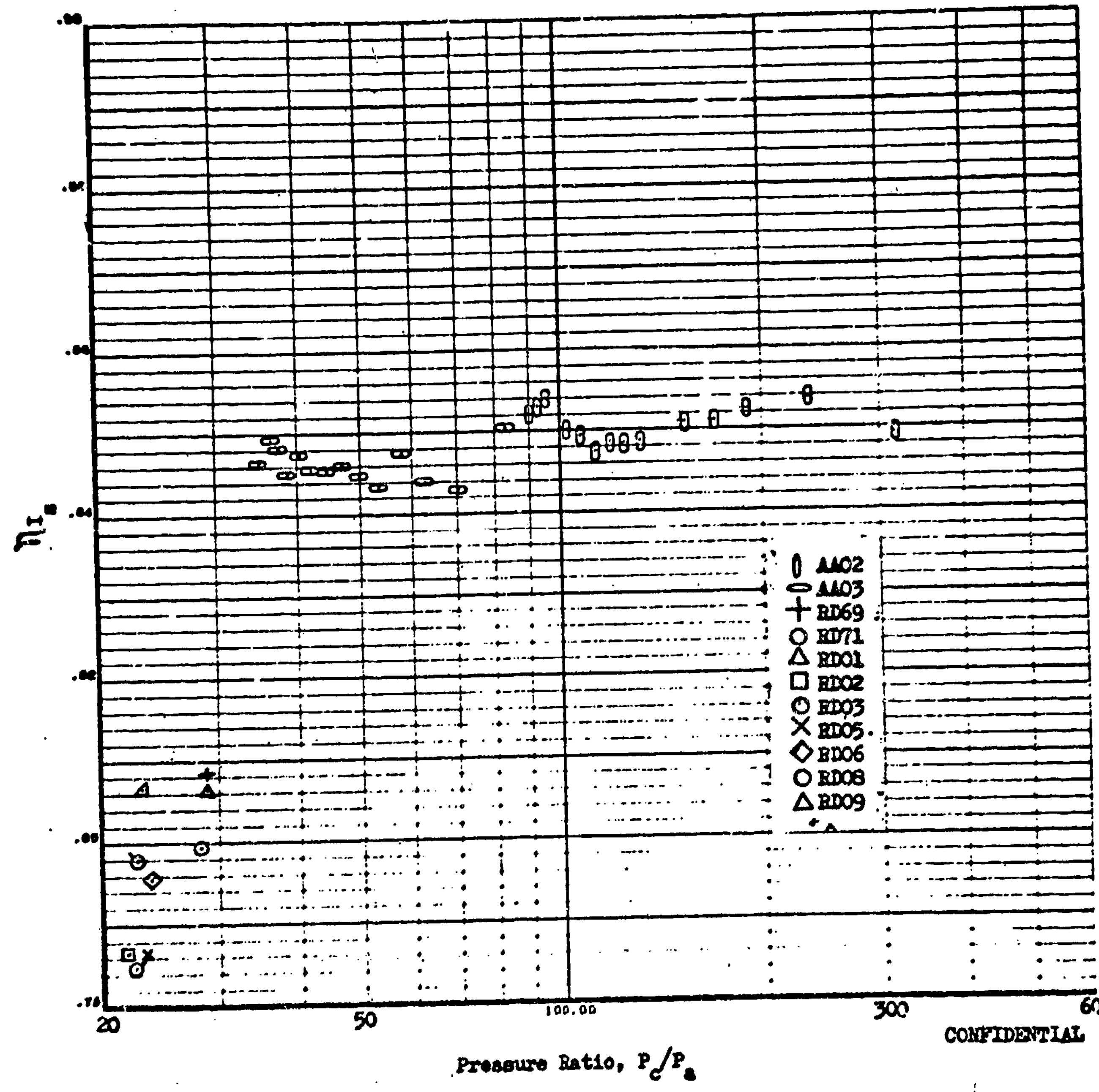

Figure 79.. Specific Impulse Efficiency vs. Pressure Ratio, $\dot{w}_s = 0$

Fig. 78 and 79 that the use of η_{I_s} does not give an accurate representation of nozzle thrust efficiency trends for this engine.

(C) The effect of approximately 1.2 percent secondary flow on aerospike performance is shown in Figs. 80 and 81. An improvement in C_T on the order of 0.3 to 0.5 percent, is indicated at design pressure ratio with this flowrate. A maximum performance increase of approximately 1.5 percent is achieved at pressure ratios from approximately 90 to 130. From the pressure ratio where nozzle recompression begins (~ 50), to a pressure ratio of 22, the performance with 1.2 percent secondary flow is equal to the performance without secondary flow. With performance referenced to primary properties only ($C_{T_{top}}$, Fig. 81), performance with 1.2 percent secondary fl , is equal to zero secondary flow performance at design pressure ratio, and a maximum of 1 percent greater than 0 secondary flow performance at a pressure ratio of approximately 110. From a pressure ratio of 50 down to 22, $C_{T,top}$, with 1.2 percent secondary flow, is approximately 0.3 percent lower than with zero secondary flow. For the sea level tests, a line joins the efficiencies obtained with and without secondary flow for the same firing.

(C) Figures 82 through 85 show the comparison of nozzle C_T and $C_{T,top}$ values for 2 to 3 percent secondary flow with those for zero secondary flow. C_T gains with secondary flow on the order of .2 to .3 percent are indicated at design pressure ratio. With 2 to 3 percent secondary flow, a maximum performance improvement of about 1.2 percent is achieved at a pressure ratio of approximately 110. Again, the C_T curves with and without secondary flow converge at a pressure ratio of 50. At a pressure ratio of 22, a loss in C_T of 0.4 percent results with the use of 2 to 3 percent secondary flow.

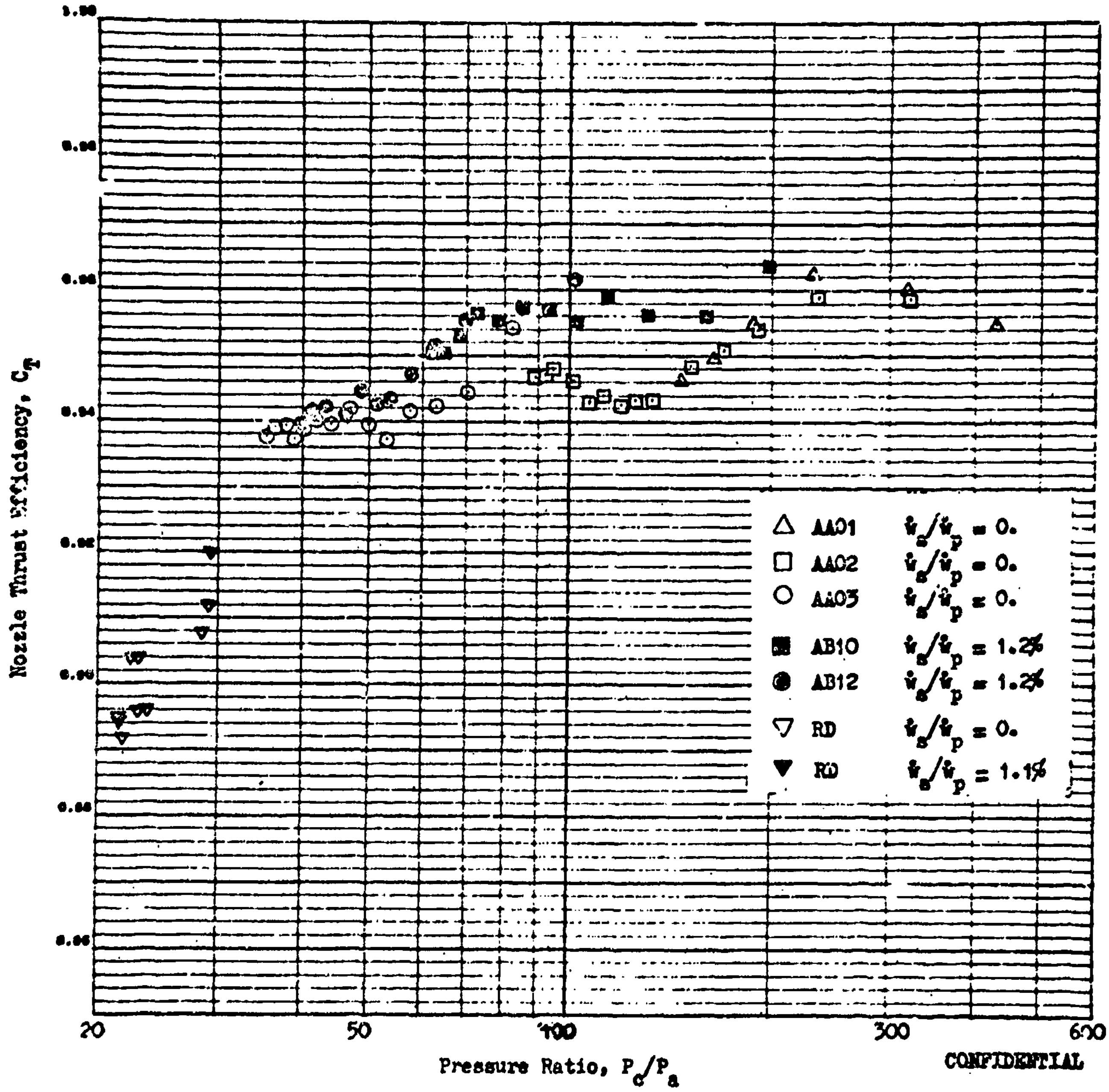

Figure 80. Nozzle Thrust Efficiency vs. Pressure Ratio, 0 and 1 Percent Secondary Flow

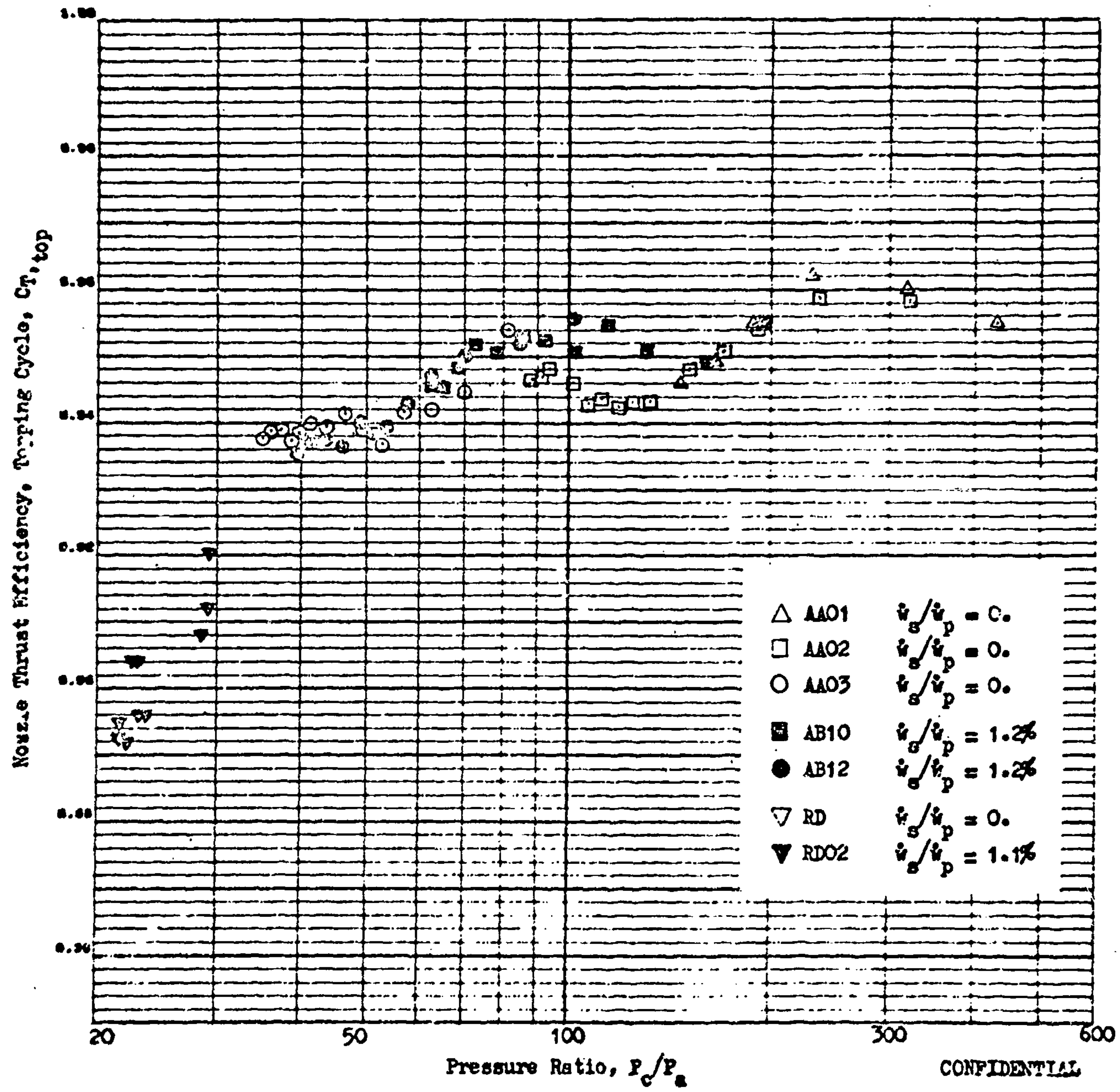

Figure 81. Nozzle Thrust Efficiency, Topping Cycle, vs. Pressure Ratio, 0 and 1 Percent Secondary Flow

UNCLASSIFIED

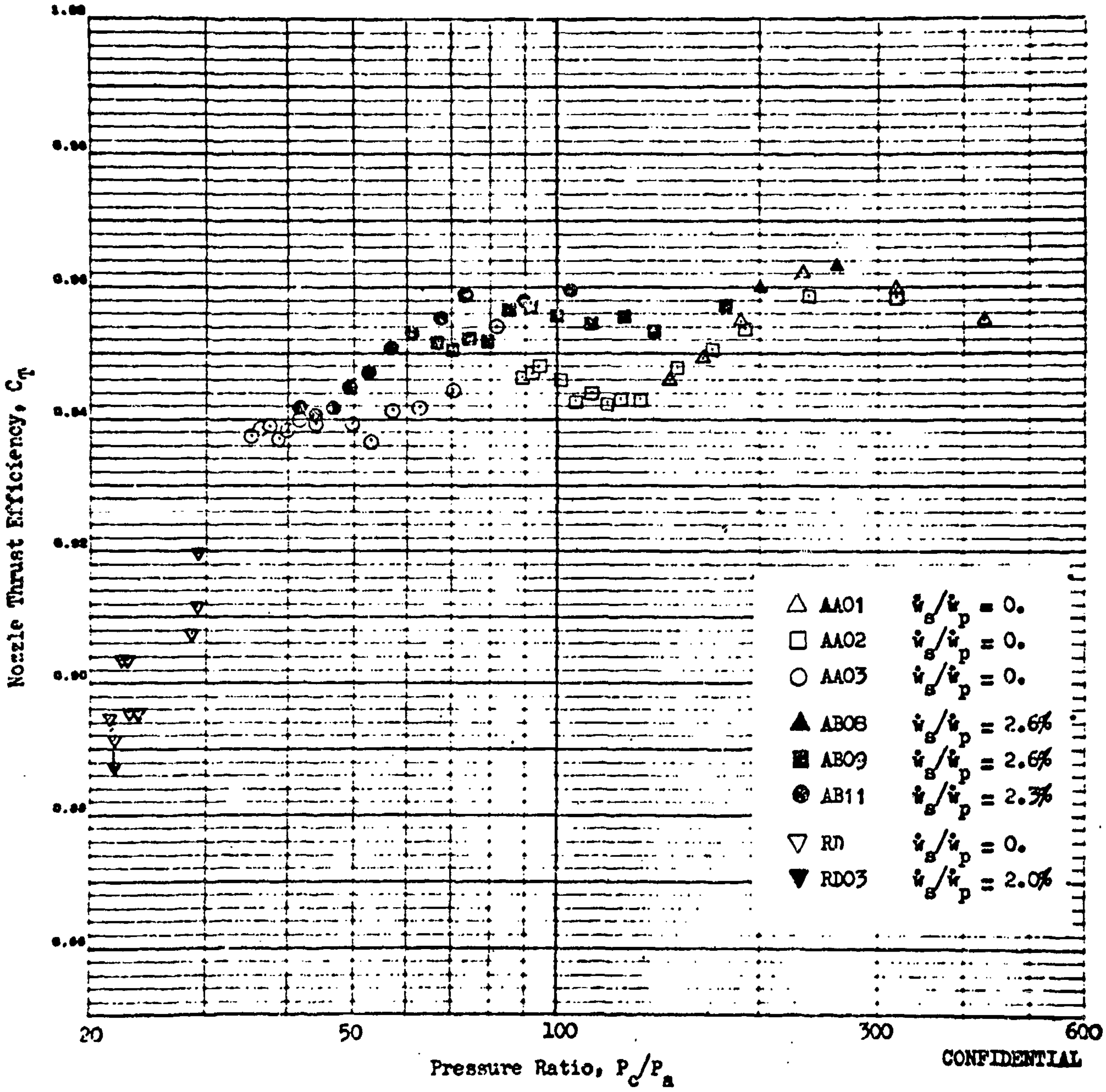

Figure 82. Nozzle Thrust Efficiency vs. Pressure Ratio, 0 and 2 Percent Secondary Flow

CONFIDENTIAL UNCLASSIFIED

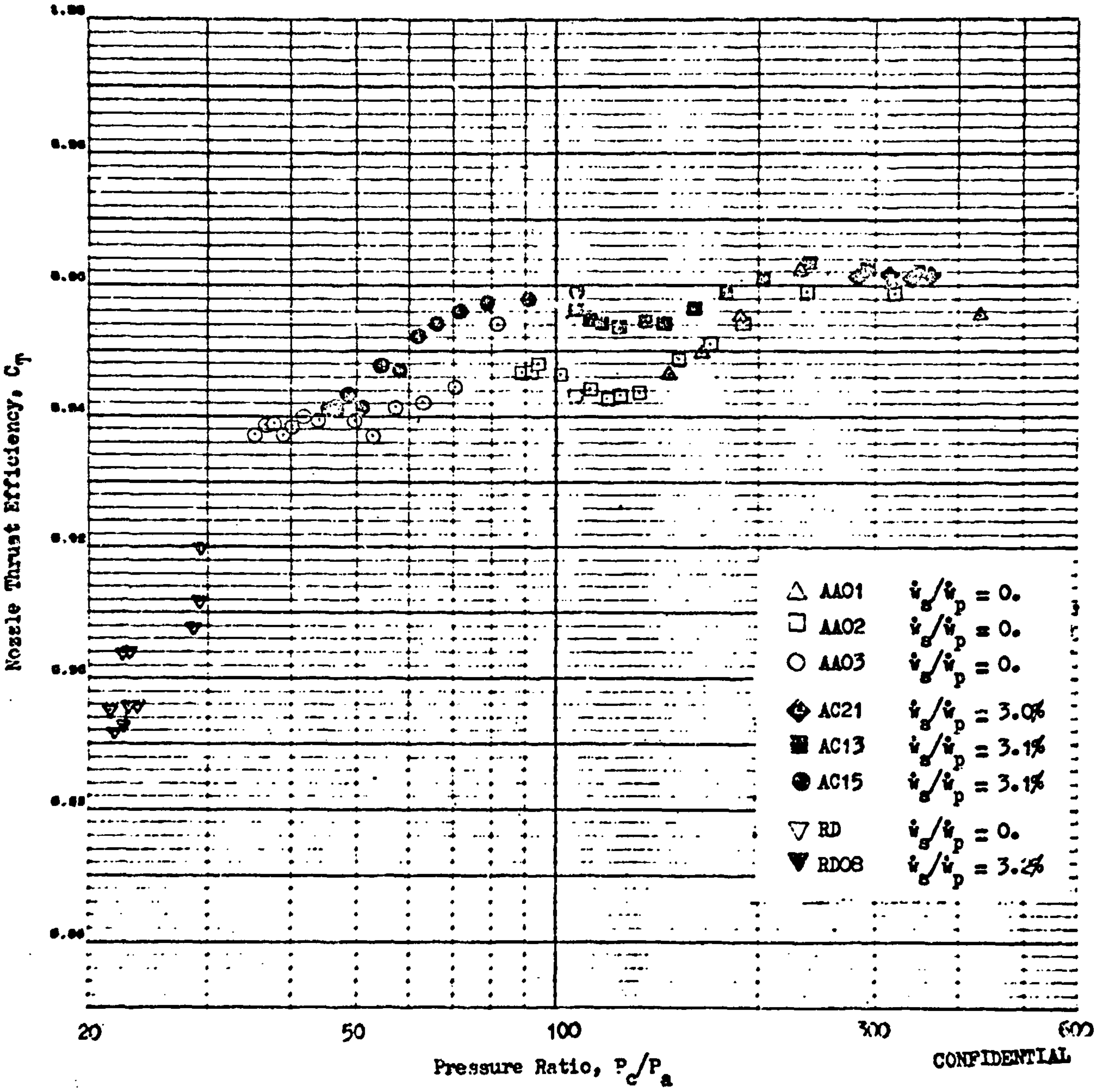

Figure 83. Nozzle Thrust Efficiency vs. Pressure Ratio, 0 and 3 Percent Secondary Flow

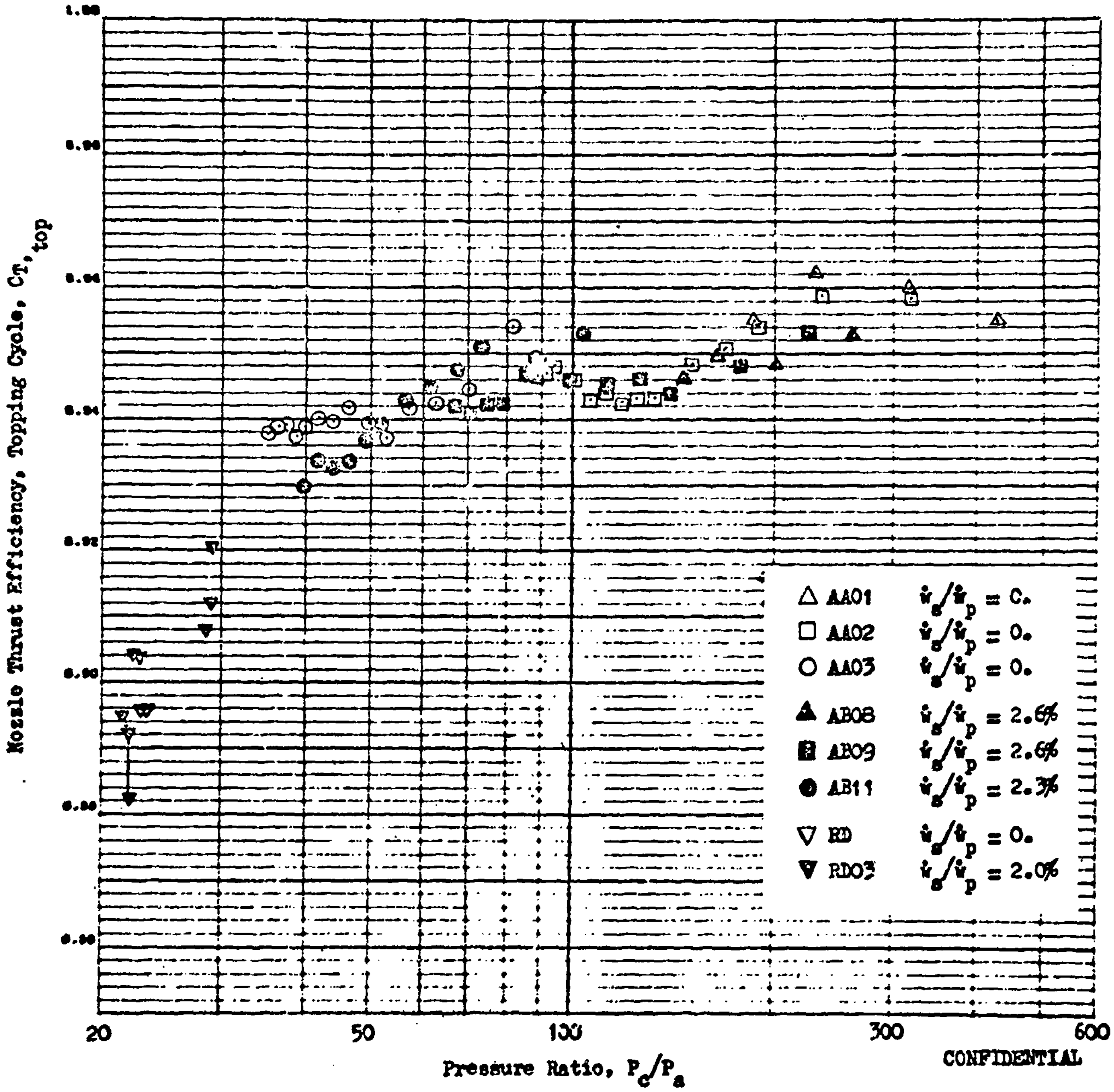

CONFIDENTIAL

Figure 84. Nozzle Thrust Efficiency, Topping Cycle, vs. Pressure Ratio, 0 and 2 Percent Secondary Flow

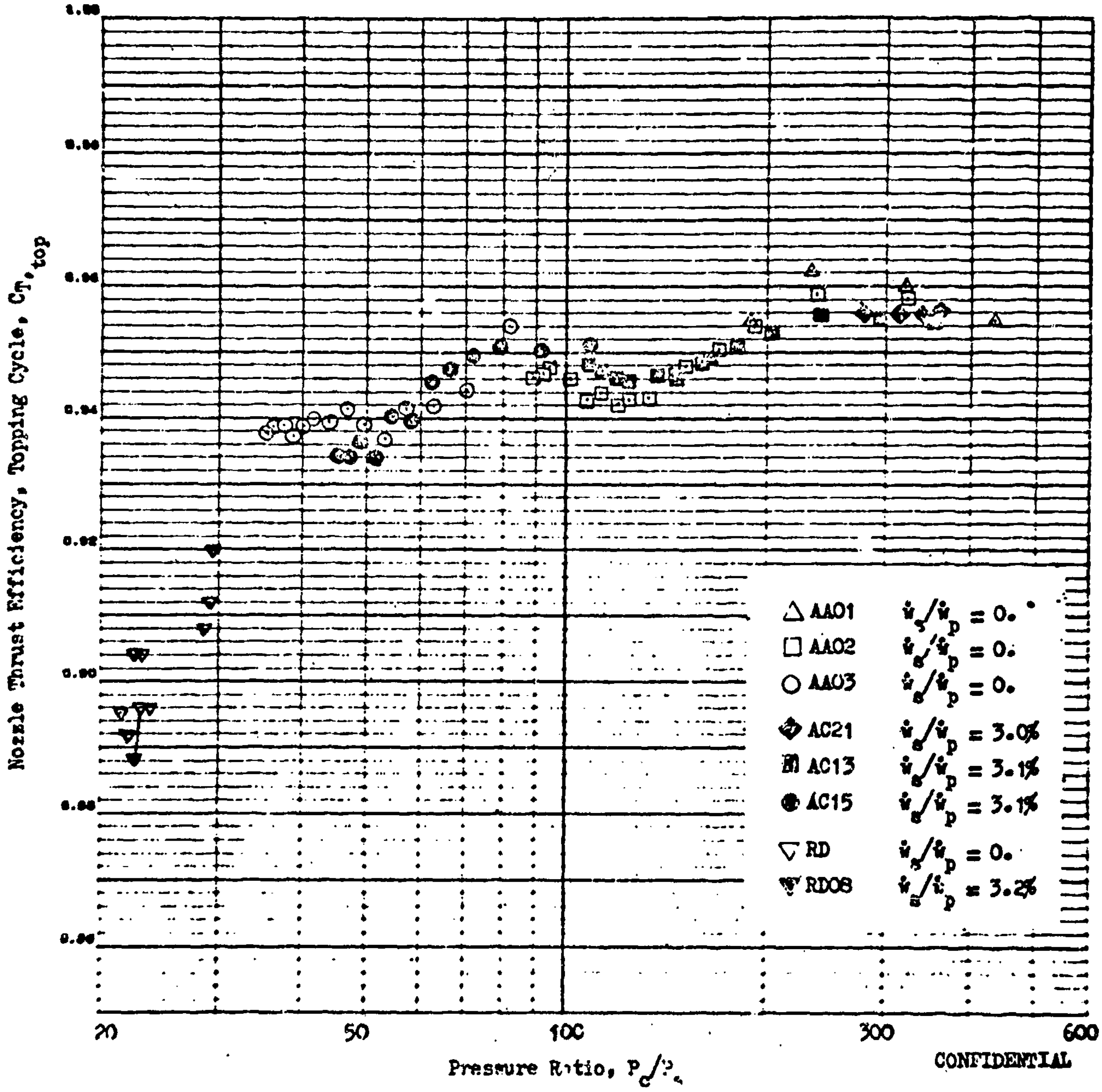

Figure 85. Nozzle Thrust Efficiency, Topping Cycle, vs. Pressure Ratio, 0 and 3 Percent Secondary Flow

(C) When performance is compared using the topping cycle definition of efficiency, $C_{T,top}$ is approximately 0.5 percent lower with 3.0 percent secondary flow at design pressure ratio.

(C) From a pressure ratio of 150 to 50, $C_{T,top}$ is higher with secondary flow by a maximum of approximately 0.5 percent. At a pressure ratio of 22, $C_{T,top}$ with 3 percent secondary flow is 0.8 percent lower than with no secondary flow.

(C) With 5.0 percent secondary flow, C_T at design pressure ratio was lower (Fig. 86) than the zero secondary flow C_T by approximately 0.6 percent. Thrust efficiency with 5.0 percent flow was slightly higher than with zero secondary flow from a pressure ratio of 150 down to approximately 50. At a pressure ratio of approximately 23, C_T was about 0.6 percent lower than 5 percent secondary flow.

(C) $C_{T_{top}}$ with 5 percent secondary flow was approximately 1.8 lower than the no secondary flow $C_{T_{top}}$ at design pressure ratio, and generally lower over the entire pressure ratio range (Fig. 87).

(C) Figures 88 and 89 show the results of the tests to determine the effect of mixture ratio on nozzle efficiency. All the tests were with approximately 3 percent secondary flow. AC13 and AC15 were high and low pressure ratio range firings, respectively, at a GG mixture ratio of .11. Test AC18 and AC17 were at a slightly lower mixture ratio of 0.10 and tests AC19 and AC20 were at a significantly higher mixture ratio of 0.18. Test AC21 was a constant altitude test at a mixture ratio of 0.11, (similar to AC13 and AC15). Table 10 lists typical secondary flow C* values for the test program. The effect of

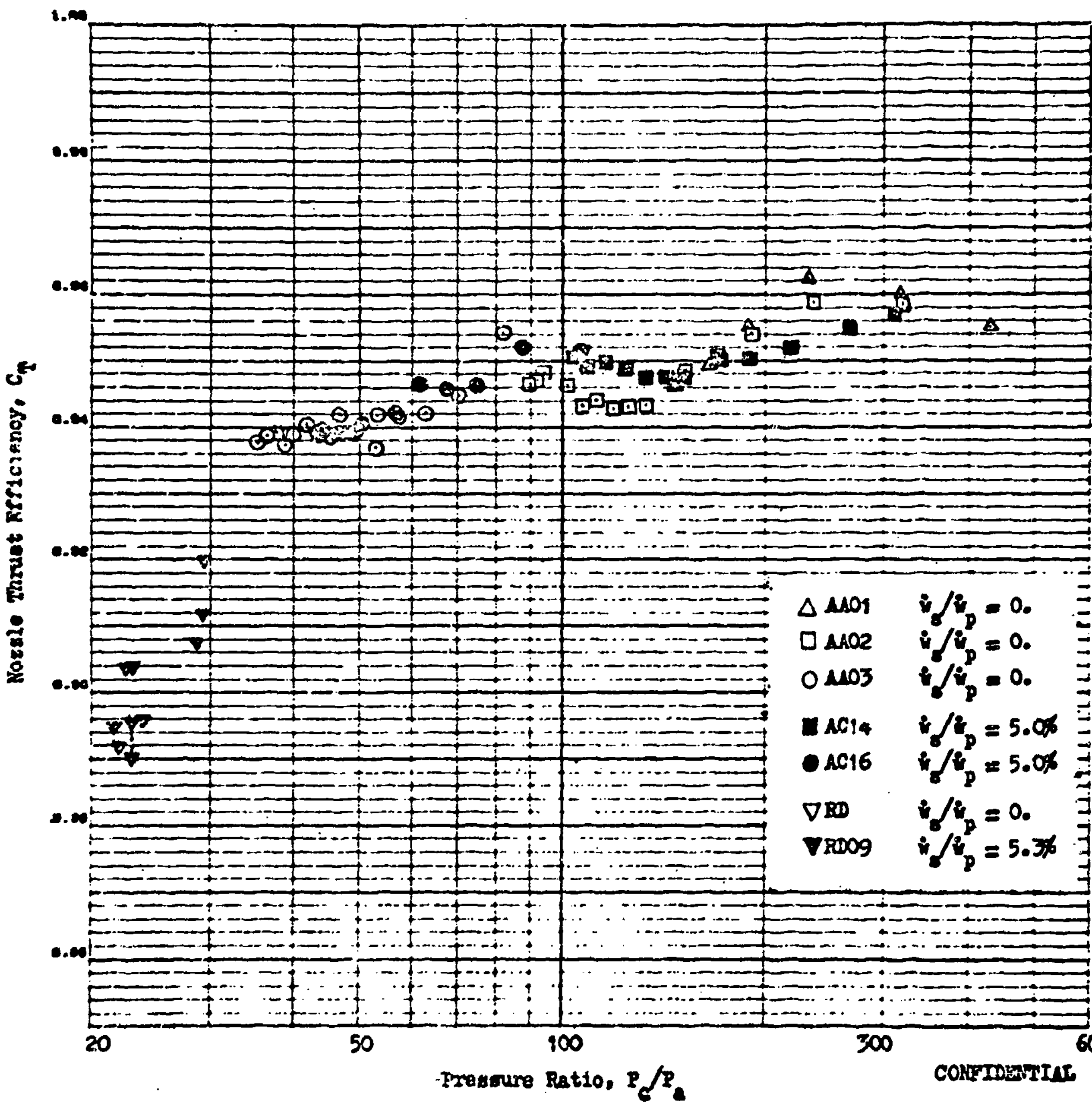

CONFIDENTIAL

Figure 86. Nozzle Thrust Efficiency vs. Pressure Ratio, 0 and 5 Percent Secondary Flow

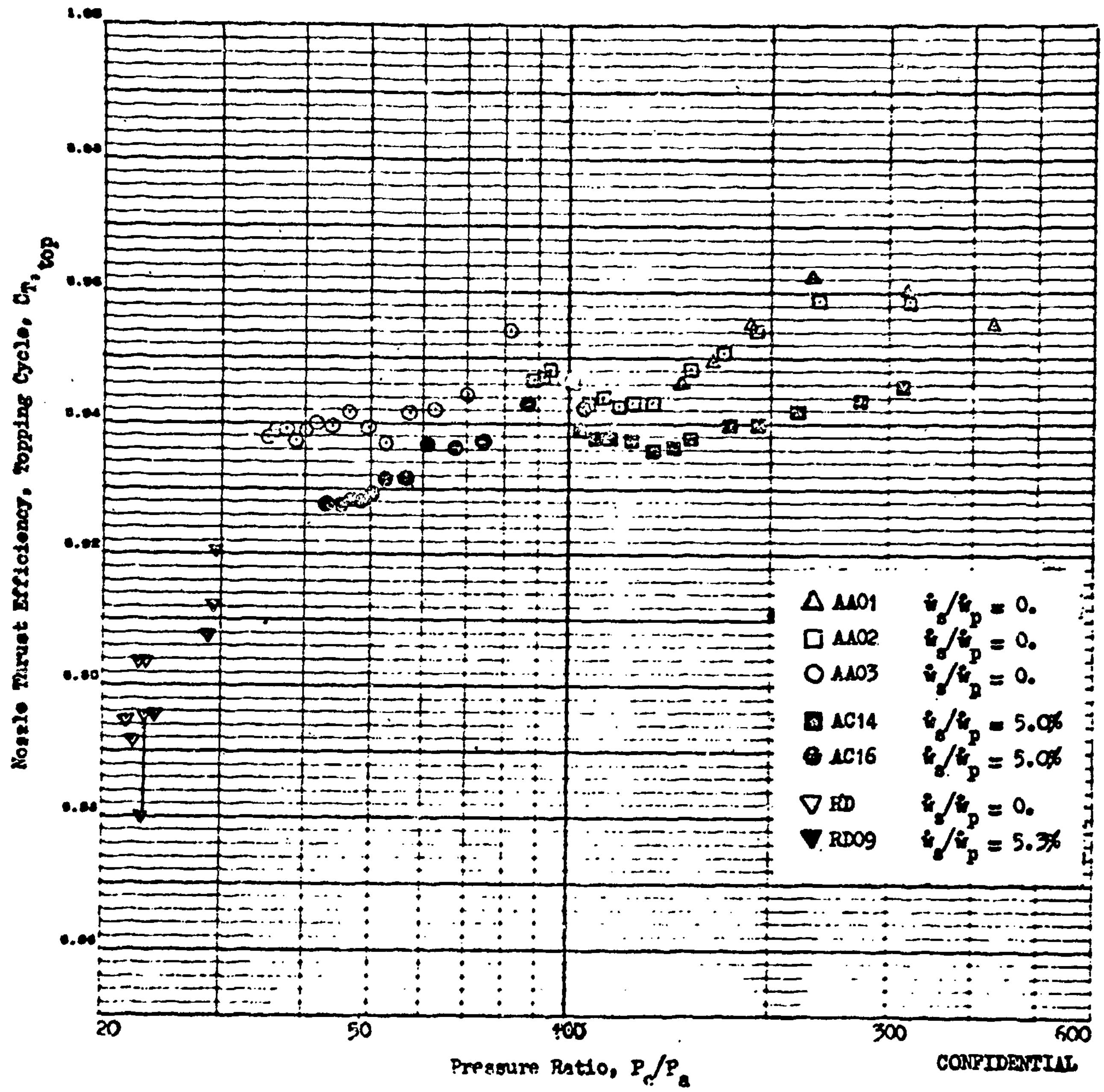

CONFIDENTIAL

Figure . 87. Nozzle Thrust Efficiency, Topping Cycle, vs. Pressure Ratio, 0 and 5 Percent Secondary Flow

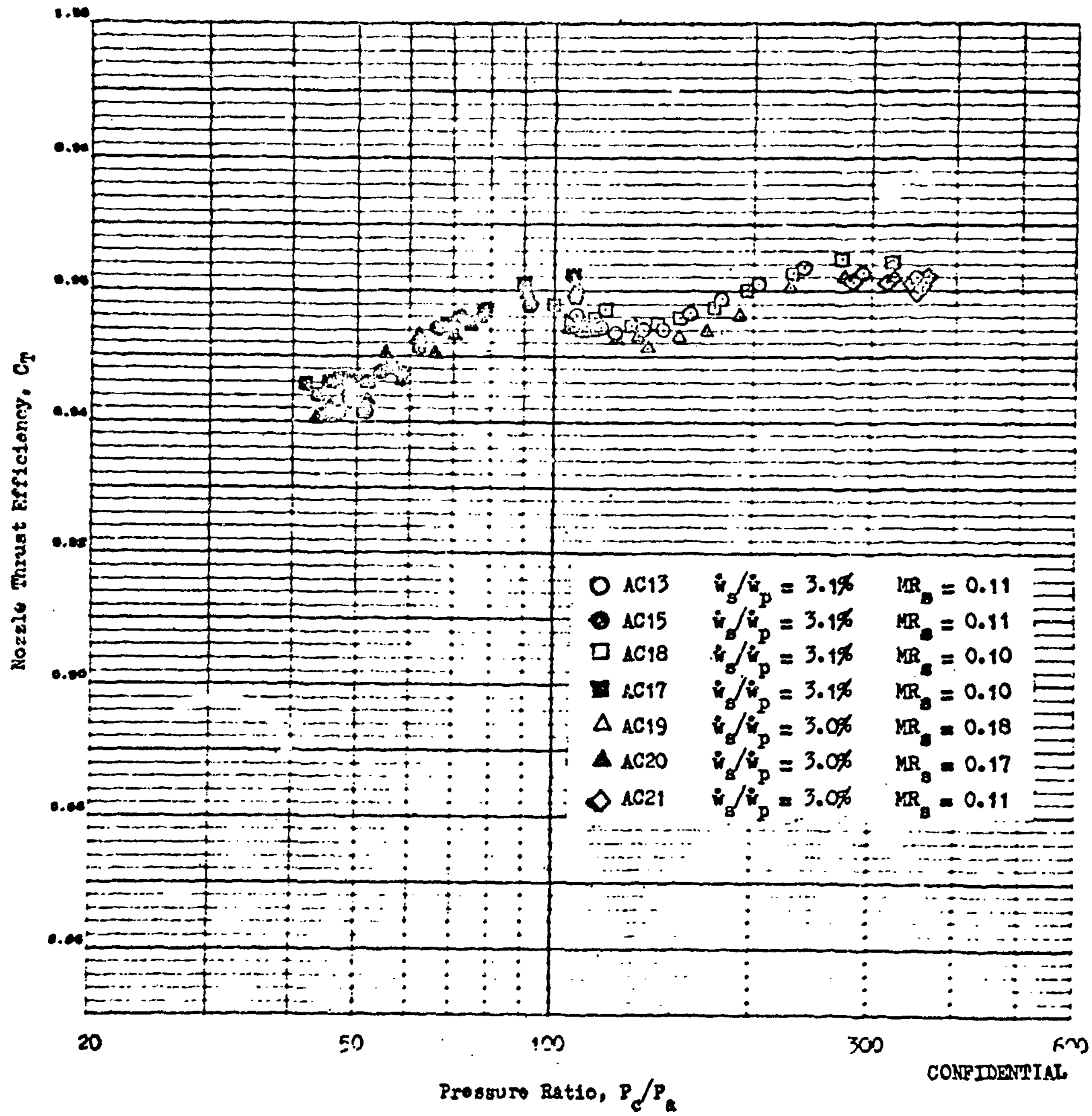

CONFIDENTIAL

Figure 88. Effect of Secondary Mixture Ratio on Nozzle Thrust Efficiency

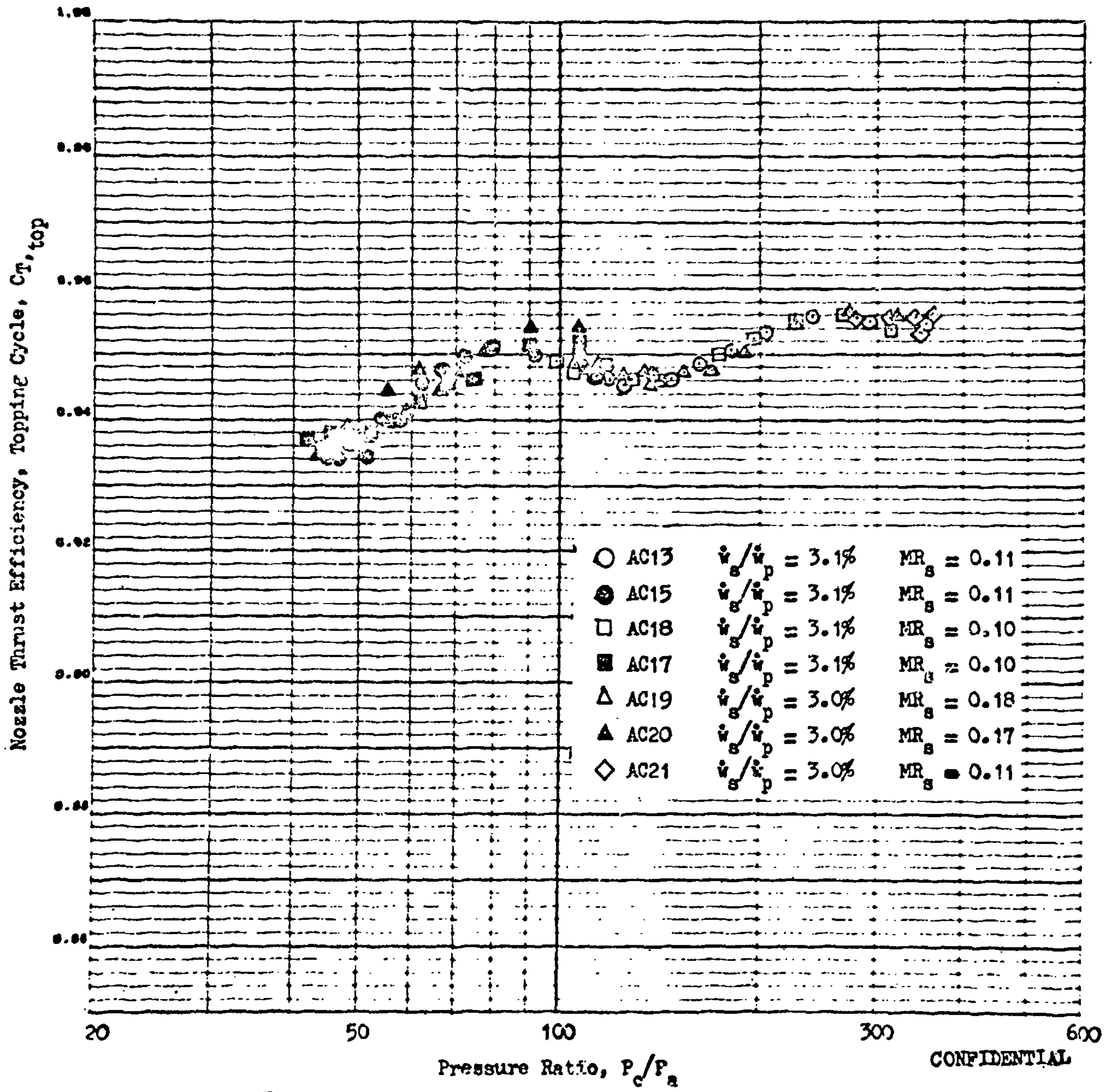

Figure 89. Effect of Secondary Mixture Ratio on Nozzle Thrust Efficiency, Topping Cycle

TABLE 10

SECONDARY FLOW PARAMETERS

CONFIDENTIAL

Test	$\dot{W}_s/\dot{W}_p$ Percent	MR_s	C^*_s ft/sec	$\eta_{C^*_s}$ Percent
RD02	1.10	.260	3768	-
RD03	1.96	.092	3632	83.7
RD08	3.23	.165	3885	88.5
RD09	5.30	.163	3979	90.0
AB08	2.59	.085	3139	72.4
AB09	2.64	.089	3138	72.5
AB10	1.21	.110	2996	69.5
AB11	2.33	.114	3233	74.1
AB12	1.22	.111	2913	67.6
AC13	3.07	.111	3661	84.6
AC14	5.03	.118	3775	86.4
AC15	3.05	.115	3801	87.7
AC16	5.02	.117	3801	87.0
AC17	3.07	.096	3651	84.8
AC18	3.06	.097	3645	84.6
AC19	2.94	.177	3944	89.8
AC20	2.96	.175	4000	91.1
AC21	3.00	.114	3929	90.7

energy level is not apparent by examining Fig. 88 alone. C_T for the high GG energy level firings (AC19 and AC20) appears generally lower than the other tests. When comparing $C_{T,top}$ values, however, tests AC19 and AC20 appear to have shifted upward approximately 0.3 percent relative to the other tests. This shift is a consequence of the defining equations (page 93) and the lower reference energy level of the low mixture ratio ($\sim$.10) secondary flow. The topping cycle definition indicates no significant differences in efficiency with energy level.

Nozzle Base Pressures

(U) Figure 90 shows the nozzle base pressures with secondary flowrates from 0 to 5 percent. Also shown are the base pressures obtained with the scaled cold-flow model (CF_4) described in Volume I of this report.

(C) With no secondary flow and in the closed wake region $\bar{P}_B/P_{C_-}$ is constant at a value of .0066. Transition to the open wake region (P_B influenced by P_a) occurs at a pressure ratio of approximately 140. From a pressure ratio of 140 to 100, $\bar{P}_B$ is slightly below ambient pressure. At lower pressure ratios $\bar{P}_B$ is higher than ambient pressure. The cold-flow data base pressures appear to be almost identical to the hot-firing values.

(C) Base pressure increases continuously with increasing secondary flowrate. It can also be seen that base pressure is influenced by ambient pressure at higher pressure ratios than with no secondary flow.

(C) Figure 91 shows the base pressures obtained with 3 percent secondary flow and different GG mixture ratios. It is difficult to distinguish any effect of GG mixture ratio on the base pressures.

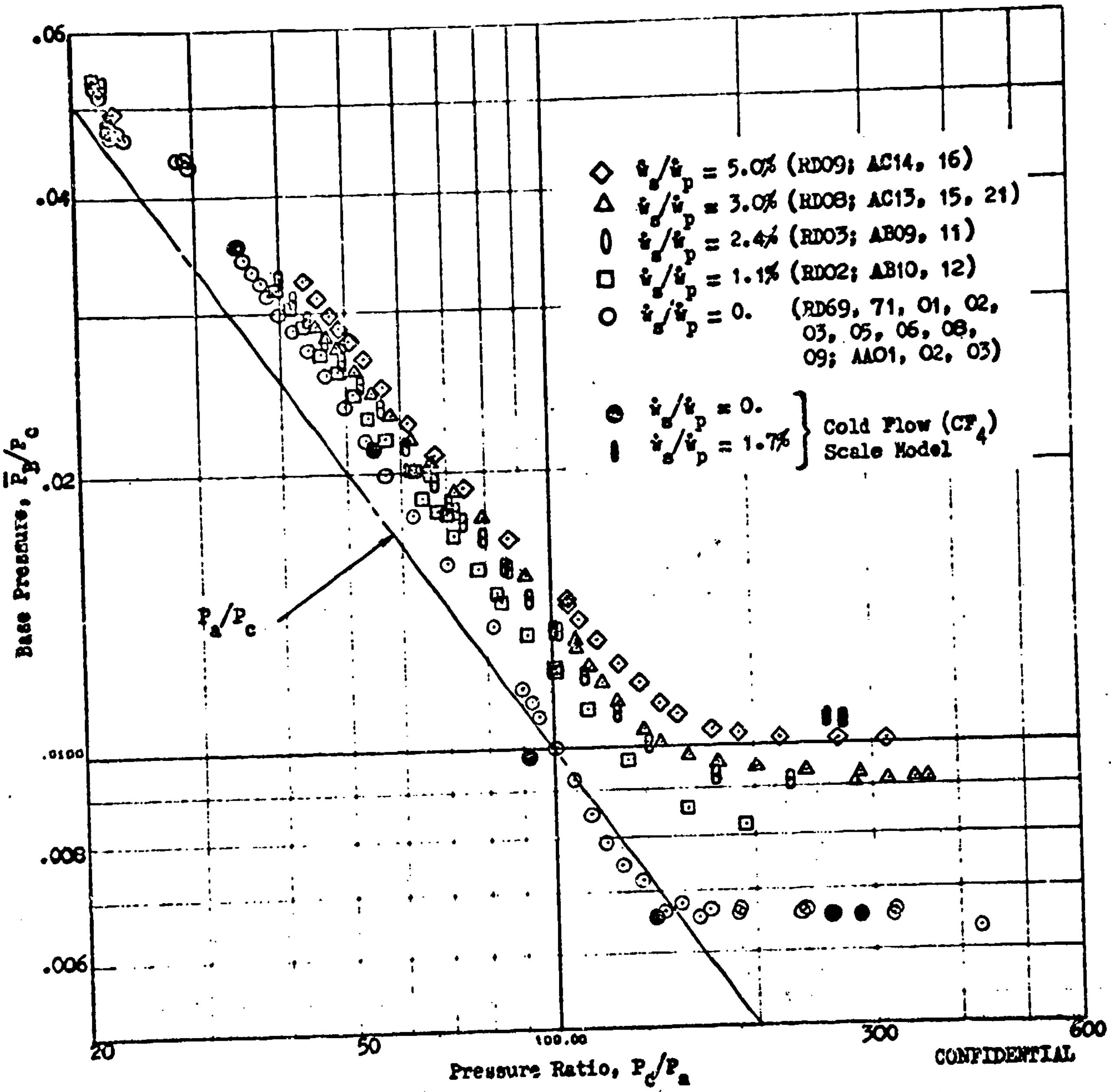

Figure . 90. Base Pressure vs. Pressure Ratio; 0, 1, 2, 3, 5 Percent Secondary Flow

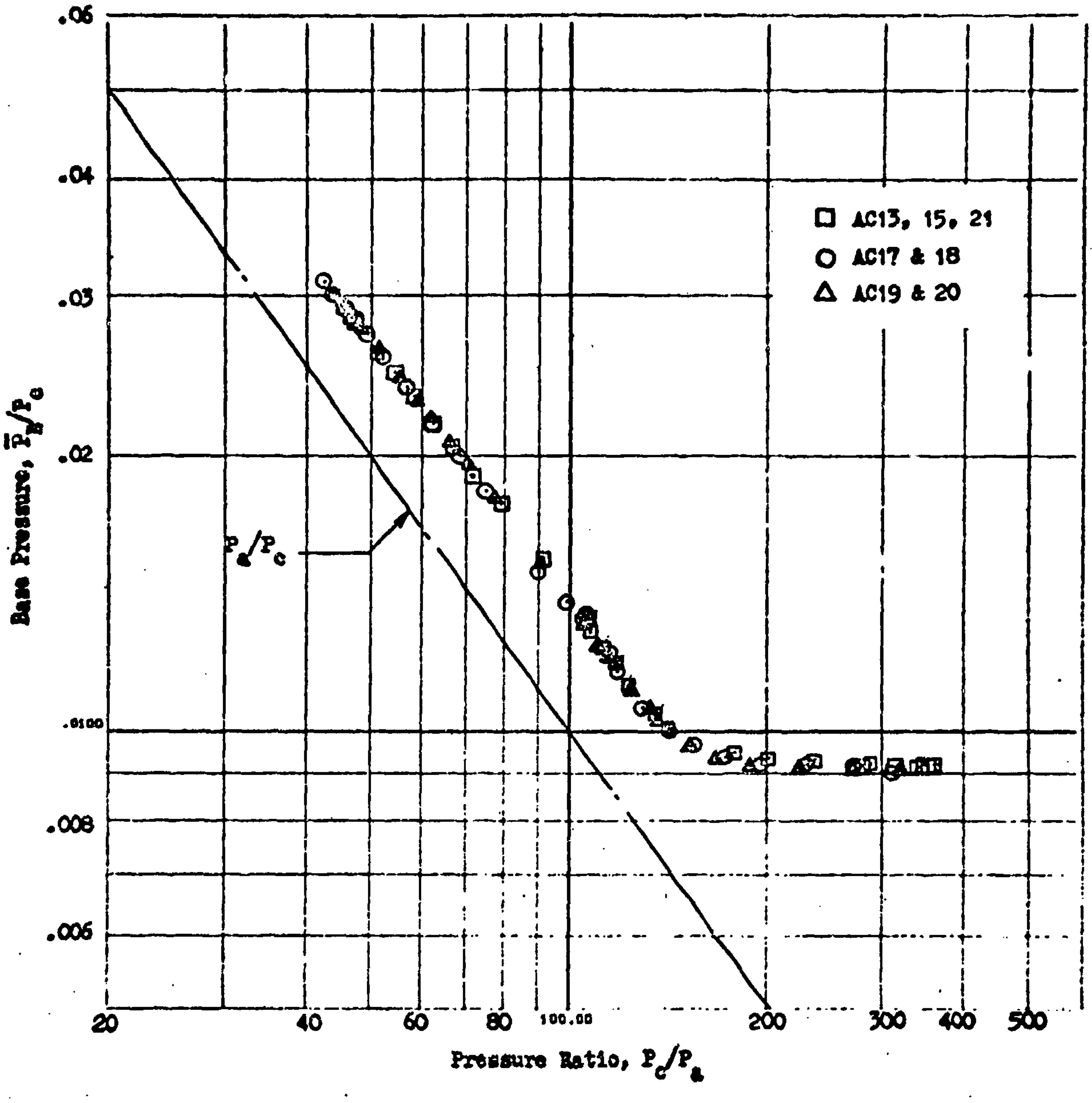

Figure . 91. Comparison of Mixture Ratio Effect on Base Pressure, $\bar{P}_B/P_c$

CONCLUSIONS AND RECOMMENDATIONS

(C) Major conclusions from the test results are

1. The method of determining relative nozzle throat areas developed in this study is an analytical approach which should prove useful in the interpretation of future data with this type nozzle.
2. A relatively high level of nozzle efficiency was achieved ($\backsim$ 96.0) at design pressure ratio with a 12 percent length aerodynamic spike nozzle with zero secondary flow. Nozzle efficiency decreased by only 2.2 percent over the pressure ratio range ($\backsim$350 to $\backsim$35) investigated at AEDC. Sea level tests with zero secondary flow at pressure ratios from 22 ($\backsim$8 percent of design PR) to 29 (10.8 percent of design PR) indicates nozzle efficiency decreased in this region to a value of about 89.5 percent.
3. Secondary flowrates from zero to 3 percent gave nozzle performance (C_T) increases of approximately 0.5 percent at design pressure ratio. The maximum gains in C_T (1 to 1.5 percent) with zero to 3 percent secondary flow were achieved over a pressure ratio range from 150 to 50.
4. At very low pressure ratios ($\backsim$22) small losses in C_T(0.1 to .3 percent) resulted with the introduction secondary flow.
5. Nozzle C_T gains at all pressure ratios were approximately the same with secondary flowrates of 1 to 3 percent.
6. Nozzle C_T was noticeably lower with 5 percent secondary flow than with the other flowrates tested.
7. When the nozzle efficiency is referenced to primary properties, a decrease in $C_{T,top}$ of from 0 to 0.5 percent results at design pressure ratio with the introduction of from 1 to 3 percent secondary. It should be noted that this small decrease in $C_{T,top}$ still represents an efficient utilization of low energy turbine exhaust gases.

No significant difference in thrust efficiency was noted for different energy level secondary flows.

9. Nozzle thrust efficiency and base pressure corresponded quite closely for the cold-flow (CF_4) model and the hot-firing thrust chamber. This suggests the use of inexpensive cold-flow tests with CF_4 will provide near quantitatively applicable design information for hot-firing engines.

Major recommendations resulting from this test program are

1. For future testing efforts, special effort should be made to determine the base thrust contribution from base pressure measurements. These measurements can provide an accurate determination of nozzle efficiency trends and serve as a valuable and independent check on efficiency trends determined from measurements of engine thrust, flows, chamber pressure and throat area.
2. Base configuration and the method of introduction of secondary flow appreciably affects performance. Hot-firing tests should be conducted to provide performance data, heat transfer rates, and other design technology with various base configurations.
3. Recent analytical studies indicate that aerospike contours other than a truncated ideal may provide a significant improvement in low pressure ratio performance. Contours can be designed specifically for the low pressure ratio region and still give altitude performance close to that of an ideal spike. Analytical contour design and cold-flow testing of several different contour designs should be conducted to verify initial analytical work.

SECTION IV

EXTERNAL FLOW EFFECTS ON AEROSPIKE PERFORMANCE

INTRODUCTION

(C) Because of interaction which occurs between external and nozzle flows, vehicle base flow characteristics encountered in missile flight differ from those prevalent in quiescent air nozzle performance investigations. These base flow characteristics are of little consequence with conventional nozzles since the expansion process is internal in this case; that is, the exhaust gases within the nozzle are shielded from the external flow by the physical expansion surface provided by the nozzle. However, with an aerospike nozzle, the external expansion boundary is formed by a gas-gas interface, and is influenced by flow interference effects. Since the position of this outer boundary in the flow affects aerospike nozzle performance at low pressure ratios where the base pressure follows changes in ambient pressure ("open wake"), the presence of an external flow can affect aerospike performance under certain conditions. Previous cold-flow testing conducted under contract NAS 8-2654 (Ref. 21) established that the effect of external flow is small and is confined to a narrow range of in-flight operating conditions. Experimental study of these effects was continued under contract AF04(611)-9948. The primary objective of this program was to confirm and extend, through hot-flow testing, the results obtained in the cold-flow slipstream study. A secondary objective was to evaluate the effect of base bleed flowrate on nozzle still air performance. Results of this investigation are discussed in the following sections.

SUMMARY

(C) A hot-flow test program was conducted to determine the influence of external flow on in-flight aerospike nozzle performance. A hot-firing aerospike engine using hydrogen peroxide propellants was enclosed by an

aerodynamic fairing constructed in the shape of a missile body to simulate an actual flight configuration. The engine generated 400 pounds of altitude thrust at a chamber pressure of 200 psia. An aerospike nozzle with an area ratio of 25 and a length equal to 20 percent of an equivalent 15 degree conical nozzle was utilized to control the expansion of engine exhaust gases. The secondary flowrate was 0.8 percent of the primary flowrate for all tests with external flow. Testing was conducted in the 16-foot transonic and supersonic propulsion wind tunnels at Arnold Engineering Development Center (AEDC). Installation of the model in the transonic wind tunnel is shown in Fig. 92.

(C) Forty tests were conducted to obtain still air and slipstream performance trends in the transonic and supersonic wind tunnels. In addition, five tests were conducted in the transonic facility to demonstrate engine performance trends with secondary flowrate. Results of these tests confirmed that high quiescent air performance (approximately 98 percent of ideal at design pressure ratio) can be obtained throughout a representative range of pressure ratios with a properly designed aerospike nozzle. The addition of secondary flow proved beneficial at all pressure ratios. It was found that the correct experimental performance level and trend with pressure ratio could be estimated above pressure ratios at which nozzle recompression occurs using previously developed semi-empirical base pressure relationships (Ref. 2) in conjunction with a potential primary flow analysis and viscous drag computations.

(C) Nozzle performance was found to be unaffected by external flow in the "closed wake" pressure ratio region (pressure ratios at which nozzle base pressure is constant in still air). At low pressure ratios ("open wake") performance of the model tested decreased at a rate which was dependent on free stream Mach number and chamber pressure ratio. When strong flow interaction effects occurred, they were found to result in

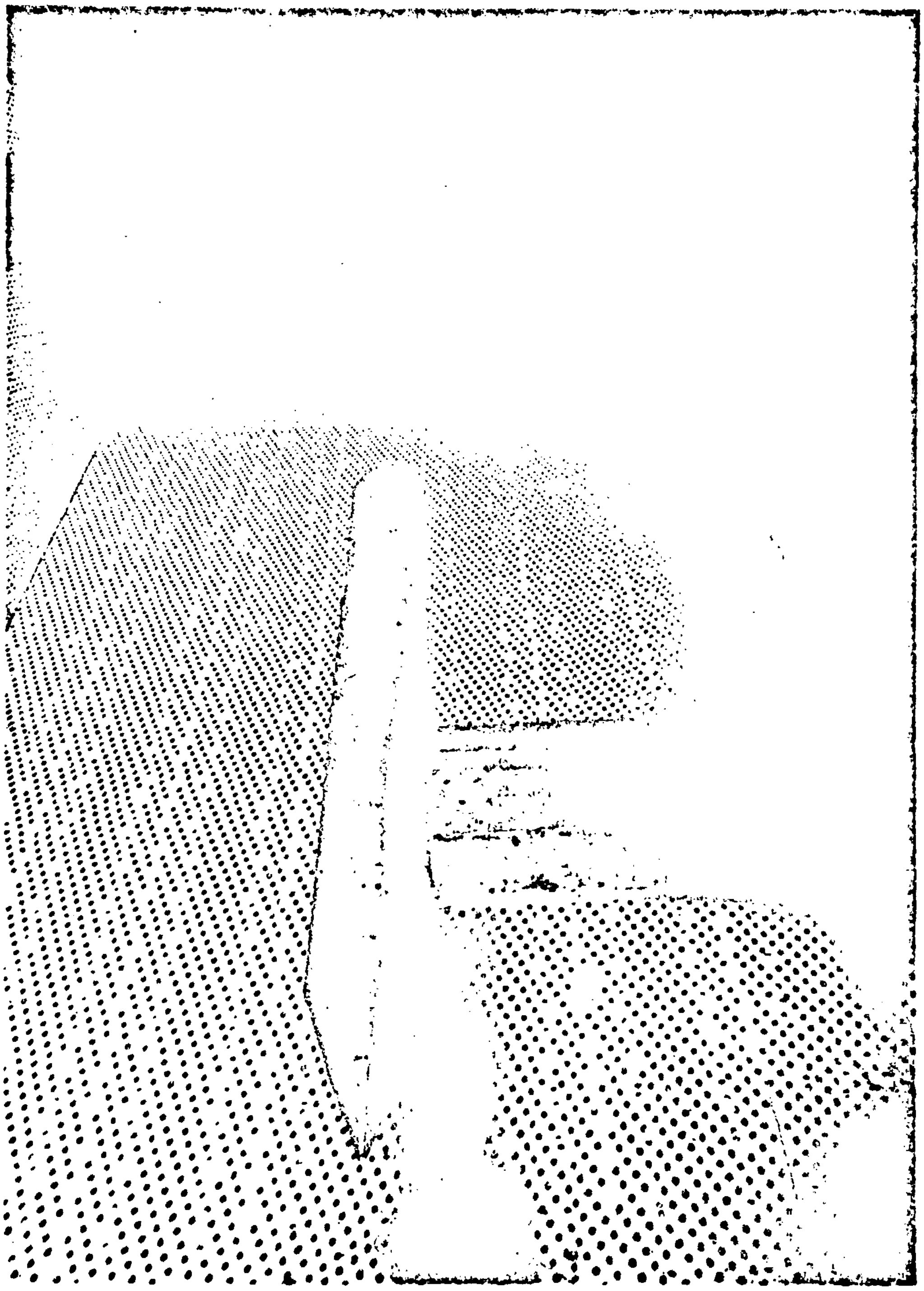

Figure 92. Test Installation in the Transonic Wind Tunnel

relatively high nozzle base pressure, which was also shown by previous cold-flow data (Ref. 21). When flow interaction did not influence nozzle base pressure, both hot- and cold-flow nozzle performance data correlated with the "effective" chamber pressure ratio, $P_c/\bar{P}_{B_v}$. On the basis of this result, it was concluded that: (1) missile base pressure approaching ambient pressure will result in nozzle efficiency in slipstream nearly identical to that obtained in still air, and (2) strong slipstream-primary flow interaction results in relatively high in-flight nozzle performance.

(C) In-flight performance estimates generated under severe assumptions demonstrated that the time-integrated external flow effects over a typical mission result in a change in average specific impulse ($\bar{I}_s$) of less than 0.2 percent. Boat-tailing, mass addition to the missile wake flow, and reduction in missile base area are shown to be effective methods of reducing these effects still further.

SLIPSTREAM TEST PROGRAM

Preliminary Analysis and Design Studies

(C) The slipstream investigation was designed to confirm and extend, through hot-flow testing, the results of previous analytical and cold-flow studies into the effects of an external flow on aerospike performance. The engine selected as the test model was a modified version of a hydrogen peroxide monopropellant engine previously used to verify cold-flow aerospike performance trends with secondary flowrate (Ref. 15). This selection was based on the demonstrated high performance of the engine, the excellent decomposition characteristics of the H_2O_2 propellant using the selected catalyst pack design, and repeatability of test results. The use of H_2O_2 monopropellant allowed a very accurate measurement of combustion efficiency, resulting in consistent and reliable determination of nozzle efficiency, C_T. C* efficiency (approximately 97.5 percent) was determined directly from the measured combustion temperature ($\approx$1350F). Testing was conducted in the Propulsion Wind Tunnel at AEDC because of the capability of this facility to simulate a wide range of potential

operating conditions. Pertinent nozzle flowfield and mission operating characteristics leading to the selection of the model design and simulated test conditions and the expected nozzle performance and base pressure trends are discussed in the following paragraphs.

(C) The external flow studies described in Ref. 21 provided invaluable insight into the flow process encountered when an aerospike nozzle operates in the presence of an external flow, and established many guidelines for the test program discussed herein. In the cold-flow testing it was established that, for the conditions investigated, the presence of an external flow influences aerospike performance only in the open wake region. In still air, the open wake region occurs below pressure ratios at which the nozzle base pressure just begins to feel the influence of ambient pressure as the chamber pressure ratio decreases. The external flow influence at these pressure ratios was found to alter the compression waves, or envelope shock, in the primary flow field which induces a change in engine thrust. This phenomena was explained on the basis of the still air nozzle flow field (illustrated schematically in Fig. 93) as follows.

(C) Initially, the primary flow undergoes a controlled expansion from the nozzle throat to the shroud exit. Beyond this point the flow expands freely about the point at the shroud exit to the local ambient pressure, P_{B_∞}. The left running expansion waves in the vicinity of the shroud exit are reflected from the outer free jet boundary as compression waves, which, in some cases, coalesce to form an envelope shock. The altitude compensating characteristics of the aerospike under still air conditions are directly related to the position of these compression waves in the flow.

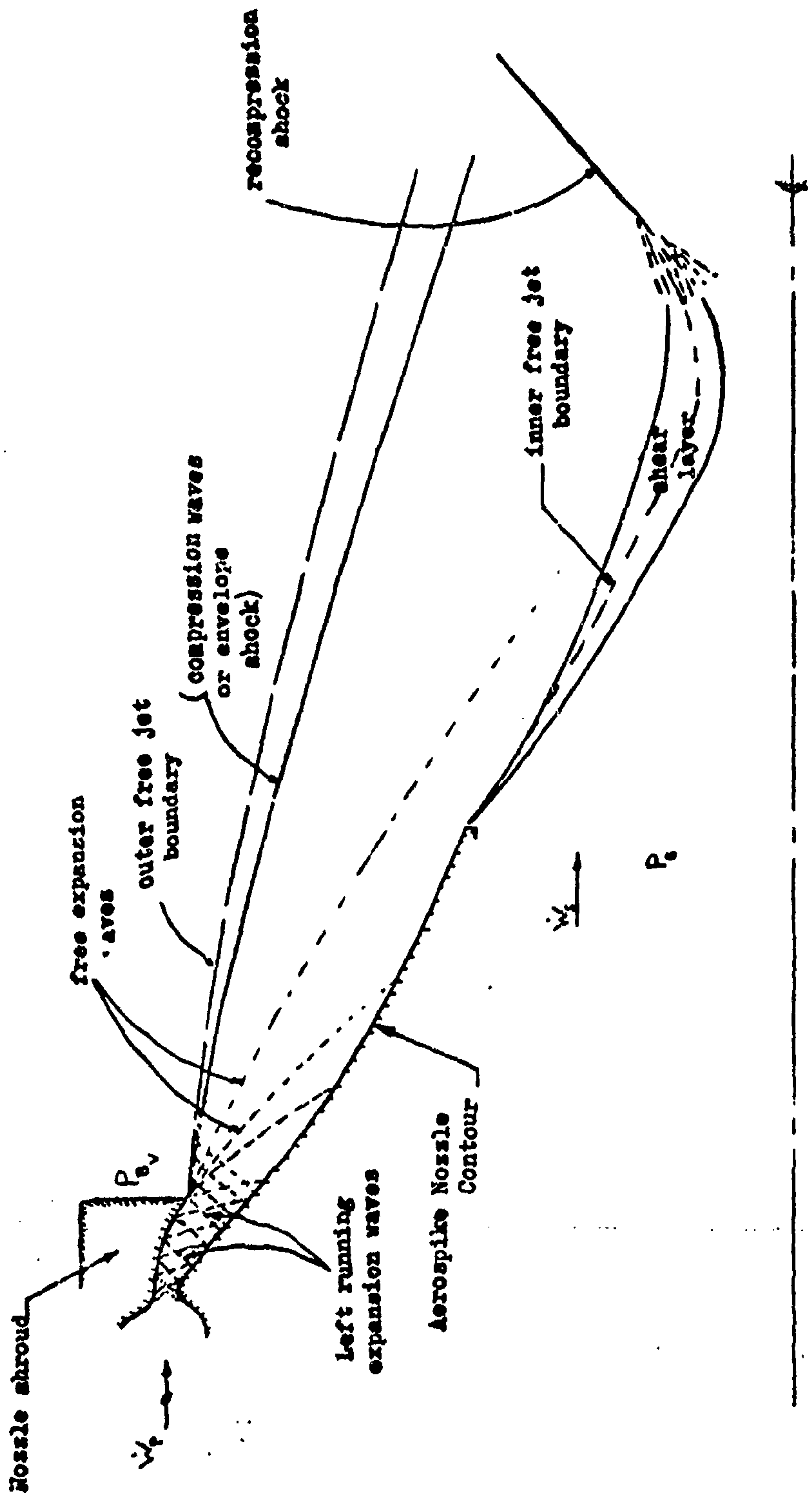

CONFIDENTIAL

Figure 93. Aerospike Flow Field

(C) At very low pressure ratios (large P_{∞}) the position of the outer free jet boundary is such that these compression waves reflect onto the nozzle contour and internal free jet boundary as shown in Fig. 94a . Both the pressures along the affected portion of the contour surface and the nozzle base pressure, P_B, are subjected to a relatively high recompression pressure (approximately equal to the local ambient pressure) which results in high nozzle performance at off-design conditions. As the ambient pressure is decreased the outer free jet boundary moves outward so that the compression waves move down the nozzle contour. Once the ambient pressure reaches a certain low value these recompression waves can no longer intersect the contour surface and the thrust developed along this surface remains unchanged with further decreases in ambient pressure. The nozzle base pressure, however, remains under the influence of the local ambient pressure (Fig.94b) until the position of the outer free jet boundary is such that the recompression waves no longer intersect the internal free jet boundary (Fig. 94c). Decreases in the ambient pressure below this value, which corresponds to a pressure ratio that is usually twenty to fifty percent of the nozzle design pressure ratio depending on the nozzle configuration, have no further effect on the nozzle base pressure.

(C) These trends with the local ambient pressure are changed slightly in the presence of an external flow. In this case there are two interrelated phenomena which influence the primary flow field. First, the local ambient pressure to the nozzle, P_{B_v}, changes relative to the slipstream static pressure, and in turn changes the initial structure of the primary flow free jet boundary. Because this missile base pressure, P_{B_v}, is normally lower than ambient (the magnitude of base pressure decrease depends on afterbody geometry and external and primary nozzle flow conditions), the position of the outer free jet boundary is moved further away from the nozzle centerline than in still air. Thus, the compression

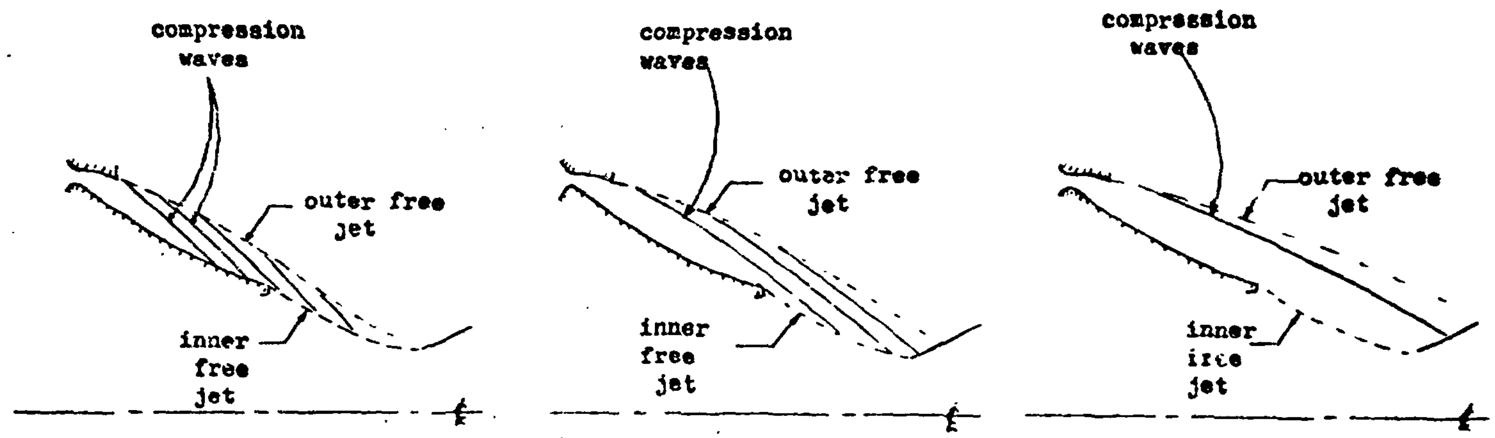

a) Very Low Pressure Ratios (Nozzle Contour and Base Pressures affected by Ambient Pressure)

b) Intermediate Pressure Ratios (Nozzle Base Pressure Affected by Ambient Pressure)

c) High Pressure Ratios (Nozzle Contour and Base Pressure Unaffected by Ambient Pressure)

CONFIDENTIAL

Figure 94. Aerdynamic Spike Flowfield at Various Pressure Ratios, $\frac{P_c}{P_\infty}$

waves emaninating from the initial portion of the outer jet boundary strike the inner jet boundary farther downstream than for still air operation as shown in Fig. 95 . This effect results in reduced recompression effects in slipstream with attendant lower nozzle base pressure than obtained in still air.

(C) Secondly, the structure of the free jet boundary of the primary exhaust stream is further altered downstream of the impingement point between the external and nozzle flows (point A in Fig. 95). Because of the flow interaction at this point, the compression waves reflecting from the free jet boundary downstream of this point, and the free jet boundary itself, are turned inward, as shown in Fig. 98 . Under these conditions, the compression waves may intersect the inner free jet boundary farther upstream and with a higher pressure than in still air. This causes the nozzle base pressure to be sensitive to changes in the ambient pressure for lower values of P_{∞} than the corresponding still air case.

(C) The net result of these two effects can be either an increase or decrease in base pressure from that obtained in still air operation, depending upon the relative strengths of the two compensating processes. The first effect described above is referred to as the influence of missile base pressure in all subsequent discussion. To facilitate this discussion the second effect is referred to as shock flow interaction, or simply interaction, in succeeding sections. However, it must be remembered that in reality both influences are interrelated, and are the result of interaction between external and nozzle flow.

(C) In the cold-flow test program it was found that missile base pressure was nearly equal to the free stream static pressure for subsonic external flow. Under these conditions, the position of the outer free jet boundary

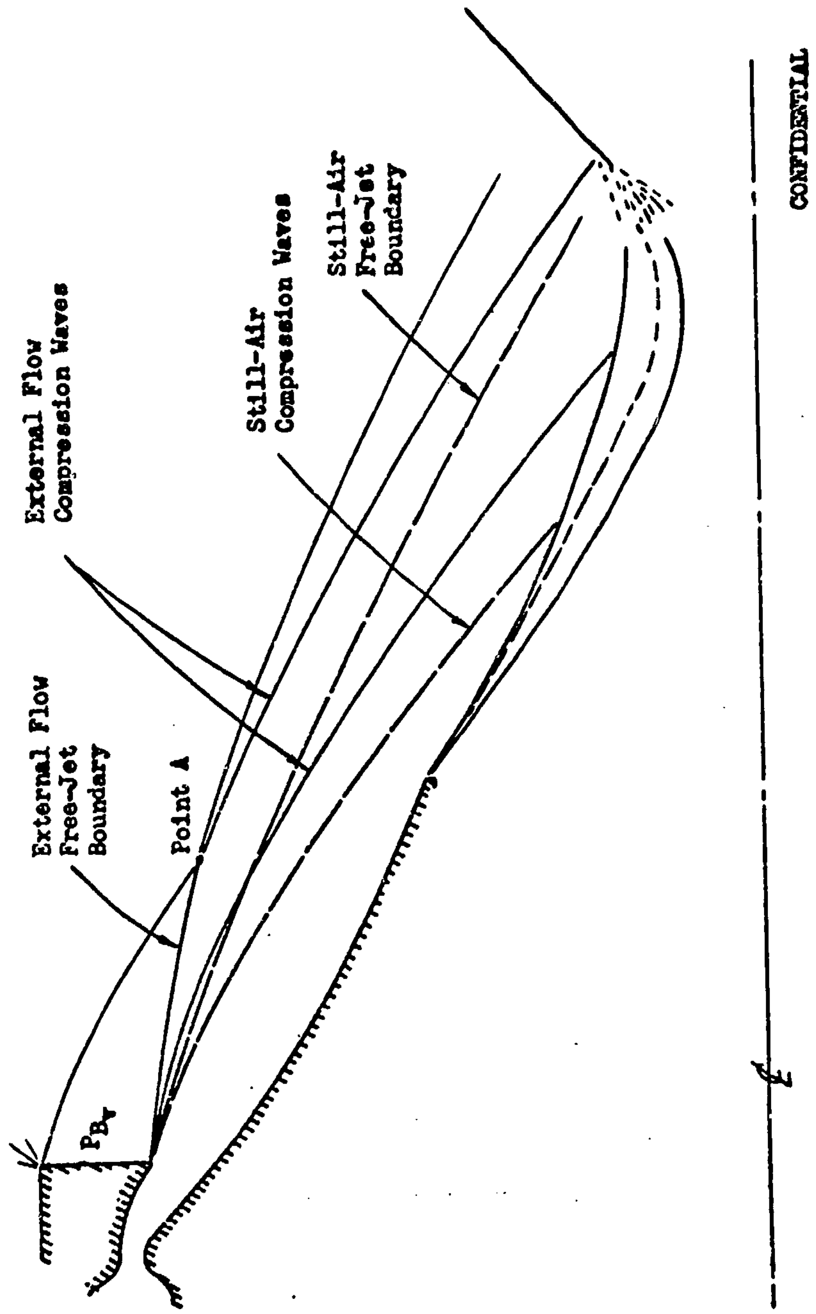

Figure 95. Effect of Reduced Missile Base Pressure

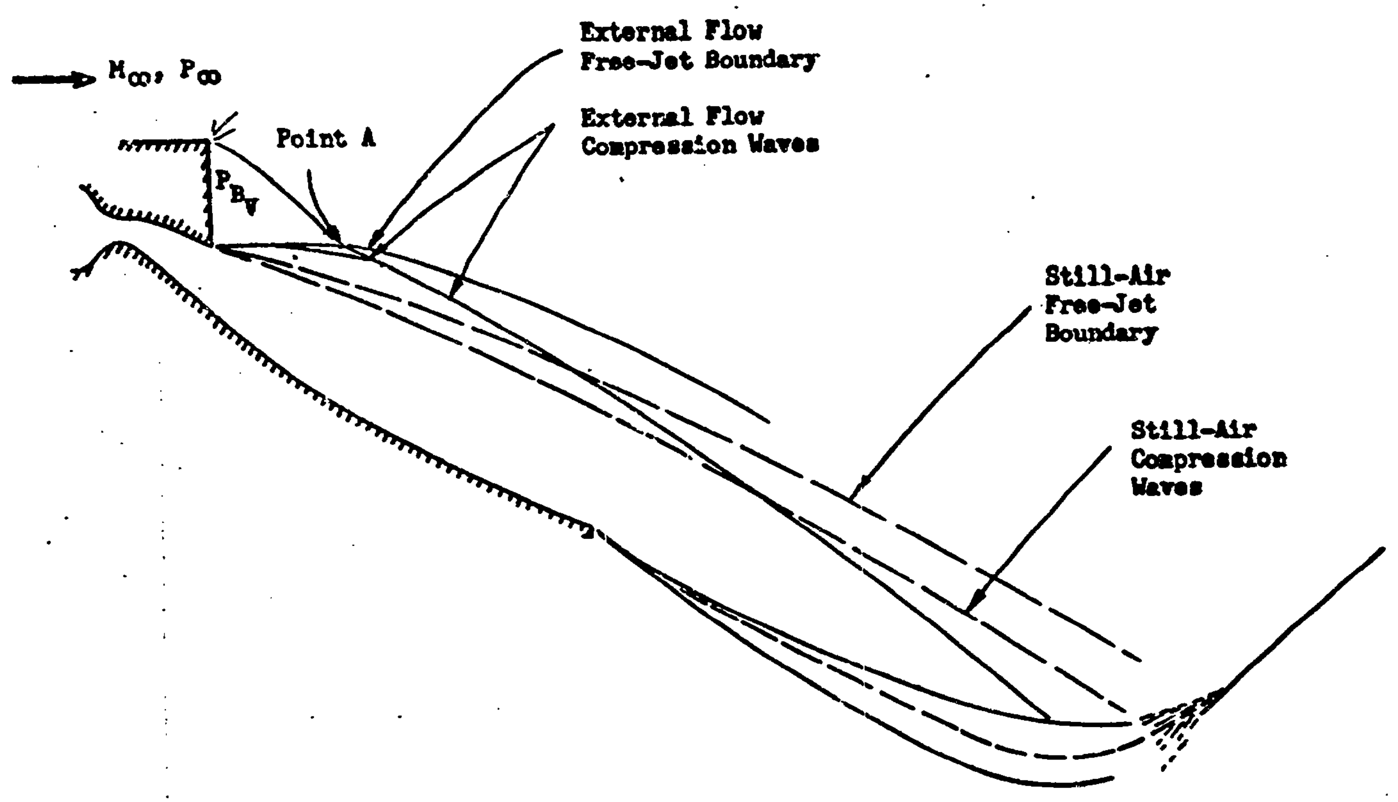

Figure 96. Effect of Slipstream and Nozzle Flow Interaction.

is nearly the same as in still air at the corresponding pressure ratio (P_c/P_∞), as shown in Fig. 97a). Hence, the influence of low missile base pressure was nearly negligible, and the shock flow interaction influence was predominate. As shown by the cold-flow data presented in Fig. 98 , the nozzle base pressures in this case are increased over those obtained in still air over a short interval in pressure ratio because of the influence of the relatively high interaction pressure acting along the affected recompression waves. This increase in base pressure results in a nozzle thrust increase as indicated in Fig. 98b .

(c) Conversely, relatively low missile base pressures were encountered in the cold-flow evaluation of supersonic external flow. In this case the position of the outer free jet boundary is as shown in Fig. 97b . Thus, although the compression waves are turned inward by the shock flow interaction process, as in the subsonic case, the initial portion of the free jet boundary is such that these waves intersect the internal free jet boundary farther downstream than in the still air case. This causes the nozzle base pressure to remain insensitive to changes in the ambient pressure, P_∞, up to higher values of P_∞ than in still air (Fig. 98a) with a subsequent loss in nozzle thrust in this region (Fig. 98 b).

(c) Since in external flow the primary flow i.e. initially expands according to the missile base pressure, P_{B_v}, nozzle performance and base pressure may correlate with P_{B_v} depending upon the relative strength of the interaction effect. Therefore, a correlating performance term has been defined to enable computation of nozzle performance under flight conditions from still air data. This parameter, Φ, is defined by the equation (refer to Appendix 2 for nomenclature):

$$\Phi = \frac{(F)\; P_c/P_{B_v}}{\left(F_{id_p}\sqrt{\frac{T_c}{T_{id}}} + F_{id_s}\sqrt{\frac{T_c}{T_{id}}}\right)_{P_c/P_{B_v}}} \qquad (1)$$

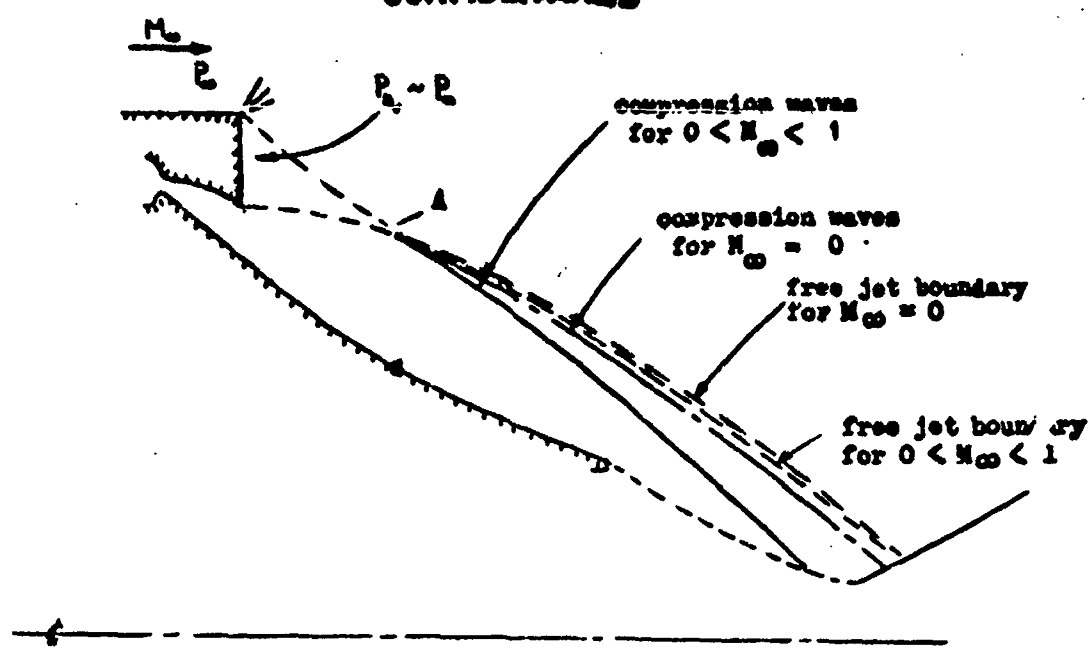

a) Subsonic External Flow

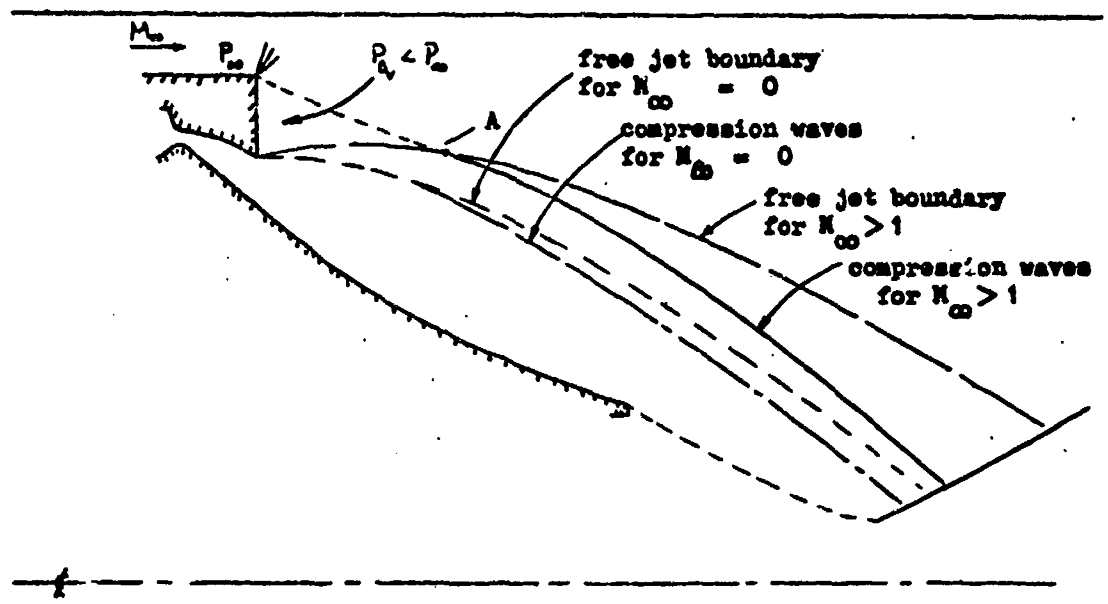

b) Supersonic External Flow

CONFIDENTIAL

Figure 97. Slipstream t on the Nozzle Flowfield

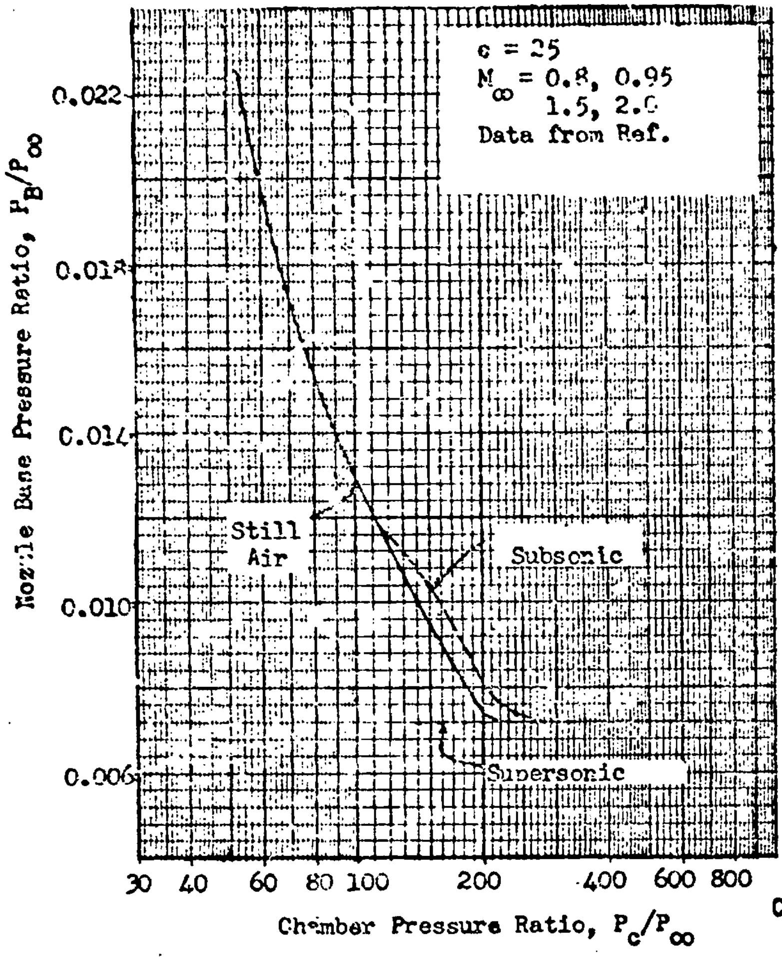

a. Base Pressure Trends

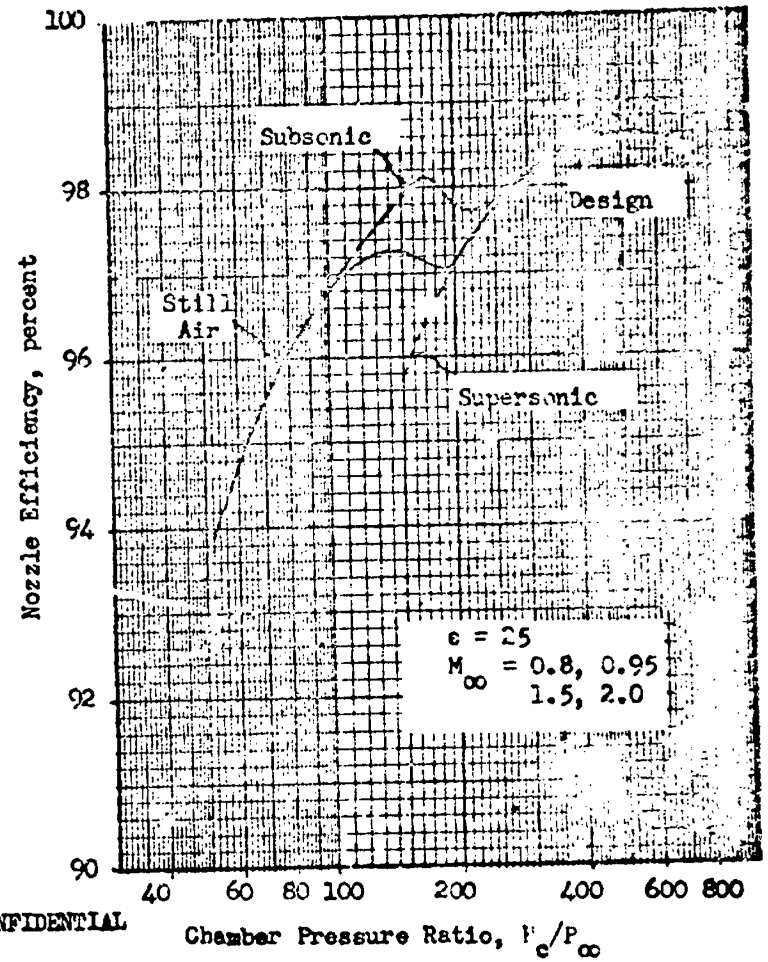

b. Nozzle Performance Trends

Figure 98. Slipstream Effects on Nozzle Base Pressure and Performance

and is referred to as a normalized thrust coefficient in subsequent discussion. When shock interaction effects do not influence nozzle performance, Eq. (1) reduces to the definition of nozzle efficiency (compare the above equation with Eq. (6) of Appendix 2), and the normalized thrust coefficient in external flow is identical to that obtained in still air for corresponding values of P_c/P_{B_v}. However, if shock interaction effects are strong (i.e., compression waves reflecting from the outer free jet boundary downstream of the impingement point are turned inward and intersect the inner free jet boundary farther upstream than if the expansion were governed only by the missile base pressure) the nozzle base pressure is higher than would be expected from the value of P_{B_v} alone. Under these conditions, the value of Φ obtained for nozzle operation in slipstream is higher than that obtained for still air operation at corresponding values of P_c/P_{B_v}.

(C) The nature of the normalized thrust coefficient, Φ, for the cold-flow test conditions is shown in Fig. 99. It can be seen that external flow thrust coefficient data correlate with still air nozzle efficiency at all but the transition pressure ratios with subsonic external flow. The base pressure data in Fig. 98a indicate that interaction effects were predominate for these conditions. Interaction effects resulted in an increased normalized thrust coefficient over that obtained in still air through the transition pressure ratios as would be expected on the basis of preceding discussion. The objective of the current program was to confirm and extend these cold-flow results.

(c) Since external flow effects on aerospike performance are dependent on the nature of both the external and nozzle flows, a trajectory study was conducted to establish representative operating conditions in terms of free stream Mach number and chamber pressure ratio combinations for pump-

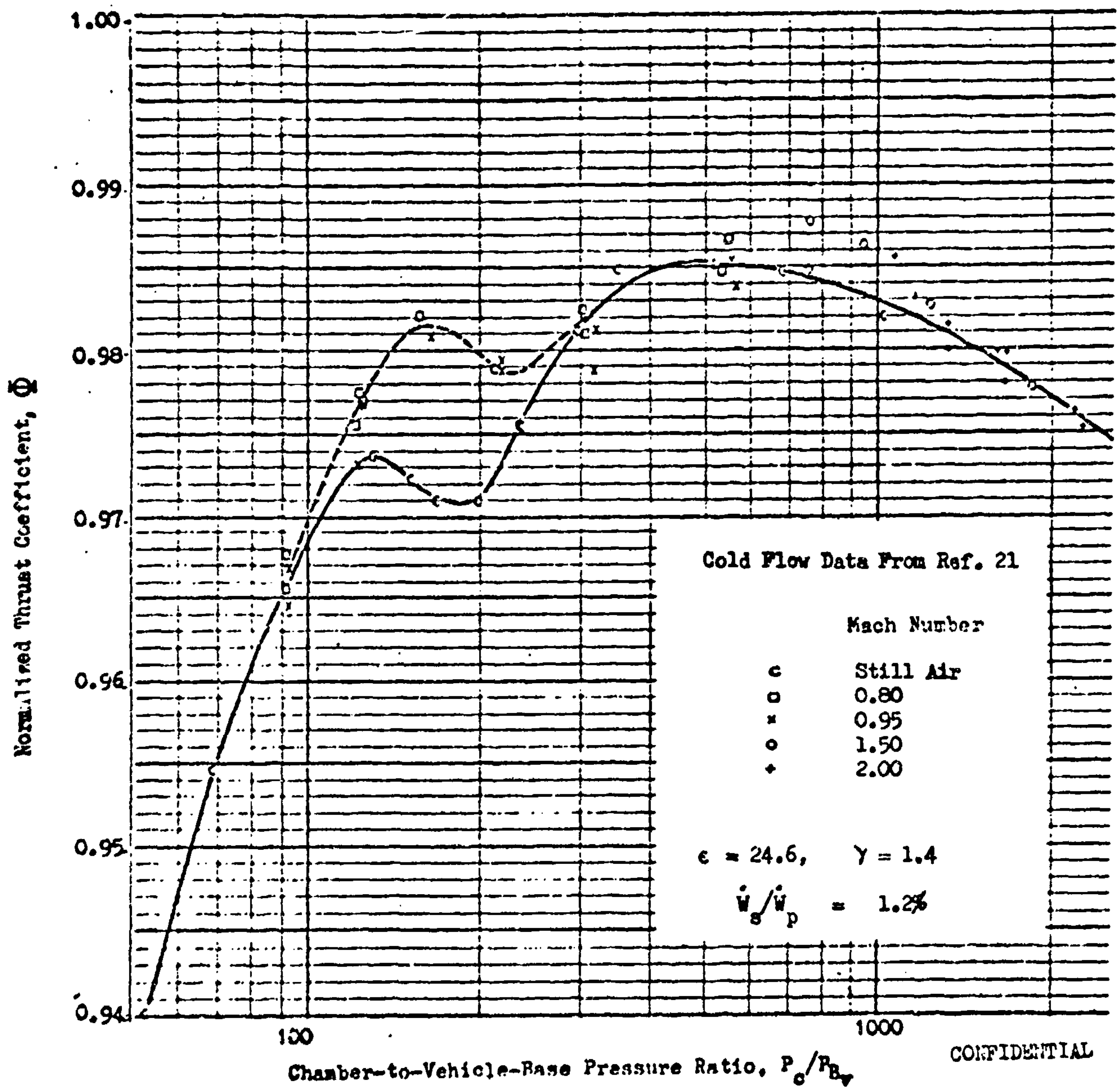

Figure 99. Nozzle Efficiency Based on Expansion to Vehicle Base Pressure, Cold-Flow Tests

and pressure-fed booster engines. This study revealed that due to differences in operating parameters a wide range of environmental conditions may arise depending on the application as shown in Fig. 100 . However, while the nature of the external flow and engine operating conditions are determined by the data in Fig. 100, the expansion characteristics of the nozzle are not reflected by these curves. In order to couple conditions in the free stream with the flow characteristics of the nozzle used in each of these applications, the ordinate in Fig. 100 was normalized in terms of the nozzle design pressure ratio, and the trajectory data were replotted versus this normalized pressure ratio as shown in Fig. 101 . The normalized trajectories allow the testing of a single nozzle at a fixed chamber pressure over a small range of ambient pressures with valid application of the data to other nozzles with different chamber pressure, expansion area ratio, and mission Mach number profile.

(U) The operating limits of the test facilities at AEDC (discussed in Ref. 20) are shown in Fig. 102. These data, and the normalized trajectory data shown in Fig. 101 were used to establish the permissable operating ranges shown in Fig. 103 for test models with various area ratios and chamber pressures. It can be seen that the desired flight conditions can be simulated with a wide range of model area ratios by proper selection of the model chamber pressure (or vice versa).

(C) The availability of comparable cold-flow data and condensation limits of the decomposition products of the hydrogen peroxide propellant led to the selection of a 25:1 nozzle area ratio and a chamber pressure of 200 psia. As shown in Fig. 103, this allows testing throughout a representative range of Mach numbers and chamber pressure ratios. A short outer shroud was utilized which was designed to yield parallel axial flow at the throat and across a linear control surface drawn from the shroud exit to the end of the full length ideal spike contour. The spike contour

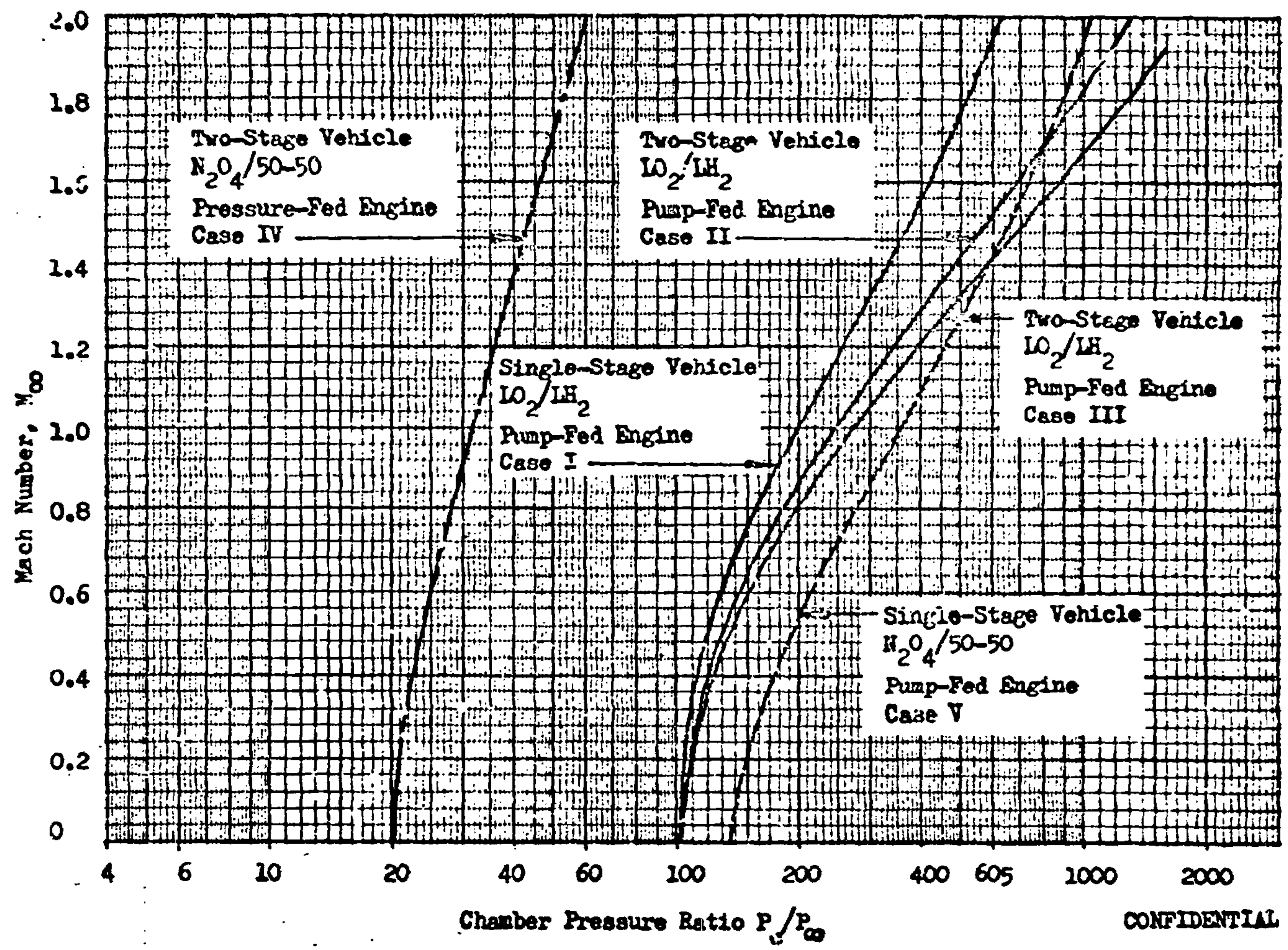

Figure 100. Typical Booster Trajectories

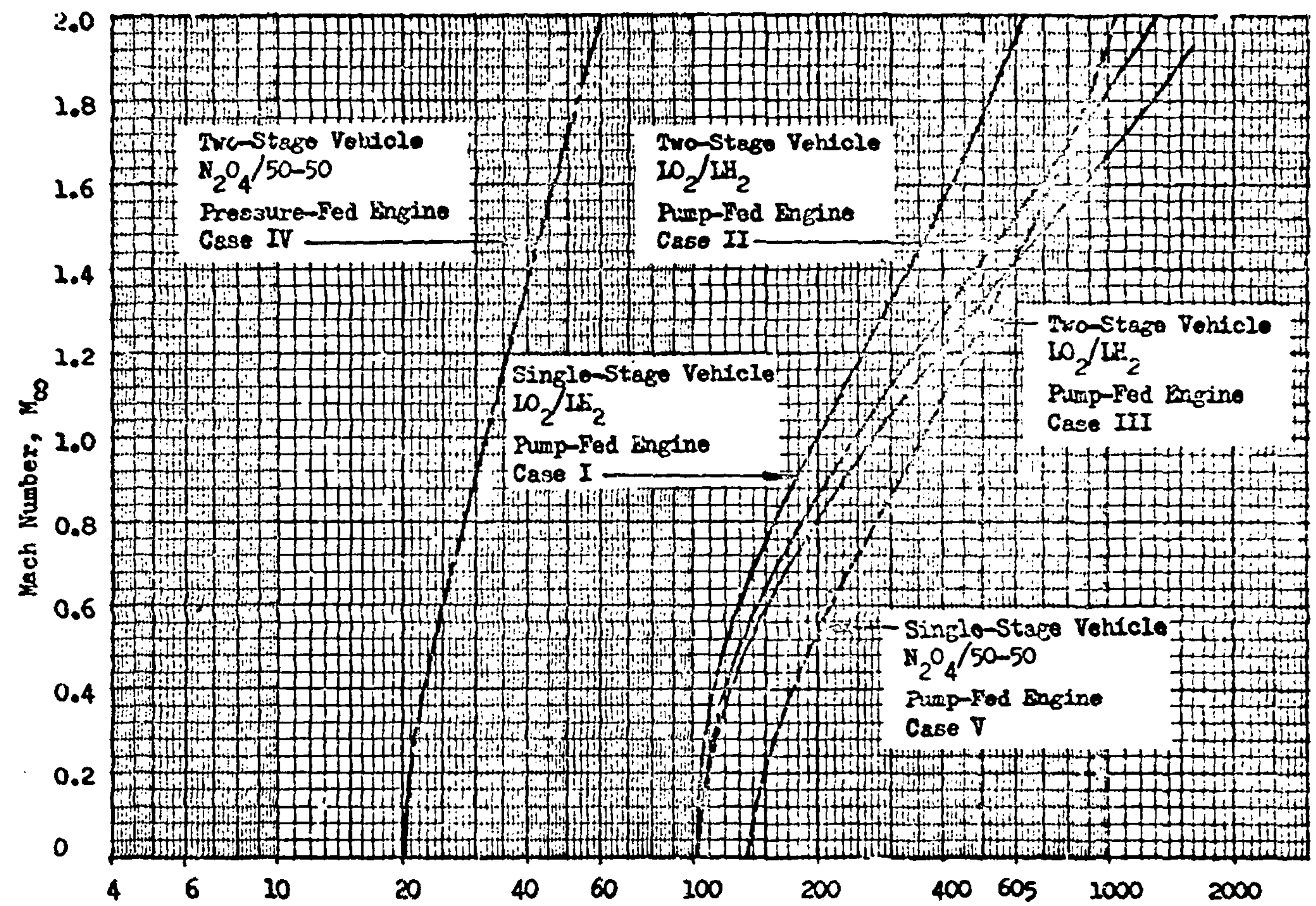

CONFIDENTIAL

Figure 100. Typical Booster Trajectories

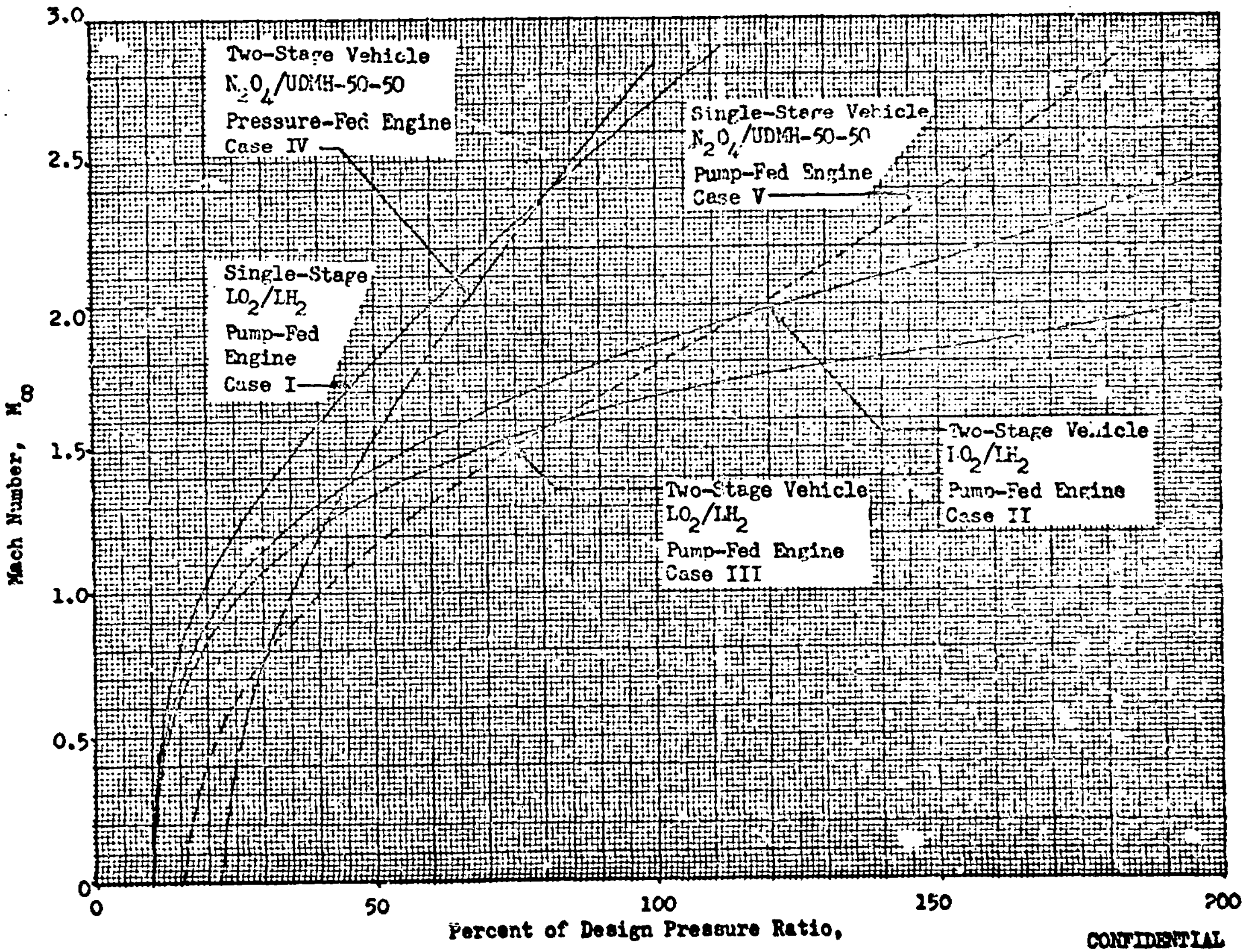

Figure 101 . Normalized Trajectory Data

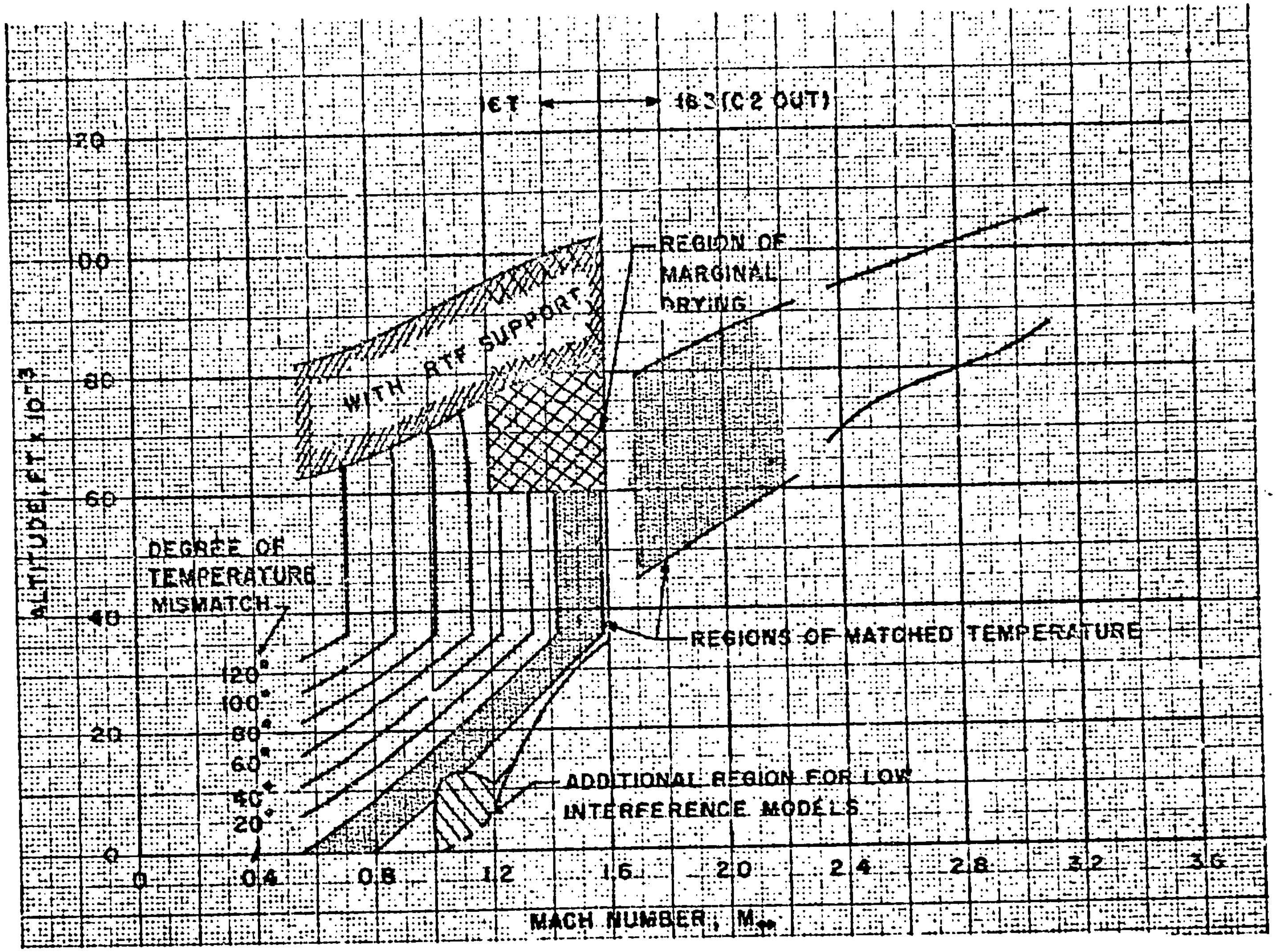

Figure 102. The Operating Range for Pressure Altitude Simulation in the PWT 16-Ft Supersonic and Transonic Tunnels

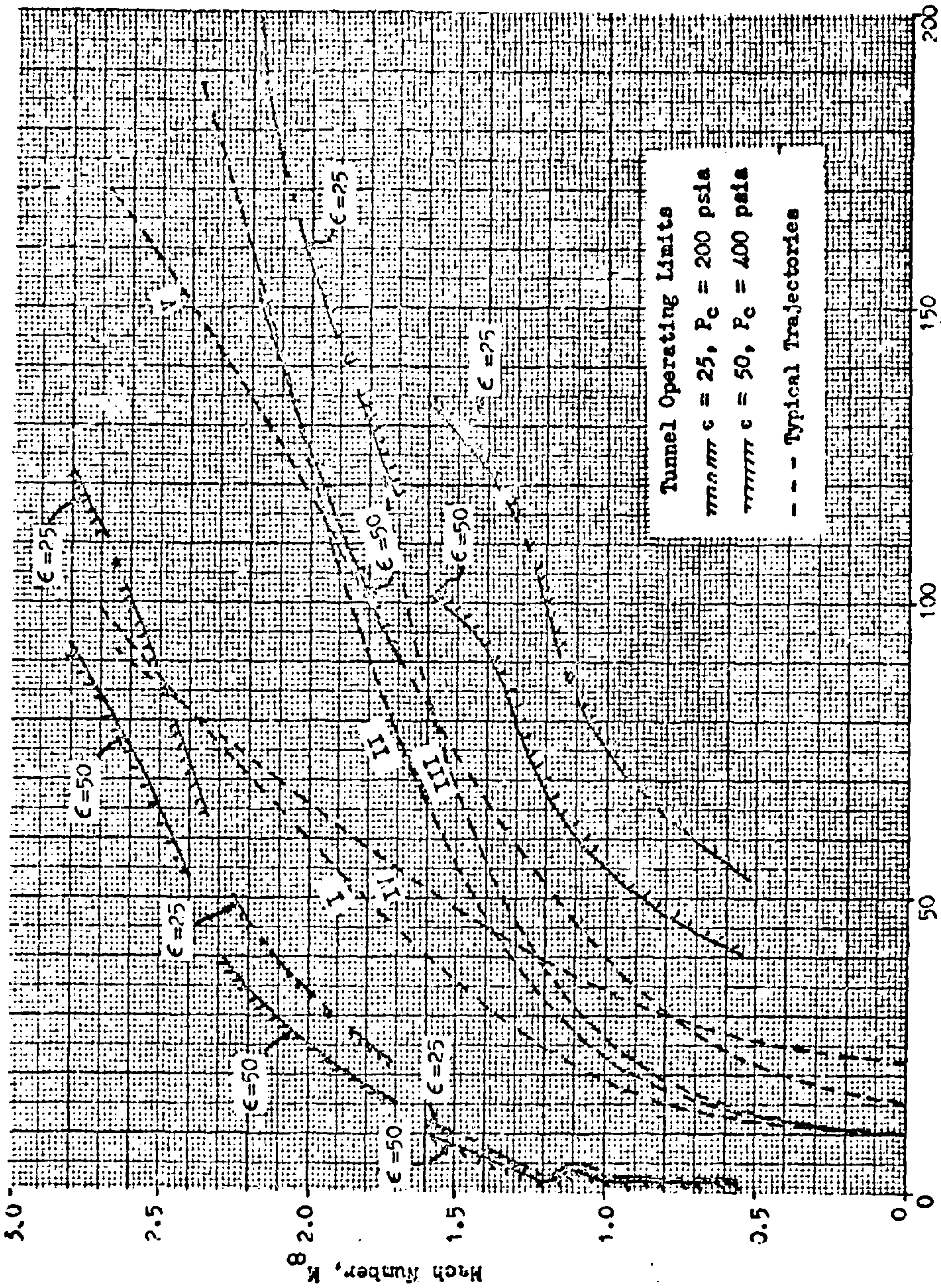

Figure 103. Permissable Operating Conditions For Various Model Selections

was truncated to an axial length which is twenty percent of the axial length of an equivalent fifteen degree conical nozzle. Ninety percent concentration hydrogen peroxide which ideally decomposes at temperatures around 1400 degrees F (depending on inlet temperature) was selected as the propellant for both the primary and secondary flows.

(C) Theoretical performance trends for this engine were determined. The primary flowfield of the nozzle was analyzed using the axially symmetric method of characteristics (programmed for automatic computation) to develop velocity and pressure profiles, and a boundary layer analysis was conducted to establish friction losses along the contour. Predicted primary nozzle wall pressure profiles are illustrated for various chamber-to-ambient pressure ratios in Fig. 104. The rise in nozzle wall pressure at low pressure ratios is caused by the recompression phenomena. This effect was found to cease at pressure ratios above approximately 63. These primary nozzle wall pressures were integrated over the nozzle surface area and combined with the pressure and momentum thrust at the throat to establish ideal primary thrust. This primary thrust value was corrected for drag losses and added to the base thrust established by estimated base pressures to obtain total nozzle thrust. Base pressure estimates were made using the empirical techniques described in Ref. 2, and are shown as a function of chamber pressure ratio for various secondary flowrates in Fig. 105. For these calculations it was assumed that $\eta C^*s = \eta C^*p$.

(C) Predicted nozzle thrust efficiency with 0.8 percent secondary flow is shown in Fig. 106 a function of the chamber pressure ratio. Efficiency gains with secondary flowrate are evident at all pressure ratios of interest; optimum secondary flowrate at design pressure ratio (PR $\approx$ 410) is approximately one percent of the primary flowrate as shown by the estimated performance trend with secondary flowrate in Fig. 107.

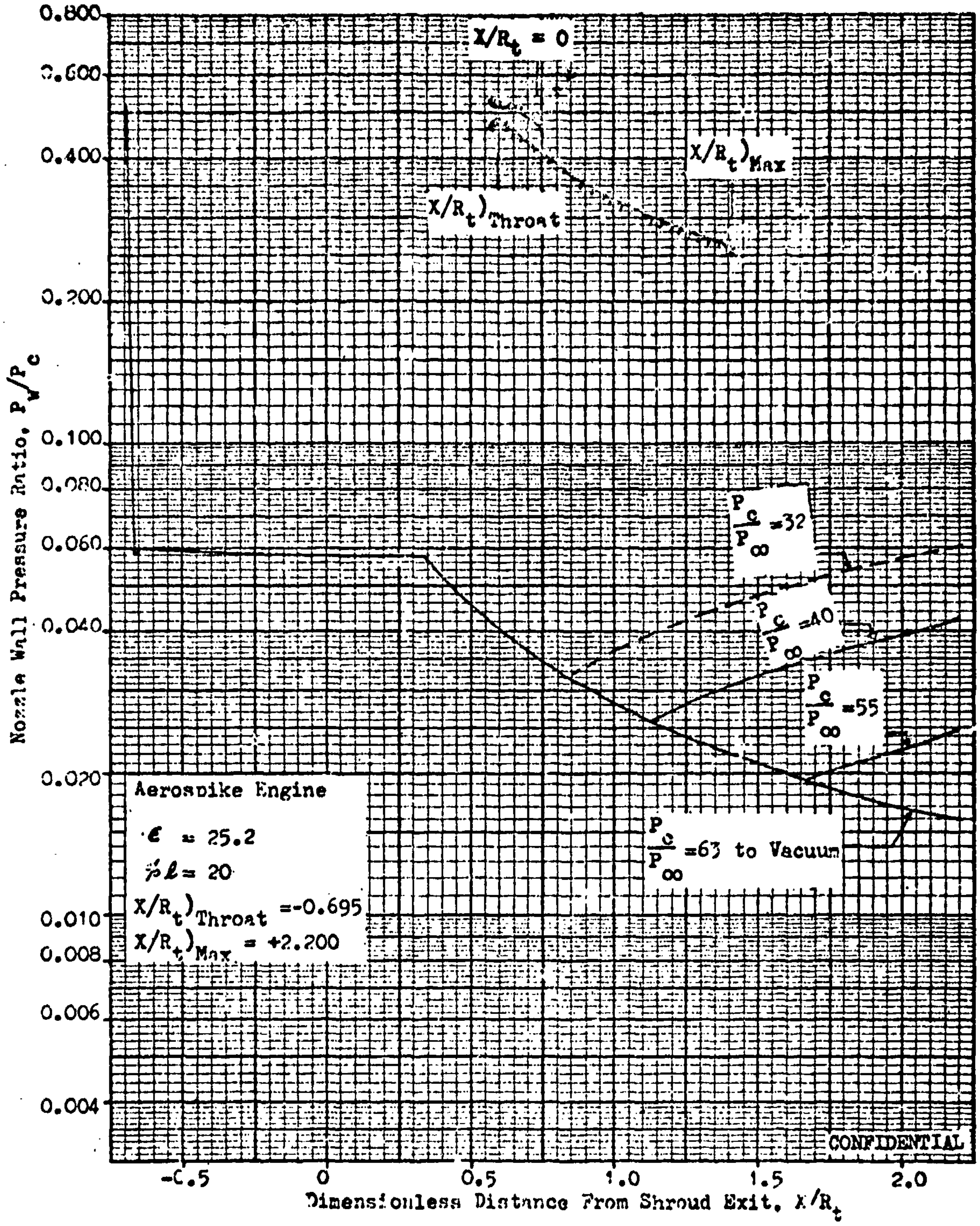

Figure 104. Theoretical Nozzle Wall Pressure Profiles

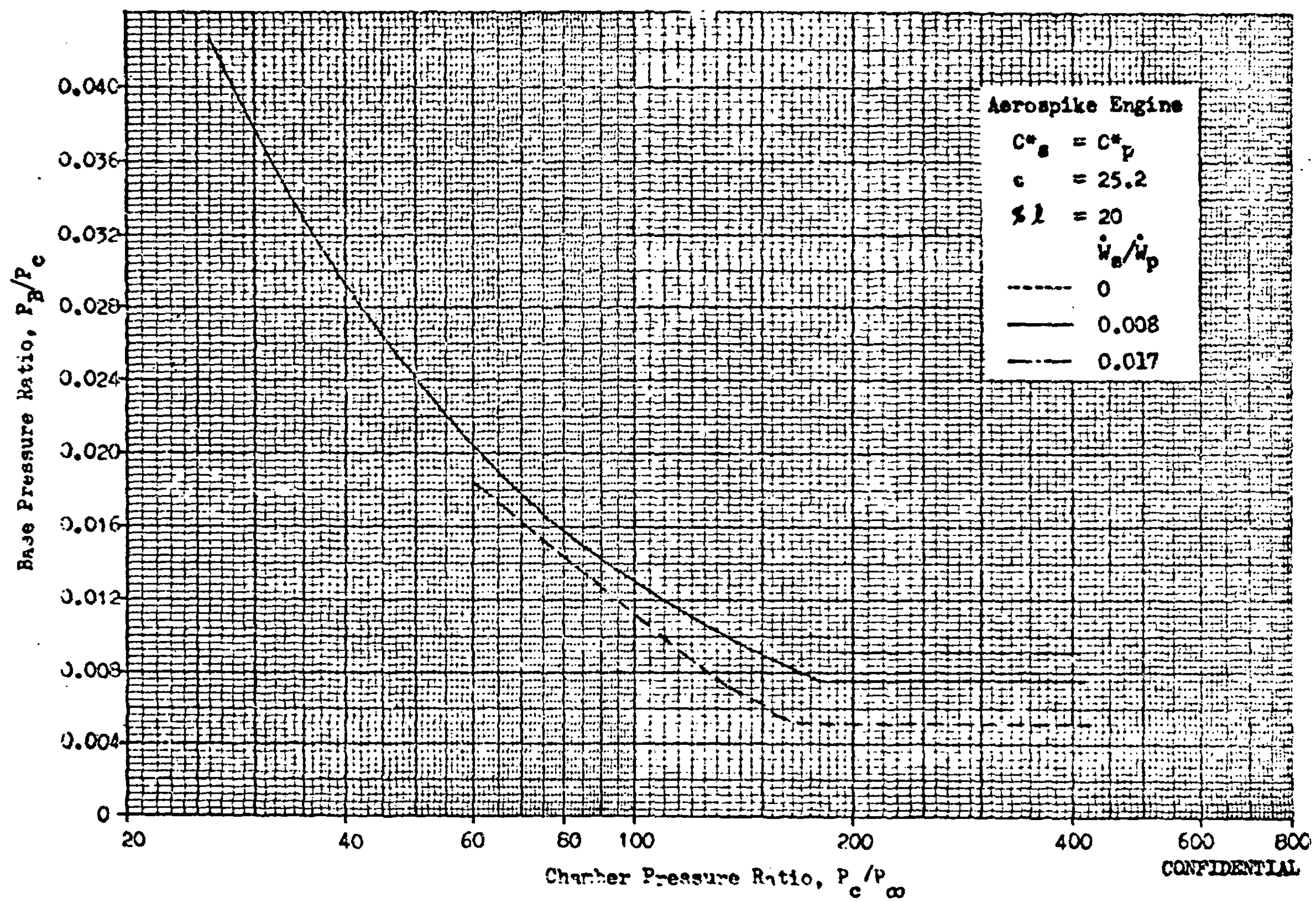

Figure 105. Estimated Base Pressure Trend With Altitude and Secondary Flowrate

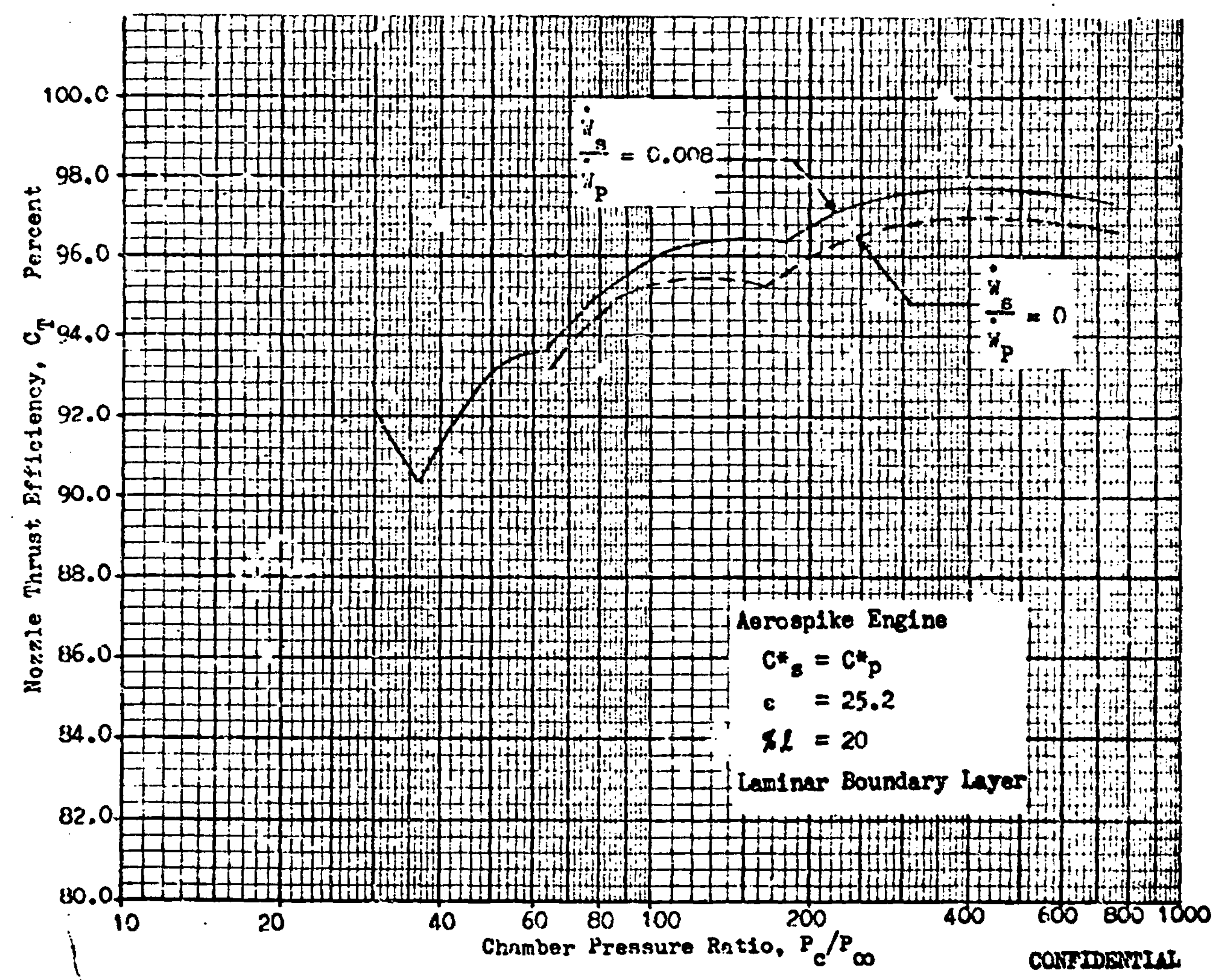

Figure 106. Estimated Performance Trend With Secondary Flowrate

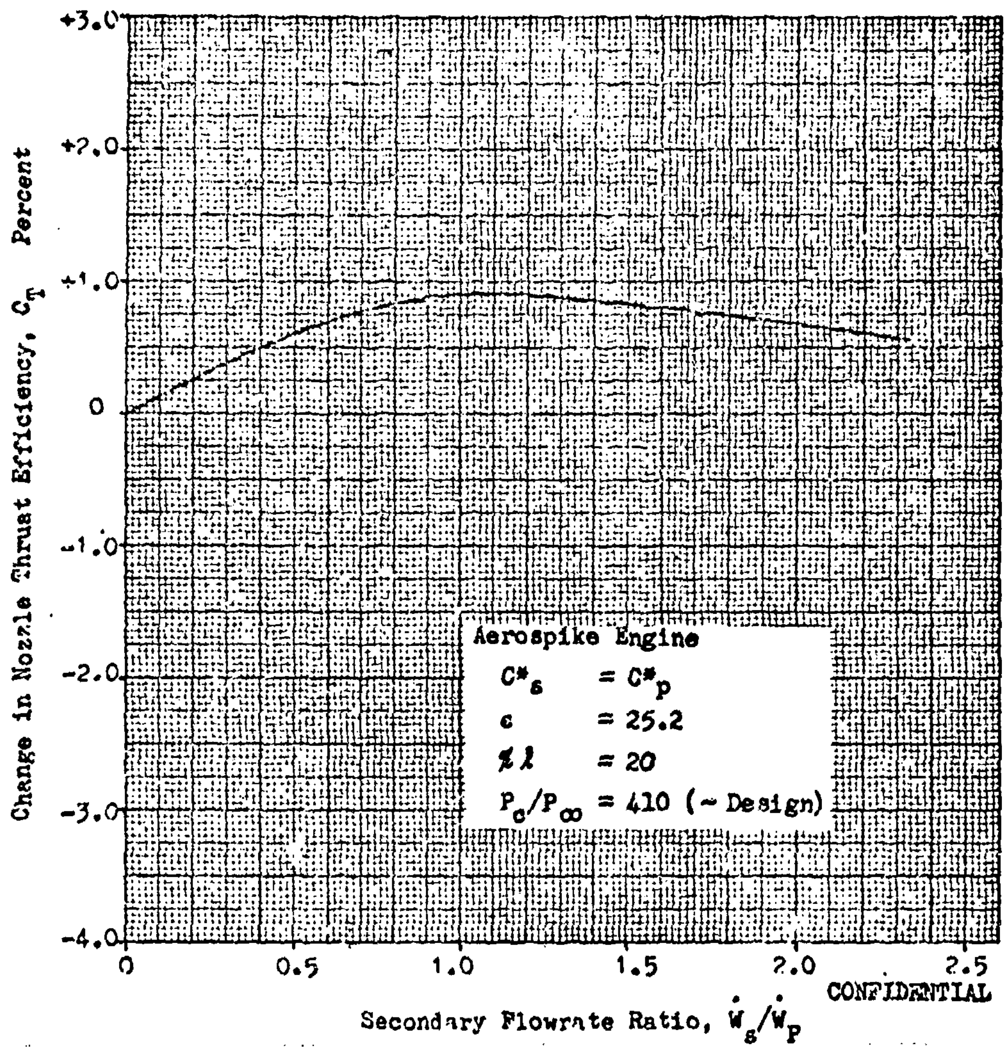

Figure 107. Estimated Efficiency Trend with Secondary Flowrate

Test Program

(C) Hardware Description. The engine assembly is shown schematically in Fig.108. The engine was operated with hydrogen peroxide monopropellant (90 percent concentration) in both the primary and secondary systems. The peroxide was decomposed in a concentric arrangement of silver screen catalyst packs located within the engine. Radial outward secondary flow injection is effected through sonic orifices located in the center of a deep base cavity. The secondary flowrate was maintained at a constant value of 0.8 percent of the primary flowrate throughout the slipstream phase of the test program. Still air tests were conducted with 0 and 1.7 percent secondary flow at the conclusion of the program. The engine is fabricated of 347 stainless steel and is uncooled with a steady state operating temperature of 1350°F (combustor and throat regions). Model dimensions were set to achieve a chamber pressure of 200 psia, design thrust level of approximately 410 lbs, and an expansion area ratio of 25 when the steady-state operating temperature was reached.

(U) The location and installation of the test article in the 16 foot transonic and supersonic wind tunnels at AEDC is shown in Figs. 109 through 112. These wind tunnels are continuous flow, closed circuit tunnels capable of operating over a range of Mach numbers from 0.55 to 1.6 and 1.7 to 3.1, respectively. Operating limits of these facilities were presented earlier in Fig.102, page 202. A detailed facility description is contained in Ref. 20.

(U) The engine was mounted on a water cooled force balance which was supported by a strut extending from the floor of the test section. In order to simulate a typical launch vehicle, the engine and force balance assembly were enclosed in an aerodynamic fairing constructed in

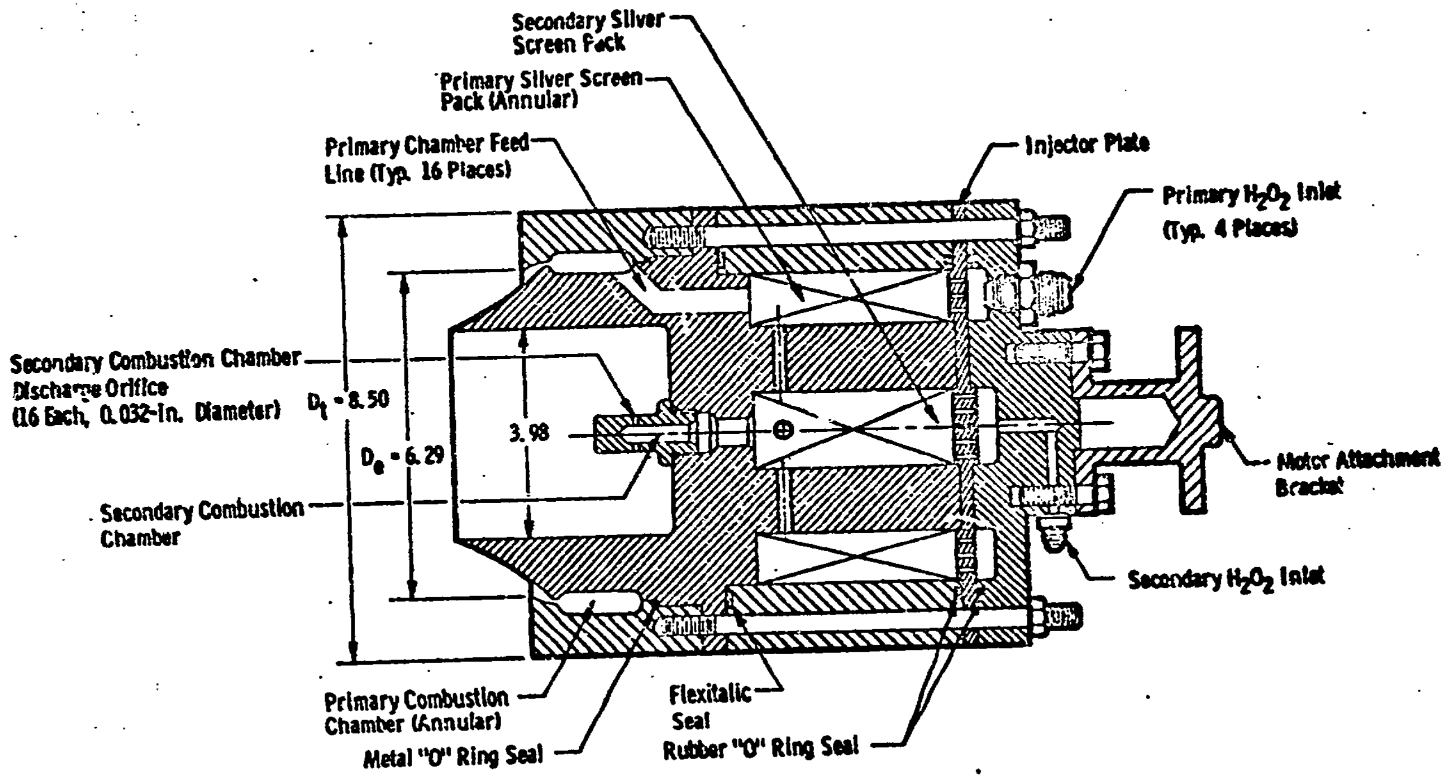

Figure 108. **Cross Section View of the Rocket Engine**

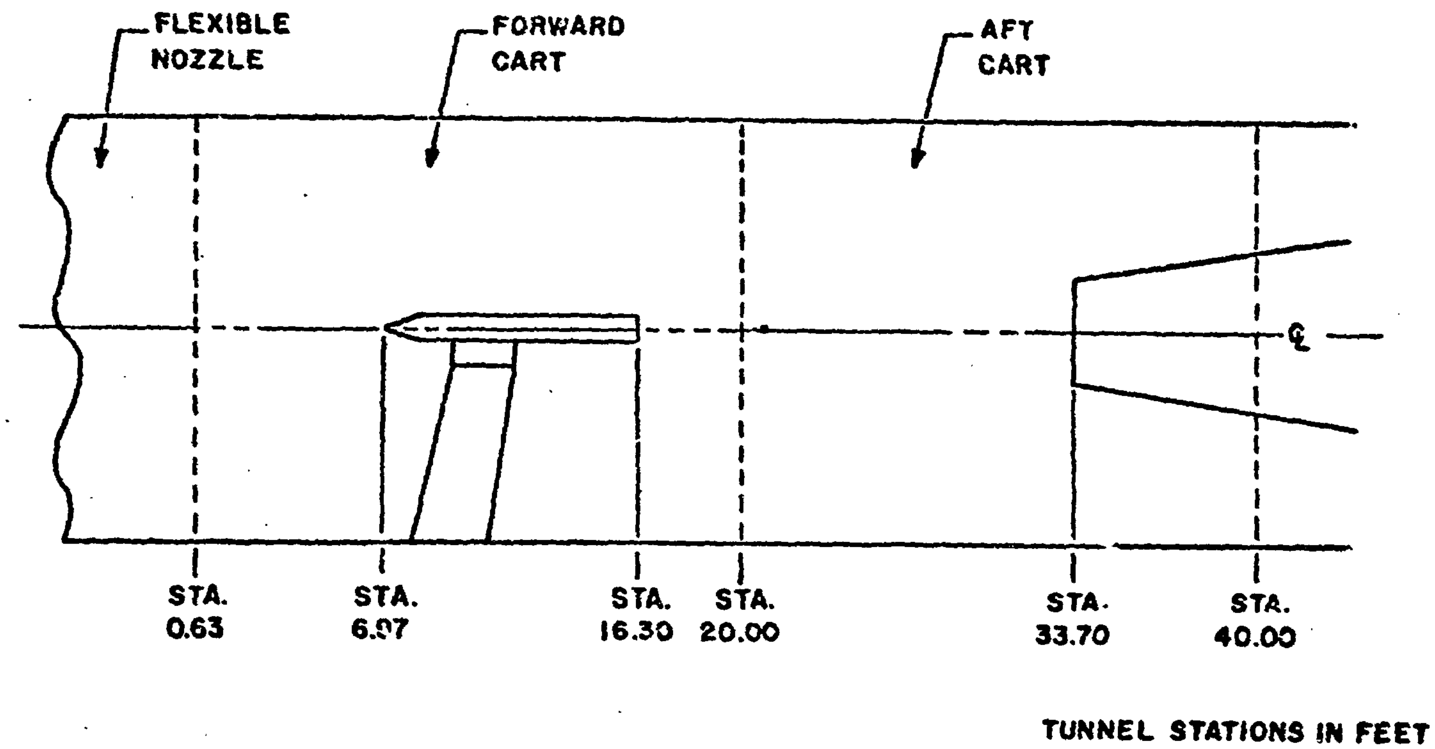

Figure 109. Test Installation in the Supersonic Wind Tunnel

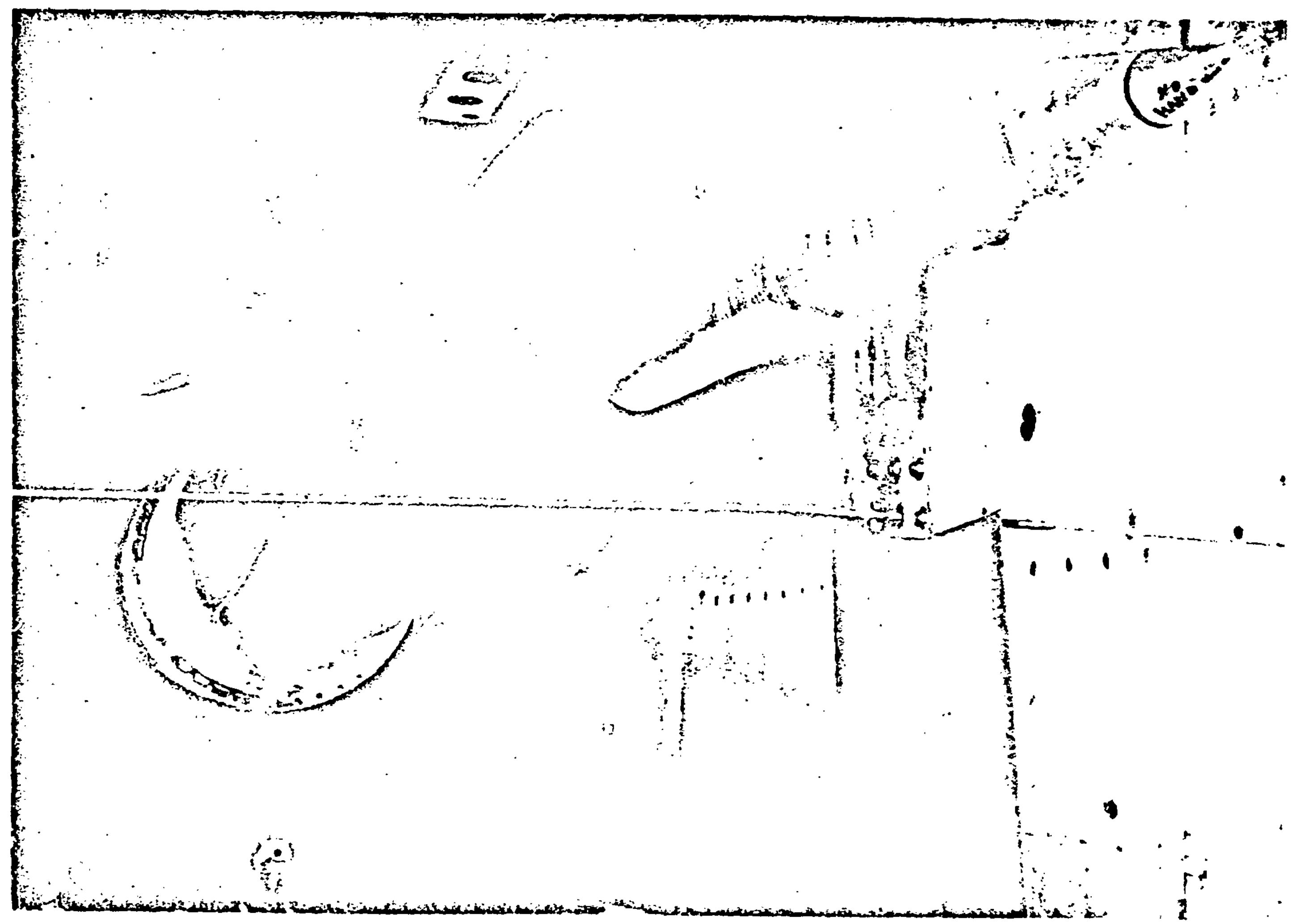

Figure 110. Test Installation in the Supersonic Wind Tunnel

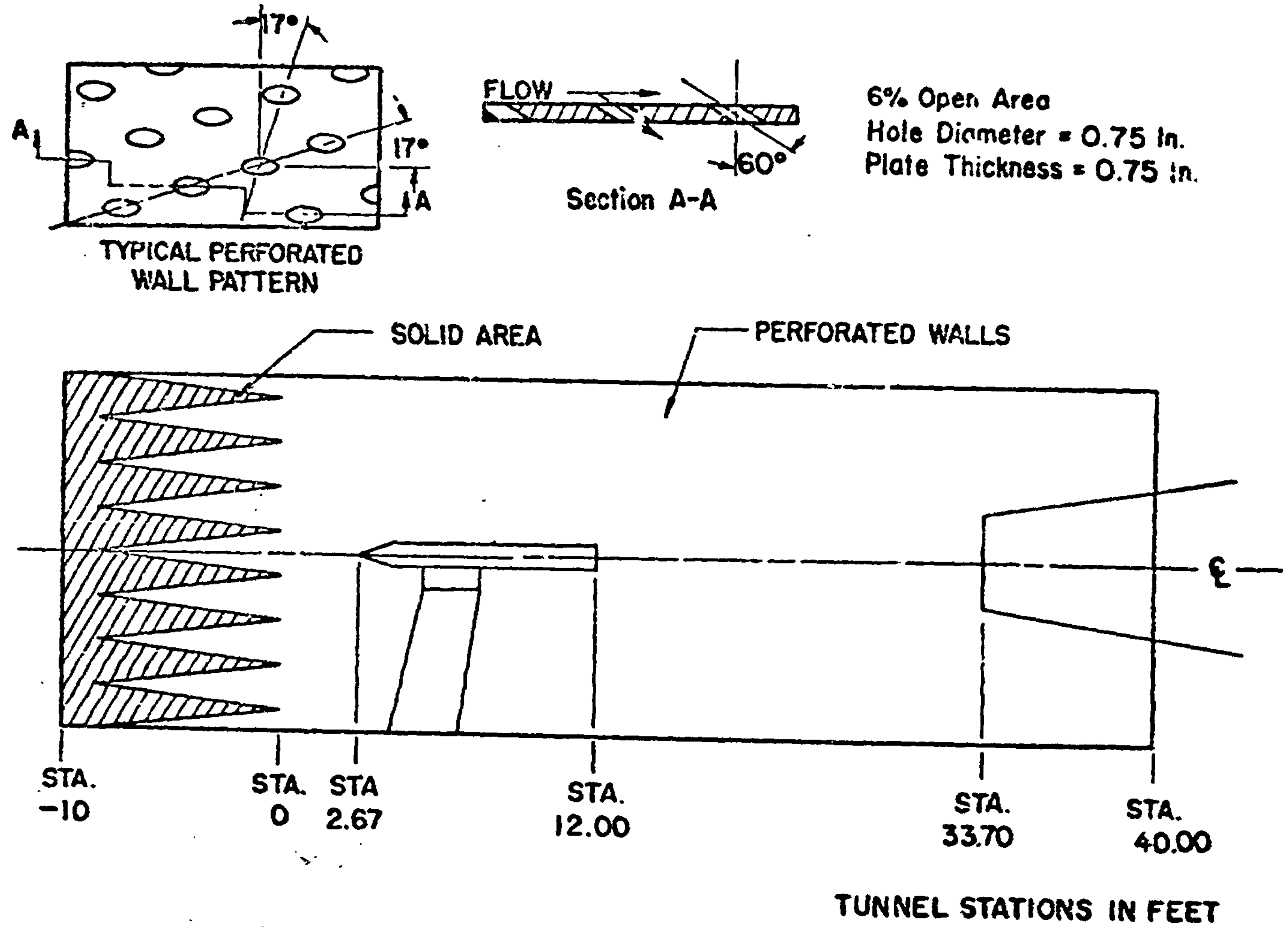

Figure 111. Test Installation in the 16T Test Section

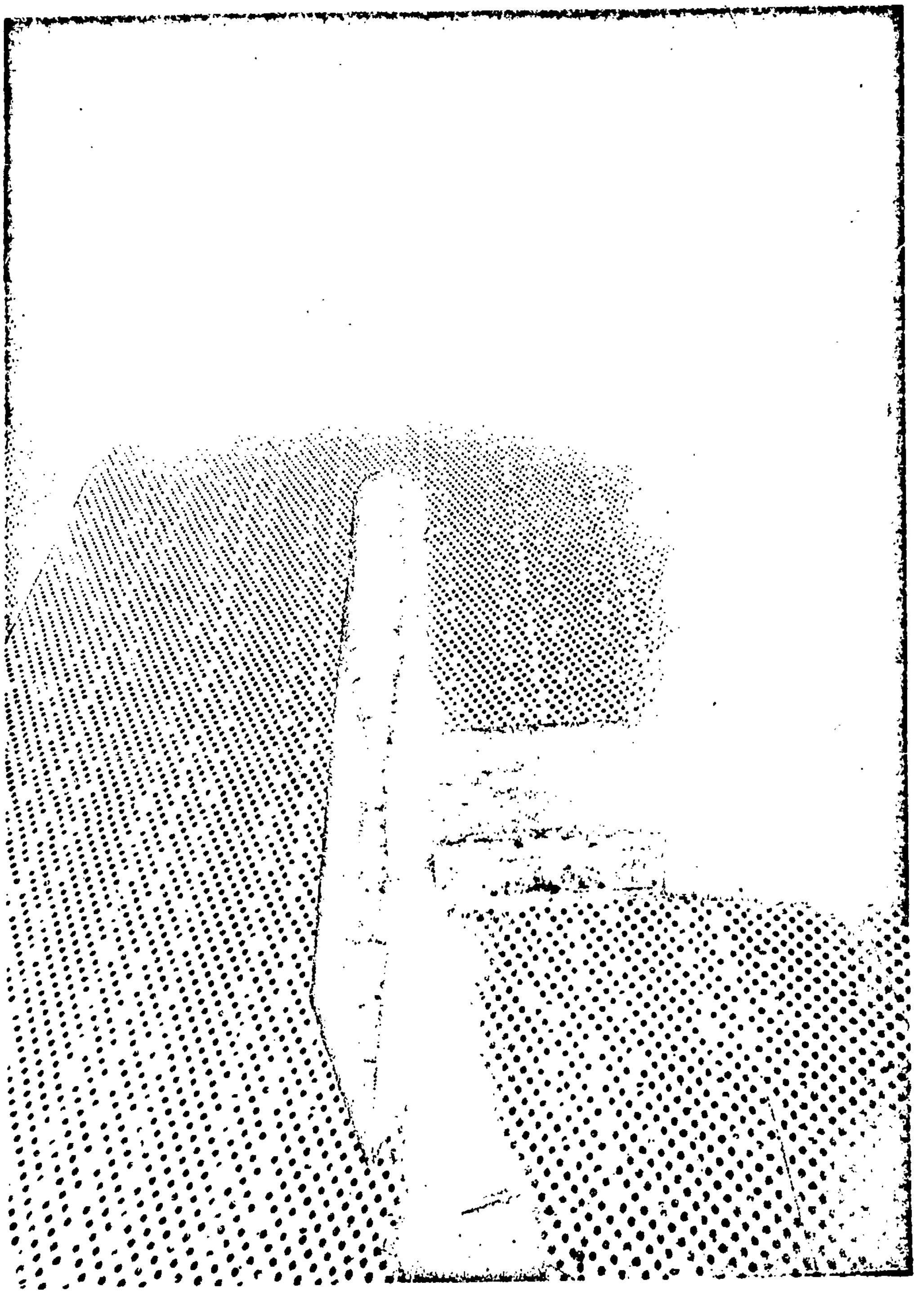

Figure 112. Installation of Slipstream Model in the Transonic Wind Tunnel at AEDC

the shape of a missile body. A dimensional sketch of the model is shown in Fig. 113, and a cross sectional view of the assembly is shown in Fig.114. The exit plane of the model extended approximately two strut chord lengths downstream of the strut trailing edge to reduce the strut interference on the model base to a minimum. In order to obtain nozzle performance as a function of the pressure which controls the expansion of primary exhaust gases, a flat, cylindrical missile boat tail was selected to insure a separated flow over the missile base with an attendant uniformly distributed missile base pressure. This is not necessarily typical of future configurations because of the relatively low missile base pressures characteristic of this geometry. Extensive testing would be required to cover all possible future boat tail geometries, and the flat, cylindrical base was chosen to simplify the interpretation of test data.

(U) Pressures along the missile base were equalized with the pressure within the simulated vehicle by providing an annular passage between the engine and outer skin which allows a gas flow from the model base to the interior of the missile body. This enables direct measurement of nozzle thrust referenced to the pressure that controls the nozzle expansion (i.e., the missile base pressure) exclusive of the missile base and skin drag. Concentricity between the engine and the missile skin was maintained by means of adjustable set screws located in the thrust mount. Pressure instrumentation was provided along the forward face of the engine and on the fore and aft sections of the force balance as a precautionary measure to enable thrust corrections in the event of an unbalance between the missile base and internal missile pressures.

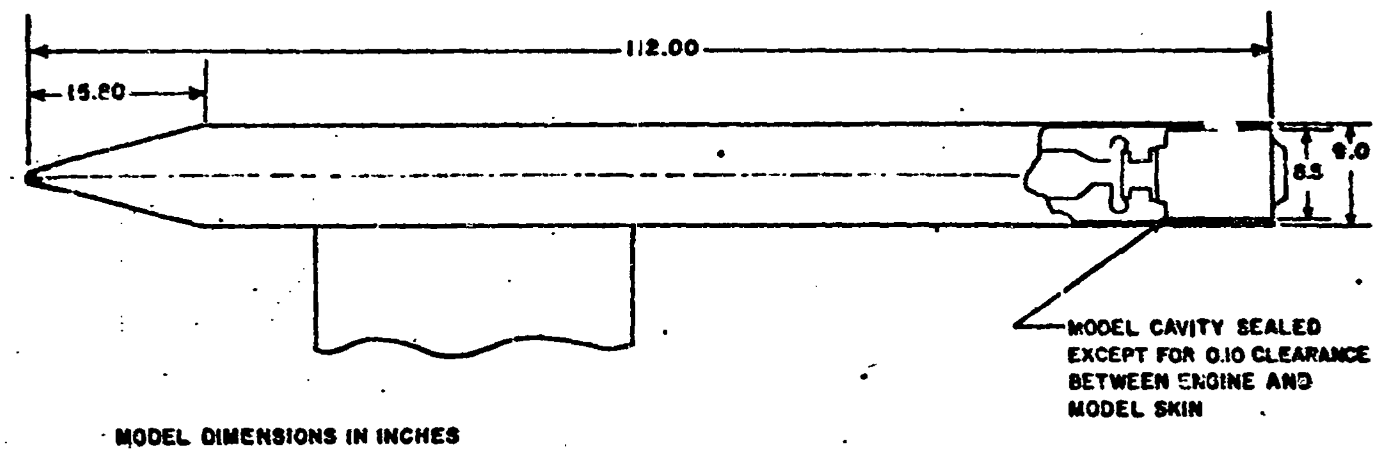

Figure 113. Dimensioned Sketch, Slipstream Model

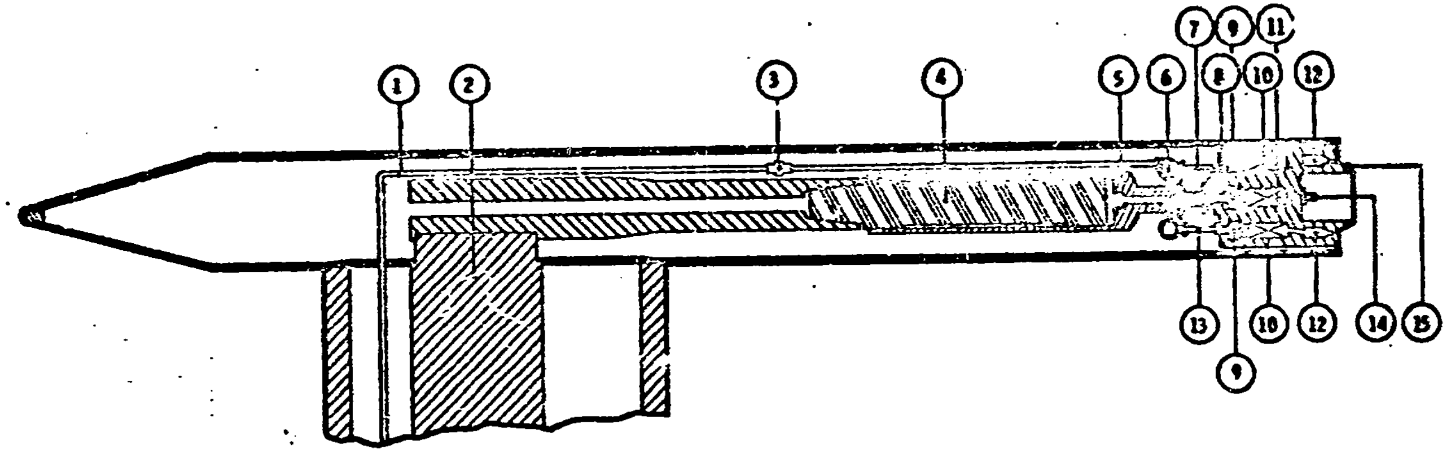

1. Propellant Supply Line
2. Model Strut Support
3. Cavitating Venturi
4. Force Balance
5. Force Balance Housing
6. Propellant Manifold
7. Secondary Propellant Line
8. Secondary Injector
9. Primary Injector
10. Primary Silver Screen Pack
11. Secondary Silver Screen Pack
12. Primary Combustion Chamber
13. Primary Propellant Line
14. Secondary Combustion Chamber
15. 20-Percent Length Aerospike

Figure 114 . Cross Section View of Slipstream Model

(U) Engine propellant lines, coolant lines for the force balance, and instrumentation lines were routed to the model assembly along the strut and enclosed by aerodynamic fairings. Propellants and coolant were supplied through rigid tubing which was free floating through a right angle turn down to a fixed cantilever point well within the support strut. This cantilever point was located such that undesirable tare forces on the balance system were negligible.

(U) As shown in Fig. 114, peroxide was supplied through four descrete feed lines to the primary annular catalyst pack from a toroidal distribution manifold located on the aft section of the force balance. A fifth feed line supplied propellant to the central secondary catalyst pack. Drilled passages in the shell separating the annular and central catalyst packs allowed communication between primary and secondary supply systems after peroxide decomposition. A facility flow schematic for these tests is shown in Fig. 115 .

(U) Pressure orifice and thermocouple locations on the H_2O_2 engine and model are shown in Fig. 116 . Steady-state pressures were measured with differential pressure transducers located in the tunnel plenum and referenced to test section wall static pressure. The rocket engine chamber pressure and injection pressures were measured with model-mounted, absolute strain-gage-type transducers. The total H_2O_2 flow rate (primary + secondary) was measured with a turbine-type flowmeter located outside the tunnel shell. A thermocouple located in the H_2O_2 supply line just upstream of the flowmeter was used to correct the measured volume flow for the H_2O_2 density. A bench calibration of the secondary flow discharge orifice was used to calculate the secondary flow rate.

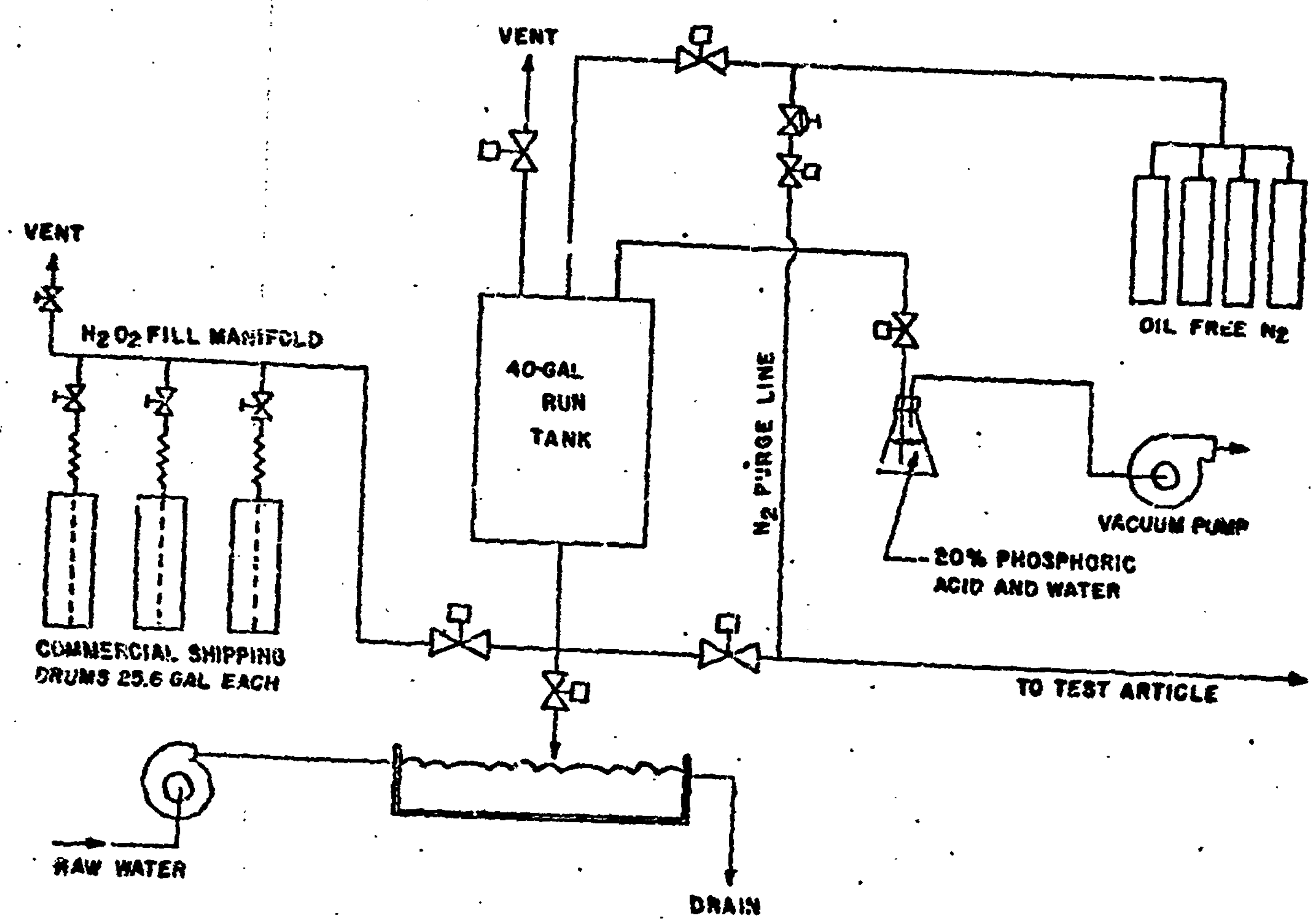

Figure 115. Hydrogen Peroxide Propellant System

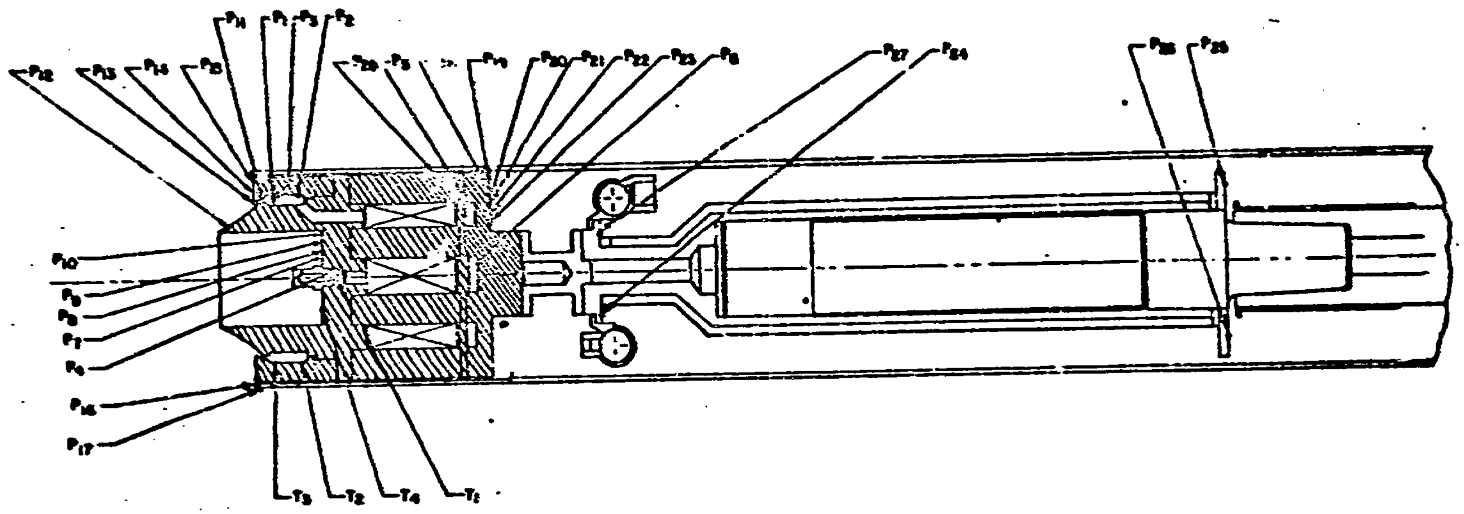

Figure 116. Pressure Orifice and Thermocouple Locations

(U) Test Procedure. The test program was designed to systematically cover the range of conditions indicated in Fig. 103. The "as tested" operating parameters are plotted along with the data of Fig. 103 in Fig. 117. As indicated, both the transonic and supersonic facilities at AEDC were used to cover the desired range of operating conditions. It can be seen that, although the testing was conducted over repeated increments in chamber pressure ratio, most of the data points were taken at conditions which closely approximate those along the trajectories in Fig. 103.

(U) During a typical test sequence, the engine was fired after the propellant system was pressurized and the desired test conditions of Mach number and total pressure were established in the test section. The correct propellant weight flow was maintained throughout the firing by supplying the run tank with regulated nitrogen flow. The rocket engine was operated for approximately 50 seconds at each of the tunnel test conditions to allow the combustion temperature to reach equilibrium. Transient data recorders and motion picture cameras were turned on just prior to the rocket firing; steady-state data points were obtained at 5-sec. intervals throughout the firing in the supersonic facility, and at 3-sec. intervals in the transonic facility.

Test Results

(U) A summary of the testing conducted in each facility is indicated in Table 11. Forty tests with $\dot{W}_s$ = 0.8 percent were conducted to evaluate slipstream effects. The remaining five tests were conducted to establish nozzle performance trends with secondary flowrate. Reduced data for each test include: nozzle thrust and specific impulse efficiency based on both ambient and missile base pressure; wall pressure ratios; P_w/P_c; average engine and missile base pressure ratios, $\overline{P}_B/P_c$ and $\overline{P}_{B_V}/P_c$; chamber and

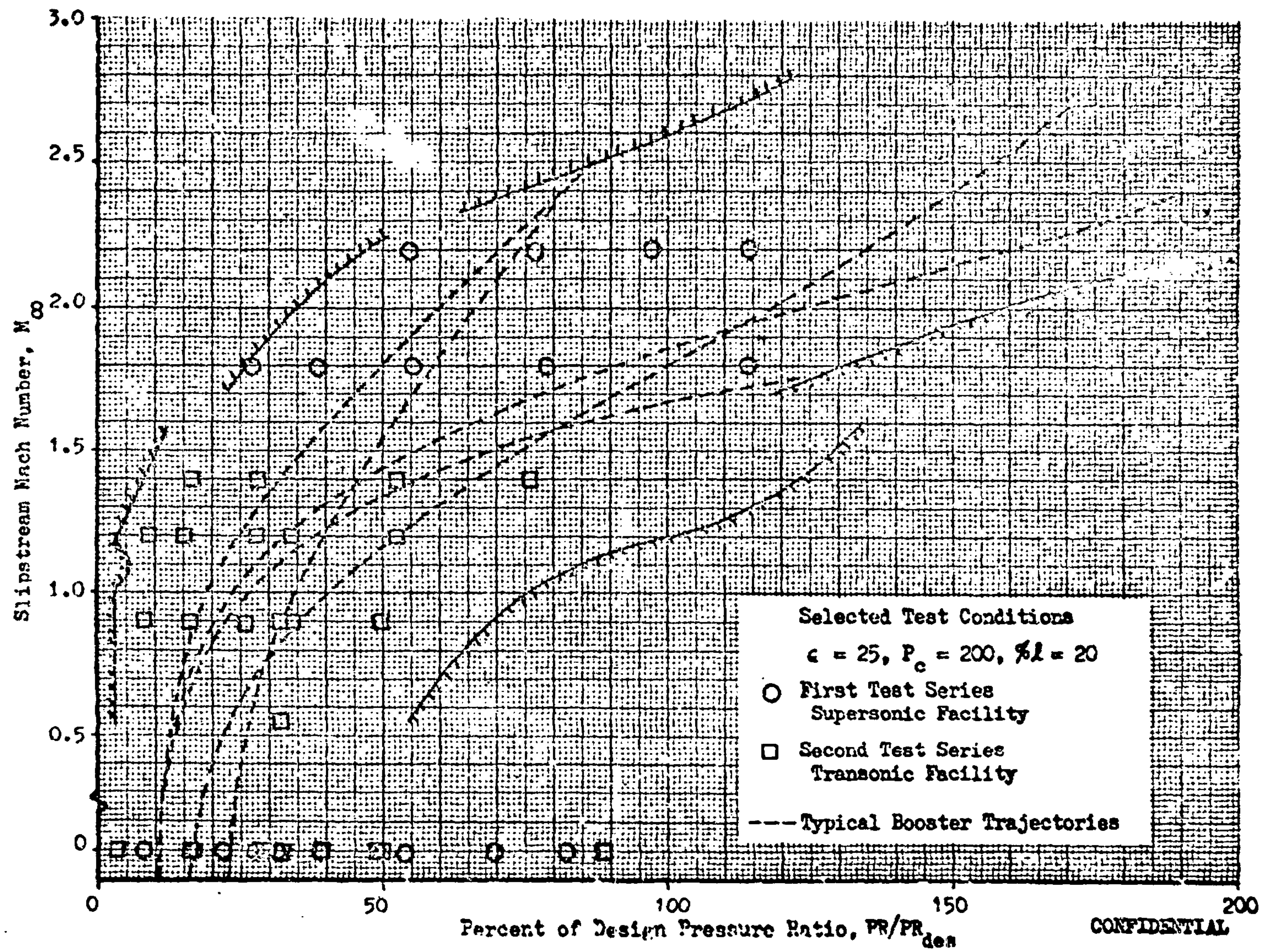

Figure 117. Still Air and External Flow Test Conditions

TABLE 11

TEST SUMMARY

CONFIDENTIAL

Number of Tests	Mach Number	Pressure Ratio Range	Secondary Flowrate (Percent)
		TRANSONIC FACILITY	
4	0	67 - 202	0
6	0	14 - 361	0.8
1	0	211	1.7
1	0.55	132	0.8
6	0.9	67 - 209	0.8
5	1.2	36 - 216	0.8
4	1.4	66 - 311	0.8
		SUPERSONIC FACILITY	
9	0	33 - 337	0.8
4	1.8	110 - 469	0.8
5	2.2	223 - 467	0.8

missile base to ambient pressure ratios, P_c/P_{oo} and $\bar{P}_{B_v}/P_{oo}$; and secondary flowrate ratio, $\dot{W}_s/\dot{W}_p$. Data reduction was performed at AEDC using automatic digital computation equipment. The techniques utilized to obtain these parameters from the measured data are discussed in Appendix 2 . Measured parameters and reduced data for each test are listed in Table 17 of Appendix 2 and Appendix 3, respectively. Engine operating characteristics established by these data in still air and in slipstream are discussed below.

(c) <u>Quiescent Air</u>. As indicated in Fig. 117, extensive testing was conducted under still air conditions to quantitatively establish performance trends with altitude and secondary flowrate for reference purposes. This testing confirmed that thrust efficiency values greater than 98 percent can be achieved at design pressure ratio with a properly designed aerospike nozzle operating with secondary flow. It was also established that off design performance with 0.8 percent secondary flow remains above 94 percent down to pressure ratios of approximately 10 percent of design pressure ratio (corresponds to sea level for most engine applications; cf Fig. 102) as demonstrated by the data presented in Fig. 118. Altitude compensation is in evidence at all pressure ratios investigated down to three percent of design pressure ratio; performance of the aerospike is seen to be considerably above that of a non-compensating nozzle at all pressure ratios below 140. The non-compensating efficiency curve was determined using the standard equations for conventional nozzle performance in conjunction with the assumption that design efficiency of the conventional and aerospike nozzles were the same. It can also be seen in Fig. 118 that good data repeatability was obtained between the transonic and supersonic test facilities at AEDC. Decomposition efficiency was nominally 97.5 percent for these tests. The shaded symbol in Fig. 118 represents questionable efficiency data and has been excluded from the remainder of the plots presented herein.

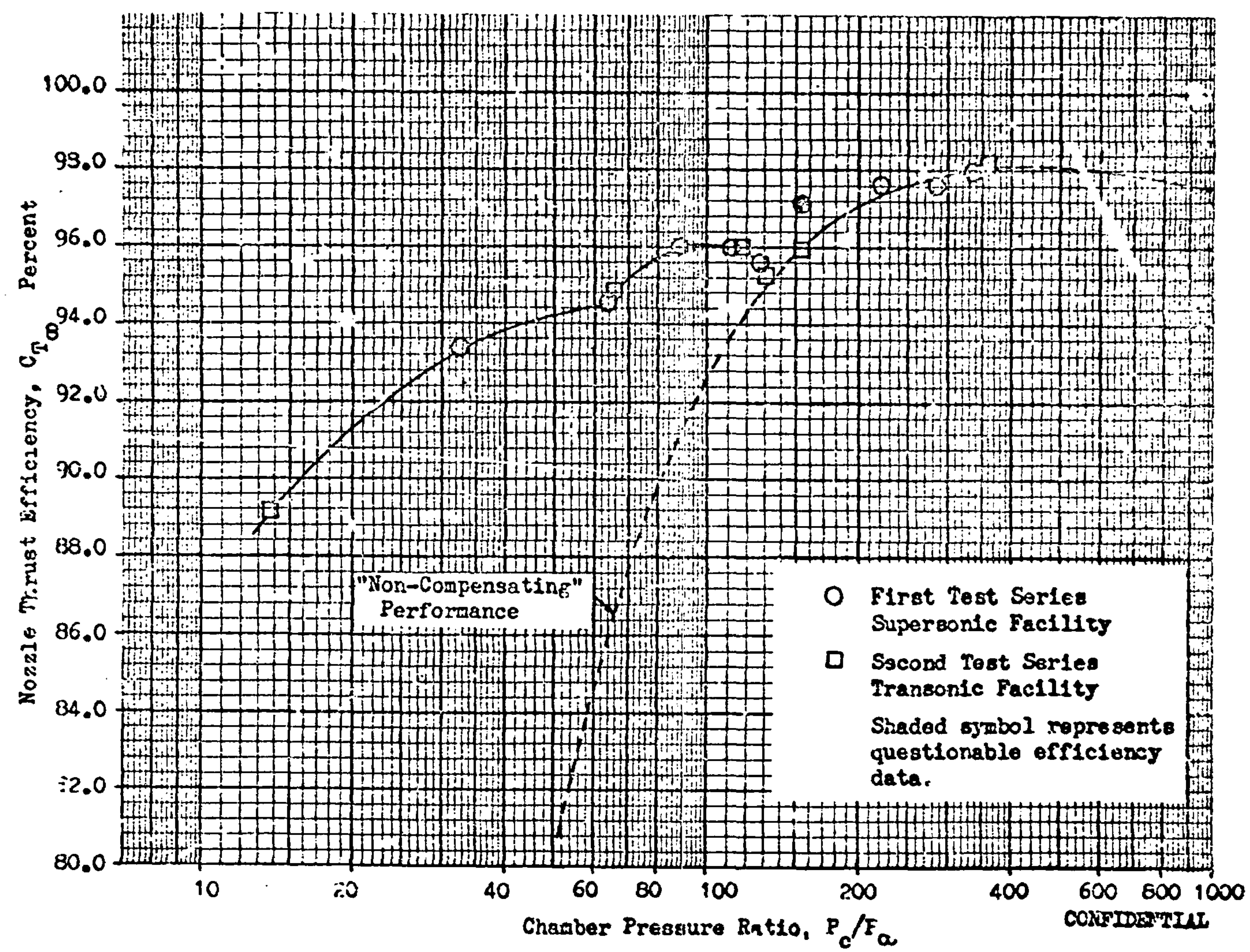

Figure 118. Still Air Nozzle Efficiency vs Chamber Pressure Ratio

(C) Aerospike "open wake" performance trends with altitude can be attributed directly to the influence of ambient pressure on nozzle base and wall pressures. Average nozzle base pressure ratio, $\overline{P}_B/P_c$, with 0.8 percent secondary flow is shown as a function of chamber pressure ratio in Fig.119. For this nozzle and secondary flowrate, base pressure remains constant (closed wake conditions) with decreasing ambient pressure for all pressure ratios greater than 150, which corresponds to a low point in the efficiency curve in Fig.118. Below this pressure ratio, base pressure is greater than ambient pressure for all of the conditions investigated. Thus, a positive thrust is developed across the engine base at all pressure ratios. The base thrust and nozzle recompression contribution becomes substantial at low pressure ratios and results in the high nozzle efficiency indicated for the aerospike at low altitudes (Fig.118).

(C) The recompression phenomena which causes base pressure to adjust to ambient pressure at low pressure ratios also causes the primary nozzle wall pressures to increase at very low pressure ratios as shown by the wall pressure data presented in Fig. 120. As indicated, the wall pressure trend with ambient pressure at locations near the end of the nozzle is similar to that predicted theoretically; good agreement between experiment and theory is evident for stations near the end of the nozzle. However, experimental data deviate from the predicted trend within the shrouded portion of the nozzle.

(C) Experimental data that show performance trends with secondary flow are presented in Fig.121. It is readily seen that the addition of secondary flow is beneficial to performance at all pressure ratios.

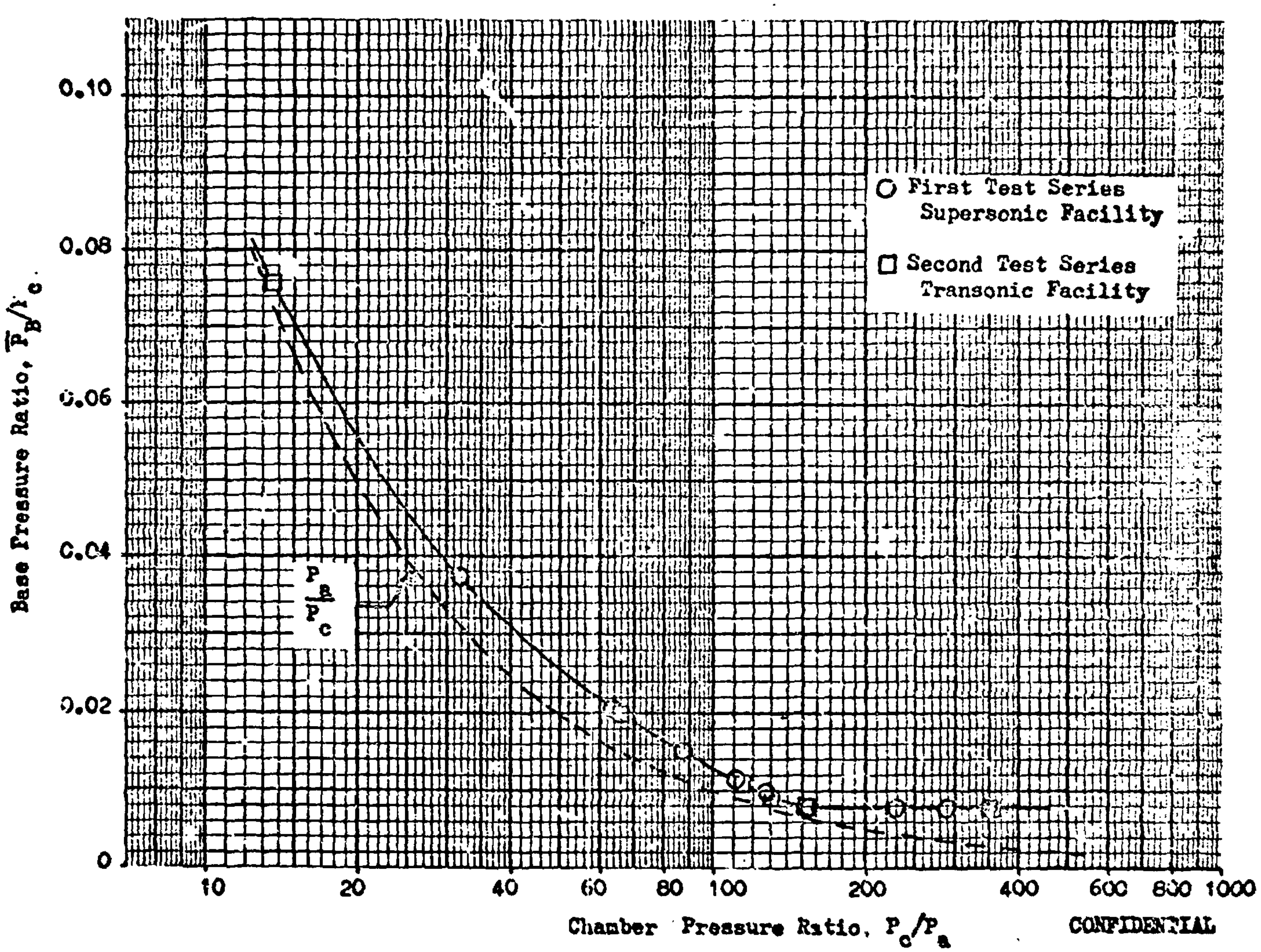

Figure 119. Engine Base Pressure vs Chamber Pressure Ratio in Still Air, $\dot{W}_s/\dot{W}_p$ = 0.8 percent

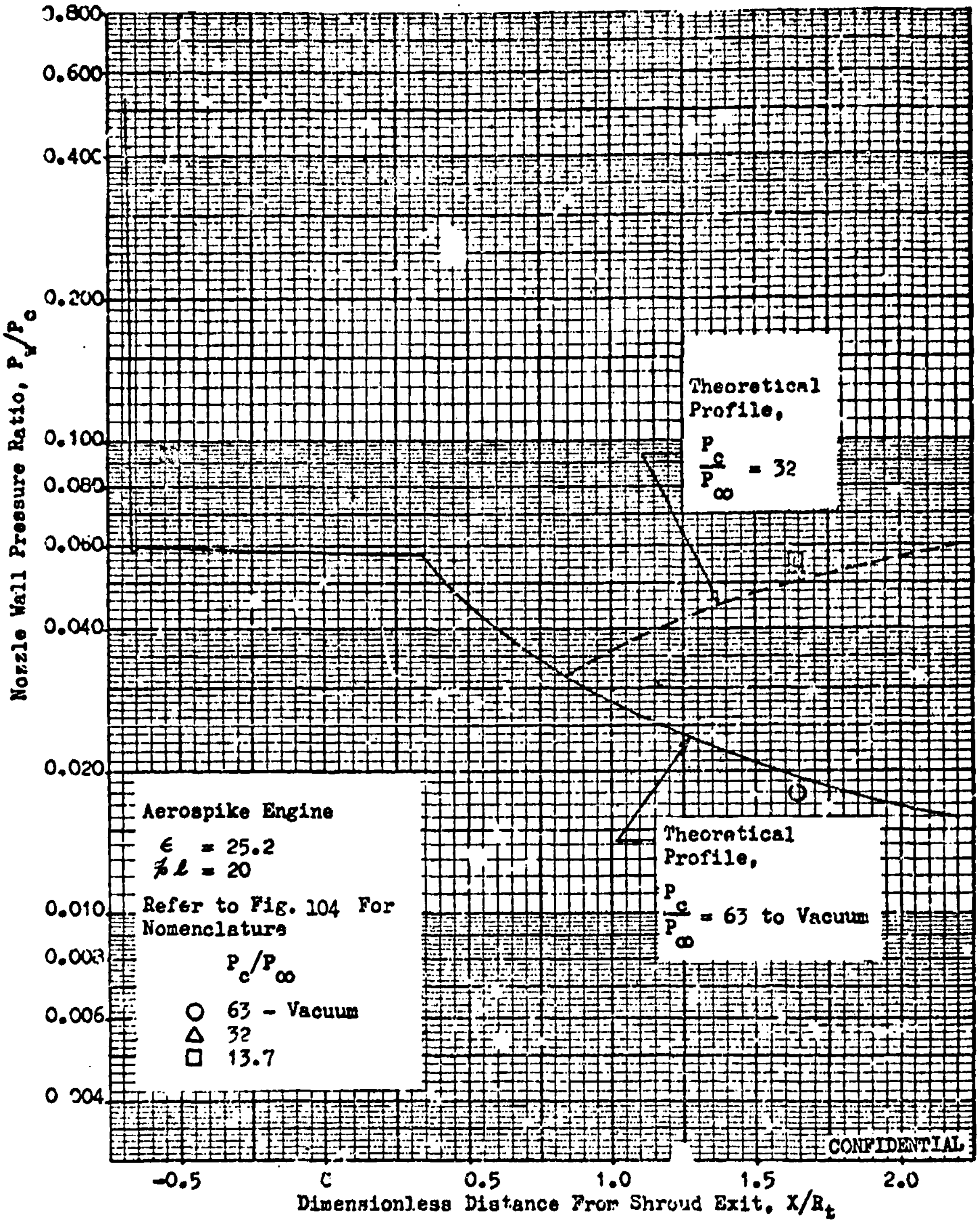

Figure 120. Comparison Between Experimental and Theoretical Wall Pressure Profiles

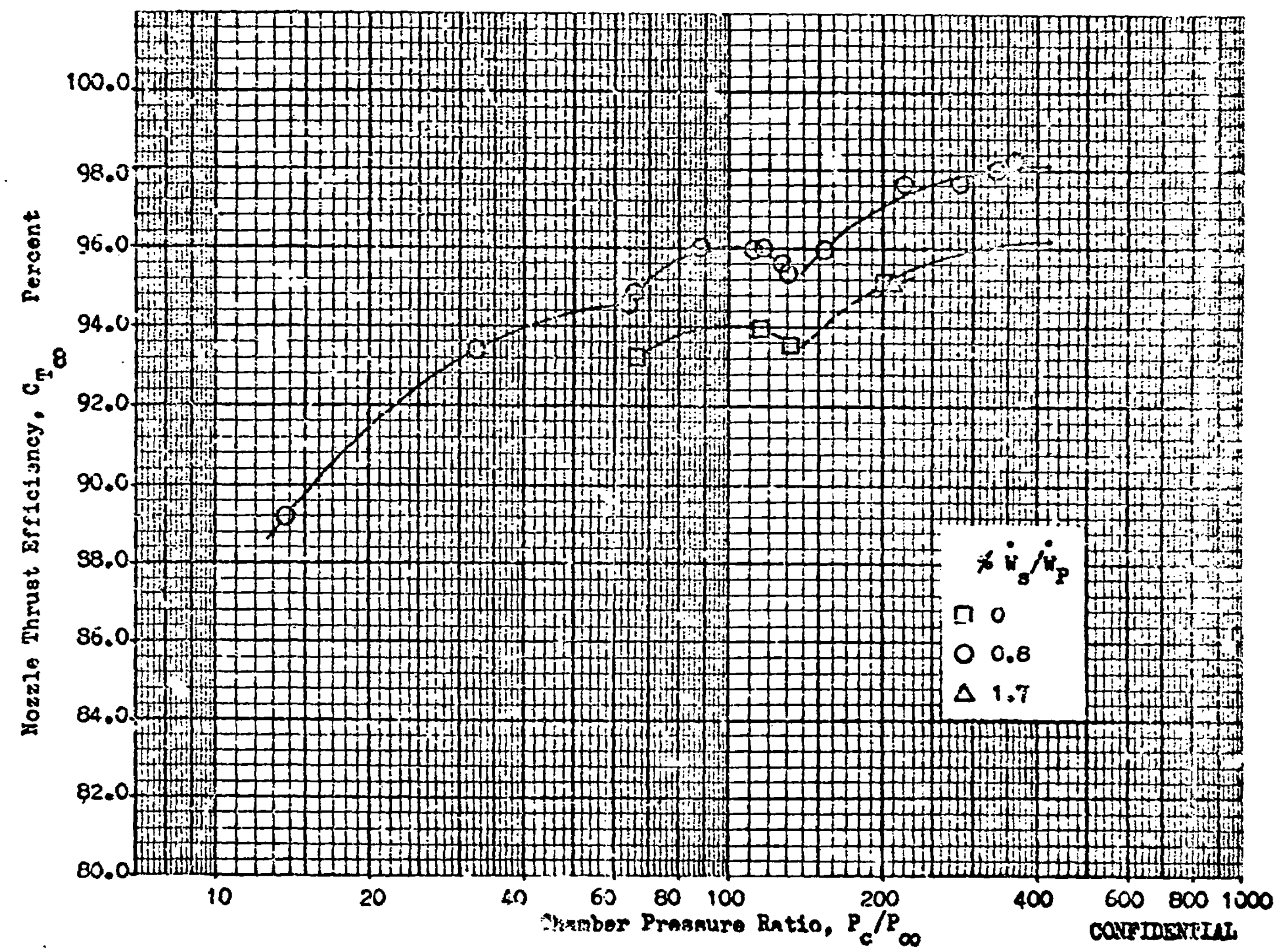

Figure 121. Measured [illegible] Efficiency Trend With Secondary Flow

(C) The experimental base pressure for secondary flowrates 0, 0.8, and 1.7 percent are shown as a function of chamber pressure ratio in Fig.122. Nozzle efficiency computed using the measured base pressure differential from base pressure for 0.8 percent secondary flow (refer to eq (10) of Appendix 2) is presented in Fig.123. Efficiency gains with secondary flow are again evident throughout the range of pressure ratios investigated, but computed efficiency without secondary flow is nominally one percent above the measured values (compare Fig.121). Also, computed performance for 1.7 percent secondary flow is nearly identical to that for 0.8 percent flow as compared to the substantial loss ($\approx$ 2 percent) indicated for 1.7 percent secondary flow in Fig.121. Although no reason could be found for this discrepancy between the measured and computed magnitude of performance gain with secondary flowrate, these hot flow data do establish the expected performance trend in both cases.

(C) A comparison between the theoretical and measured nozzle efficiency is presented in Fig.124. Measured base pressure (from Fig.122) was utilized to compute the predicted performance. As indicated, good agreement exists between experiment and theory.
The efficiency trend with secondary flow computed from the measured change in base pressure follows the predicted trend very closely as shown in Fig.125.

(C) Base pressure estimated using the empirical technique developed in Ref. 2 (Fig.105, page 206) was found to be slightly higher than that measured for 0.8 percent secondary flow in the "closed wake" and "transition" pressure ratio regimes as shown in Fig.126. A cross-over point between measured and estimated base pressure occurs at a pressure ratio of 100. Estimated base pressures fall slightly below the measured values at pressure ratios less than 100. The percent deviation ranges from -7 percent at low pressure

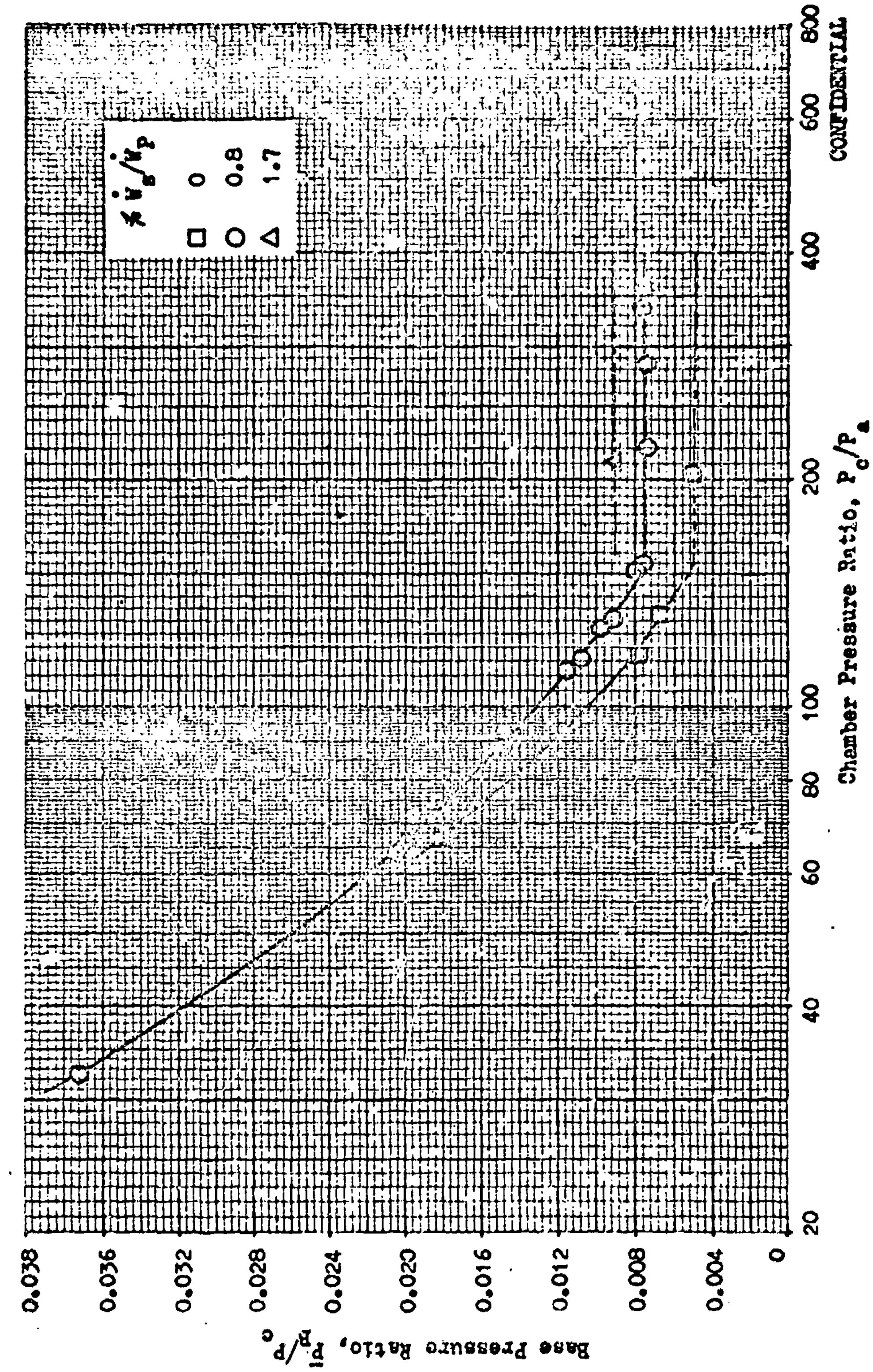

Figure 122. Measured Base Pressure Trend With Secondary Flow

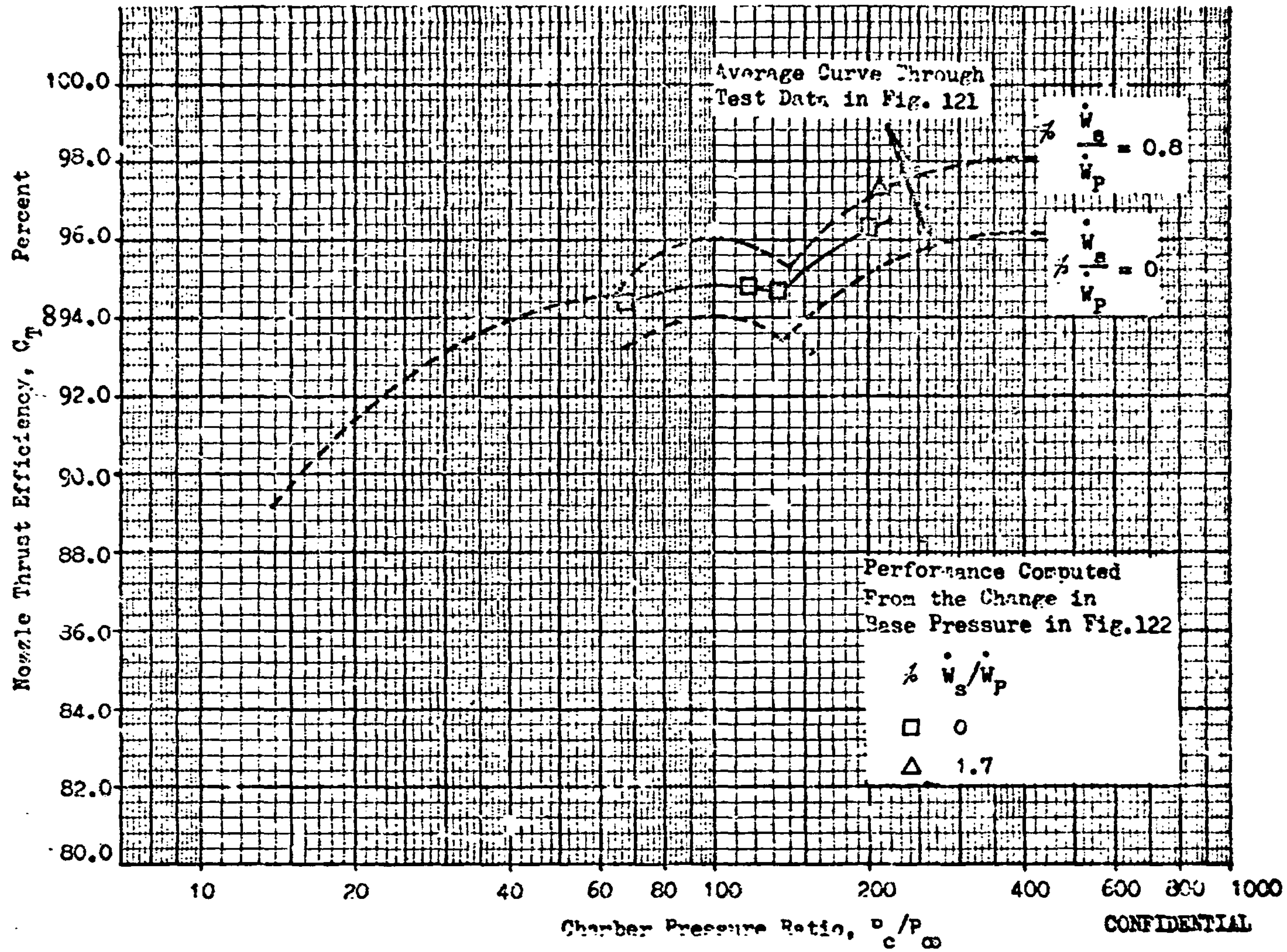

Figure 123. Still Air Nozzle Efficiency Trend with Secondary Flowrate and Chamber Pressure Ratio Computed from the Measured Change in Nozzle Base Pressure.

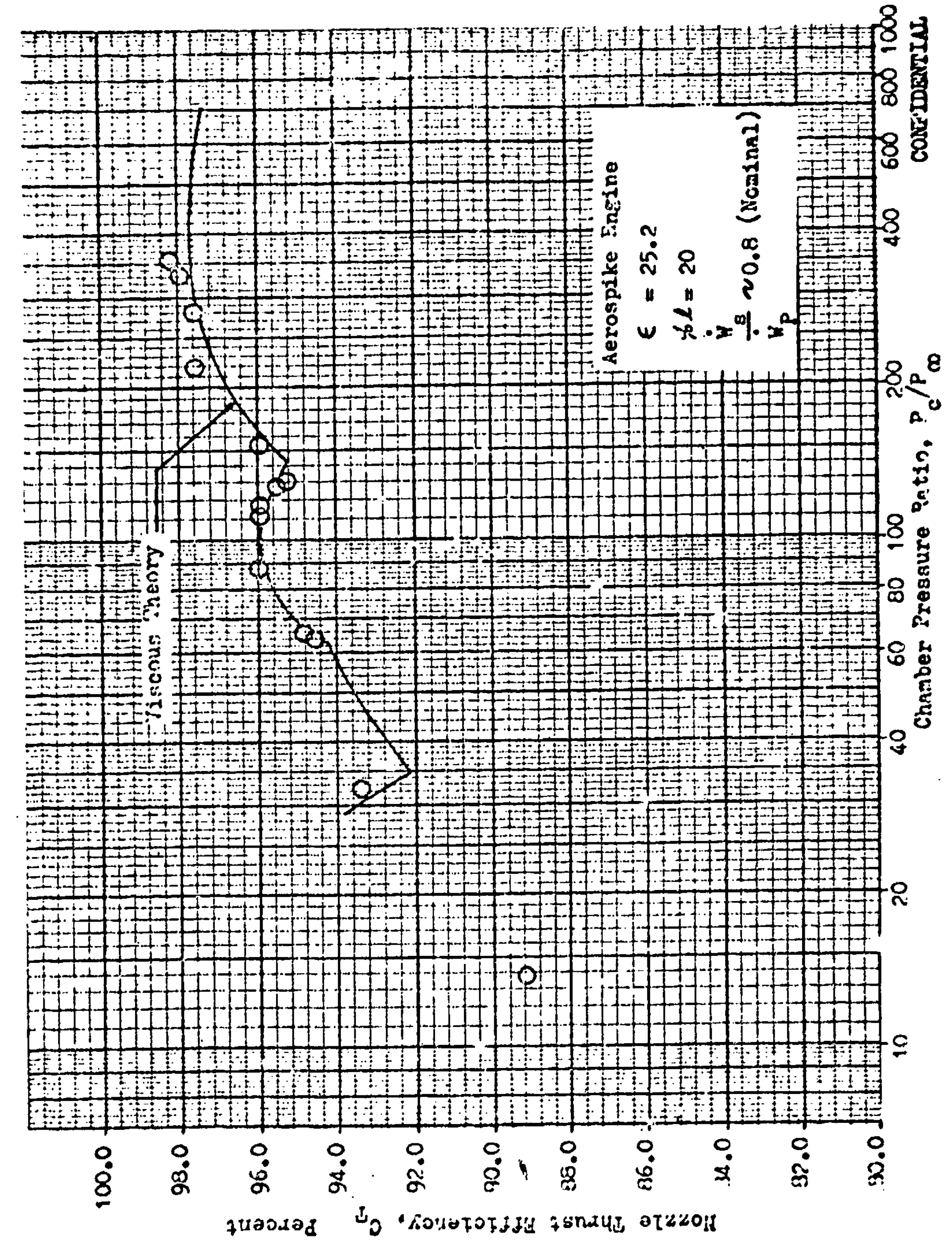

Figure 124. Comparison Between Estimated and Measured Efficiency Using Measured Base Pressure Data

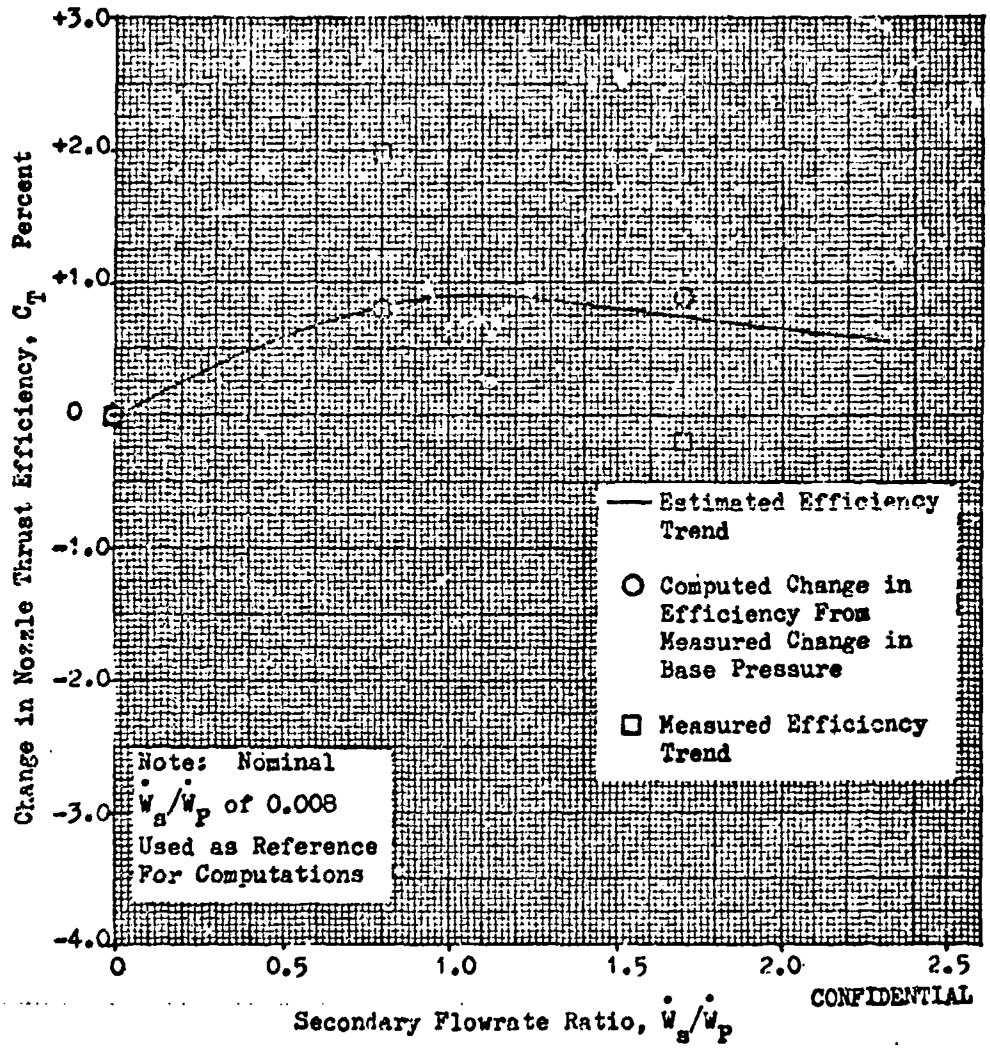

Figure 125. Comparison Between Estimated and Measured Efficiency Trend with Secondary Flowrate

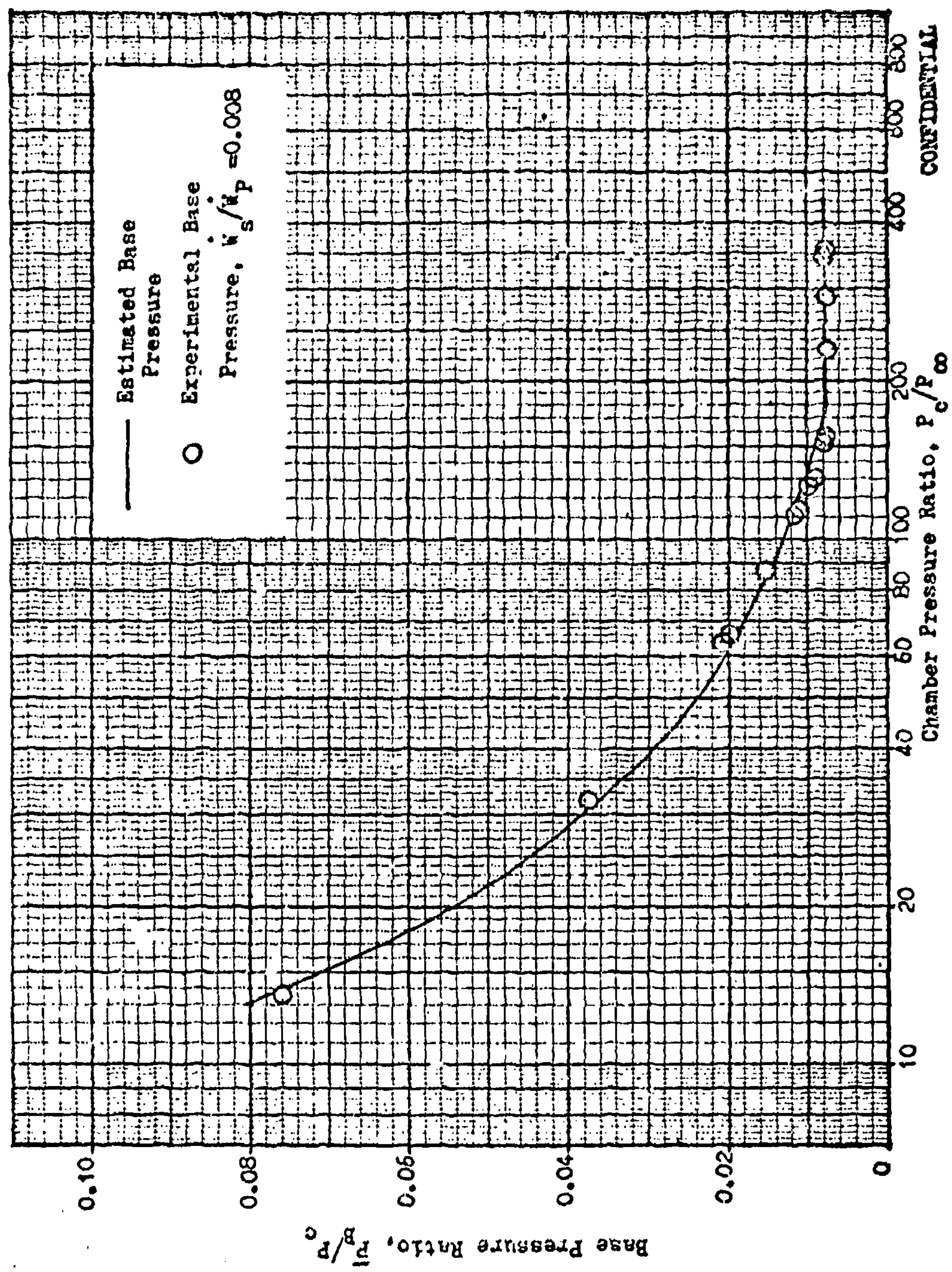

Figure 126. Comparison Between Estimated and Measured Base Pressure

ratios to +17 percent at a pressure ratio of 150 and back to +3 percent in the closed wake regime. Similar results were obtained with zero and 1.7 percent secondary flow as shown in Fig.127.

(C) External Flow. Slipstream testing was conducted over a range of Mach numbers from 0.55 to 2.2 and a range of chamber pressure ratios from 8 to 115 percent of the model design pressure ratio (PR = 410). Nozzle efficiency data (referenced to the static pressure of the free stream as in eq 6 of Appendix 2) obtained under these conditions are presented as a function of the chamber pressure ratio, P_c/P_{oo}, in Fig. 128. Performance is seen to be unaffected by free stream conditions at all pressure ratios above approximately 150, which closely approximates the pressure ratio of base closure as shown by the data in Fig.122. Below this pressure ratio, efficiency decreases at a rate which is dependent on the free stream Mach number; performance at low pressure ratios is lowest for high (supersonic) Mach numbers.

(C) These efficiency data are replotted as a function of percent of design pressure ratio in Fig.129. The flight trajectory data shown in Fig.101, page 201, were used to obtain the indicated nozzle efficiency limits for the most adverse flight conditions. Typical aerospike booster performance below the closed-wake pressure ratio (in still air) will lie above the shaded region and the non-compensating performance curve. For higher pressure ratios, nozzle performance is unaffected by Mach number. It can be seen that nozzle performance is only moderately reduced under typical flight conditions. Application of the data to a typical trajectory will be discussed in more detail in a later section.

(C) The indicated decrease in performance with increasing free steam Mach number was found to result directly from a similar trend in nozzle base pressures at low pressure ratios. Engine base pressure data measured

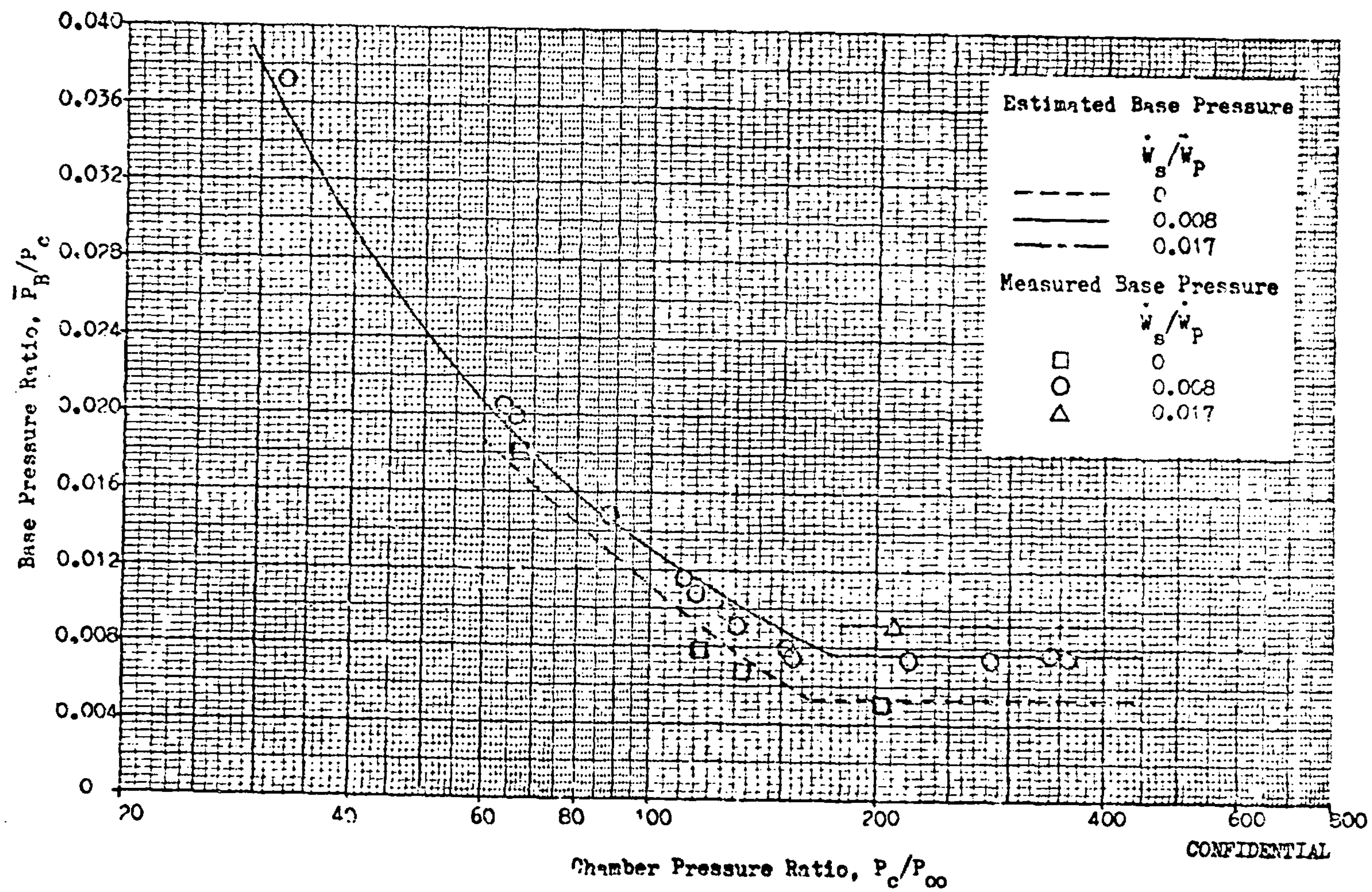

Figure 127. Comparison Between Measured and Estimated Base Pressure Trend With Secondary Flowrate

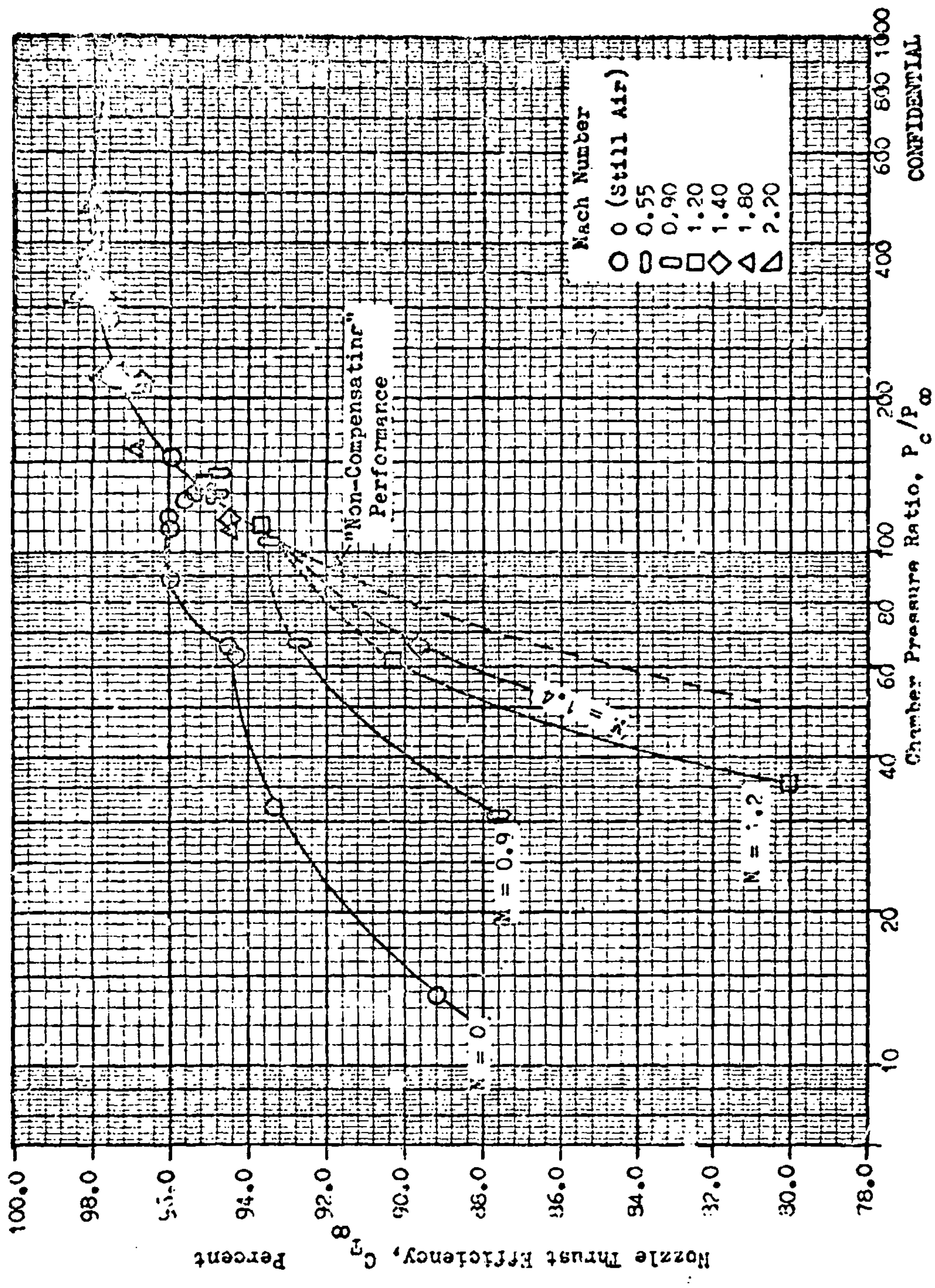

Figure 128. Aerospike Nozzle Efficiency vs Chamber Pressure Ratio With External Flow

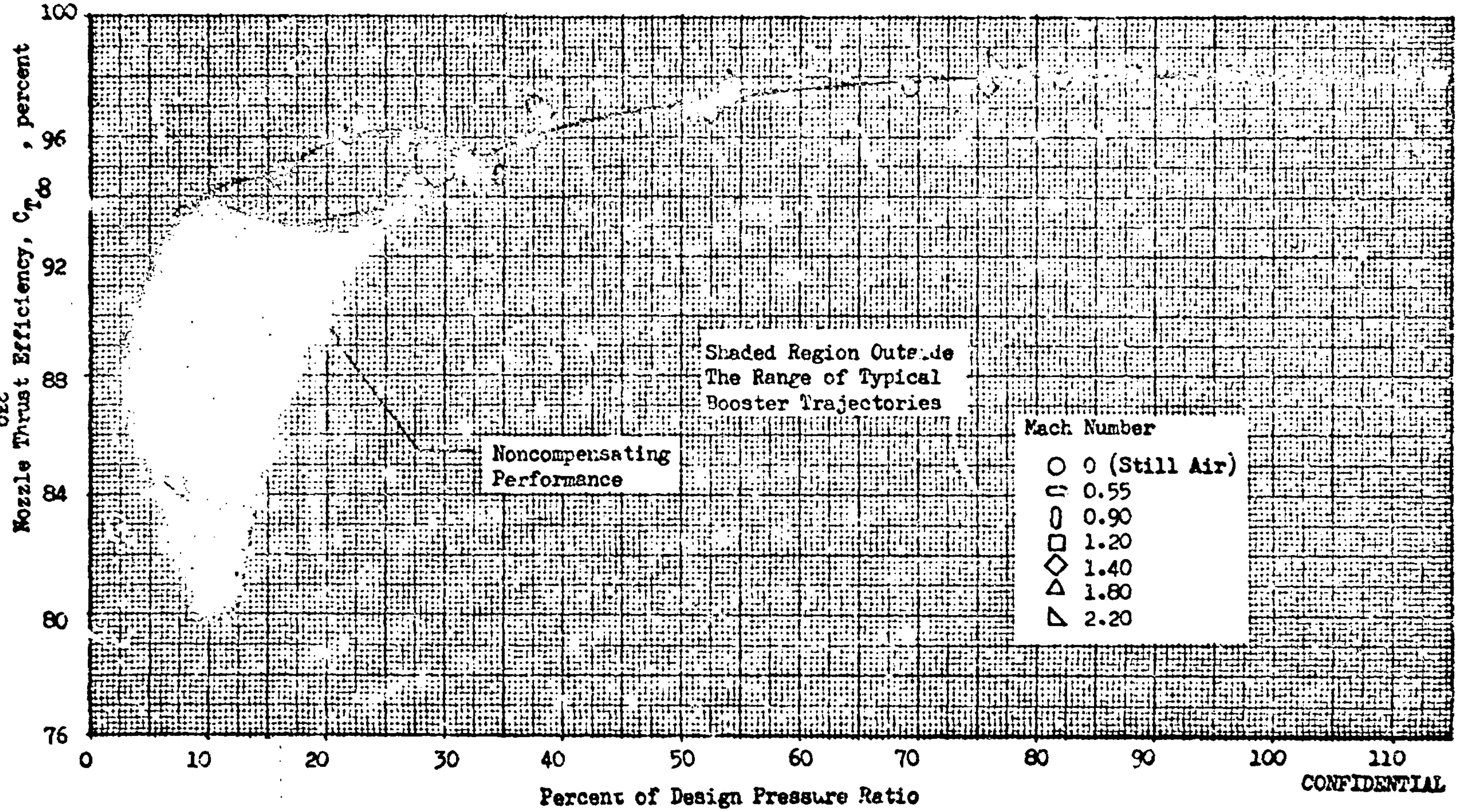

Figure 129. Aerospike Nozzle Efficiency vs Percent of Design Pressure Ratio

under the aforementioned external flow conditions are indicated in Fig. 130. As shown, a closed wake condition occurs at lower pressure ratios in slipstream than in still air, and base pressure is unaffected by the presence of external flow at high pressure ratios. Also, at low pressure ratios, base pressure does not recover to the same value in slipstream as it does in still air. The magnitude of base pressure in the open wake is seen to be a strong function of free stream Mach number, and forms the basis for the trend in nozzle efficiency indicated in Fig. 128.

(C) Nozzle wall pressures were found to be unaffected by external flow except at Mach number 0.9 at a pressure ratio of 32 where a slight decrease occurred. These data are presented in Fig. 131.

(C) These efficiency and nozzle base pressure trends in slipstream are similar to those obtained through the cold-flow testing discussed previously at pressure ratios above which base pressure is constant in still air. Trends at low pressure ratios with subsonic external flow differ from those established by the cold-flow data, and were found to be the result of lower missile base pressures than those measured in the cold-flow program. The average pressure acting over the missile base with the hot-flow model is shown plotted against the chamber pressure ratio of the engine in Fig. 132. It is readily seen that sub-ambient missile base pressures were obtained for all tests with external flow. Missile base pressure ratio decreases with increasing pressure ratio in subsonic external flow, while the opposite trend occurs with supersonic slipstream air. A reversal in this trend is observed at very low pressure ratios with free stream Mach number of 1.2, indicating a probable "opening" of the wake flow downstream of the missile base (Fig. 133) with corresponding tendency for missile base pressure to approach the free stream static pressure.

(C) A crossplot of the curves in Fig. 132 was made to show the effect of free stream velocity, and is presented along with cold-flow data from Ref. 21 in Fig. 134. As shown, the rate of missile base pressure decrease with increasing

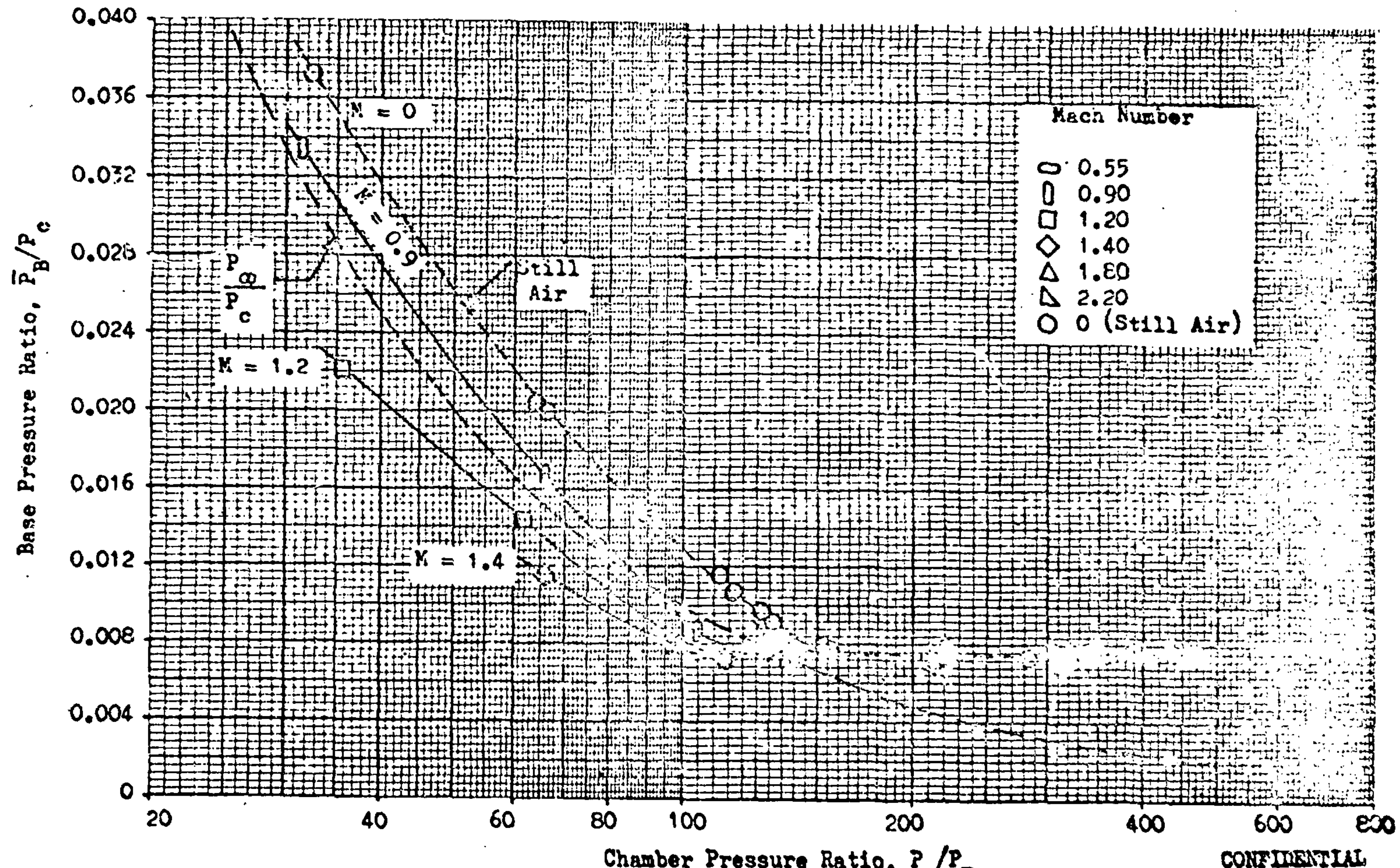

Figure 130. Engine Base-To-Chamber Pressure Ratio vs Chamber Pressure Ratio

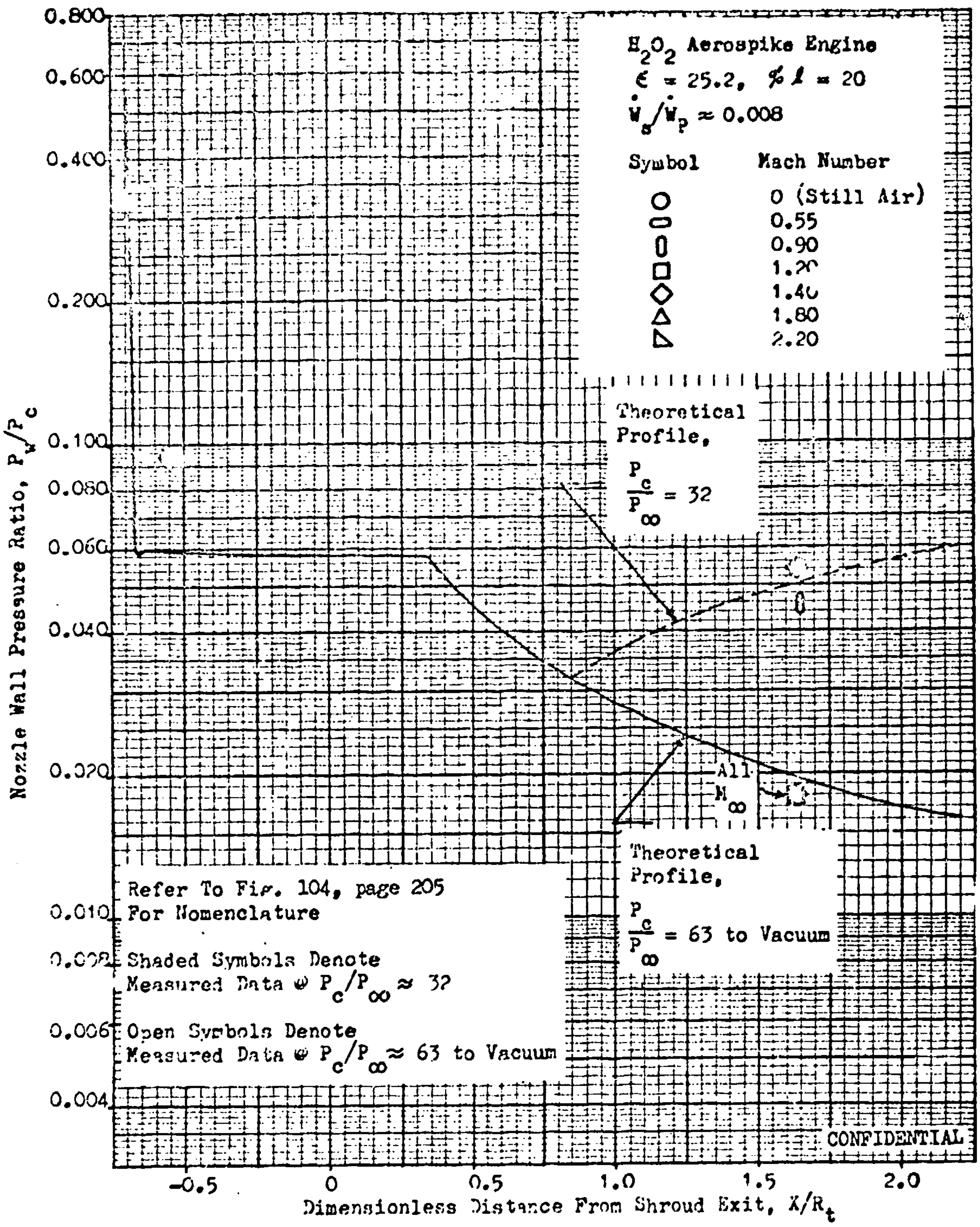

Figure 131. Nozzle Wall Pressure Trend in External Flow

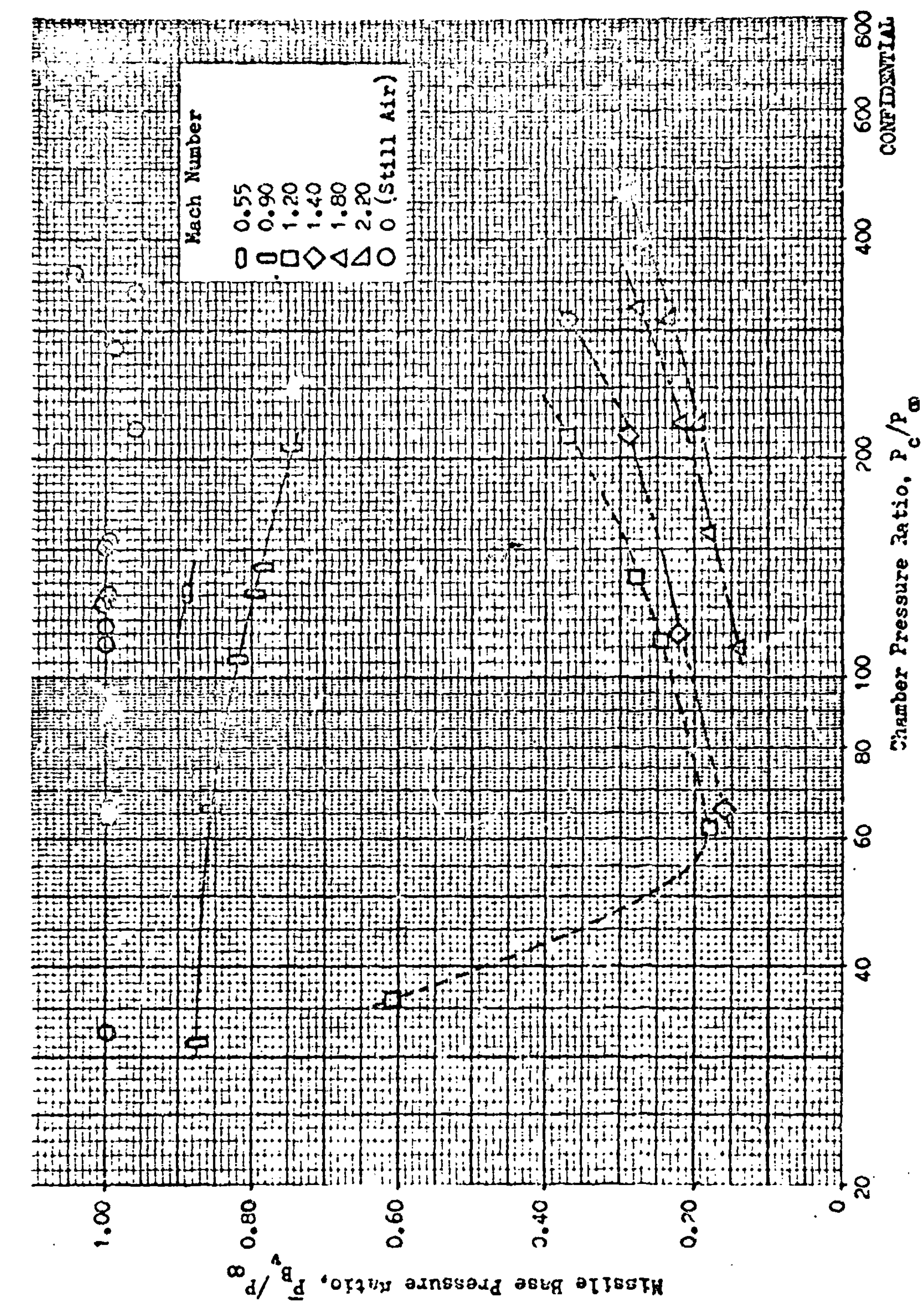

Figure 132. Missile Base-To-Ambient Pressure Ratio vs Chamber Pressure Ratio

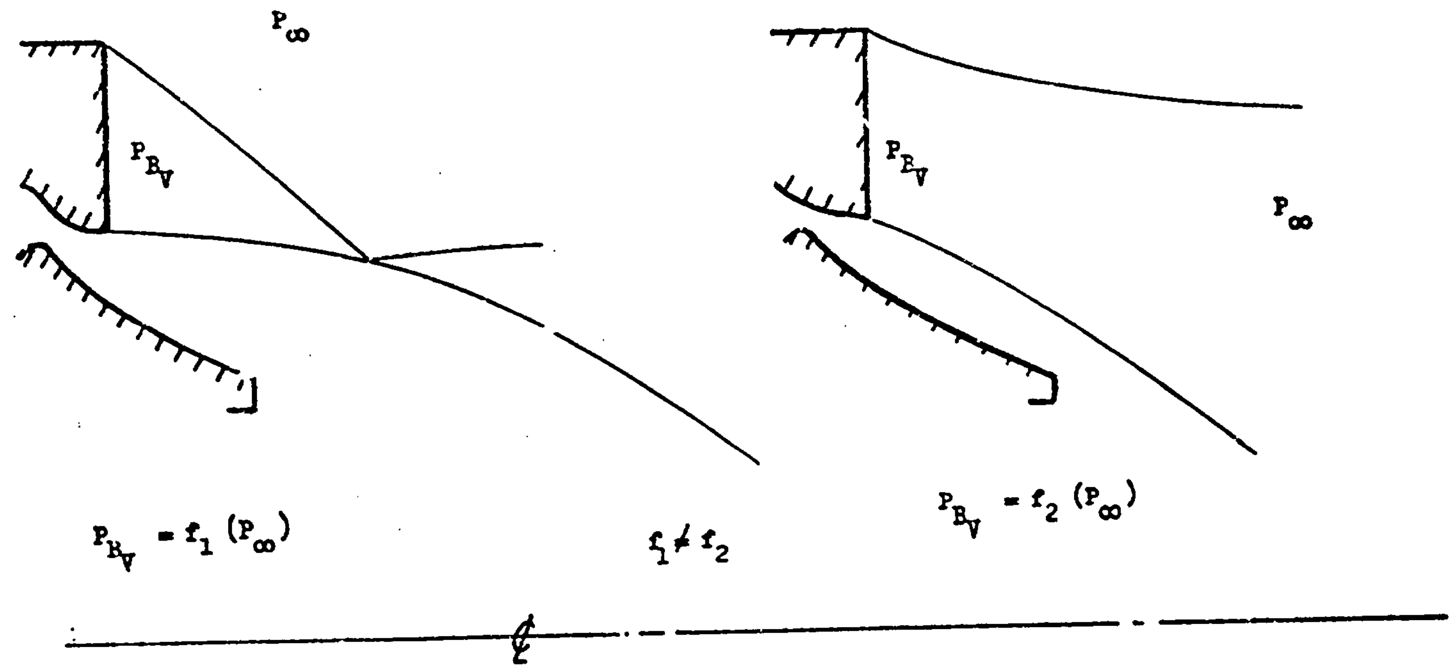

a. Closed-Missile Wake

b. Open-Missile Wake

Figure 133. Flow Regions for the Missile Base Flow

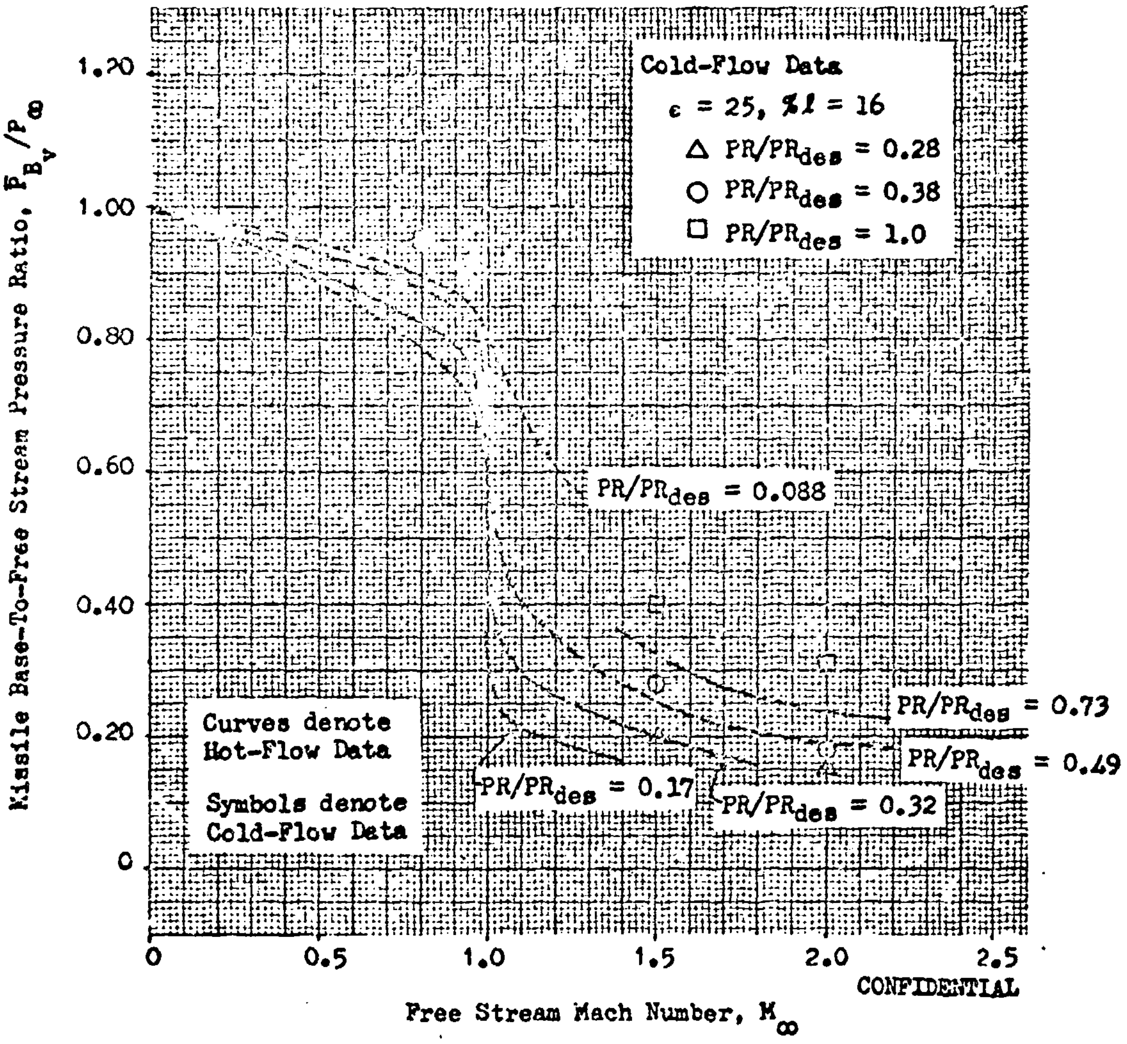

Figure 134. Effect of Free Stream Mach Number and Chamber Pressure Ratio on Missile Base-To-Ambient Pressure Ratio (Cross Plot From Fig. 41)

(C) Mach number is approximately the same in subsonic flow as in supersonic flow in both cases. A discontinuity occurs for sonic slipstream velocity. At this free stream velocity, a reversal in trend with chamber pressure ratio also occurs except at a chamber pressure ratio of 36 (PR/PR_{des} = 0.088) which is felt to be an "open wake" condition at the base of the missile with the hot-flow engine. The hot-flow missile base pressures fall below those obtained with the cold-flow configuration for subsonic free stream Mach numbers. This is apparently a consequence of slightly dissimilar gas properties, nozzle contours, and afterbody configurations between the hot- and cold-flow models.

(C) The open-wake nozzle performance trends in external flow (Fig.128, page 238) are attributable to the combined influence of the reduced missile base shown in Fig.134, and shock flow interaction effects. It was discussed previously that the relative influence of these effects could be distinguished by means of the normalized thrust coefficient, Φ (cf Eq. (7), page 441). If the effect of reduced missile base pressure predominates, this parameter reduces to the definition of nozzle efficiency, and the thrust coefficient data obtained in external flow correlates with that obtained in still air when plotted versus the "effective" chamber pressure ratio, P_c/P_B. When shock flow interaction occurs the normalized thrust coefficient is higher than that obtained in still air for corresponding values of P_c/P_B, because of higher nozzle base pressure under these conditions than would be expected on the basis of P_B alone. The shock interaction effect was defined earlier as an influence on performance caused by compression waves emanating from the outer free jet boundary downstream of the impingement point (point A in Fig. 96, page 193) which are turned inward as a result of strong flow interaction. These compression waves intersect the inner free jet boundary farther upstream than if the expansion were controlled only by the missile base pressure.

(C) Normalized thrust coefficient trends with the chamber-to-missile base pressure ratio, P_c/P_B, are shown in Fig.135. The normalized thrust coefficient is higher than that obtained in still air for M_∞ = 1.2 and 1.4 at effective pressure ratios of 350 and 410 respectively. For these two tests, the nozzle

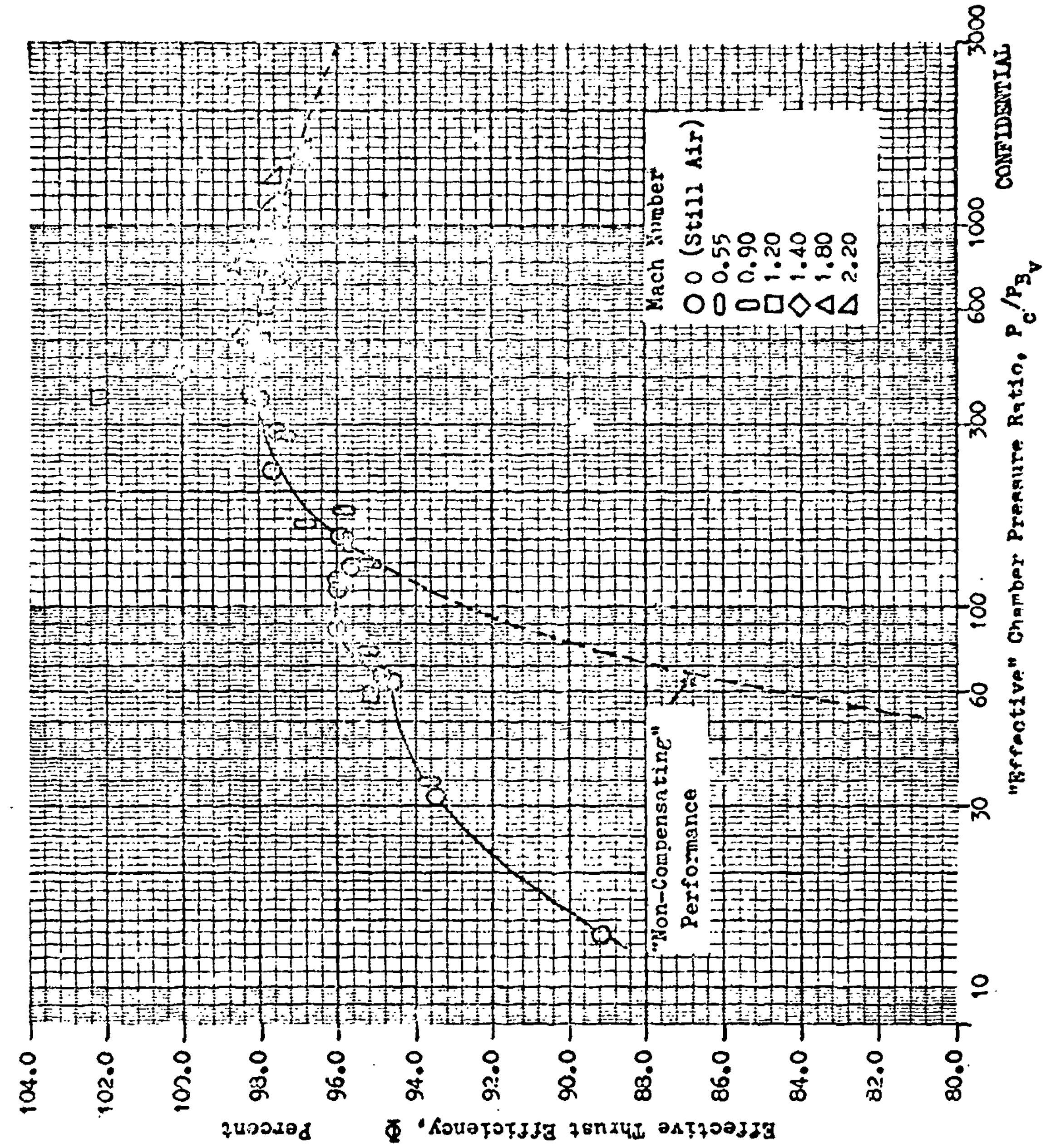

Figure 135. Effective Thrust Efficiency vs Chamber-To-Missile Base Pressure Ratio

base pressure was increased through relatively strong flow interaction at these effective pressure ratios as shown in Fig.136. The correlations in Figs.135 and136 indicate that the influence of reduced missile base pressure was the predominate effect in establishing nozzle performance and base pressure trends in Figs.128 and130 for all of the remaining hot-flow test conditions. The absence of flow interaction effects with subsonic external flow in the transition pressure ratio regime explains the discrepancy between hot- and cold-flow efficiency trends in this region. The correlating parameter, Φ, in Fig.135 can be used to obtain in-flight performance estimates by means of still air performance and known missile base pressure, but these estimates will be conservative because shock effects are neglected using this procedure.

(C) The results in Figs.134 and136 indicate that both missile base pressure and interaction effects are dependent on the physical and dynamic properties of the primary and slipstream flows, and on the missile and nozzle geometry. However, more work is needed to establish the relative influence of these parameters on missile base pressure and interaction effects. Once the nature of these effects is fully defined, a more detailed study of nozzle performance trends in external flow can be conducted. It is felt that, for the most part, these aspects can be evaluated theoretically.

APPLICATION OF TEST RESULTS

Mission Analysis

(C) The nozzle efficiency data discussed in the previous section is a combined function of Mach number and pressure ratio. Therefore, a typical booster trajectory must be examined to assess the overall effect on in-flight system performance. The correlations presented in Figs. 135 and 136 demonstrate that aerospike nozzle performance and base pressure trends in slipstream are identical to those in still air (except when slipstream

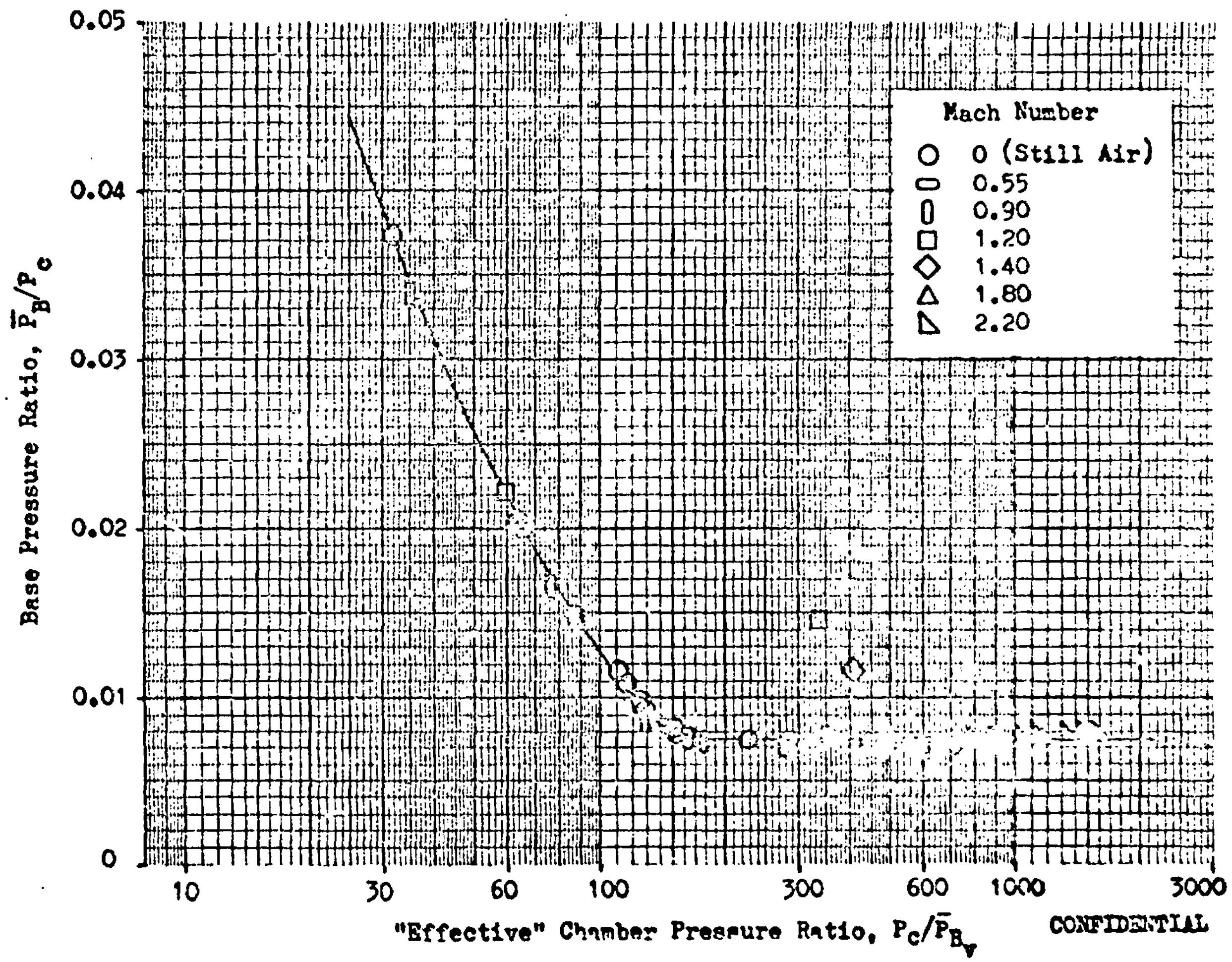

Figure 136. Engine Base-To-Chamber Pressure Ratio vs Effective Chamber Pressure Ratio

interaction occurs) if represented as a function of the local ambient pressure. (P_{B_v}) to the nozzle. Therefore, nozzle performance trends such as those in Fig. 128 can be established for any engine-vehicle configuration through knowledge of still air performance and missile base pressure as a function of altitude by means of the normalized thrust coefficient, Φ.

(C) For cases without interaction, nozzle performance based on the chamber-to-ambient pressure ratio, P_c/P_{oo} can be obtained by first determining P_c/P_{B_v}. Then, engine thrust is obtained from the still air performance curve for the nozzle in question through the normalized thrust coefficient, Φ, and the estimated value of P_c/P_{B_v} as follows:

$$F)_{\frac{P_c}{P_{B_v}}} = (F_{id_p} + F_{id_s})_{\frac{P_c}{P_{B_v}}} \; \Phi$$

(C) The thrust corresponding to the true ambient pressure, P_{oo}, is then obtained from:

$$F)_{\frac{P_c}{P_{oo}}} = F)_{\frac{P_c}{P_{B_v}}} - A_e \, (P_{oo} - P_{B_v})$$

where A_e is the nozzle exit area. Performance corresponding to P_{oo} is given by:

$$C_{T_{oo}} = \frac{F)_{P_c/P_{oo}}}{(F_{id_p} + F_{id_s})_{P_c/P_{oo}}}$$

(C) For isoenergetic primary and secondary flows with equal specific heat ratios, this procedure can be abbreviated as follows:

$$C_{T_{oo}} = \frac{(\Phi \, C_{F_{opt}})_{P_c/P_{B_v}} - \frac{\epsilon}{PR_{oo}} \left(1 - \frac{P_{B_v}}{P_{oo}}\right)}{(C_{F_{opt}})_{P_c/P_{oo}}} \qquad (2)$$

(C) As indicated by the results of this hot-flow program, the occurrence of external flow interaction effects are difficult to predict without detailed study of flow processes involved in each case. However, conservative estimates of nozzle efficiency in external flow can be obtained simply by ignoring interaction effects (both the hot-flow and cold-flow data indicate that these effects are beneficial to performance).

(C) In order to obtain a "worst case" estimate for the magnitude of external flow influence over a typical booster mission, it was assumed that the still air expansion characteristics in Fig.118 (in percent of design pressure ratio), and missile base pressure trends in Fig.134 were representative of an LO_2/LH_2 aerospike engine with area ratio of 80 and chamber pressure of 1500 psia. Interaction effects were assumed to be negligible. The assumed trajectory corresponds to Case II in Fig.101, page 201 (two-stage vehicle), which is reproduced in Fig.137. In order to facilitate performance computations, the nozzle efficiency in slipstream was normalized in terms of the still air nozzle performance, and plotted versus the free stream Mach numbers for various values of the percent of the nozzle design pressure ratio as shown in Fig.138. The interpolation at subsonic Mach numbers was accomplished by using the data in Fig. 134 in conjunction with eq (2). These performance estimates are somewhat conservative, because in-flight missile base pressure can probably be made higher than indicated in Fig.134 as discussed in a later section.

(C) Application of the generalized efficiency data in Fig.138 leads to an in-flight specific impulse variation as shown in Fig.139. It can be seen that slipstream effects are influential only during approximately 15 percent of the total trajectory time. The overall slipstream effect is to decrease the time-integrated specific impulse by 0.17 percent.

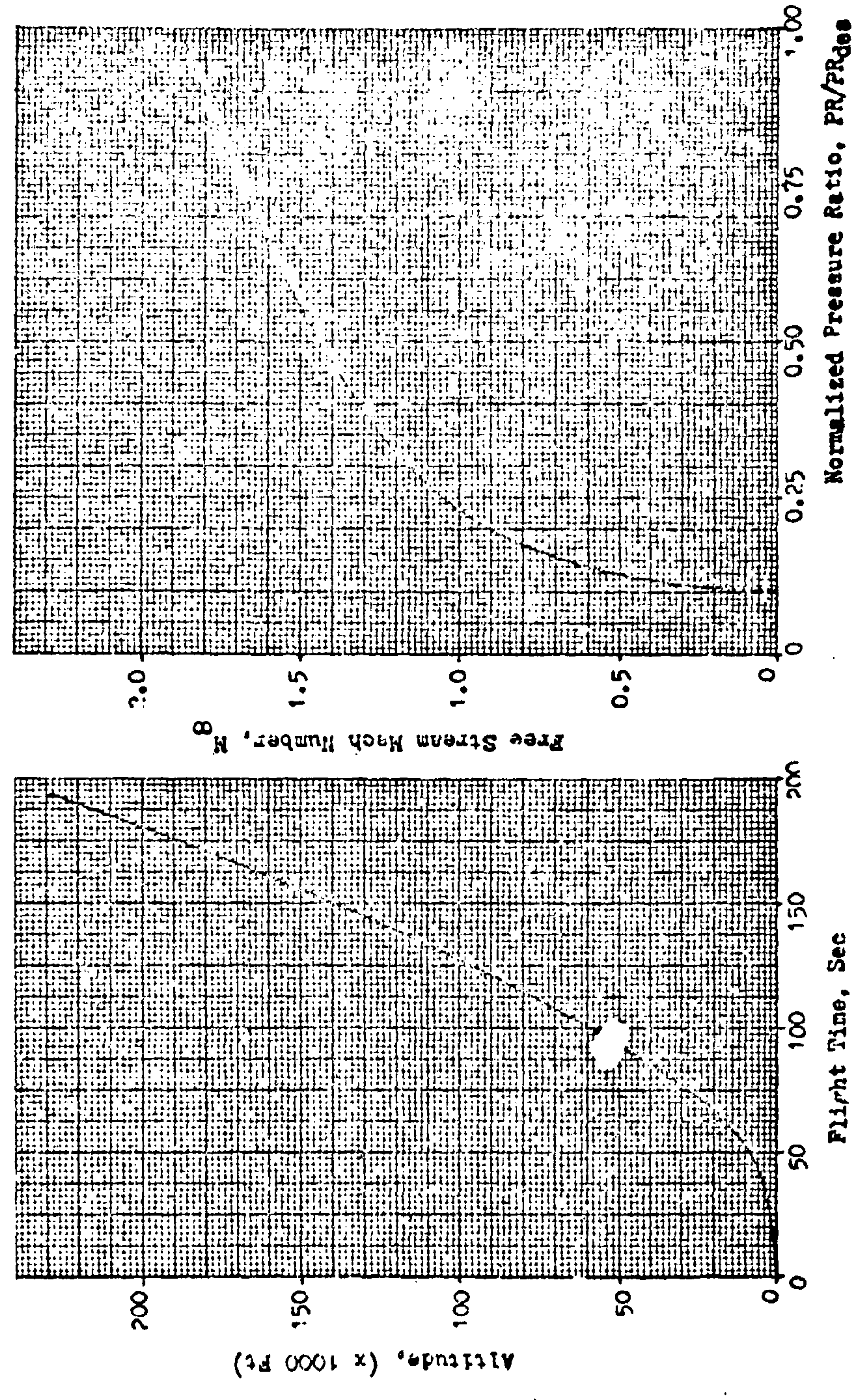

Figure 137. Trajectory Data Used in Mission Analysis

CONFIDENTIAL

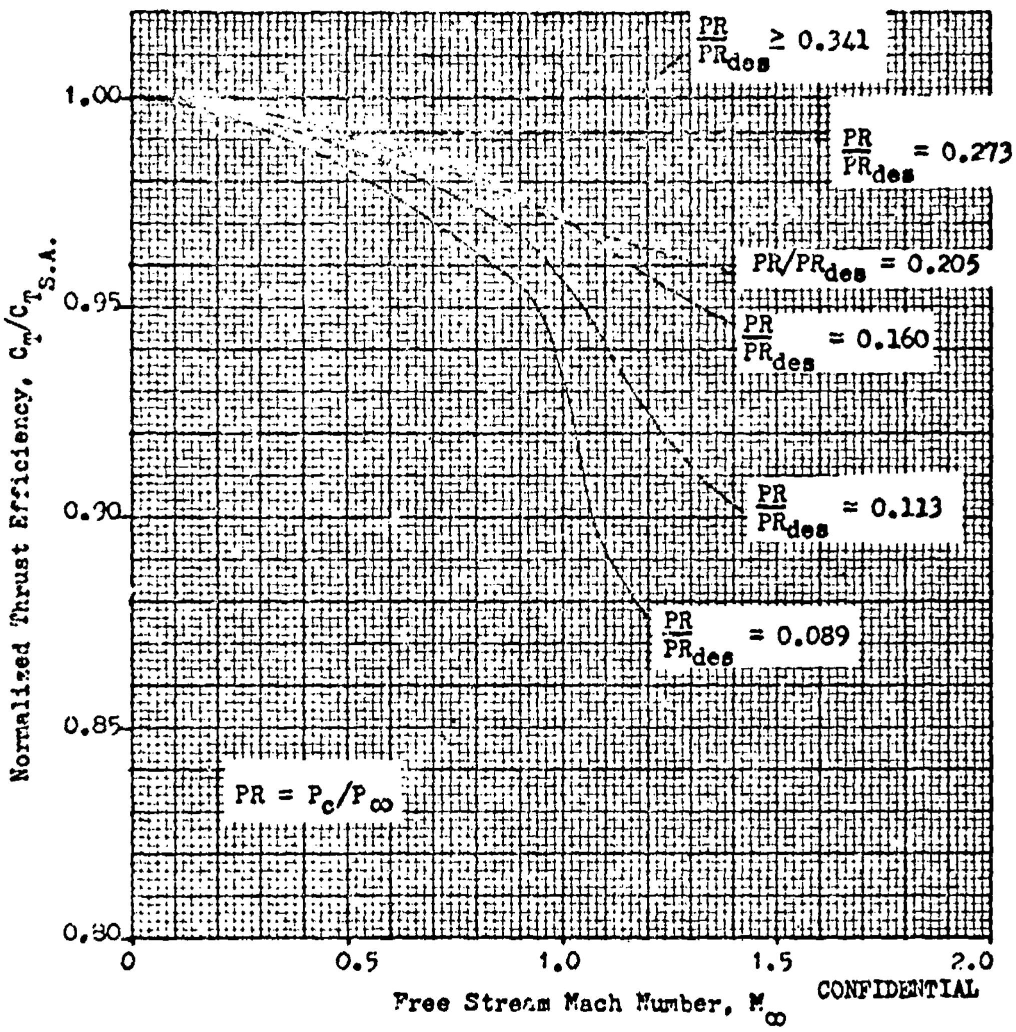

Figure 138. Normalized Performance Data For Mission Analysis

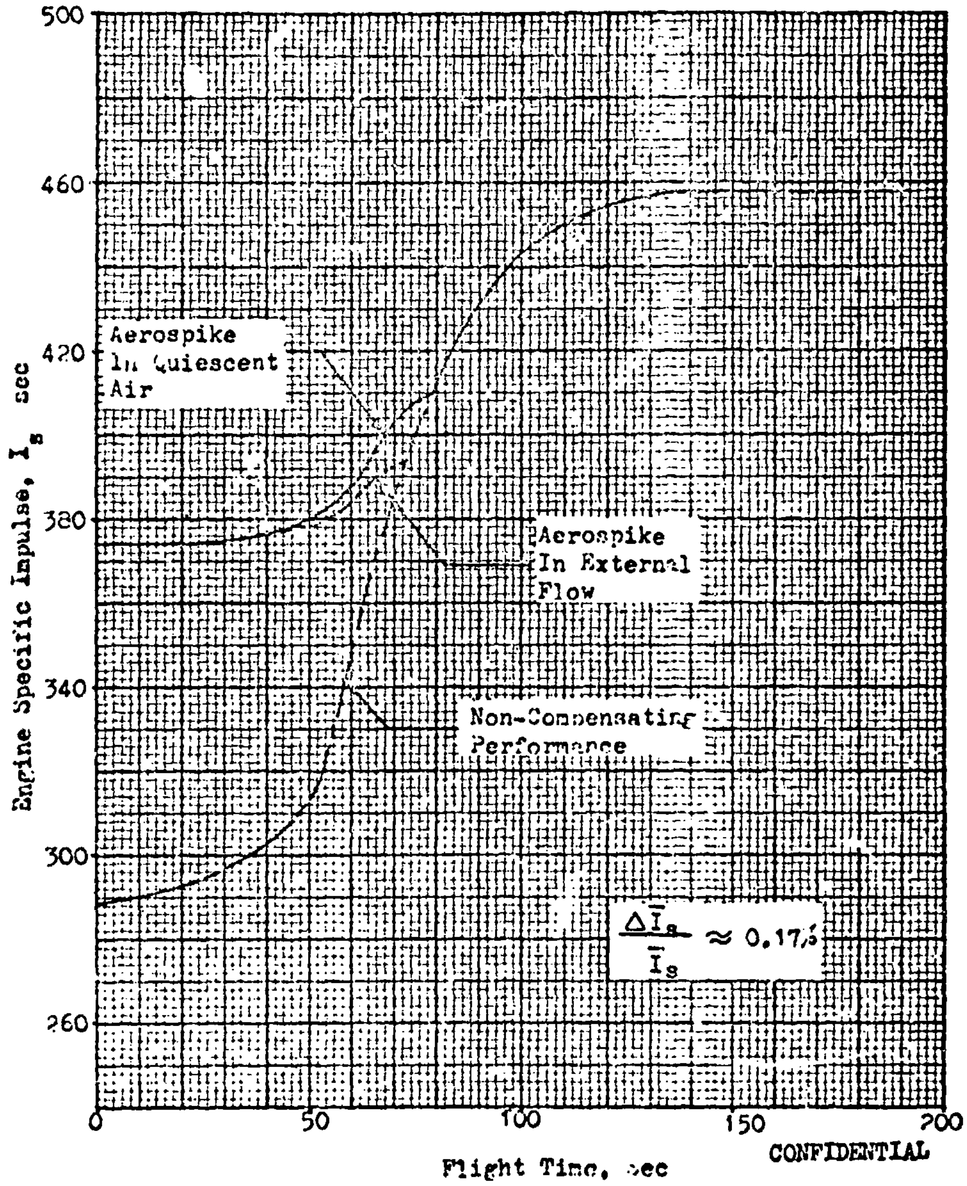

Figure 139. In-Flight Specific Impulse With and Without External Flow

Methods of Reducing Slipstream Effects

(C) The hot- and cold-flow data discussed herein have shown that the presence of an external flow can influence aerospike nozzle performance in two ways; both are closely coupled with the gas properties and expansion characteristics of the nozzle. The first effect of slipstream results from a decrease in vehicle base pressure with increasing free stream Mach number which causes the nozzle exhaust flow to expand through higher pressure ratios than in still air. Secondly, nozzle performance is affected when strong shock interaction between slipstream and nozzle flows is such that some of the recompression waves emanating from the outer free jet boundary strike the inner free jet boundary farther upstream than for the case where the missile base pressure is the sole factor governing the nozzle expansion process.

(C) The increased expansion caused by low missile base pressures results in low nozzle base pressure relative to that obtained in still air with an attendant reduction in performance at low pressure ratios. This is caused by increased turning of the outer free jet boundary of the aerospike thereby reducing the effectiveness of recompression waves in the nozzle flow as illustrated in Fig. 95, page 192. Thus, one way of increasing in-flight nozzle performance at low altitudes is to increase the pressure acting along the outer free jet boundary which controls the expansion process. Missile base pressures approaching ambient pressure result in negligible slipstream effects. Past study has shown that the most effective means of obtaining high missile base pressure is through proper design of the missile base geometry and/or through mass addition into the base wake flow. Afterbody configurations found to result in relatively high afterbody thrust through previous investigation (e. g. Ref. 22 and illustrated in Fig. 140. Missile base pressures obtained from the circular arc boat-tail configuration (Fig. 140b) are shown in Fig. 141 compared to that

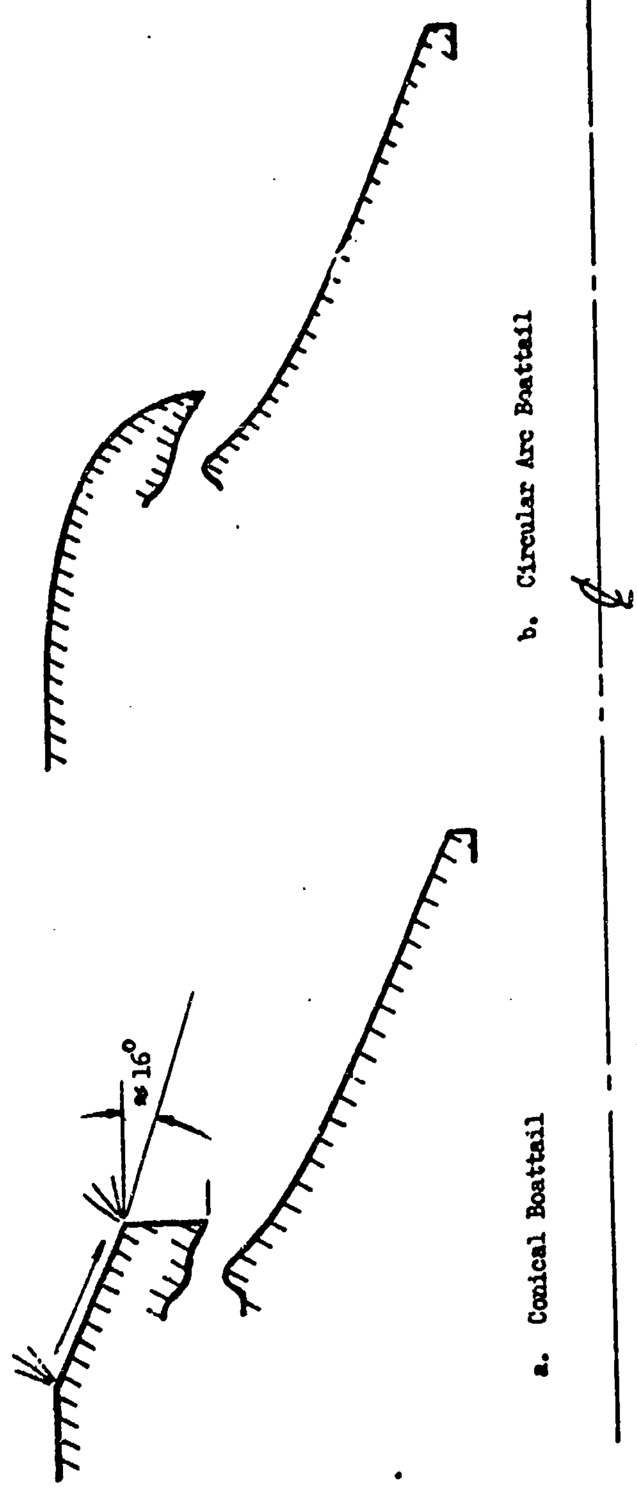

Figure 140. Boattail Geometry Producing High Missile-Base Pressure

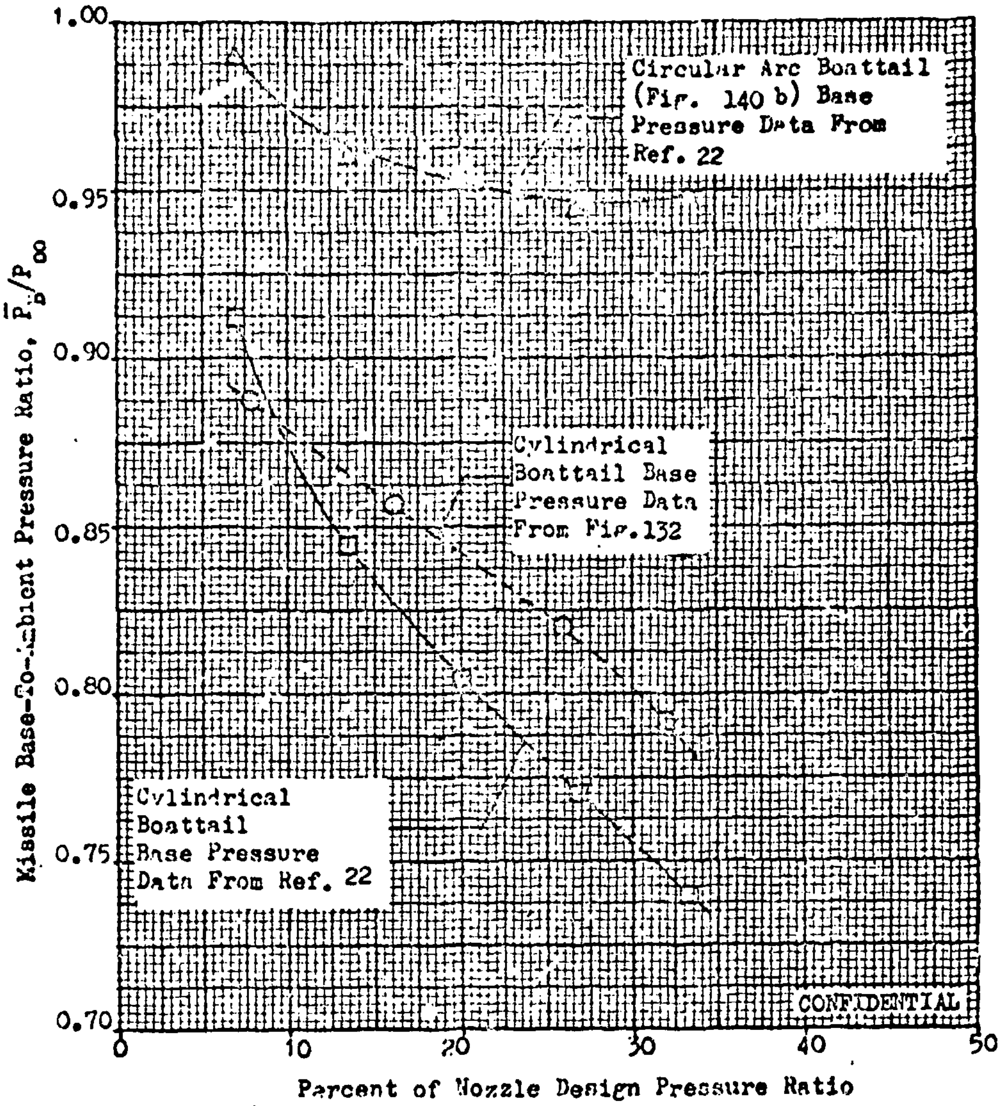

Figure 141. Effect of Afterbody Geometry on Missile Base Pressure at High Subsonic Mach Numbers ($M_\infty = 0.9$)

obtained from a simple cylindrical boat-tail similar to that tested in this program. It can be seen that substantial increases in missile base pressure are possible through proper afterbody design. The effect of mass addition into the wake flow downstream of a rearward facing step is illustrated schematically in Fig. 142, and is discussed in Ref. 23. As shown in Fig. 142 the base pressure increases markedly through the addition of a small amount of bleed flow.

(C) Results obtained to date have shown that when flow interaction does change the intrinsic operation of the nozzle, the overall effect is an increase in base pressure over that obtained without flow interaction as shown in Fig. 136. To show the nature of interaction effects, the average curve through the missile base pressure data in Fig. 132, page 243, is shown along with nozzle base pressure data from Fig. 136, page 249, in Fig. 143. The nozzle base pressure tends to follow changes in the free stream static pressure in the "open-wake regime just as in still air (also shown by the data in Fig. 130). In slipstream, communication between the nozzle flow field and free stream conditions is achieved directly through the missile base pressure as shown by the majority of this data, and through flow interaction (M_∞ = 1.2, 1.4) at chamber-to-missile base pressure ratios of 300 and 410, respectively. However, only the portion of the outer free jet boundary of the nozzle downstream of the point of flow impingement (point A in Fig. 95, page 192) is influenced by P_∞ in the latter case. Therefore, the base pressure increase is not as pronounced as it is for the corresponding case in still air.

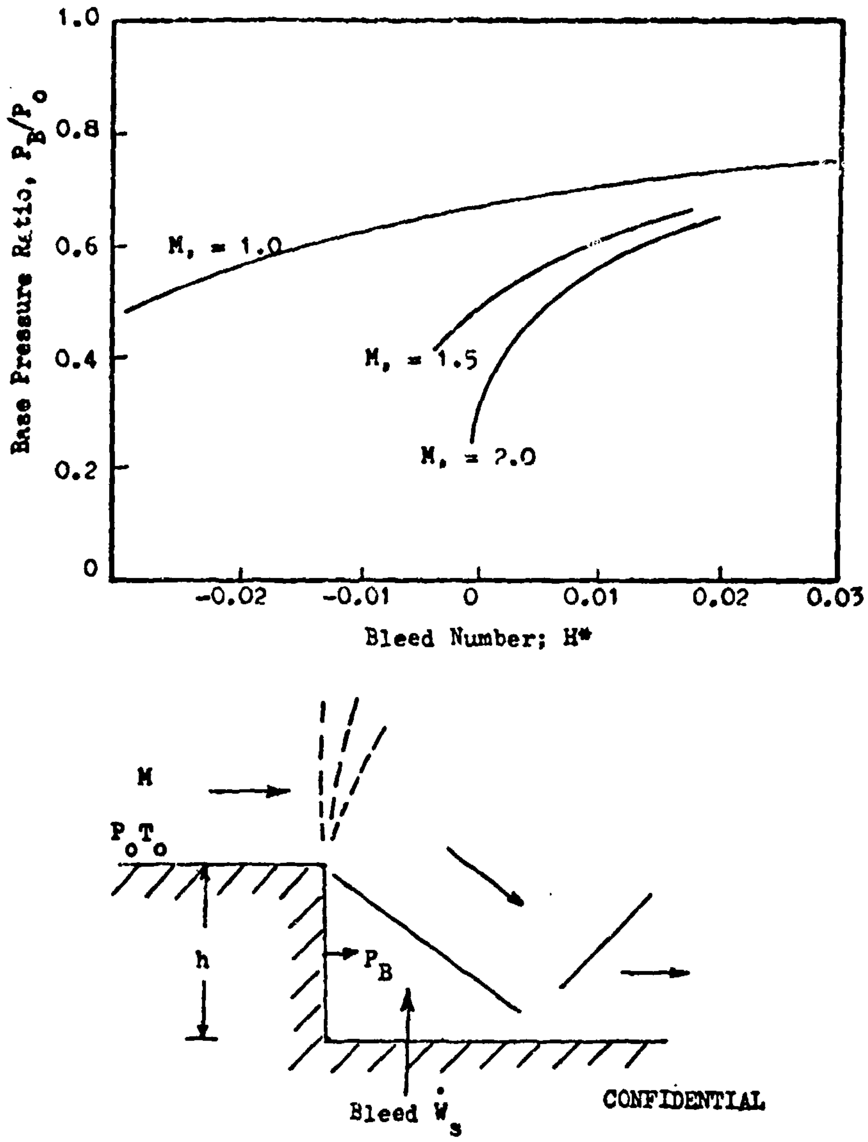

$$^*H = \Gamma \sqrt{\frac{RT_o}{g\gamma}}$$

where Γ = mass bleed flow per unit area

Figure 142. Effect of Bleed on Base Pressures in Two-Dimensional Flow Over a Back Step.

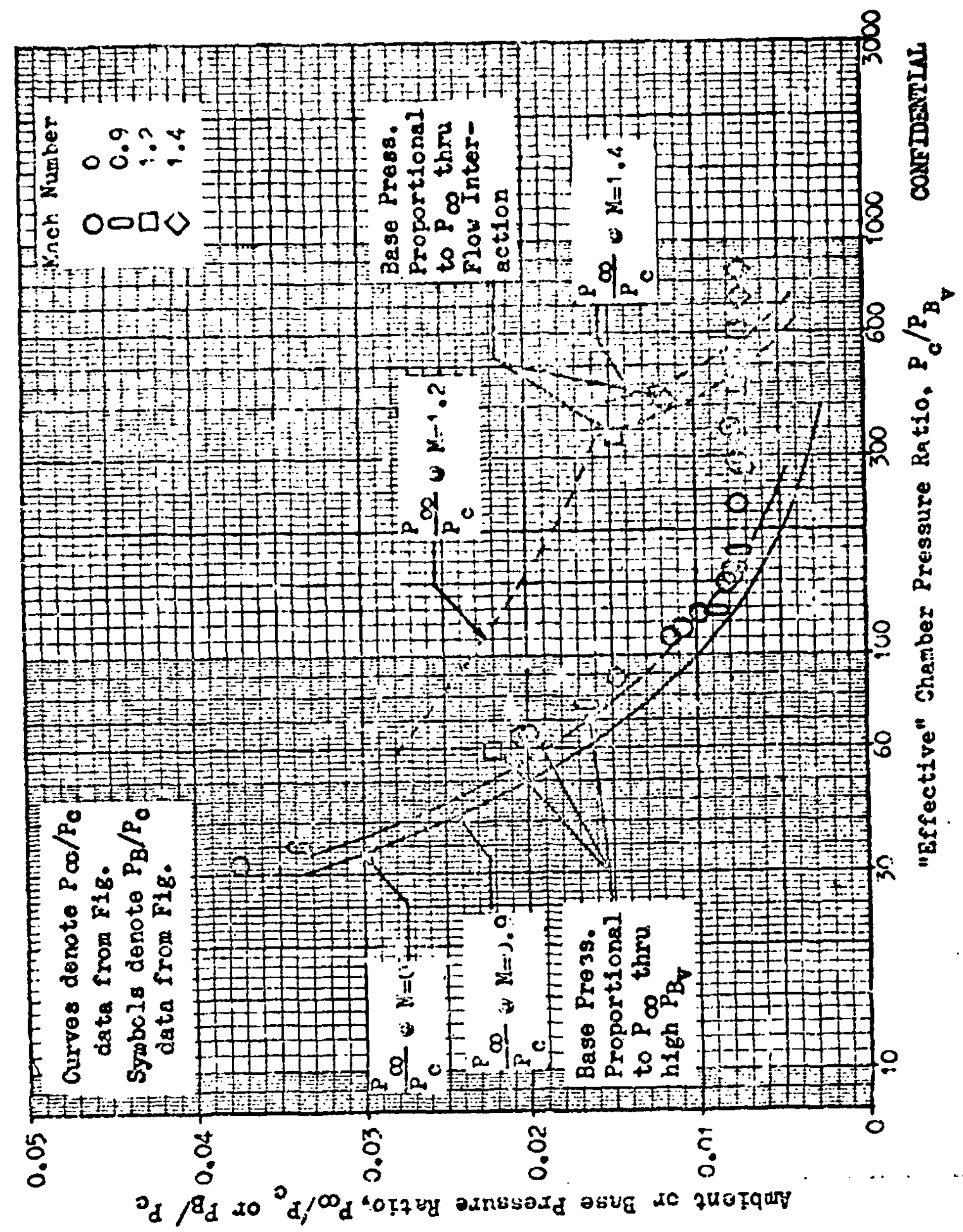

Figure 143 . Influence of Flow Interaction on Base Pressure

(C) Reducing the portion of the nozzle free jet boundary exposed to the relatively low missile base pressure as shown in Fig. 144 b will alleviate this situation. Altering the afterbody design in this manner will allow the free stream static pressure to act over nearly the entire free jet boundary, and nozzle base pressure will recover to this pressure rather than the missile base pressure, just as in still air. Consequently, nozzle performance in slipstream will be similar to that in still air. Actually, if compression waves in the nozzle flow are turned inward by the interaction process as illustrated in Fig.96 , performance obtained in external flow may be slightly higher than that obtained in still air at low pressure ratios. This apparently was the case in the cold-flow program where relatively high missile base pressures combined with flow interaction resulted in an increase in efficiency with subsonic external flow. Since the missile base pressure is no longer the predominate influence for small base areas, the correlation presented in Figs.135 and 136will not represent a true indication of the expansion process. Of course, this afterbody design will also be beneficial to vehicle base drag characteristics, since the area subjected to sub-ambient pressure is minimized.

A recent paper (Ref.24) presented results of an experimental study of the performance of low angle plug nozzle performance in slipstream. The same interaction effects discussed herein were observed and the use of a slender base lip improved performance considerably.

CONCLUSIONS AND RECOMMENDATIONS

(C) Analysis of the data presented herein leads to several conclusions regarding aerospike performance in still air and with external flow. These are the following:

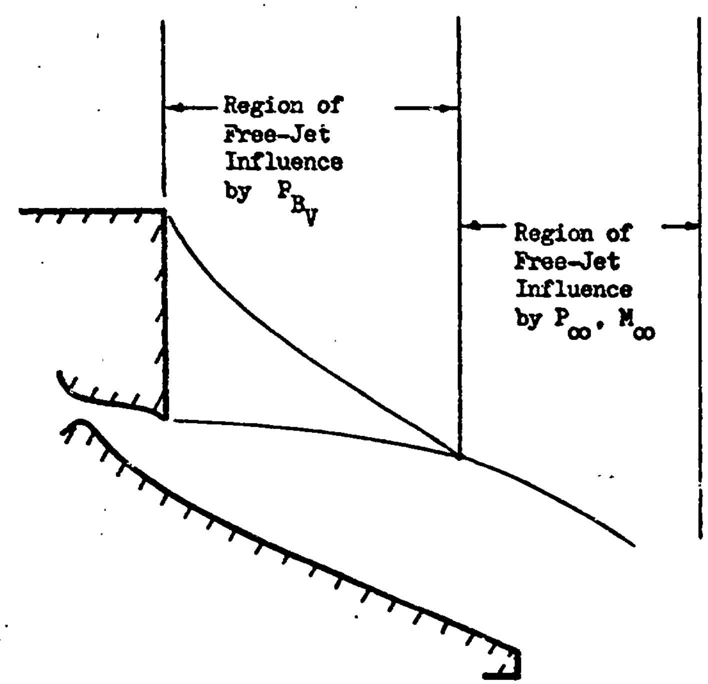

a. Large-Missile Base Area

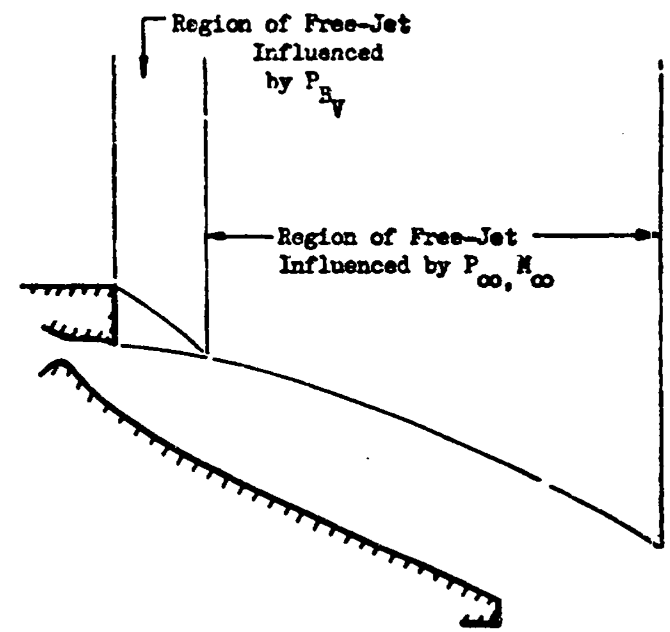

b. Small-Missile Base Area

Figure 144. Qualitative Influence Regions of External Ambient Pressures

1) Still air performance of a properly designed aerospike thrust chamber is approximately 98 percent of ideal at design pressure ratio under the conditions tested in this program. Altitude compensation is obtained at all pressure ratios.
   a) The addition of secondary flow is beneficial to performance at all pressure ratios. Optimum secondary flow is between 0.8 and 1.7 percent of the primary flow for the conditions tested.
   b) Excellent agreement between predicted and experimental performance was obtained for all pressure ratios greater than 32.

2) Aerospike performance is unaffected by external flow in the closed wake pressure ratio region. In the open wake region, performance and base pressure of configurations similar to that tested in this program decrease at a rate which is Mach number and pressure ratio dependent. Similar results are obtained through cold-flow testing except when flow interaction influences performance.
   a) For cases without flow interaction, both hot- and cold-flow nozzle performance and base pressure data tend to correlate with the chamber-to-missile base pressure ratio. This indicates that the missile base pressure, in most cases, controls the nozzle expansion and can be used to form the basis for conservative in-flight performance estimates.
   b) Hot- and cold-flow missile base pressure and interaction effects differ indicating an influence of nozzle gas properties on slipstream effects.

3) External flow effects integrated over a typical mission are small and can be further reduced by proper afterbody design.
   a) Conservative performance estimates based on the missile base pressure data presented herein indicate that time integrated specific impulse $(\bar{I}_s)$ is reduced by 0.17 percent because of the influence of external flow.
   b) Missile base pressure can be increased substantially through boat-tailing (Fig. 141) and/or mass addition to the base wake (Fig. 142) thereby increasing performance in external flow.
   c) Communication with free stream static pressure can be induced at all altitudes by causing flow interaction for all conditions through minimization of vehicle base area. Nozzle performance under these conditions will be similar to that obtained in still air at low pressure ratios.

(C) Based on these results, it can be seen that external flow effects are small even under severe conditions, and can be reduced still further by proper afterbody design. Further analytical studies can be conducted to theoretically determine missile base pressure trends with the following: primary nozzle geometry, gas properties and flow conditions of the primary flowfield, missile afterbody geometry, and external flow conditions. These studies should also attempt to establish the nature of external and nozzle flow interaction effects, and the conditions under which these effects influence performance. The results of these studies should be used to devise methods of reducing adverse slipstream effects incurred because of sub-ambient missile base pressure, and to quantitati[illegible]mine various means of using flow interaction effects to advantage. En[illegible]ental testing should be conducted to verify the results of the analytical study.

SECTION V

AEROSPIKE LIQUID INJECTION THRUST VECTOR CONTROL INVESTIGATION

INTRODUCTION

(U) Recent advances in rocket engine technology have resulted in a need for increased study of means for providing directional thrust control for future generation rocket vehicles. Secondary injection of fluids into the engine exhaust streams has proven to be an effective and efficient method of thrust vector control (TVC) in several present applications; and cold-flow testing, complemented by analytical engine system studies, has shown that this is also a competitive TVC technique for advanced aerospike engines. One of the objective of the Advanced Aerodynamic Spike Configurations Program (AF04(611)-9948) was to supplement current aerospike TVC technology by providing sufficient hot-flow liquid injection thrust vector control (LITVC) test data to establish design criteria and enable quantitative performance evaluations for future high-thrust aerospike engines.

(C) A test program was formulated so that this TVC technique could be studied using a modified version of the storable propellant (N_2O_4/UDMH-N_2H_4,50-50) aerospike thrust chamber tested previously in this program. Chamber pressure selected for the TVC testing was 200 psia with an attendant thrust level of approximately 5600 pounds at vacuum. Area ratio of the aerospike nozzle was 25:1, and the axial length was 25 percent of the axial length of a 15-degree conical nozzle with equivalent area ratio. Injection of the TVC flow was effected through orifices located in uncooled contoured flow rings which comprised the aft section of the nozzle. Testing was conducted in an altitude facility at Arnold Engineering Development Center (AEDC), J2 cell. A typical test configuration is illustrated along with the flow field accompanying liquid N_2O_4 injection into aerospike mainstream gases in Fig.145 . The previous SITVC analytical and test results leading to the selection of test configurations are described in the following sections, along with the TVC performance trends that were established through this testing.

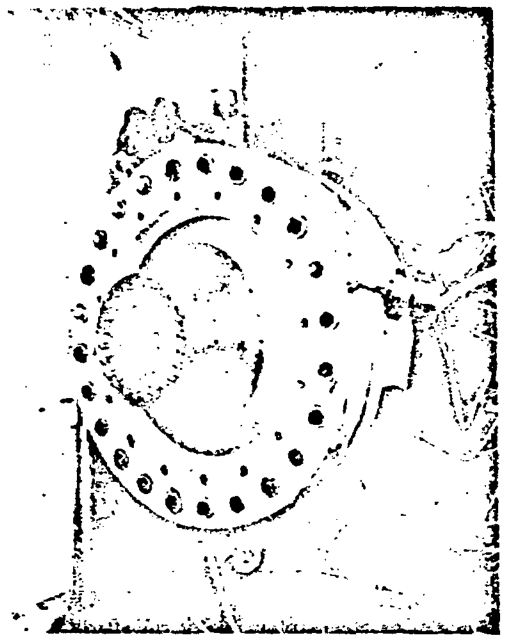

a. Sea Level Checkout Installation

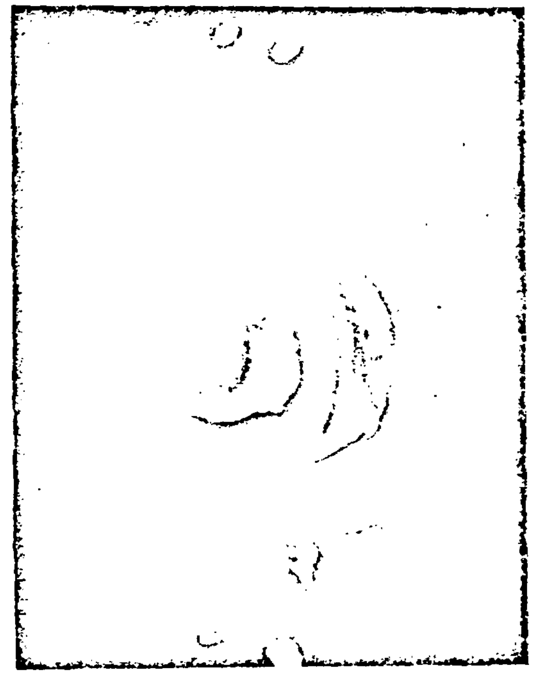

b. AEDC Altitude Firing

Figure 145. Aerospike TVC Engine. Rocketdyne Installation and Firing at AEDC

SUMMARY

(U) Thirty-three firings of 6 second's duration were conducted at altitude to establish engine performance without TVC, and to determine LITVC performance trends with variations in the injection parameters. Five sea level check-out tests of from 1/2 to 5 second's durations were conducted at Rocketdyne prior to the altitude testing. Measured thrust efficiency of the engine was 95.1 percent for $\dot{W}_s/\dot{W}_p = 0$ and 95.2 percent for $\dot{W}_s/\dot{W}_p = 0.017$. Combustion efficiency (η_{C*}) was nominally 89 percent throughout the program. The measured nozzle thrust efficiency without secondary flow was 0.8 percent greater than that estimated theoretically. Because of its magnitude, this discrepancy was attributed to effects such as downstream burning which may result from the relatively low combustion efficiency, and which cannot be accounted for theoretically.

(C) The semi-empirical blast-wave theory of Ref. 1 was utilized in conjunction with experimental data from various sources to provide a basis for selection of SITVC test configurations. Testing of these configurations established that measured LITVC side-force efficiency trends with an aerospike are similar to those expected on the basis of preliminary analysis: injection near the throat provides higher side-force efficiency than injection near the nozzle exit, multiple-port injectors are superior to single-port designs, port spacing and axial port inclination have no influence on LITVC performance in the range tested near the nozzle exit, and parallel stream injection affords higher performance than radial stream injection at both locations studied. Control moment and nozzle specific impulse efficiency trends were found to be dependent upon the engine-vehicle geometric relationship. These efficiencies followed trends established by the side-force efficiency for boost vehicles ($r_e/h = 0.25$), but in some cases optimized differently for upper-stage configurations ($r_e/h = 1.0$).

(C) Comparison of the side-thrust efficiency TVC data obtained in this program with that obtained from other nozzles revealed that LITVC performance with an aerospike is equal to or less than with other nozzles, because of the relatively short length of the aerospike. The level of side thrust efficiency for N_2O_4 injection established through this testing was also found to be lower than that estimated using the blast wave analysis in conjunction with an empirical coefficient obtained for gas injection into flow over a flat plate. It was necessary to revise this coefficient to obtain quantitative agreement between theory and experiment for the configuration tested. Application of the test data to full-scale engine systems showed that liquid injection may be competitive with gas injection under certain conditions. In general, fuel injection provides higher in-flight engine specific impulse efficiency but lower density impulse than oxidizer injection if vaporization and reaction do not occur within the nozzle.

(C) On the basis of these results, it is recommended that the relative merits of liquid injection TVC be investigated through comparative systems analysis using the conservative performance estimates presented herein for full-scale engines. It is also recommended that improved LITVC designs such as a bipropellant injection technique be studied, and that the performance and operating characteristics of attractive systems be evaluated through large-scale environmental hot-flow testing.

THRUST VECTOR CONTROL STUDY PROGRAM

Preliminary Analysis and Design Studies

(C) The design of the engine utilized for the TVC testing was basically identical to that of the 12-percent length engine tested previously in this program. Modification to the previous test hardware consisted of: an increase in

length from 12 to 25 percent of the length of an equivalent area ratio ($\epsilon = 25$) 15-degree conical nozzle to accommodate the liquid injection orifices in uncooled nozzle extensions, and use of a porous base plate flush with the base exit plane for injection of secondary bleed flow. The engine was operated with N_2O_4/UDMH-N_2H_4,(50-50) propellants at a mixture ratio of 2.0 and with a chamber pressure of 200 psia. Under these conditions vacuum thrust of the engine was approximately 5600 pounds. The nozzle contour is shown in Fig. 146.

(C) This modified engine was analyzed for constant γ expansion using the axially symmetric method of characteristics to describe the inviscid portion of the primary flow field from which the intrinsic primary thrust is determined, a boundary layer analysis to establish thrust corrections for viscosity effects, and a Bray analysis to determine thrust corrections for reaction kinetics. The total primary thrust coefficient, C_{F_p}, is derived from the summation of these contributions by the expression (Refer to Nomenclature):

$$C_{F_p} = \frac{F_p}{P_c A_p^*} = C_{F_{int}} - \Delta C_{F_D} - (1 - \eta_K)\, C_{F_{id_v}}$$

where $C_{F_{id_v}}$ is the full shifting one-dimensional ideal thrust coefficient at vacuum for $\epsilon = 25$. The performance contributions from these analyses for a thrust chamber mixture ratio of 2.0 are as follows:

$C_{F_{int}}$ = 1.7364

ΔC_{F_D} = 0.0245

η_K = 0.9749

$C_{F_{id_v}}$ = 1.887

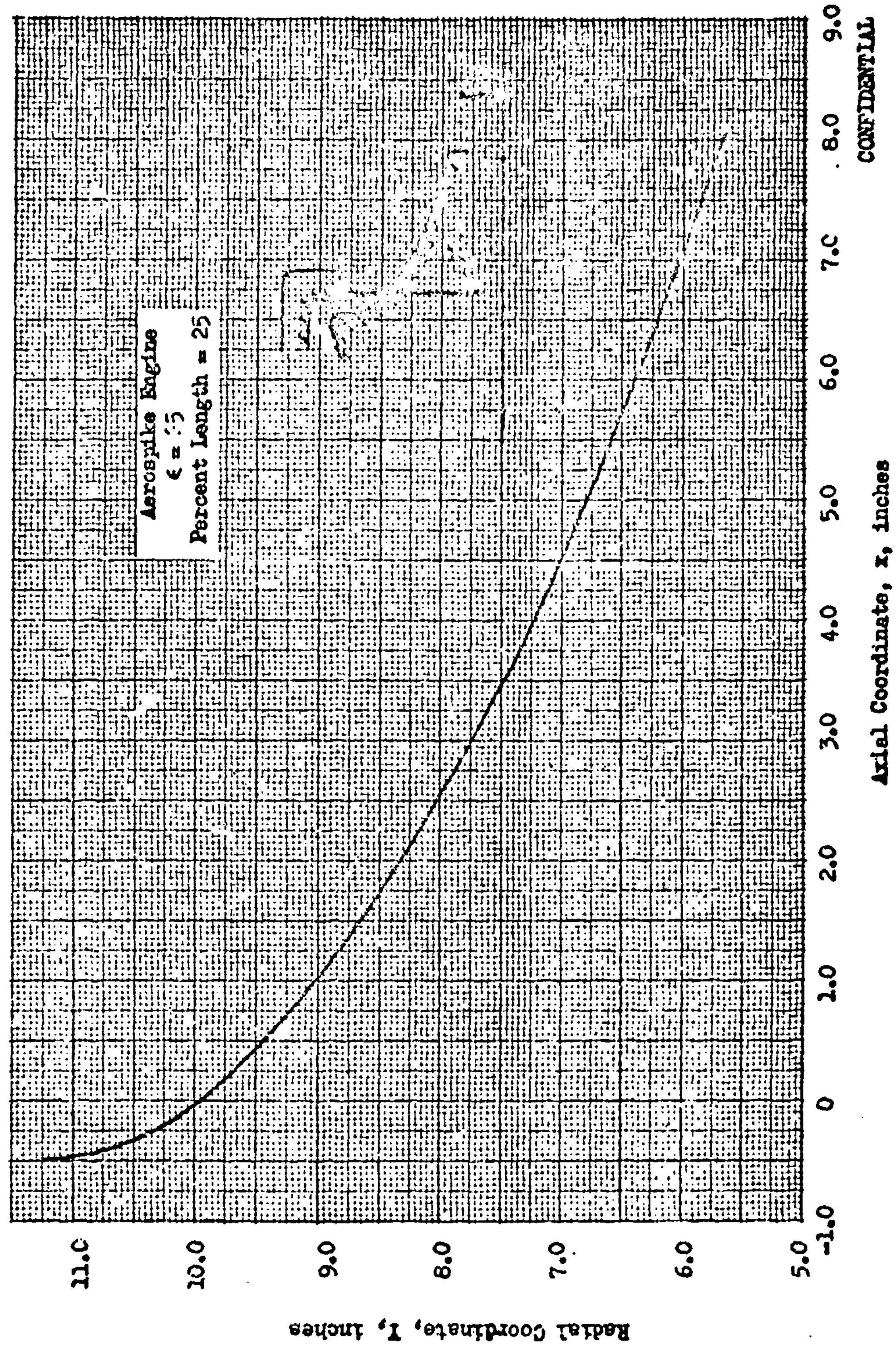

Figure 146. Nozzle Inner Contour Design

(U) The nozzle base pressure, $\bar{P}_B$, was obtained by means of the semiempirical techniques outlined in Ref. 2 and utilized to obtain a base thrust coefficient through the relation:

$$C_{F_B} = \frac{F_B}{P_c A_p^*} = \frac{P_B}{P_c} \frac{A_B}{A_p^*} = \frac{P_B}{P_c} \epsilon_B$$

(U) Thus, the nozzle thrust coefficient at any pressure ratio is given by:

$$C_F = C_{F_p} + C_{F_B} - \epsilon/PR$$

and the nozzle specific impulse and thrust efficiency are obtained from Eq. (1) and (2) below.

$$\eta_{I_s} = \left.\frac{\eta_{C_p^*} \; C_F}{C_{F_{opt_p}} \left(1 + \frac{I_{s_{opt_s}}}{I_{s_{opt_p}}} \frac{\dot{W}_s}{\dot{W}_p}\right)}\right|_{P_c/P_a} \qquad (1)$$

$$C_T = \left.\frac{C_F}{C_{F_{opt_p}} \left(1 + \frac{\eta_{C_s^*}}{\eta_{C_p^*}} \frac{I_{s_{opt_s}}}{I_{s_{opt_p}}} \frac{\dot{W}_s}{\dot{W}_p}\right)}\right|_{P_c/P_a} \qquad (2)$$

(C) The variation in kinetic efficiency with engine mixture ratio is shown in Fig.147 for 12- and 25-precent length nozzles with chamber pressure of 200 psia. A theoretical wall pressure profile for vacuum expansion is shown in Fig.148. The base pressure trend with secondary flowrate was estimated using the empirical design procedure discussed in Ref. 2 , and is shown in Fig.149. These data were used in conjunction with the theoretical primary nozzle thrust contribution to develop semiempirical nozzle performance estimates as a function of secondary flowrate. These estimates are shown in Fig. 150. Values used for $\eta_{C_p^*}$ and $\eta_{C_s^*}$ were 0.89 and 0.60, respectively, on the basis of previous testing. Reference performance data were obtained both with and without secondary flow. Reference data for the TVC testing were obtained with a nominal secondary flowrate which was 1.6 percent of the primary flowrate. As shown in Fig.150a, this corresponds to the peak value of nozzle thrust efficiency, C_T.

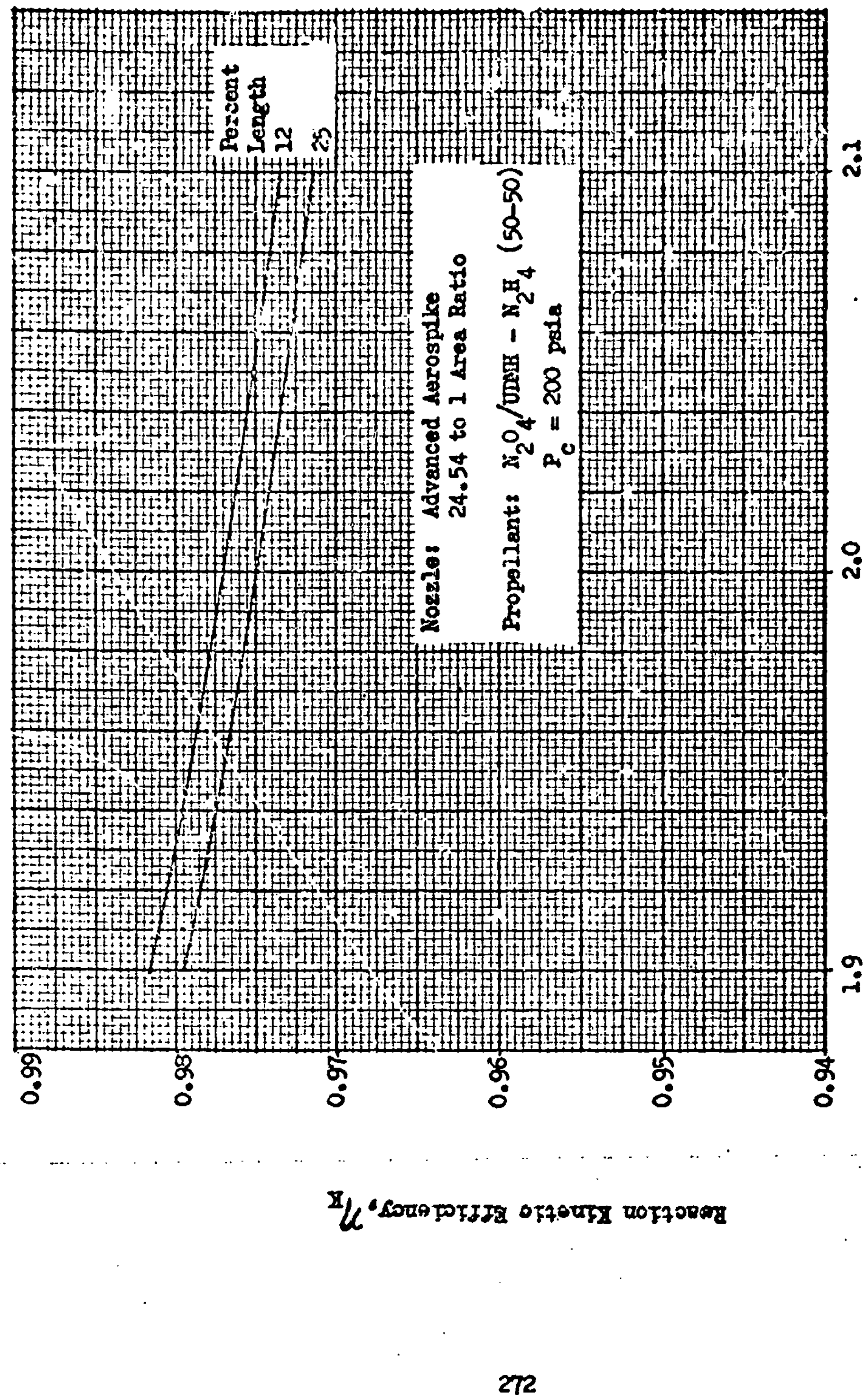

CONFIDENTIAL

Figure 147. Kinetic Efficiency Dependence on Axial Length and Thrust Chamber Mixture Ratio

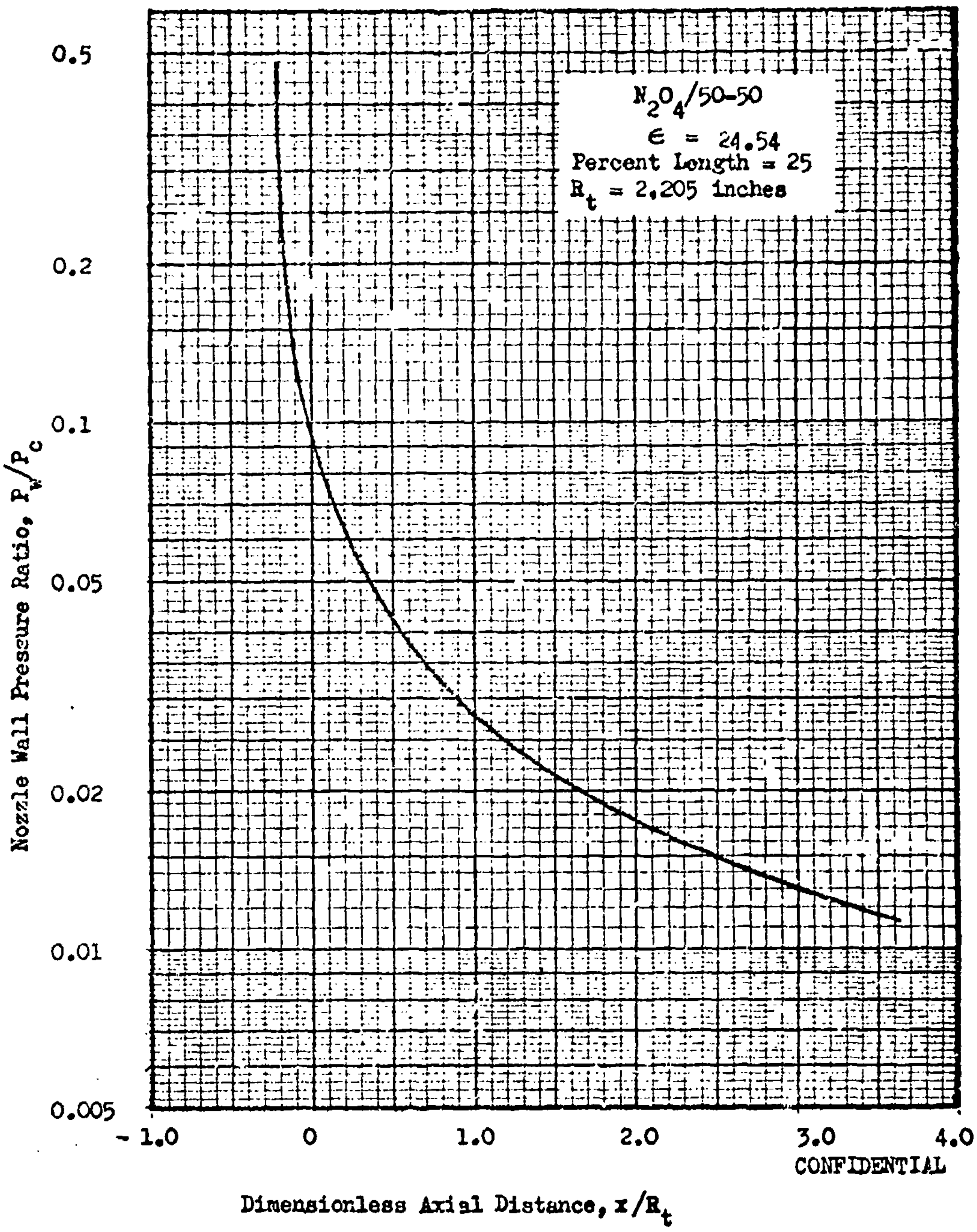

Figure 148. Theoretical Wall Pressure Distribution for Aerospike Engine

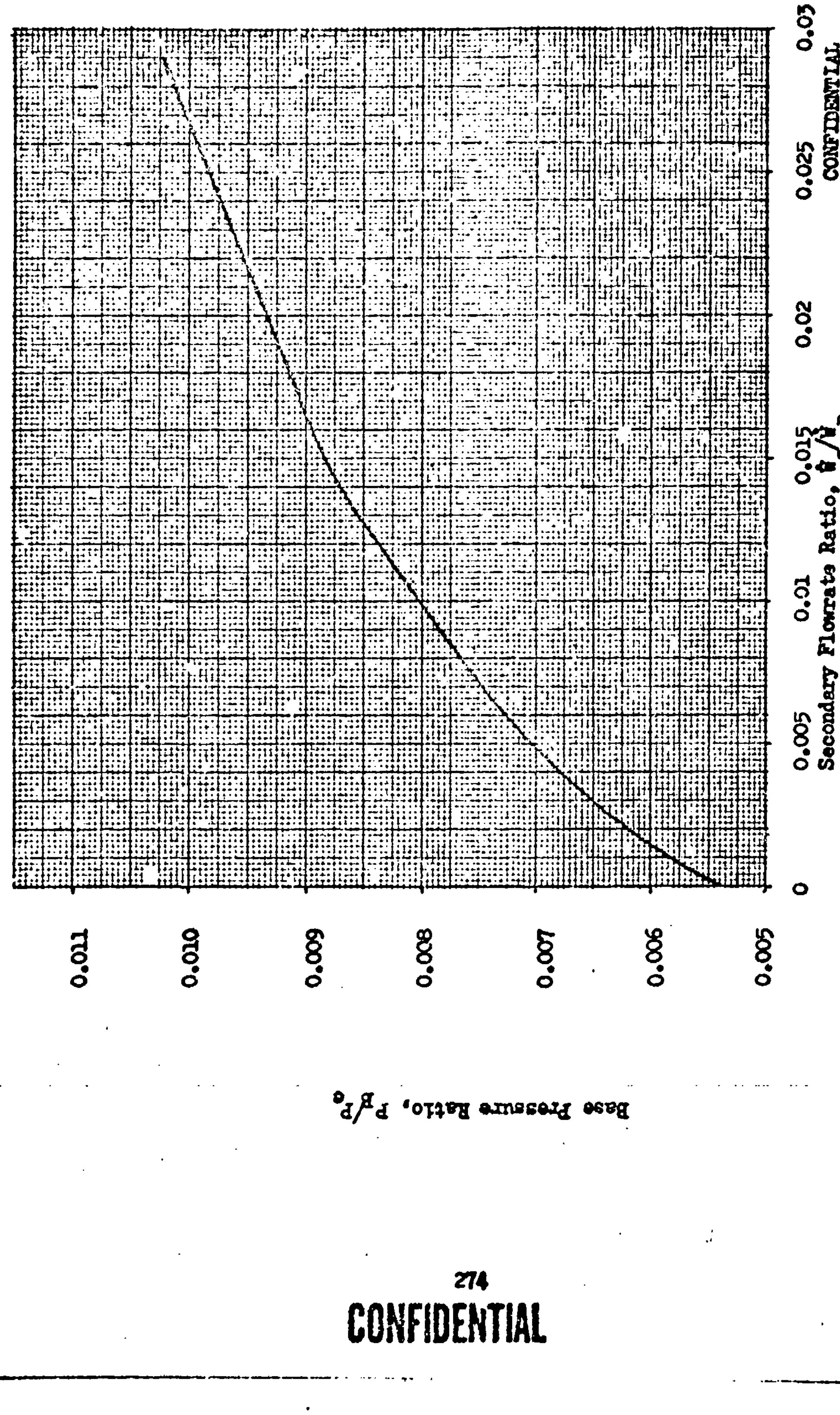

Figure 149. Estimated Base Pressure Dependence on Secondary Flowrate, Closed Wake

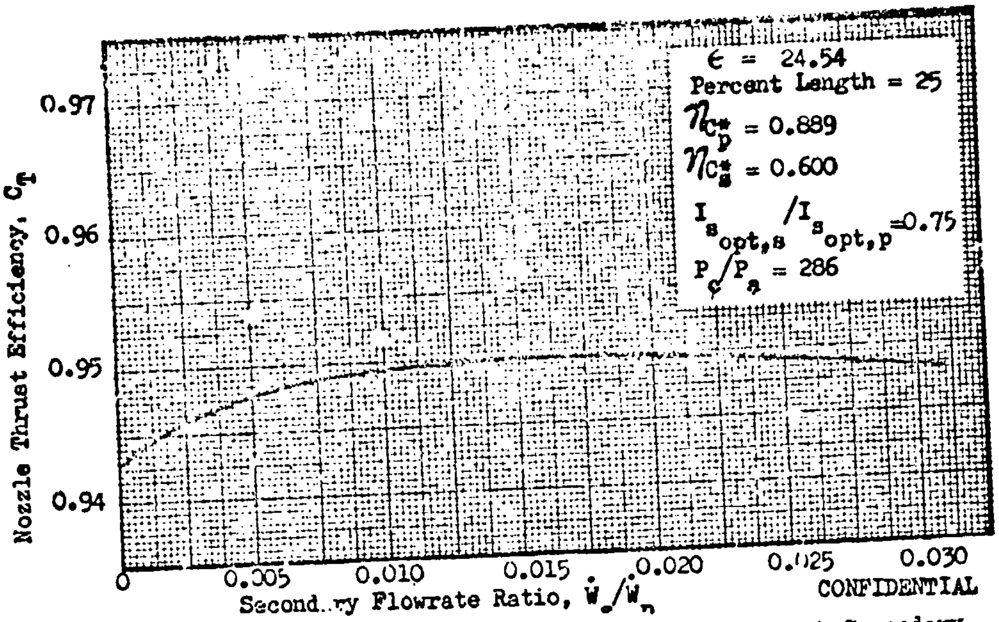

Figure 150. Estimated Nozzle Performance Trend with Secondary Flowrate for Aerospike Engine

(U) To establish guidelines for the TVC testing, a literature review was conducted to determine high-performing TVC injector designs and performance trends with the system variables. This preliminary study revealed that the efficiency of this TVC technique is a function of parameters such as the physical and chemical properties of the injectant, orientation and location of the injector, injection velocity and flow characteristics, etc. The secondary injectant may be an inert or reactive gas or liquid, giving rise to complex fluid dynamics and chemical kinetic interference with the supersonic mainstream flow.

(C) Theoretical interpretation of this flow process is desirable since it enables comparisons on a common basis, facilitates isolated study of influential parameters, and provides a basis for design selections. Because of the complex interference phenomena induced by secondary fluid injection, a rigorous solution is intractable. Nevertheless, flow visualization such as that reported in Ref. 3 and 4 have provided a basis for formulating a simplified model of fluid injection which is amenable to practical analysis. The data presented in these references indicate that the TVC flow remains essentially intact after injection, and forms an effective body downstream of the injection port which provides an obstruction to the mainstream flow (i.e., very little mixing occurs between the two streams for some distance downstream of the injection port). Based upon this result, an idealized flow model can be constructed as illustrated in Fig. 151.

(C) A variety of approaches used in the analysis of this flow model are reported in the general literature. Several of these have been evaluated and it has been found that, of the techniques investigated, the semi-empirical blast wave theory developed in Ref. 1 provided the most accurate representation of the flow process illustrated in Fig. 151. This theory was used to establish

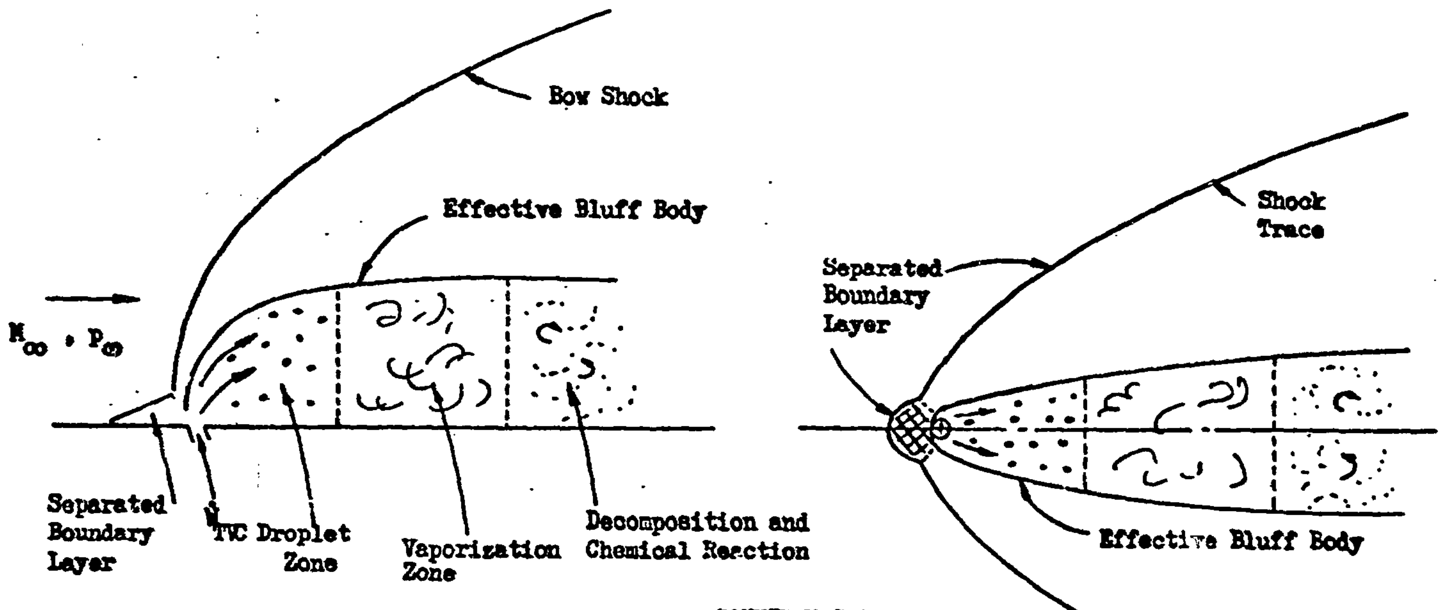

CONFIDENTIAL

a. Cross-Section

b. Plan View

Figure 151. Analytical Aspects: Flow Model of Fluid Injection

qualitative liquid injection TVC performance trends with the injection parameters to select meaningful test conditions. Experimental data and results of similar analytical studies obtained from various sources were used to support the theoretical trends where necessary, and to provide the basis for design selections for parameters whose influence is not predictable by the theory (e.g., interaction losses between ports in multiport configurations).

(C) The blast wave theory is based upon the similarity that exists between the effective body formed by the injectant in the mainstream flow and a linear explosion in the plane of the wall and parallel to the mainstream, which, on detonation, supplies a uniform energy per unit length of charge to the surroundings. The energy supplied to the mainstream is derived through consideration of the work that is done on portions of the primary fluid by the secondary injectant through various thermodynamic processes, and through consideration of certain modifications required to satisfy the boundary conditions specified in the original blast wave theory of Ref. 6 and 7 (used to compute the flow field surrounding the charge). The treatment in Ref. 1 results in the following approximate expression for the interaction force induced by secondary injection through single circular ports. (Refer to Nomenclature):

$$F_{si} = G\left(\frac{4}{\pi J_o}\right)^{3/4} \left(k_1^2 M_\infty s \sqrt{p_\infty \dot{m}_j^3 u_\infty^3 w_2^3}\right)^{1/2} \cos\alpha \qquad (3)$$

(C) A format for prediction of either liquid or gaseous SITVC data is provided by Eq. (3). Correlations presented for gas injection in Ref. 8 indicated that to obtain agreement with the experimental data, Eq. (3) must be prefixed by a spreading correction denoted by G in Eq. (3) which empirically was found to depend upon the distance between the TVC port and the nozzle exit. The form of this correction for gas injection into conical nozzles is illustrated in Fig. 152. The quantity w_2 in Eq. (3) is related to the charge energy per unit mass of

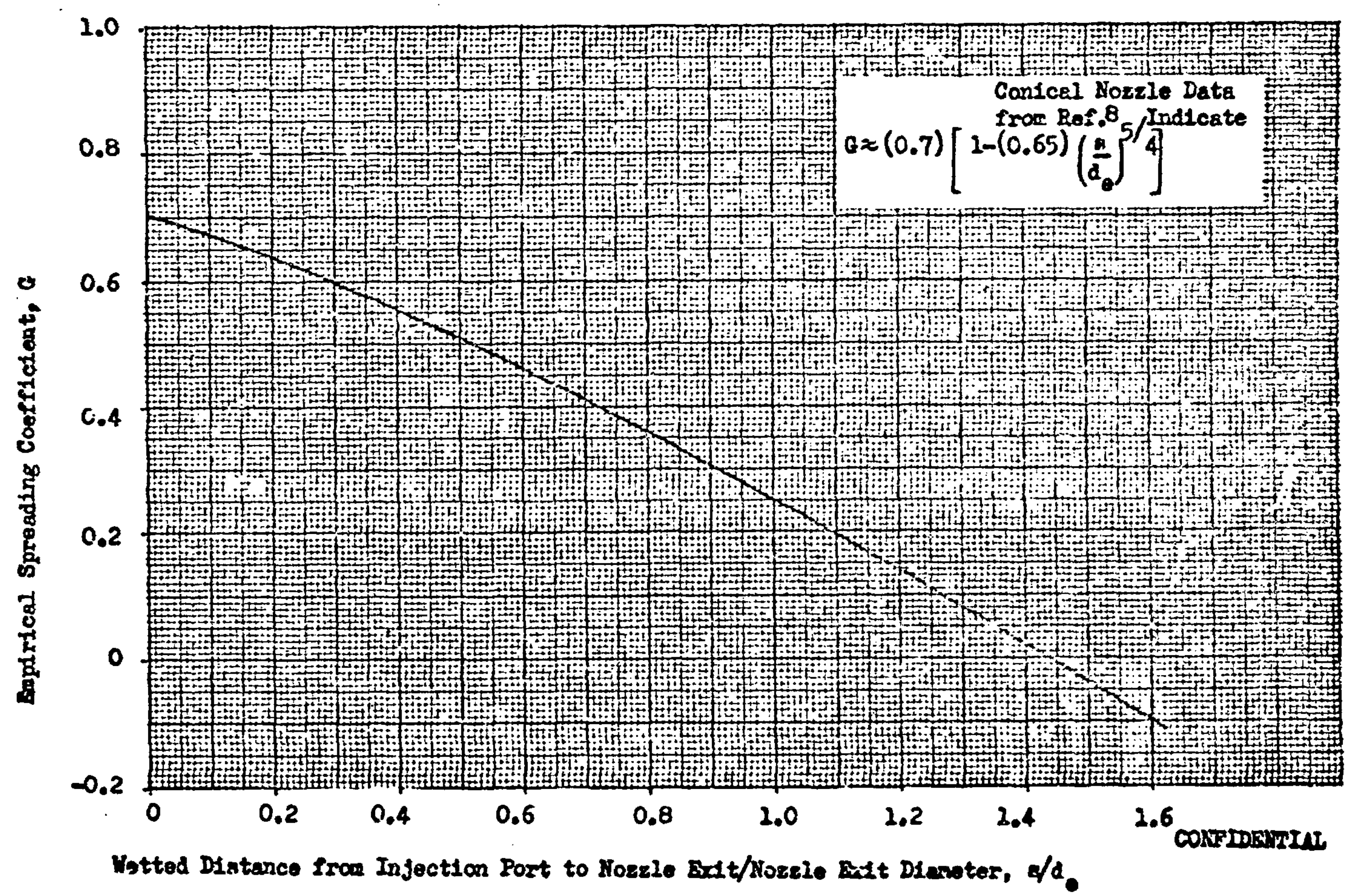

Figure 152. Empirical Spreading Coefficient for Gas Injection into Conical Nozzle from Ref. 8.

charge which is in turn related to the energy of the secondary injectant. It is pointed out in Ref. 9 that this quantity can be represented in the following manner for both gaseous and liquid injection:

$$\omega_2 = \frac{1}{2} + \frac{v_i}{u_\infty} \cos\lambda + \frac{1}{2}\left(\frac{v_i}{u_\infty}\right)^2 + \frac{\mathcal{M}_p/\mathcal{M}_i}{(\gamma-1)\,M_\infty^2}\left(1 + \frac{\overline{\mathcal{M}_i C_{p_i}}}{\mathcal{M}_p C_{p_\infty}}\right) \quad (4)$$

where $\mathcal{M}_j C_{p_j}$ is the effective molar specific heat of all processes occurring (evaporation, reaction, etc.), and is defined as $\sum \Delta H/T_\infty$. This quantity is dependent upon factors such as: mixing efficiency of injectant and mainstream gases, injectant stay time within the nozzle, droplet formation and vaporization. Since mixing efficiency is normally low, and injectant stay times are very short for small-scale nozzles this term has been assumed negligible in subsequent discussion relating to the short length aerospike tested in this program. Inserting Eq. (4) into Eq. (3) and rearranging results in the following expression for F_{si};

$$F_{si} = G\left(\frac{4k_i^{4/3}}{\pi J_o}\right)^{3/4} \left(M_\infty s \sqrt{p_\infty \; \dot{m}_j^3 u_\infty^3}\right)^{1/2} \left\{\frac{1}{2} + \frac{v_i}{u_\infty}\cos\lambda + \frac{1}{2}\left(\frac{v_i}{u_\infty}\right)^2 + \frac{\mathcal{M}_p/\mathcal{M}_i}{(\gamma-1)\,M_\infty^2}\right\}^{3/4} \cos\alpha \quad (5)$$

(C) The geometric parameters appearing in the above equation and in subsequent equations are illustrated in Fig. 153. For the aerospike engine used in this test program, the dimensionless induced force becomes:

$$\frac{F_{si}}{F_v} = (0.233)\; c_N^{1/4} \cos\alpha \left(\frac{M_\infty^{5/4}}{V_\infty^{1.625}}\right)\left(\frac{s}{d_e}\right)^{\frac{1}{2}} \left\{\frac{1}{2} + \frac{v_i}{u_\infty}\cos\lambda + \frac{1}{2}\left(\frac{v_i}{u_\infty}\right)^2 + \frac{\mathcal{M}_p/\mathcal{M}_i}{(\gamma-1)\,M_\infty^2}\right\}^{3/4} \left(\frac{\dot{w}_i}{\dot{w}_e}\right)^{3/4}$$

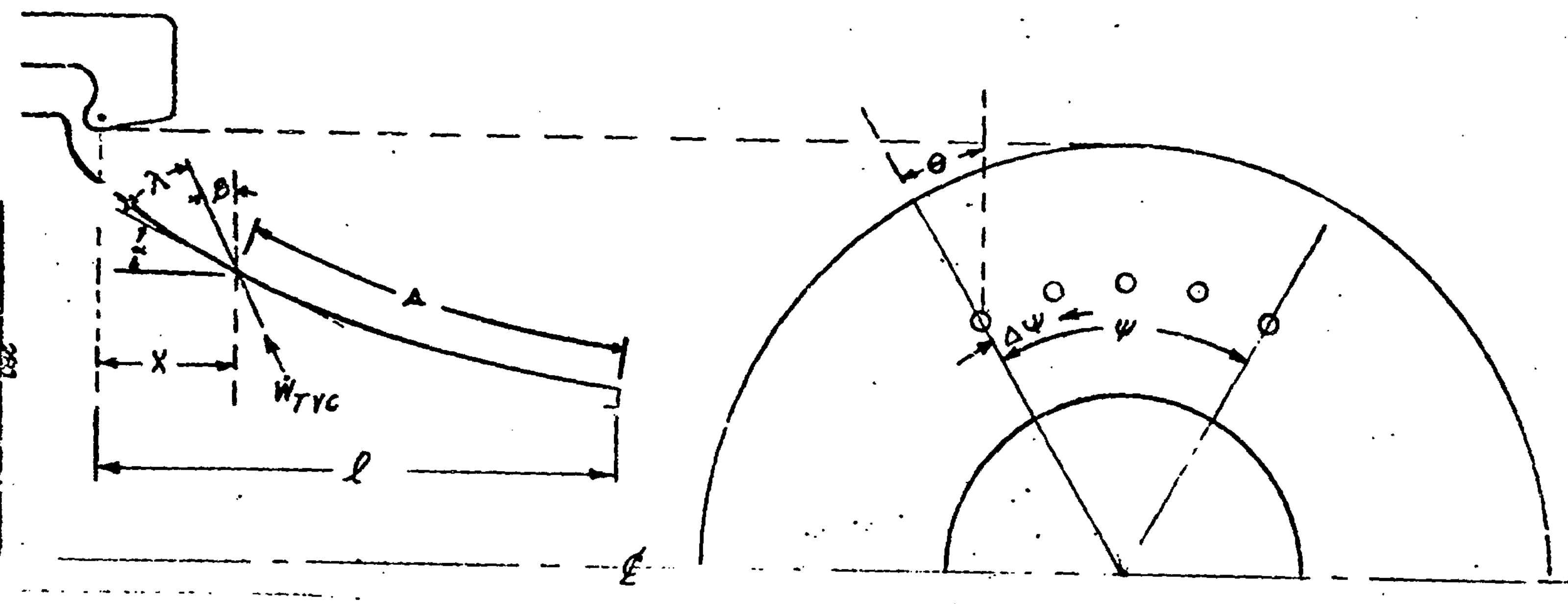

Figure 153. Geometric Design Parameters with Secondary Liquid Injection TVC

since

$$\mathfrak{M}_p = 23.7$$

$$\bar{\gamma}_p = 1.25$$

$$\epsilon_n^{\frac{1}{4}} = 2.24$$

$$C_p^* = 5029 \text{ ft/sec } (MR = 2.0,\ \eta_{C_p^*} = 0.89)$$

(C) Since liquid injection test data were not available for the aerospike nozzle prior to this program, a constant value of 0.7 (flat plate from Ref. 8 used for the empirical spreading coefficient, G . Thus, the form of the expression for the side thrust amplification factor, which is a measure of LITVC efficiency relative to main engine performance as discussed in Appendix 4, is as follows:

$$K_s = I_{s_s}/I_{s_e} = \frac{(F_{si} + F_{sr})/F_v}{\dot{W}_{TVC} / \dot{W}_e}$$

$$= (0.521) \cos\alpha \left(\frac{M_\infty^{1.25}}{V_\infty^{1.625}}\right)\left(\frac{s}{d_e}\right)^{\frac{1}{2}} \left\{\frac{1}{2} + \frac{v_j}{u_\infty}\cos\lambda + \left(\frac{v_j}{u_\infty}\right)^2 + \right.$$

$$\left.\frac{\mathfrak{M}_p/\mathfrak{M}_j}{(\gamma-1)\, M_\infty^2}\right\}^{3/4} \left(\frac{\dot{W}_j}{\dot{W}_p}\right)^{-\frac{1}{4}} + (1.105)(10^{-4})\, v_j \sin(\alpha+\lambda) \qquad (6)$$

where

$$F_{sr} = \dot{m}_j\, v_j \sin(\alpha + \lambda)$$

(C) For multiport injection, it was assumed that flow interaction losses between ports are small if the proper port spacing is maintained. Under this assumption, the amplification factor, K_s, can be expressed as:

$$K_s = K_s)_{n=1} \left[1 + 2 \sum_{k=1,3,5\ldots}^{n} \cos \left(\frac{k-1}{2}\right) \Delta\Psi \right] \left(\frac{1}{n}\right) \qquad (7)$$

for odd port groupings and:

$$K_s = K_s)_{n=1} \left[\frac{2}{n} \sum_{k=2,4,6\ldots}^{n} \cos \left(\frac{k-1}{2}\right) \Delta\Psi \right] \qquad (8)$$

for even port groupings.

(C) It is demonstrated by Eq. (6, 7, and 8) that the performance of liquid injection TVC systems is sensitive to a wide range of operating variables. These variables include: injection flowrate and velocity, injector location, number of ports and port spacing, axial and radial port inclination, and injectant properties. The influence of injection flowrate and velocity is illustrated graphically in Fig. 154 for upstream injection through a single port located near the nozzle throat. The TVC flowrate is seen to have a strong influence upon the efficiency of this secondary injection system;

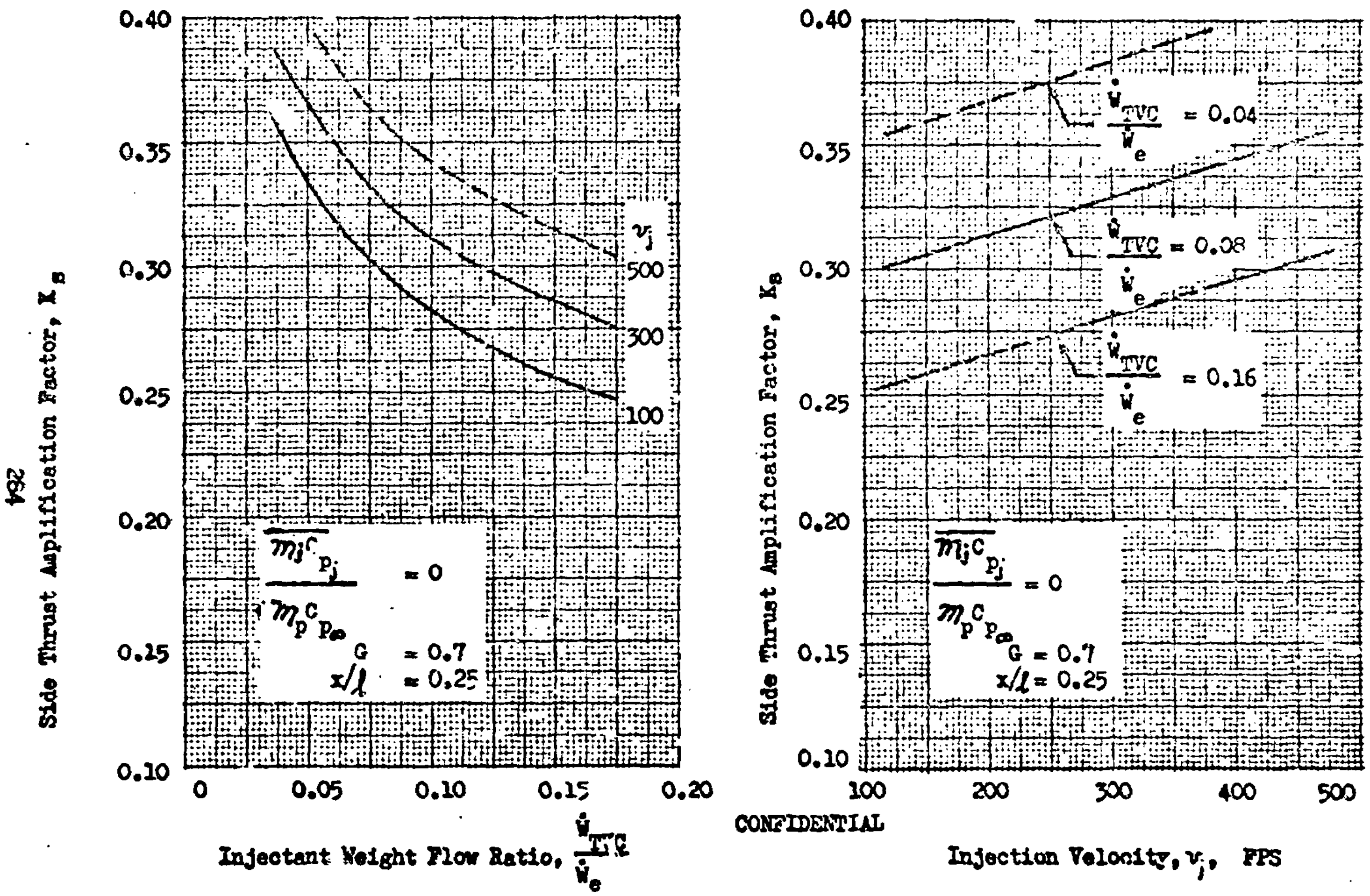

CONFIDENTIAL

Figure 154. Estimated Influence of Injection Flowrat· and Velocity

performance decreases sharply with increasing flowrate for all injection velocities. Performance is a weaker function of the injection velocity, and, since $(v_j/u_\infty)^2 \ll 1$, K_s increases almost linearly with increasing velocity. However, a large expenditure in system pressure drop is required to achieve a relatively small gain in efficiency as shown by the data in Fig. 155.

(C) At first glance it would appear that the best simulation of a full-scale, high-chamber-pressure engine would be to test with an injection velocity and pressure drop compatible with the large engine operating conditions; e.g., v_j = 300 ft/sec and Δp = 1800 psia. However, this requires abnormally small TVC orifices for the weight flowrates of the small-scale test configuration. From previous testing with this type of configuration (Ref. 11) it has been shown that very low performance may be encountered because of breakup and atomization of the injectant stream at the injection port (experience to date indicates that the best performance is obtained with a well-collimated fluid stream at the injection orifice as discussed in Ref. 12). Thus, an injection velocity of 100 ft/sec was selected for the majority of the testing conducted in this program. This value results in an orifice Δp compatible with the engine chamber pressure as shown in Fig. 155; that is, similitude between small- and large-scale engines is maintained through the parameter P_j/P_c rather than through the absolute magnitude of the injection velocity. Since this study and various experimental data (e.g., Ref. 12 and 13) indicate that the injection velocity is an influential parameter, the test program was designed to evaluate several injection velocities over a range of TVC flowrates at two injector locations.

(C) The theoretical performance trend with flowrate at various injector locations, and with injector location for various TVC flowrates is shown in Fig. 156. Both parameters are seen to have a strong influence on performance, and the performance trend with flowrates noted earlier for constant velocity injection near the nozzle throat persists for injection near the end of the

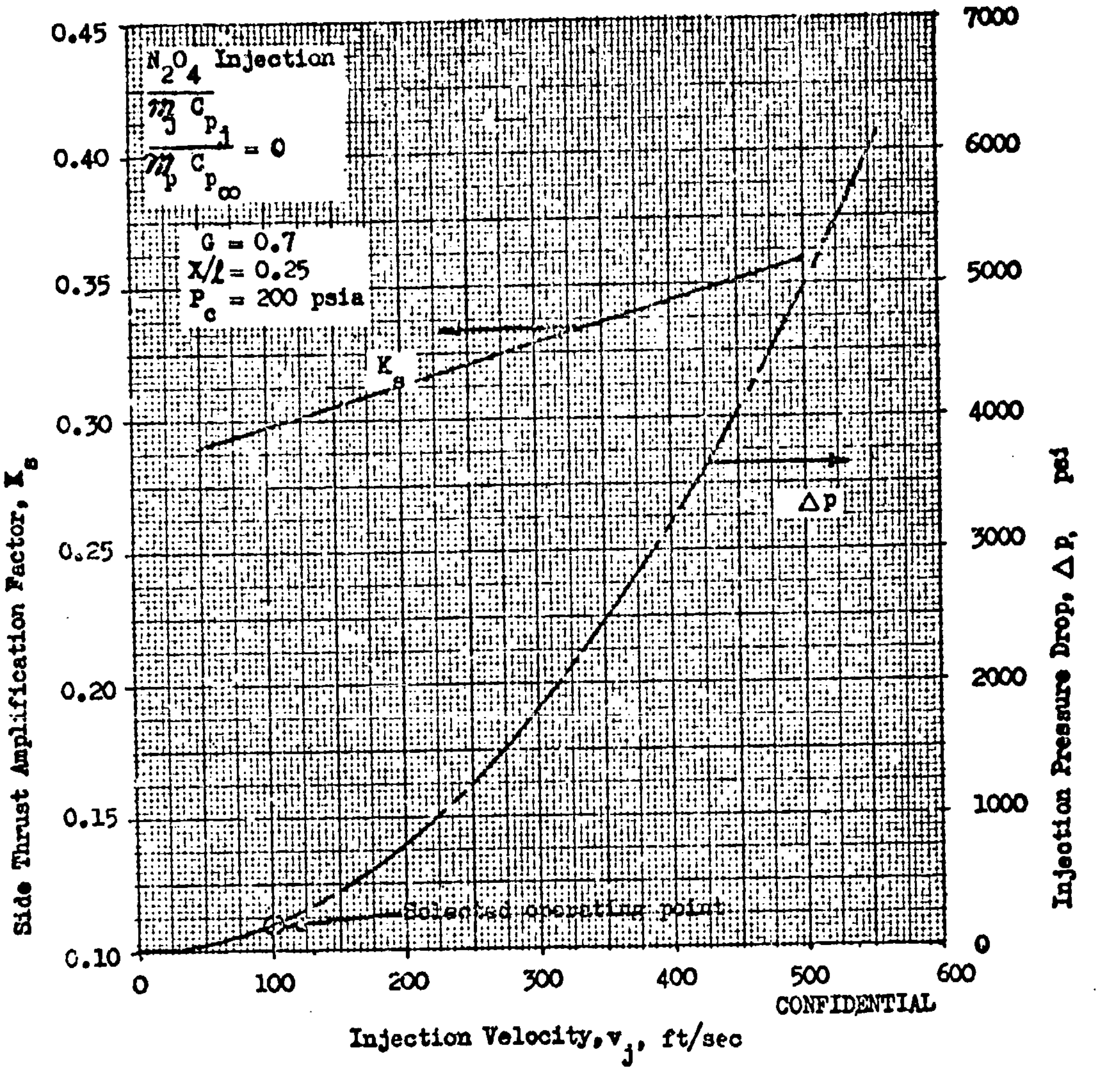

Figure 155. Estimated Influence of Injection Velocity on SITVC Performance and System Pressure Drop

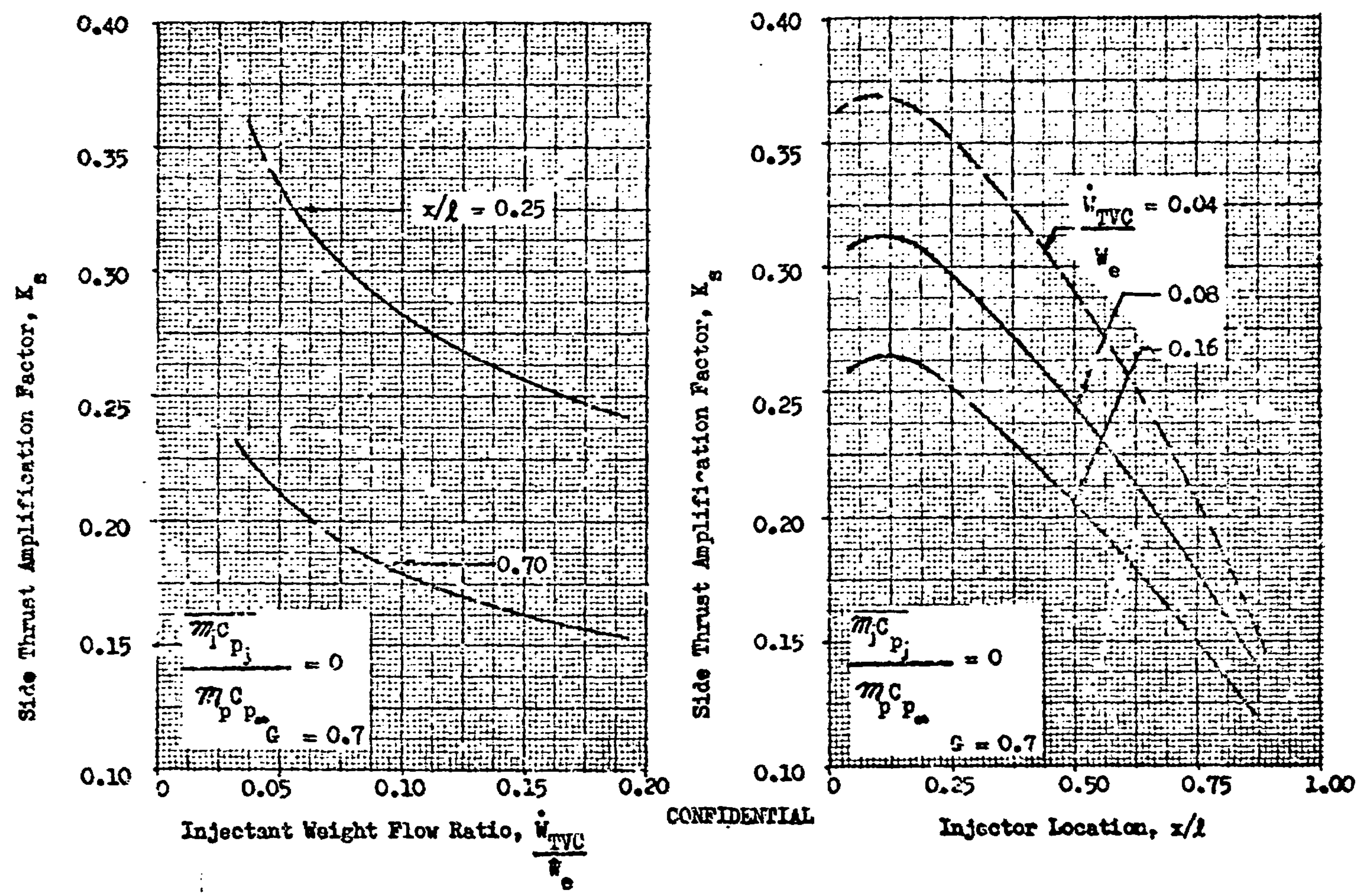

CONFIDENTIAL

Figure 156. Estimated Influence of Injector Flowrate and Location

nozzle. It should be pointed out that to develop these curves, it was assumed that the location of the effective side force vector is at the injection port so the angle α in Eq. (6) is the wall angle at the point of injection. In reality, the effective side-force vector is located some distance downstream of the TVC port so the wall angle at the point of application of this vector is less than that at the injection port. Also, the spreading coefficient, G, was assumed to be independent from the injector location. In view of the trend established for conical nozzles (Fig. 152), some variation in the spreading coefficient with axial location can be expected for the aerospike. Thus, while the approximation that vaporization, decomposition, and reactivity influences are negligible become less valid for injector locations far upstream of the nozzle exit and offsets these latter approximations, both of these assumptions tend to exaggerate the influence of the parameter x/ℓ. Nevertheless, the results of this and related study (e.g., the experimental and theoretical data for the Lance thrust chamber discussed in Ref. 12) do indicate that the injector location is an important performance parameter. Therefore the test configuration was designed to incorporate TVC injectors at three locations: $x/\ell = 0.25$, $x/\ell = 0.40$, and $x/\ell = 0.7$. Separate contoured TVC flow rings were used for each location.

(C) The pronounced decrease in performance with increasing flowrate indicated for single-port injection in Fig. 156 demonstrates the desirability of operating continuously in the low flowrate range. This can be accomplished by injecting the TVC flow through a number of ports, each operating over a range of relatively low flowrates. Because the pressure acting over the downstream area affected by overlapping induced shock fields is not increased significantly by overlap, care must be taken to space the TVC ports around the nozzle circumference such that these flow interaction losses are held to a minimum. Cosine losses coupled with interference effects lead to the

the type of optimization indicated in Fig.157 and discussed in detail in Ref. 12. Data for conical nozzles compiled in Ref.10 indicate that near-optimum performance is obtained for ports radially spaced approximately 15 degrees apart around the nozzle circumference as shown in Fig.158. Assuming that interaction effects are negligible for this port spacing, theoretical LITVC performance varies with the number of ports as shown in Fig. 159, odd port groupings and as shown in Fig.160 for even port groupings. Substantial performance increases are realized by increasing the number of ports from one to five (or six), which is near optimum for ports spaced 15 degrees apart.

(C) Identical results are obtained for both odd and even port groupings, so odd groupings were arbitrarily chosen for evaluation in this program. Because spreading and interaction losses are dependent upon the injector location, provision was made to test three- and five-port configurations at each of the three selected injector locations. The ports were spaced 15 degrees apart in all cases. A single port configuration was incorporated into a flow ring at $x/\ell = 0.25$ to provide reference data. A three-port configuration with 30 degrees between ports was included in the flow ring at $x/\ell = 0.7$ to allow evaluation of flow interference effects at this location. The nominal flowrate selected for this testing was 8 percent for $n = 1$ and 3, and 13 percent for $n = 5$. Provisions were also made to confirm the theoretical performance trend with flowrate at constant velocity by testing various port sizes at $x/\ell = 0.25$ with the flowrates indicated in Fig. 159 and with flowrates of 4 and 8 percent ($n = 3$) and 7 and 13 percent ($n = 5$) at $x/\ell = 0.4$.

(C) For the nominal injection velocity of 100 ft/sec selected for the majority of this testing, it was found theoretically (Eq. 6) that the effect of the injector axial inclination is nearly negligible as shown in Fig. 161. Similar results have been obtained experimentally for moderate variations in

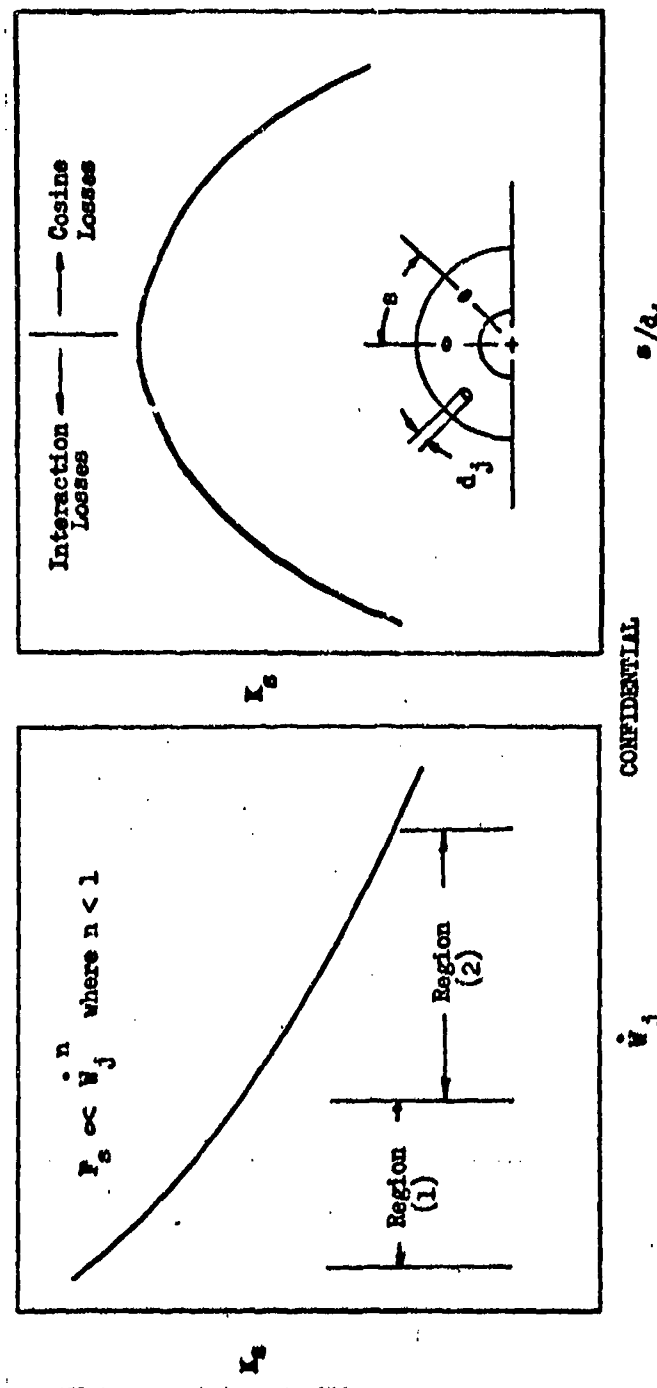

Figure 157. Influence of Number of Injection Ports and Port Spacing

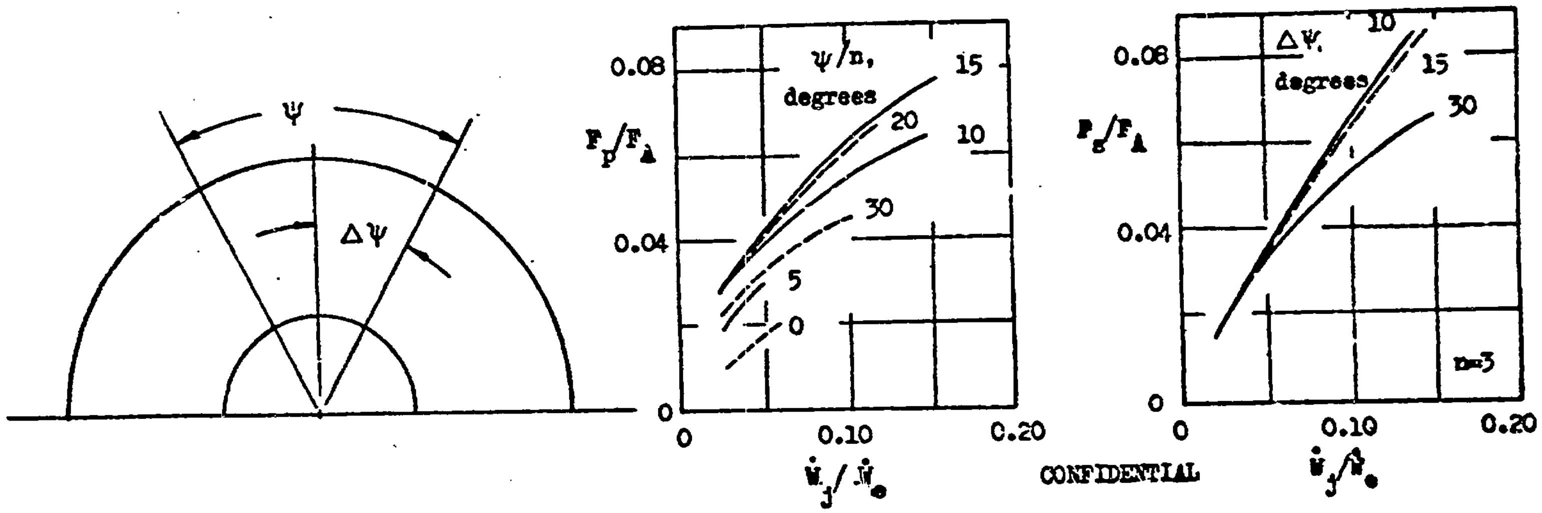

a. Freon Injection

CONFIDENTIAL

b. Sr $(ClO_4)_2$ Injection

Figure. 158. Effect of Port Spacing on Conical Nozzle Performance (Ref. 10)

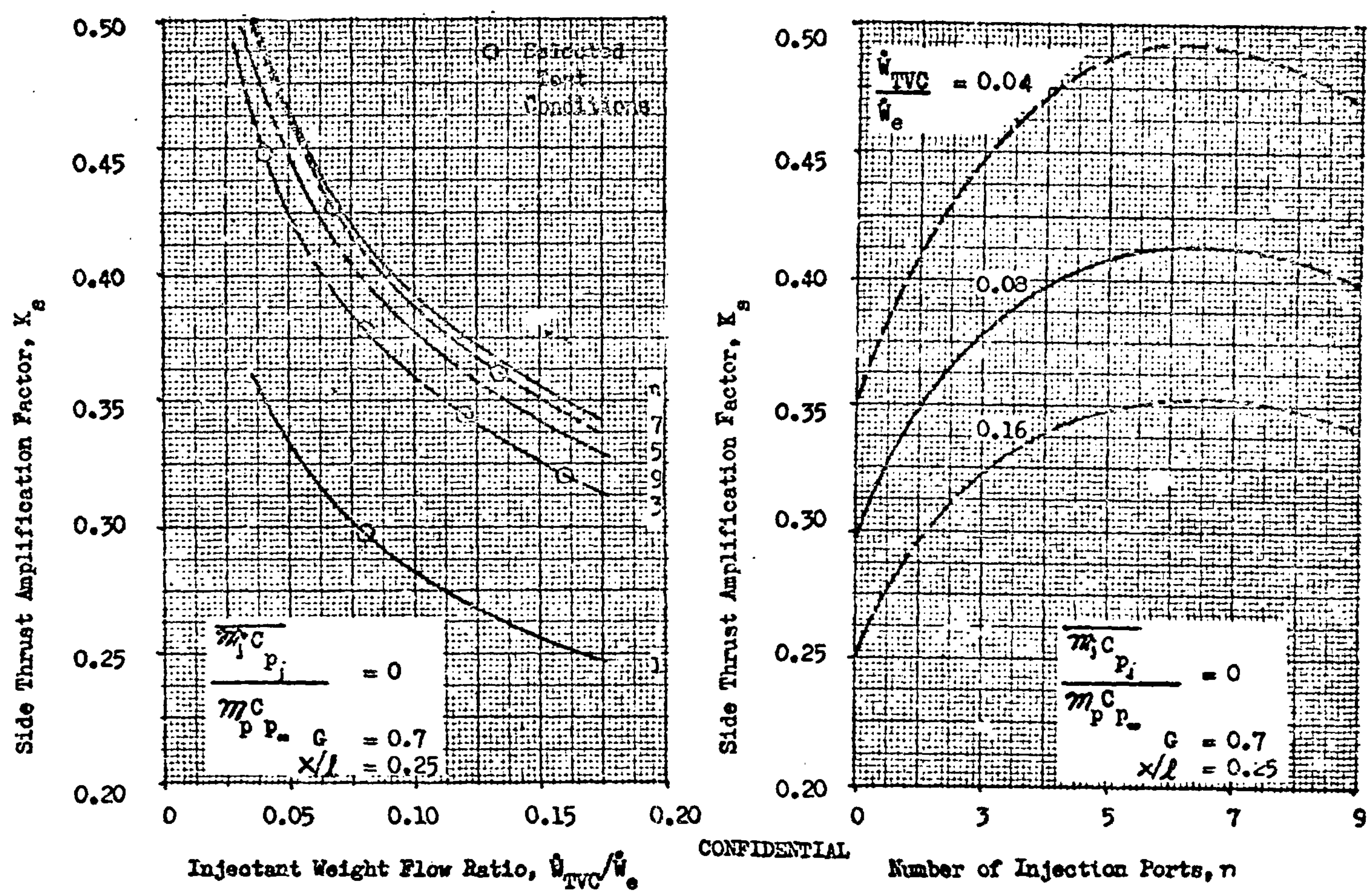

Figure 159. Estimated Influence of the Injectant Flowrate and the Number of Ports (n odd)

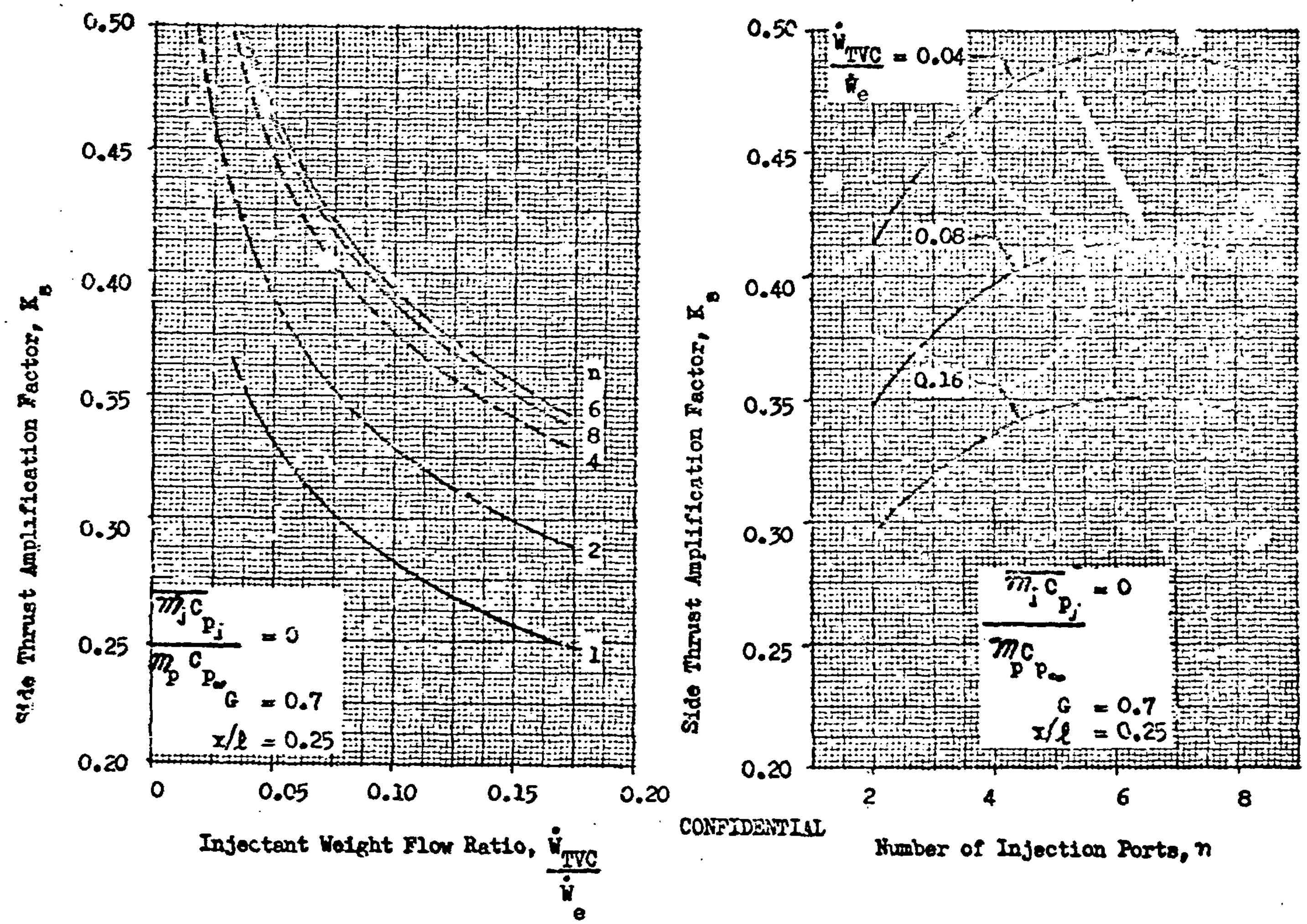

Figure 160. Estimated Influence of the Injectant Flowrate and Number of Injection Ports (n even)

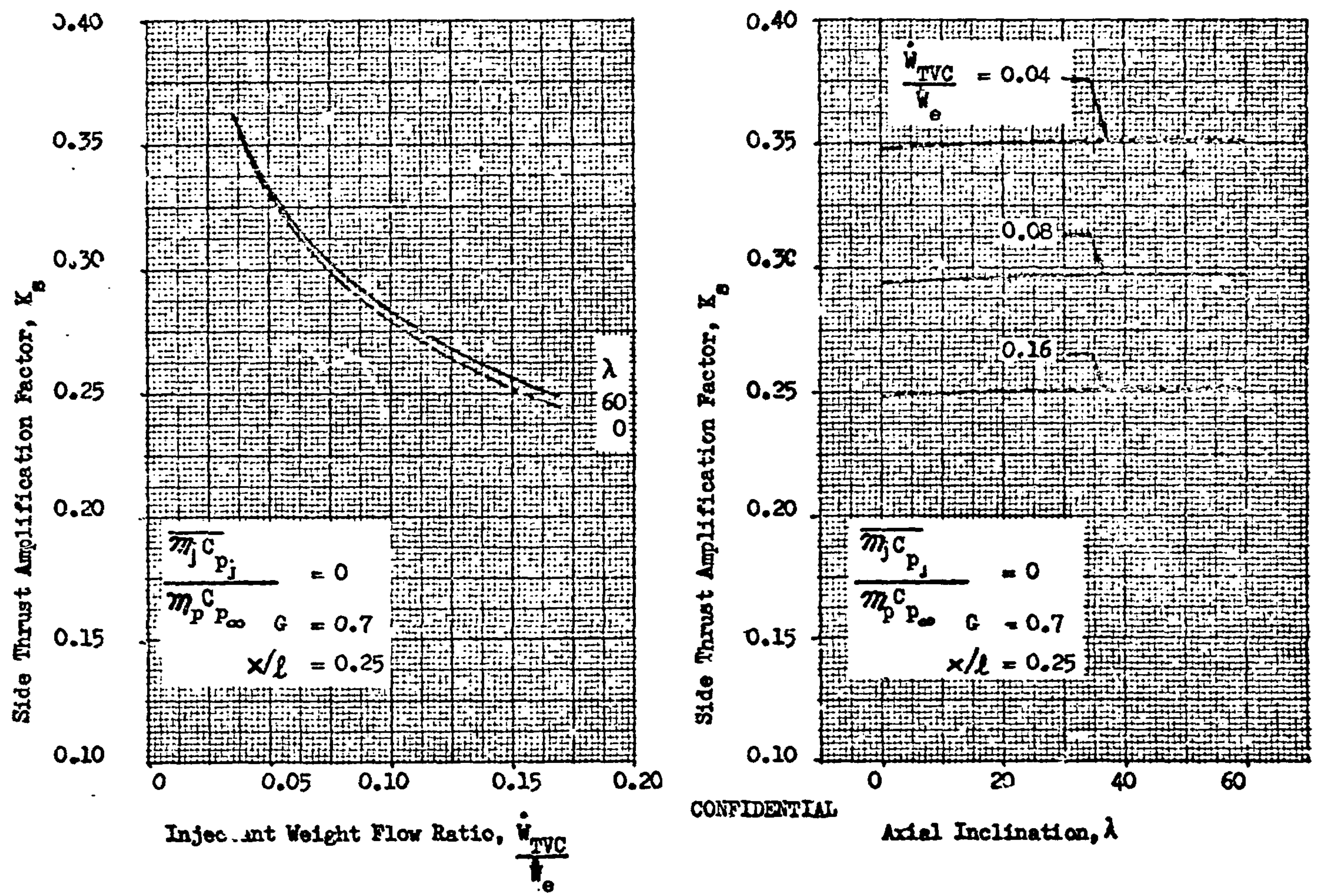

Figure 161. Estimated Influence of the Injectant Flowrate and the Axial Port Inclination

λ as shown by the data from Ref. 10 presented in Fig. 162. Thus, this parameter was not emphasized in this program. An axial inclination of 45 degrees measured with respect to the contour as shown in Fig.153 was chosen as the nominal value to prolong the injectant stay time within the nozzle. To verify the indicated trend for the aerospike, three and five port configurations with an axial inclination of 60 degrees were provided at $x/\ell = 0.4$ and $x/\ell = 0.7$.

(C) Because of the variable influence of flow interference effects with multiport injection and asymmetric flow field surrounding radially inclined ports, the effect of the radial inclination of ports is not predictable theoretically. However, experimental data such as those presented in Fig. 163 (from Ref. 13) indicate that this may be an influential parameter for certain configurations. As indicated in the figure, injecting the flow through parallel ports resulted in a performance loss as compared with radial injection. This can be attributed to an unfavorable spread of the pressure field surrounding the parallel injectors in a conical nozzle which increases cosine losses to a point where they more than offset the gain in side thrust produced by the increased injection momentum in the lateral direction. Because of a reversal in nozzle geometry, including the ports in an aerospike such that all of the TVC flow streams are parallel or convergent may tend to concentrate the pressure field in a more favorable manner if the ports are spaced far enough apart to avoid severe interaction losses. Therefore, capability was incorporated into the LITVC system design to test parallel stream injectors at each of the three selected injector locations with 8 and 13 percent flow for $n = 3$ and $n = 5$ respectively. Additionally, capability for testing a parallel stream injector with 4 percent ($n = 3$) and 6 ($n = 5$) percent flow and a converging stream injector with 8 ($n = 3$) and 13 ($n = 5$) percent flow was included at $x/\ell = 0.25$. All of the remaining parameters were investigated with radial injection orifices.

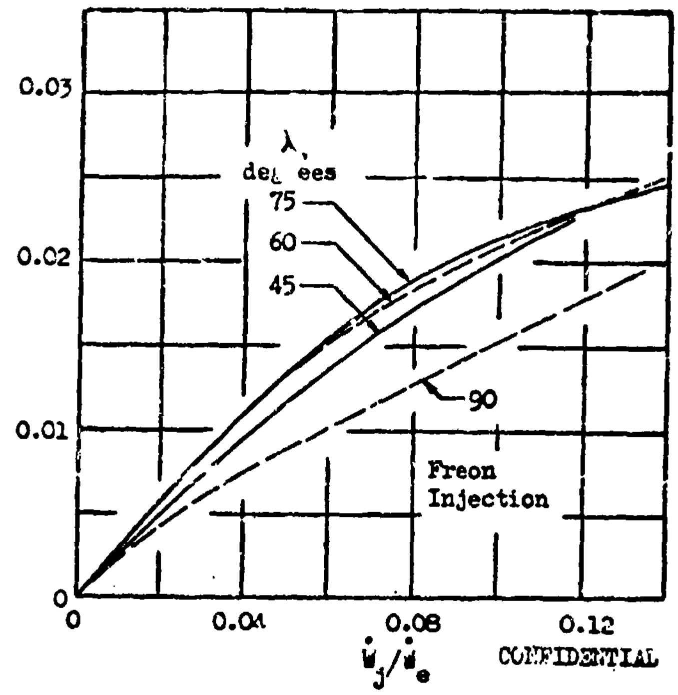

Figure 162. Measured Influence of the Axial Port Inclination for Conical Nozzles (Ref. 10)

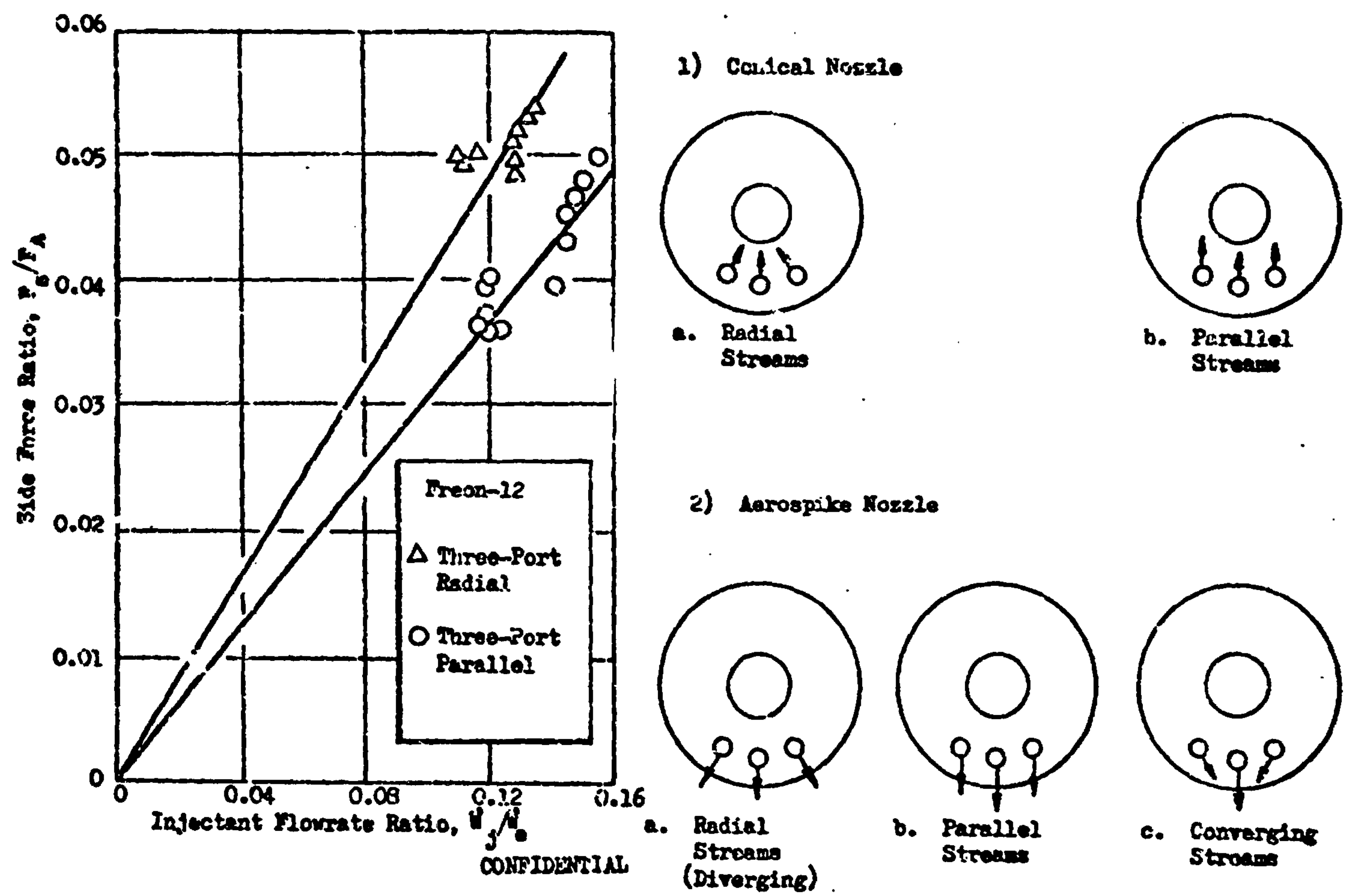

Figure 163. Measured Influence of the Radial Port Inclination with Conical Nozzles (Ref. 33)

(C) Fast testing with various nozzles has shown that, in addition to the injector and flow characteristics discussed above, injectant properties exert a strong influence on the performance of the TVC systems. Parametric studies conducted in conjunction with the Lance engine optimization study (Ref. 16) indicate that side force tends to correlate with the volume flowrate of injectant for systems with equal pressure drop as shown in Fig. 164. This correlation, if valid for the aerospike, results in the LITVC performance comparison between N_2O_4 and UDMH-N_2H_4 (50-50) shown in Fig. 165a. The accompanying data in Fig. 165b represent the trend estimated theoretically by using Eq. (6) and neglecting the energy release caused by vaporization, decomposition, and reaction. The estimated influence of injectant properties is weaker using the latter method, but the trend is the same in both cases. In view of the apparent performance advantage of UDMH-N_2H_4 (50-50) over N_2O_4, the test program was arranged to allow evaluation of UDMH-N_2H_4 (50-50) as an injectant with the injector designs selected at $x/\ell = 0.25$ and $x/\ell = 0.4$.

(C) Nozzle recompression at low altitudes strongly affects the undisturbed nozzle pressure profile indicating that the ambient pressure may have a strong influence on LITVC performance at low pressure ratios. Therefore, provisions were incorporated into the test program to study this influence by testing at low altitudes with the flow ring at $x/\ell = 0.4$.

(U) To summarize, the engine was designed to enable experimental study of: (1) constant-velocity flowrate variation, and radial, parallel and convergent stream injection with three-and five-port configurations at $x/\ell = 0.25$, and single port injection at $x/\ell = 0.25$; (2) constant-velocity flowrate variation, radial and parallel stream injection and variable axial inclination with three-and five-port configurations at $x/\ell = 0.4$; (3) radial and parallel stream injection and variable axial inclination for three- and

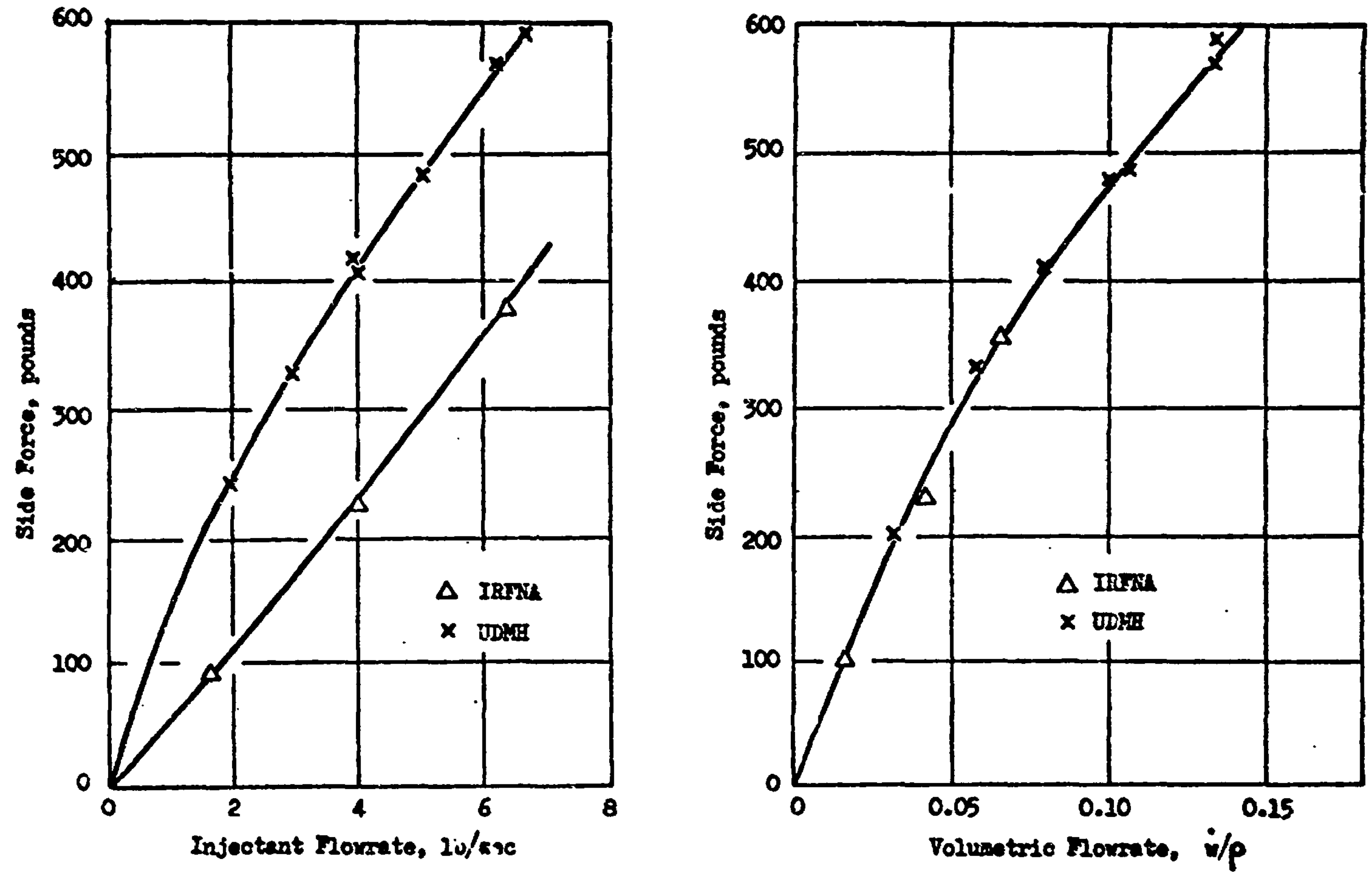

Figure 164. Measured Effect of Injectant Density
(Ref. 16)

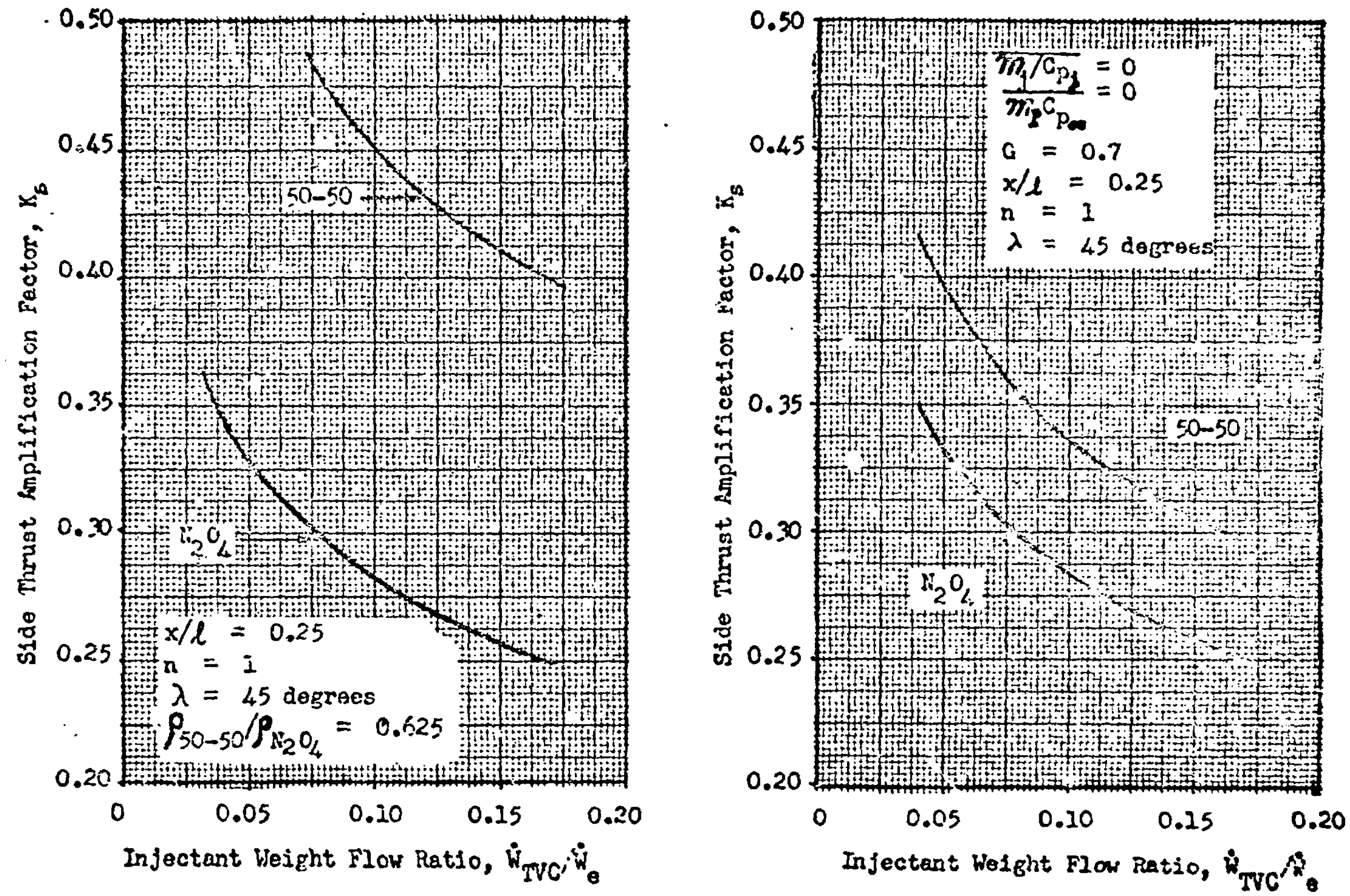

a. Volumetric Flowrate Correlation

b. Blast Wave Theory

Figure 165. Estimated Influence of Injectant Properties

five-port configurations along with variable port spacing for a three-port configuration at $X/\ell = 0.7$. TVC flow rings designed to incorporate these features are illustrated schematically in Figs. 166 and 167. It is readily seen from the selected designs that the intent of the program was to determine the parameters which exert the strongest influence on LITVC performance with an aerospike and to establish the relative magnitude of this influence, rather than to optimize each of the many variables for one particular test configuration.

Test Program

(U) Hardware Description. The aerospike thrust chamber tested in the TVC phase of the Advanced Aerodynamic Spike Configuration Program is shown in Fig. 168. The TVC hardware assembly is identical to the 12-percent length nozzle tested previously in the program with the exception that a new inner throat and nozzle section with liquid injection thrust vector control capability was utilized. The inner contour is 25 percent of the axial length of an equivalent 15-degree conical nozzle with an area ratio of 25. Secondary gas is supplied from a gas generator mounted directly within the center of the inner nozzle. The secondary gas is diffused through a porous base plate mounted at the nozzle exit. Fluid systems consist of the primary propellant (N_2O_4/UDMH-N_2H_4, 50-50), secondary propellant (N_2O_4/UDMH-N_2H_4, 50-50), TVC fluid (N_2O_4 and UDMH-N_2H_4, 50-50),

(U) The thrust chamber contains the following basic components: the injector, a removable water cooled combustion chamber, a water cooled throat and inner nozzle section, and removable uncooled nozzle extensions which contain the TVC injection orifices. Each of these components, except for the nozzle extensions, was discussed in detail previously, but is reviewed below to show the relationship between the hardware assemblies.

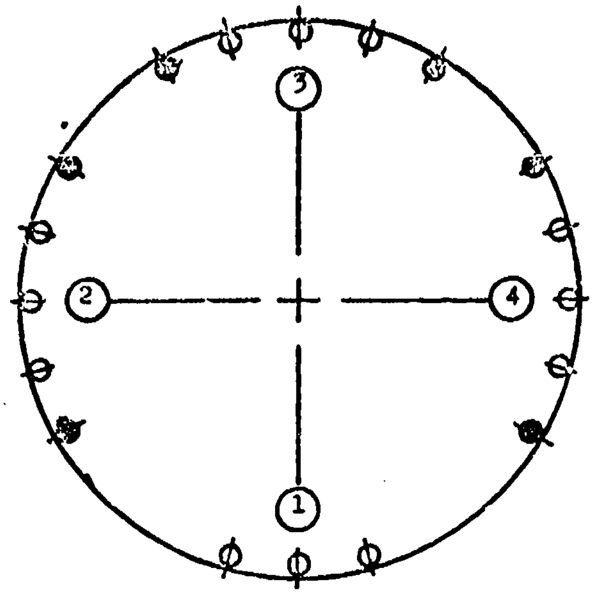

Quadrant	$\frac{\dot W_s}{\dot W_p}$ (%)	ψ	λ	θ
1	16	30	45	0
2	12,20	30,60	45	0
3	8,13	30,60	45	0
4	4, 7	30,60	45	0

Nominal v_j = 100 FPS

Figure 166a, Nominal Geometry, Ring A

θ = 0: Radial Streams

θ = Δ: Converging Streams

θ = ||: Parallel Streams

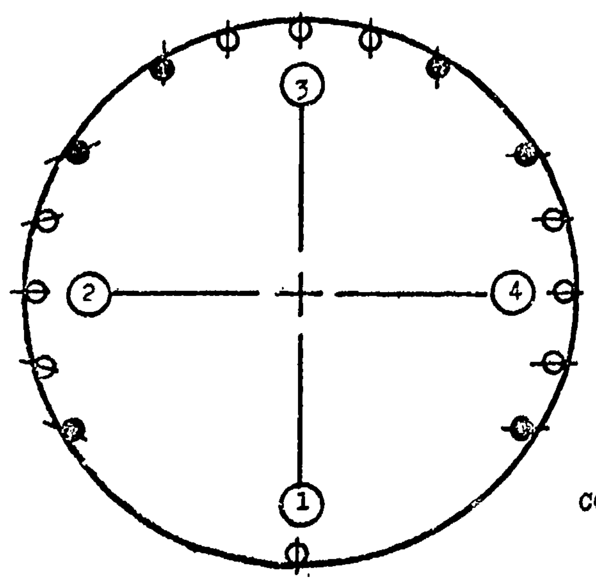

Quadrant	$\frac{\dot W_s}{\dot W_p}$ (%)	ψ	λ	θ
1	8	0	45	0
2	8,13	30,60	45	Δ
3	8,13	30,60	45	||
4	4, 7	30,60	45	||

Nominal v_j = 100 FPS

CONFIDENTIAL

Figure 166b, Parallel and Converging Ports, Ring B

Figure 166. Test Configurations at x/ℓ = 0.25

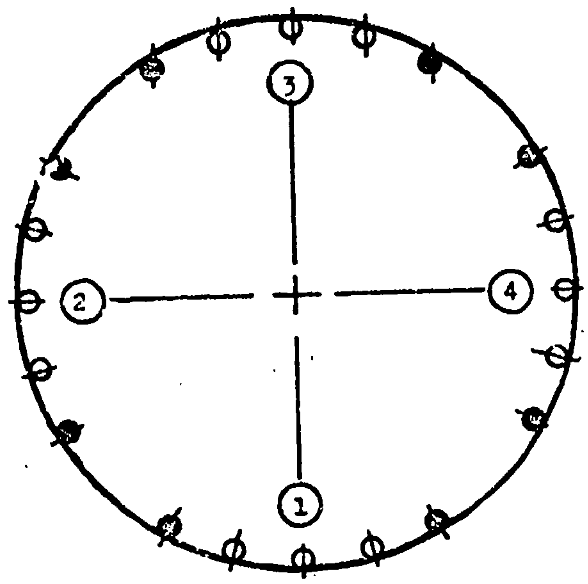

Quadrant	$\frac{\dot{w}_i}{\dot{w}_p}$ (%)	ψ	λ	θ
1	8,13	30,60	60	0
2	8,13	30,60	45	0
3	8,13	30,60	45	||
4	4, 7	30,60	45	0
Nominal v_j = 100 FPS				

Figure 167a, x/ℓ = 0.4 , Ring C

θ = 0: Radial Streams

θ = ||: Parallel Streams

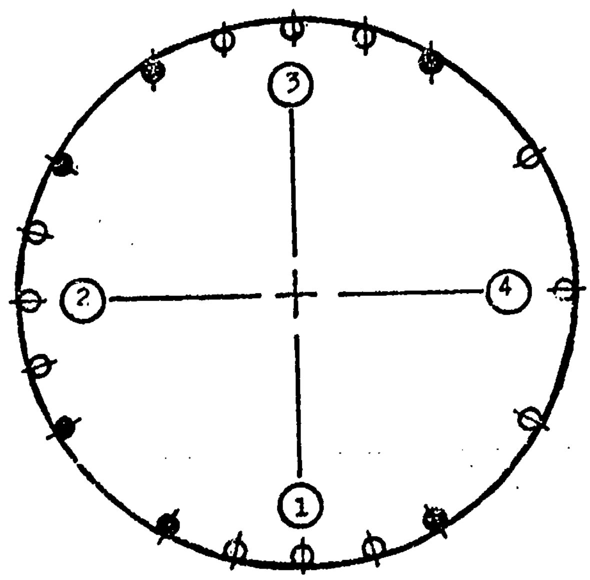

Quadrant	$\frac{\dot{w}_i}{\dot{w}_p}$ (%)	ψ	λ	θ
1	8,13	30,60	60	0
2	8,13	30,60	45	0
3	8,13	30,60	45	||
4	8	30,60	45	0
Nominal v_j = 100 FPS				

Figure 167b, x/ℓ = 0.7 , Ring D

Figure 167. Test Configurations at x/ℓ = 0.4 and x/ℓ = 0.7

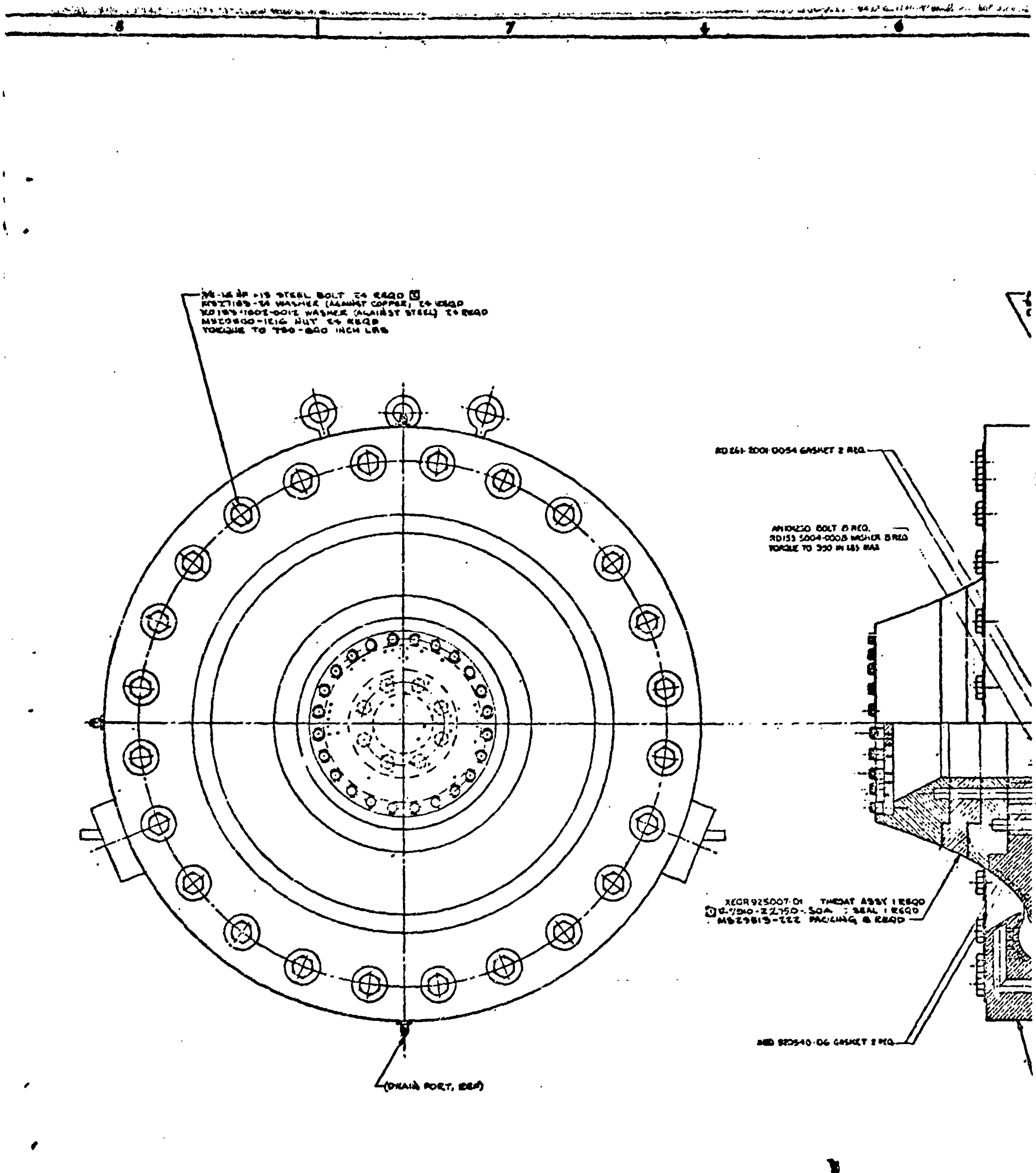

STEEL BOLT 24 REQD
WASHER (AGAINST COPPER) 24 REQD
WASHER (AGAINST STEEL) 24 REQD
NUT 24 REQD
INCH LBS
RD 261-2001-0054 GASKET 2 REQ.
BOLT 8 REQ.
RD153-5004-0008 WASHER 8 REQ
TORQUE TO 350 IN LBS MAX
XEGR 925007-01 THROAT ASSY 1 REQD
SEAL 1 REQD
PACKING 8 REQD
GASKET 2 REQ.
(DRAIN PORT, REF)

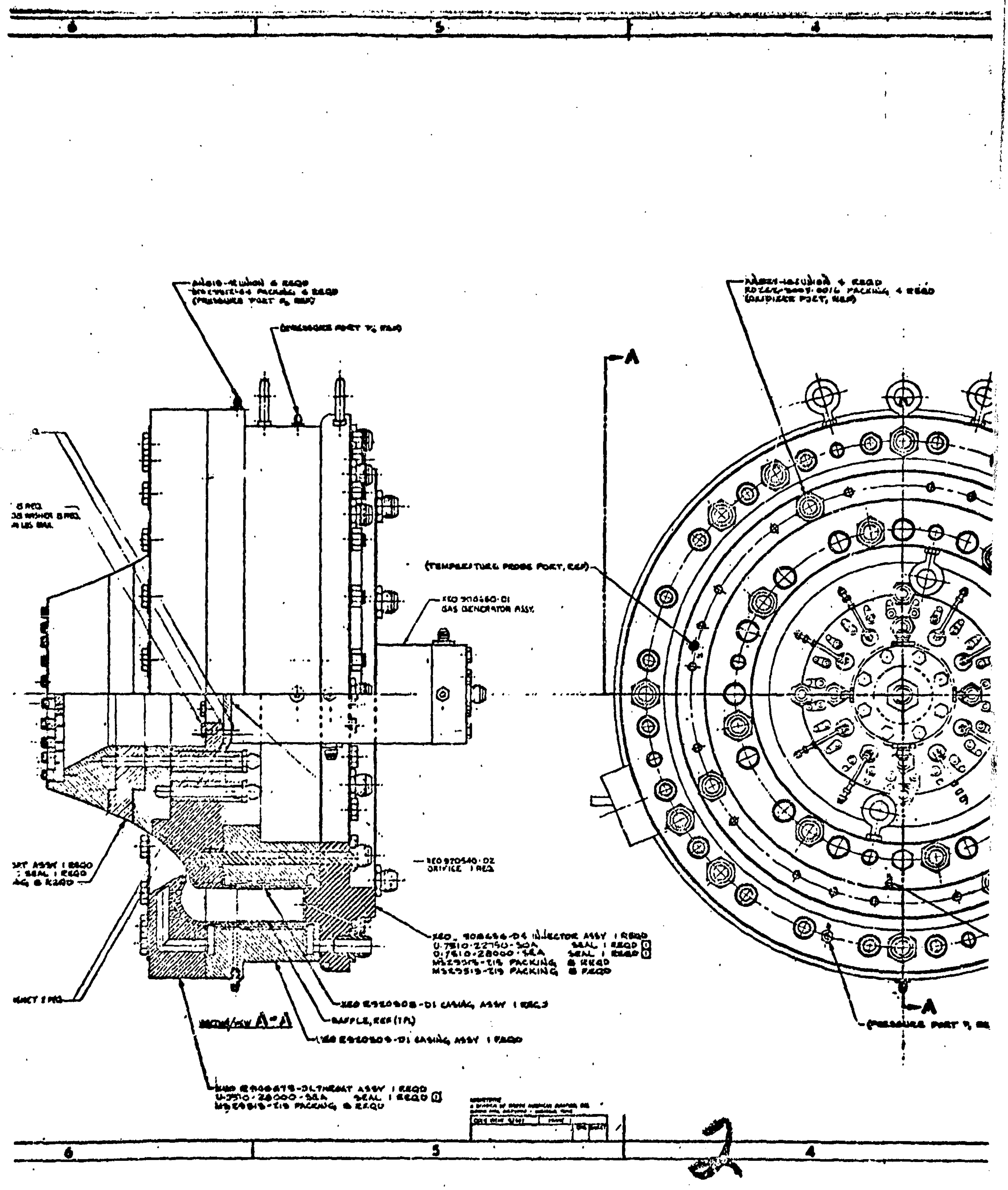
6
5
4
(TEMPERATURE PROBE PORT, REF)
REQ 970460-01 GAS GENERATOR ASSY.
REQ 970540-02 ORIFICE 1 REQ
BAFFLE, REF (TYP)
SECTION/VIEW A-A
A

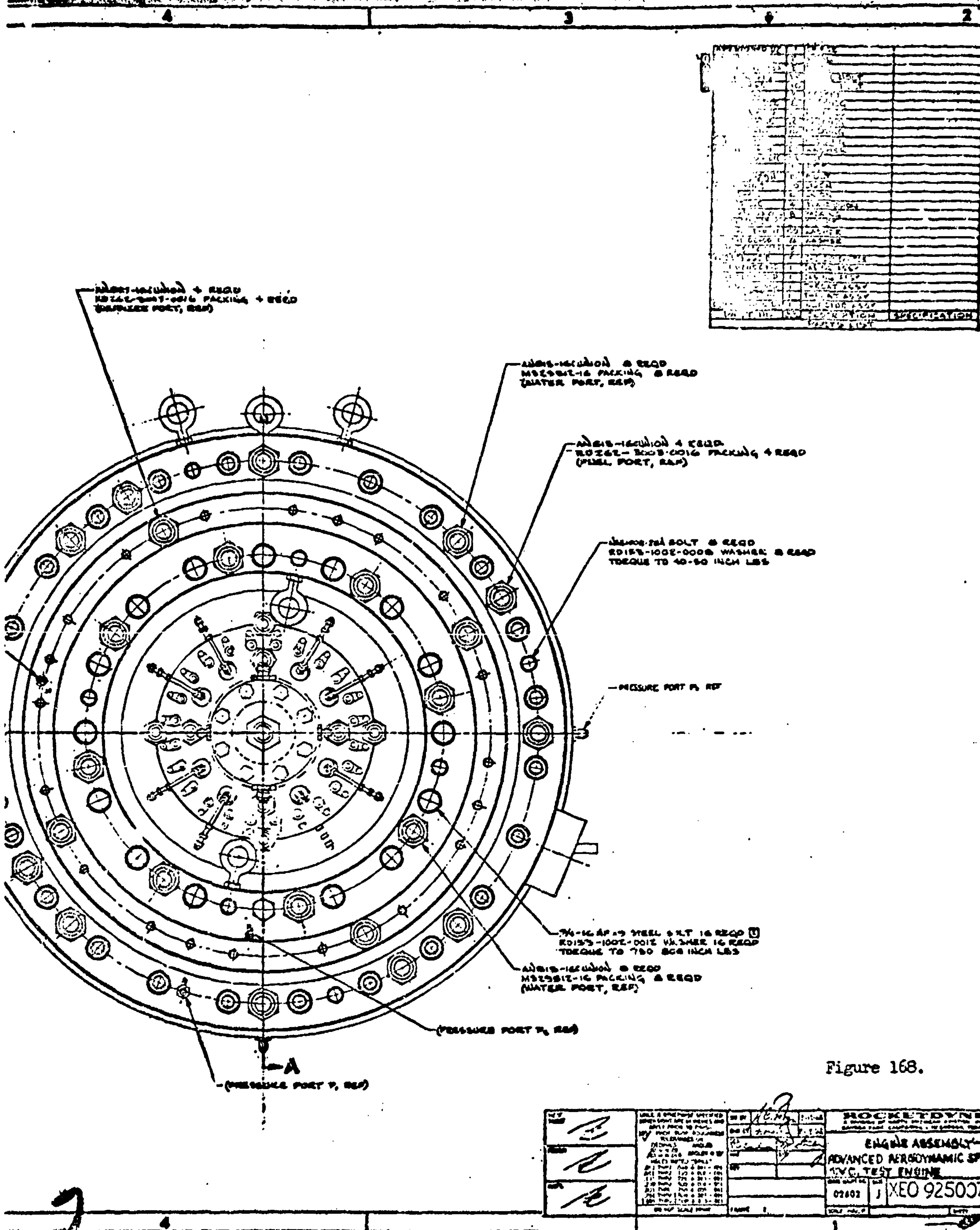
ROCKETDYNE
ENGINE ASSEMBLY—
ADVANCED AERODYNAMIC SPI
TVC TEST ENGINE
02602
J
XEO 925007
WATER PORT, REF
FUEL PORT, REF
TORQUE TO 40-50 INCH LBS
A

Figure 168.

(U) The stainless steel injector face (Fig. 169) contains three propellant injectant rings, the center ring (stainless steel) has the oxidizer orifices and is bounded on each side by fuel rings (copper). A like-on-like doublet orifice pattern is used. Distribution manifolds behind the injector rings are machined into the body and are fed through a series of drilled holes from the primary manifolds. The injector is divided into thirteen equal compartments by uncooled copper baffles brazed to the injector face.

(U) The water cooled casings and throat assemblies are constructed entirely of oxygen-free, high-conductivity copper. Coolant water enters the thrust chamber assembly through ports in the injector body. Four water inlets and four water outlets are provided for both the inner and outer sections of the chamber; each section having independent cooling circuits. The straight inner and outer chamber pieces have eight water manifolds at either end between 5/16inch axially drilled coolant holes. The cooling circuit in each throat piece consists of eight drilled manifolds (four inlets and four outlets) from which a series of smaller holes lead into circumferential passages. Water enters these small holes from the four manifolds, passes circumferentially along a 45-degree arc, and is discharged through adjacent outlet holes.

(U) A gas generator, designed to operate on the same propellants as the main chamber, supplies the secondary flow to the base region of the nozzle. It is designed to operate uncooled at a maximum steady-state temperature of approximately 1800 F, based upon hardware (347 CRES) limitations. The low-flow injector, which supplies secondary flow in the range from 1 to 2 percent of the primary flow, was used for the TVC testing. The injector flow pattern consists of four fuel streams impinging on one oxidizer stream. The porous plate base configuration is shown in Fig. 170.

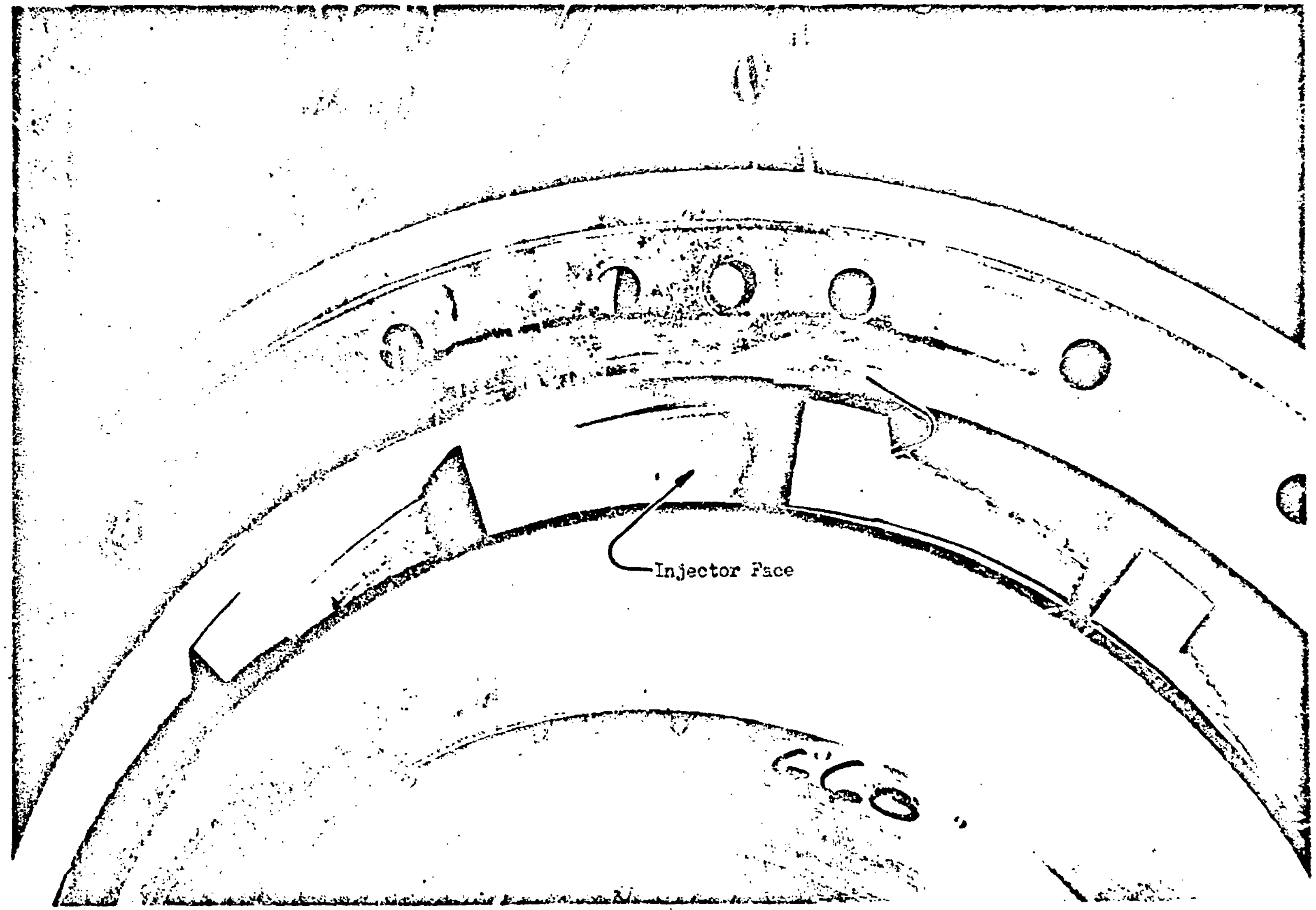

Figure 169. Injector and Chamber Baffles

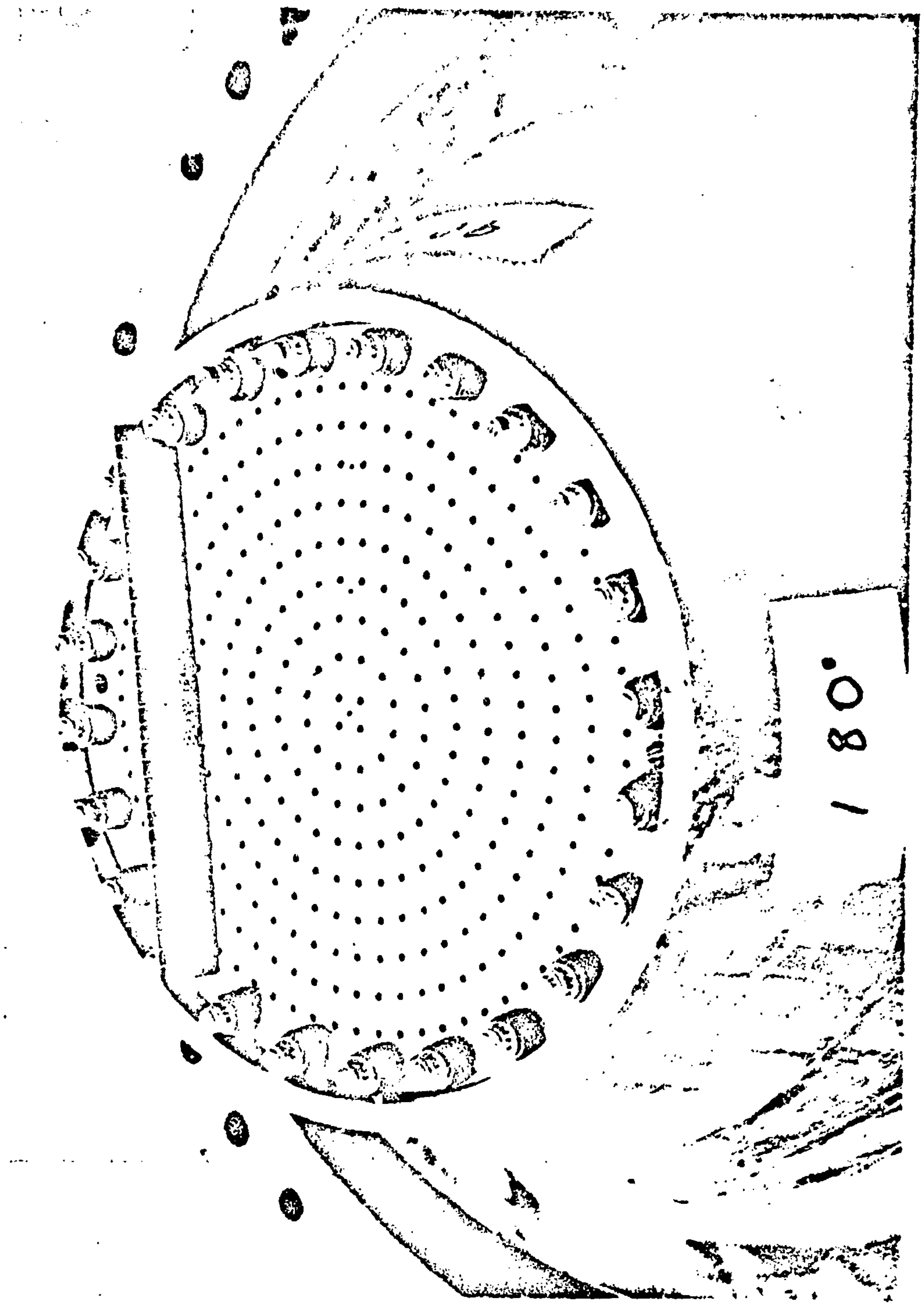

Figure 170. Porus Base Plate Configuration

(U) The uncooled portion of the nozzle is made up of three in-line removable stainless steel flow rings, two of which (Fig.168) contain TVC injection orifices in all four quadrants. The TVC flow is supplied to short circumferential manifolds in each quadrant though discrete feed lines (eight in all) so that the operation of one quadrant is independent from the other three. The manifolds serve as a common plenum for the drilled injection orifices in each quadrant.

(U) A total of six flow rings, two for each injection location, was fabricated. The second flow ring at each location was used to serve as a backup in the event of hardware damage, and to provide a means of extending the range of parametric variation if necessary. Both rings at $x/\ell = 0.25$ contain injection orifices in each quadrant. At each of the other locations, $x/\ell = 0.4$ and 0.7, one blank ring and one ring with TVC injection orifices was employed. The injection orifice pattern in each operational flow ring is illustrated in Fig. 166 and 167.

(U) As shown in these figures, most of the configurations contain five injection orifices in each quadrant and make up the five-port geometries discussed previously. During the testing, the ports indicated by the darkened symbols in these figures, were plugged with steel pins to provide three-port configurations. The assemblies that were used in the TVC testing at AEDC are shown in Fig. 171, and 172. Note that by providing the passages in the blank ring at $x/\ell = 0.4$ through to the flow ring at $x/\ell = 0.7$, this piece becomes an integral part of the system design. This procedure is advantageous since it simplifies the propellant feed system to the flow rings at $x/\ell = 0.4$ and 0.7 (both rings are supplied with TVC flow through the same feed lines); however, it also required that the operational rings at these locations be tested separately. A typical set of flow rings used in this testing (BE series) is shown in Fig. 173.

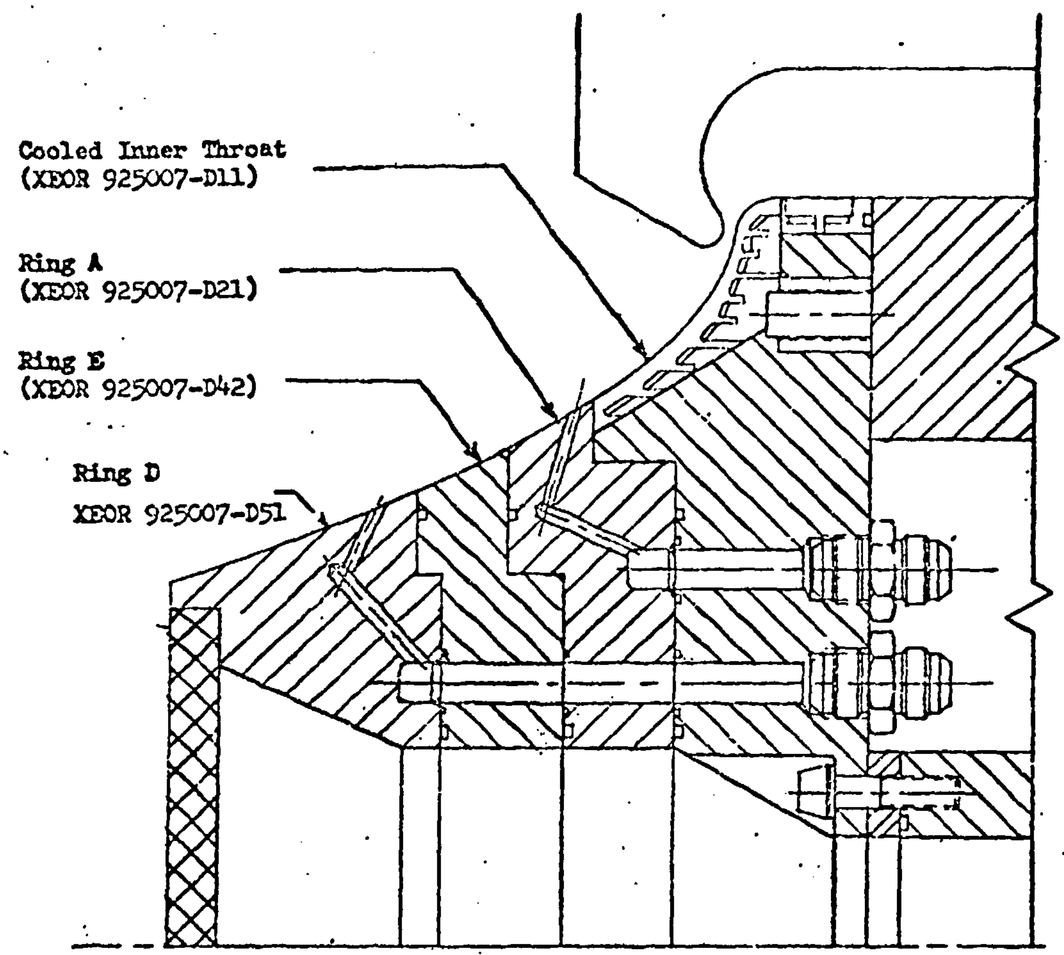

Figure 171. TVC Nozzle Ring Configuration Number 1

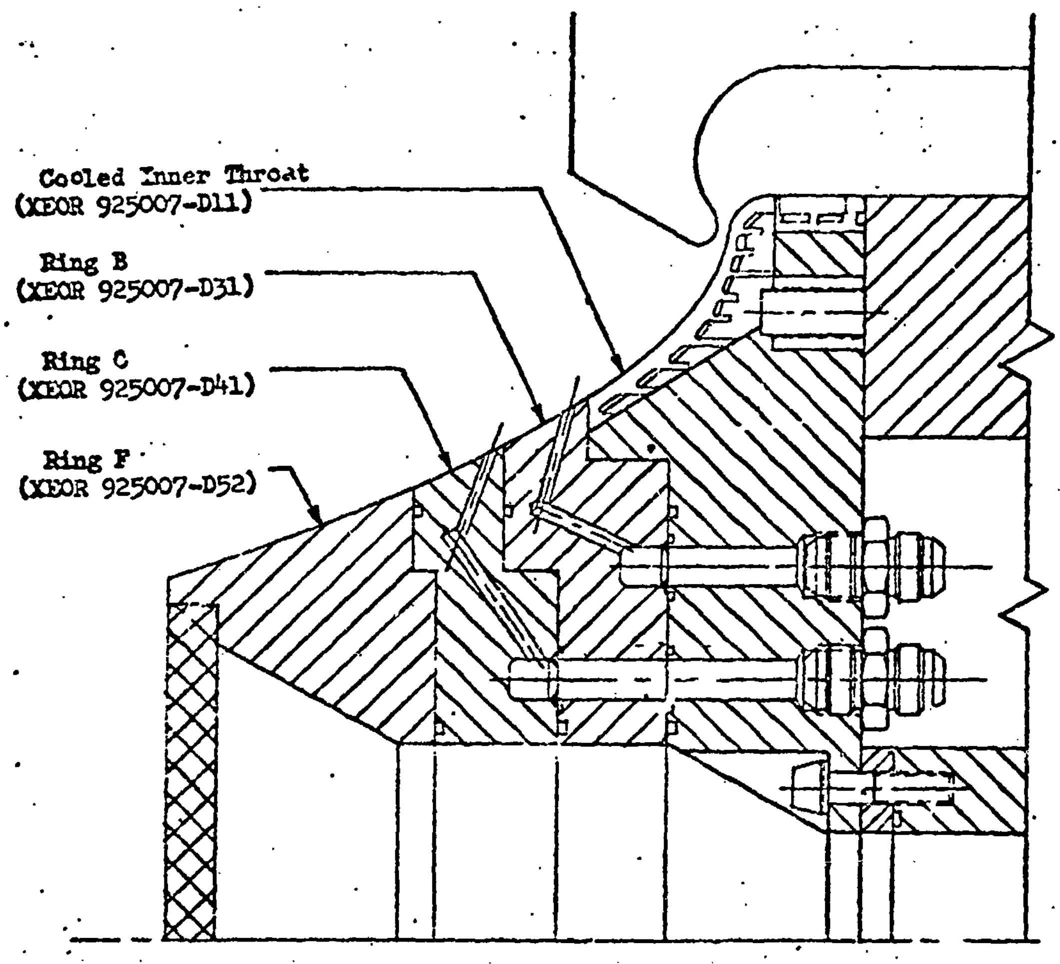

Figure 172. TVC Nozzle Ring Configuration Number 2

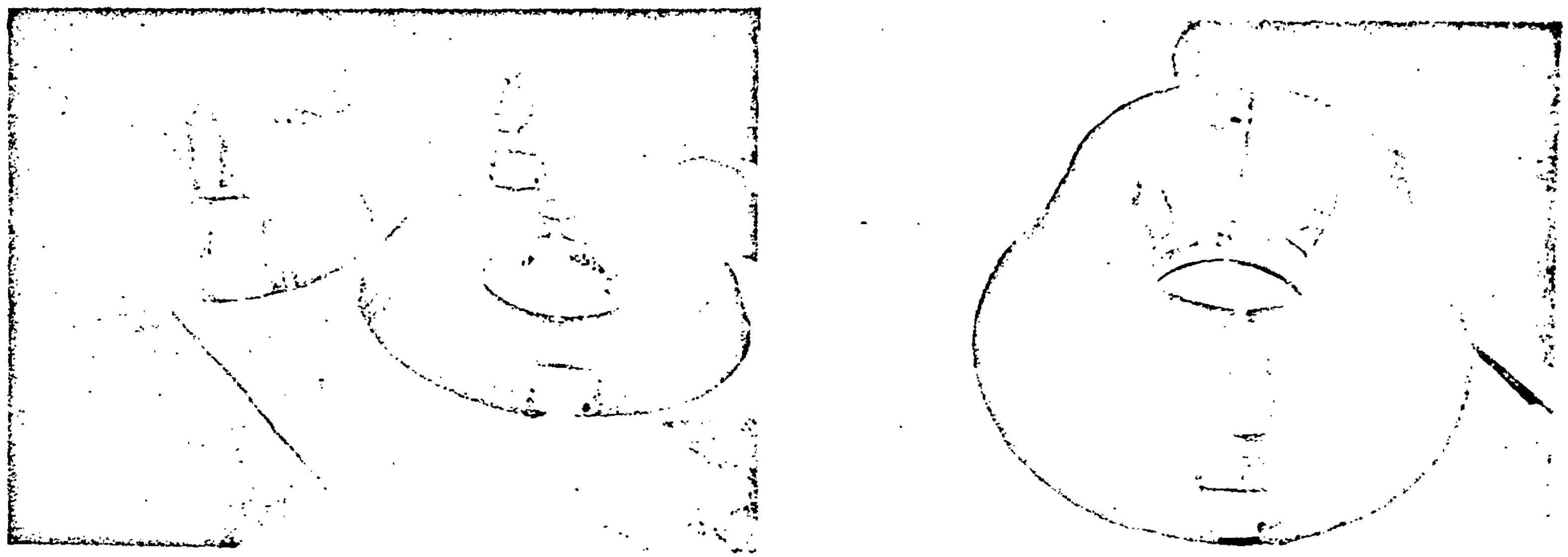

Figure 173. Typical TVC Flow Ring Assembly

(U) The thrust chamber was instrumented to provide information regarding primary and secondary chamber pressure, primary wall pressure, secondary cavity pressure, primary and secondary injection pressures, and secondary chamber temperature. The approximate location of this instrumentation is shown in Fig. 174 through 177. Facility instrumentation provided: force, weight flow, tank pressure, propellant line temperature, water temperature and cell pressure data. Approximate ranges for these parameters are indicated in Table 19 of Appendix 4.

(U) Test Procedure. TVC testing was conducted at design pressure ratio for this nozzle (PR≈290) in an altitude chamber (J-2 cell) at the Rocket Test Facility, AEDC. The operational characteristics of this facility are discussed in Ref. 20 . A six-component load cell arrangement was used to monitor the forces and moments induced by secondary injection during each test. The engine mounting assembly is illustrated schematically in Fig. 178, and a photo of the test installation is shown in Fig. 179. Only the flow-ring quadrants situated in the yaw plane were tested in any given "air-on" (test) period. The five port configurations were evaluated initially. The outer two orifices were then plugged (during the "air-on" period whenever possible) and these quadrants in the yaw plane were retested to evaluate the three port geometries. After the quadrants initially in the yaw plane were tested, both flow rings were rotated through an angle of 90 degrees and retested to evaluate the parameters contained in the remaining two quadrants.

(U) During each test, the engine was initially operated for 3-1/2 seconds without TVC flow to establish reference data for each parameter. Nitrogen tetroxide was injected for thrust vector control during the last 2-1/2 seconds of each firing. Nitrogen purges were used to clear all propellant lines. Primary oxidizer and fuel purges were operative continuously prior to ignition and came on immediately at engine shutdown. Secondary purges were on

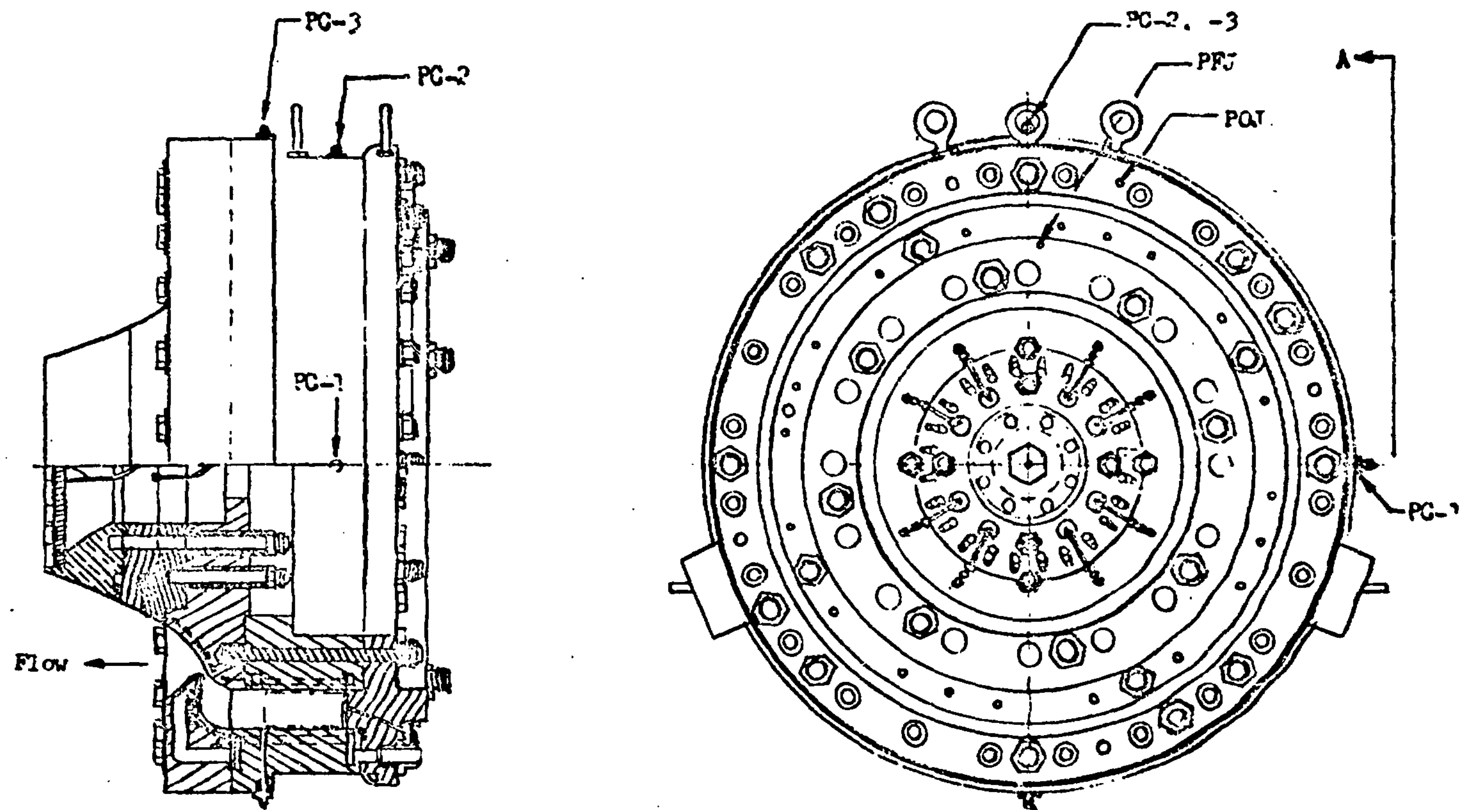

View "AA"

Looking Downstream

Figure 174. Main Engine Chamber Instrumentation

Press. Tap	Dist. Outer Edge X, Inches
PN-2	0.625
PN-3	1.500
PN-4	0.125
PN-5	0.125

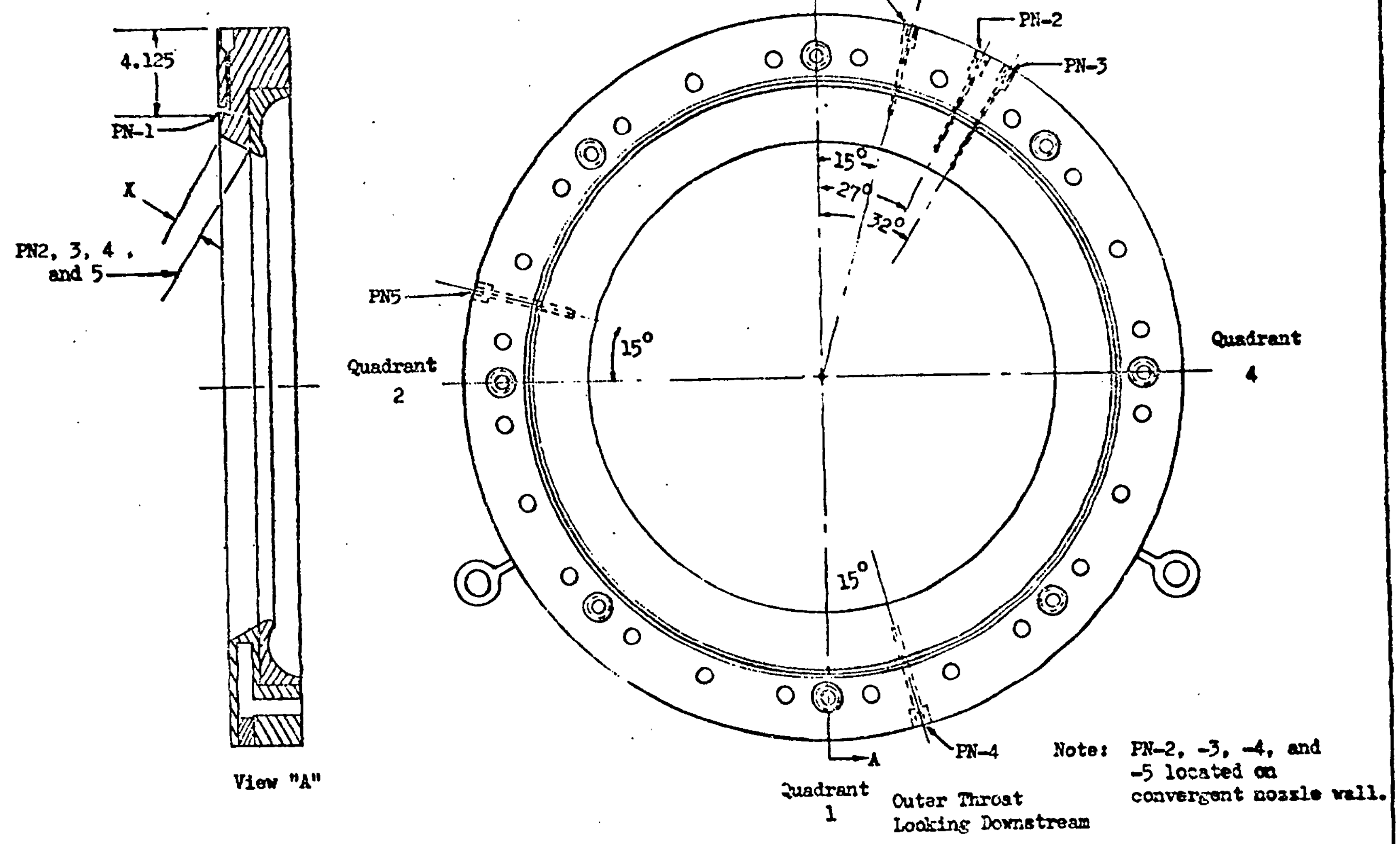

Figure 175. Aerospike Engine, Outer Throat Instrumentation

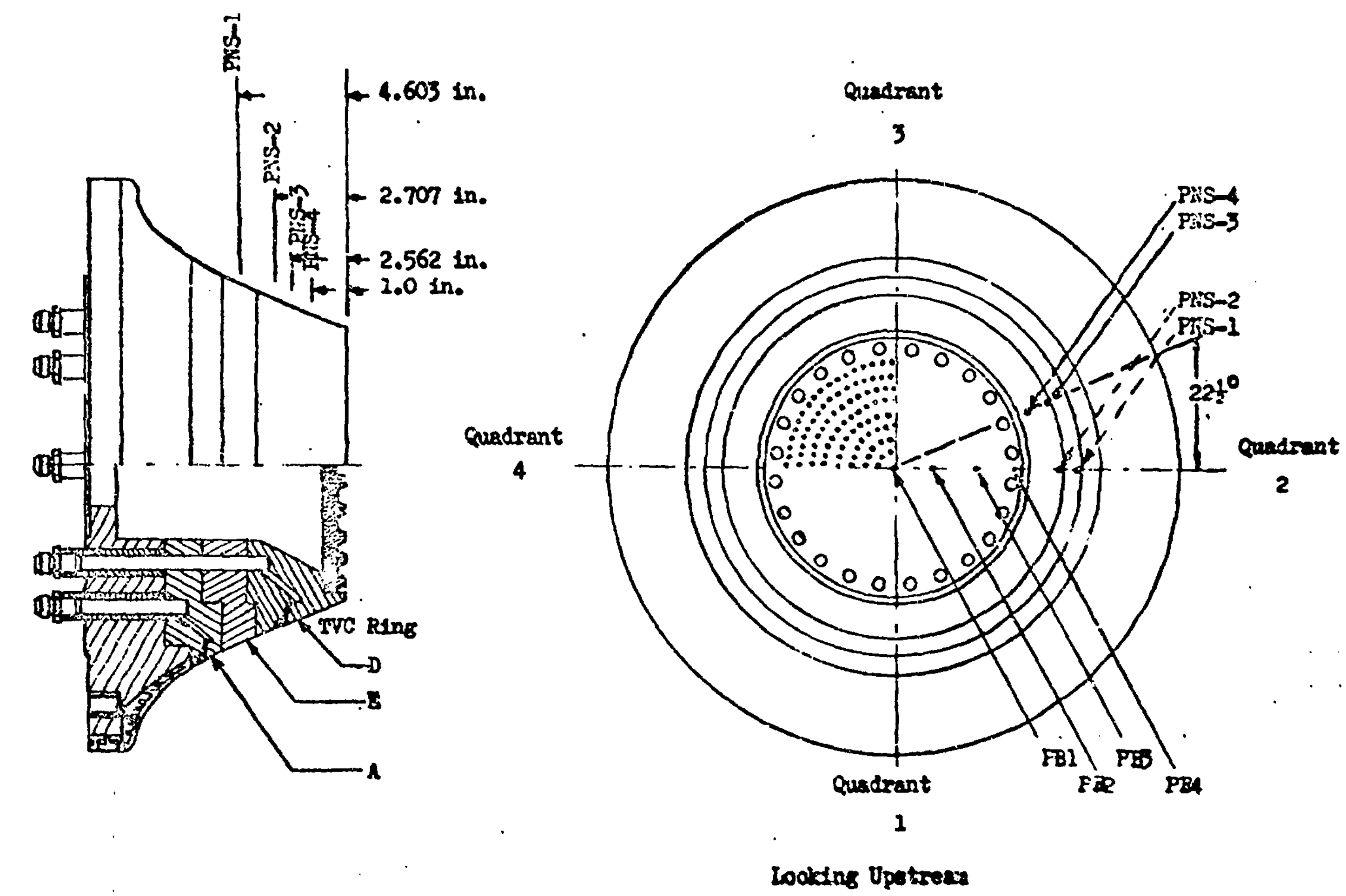

Figure 176. Engine Inner Nozzle Instrumentation

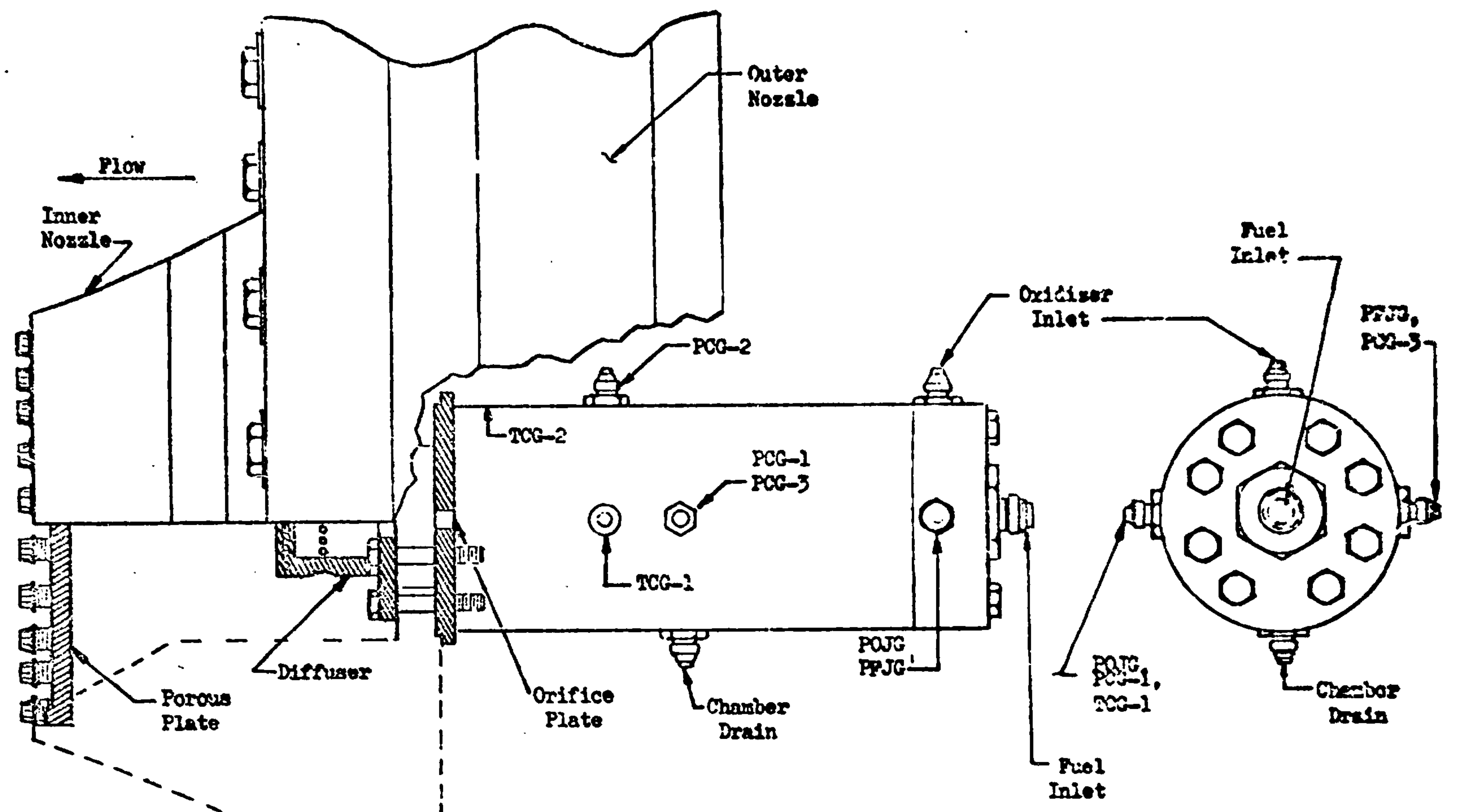

Note: POJG-1 and PFJG-1 are located in the lines leading to injector

Figur 177. Gas Generator Instrumentation

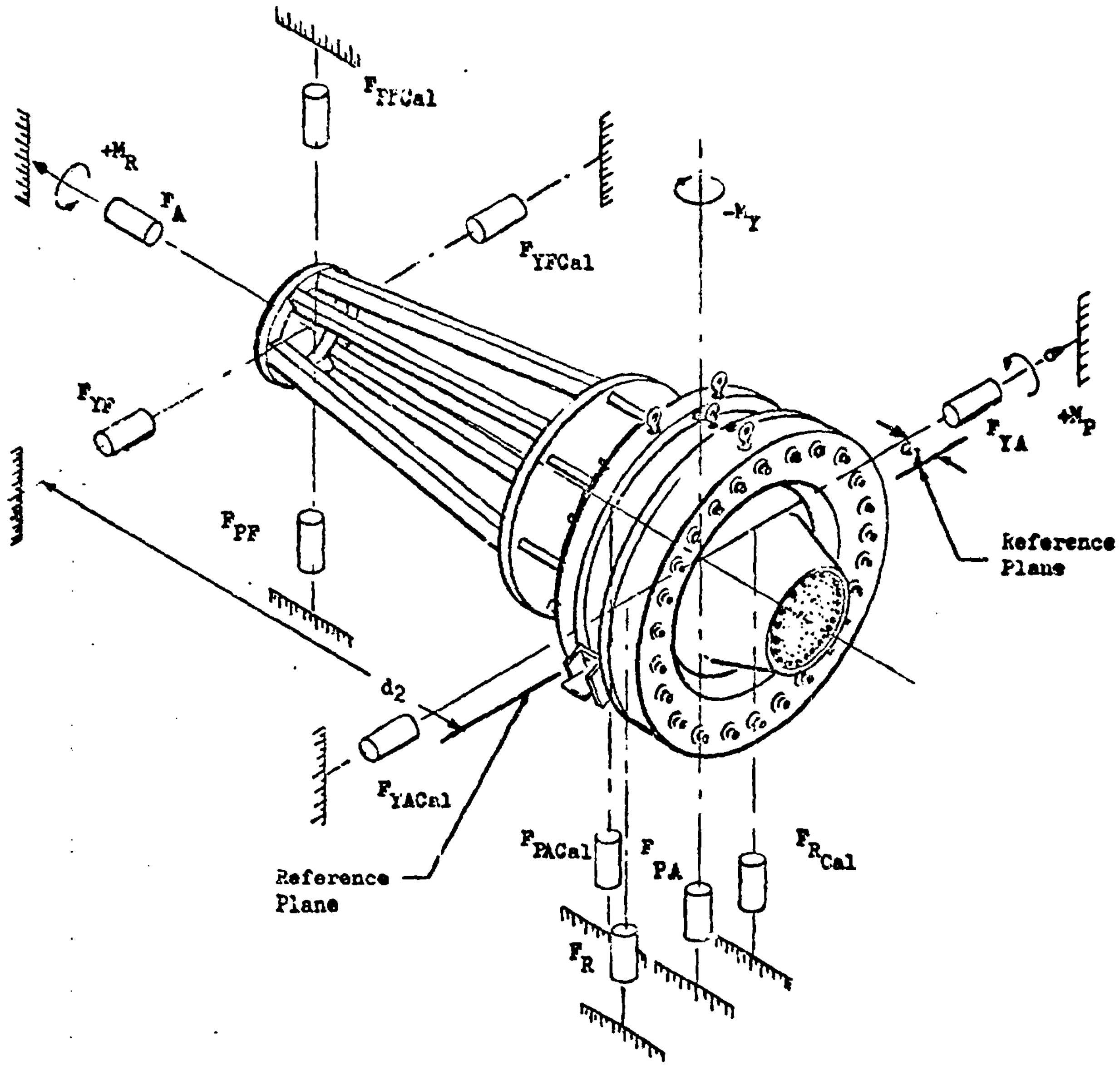

Figure 178. Six-Component Thrust Stand

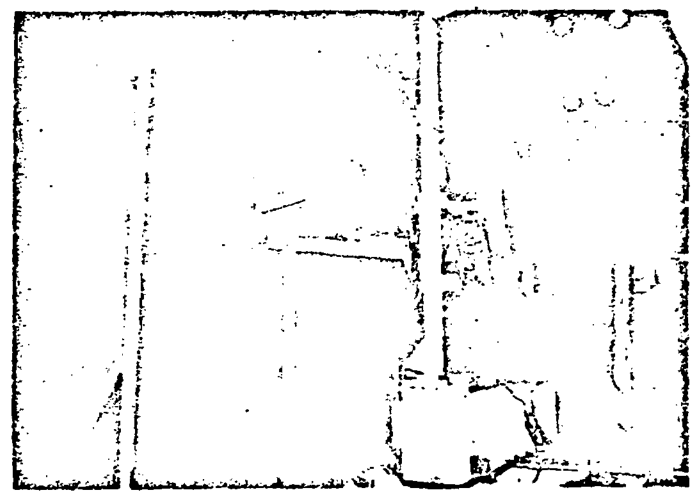

a. Side View

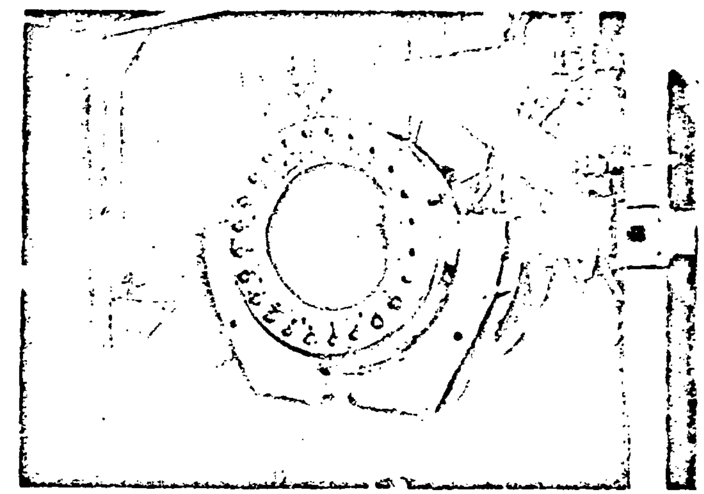

b. Front View

Figure 179. Test Installation at AEDC

prior to each run sequence, and were performed manually at the conclusion of the firing. A typical run sequence is illustrated in Fig. 180, and the facility flow system used for this testing is shown in Figs. 181 and 182.

(U) The planned altitude test schedule is shown in Table 12. Provisions to supply TVC flow to two quadrants during each test were incorporated into the plumbing system, and it was originally planned to test both TVC quadrants during 10-second firings as indicated in the table. However, after the program was initiated, it was found more desirable to shorten the test duration to 6 seconds, and test only one TVC quadrant in each firing. Hardware difficulties encountered during the checkout testing at Rocketdyne caused a delay in the program, so several of the originally planned tests were not conducted. Only the data in Table 12 denoted by an asterisk were obtained in the resulting abbreviated program.

Test Results

(U) Thirty-three firings were conducted over a series of five test periods. Performance and thrust vector control data from these firings are presented in Tables 13 and 14 respectively. A sea level data point (5-second duration test) obtained in the checkout testing conducted at Rocketdyne is included in Table 13. Four additional short-duration (two at 0.5 seconds and two at 1.5 seconds) checkout tests were conducted at Rocketdyne; however, performance data were not obtained and these tests are not tabulated. The measurements indicated in Table 19, Appendix 4 were used to compute reference nozzle performance without TVC, side forces and total control moments generated during TVC operation, and nozzle wall and base pressure profiles for each test. The methods by which these parameters were determined from the measured data obtained in this test program are discussed in Appendix 4.

NOTE: Propellant Flow Times Refer to Full Injection Pressure and not to Valve Openings.

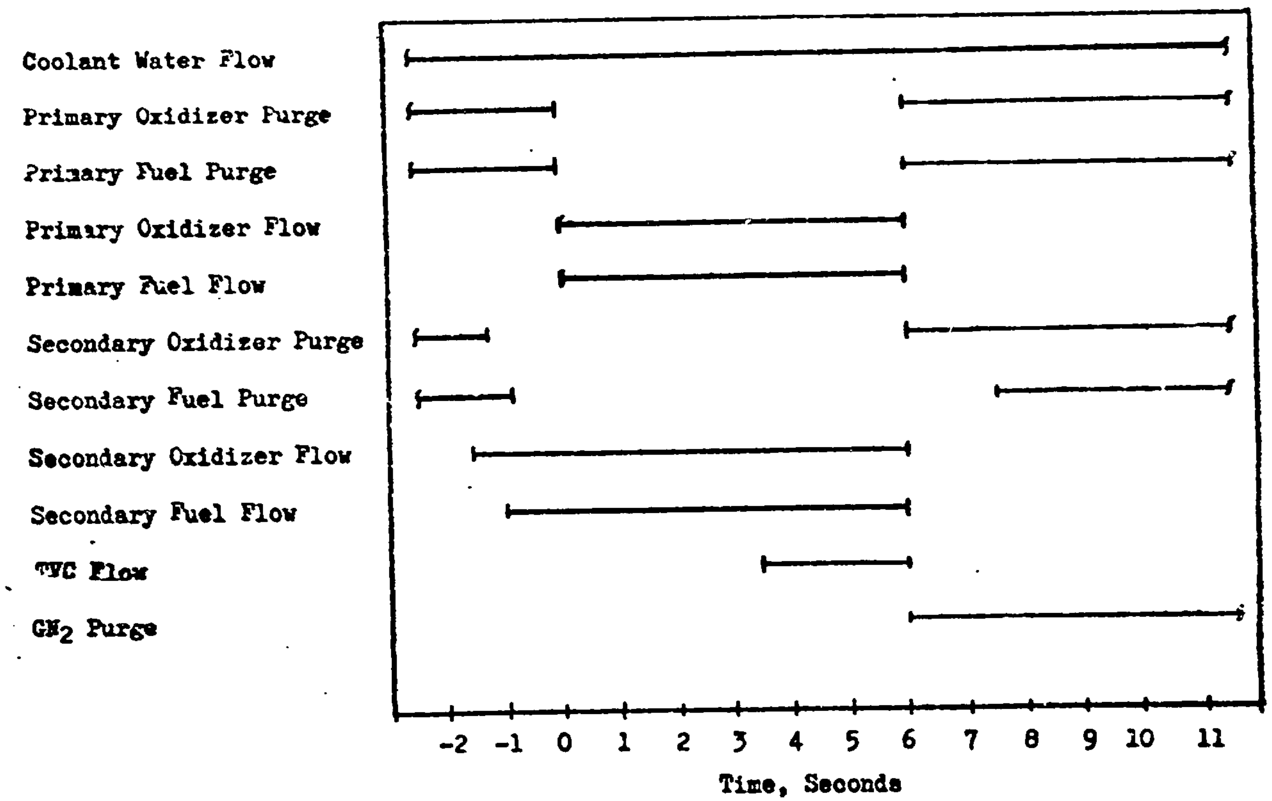

Figure 180. Test Sequence

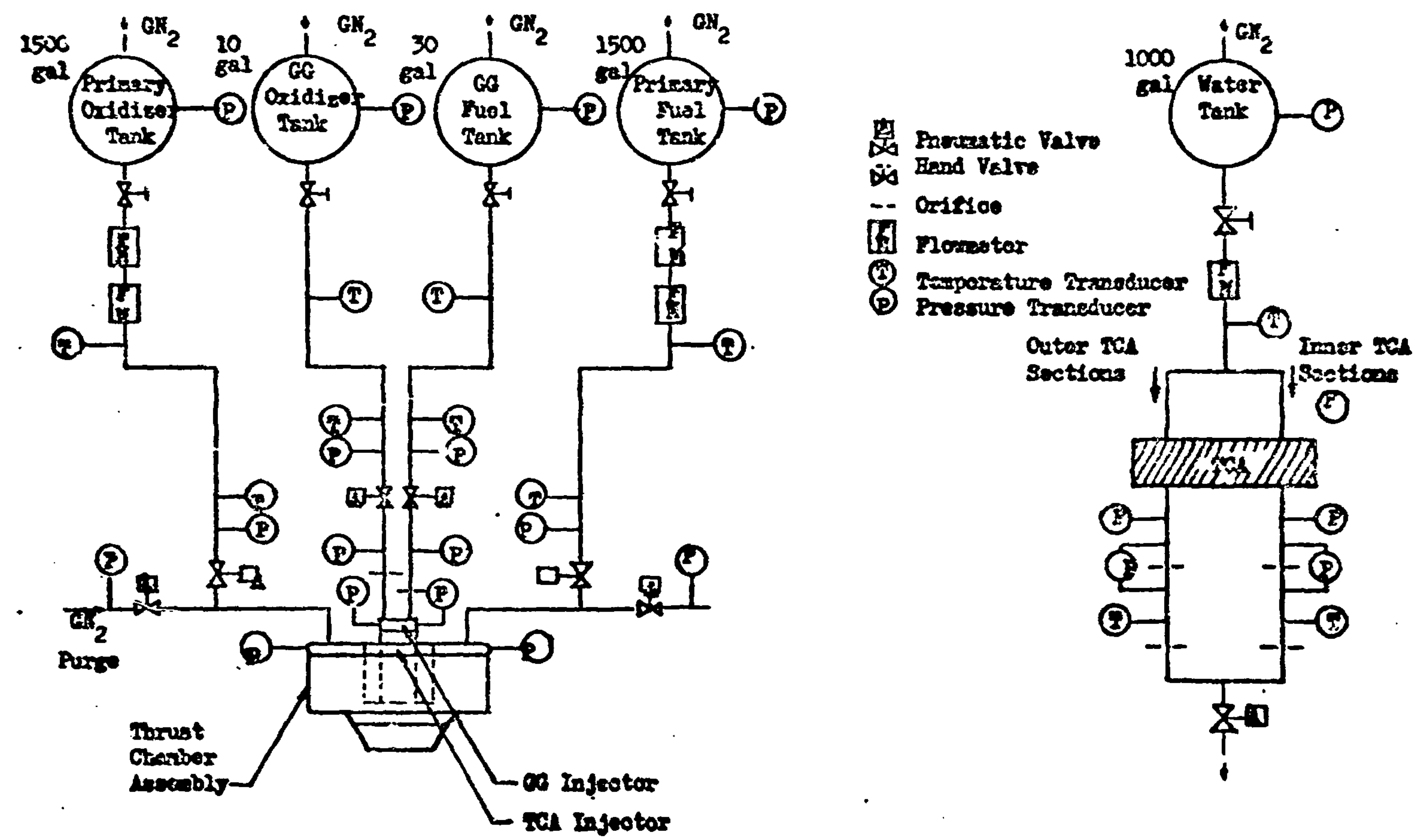

a. Primary and Secondary (GG) Propellant Supply System

b. Primary Engine Cooling Water Supply System

Figure 181. Facility Propellant and Cooling Water Supply System Instrumentation

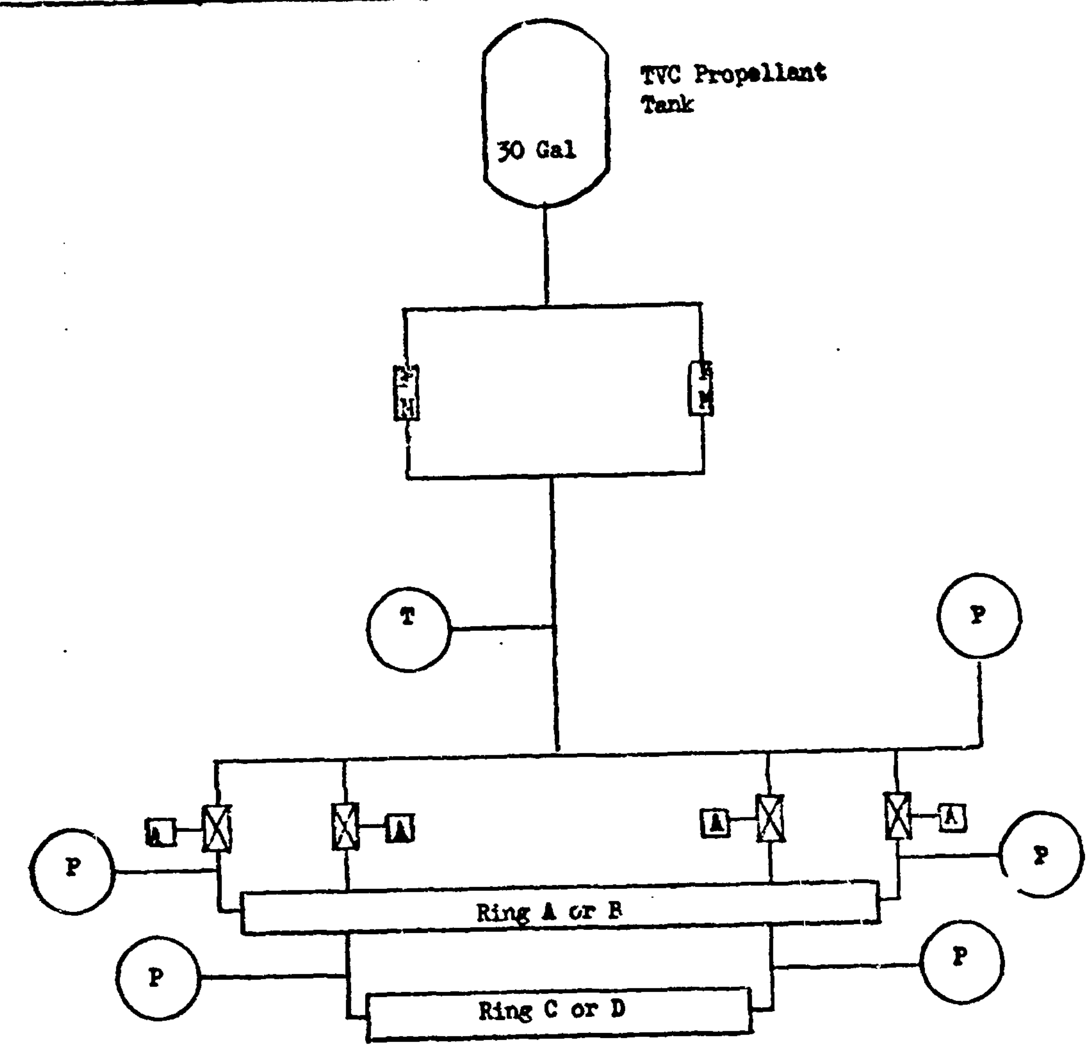

Figure 182 . TVC Propellant Supply System

Vacuum Period	Firing	Ring	Quadrant	TVC Flowrate, percent W_p	TVC Flowrate lb/sec	TVC Velocity ft/sec	TVC Supp Pressu lb/in^2
1a	1	-	CHECKOUT	TEST	-	-	-
	2	D1	2	13.33*	2.67	106	239
	3		4	8.00*	1.60	105	233
	4	A1	2	20.00*	4.00	105	234
	5		4	6.67*	1.33	110	263
1b	6	D2	2	8.00*	1.60	106	239
	7		4	8.00*	1.60	105	233
	8	A2	2	12.00*	2.40	105	234
	9		4	4.00*	0.80	110	263
	10		4	5.65*	1.13	156	559
	11		2, 4	11.68*, 4.13	2.34, 0.83	107, 108	249
2a	12	D1	1, 3	12.63* 14.20*	2.53, 2.84	100, 113	252
	13	A1	3, 1	13.30* 16.10*	2.66, 3.22	106, 109	233
2b	14	D2	1, 3	7.58* 8.51*	1.52, 1.71	100, 113	252
	15	A2	3, 1	7.98* 16.10*	1.60, 3.22	106, 109	233
	16		3, 1	3.99* 8.10*	0.80, 1.62	53, 55	52
	17		3, 1	5.65* 11.40*	1.13, 2.28	75, 77	114
	18		3, -	11.27* -	2.26, -	150, -	495
	19	D2	1	11.31*	2.27	170	1000
	20	-	-	-	-	-	-
	21	-	-	-	-	-	-
			REMOVE BASE PLATE				
2c	22	-	-	-	-	-	-
	23	-	-	-	-	-	-
3a	24	B1	4 2	7.05, 13.29	1.41, 2.60	108, 101	207
	25	C1	4 2	6.31, 14.20	1.26, 2.84	98, 101	215
3b	26	B2	4 2	4.23, 7.98	0.85, 1.56	108, 101	207
	27	C2	4 2	3.79, 8.52	0.76, 1.71	98, 101	215
	28		4 2	3.79, 8.52	0.76, 1.71	98, 101	215
	29		4 2	3.79, 8.52	0.76, 1.71	98, 101	215
	30		4 2	3.79, 8.52	0.76, 1.71	98, 101	215
	31		4 2	2.68, 6.04	0.54, 1.21	69, 72	105
	32		4 2	5.35, 12.08	1.08, 2.42	139, 143	439
4a	33	B1	3 1	13.93* 7.70*	2.79, 1.54	111, 103	243
	34		1 -	3.85, -	0.77, -	57, -	61
	35		1 -	5.45, -	1.09, -	73, -	115
	36		1 -	10.90, -	2.18, -	146, -	503
	37	C1	1 3	13.22* 13.46	2.65, 270	108, 107	227
4b	38	B2	3 1	8.35, 7.70	1.68, 1.54	111, 103	243
	39	C2	3 1	7.94, 8.06	1.59, 1.62	108, 107	227
5	40	A2	4 2	2.58, 7.30	0.52, 1.46	107, 108	149
	41		4 -	3.65,	0.74, -	156, -	349
	42		4 2	2.58, 7.30	0.52, 1.46	107, 108	149
	43	C2	4 2	2.37, 5.34	0.48, 1.07	98, 101	134
	44		4 2	1.68, 3.78	0.34, 0.76	69, 72	66
	45		4 2	3.34, 7.55	0.68, 1.51	139, 143	274
6	46	A2	3 1	4.99, 10.07	1.00, 2.01	106, 109	146
	47		3 1	3.53, 7.12	0.71, 1.43	75, 77	71
	48		3 -	7.04,	1.41, -	150, -	310
	49	C2	3 1	4.96, 5.05	0.99 1.01	108, 107	142

CONFIDENTIAL

...ity ...ec	TVC Supply Pressure lb/in^2	Primary Mixture Ratio	$\dot{W}_s/\dot{W}_p$ percent	Number of Ports	Ambient Pressure, psia	Duration, seconds
	-	1.8	*	-	0.65	6
	239		1.5	5		
	233					
	234					
	263					
	239			3		
	233					
	234					
	263					
	559					
108	249	1.6				10
113	252	1.8	1.5	5	0.65	10
109	233			5, 3		
113	252			3		
109	233					
55	52					
77	114					
-	495					6
	1000		1.5			
	-		0*	-		
	-		1.5*	-		
	-		1.5	-		
	-		0	-		
101	207	1.8	1.5	5	0.65	10
101	215					
101	207			3		
101	215					
101	215				7.27	
101	215				4.85	
101	215				3.64	
72	105				.65	
143	439					
103	243	1.8	1.5	5, 1	0.65	10
-	61			1		
-	115					
-	503					
107	227			5		
103	243			3, 1		
107	227			3		
108	149	1.8	1.5	3	0.65	10
-	349					
108	149	2.0				
101	134	1.8				
72	66					
143	274					
109	146	1.8	1.5	3	0.65	10
77	71					
-	310					
107	142					

CONFIDENTIAL

TABLE 12

PLANNED TVC TEST SCHEDULE

Note: Only those tests marked with an asterisk were accomplished.

2

1

TABLE 13

REFERENCE PERFORMANCE DATA* AT P_a = 0.7 psia

CONFIDENTIAL

Test	A^*	ϵ^*	C^*_s	C^*_p	$\eta_{C^*_s}$	$\eta_{C^*_p}$	η_{I_s}	$\eta_{I_{s_{top}}}$	C_T	$C_{T_{top}}$
1**	15.750	23.6	-	5104	-	0.897	0.835	0.836	0.932	0.932
BA01	15.407	24.1	-	4999	-	0.891	0.846	0.846	0.949	0.949
BA02			2790	5003	0.650	0.892	0.844	0.840	0.946	0.942
BA03			2716	5004	0.633	0.890	0.841	0.838	0.948	0.942
BA04			2680	4978	0.625	0.885	0.840	0.837	0.953	0.946
BA05			2750	4983	0.641	0.886	0.844	0.841	0.956	0.949
BB06	15.407	24.1	2712	4948	0.633	0.878	0.846	0.842	0.957	0.959
BB07			2822	4944	0.658	0.877	0.843	0.840	0.965	0.958
BB08			2728	4963	0.636	0.880	0.844	0.841	0.963	0.956
BB09			2655	4943	0.619	0.876	01840	0.836	0.963	0.954
BB10			2763	4938	0.644	0.875	0.845	0.841	0.969	0.951
BB11			2720	4940	0.634	0.875	0.847	0.844	0.972	0.965
BC12	15.825	23.4	2396	4992	0.559	0.883	0.840	0.836	0.955	0.947
BC13			2472	5011	0.577	0.886	0.843	0.839	0.953	0.947
BC14			2499	5023	0.583	0.888	0.844	0.840	0.954	0.946
BC15			2539	5023	0.592	0.888	0.843	0.839	0.953	0.945
BC16			2562	5009	0.597	0.886	0.841	0.837	0.953	0.945
BC17			-	5027	-	0.889	0.847	0.847	0.953	0.953
BC18			2569	5028	0.599	0.889	0.843	0.839	0.952	0.944
BD19	15.999	23.2	2741	5014	0.637	0.885	0.839	0.836	0.951	0.945
BD20			3178	5063	0.738	0.893	0.846	0.843	0.949	0.944
BD21			3113	5059	0.723	0.892	0.844	0.842	0.949	0.944

*Performance corrected for heat loss
**Rocketdyne sea level test (Performance Data Computed for P_a = 13.7 psia)

TABLE 13

(Continued)

CONFIDENTIAL

Test	P_c	P_c/P_a	P_{c_s}	F_{A_c}	$\dot{w}_s/\dot{w}_p$	$\dot{w}_T$	MR_p	MR_s	I_s
1**	197.2	14.4	-	3932	0	19.58	1.54	-	200.8
BA01	196.9	281	-	5275	0	19.70	2.10	0	267.8
BA02	197.5	282	106.9	5333	0.0162	20.05	2.08	0.100	266.0
BA03	197.7	282	106.2	5334	0.0164	20.1[illegible]	2.07	0.099	265.2
BA04	197.1	282	104.5	5339	0.0163	20.15	2.07	0.098	265.0
BA05	197.4	282	106.3	5368	0.0162	20.16	2.07	0.099	266.3
BB06	197.4	282	107.6	5414	0.0165	20.31	2.04	0.094	266.6
BB07	197.4	282	110.1	5398	0.0162	20.30	2.04	0.095	265.9
BB08	197.6	282	108.5	5389	0.0166	20.25	2.03	0.097	266.1
BB09	197.6	282	107.3	5384	0.0168	20.34	2.02	0.098	264.7
BB10	197.4	282	109.7	5415	0.0165	20.34	2.02	0.097	266.2
BB11	197.5	282	109.1	5431	0.0166	20.34	2.01	0.097	267.0
BC12	195.4	279	97.3	5406	0.0168	20.45	1.99	0.103	264.4
BC13	196.3	280	101.7	5419	0.0170	20.40	1.99	0.098	265.6
BC14	196.3	280	102.5	5420	0.0170	20.40	1.99	0.099	265.7
BC15	196.4	280	103.4	5422	0.0168	20.42	1.99	0.100	265.5
BC16	196.2	280	103.8	5420	0.0167	20.45	1.99	0.101	264.9
BC17	196.1	280	-	5368	0	20.04	1.99	-	267.9
BC18	196.1	280	103.8	5412	0.0167	20.39	1.99	0.100	265.4
BD19	195.6	279	102.5	5442	0.0153	20.60	1.97	0.115	264.2
BD20	196.2	280	110.0	5442	0.0143	20.43	1.95	0.113	266.4
BD21	196.0	280	109.3	5440	0.0145	20.44	1.95	0.113	266.1

*Performance corrected for heat loss
**Rocketdyne sea level test (Performance Data Computed for P_a = 13.7 psia)

TABLE 14

SITVC PERFORMANCE DATA

CONFIDENTIAL

Test	x/ℓ	n	$\Delta\psi$	λ	θ	ν_J	F_v*	F_a	K_T
BA02	0.70	5	15	45	0	106	5483	104	355.3
BA03	0.70	3	30	45	0	102	5475	63	144.6
BA04	0.25	5	15	45	0	102	5480	141	479.9
BA05	0.25	5	15	45	0	99	5509	68	-181.7
BB06	0.70	3	15	45	0	112	5556	60	459.6
BB07	0.70	3	30	45	0	102	5546	61	113.3
BB08	0.25	3	15	45	0	115	5533	82	357.6
BB09	0.25	3	15	45	0	109	5532	50	- 17.1
BB10	0.25	3	15	45	0	157	5565	55	- 31.2
BB11	0.25	3	15	45	0	113	5579	88	437.2
BC13	0.70	5	15	60	0	100	5561	81	645.5
BC14	0.70	5	15	45	11	136	5562	128	344.0
BC15	0.25	5	15	45	0	118	5563	122	- 57.2
BC16	0.25	3	15	45	0	132	5562	116	165.3
BD19	0.70	3	15	60	0	90	5570	59	277.3
BD20	0.70	3	15	45	11	109	5575	77	218.3
BD21	0.25	3	15	45	0	108	5565	74	160.5
BE30	0.25	5	15	45	11	95	5703	117	-263.7
BE31	0.25	1	-	45	0	95	5670	48	111.0
BE33	0.40	5	15	60	0	131	5774	110	4.2

*Measured vacuum thrust (not corrected for heat loss)

TABLE 14

(Continued)

CONFIDENTIAL

Test	ΔF_A	$\dot{W}_{TVC}$	$\dot{W}_{TVC}/\dot{W}_e$	F_s/F_v	F_{oc}/F_v	$\Delta F_A/F_T$	$\Delta I_s/I_s$	K_s	K_M
BA02	44	2.712	0.135	0.0190	0.0065	0.0080	0.112	0.140	0.048
BA03	22	1.651	0.082	0.0115	0.0024	0.0040	0.072	0.140	0.029
BA04	82	4.136	0.205	0.0257	0.0084	0.0150	0.153	0.125	0.041
BA05	36	1.280	0.064	0.0125	0.0030	0.0065	0.054	0.194	-0.047
BB06	26	1.693	0.083	0.0108	0.0076	0.0047	0.073	0.129	0.092
BB07	25	1.637	0.081	0.0110	0.0019	0.0045	0.070	0.137	0.023
BB08	54	2.771	0.137	0.0148	0.0060	0.0098	0.112	0.109	0.044
BB09	25	0.838	0.041	0.0090	0.0003	0.0045	0.035	0.218	-0.007
BB10	25	1.213	0.060	0.0099	0.0005	0.0045	0.052	0.166	-0.008
BB11	43	2.745	0.135	0.0158	0.0072	0.0077	0.112	0.117	0.053
BC13	44	2.608	0.128	0.0146	0.0107	0.0079	0.106	0.114	0.084
BC14	49	3.483	0.171	0.0230	0.0057	0.0088	0.138	0.135	0.033
BC15	39	2.965	0.145	0.0219	0.0010	0.0070	0.121	0.151	-0.007
BC16	28	3.944	0.193	0.0209	0.0031	0.0050	0.157	0.108	0.016
BD19	15	1.392	0.068	0.0106	0.0046	0.0027	0.061	0.157	0.068
BD20	13	1.689	0.083	0.0138	0.0036	0.0023	0.074	0.167	0.043
BD21	24	1.629	0.080	0.0133	0.0027	0.0043	0.070	0.167	0.034
BE30	29	2.40	0.116	0.0205	0.0043	0.0051	0.100	0.176	-0.037
BE31	6	1.40	0.068	0.0085	0.0018	0.0011	0.063	0.125	0.026
BE33	29	3.36	0.161	0.0190	0.0001	0.0050	0.134	0.118	0.001

Note: Six tests (BD22 through BD29) were invalid because of broken load cell linkage. Test BE32 was invalid because of instability.

(U) Post test inspection of the engine after the BB test series revealed that a substantial water leakage along the contour occurred during this test series, and, to a lesser degree, during the BA test series. Therefore, the reference performance data listed in Table 13 for these tests is somewhat questionable. However, the TVC performance data for these tests are consistent with the trends established by the data obtained in subsequent testing after the water leakage along the contour was eliminated. Thus, the TVC performance data for the BA and BB test series in Table 14 are felt to be of good quality. A failure in the aft yaw plane load cell which occurred during test BD22 resulted in inaccurate side and axial thrust data for firings BD22 through BD29, and therefore, data from these firings have been excluded from Tables 13 and 14. A low frequency (≈ 180 cpm) instability with peak-to-peak amplitude of approximately 60 psia occurred during test BE32 which resulted in moderate hardware damage. Post test inspection of the hardware indicated that portions of the chamber baffles and throat region had been eroded (Fig.183). Hence, the TVC data for test BE31 (in Table 14) is also considered questionable. Reference and LITVC performance trends established by the remaining data presented in Tables 13 and 14 are discussed in the following paragraphs.

(U) Reference Performance. Except for the sea-level firing, all of the data listed in Table 13 were obtained from a 0.5-second time slice approximately 3 seconds after the beginning of the run. Because of the shorter duration of the sea-level firing (five seconds), TVC flow was injected during the final 2 seconds of the test, and performance data were averaged over a 0.5-second time interval just prior to actuation of the thrust vector control system. Time variations of critical parameters for a typical altitude test without TVC are shown in Fig. 184. It can be seen that all performance parameters reach essentially stable values after approximately 2.5 seconds of test operation.

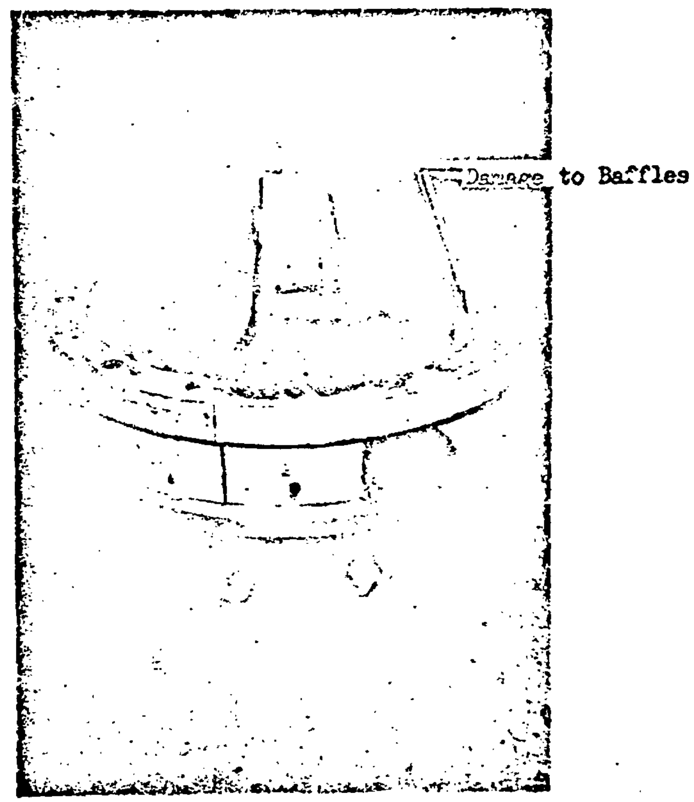

a. Damage to Chamber Baffles

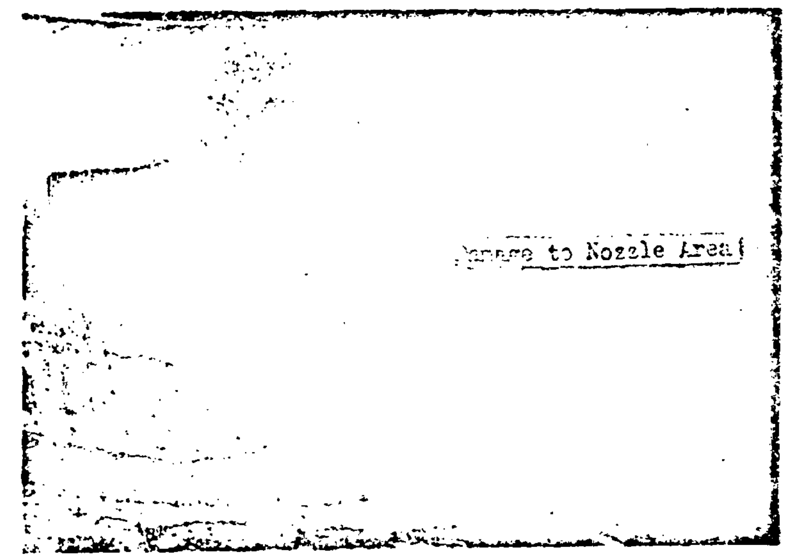

b. Damage to Nozzle

Figure 183. Hardware Damage Incurred During Test BE32

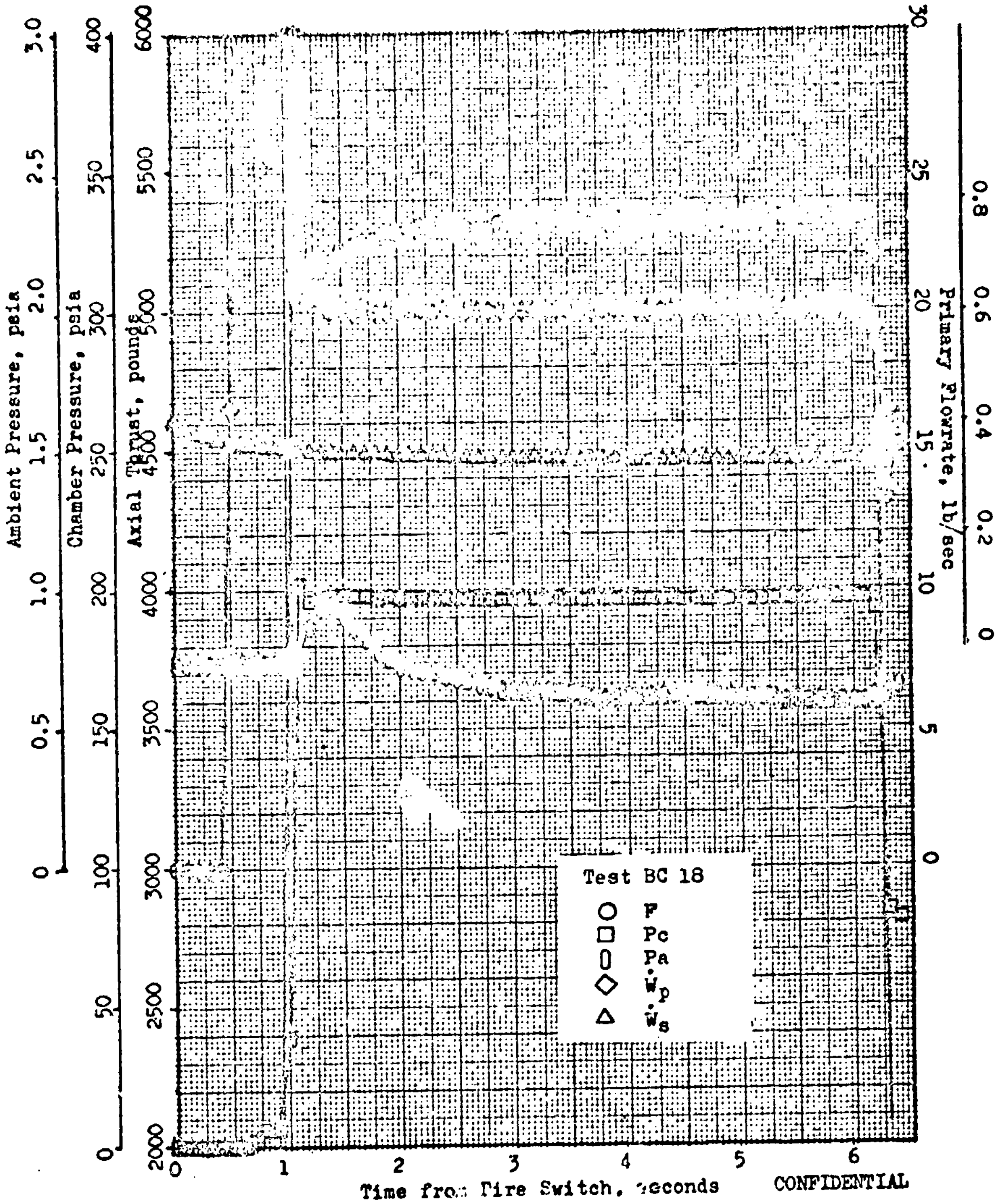

Figure 124. Critical Parameters for a Reference Test (No TVC) with Secondary Flow

(C) Average thrust efficiency of the nozzle is 95.1 percent without secondary flow from Table 13. This value is 0.8 percent above the predicted nozzle efficiency without secondary flow as seen by comparison with Fig. 150 page 275. The difference could arise from any of the following factors:

1 Experimental inaccuracies
2) Primary inviscid flow field analysis
3) Boundary layer analysis
4) Kinetics analysis
5) Base pressure estimate
6) Downstream combustion phenomena
7) Differences in geometry between analytical model and actual hardware
8) Differences in overall gas properties between the analytical model and the actual hardware

(C) Consideration of each of these factors indicated items (7) and (8) to be the most probable causes for the difference noted.

(C) A comparison of the nozzle and specific impulse efficiencies between the Rocketdyne sea level test and the AEDC altitude tests is represented in the table below. A decrease of only 2 percent in nozzle efficiency and 1 percent

TABLE 15

COMPARISON OF SEA LEVEL AND ALTITUDE PERFORMANCE, $\dot{W}_s = 0$

Test	P_c/P_a	$\eta_{C^*_p}$	η_{I_s}	C_T	MR_p	P_c, psia
1	14.4	0.897	0.836	0.932	1.54	197.2
BA01	281	0.891	0.846	0.949	2.10	196.1
BC17	280	0.889	0.847	0.953	1.99	196.9

in specific impulse efficiency was experienced with operation between 100 percent and 5 percent of design pressure ratio. It should be noted that the mixture ratio was significantly different for the sea level test, and chemical reaction effects could be a factor causing a relatively higher nozzle efficiency for the lower mixture ratio. The results clearly show a high degree of altitude compensation was obtained.

(C) LITVC Performance. Liquid N_2O_4 performance data were obtained from a 0.5-second average time slice near the end of the firing after all critical parameters were essentially stabilized. Time variations of these parameters during a typical test with TVC are shown in Fig.185. As seen, these data stabilized approximately 0.5-second after signaling for the injection of TVC flow. Basic test results are presented as curves of F_s/F_v, F_{oc}/F_v, and $\Delta F_A/F_v$ vs $\dot{W}_{TVC}/\dot{W}_e$ in Fig.186 through 191. Each of these parameters is defined and discussed in Appendix 4. The off-center force ratio represents the dimensionless moment about the reference set of axis used to define the nozzle contour design (Fig.146, page 270).

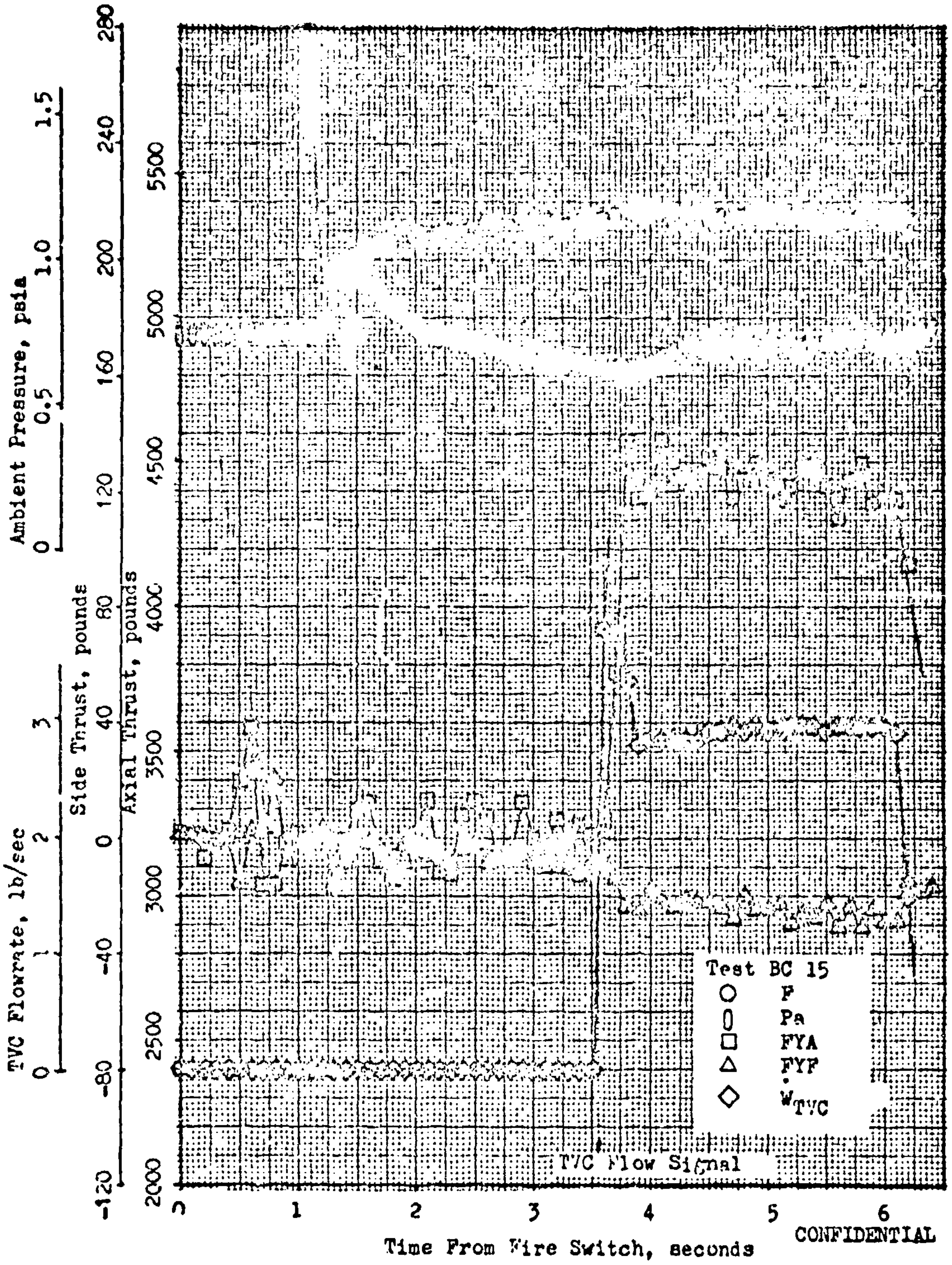

Figure 185. Time Variation of Critical SITVC Parameters

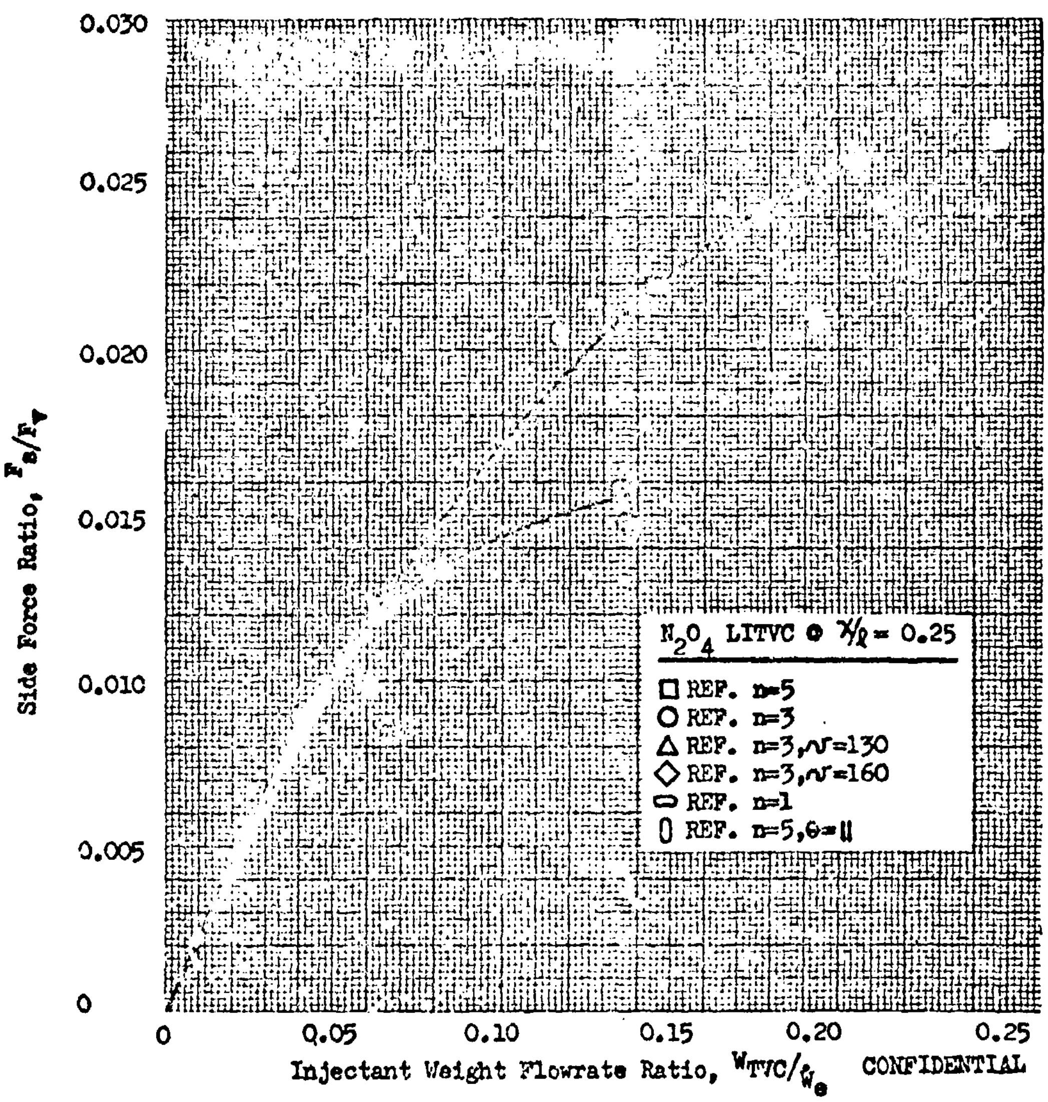

Figure 186. Side Force Ratio vs Flowrate Ratio for Liquid Injection at $X/\ell = 0.25$

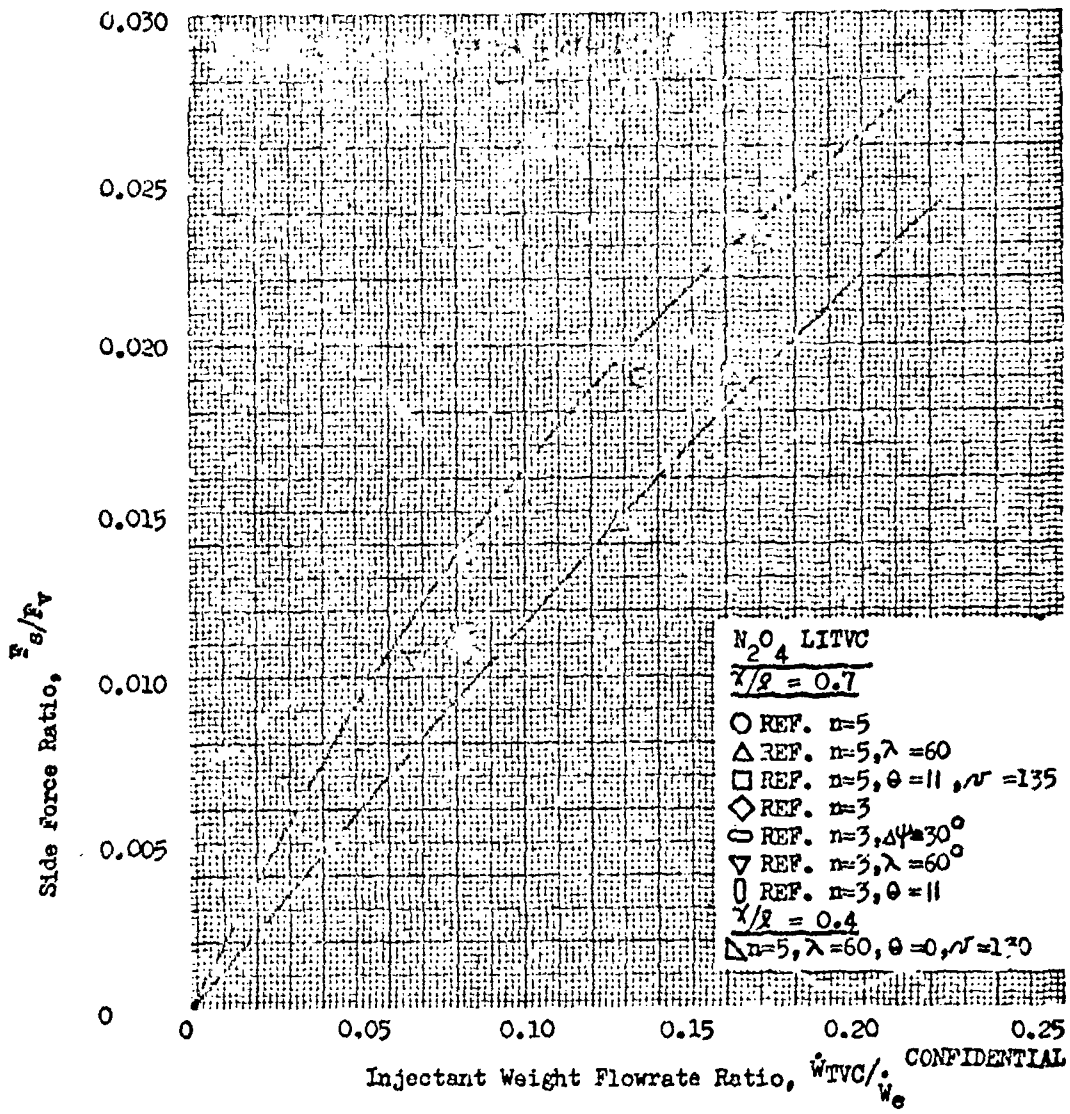

Figure 187. Side Force Ratio vs Flowrate Ratio for Liquid Injection at X/ℓ = 0.4, 0.7

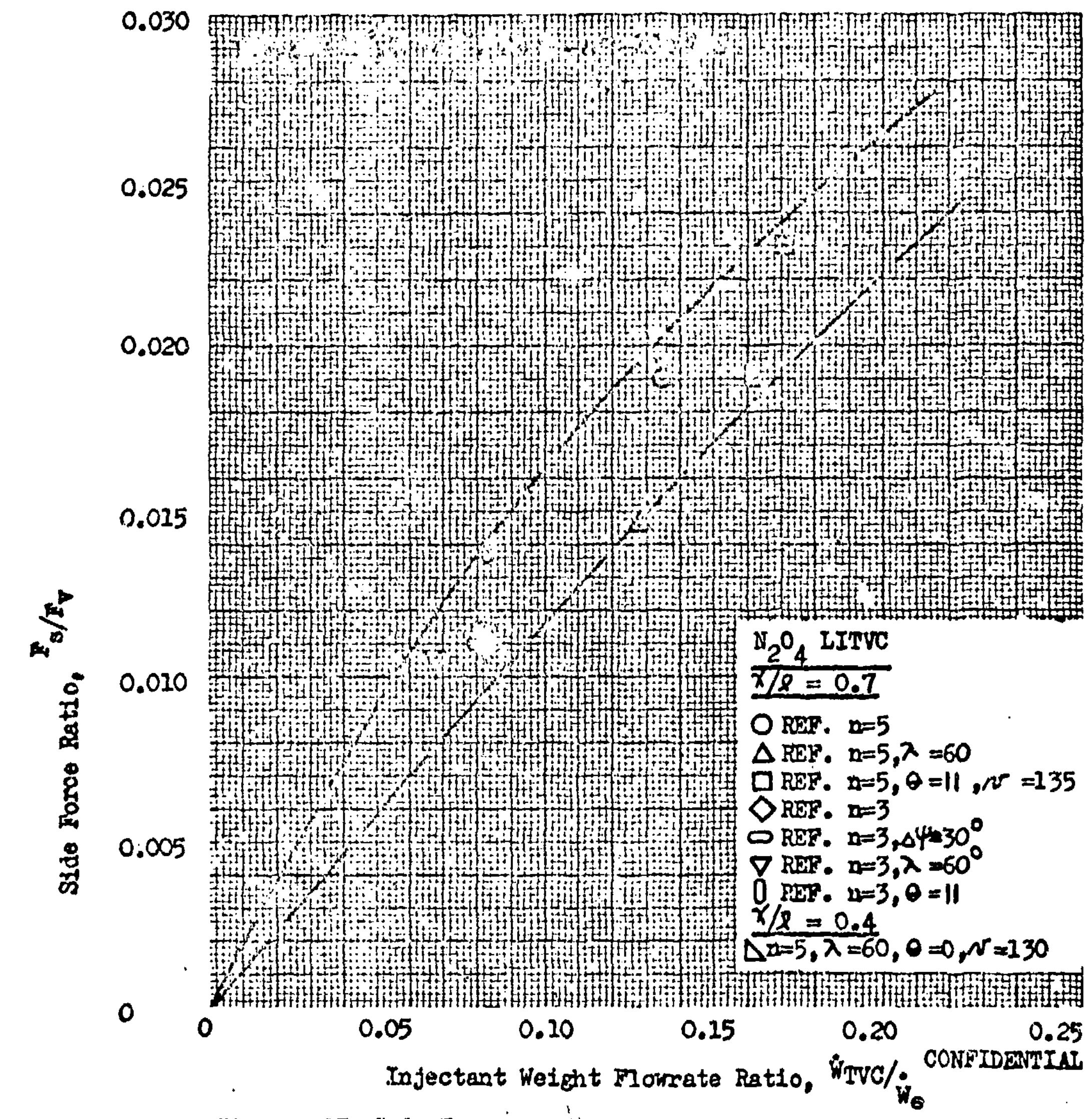

Figure 187. Side Force Ratio vs Flowrate Ratio for Liquid Injection at X/ℓ = 0.4, 0.7

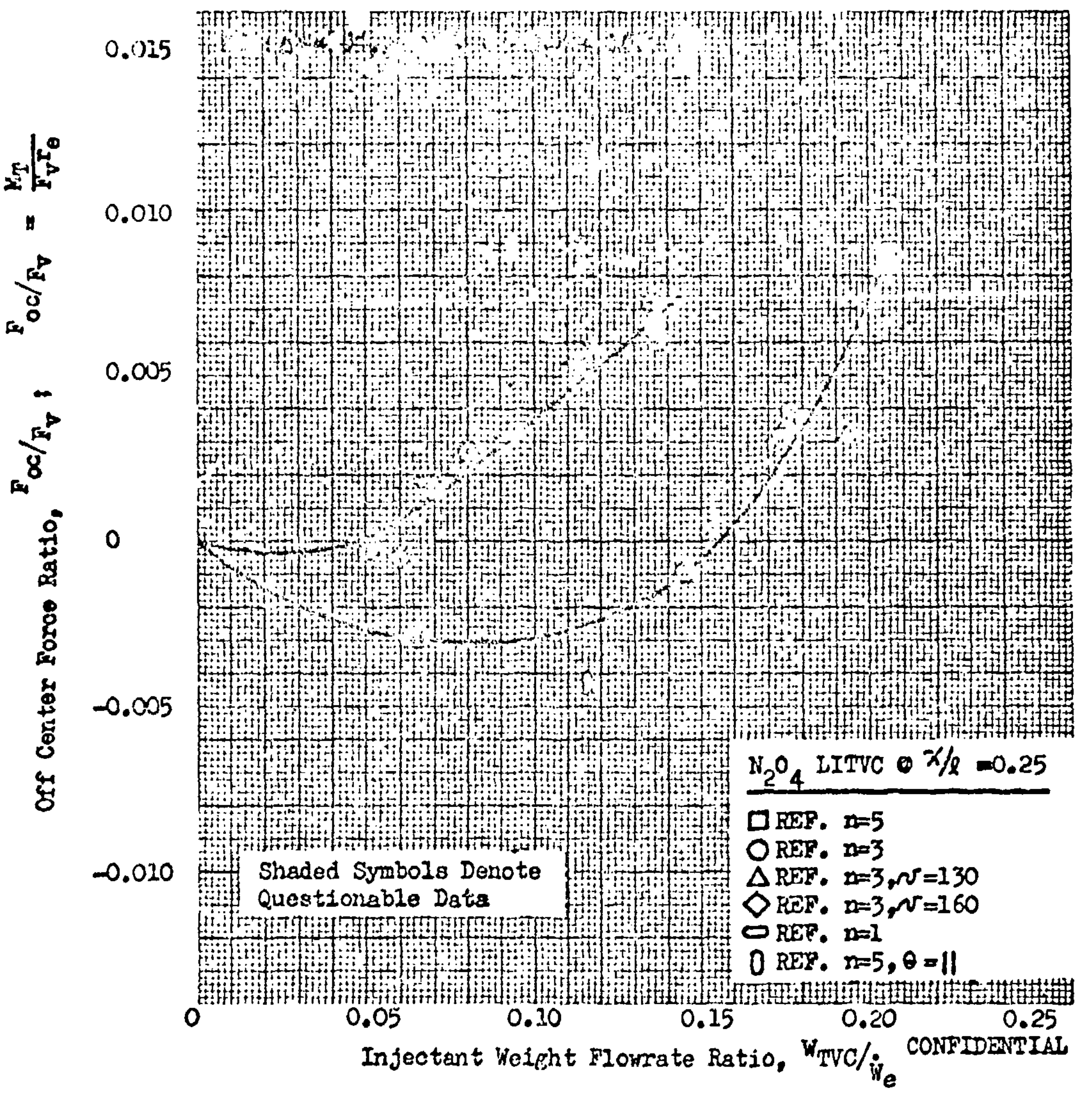

Figure 188. Off Center Force Ratio vs Flowrate Ratio for Liquid Injection at x/ℓ = 0.25

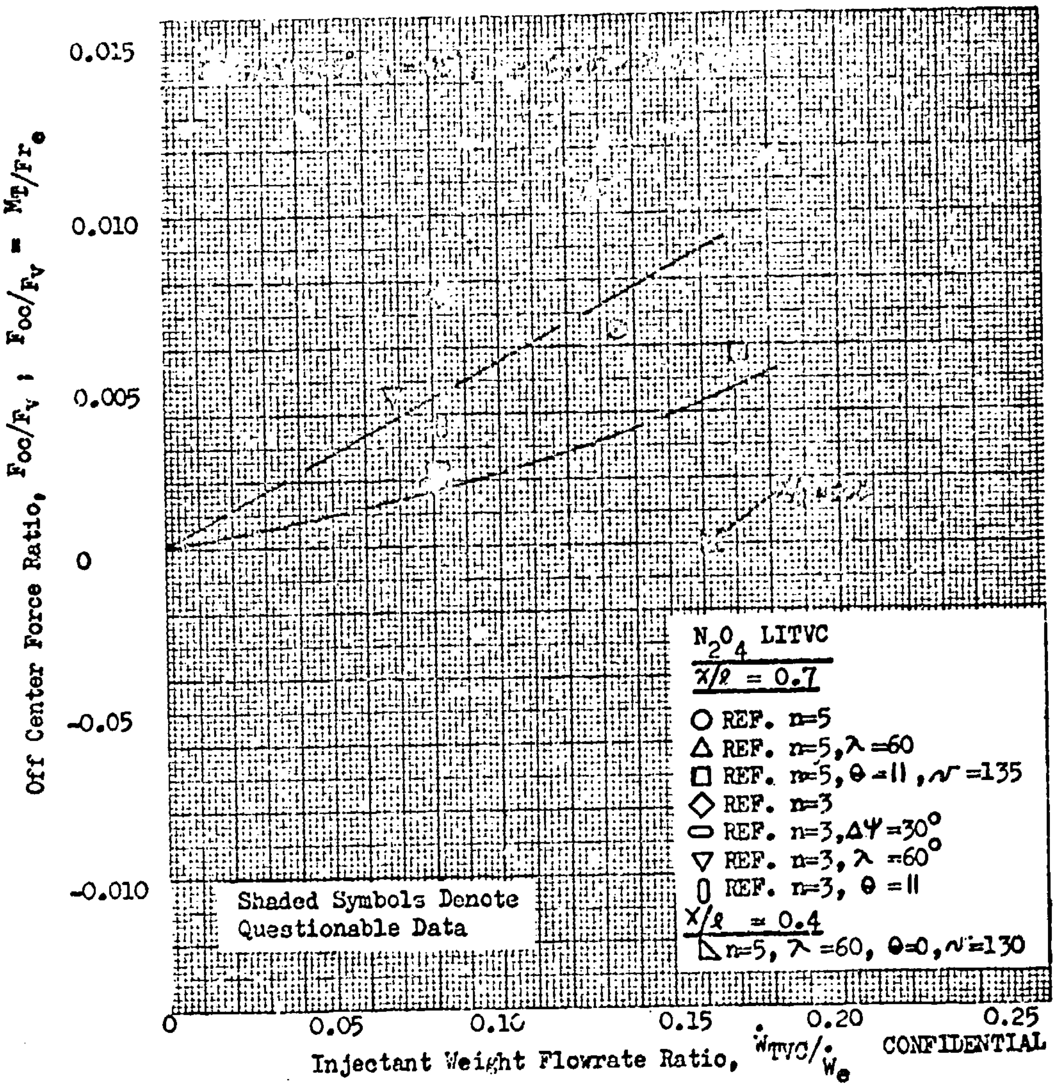

Figure 189. Off Center Force Ratio vs Flowrate Ratio for Liquid Injection at X/ℓ = 0.4, 0.7

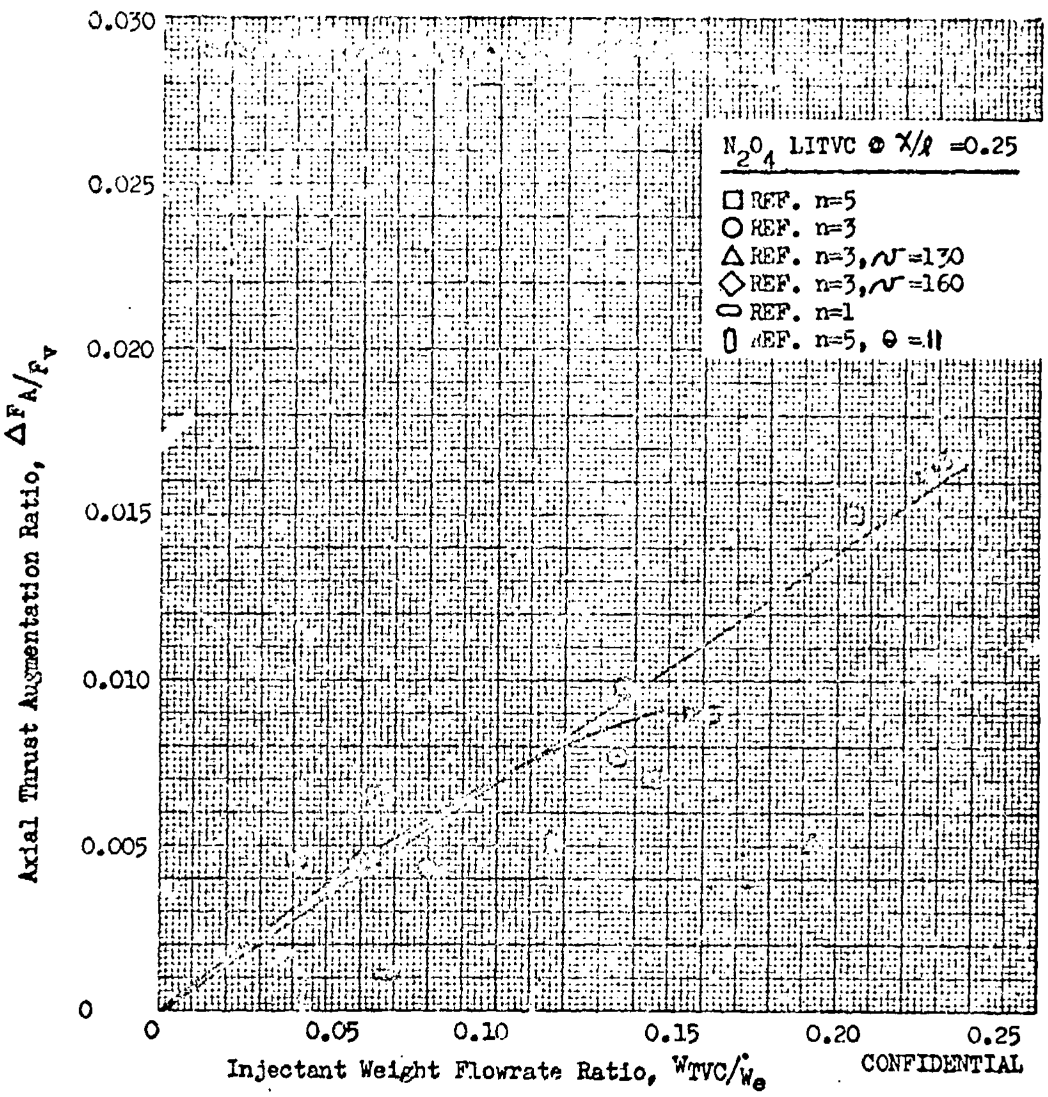

Figure 190. Relative Change in Axial Thrust vs Flowrate Ratio for Liquid Injection at X/ℓ = 0.25

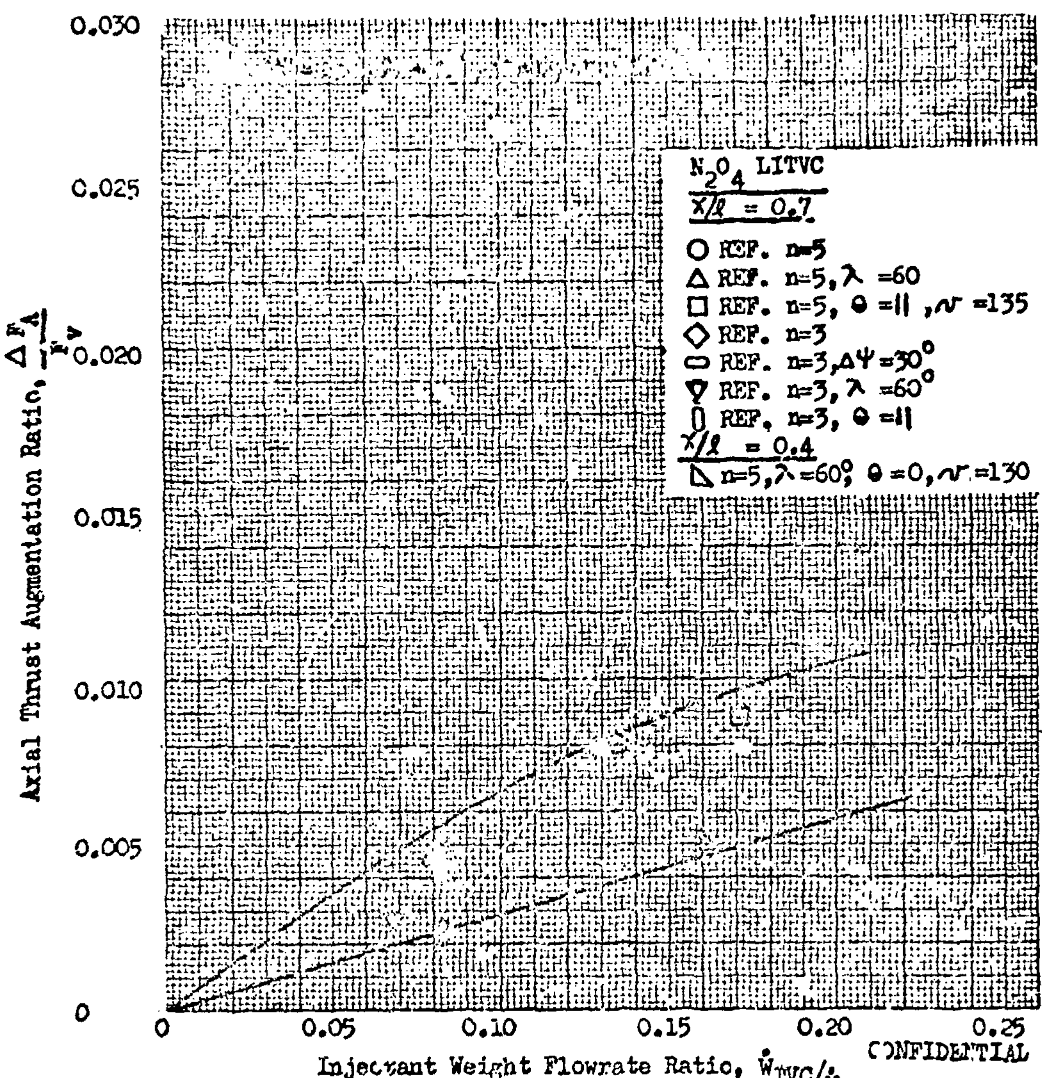

Figure 191. Relative Change in Axial Thrust vs Flowrate Ratio for Liquid Injection at X/ℓ = 0.4, 0.7

(C) Side force increases with the addition of TVC flow throughout the range of flowrates tested at $x/\ell = 0.25$ as shown by the data in Fig. 186. For a given flowrate, injecting liquid N_2O_4 through multiple orifices results in higher side force than single-port injection at this location. Parallel stream injection ($\theta = \parallel$) also yields higher side force than radial stream injection ($\theta = 0$) with five injection ports at $x/\ell = 0.25$. Similar results were obtained at $x/\ell = 0.7$ with both three- and five-port configurations as shown in Fig. 187. However, port spacing and axial inclination did not appear to influence the induced side force significantly at the latter location.

(C) Both positive and negative off-center forces were generated during this testing as shown by the data in Fig. 188 and 189. The trends at $x/\ell = 0.25$ imply that at low flows, the side force vector effectively acts near the injection ports, thereby producing a subtractive moment about the throat plane. As the TVC flowrate is increased this vector moves down the contour causing the throat moment to become positive. The relationship between side-force location and throat moment derived and discussed in Appendix 4 is illustrated in Fig. 192. It can be seen that to obtain additive moments, the effective side-force vector must be located along the aft portion of the nozzle. Five port injection results in lower throat plane moments than three-port injection because of a higher concentration of side force (Fig. 186) near the nozzle throat. Off-center forces are understandably slightly higher for injection near the nozzle exit (Fig. 189) simply because of the more favorable port location as shown by the curve in Fig. 192.

The axial thrust data in Fig. 190 and 191 reflect trends that are similar to those established by the side force data in Fig. 186 and 187 as would be expected if the effective TVC forces are normal to the contour. However,

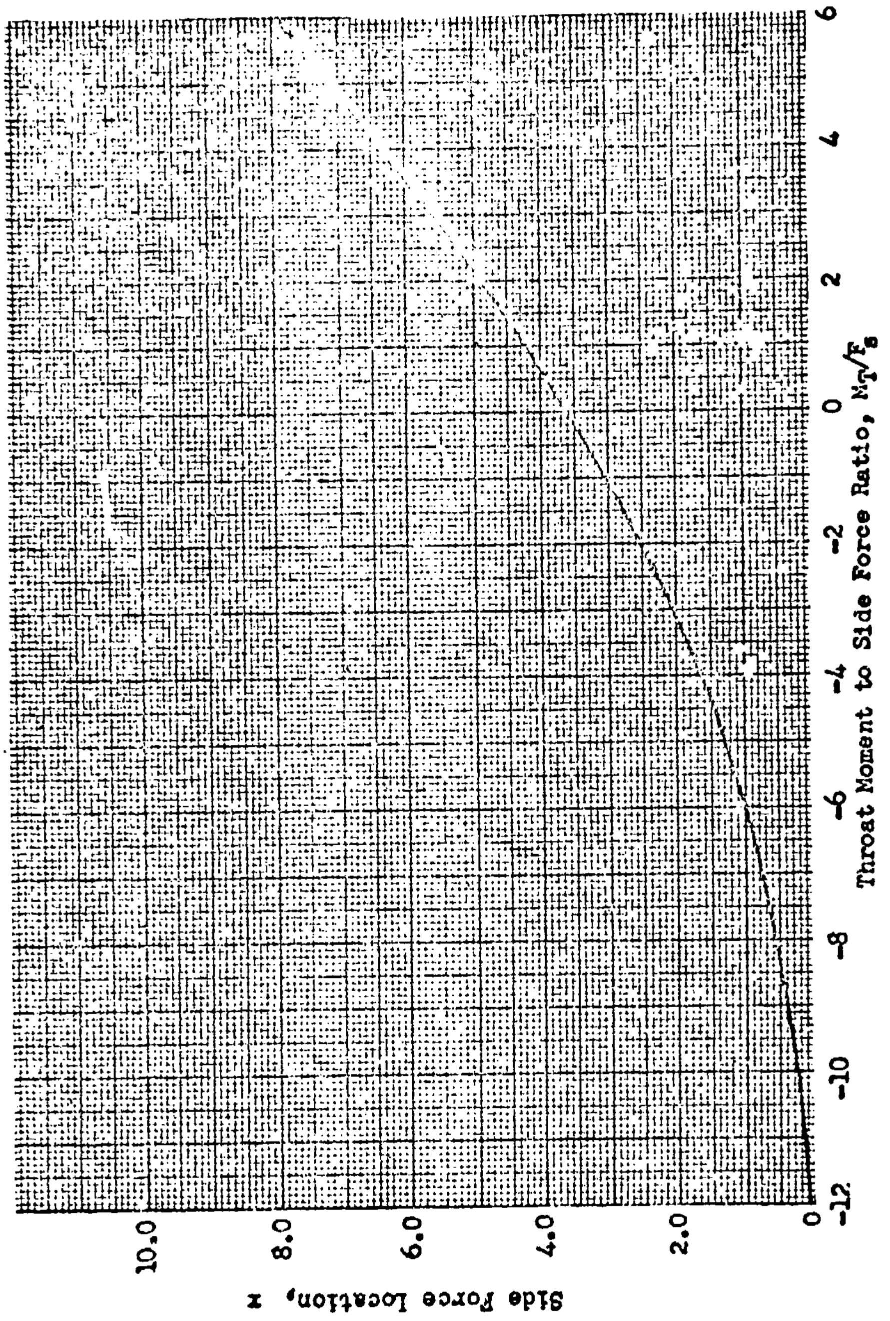

Figure 192. Variation of Side Force Location with Throat Moment-to-Side Force Ratio

because of the small magnitude of the axial thrust differences it is not possible to distinguish trends in the change in axial thrust with variations in the injection parameters.

(C) The change in nozzle wall pressure during TVC is illustrated by the data in Fig. 193. It can be seen that pressure is increased both upstream and downstream of the TVC port, and remains above the undisturbed wall pressure for some distance downstream of the injector. The test-to-test base pressure variation noted earlier during the reference performance testing persisted throughout the TVC testing. In general, it appeared that nozzle base pressure remained constant or decreased slightly during liquid injection, but definite trends with the injection parameters could not be determined from the measured data.

(C) The basic data presented in Fig. 186 and 187 were used to develop side thrust amplification factors to provide LITVC efficiency comparisons for N_2O_4 injection with this aerospike nozzle. The constant velocity SITVC performance trend with flowrate established for three- and five-port injection at x/ℓ = 0.25 is similar to the expected trend (Fig. 159 as shown by the data in Fig. 194. Performance decreases with increasing flowrate, and five-port injection provides the highest performance in the range tested. Parallel-stream injection affords slightly higher performance than radial-stream injection for the five-port configuration, indicating that a more concentrated injection pattern such as that provided by radial streams in a conical nozzle (Fig. 163) is superior to a divergent flow pattern. The magnitude of performance benefit is expected to be a function of factors such as: port spacing, exposed area downstream of the port, axial inclination, and injectant properties.

(C) Parallel-stream injection also affords higher side thrust efficiency than radial injection with both three- and five-port configurations at x/ℓ = 0.7

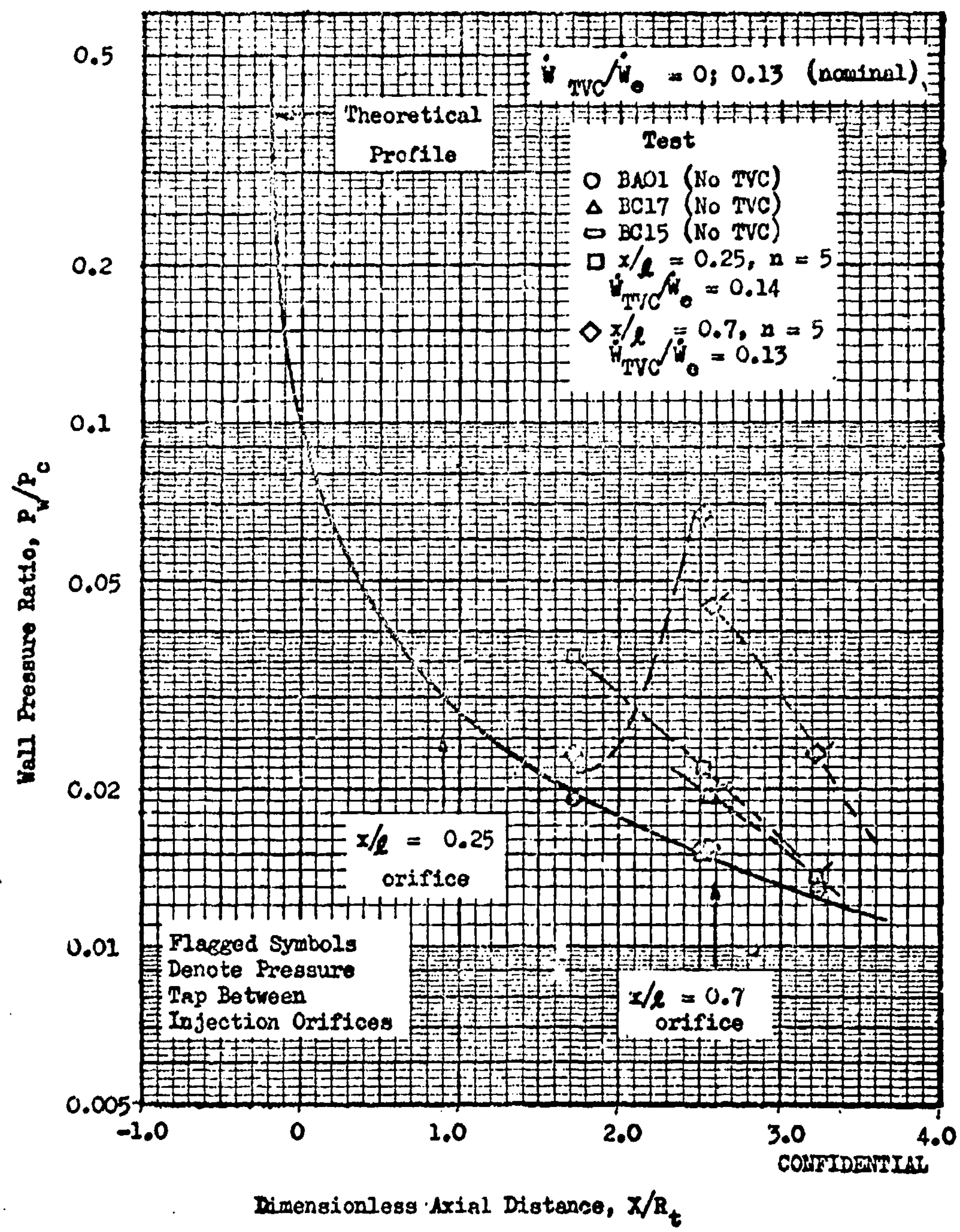

Figure 193. Wall Pressure Profile with Liquid N_2O_4 Injection at x/ℓ = 0.25 and x/ℓ = 0.7 for Aerospike Engine

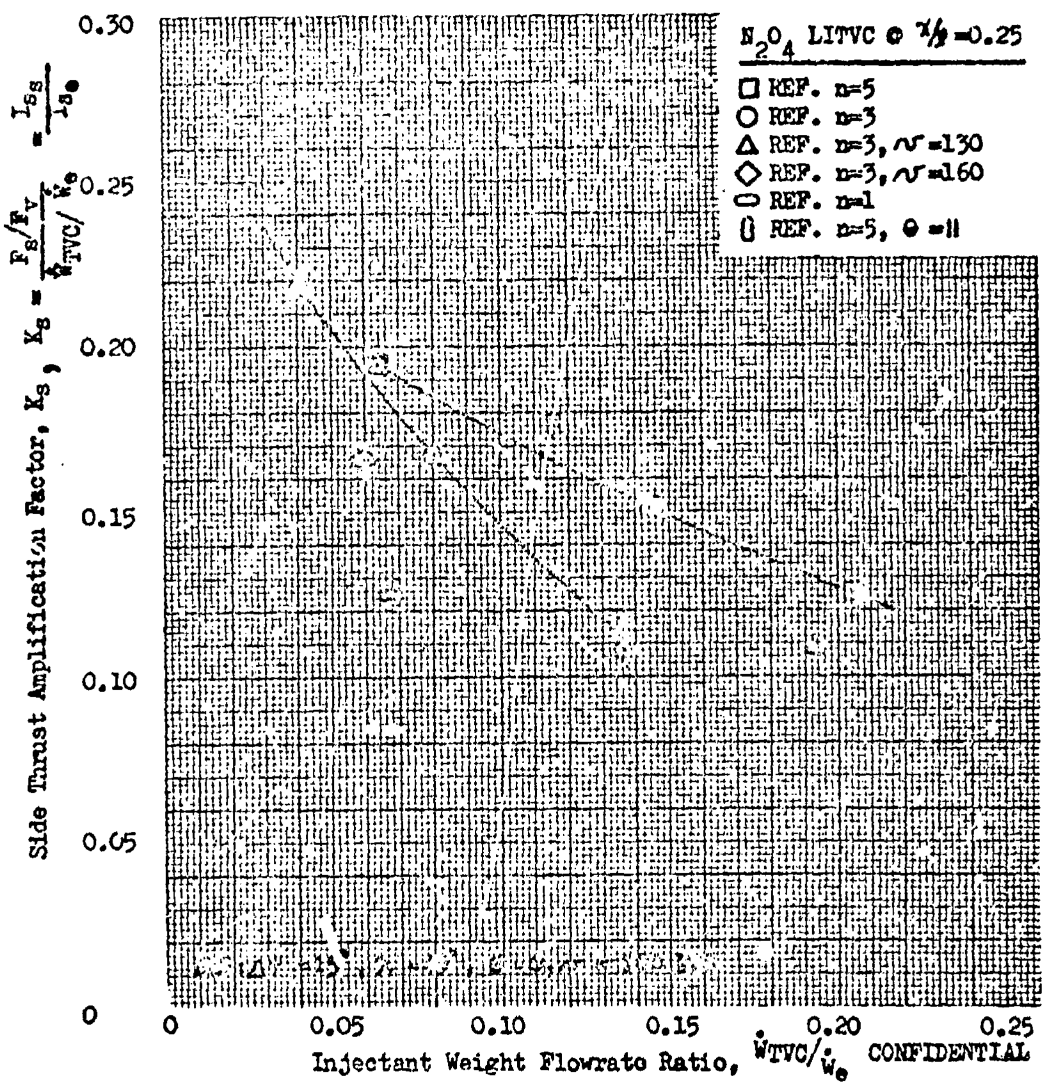

CONFIDENTIAL

Figure 194. Side Thrust Amplification Factor for Liquid N_2O_4 Injection at X/ℓ = 0.25

as shown in Fig. 195. However, the absolute performance level at this location is lower than at $x/l = 0.25$ as can be seen by comparison with the nominal performance trend for three- and five-port injection at $x/l = 0.25$ (from Fig. 194). The indicated performance insensitivity to the port spacing may not hold true for injection nearer the throat because interference losses are a direct function of the influenced area downstream of the injection port. That is, the parameter, $\Delta\psi$, may optimize differently for different stations along the nozzle.

(C) As expected, the axial inclination of the TVC ports did not significantly influence performance with the variation investigated at $x/l = 0.7$. Although the data for injection at $x/l = 0.4$ is somewhat questionable (Test BE33), the performance level established with the five-port configuration at this location is consistent with the data obtained at the other locations tested.

(C) A parameter similar to the side thrust amplification factor was used to represent off-center thrust efficiency for the various injection techniques. This parameter, which is termed the off-center thrust amplification factor, K_{γ} (defined and discussed in Appendix 4) is shown for N_2O_4 injection at $x/l = 0.25$ in Fig. 196. At low flows, negative off-center thrust amplification factors were obtained because the effective side force vector is apparently located near the injection port as discussed previously. The off-center thrust amplification factor increases with flowrate throughout the range of flowrates. Except for the data points that denote variations in injection velocity, those conditions that yield high side force amplification (Fig. 194) also yield relatively low off-center thrust amplification at this location.

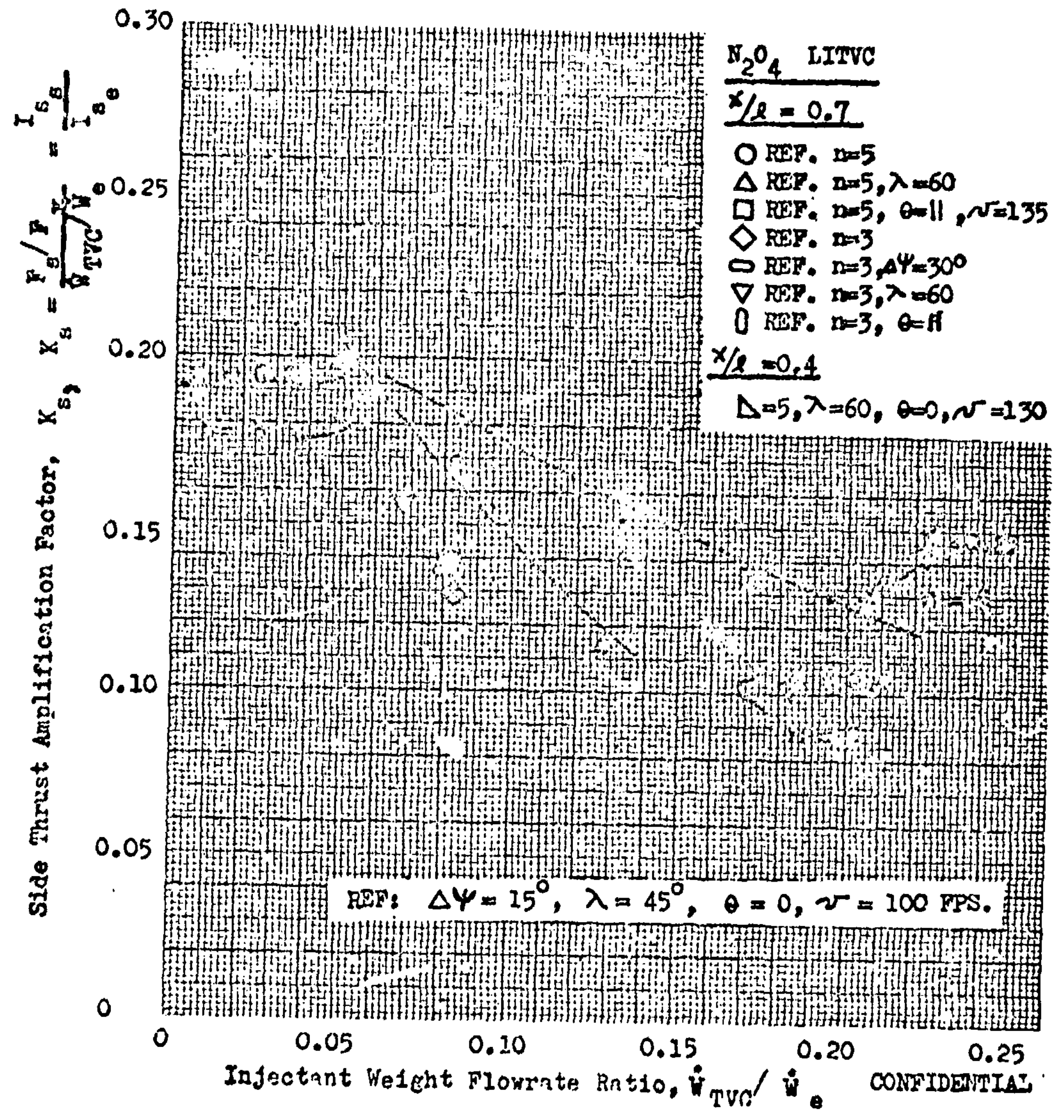

Figure 195. Side Thrust Amplification Factor for Liquid N_2O_4 Injection at x/ℓ = 0.4, 0.7

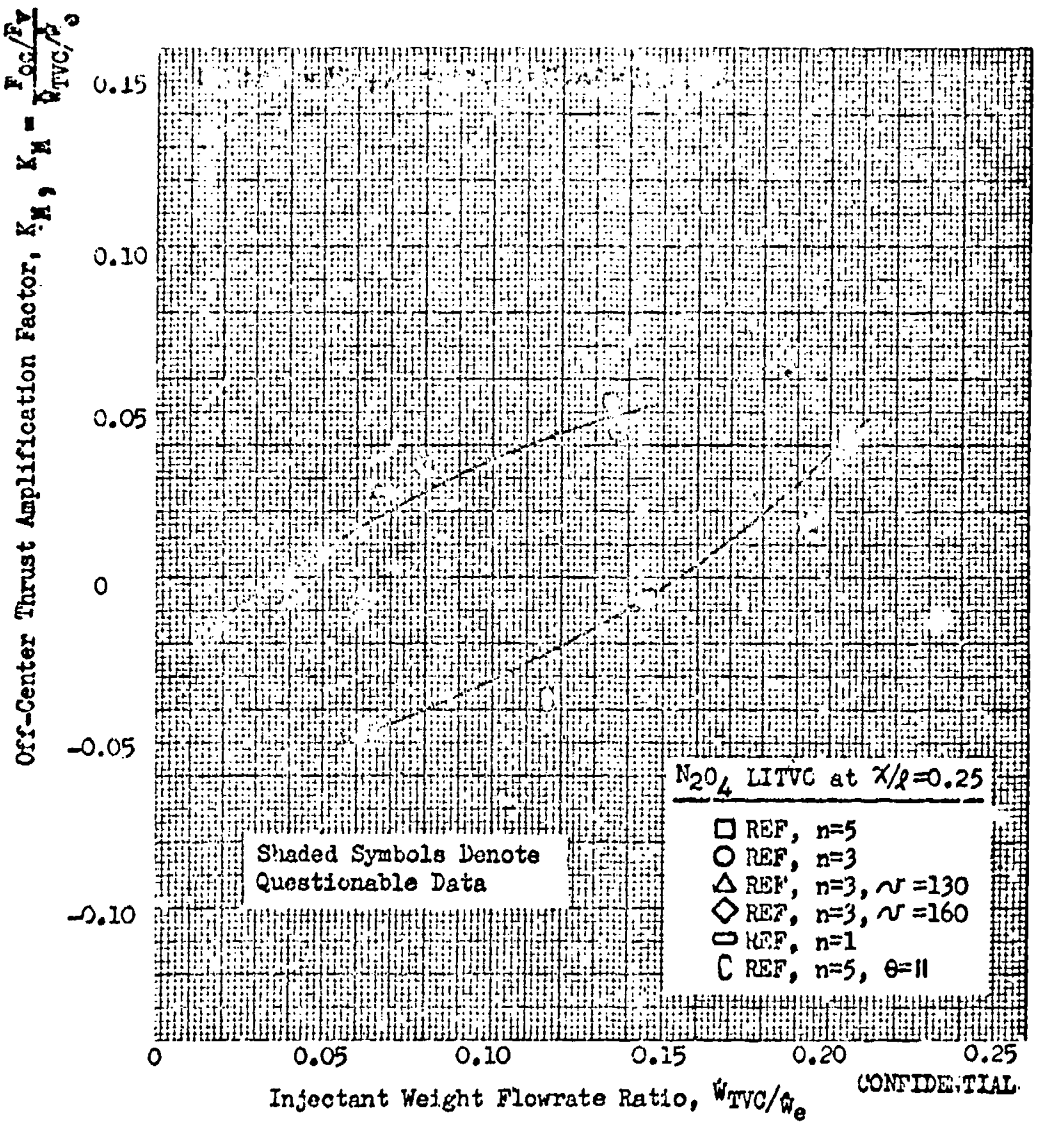

Figure 196. Off Center Thrust Amplification Factor for Liquid N_2O_4 Injection at $x/\ell \approx 0.25$

(C) Off-center thrust performance data for injection at $x/\ell = 0.4$ and $x/\ell = 0.7$ are shown along with the nominal trends at $x/\ell = 0.25$ (from Fig. 196) in Fig. 197. It can be seen that for locations near the end of the nozzle, the off-center thrust efficiency is higher than for injection near the nozzle throat, and tends to follow side thrust efficiency trends more closely than in the latter case. No reason could be found for the relatively low off-center thrust efficiency displayed for the configuration with $\Delta\psi = 30$ degrees at $x/\ell = 0.7$ and with $\lambda = 60$ degrees at $x/\ell = 0.4$; these data points are considered questionable in view of the performance level established by the other data and the relationship required between side and off-center thrust indicated by the curve in Fig. 192.

(C) To provide a basis for more meaningful comparison of injection techniques, the side and off-center thrust amplification factors in Fig. 194 through 197 were combined to form a control moment performance factor, $\bar{K}$, which reflects the influence of both quantities. Since $\bar{F}$ is indicative of the total control moment about the vehicle center of gravity, a geometric relationship between the engine and vehicle must be assumed to completely determine this quantity. As discussed in Appendix 4, this is accomplished by means of the parameter r_e/h where r_e is the engine radius and h is the distance from the reference gimbal plane to the vehicle center of gravity.

(C) Results are presented for N_2O_4 injection at $x/\ell = 0.25$ and for r_e/h values of 0.25 (typical boost vehicle) and 1.0 (typical upper stage vehicle) in Fig. 198a and 198b, respectively. Overall TVC performance trends with flowrate are nearly identical to side-force efficiency trends for $r_e/h = 0.25$, because of the relatively weak influence of the quantity, K_H. However, performance trends with flowrate and configuration are changed for r_e/h . 1.0 indicating that the vehicle geometry may have an influence on the selection of an LITVC injector design under certain conditions. Similar results were obtained for injection at $x/\ell = 0.7$ as shown

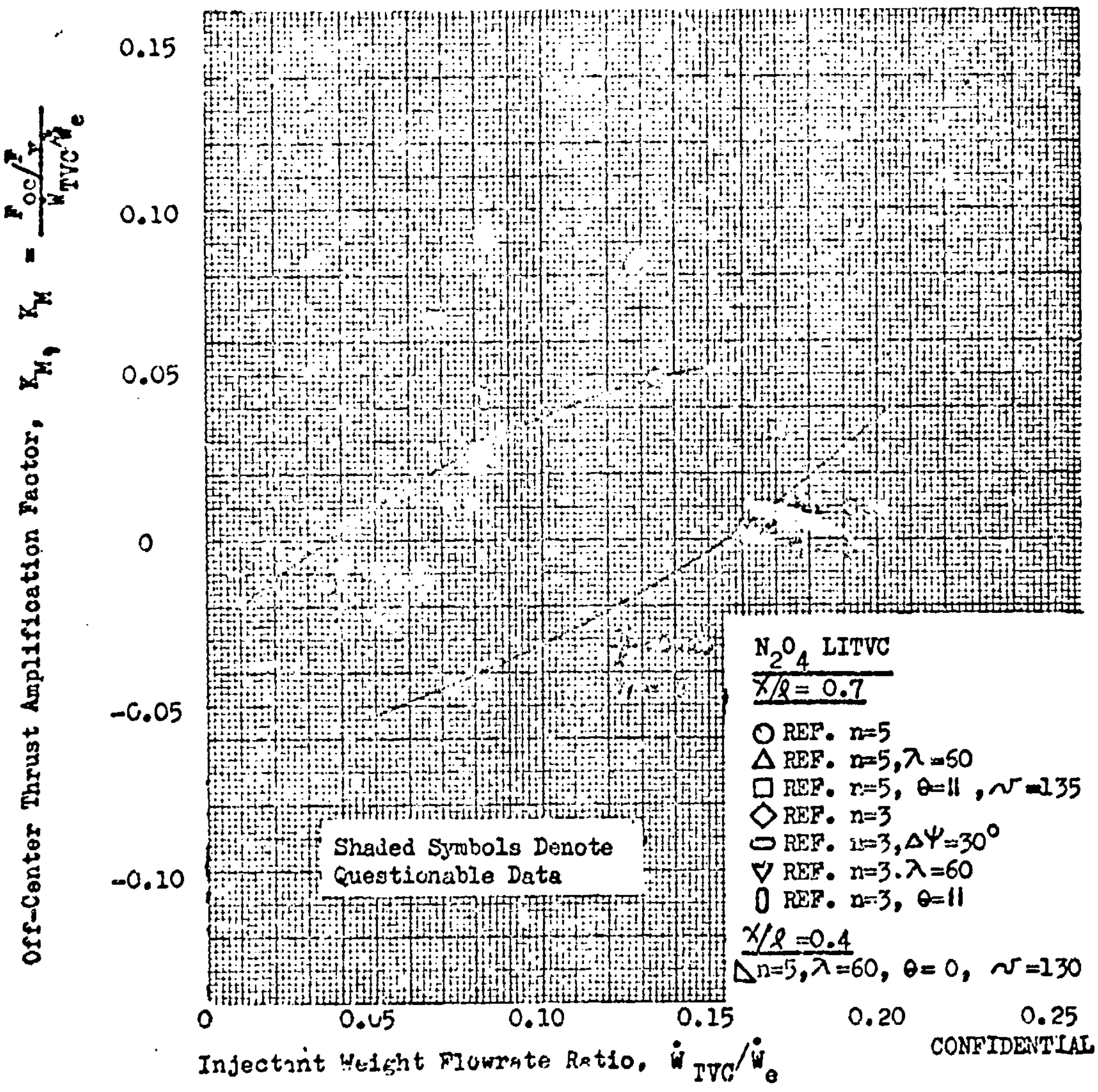

Figure 197. Off Center Thrust Amplification Factor for Liquid N_2O_4 Injection at $\frac{X}{\ell} = 0.4, 0.7$

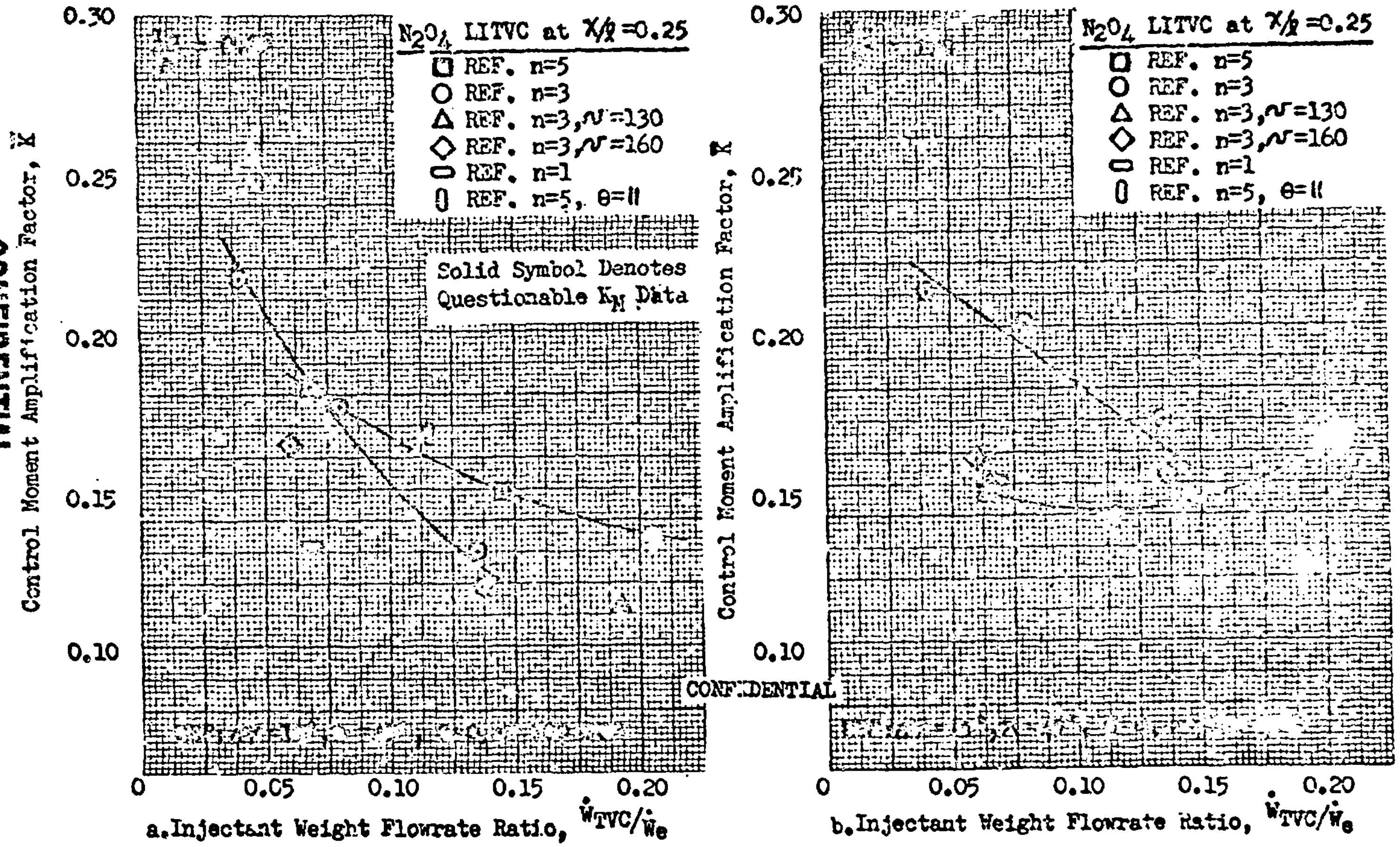

Figure 198 . Total Control Moment Amplification Factor for Liquid N_2O_4 Injection at $X/\ell = 0.25$

by the data in Fig. 199. The nominal trends established for three- and five-port injection at $x/\ell = 0.25$ are included in Fig. 199 for comparison. Control moment efficiency is seen to be higher when the TVC flow is injected near the nozzle throat if $r_e/h = 0.25$, while the opposite is true if $r_e/h = 1.0$.

(C) The moment efficiency data in Fig. 198 and 199 were used in conjunction with the axial thrust data in Fig. 190 and 191 to establish the change in engine specific impulse as a function of the equivalent gimbal angle, φ, developed during liquid injection thrust vector control. The relative change in engine specific impulse was obtained from the relation:

$$\frac{\Delta I_s}{I_s} = \frac{1 + \Delta F_A/F_V}{1 + \dot{w}_{TVC}/\dot{w}_e}$$

and the equivalent gimbal angle is defined as (from Appendix 4):

$$\varphi = \arcsin \quad \bar{K}\left(\frac{\dot{w}_{TVC}}{\dot{w}_e}\right)$$

(C) These results are presented for N_2O_4 injection at $x/\ell = 0.25$ and $x/\ell = 0.4$, 0.7 in Fig. 200 and 201, respectively. Reference to Fig. 200 shows that engine specific impulse decreases sharply with increases in the control requirements. The rate of decrease is dependent upon the number of injection ports and the engine-vehicle similarity parameter, r_e/h . Five-port injection provides the highest engine performance for $r_e/h = 0.25$, while three-port injection appears to be optimum for $r_e/h = 1.0$ (at least for the port spacing utilized in this program). Engine performance during TVC for injection at $x/\ell = 0.7$ is nearly identical to that obtained at $x/\ell = 0.25$ for $r_e/h = 0.25$ as shown in Fig. 201 a. However, if $r_e/h = 1.0$ the data in Fig. 201 b indicate that engine performance is higher for injection of TVC flow near the end of the nozzle than for injection near the throat.

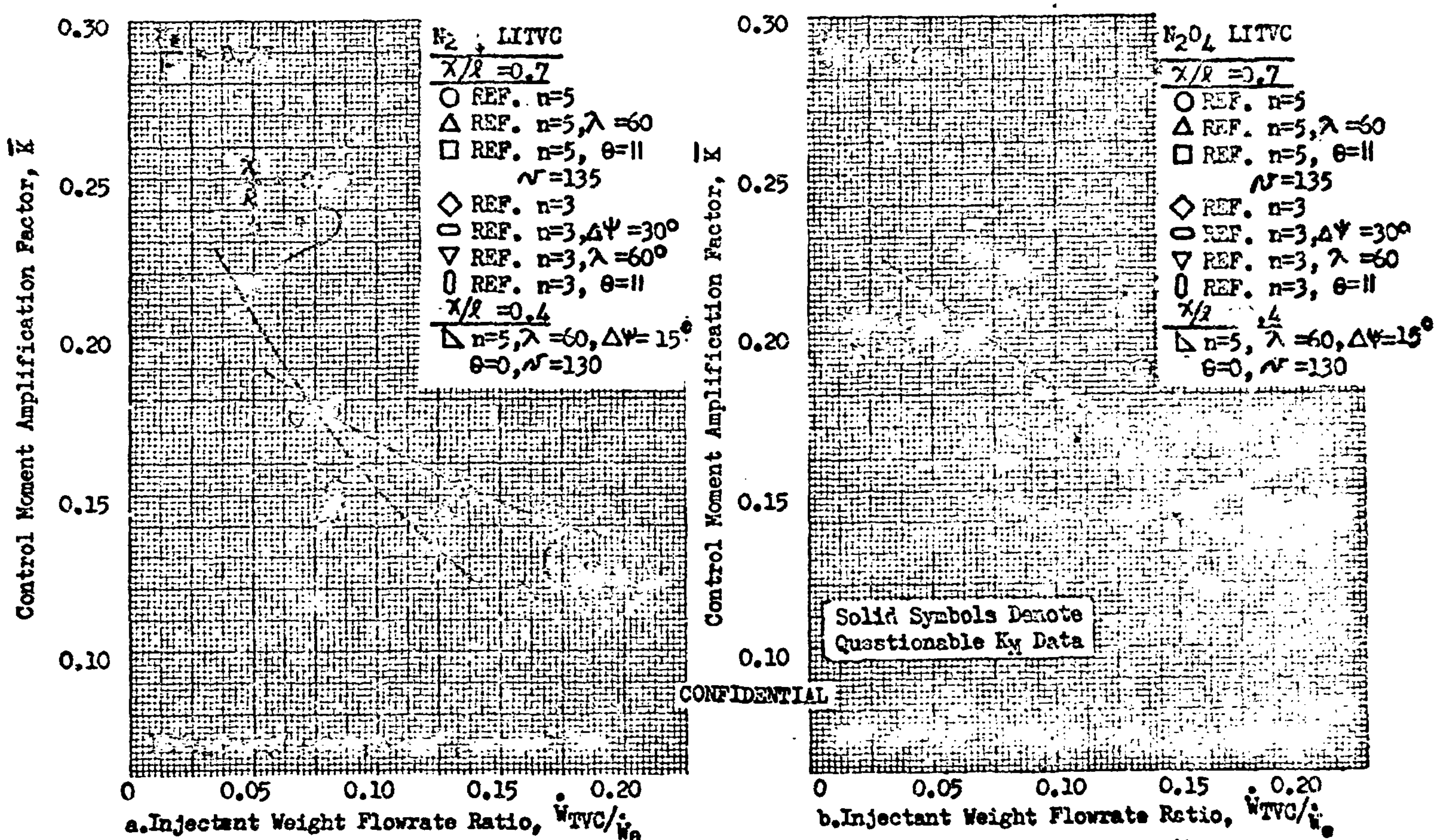

Figure 199 . Total Control Moment Amplification Factor for Liquid N_2O_4 Injection at x/l = 0.4, 0.7

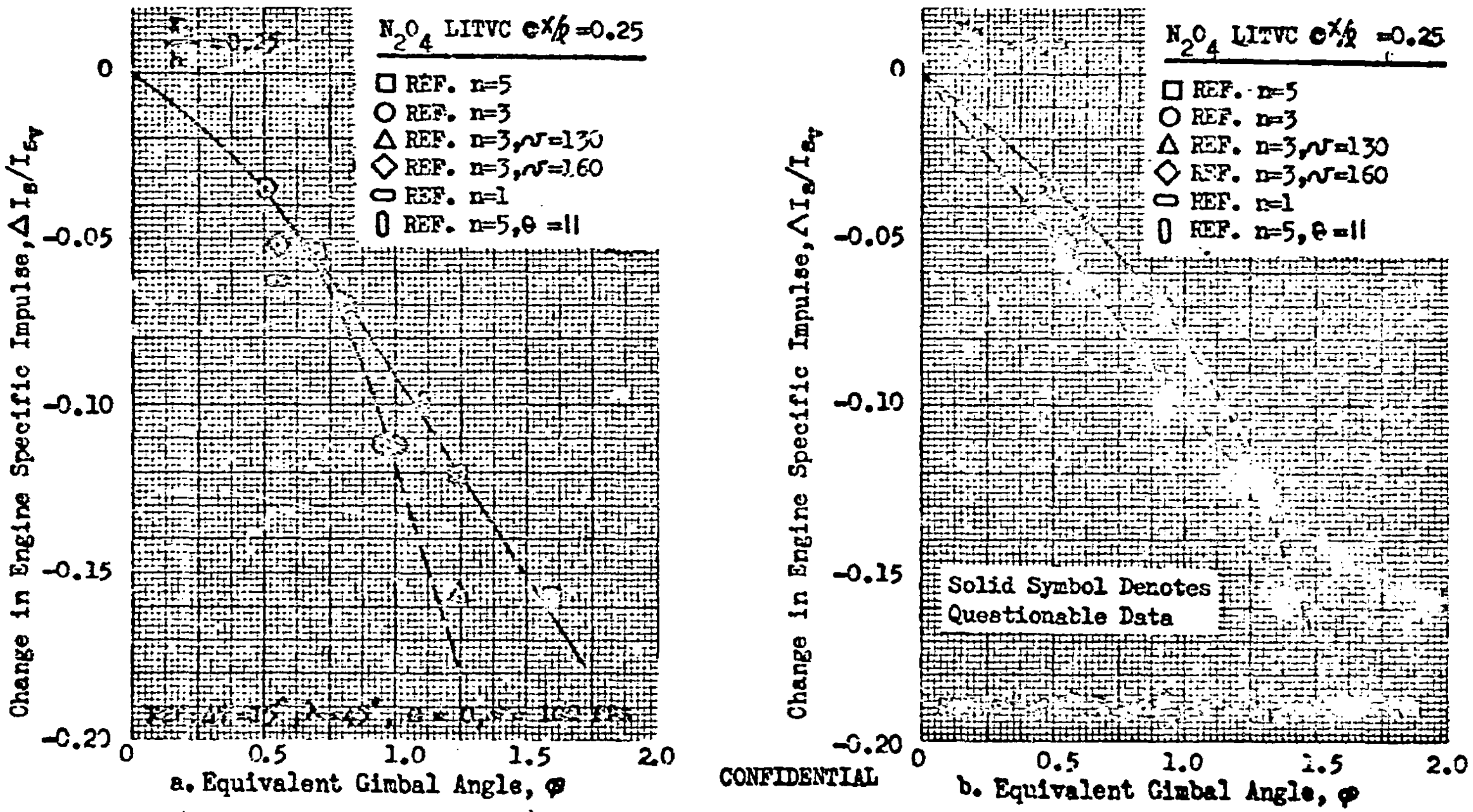

CONFIDENTIAL

Figure 200 . Change in Engine Performance During Liquid N_2O_4 Injection TVC at $X/\ell = 0.25$

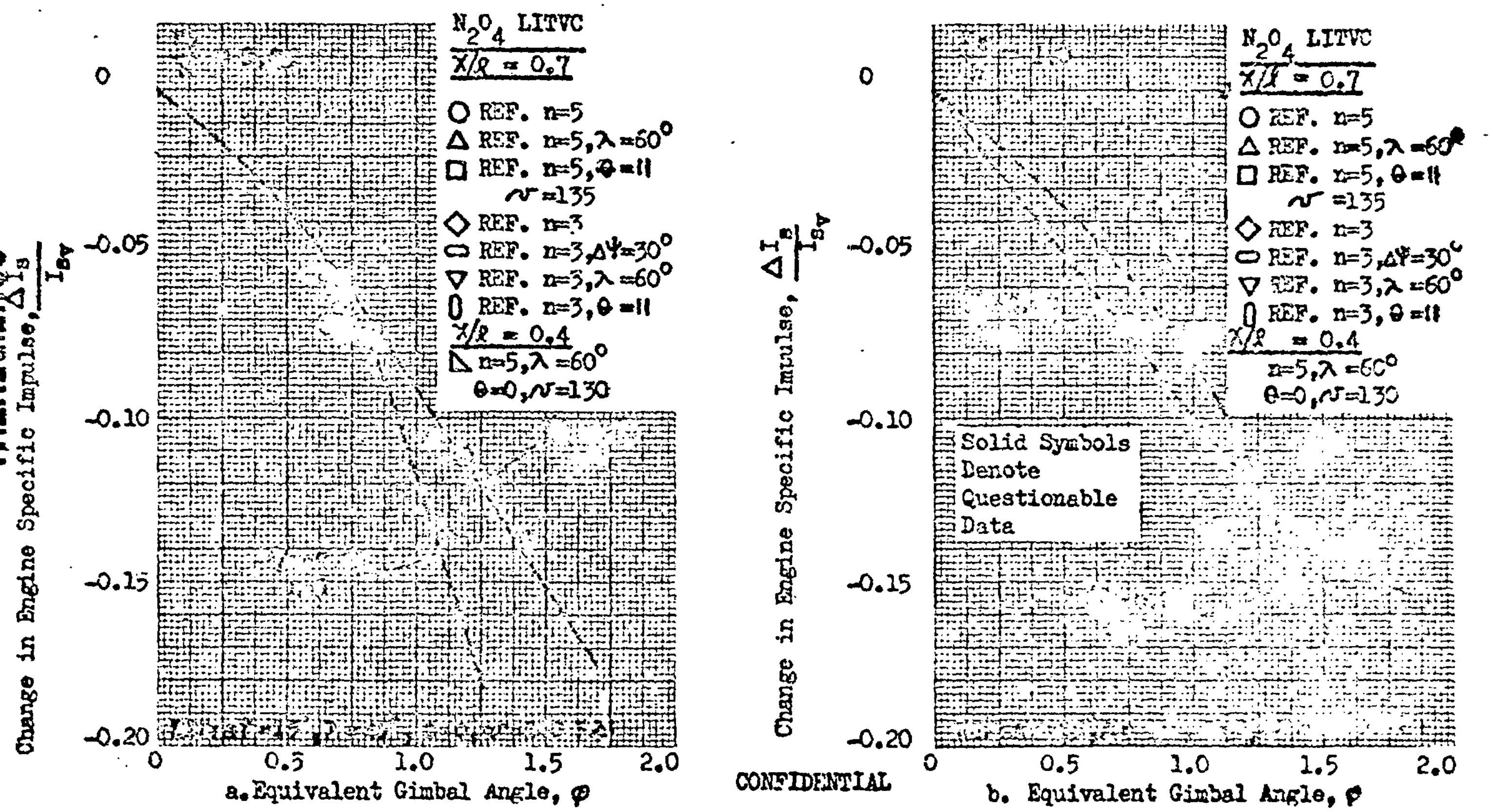

Figure 201. Change in Engine Performance during Liquid N_2O_4 Injection TVC at x/l = 0.4 and 0.7

(C) In general, these trends in engine performance during TVC are identical to those exhibited by the control moment coefficient, $\overline{K}$, with variations in TVC flowrate ratio (or with variations in the equivalent gimbal angle since these quantities are proportional). This indicates that the TVC injector designs that result in high side force and moment efficiency will also result in high engine performance during liquid injection TVC, which is a result that is not necessarily true of gaseous injection TVC systems as shown by the data presented in Ref. 15.

Application of LITVC Test Results

(C) Comparison with LITVC Performance Data for Other Nozzles. Previous test programs conducted by Rocketdyne have established performance trends for liquid oxidizer injection into high area ratio bell and H-F nozzles (Ref. 14) and a low area ratio annular bell nozzle (Ref. 16). The LITVC design utilized for the high-area-ratio testing incorporated multiple, closely spaced ports that were inclined 30 degrees upstream with respect to the engine centerline. Testing was conducted over a range of axial locations and TVC flowrates with both engines. Vacuum thrust and chamber pressure of these engines were 10,000 pounds and 225 psia respectively. Propellants were N_2O_4/UDMH-N_2H_4, 50-50 for the bell nozzle, and N_2O_4/UDMH for the F-H nozzle.

(C) The Lance annular bell nozzle ($\epsilon = 5.6$) utilizes single-port injection at a location near the throat. The TVC flow is injected into the nozzle at an angle of ninety degrees with respect to the engine centerline. Flow modulation is accomplished by means of a variable-area pintle valve. Experimental evaluation of this LITVC design was conducted with a 90-degree segment of the full-scale Lance engine, which operates with IRFNA/UDMH propellants at a chamber pressure of approximately 900 psia. Thrust level of the segment is approximately 10,000 pounds under these conditions.

(C) Typical SITVC performance results from these programs are shown in Fig. 202 along with aerospike LITVC side-force efficiency data from Fig. 194. Since the injection ports were closely spaced in the high-area-ratio nozzles, the trends displayed for these configurations are more representative of single- than multiple-port injection as shown by the data in Ref. 10. It can be seen that the performance level of liquid injection with an aerospike nozzle is somewhat lower than with high-area-ratio bell and H-F nozzles. This can be attributed to the much shorter length of the lower area ratio aerospike nozzle (even at the same area ratio, axial length of the aerospike nozzle is only 30 percent of the bell and 60 percent of the H-F nozzles). Similar results can be expected at higher thrust levels, but if scale effects exist, they are expected to be slightly more influential with an aerospike because of its shorter length. Thrust vector control demands for the Lance engine are relatively small so testing was conducted over a limited range of low flowrates. Comparison with aerospike side force efficiency under these conditions is difficult because of the rapidly changing slope of the side force efficiency curve at low flows. However, the level of aerospike side force efficiency does appear to be consistent with that obtained with the annular bell configuration at low flows.

(C) Comparison with Semi Empirical LITVC Performance Estimates. The side force efficiency data presented in Fig.194 and 195 have established performance trends with injection variables. that are in qualitative agreement with the estimated performance trends presented earlier. However, the measured performance level is lower than that estimated theoretically as shown in Fig. 203.

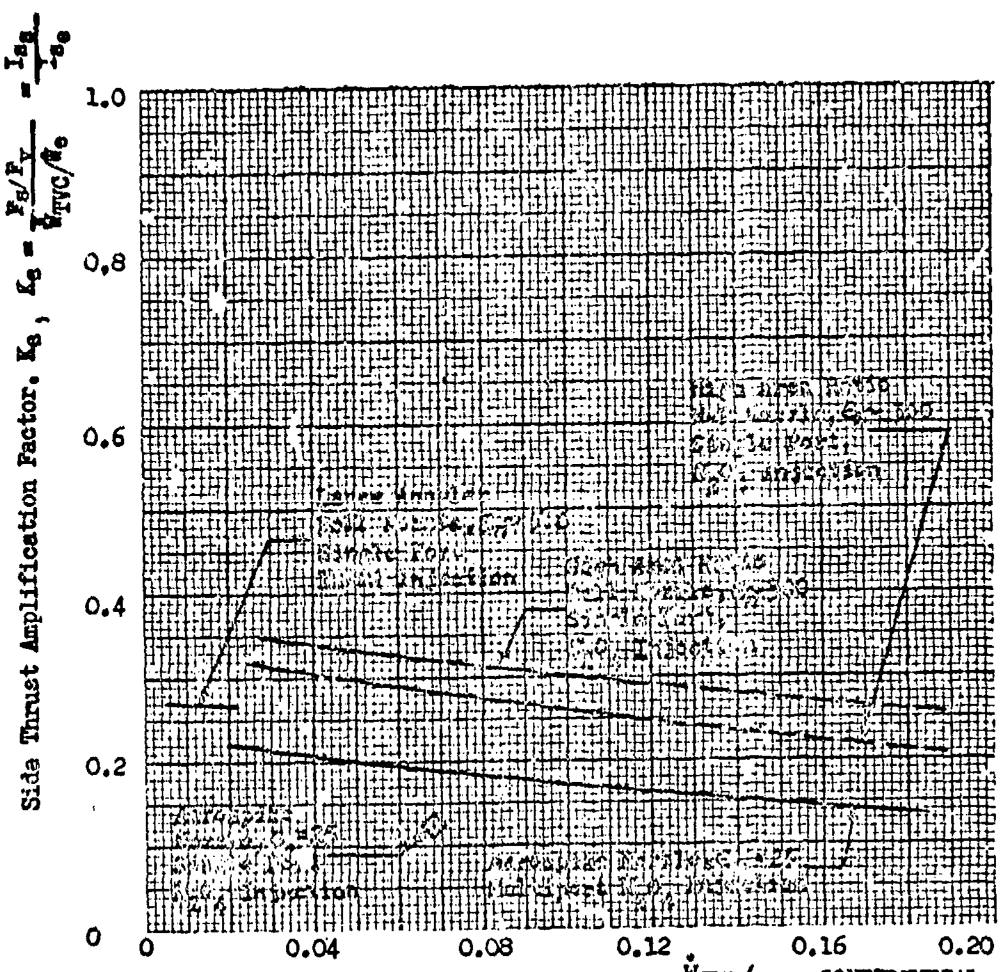

CONFIDENTIAL

Figure 202. Side Thrust Amplification Factor for Liquid Injection with Various Nozzles

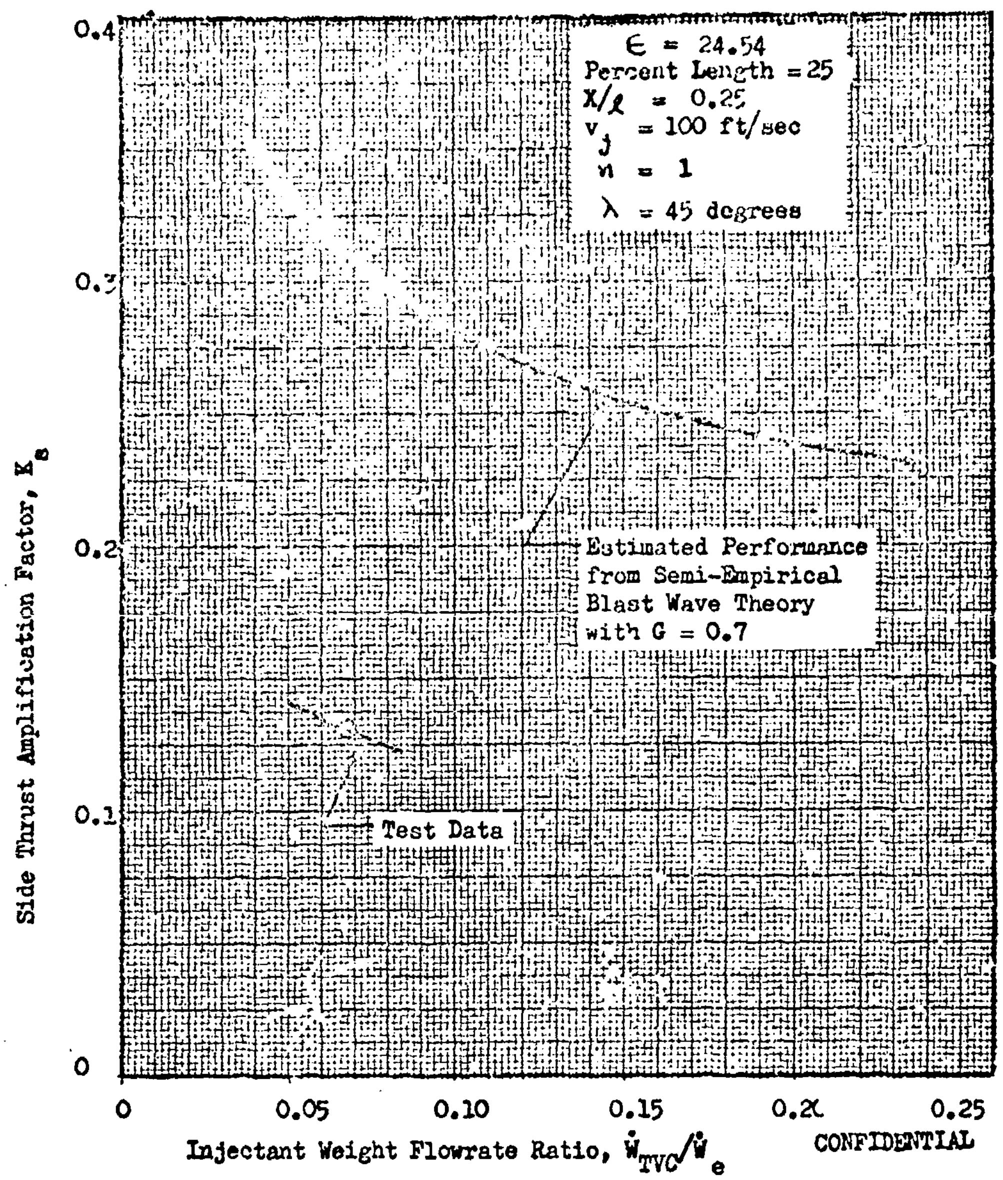

Figure 203. Comparison Between Estimated and Measured SITVC Performance Level for Aerospike Engines

(C) To obtain agreement with the test data the spreading coefficient, G, was revised to match the single port data at $x/\ell = 0.25$ and the three port data with $\Delta\psi = 30$ degrees at $x/\ell = 0.7$ (interference effects are minimal with the latter configuration). Because it was derived from experimental data, this revised spreading coefficient, G, which is presented in Fig. 204, includes: (1) corrections for nonuniform nozzle flow similar to the coefficient for gas injection into flow over a flat plate used in previous analysis, (2) corrections for variable wall angle and spreading (cosine) losses with length, and (3) corrections for the effects of injectant vaporization and reaction. While the data in Fig. 204 applies quantitatively only to the aerospike nozzle geometry tested in this program, its use to estimate LITVC performance trends for larger engines than that tested should yield conservative results. The correlation shown in Fig. 205 indicates that once the performance level is established, correct trends with the injection parameters are predicted by the blast wave theory. The deviation in Fig. 205a can be attributed to flow interference effects (which are apparently small) and/or to slight inaccuracy in the blast wave representation of the influence of the injectant flowrate (the blast wave theory indicates that $K_s \propto \left(\frac{\dot{w}_{TVC}}{\dot{w}_e}\right)^{-\frac{1}{4}}$ which may not be exactly true for the aerospike).

(C) Comparison Between Aerospike Liquid and Gas Injection Performance. Coldflow testing conducted during the Aerodynamic Nozzle Study (Ref. 15) established the like-into-like gaseous injection performance characteristics to be expected from an aerospike nozzle. Injection parameters studied include: TVC injection location and axial inclination, TVC flowrate and injection velocity, and the nozzle chamber to ambient pressure ratio. Area ratio of the aerospike nozzle tested was 25:1 and its length was 16 percent of a conical nozzle with equivalent area ratio and throat area. Typical results of this investigation are shown in Fig. 206. comparable LITVC data obtained for five-port N_2O_4 injection at $x/\ell = 0.25$.

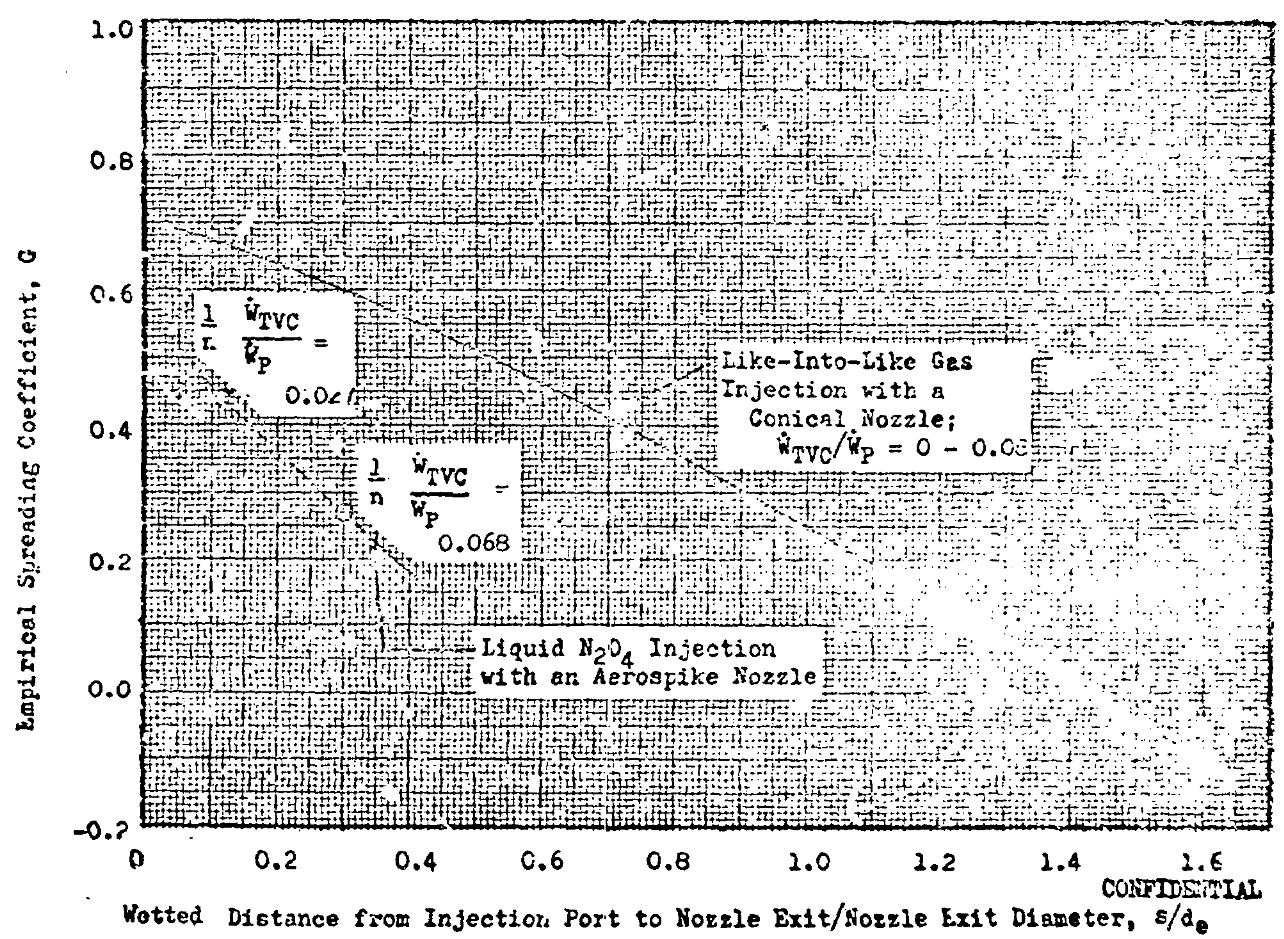

Figure 204. Empirical Spreading Coefficient for Gas Injection into Conical Nozzles (Ref. 8) and Liquid Injection into an Aerospike Nozzle.

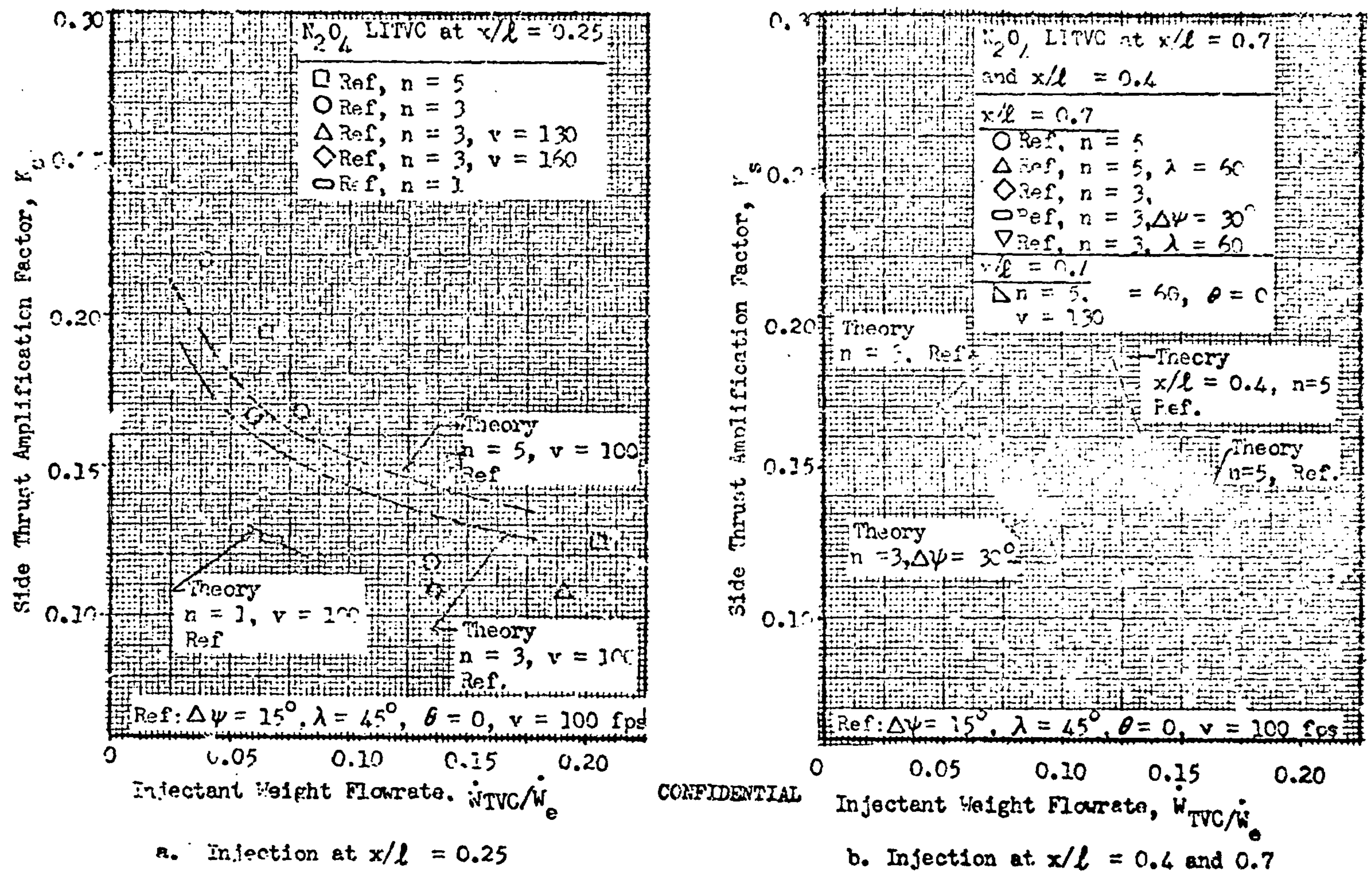

CONFIDENTIAL

Figure 205. Comparison Between Estimated and Measured SITVC Performance Trends Using the Revised Spreading Coefficient from Fig. 204.

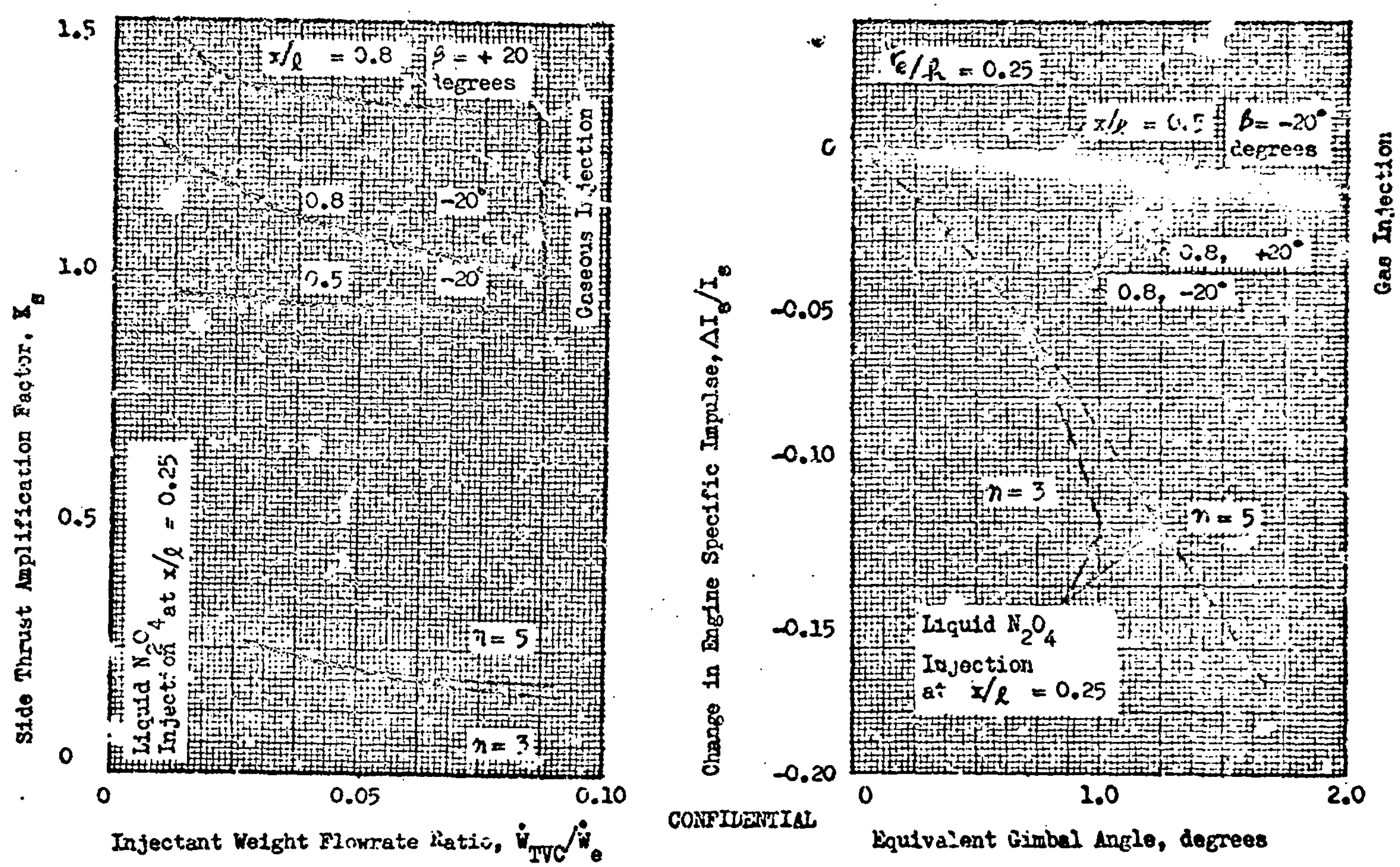

SITVC Performance

Engine Performance During SITVC

CONFIDENTIAL

Figure 206. Comparison Between Liquid and Gaseous Injection Performance with an Aerospike

(C) Reference to Fig. 206a reveals that much lower flows are required to produce the same side force if liquid N_2O_4 is replaced by a high-energy gaseous fluid. As indicated, performance trends with the injection variables are more pronounced with gaseous injection than with liquid injection; it was found in the cold-flow testing that those injector designs which provide high control moment efficiency for gas injection also result in relatively low nozzle performance at the corresponding TVC flowrate. This characteristic resulted in nearly identical nozzle performance during TVC from all of the configurations tested in the cold-flow program as indicated in Fig. 206b. The nozzle performance level established by this cold-flow data (Fig. 206b) is significantly higher than that obtained with liquid N_2O_4 injection, because of the lower flows needed to produce equivalent control moments. The high-area-ratio bell and H-F nozzle TVC data presented in Ref. 14 indicate that similar comparisons can be expected from hot-flow gaseous injection TVC systems.

(C) <u>Estimated SITVC Performance For Full Scale Engines</u>. To make a more meaningful comparison between injectants and to provide a basis for future systems analysis, the data obtained in this program were used to generate performance estimates subject to the operating requirements expected of future aerospike engine applications. Two methods were used to estimate LITVC performance to ensure that realistic efficiencies were obtained.

The first method involved direct scaling of the LITVC control moment and nozzle efficiency data obtained for five-port injection at $x/\ell = 0.25$ (Fig. 198 and 200) by means of the volumetric flowrate correlation discussed earlier. With the other method, performance was estimated theoretically using the blast wave analysis and corrected for spreading losses by means of the revised spreading coefficient obtained for the aerospike nozzle tested in this program (Fig. 204). Both methods of estimating liquid injection performance should tend towards conservatism since the influence of injectant vaporization and reaction is assumed

constant and is believed to be negligible for the nozzle size tested. In reality, these effects become more pronounced as the engine thrust level and size increase. Like-into-like gas injection performance was obtained through direct scaling of the cold-flow data in Fig. 204. Performance of low-energy gas injection was estimated by means of the characteristic velocity correlation discussed in Ref. 15.

(C) High- and low-energy gas injection performance was compared with that of liquid fuel and oxidizer injection for two potential aerospike booster engine applications, and an upper-stage engine system. The first of these boost applications utilizes a 1.8-million-pound thrust engine (sea level) with N_2O_4/50-50 propellants. Chamber pressure of the engine is 2000 psia, and the area ratio of the aerospike nozzle is 55. The other booster engine also operates with a chamber pressure of 2000 psia. Propellants in the latter case are LO_2/LH_2, sea-level thrust is 24 million pounds, and the area ratio of the nozzle is 78. Vacuum thrust of the upper stage engine is 250K; area ratio of the aerospike nozzle is 78. This engine operates with LO_2/LH_2 propellants at a chamber pressure of 1500 psia. Thrust vector control requirements expected of these engines are shown in Fig. 207.

(C) Results of this analysis are presented in Fig. 208 through 210. Reference to Fig. 208 reveals that in-flight engine performance with liquid injection TVC is considerably lower than when gas injection is used for TVC in typical storable propellant booster engine applications. Comparison between Fig. 208a and Fig. 208b shows that similar results are obtained for both methods of LITVC performance prediction, but the influence of liquid injectant properties is more pronounced for performance data generated using the volumetric flowrate correlation. Liquid hydrogen injection can be expected to provide in-flight performance comparable to low-energy gas injection TVC in a typical LOX/H_2 booster engine system as shown in Fig. 209. The data in Fig. 210 indicate that similar results are obtained from upper-stage LOX/H_2 engines.

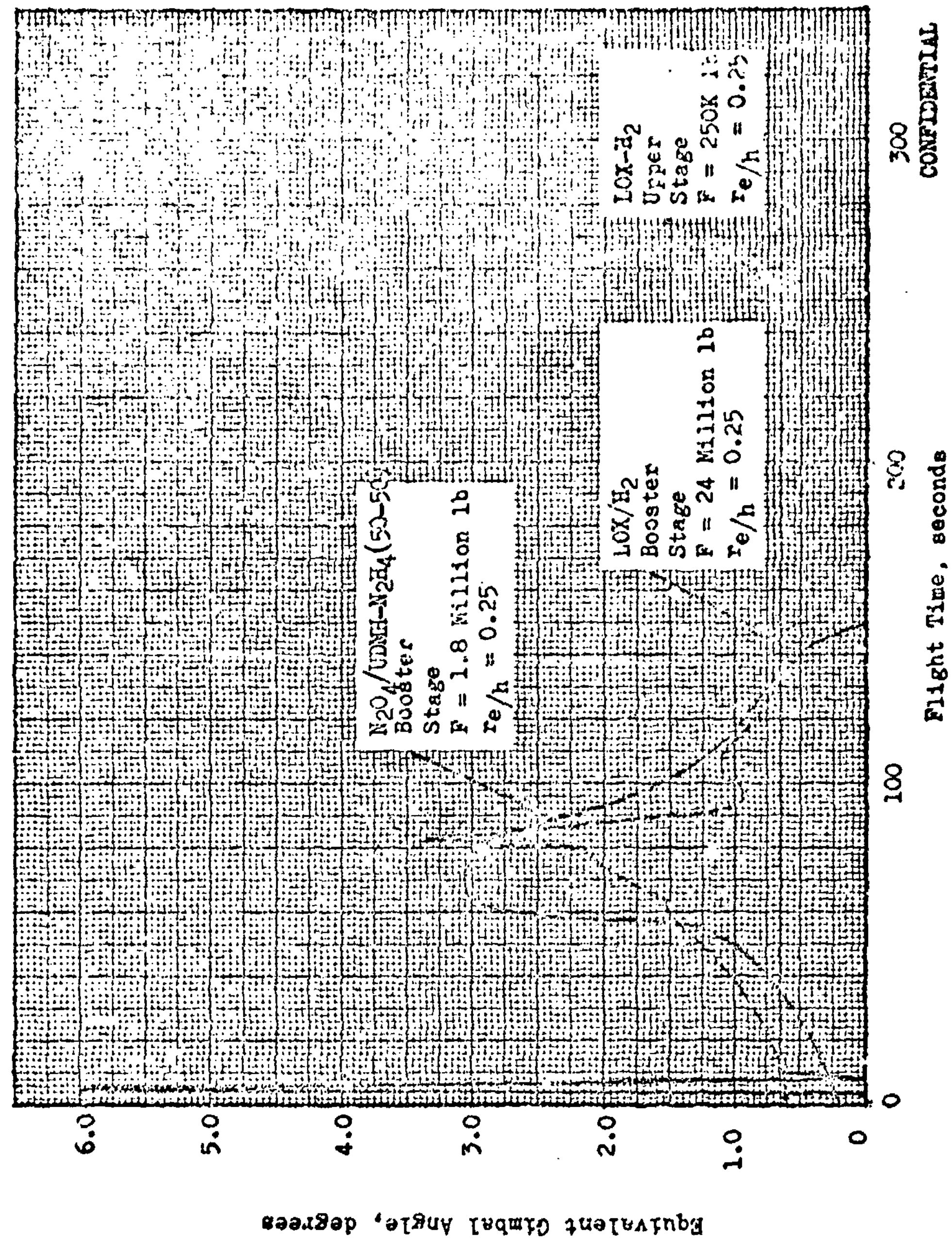

Figure 207. Typical In-Flight TVC Duty Cycle Requirements.

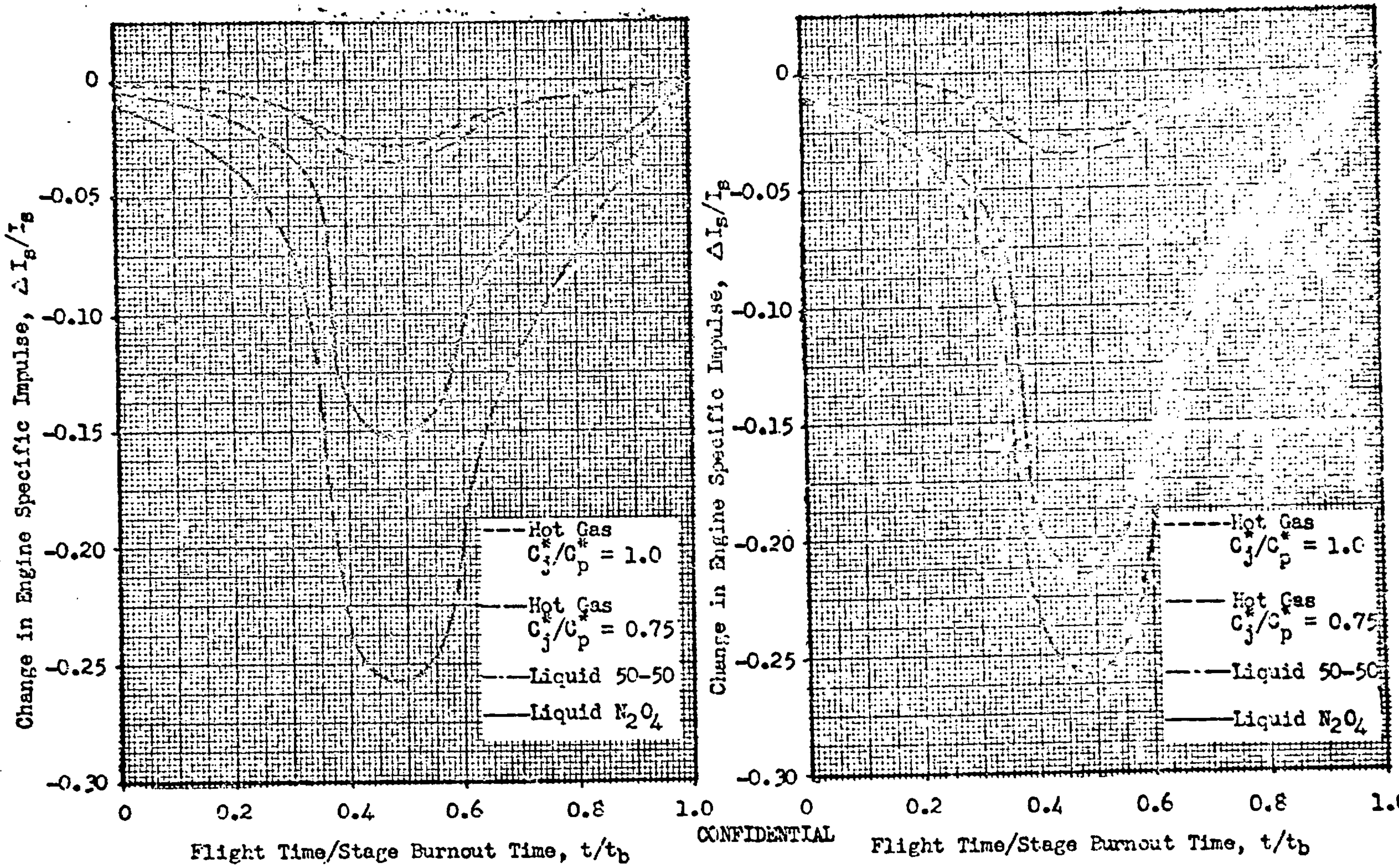

a. Performance Estimate Using the Volumetric Flowrate Correlation

b. Performance Estimate Using the Semi-Empirical Blast Wave Theory

Figure 208. In-Flight Performance Loss Associated With Fluid Injection TVC for a Low Thrust Storable Propellant Booster Engine, Thrust = 1.8 Million Pounds in Fig. 207.

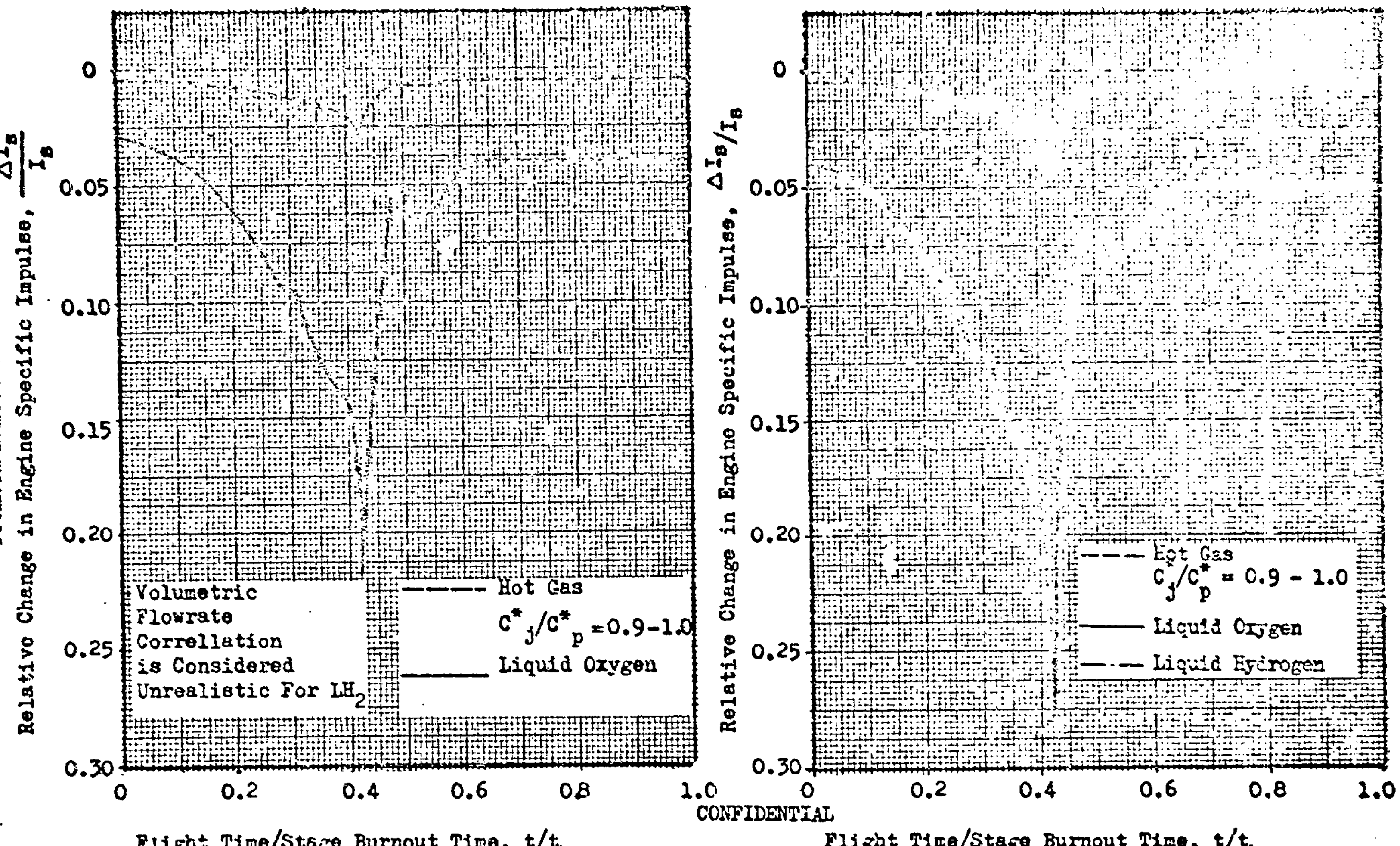

a) Performance Estimate Using the Volumetric Flowrate Correlation (Liquid)

b) Performance Estimate Using the Semi-Empirical Blast Wave Theory (Liquid)

CONFIDENTIAL

Figure 209. In-Flight Performance Loss Associated with Fluid Injection TVC for a High Thrust O_2/H_2 Booster Engine (F = 24 Million Pounds in Figure 207.)

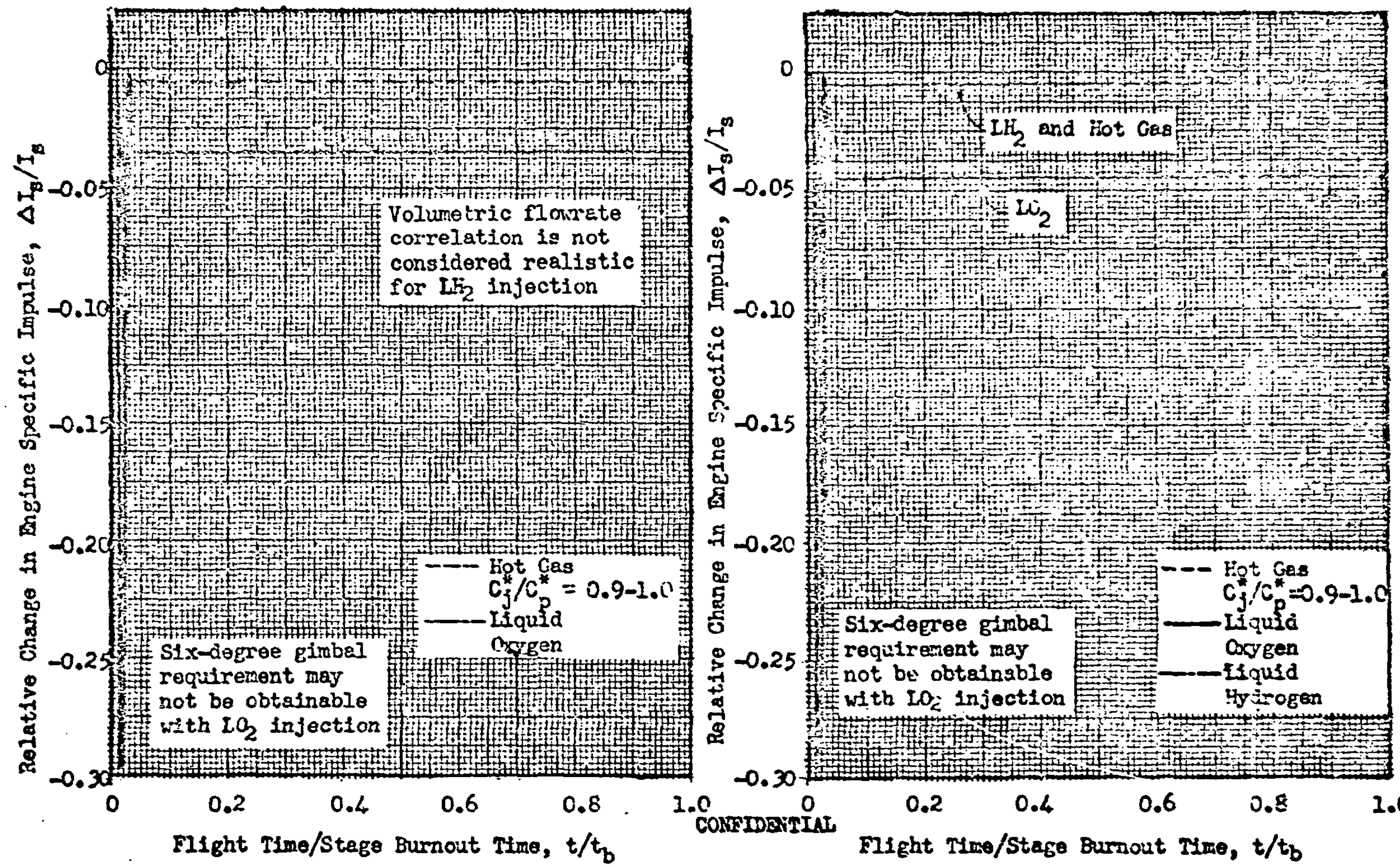

a. Performance Estimate Using the Volumetric Flowrate Correlation

b. Performance Estimate Using the Semi-Empirical Blast Wave Theory

Figure 210. In-Flight Performance Loss Associated With Fluid Injection TVC for an Upper Stage Engine (Thrust = 250K in Figure 207).

(C) It can be seen that in all cases liquid fuel injection affords higher engine specific impulse efficiency than liquid oxidizer injection. However, liquid fuel injection also results in much lower density impulse than obtained with liquid oxidizer injectants. For example, the tank mixture ratio for the LOX/H_2 booster engine (engine MR without TVC is 6.0) with liquid fuel injection (Fig. 209) is approximately 5.6 for the mission shown in Fig 207 as opposed to the more favorable mixture ratio of 6.7 if liquid oxygen is utilized for thrust vector control. A detailed systems study is required to determine the overall merits including total system weight, of each injectant. The data in Fig. 209 indicate that liquid injection with N_2O_4 or UDMH-N_2H_4 (50-50) is not competitive with practical (low energy) gaseous injection TVC systems. However, LOX/H_2 engines utilizing either liquid fuel or oxidizer as the TVC injectant may be competitive since both fluids are expected to exhibit much more favorable vaporization and reaction characteristics than the N_2O_4 data which was used as the basis for the above analysis.

CONCLUSIONS AND RECOMMENDATIONS

(C) The performance data obtained in the hot-flow test program discussed above lead to several conclusions regarding engine efficiency and liquid injection thrust vector control with an aerospike nozzle. These conclusions are as follows:

1. Measured thrust efficiency (without TVC flow) at design pressure ratio of the aerospike engine tested in this program was 95.1 percent without secondary flow and 95.2 percent with secondary flow. The measured thrust efficiency without secondary flow was 0.8 percent above the theoretical estimate. The difference is probably attributable to variations between the theoretical and actual geometries and gas properties.

2. Test data indicate that a large degree of altitude compensation was obtained with this aerospike engine in the range from 100 to 5 percent of design pressure ratio.
3. SITVC side-force efficiency trends were as expected for the most part, indicating that the effects of the injection variables can be qualitiatively determined through analysis.
   a. Multiport injection is superior to single-port injection; five-port injection provided the highest side-force efficiency of the configurations tested.
   b. Parallel-stream injection affords higher performance than radial-stream injection. The axial port inclination did not influance performance in the range tested.
   c. Port spacing did not influence performance at $x/\ell = 0.7$, but the influence of this parameter is expected to be variable with axial location.
   d. Side-force efficiency is higher if the TVC flow is injected near the throat than if injection is affected near the nozzle exit.
4. Control moment and nozzle performance trends with the injection variables are dependent upon the vehicle application.
   a. For $r_e/h = 0.25$, (typical boost vehicle) control moment and nozzle performance trends duplicate side force efficiency trends with variations in the injection parameters.
   b. If $r_e/h = 1.0$ (typical upper stage) three port injection appears to be optimum at $x/\ell = 0.25$; also, multiport injection near the nozzle exit provides higher performance than injection near the throat.

5. LITVC performance with an aerospike nozzle is generally less than that obtained with other nozzles because of the relatively short length of the aerospike.
6. Empirical coefficients utilized in the blast wave analysis of secondary injection flow phenomena must be revised to obtain quantitative agreement between experimental and theoretical performance for the configuration tested.
7. Application of the test results to typical advanced engine-vehicle configurations shows that N_2O_4 liquid injection TVC systems are not competitive with gas injection systems from the standpoint of in-flight engine performance with TVC. However, this TVC technique may be attractive for application to LO_2/LH_2 engine systems.

(C) If the relatively low TVC performance obtained in this program is the result of negligible vaporization and reaction within the nozzle, then performance may be improved through bipropellant injection. However, since maximum injectant collimation and penetration is desirable at the injection port (Ref. 12), the second fluid (fuel or oxidizer) should be injected downstream of main port as shown in Fig. 211 to ensure that the initial structure of the injectant stream is not impaired. Injectant stay time should be increased, and mixing and atomization efficiencies should also be improved downstream of the injection port. An attractive source for the secondary TVC flow is the high-temperature, fuel-rich flow available in the form of excess turbine exhaust gases.

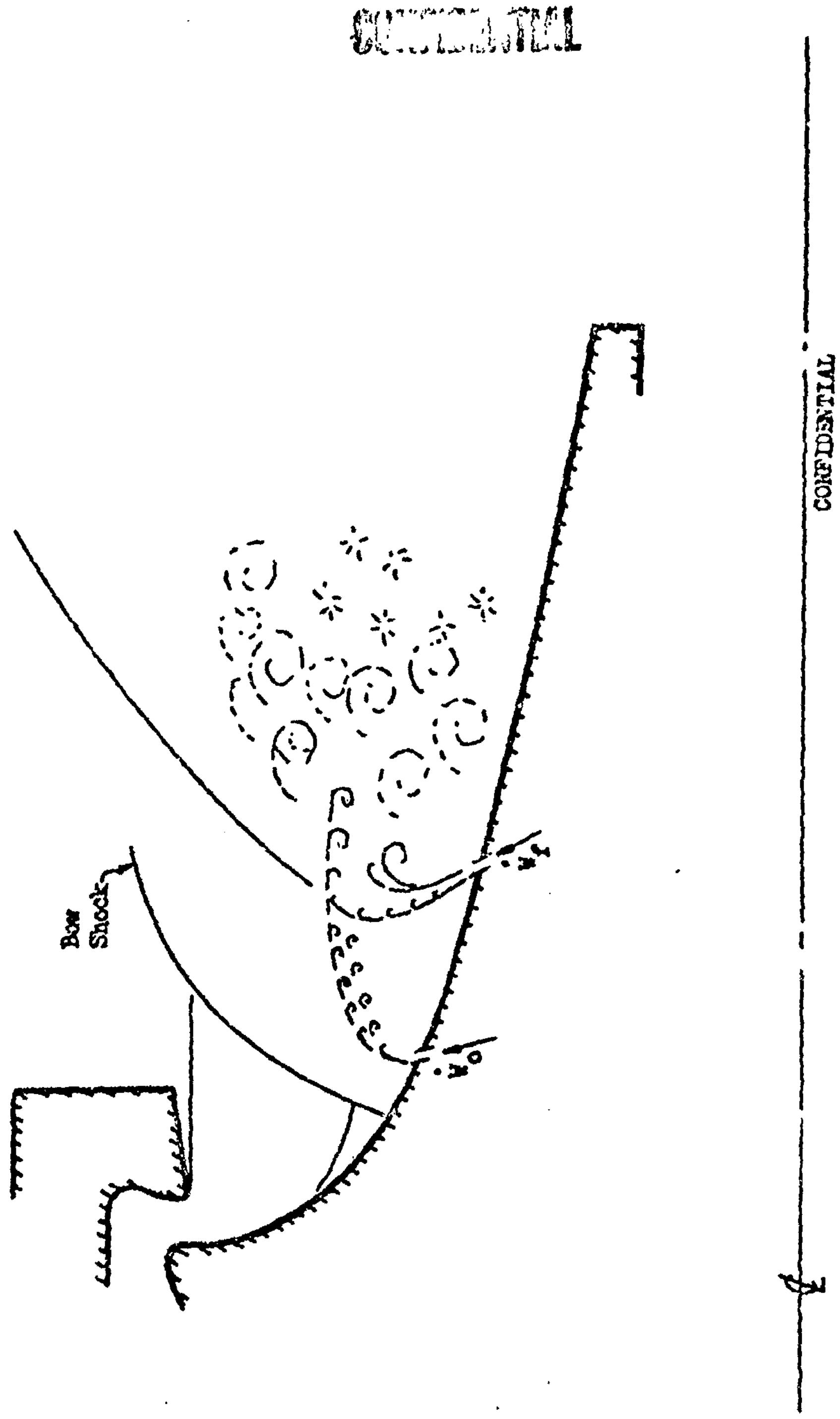

Figure 211. Improved Bipropellant Injector

(c) The test results presented herein have established the level of SITVC performance to be expected for N_2O_4 injection with an aerospike nozzle, and have verified expectations regarding the influence of the injection parameters. While the performance of liquid N_2O_4 injection was relatively low with the engine tested, several techniques not investigated may prove attractive pending further study. Liquid UDMH/N_2H_4(50-50) should provide higher performance in storable propellant engines, particularly if exothermic decomposition occurs within the nozzle. Both LO_2 and LH_2 are expected to yield higher performance than that obtained in this program because of their more favorable reactivity and vaporization characteristics. Bipropellant injection techniques such as that suggested above are attractive because of their potential for chemical reaction without having to rely on mixing with mainstream gases. Tertiary LITVC propellants such as perclorate solutions or hydrogen peroxide may be advantageous as indicated by the high performance shown for these fluids in Refs. 10 and 17. Gaseous injection TVC also yields relatively high performance as shown by the cold-flow data in Fig. 206, but further work is needed to quantitatively establish the performance of low energy gas injection systems. It is therefore recommended that studies be initiated to more fully investigate these possibilities. Complete evaluation of the SITVC concepts described above would entail the following: (1) comparative systems analysis of operational engine systems that utilize all of the forms of SITVC mentioned above, (2) development and/or refinement of theoretical SITVC performance and design analysis for both liquid and gaseous injection with emphasis on aerospike nozzle geometry, and (3) further hot- and cold-flow experimental study of various liquid and gaseous injectants.

(C) The system design studies should include evaluation of engine weights, cost, controls, and reliability as well as performance. Stress and heat transfer analysis should be performed to establish application restrictions, if any.

(C) The theoretical studies should be conducted to establish a basis for accurately determining induced pressure profiles and side forces for fluid injection TVC. This theory should incorporate provisions to establish the influence of injectant reaction (and vaporization if the injectant is a liquid) and to determine if injectant stay time and mixing is such that reaction will occur. For liquid injection, the theoretical models used in this program could be refined as proposed in Ref. 18 and 19. The primary objective of the theoretical study should be to determine attractive injectants, both inert and reactive, and establish performance and design criteria for their use in advanced aerospike SITVC systems.

(U) Experimental studies should be conducted to support the theoretical analysis where necessary, and to provide required information in areas not covered by analysis.

APPENDIX 1

TWELVE PERCENT LENGTH AEROSPIKE DATA SUMMARY

APPENDIX 1

TWELVE PERCENT LENGTH AEROSPIKE DATA SUMMARY

(U) A compilation of hot-firing data obtained with the twelve percent length water cooled aerospike is presented. Performance parameters [thrust, I_s, C^*_p, $\eta_{C^*_p}$, η_{I_s}, $\eta_{I_{s, top}}$, C_T, $C_{T_{top}}$, $(\dot{w}_s/\dot{w}_p)_{eff}$] have heat loss and water content factors applied to them. The values of the factors applied are presented in Table .

(U) Performance parameters are presented vs. time for each test. For the sea level tests (RD designation), TIME = 0.00 corresponds to ignition. For the AA test series, TIME = 4.70 is thrust chamber ignition. For the AB and AC series, TIME = 3.95 is ignition. Peak thrust occurs within approximately 90 milliseconds for all tests.

(U) An explanation of the headings in the data summary is given below.

TIME - Arbitrary reference time during firing, seconds

LAMBDAP - P_c/P_a, primary nozzle stagnation pressure to ambient pressure ratio

PA - P_a, ambient pressure, psia

PC - P_c, primary nozzle stagnation pressure, psia

PCS - $P_{c,s}$, G.G. stagnation pressure, psia (PCS = 0.0 designates GG is not firing.) ($P_{c,s}$ is actually approximately equal to $\overline{P}_B$ at this time.)

PB - $\overline{P}_B$, Average nozzle base pressure, psia

F - Measured thrust adjusted for heat loss, pounds

WS/WP - $\dot{w}_s/\dot{w}_p$, Secondary to primary flowrate ratio

WS/WP,EFF - $(\dot{w}_s/\dot{w}_p)(C^*_s/C^*_p)$, Effective Secondary flowrate ratio

WT - $\dot{w}_T$, Total engine propellant flowrate, pounds/sec.

MRP - MR_p, Primary thrust chamber propellant mixture ratio

MRS - MR_s, G.G. propellant mixture ratio

IS - $I_s = F/\dot{w}_T$, Engine specific impulse, sec.

A* - $A^*_p = .9893\ A_p$, Primary nozzle aerodynamic throat area, sq.in.

EPSILON* - $\epsilon^* (= A^*_p/A_e)$, Primary nozzle aerodynamic area ratio

PB/PC - $\bar{P}_B/P_c$

PB/PA - $\bar{P}_B/P_a$

C*S - C^*_s, G.G. characteristic velocity, ft./sec.

C*P - C^*_p, Primary thrust chamber characteristic velocity (adjusted for heat loss) ft./sec.

NC*P - $\eta_{C^*_p} (= C^*_p/C^*_{p,th})$, Primary thrust chamber characteristic velocity efficiency ($C^*_{p,th}$ adjusted for water coolant), ft./sec.

NC*S - $\eta_{C^*_s} (= C^*_s/C^*_{s,th})$, G.G. characteristic velocity efficiency, ft./sec.

NIS - $\eta_{I_s} [= F/(F_{p,th} + F_{s,th})]$, Engine specific impulse efficiency referenced to theoretical primary and theoretical secondary propellant properties.

NIS,TOP - $\eta_{I_{s,top}} [= F/F_{p,th}(1 + \dot{w}_s/\dot{w}_p)]$, Engine specific impulse efficiency referenced to theoretical primary propellant properties.

CT - $C_T [= F/(\eta_{C^*_p} F_{p,th} + \eta_{C^*_s} F_{s,th})]$, Nozzle thrust efficiency referenced to theoretical primary and secondary propellant peroperties.

CT,TOP - $C_{T,top} [= F/\eta_{C^*_p} F_{p,th}(1 + \dot{w}_s/\dot{w}_p)]$, Nozzle thrust efficiency referenced to theoretical primary propellant properties.

(c) Tabulated values of $\bar{P}_B/P_c$ were computed from measured base pressures and the averaging equation (p. 117). Analysis of the last two seconds of each test during which the GG was shut off indicated that base thrust was higher than that computed by the average base pressure method for the AC test series. It is therefore recommended that $\bar{P}_B/P_c$ values for this series be increased by the following amounts:

Test	$\Delta\bar{P}_B/P_c$
AC 14, 16	.00062
AC 19,20	.00044
AC 13,15,17,18,21	.00048

APPENDIX 1 (Cont'd)

TABLE 16

HEAT LOSS AND WATER CONTENT FACTORS APPLIED TO MEASURED AND THEORETICAL (PRIMARY ONLY) DATA

CONFIDENTIAL

Test	$\Delta I_{s_{H.L.}}$ Sec.	$\eta_{C^*_{H.L.}}$	$\Delta I_{s_{H_2O}}$, sec.	$\eta_{C^*_{H_2O}}$
RD69	+6.27	.9902	-0.30	.9987
71	+6.05	.9906	-0.30	.9987
01	+6.16	.9904	-0.30	.9987
02	+7.65	.9878	-0.30	.9987
03	+8.25	.9872	-0.30	.9987
05	+9.23	.9856	-0.20	.9994
06	+9.00	.9860	-0.20	.9994
08	+9.12	.9858	-0.20	.9994
09	+9.33	.9853	-0.20	.9994
AA01	+6.90	.9891	-0.26	.99915
02	+6.70	.9896	-0.26	.99915
03	+7.16	.9888	-0.26	.99915
AB08	+7.37	.9884	-0.21	.99937
09	+7.37	.9884	-0.21	.99937
10	+7.56	.9881	-0.21	.99937
11	+7.79	.9878	-0.21	.99937
12	+7.94	.9875	-0.21	.99937
AC13	+7.88	.9874	-0.19	.99943
14	+7.54	.9883	-0.19	.99943
15	+8.29	.9869	-0.19	.99943
16	+8.26	.9867	-0.19	.99943
17	+8.13	.9871	-0.19	.99943
18	+8.06	.9874	-0.19	.99943
19	+7.91	.9876	-0.19	.99943
20	+8.20	.9872	-0.19	.99943
21	+7.91	.9876	-0.19	.99943

APPENDIX 1 (Cont'd)

HOT - FIRING TEST DATA -- 12 PERCENT LENGTH AEROSPIKE NOZZLE
TEST NUMBER AA01, PAGE 1

CONFIDENTIAL

TIME (SECONDS)	LAMBDAP (DMNLESS)	PA (PSIA)	PC (PSIA)	PCS (PSIA)	PB (PSIA)	F (POUNDS)
4.95	432.92	0.6535	282.91	0.0	1.8038	6961.
5.25	319.45	0.8815	281.59	0.0	1.8621	6878.
5.75	232.95	1.2024	280.09	0.0	1.8656	6763.
6.25	187.56	1.4903	279.52	0.0	1.8607	6638.
6.75	165.13	1.6918	279.37	0.0	1.8380	6560.
7.25	146.56	1.9047	279.16	0.0	1.8655	6497.

TIME (SECONDS)	WS/WP (DMNLESS)	WS/WP, EFF (DMNLESS)	WT (LBS/SEC)	KRP (DMNLESS)	MRS (DMNLESS)	IS (SECONDS)
4.95	0.0	0.0	25.4017	1.7218	0.0	274.05
5.25	0.0	0.0	25.4558	1.7129	0.0	270.18
5.75	0.0	0.0	25.2814	1.6929	0.0	267.53
6.25	0.0	0.0	25.3527	1.6927	0.0	261.82
6.75	0.0	0.0	25.2388	1.6885	0.0	259.92
7.25	0.0	0.0	25.1406	1.6935	0.0	258.45

CONFIDENTIAL

CONFIDENTIAL

APPENDIX I (Cont'd)

HOT - FIRING TEST DATA -- 12 PERCENT LENGTH AEROSPIKE NOZZLE
TEST NUMBER AA01, PAGE 2

CONFIDENTIAL

TIME (SECONDS)	A* (SQ. IN.)	EPSILON* (DMNLESS)	PB/PC (DMNLESS)	PB/PA (DMNLESS)	C*S (FT/SEC)	C*P (FT/SEC)
4.95	14.205	26.156	0.00638	2.760	0.	5146.
5.25	14.241	26.089	0.00661	2.113	0.	5124.
5.75	14.298	25.985	0.00666	1.552	0.	5153.
6.25	14.342	25.906	0.00666	1.249	0.	5144.
6.75	14.370	25.855	0.00658	1.086	0.	5174.
7.25	14.392	25.816	0.00668	0.979	0.	5198.

TIME (SECONDS)	NC*P (DMNLESS)	NC*S (DMNLESS)	NIS (DMNLESS)	NIS, TOP (DMNLESS)	CT (DMNLESS)	CT, TOP (DMNLESS)
4.95	0.8962	0.0	0.8559	0.8559	0.9550	0.9550
5.25	0.8922	0.0	0.8563	0.8563	0.9598	0.9598
5.75	0.8967	0.0	0.8626	0.8626	0.9620	0.9620
6.25	0.8951	0.0	0.8546	0.8546	0.9547	0.9547
6.75	0.9004	0.0	0.8549	0.8549	0.9495	0.9495
7.25	0.9047	0.0	0.8560	0.8560	0.9462	0.9462

CONFIDENTIAL

APPENDIX 1 (Cont'd)

HOT - FIRING TEST DATA -- 12 PERCENT LENGTH AEROSPIKE NOZZLE
TEST NUMBER AA02, PAGE 1

CONFIDENTIAL

TIME (SECONDS)	LAMBDAP (DMNLESS)	PA (PSIA)	PC (PSIA)	PCS (PSIA)	PB (PSIA)	F (POUNDS)
5.25	320.47	0.9568	306.63	0.0	2.0267	7435.
5.75	235.48	1.2986	305.81	0.0	2.0220	7326.
6.25	189.51	1.6095	305.03	0.0	2.0229	7208.
6.75	168.84	1.8036	304.52	0.0	2.0208	7134.
7.25	151.41	2.0115	304.56	0.0	2.0462	7082.
7.75	132.32	2.3008	304.45	0.0	2.1647	6976.
8.25	123.83	2.4558	304.11	0.0	2.2494	6944.
8.75	118.23	2.5714	304.00	0.0	2.3755	6913.
9.25	111.85	2.7158	303.76	0.0	2.5688	6886.
9.75	106.39	2.8545	303.70	0.0	2.7964	6862.
10.25	100.66	3.0172	303.70	0.0	3.0290	6852.
10.75	95.03	3.1978	303.87	0.0	3.3135	6841.
11.25	93.05	3.2648	303.78	0.0	3.4223	6825.
11.75	89.83	3.3807	303.69	0.0	3.5498	6801.

TIME (SECONDS)	WS/WP (DMNLESS)	WS/WP, EFF (DMNLESS)	WT (LBS/SEC)	MRP (DMNLESS)	MRS (DMNLESS)	IS (SECONDS)
5.25	0.0	0.0	27.6638	1.7744	0.0	268.76
5.75	0.0	0.0	27.5478	1.7704	0.0	265.95
6.25	0.0	0.0	27.4761	1.7709	0.0	262.34
6.75	0.0	0.0	27.4311	1.7665	0.0	260.07
7.25	0.0	0.0	27.4084	1.7715	0.0	258.38
7.75	0.0	0.0	27.3148	1.7627	0.0	255.38
8.25	0.0	0.0	27.3044	1.7772	0.0	254.34
8.75	0.0	0.0	27.2601	1.7729	0.0	253.58
9.25	0.0	0.0	27.3128	1.7632	0.0	252.13
9.75	0.0	0.0	27.2311	1.7783	0.0	251.99
10.25	0.0	0.0	27.2843	1.7685	0.0	251.12
10.75	0.0	0.0	27.2134	1.7690	0.0	251.39
11.25	0.0	0.0	27.2308	1.7782	0.0	250.65
11.75	0.0	0.0	27.2328	1.7781	0.0	249.72

APPENDIX 1 (Cont'd)

HOT - FIRING TEST DATA -- 12 PERCENT LENGTH AERUSPIKE NOZZLE
TEST NUMBER AA32, PAGE 1

CONFIDENTIAL

TIME (SECONDS)	LAMBDAP (DMNLESS)	PA (PSIA)	PC (PSIA)	PCS (PSIA)	PB (PSIA)	F (POUNDS)
5.25	320.47	0.9568	306.63	0.0	2.0267	7435.
5.75	235.48	1.2986	305.81	0.0	2.0220	7326.
6.25	189.51	1.6095	305.33	0.0	2.0229	7208.
6.75	168.84	1.8036	304.52	0.0	2.0208	7134.
7.25	151.41	2.0115	304.55	0.0	2.0462	7062.
7.75	132.32	2.3008	304.45	0.0	2.1647	6976.
8.25	123.83	2.4558	304.11	0.0	2.2494	6944.
8.75	118.23	2.5714	304.00	0.0	2.3755	6913.
9.25	111.85	2.7158	303.76	0.0	2.5688	6886.
9.75	106.39	2.8545	303.70	0.0	2.7984	6862.
10.25	100.66	3.0172	303.70	0.0	3.0290	6852.
10.75	95.03	3.1978	303.87	0.0	3.3135	6841.
11.25	93.05	3.2648	303.78	0.0	3.4223	6825.
11.75	89.83	3.3807	303.69	0.0	3.5498	6801.

TIME (SECONDS)	WS/WP (DMNLESS)	WS/WP, EFF (DMNLESS)	WT (LBS/SEC)	MRP (DMNLESS)	MRS (DMNLESS)	IS (SECONDS)
5.25	0.0	0.0	27.6638	1.7744	0.0	268.76
5.75	0.0	0.0	27.5478	1.7704	0.0	265.95
6.25	0.0	0.0	27.4761	1.7709	0.0	262.34
6.75	0.0	0.0	27.4311	1.7665	0.0	260.07
7.25	0.0	0.0	27.4084	1.7715	0.0	258.38
7.75	0.0	0.0	27.3148	1.7527	0.0	255.38
8.25	0.0	0.0	27.3044	1.7772	0.0	254.34
8.75	0.0	0.0	27.2601	1.7729	0.0	253.58
9.25	0.0	0.0	27.3128	1.7632	0.0	252.13
9.75	0.0	0.0	27.2311	1.7783	0.0	251.99
10.25	0.0	0.0	27.2843	1.7685	0.0	251.12
10.75	0.0	0.0	27.2134	1.7690	0.0	251.39
11.25	0.0	0.0	27.2308	1.7782	0.0	250.65
11.75	0.0	0.0	27.2328	1.7781	0.0	249.72

CONFIDENTIAL

CONFIDENTIAL

APPENDIX 1 (Cont'd)

HOT - FIRING TEST DATA -- 12 PERCENT LENGTH AEROSPIKE NOZZLE
TEST NUMBER AA02, PAGE 2

TIME (SECONDS)	A* (SQ. IN.)	EPSILON* (DMNLESS)	PB/PC (DMNLESS)	PB/PA (DMNLESS)	C*S (FT/SEC)	C*P (FT/SEC)
5.25	14.096	26.358	0.00661	2.118	0.	5060.
5.75	14.153	26.252	0.00661	1.557	0.	5108.
6.25	14.196	26.172	0.00663	1.257	0.	5124.
6.75	14.225	26.119	0.00664	1.120	0.	5134.
7.25	14.246	26.080	0.00672	1.017	0.	5147.
7.75	14.246	26.080	0.00711	0.941	0.	5163.
8.25	14.246	26.080	0.00740	0.916	0.	5159.
8.75	14.246	26.080	0.00781	0.924	0.	5165.
9.25	14.246	26.080	0.00846	0.946	0.	5151.
9.75	14.246	26.080	0.00921	0.980	0.	5166.
10.25	14.246	26.080	0.00997	1.004	0.	5156.
10.75	14.246	26.080	0.01090	1.036	0.	5172.
11.25	14.246	26.080	0.01127	1.048	0.	5167.
11.75	14.246	26.080	0.01169	1.050	0.	5165.

TIME (SECONDS)	NC*P (DMNLESS)	NC*S (DMNLESS)	NIS (DMNLESS)	NIS, TOP (DMNLESS)	CT (DMNLESS)	CT, TOP (DMNLESS)
5.25	0.8856	0.0	0.8490	0.8490	0.9587	0.9587
5.75	0.8904	0.0	0.8537	0.8537	0.9589	0.9589
6.25	0.8932	0.0	0.8526	0.8526	0.9546	0.9546
6.75	0.8948	0.0	0.8511	0.8511	0.9511	0.9511
7.25	0.8972	0.0	0.8511	0.8511	0.9486	0.9486
7.75	0.8996	0.0	0.8488	0.8488	0.9434	0.9434
8.25	0.8994	0.0	0.8486	0.8486	0.9434	0.9434
8.75	0.9004	0.0	0.8488	0.8498	0.9426	0.9426
9.25	0.8977	0.0	0.8474	0.8474	0.9440	0.9440
9.75	0.9007	0.0	0.8495	0.8495	0.9431	0.9431
10.25	0.8986	0.0	0.8501	0.8501	0.9460	0.9460
10.75	0.9015	0.0	0.8546	0.8546	0.9479	0.9479
11.25	0.9009	0.0	0.8531	0.8531	0.9469	0.9469
11.75	0.9006	0.0	0.8522	0.8522	0.9463	0.9463

CONFIDENTIAL

CONFIDENTIAL

APPENDIX 1 (Cont'd)

HOT - FIRING TEST DATA -- 12 PERCENT LENGTH AEROSPIKE NOZZLE
TEST NUMBER AA03, PAGE 1

CONFIDENTIAL

TIME (SECONDS)	LAMBDAP (DMNLESS)	PA (PSIA)	PC (PSIA)	PCS (PSIA)	PR (PSIA)	F (POUNDS)
5.25	82.14	3.7446	307.57	0.0	4.2063	6857.
5.75	70.09	4.3789	306.90	0.0	4.9030	6797.
6.25	62.74	4.8572	305.96	0.0	5.5019	6675.
6.75	57.19	5.3406	305.42	0.0	6.1089	6573.
7.25	53.12	5.7429	305.05	0.0	6.6013	6498.
7.75	49.62	6.1459	304.96	0.0	7.2062	6469.
8.25	46.50	6.5551	304.91	0.0	7.7078	6443.
8.75	43.93	6.9285	304.34	0.0	8.2583	6395.
9.25	41.65	7.2982	304.29	0.0	8.7248	6356.
9.75	39.96	7.6140	304.24	0.0	9.1174	6316.
10.25	38.46	7.9047	304.04	0.0	9.5366	6284.
10.75	37.27	8.1548	303.90	0.0	9.8241	6277.
11.25	36.20	8.3935	303.87	0.0	10.1210	6253.
11.75	35.07	8.6595	303.65	0.0	10.4348	6221.

TIME (SECONDS)	WS/WP (DMNLESS)	WS/WP, EFF (DMNLESS)	WT (LBS/SEC)	MRP (DMNLESS)	MRS (DMNLESS)	TS (SECONDS)
5.25	0.0	0.0	27.6888	1.7790	0.0	247.63
5.75	0.0	0.0	27.6862	1.7700	0.0	242.24
6.25	0.0	0.0	27.5615	1.7802	0.0	240.36
6.75	0.0	0.0	27.4467	1.7763	0.0	239.48
7.25	0.0	0.0	27.4462	1.7762	0.0	236.77
7.75	0.0	0.0	27.4566	1.7621	0.0	235.61
8.25	0.0	0.0	27.4563	1.7620	0.0	234.67
8.75	0.0	0.0	27.3850	1.7625	0.0	233.15
9.25	0.0	0.0	27.3854	1.7626	0.0	232.08
9.75	0.0	0.0	27.2715	1.7586	0.0	231.60
10.25	0.0	0.0	27.3048	1.7773	0.0	230.13
10.75	0.0	0.0	27.2512	1.7872	0.0	230.33
11.25	0.0	0.0	27.1914	1.7733	0.0	229.07
11.75	0.0	0.0	27.2409	1.7778	0.0	228.35

CONFIDENTIAL

APPENDIX 1 (Cont'd)

HOT - FIRING TEST DATA -- 12 PERCENT LENGTH AEROSPIKE NOZZLE
TEST NUMBER AA03, PAGE 2

CONFIDENTIAL

TIME (SECONDS)	A* (SQ. IN.)	EPSILON* (DMNLESS)	PB/PC (DMNLESS)	PB/PA (DMNLESS)	C*S (FT/SEC)	C*P (FT/SEC)
5.25	14.162	26.235	0.01368	1.123	0.	5119.
5.75	14.196	26.172	0.01598	1.120	0.	5120.
6.25	14.229	26.111	0.01799	1.133	0.	5138.
6.75	14.262	26.051	0.02000	1.144	0.	5164.
7.25	14.279	26.020	0.02164	1.149	0.	5164.
7.75	14.279	26.020	0.02363	1.173	0.	5161.
8.25	14.279	26.020	0.02558	1.190	0.	5158.
8.75	14.279	26.020	0.02714	1.192	0.	5164.
9.25	14.279	26.020	0.02867	1.195	0.	5163.
9.75	14.279	26.020	0.02997	1.197	0.	5183.
10.25	14.279	26.020	0.03137	1.206	0.	5174.
10.75	14.279	26.020	0.03233	1.205	0.	5181.
11.25	14.279	26.020	0.03331	1.206	0.	5192.
11.75	14.279	26.020	0.03436	1.205	0.	5179.

TIME (SECONDS)	NC*P (DMNLESS)	NC*S (DMNLESS)	NIS (DMNLESS)	NIS, TRP (DMNLESS)	CT (DMNLESS)	CT, TRP (DMNLESS)
5.25	0.8922	0.0	0.8509	0.8509	0.9538	0.9538
5.75	0.8925	0.0	0.5428	0.8428	0.9444	0.9444
6.25	0.8959	0.0	0.8438	0.8438	0.9418	0.9418
6.75	0.9003	0.0	0.8475	0.8475	0.9413	0.9413
7.25	0.9003	0.0	0.8433	0.8433	0.9367	0.9367
7.75	0.8993	0.0	0.8446	0.8446	0.9392	0.9392
8.25	0.8988	0.0	0.8463	0.8463	0.9415	0.9415
8.75	0.8998	0.0	0.8453	0.8453	0.9394	0.9394
9.25	0.8997	0.0	0.8457	0.8457	0.9400	0.9400
9.75	0.9032	0.0	0.8475	0.8475	0.9384	0.9384
10.25	0.9020	0.0	0.8451	0.8451	0.9369	[illegible]
10.75	0.9037	0.0	0.8485	0.8485	0.9389	0.9389
11.25	0.9052	0.0	0.8498	0.8498	0.9389	0.9389
11.75	0.9030	0.0	0.8466	0.8466	0.9376	0.9376

APPENDIX 1 (Cont'd)

HOT - FIRING TEST DATA -- 12 PERCENT LENGTH AEROSPIKE NOZZLE
TEST NUMBER AB08, PAGE 1

CONFIDENTIAL

TIME (SECONDS)	LAMBDAP (DMNLESS)	PA (PSIA)	PC (PSIA)	PCS (PSIA)	PB (PSIA)	F (POUNDS)
4.45	257.62	1.1853	305.36	278.54	2.7672	7426.
4.75	200.53	1.5126	303.48	268.97	2.7837	7261.

TIME (SECONDS)	WS/WP (DMNLESS)	WS/WP, EFF (DMNLESS)	WT (LBS/SEC)	MRP (DMNLESS)	MRS (DMNLESS)	IS (SECONDS)
4.45	0.0254	0.0163	27.7242	1.7261	0.0840	267.86
4.75	0.0259	0.0158	27.6777	1.7267	0.0850	262.34

APPENDIX 1 (Cont'd)

HOT - FIRING TEST DATA -- 12 PERCENT LENGTH AEROSPIKE NOZZLE
TEST NUMBER A808, PAGE 2

CONFIDENTIAL

TIME (SECONDS)	A* (SQ. IN.)	EPSILON* (DMNLESS)	PB/PC (DMNLESS)	PB/PA (DMNLESS)	C*S (FT/SEC)	C*P (FT/SEC)
4.45	14.038	26.467	0.00906	2.335	3311.	5161.
4.75	14.059	26.427	0.00917	1.843	3139.	5148.

TIME (SECONDS)	NC*P (DMNLESS)	NC*S (DMNLESS)	NIS (DMNLESS)	NIS, TOP (DMNLESS)	CT (DMNLESS)	CT, TOP (DMNLESS)
4.45	0.8982	0.7636	0.8625	0.8574	0.9631	0.9546
4.75	0.8960	0.7242	0.8566	0.8513	0.9596	0.9502

CONFIDENTIAL

CONFIDENTIAL

CONFIDENTIAL

APPENDIX 1 (Cont'd)

HOT - FIRING TEST DATA -- 12 PERCENT LENGTH AEROSPIKE NOZZLE
TEST NUMBER ABD9, PAGE 1

CONFIDENTIAL

TIME (SECONDS)	LAMBDAP (DMNLESS)	PA (PSIA)	PC (PSIA)	PCS (PSIA)	PB (PSIA)	F (POUNDS)
4.45	224.32	1.3597	305.01	283.63	2.7795	7318.
4.75	177.72	1.7090	303.74	271.22	2.8063	7163.
5.25	139.28	2.1726	302.61	269.26	3.0364	7014.
5.75	125.49	2.4032	301.59	269.40	3.3008	6975.
6.25	112.20	2.6822	300.94	269.40	3.6479	6905.
6.75	100.86	2.9788	300.44	269.87	4.0304	6860.
7.25	92.02	3.2650	300.46	270.29	4.4402	6834.
7.75	85.27	3.5210	300.26	269.85	4.7747	6796.
8.25	79.17	3.7869	299.82	270.14	5.1036	6722.
8.75	74.81	4.0072	299.79	270.68	5.2170	6696.
9.25	70.58	4.2388	299.18	271.03	5.5161	6645.
9.75	67.18	4.4417	298.39	271.23	5.8675	6606.

TIME (SECONDS)	WS/WP (DMNLESS)	WS/WP, EFF (DMNLESS)	WT (LBS/SEC)	MRP (DMNLESS)	MRS (DMNLESS)	IS (SECONDS)
4.45	0.0255	0.0167	27.6365	1.7388	0.0873	264.72
4.75	0.0262	0.0160	27.5405	1.7348	0.0884	260.08
5.25	0.0262	0.0159	27.6044	1.7261	0.0886	254.08
5.75	0.0263	0.0160	27.5153	1.7374	0.0886	253.51
6.25	0.0263	0.0160	27.4510	1.7269	0.0887	251.54
6.75	0.0263	0.0160	27.4446	1.7320	0.0886	249.94
7.25	0.0263	0.0160	27.3930	1.7414	0.0886	249.47
7.75	0.0265	0.0160	27.2991	1.7469	0.0887	248.95
8.25	0.0264	0.0160	27.3217	1.7414	0.0886	246.02
8.75	0.0264	0.0161	27.2814	1.7374	0.0886	245.44
9.25	0.0263	0.0161	27.3888	1.7412	0.0886	242.62
9.75	0.0266	0.0161	27.1331	1.7154	0.0886	243.48

CONFIDENTIAL

APPENDIX 1 (Cont'd)

HOT - FIRING TEST DATA -- 12 PERCENT LENGTH AEROSPIKE NOZZLE
TEST NUMBER AB39, PAGE 2

CONFIDENTIAL

TIME (SECONDS)	A* (SQ. IN.)	EPSILON* (DMNLESS)	PB/PC (DMNLESS)	PB/PA (DMNLESS)	C*S (FT/SEC)	C*P (FT/SEC)
4.45	13.959	26.617	0.00911	2.044	3377.	5143.
4.75	13.980	26.577	0.00924	1.642	3150.	5150.
5.25	14.009	26.521	0.01003	1.398	3119.	5130.
5.75	14.030	26.482	0.01094	1.373	3123.	5137.
6.25	14.047	26.450	0.01212	1.360	3124.	5145.
6.75	14.061	26.423	0.01341	1.353	3133.	5142.
7.25	14.072	26.403	0.01478	1.360	3140.	5157.
7.75	14.086	26.377	0.01590	1.356	3133.	5177.
8.25	14.101	26.348	0.01702	1.348	3138.	5170.
8.75	14.112	26.328	0.01759	1.316	3147.	5181.
9.25	14.119	26.315	0.01844	1.301	3153.	5152.
9.75	14.132	26.291	0.01966	1.321	3156.	5193.

CONFIDENTIAL

TIME (SECONDS)	NC*P (DMNLESS)	NC*S (DMNLESS)	NIS (DMNLESS)	NIS, TOP (DMNLESS)	CT (DMNLESS)	CT, TOP (DMNLESS)
4.45	0.8953	0.7777	0.8585	0.8533	0.9613	0.9531
4.75	0.8966	0.7257	0.8549	0.8496	0.9570	0.9476
5.25	0.8928	0.7186	0.8480	0.8427	0.9534	0.9439
5.75	0.8944	0.7196	0.8514	0.8461	0.9556	0.9461
6.25	0.8954	0.7198	0.8515	0.8462	0.9546	0.9450
6.75	0.8952	0.7218	0.8522	0.8469	0.9557	0.9461
7.25	0.8979	0.7234	0.8560	0.8506	0.9570	0.9474
7.75	0.9015	0.7218	0.8589	0.8535	0.9565	0.9463
8.25	0.9003	0.7229	0.8537	0.8484	0.9519	0.9423
8.75	0.9021	0.7250	0.8555	0.8502	0.9521	0.9425
9.25	0.8972	0.7264	0.8495	0.8442	0.9504	0.9410
9.75	0.9037	0.7272	0.8567	0.8513	0.9516	0.9420

CONFIDENTIAL

CONFIDENTIAL

APPENDIX 1 (Cont'd)

HDT - FIRING TEST DATA -- 12 PERCENT LENGTH AEROSPIKE NOZZLE
TEST NUMBER AB13, PAGE 1

CONFIDENTIAL

TIME (SECONDS)	LAMBDAP (DMNLESS)	PA (PSIA)	PC (PSIA)	PCS (PSIA)	PB (PSIA)	F (POUNDS)
4.45	195.16	1.5375	300.05	91.69	2.4444	7047.
4.75	158.09	1.8901	298.81	101.41	2.5413	6890.
5.25	129.63	2.2983	297.46	112.95	2.8810	6800.
5.75	113.38	2.6151	296.50	116.17	3.2699	6743.
6.25	101.32	2.9216	296.01	116.66	3.5929	6666.
6.75	92.60	3.1901	295.40	116.57	3.9686	6630.
7.25	85.23	3.4627	295.11	116.75	4.3250	6598.
7.75	78.06	3.7745	294.54	116.67	4.6952	6532.
8.25	72.45	4.0665	294.50	116.89	5.1054	6505.
8.75	68.19	4.3177	294.43	116.97	5.4037	6461.
9.25	64.93	4.5303	294.17	117.11	5.5767	6406.
9.75	62.24	4.7169	293.57	116.83	5.9316	6375.

TIME (SECONDS)	WS/WP (DMNLESS)	WS/WP, EFF (DMNLESS)	WT (LBS/SEC)	MRP (DMNLESS)	MRS (DMNLESS)	IS (SECONDS)
4.45	0.0146	0.0055	26.9082	1.7337	0.1075	261.90
4.75	0.0137	0.0061	26.9128	1.7289	0.1079	256.02
5.25	0.0125	0.0068	26.8003	1.7439	0.1086	253.71
5.75	0.0122	0.0070	26.6847	1.7299	0.1090	252.69
6.25	0.0122	0.0071	26.6822	1.7453	0.1092	249.91
6.75	0.0122	0.0071	26.6630	1.7464	0.1093	248.68
7.25	0.0121	0.0071	26.6708	1.7618	0.1094	247.37
7.75	0.0122	0.0071	26.5863	1.7526	0.1095	245.69
8.25	0.0121	0.0071	26.6278	1.7489	0.1095	244.30
8.75	0.0121	0.0071	26.5822	1.7679	0.1096	243.04
9.25	0.0121	0.0071	26.5926	1.7535	0.1096	240.90
9.75	0.0122	0.0071	26.3582	1.7449	0.1095	241.87

CONFIDENTIAL

CONFIDENTIAL

APPENDIX 1 (Cont'd)

HOT - FIRING TEST DATA -- 12 PERCENT LENGTH AEROSPIKE NOZZLE
TEST NUMBER AB13, PAGE 2

CONFIDENTIAL

TIME (SECONDS)	A* (SQ. IN.)	EPSILON* (DMNLESS)	PB/PC (DMNLESS)	PB/PA (DMNLESS)	C*S (FT/SEC)	C*P (FT/SEC)
4.45	13.893	26.743	0.00815	1.590	1932.	5119.
4.75	13.914	26.703	0.00850	1.345	2277.	5099.
5.25	13.942	26.649	0.00969	1.254	2780.	5102.
5.75	13.963	26.609	0.01103	1.250	2945.	5113.
6.25	13.980	26.577	0.01214	1.230	2975.	5111.
6.75	13.994	26.550	0.01343	1.244	2973.	5110.
7.25	14.006	26.527	0.01466	1.249	2986.	5107.
7.75	14.020	26.501	0.01594	1.244	2984.	5121.
8.25	14.034	26.474	0.01733	1.255	2996.	5117.
8.75	14.045	26.454	0.01835	1.252	3002.	5127.
9.25	14.052	26.440	0.01896	1.231	3010.	5123.
9.75	14.065	26.416	0.02021	1.258	2995.	5163.

TIME (SECONDS)	NC*P (DMNLESS)	NC*S (DMNLESS)	NIS (DMNLESS)	NIS, TOP (DMNLESS)	CT (DMNLESS)	CT, TOP (DMNLESS)
4.45	0.8911	0.4499	0.8540	0.8510	0.9636	0.9550
4.75	0.8876	0.5300	0.8452	0.8424	0.9561	0.9490
5.25	0.8885	0.6458	0.8475	0.8449	0.9563	0.9510
5.75	0.8902	0.6839	0.8519	0.8494	0.9591	0.9542
6.25	0.8902	0.6906	0.8487	0.8462	0.9553	0.9505
6.75	0.8900	0.6903	0.8500	0.8475	0.9570	0.9522
7.25	0.8900	0.6932	0.8503	0.8478	0.9573	0.9526
7.75	0.8921	0.6927	0.8504	0.8479	0.9553	0.9505
8.25	0.8913	0.6954	0.8507	0.8482	0.9563	0.9516
8.75	0.8936	0.6967	0.8500	0.8475	0.9531	0.9484
9.25	0.8925	0.6986	0.8462	0.8437	0.9501	0.9454
9.75	0.8993	0.6952	0.8529	0.8503	0.9504	0.9456

CONFIDENTIAL

CONFIDENTIAL

APPENDIX 1 (Cont'd)

HOT - FIRING TEST DATA -- 12 PERCENT LENGTH AEROSPIKE NOZZLE
TEST NUMBER AB11, PAGE 1

CONFIDENTIAL

TIME (SECONDS)	LAMBDAP (DMNLESS)	PA (PSIA)	PC (PSIA)	PCS (PSIA)	PB (PSIA)	F (POUNDS)
4.45	103.77	2.9305	334.10	262.31	4.0875	6901.
4.75	87.83	3.4482	332.87	244.55	4.7766	6783.
5.25	72.90	4.1383	331.68	246.49	5.5418	6681.
5.75	67.02	4.4893	330.86	246.63	6.0069	6601.
6.25	60.96	4.9316	333.65	245.16	6.5102	6538.
6.75	56.47	5.3244	300.68	246.18	7.1116	6485.
7.25	52.20	5.7582	300.56	246.18	7.5384	6420.
7.75	49.07	6.1217	300.39	246.35	8.0906	6373.
8.25	46.36	6.4761	300.21	246.71	8.4763	6318.
8.75	43.93	6.8316	300.10	246.75	8.9504	6285.
9.25	41.63	7.1969	299.52	246.48	9.4243	6253.
9.75	39.67	7.5402	299.11	246.39	9.8149	6190.

TIME (SECONDS)	WS/WP (DMNLESS)	WS/WP, EFF (DMNLESS)	WT (LBS/SEC)	MRP (DMNLESS)	MRS (DMNLESS)	IS (SECONDS)
4.45	0.0223	0.0157	27.5707	1.7613	0.1140	250.30
4.75	0.0235	0.0146	27.4644	1.7630	0.1133	246.98
5.25	0.0233	0.0147	27.4571	1.7627	0.1136	243.32
5.75	0.0234	0.0148	27.3309	1.7546	0.1139	241.52
6.25	0.0234	0.0147	27.3412	1.7615	0.1140	239.12
6.75	0.0233	0.0147	27.3731	1.7572	0.1141	236.90
7.25	0.0233	0.0147	27.3362	1.7588	0.1140	234.84
7.75	0.0233	0.0147	27.3356	1.7662	0.1140	233.15
8.25	0.0233	0.0147	27.3201	1.7563	0.1139	231.26
8.75	0.0234	0.0147	27.2222	1.7618	0.1139	230.88
9.25	0.0235	0.0147	27.2231	1.7620	0.1138	229.69
9.75	0.0235	0.0147	27.1798	1.7577	0.1138	227.76

CONFIDENTIAL

APPENDIX 1 (Cont'd)

HOT - FIRING TEST DATA -- 12 PERCENT LENGTH AEROSPIKE NOZZLE
TEST NUMBER AB11, PAGE 2

CONFIDENTIAL

TIME (SECONDS)	A* (SQ. IN.)	EPSILON* (DMNLESS)	PB/PC (DMNLESS)	PB/PA (DMNLESS)	C*S (FT/SEC)	C*P (FT/SEC)
4.45	13.862	26.903	0.01344	1.395	3568.	5092.
4.75	13.[illegible]	26.762	0.01577	1.385	3173.	5104.
5.25	13.912	26.706	0.01837	1.339	3219.	5095.
5.75	13.933	26.666	0.01997	1.338	3228.	5112.
6.25	13.949	26.636	0.02165	1.320	3203.	5113.
6.75	13.964	26.607	0.02365	1.336	3226.	5112.
7.25	13.975	26.586	0.02508	1.309	3224.	5122.
7.75	13.989	26.559	0.02693	1.322	3228.	5124.
8.25	14.003	26.533	0.02823	1.309	3233.	5129.
8.75	14.014	26.512	0.02982	1.310	3234.	5150.
9.25	14.021	26.499	0.03145	1.310	3228.	5144.
9.75	14.034	26.474	0.03281	1.302	3225.	5148.

TIME (SECONDS)	NC*P (DMNLESS)	NC*S (DMNLESS)	NIS (DMNLESS)	NIS, TOP (DMNLESS)	CT (DMNLESS)	CT, TOP (DMNLESS)
4.45	0.8976	0.81[illegible]	0.8500	0.8456	0.9595	0.9533
4.75	0.8892	0.7275	0.8491	0.8445	0.9580	0.9497
5.25	0.8877	0.7379	0.8486	0.8440	0.9588	0.9507
5.75	0.8905	0.7399	0.8482	0.8436	0.9553	0.9473
6.25	0.8909	0.7342	0.8463	0.8417	0.9530	0.9448
6.75	0.8906	0.7394	0.8441	0.8395	0.9506	0.9426
7.25	0.8923	0.7390	0.8425	0.8379	0.9471	0.9391
7.75	0.8929	0.7398	0.8411	0.8365	0.9448	0.9368
8.25	0.8935	0.7411	0.8358	0.8342	0.9416	0.9337
8.75	0.8973	0.7412	0.8416	0.8370	0.9408	0.9328
9.25	0.8963	0.7398	0.8416	0.8370	0.9419	0.9338
9.75	0.8970	0.7393	0.8386	0.8340	0.9378	0.9298

CONFIDENTIAL

APPENDIX 1 (Cont'd)

HOT - FIRING TEST DATA -- 12 PERCENT LENGTH AEROSPIKE NOZZLE
TEST NUMBER AB12, PAGE 1

CONFIDENTIAL

TIME (SECONDS)	LAMBDA (DMNLESS)	PA (PSIA)	PC (PSIA)	PCS (PSIA)	PB (PSIA)	F (POUNDS)
4.45	101.02	2.9839	301.44	107.17	3.7031	6788.
4.75	84.60	3.5484	300.19	110.97	4.4732	6659.
5.25	70.02	4.2753	299.36	114.02	5.4414	6541.
5.75	62.53	4.7764	298.69	116.00	6.0125	6456.
6.25	57.63	5.1745	298.20	117.55	6.5064	6376.
6.75	53.92	5.5302	298.20	117.74	6.6830	6326.
7.25	51.31	5.8141	298.30	117.92	7.3237	6304.
7.75	48.82	6.1055	298.06	113.94	7.7422	6285.
8.25	46.16	6.4540	297.92	114.70	8.0539	6228.
8.75	43.78	6.8015	297.74	114.91	8.6145	6197.
9.25	41.48	7.1755	297.65	115.44	9.0357	6158.
9.75	39.65	7.5102	297.75	116.07	9.4179	6125.

TIME (SECONDS)	WS/WP (DMNLESS)	WS/WP, EFF (DMNLESS)	WT (LBS/SEC)	MRP (DMNLESS)	MRS (DMNLESS)	IS (SECONDS)
4.45	0.0129	0.0064	27.0407	1.7008	0.1096	251.03
4.75	0.0125	0.0066	27.0304	1.7082	0.1100	246.35
5.25	0.0123	0.0068	26.8535	1.6983	0.1104	243.57
5.75	0.0120	0.0070	26.9432	1.7104	0.1108	239.63
6.25	0.0119	0.0070	26.8220	1.7031	0.1111	237.79
6.75	0.0118	0.0071	26.8088	1.7013	0.1112	235.97
7.25	0.0118	0.0071	26.8140	1.7072	0.1114	235.11
7.75	0.0123	0.0068	26.7497	1.7141	0.1110	234.95
8.25	0.0122	0.0069	26.7604	1.7152	0.1112	232.74
8.75	0.0122	0.0069	26.7132	1.7136	0.1113	232.00
9.25	0.0121	0.0069	26.7345	1.7058	0.1115	230.36
9.75	0.0120	0.0070	26.6748	1.7154	0.1116	229.62

CONFIDENTIAL

CONFIDENTIAL

APPENDIX 1 (Cont'd)

HOT - FIRING TEST DATA -- 12 PERCENT LENGTH AEROSPIKE NOZZLE
TEST NUMBER AB12, PAGE 2

CONFIDENTIAL

TIME (SECONDS)	A* (SQ. IN.)	EPSILON* (DMNLESS)	PB/PC (DMNLESS)	PB/PA (DMNLESS)	C*S (FT/SEC)	C*P (FT/SEC)
4.45	13.931	26.670	0.01228	1.241	2534.	5126.
4.75	13.951	2[illegible].632	0.01490	1.261	2707.	5111.
5.25	13.979	26.578	0.01818	1.273	2858.	5140.
5.75	14.001	26.537	0.02013	1.259	2965.	5118.
6.25	14.021	26.499	0.02183	1.258	3052.	5139.
6.75	14.039	26.465	0.02308	1.245	3066.	5148.
7.25	14.056	26.433	0.02455	1.260	3081.	5155.
7.75	14.056	26.433	0.02598	1.268	2871.	5165.
8.25	14.056	26.433	0.02703	1.248	2913.	5160.
8.75	14.056	26.433	0.02893	1.267	2926.	5166.
9.25	14.056	26.433	0.03036	1.259	2956.	5160.
9.75	14.056	26.433	0.03163	1.254	2989.	5173.

TIME (SECONDS)	NC*P (DMNLESS)	NC*S (DMNLESS)	NIS (DMNLESS)	NIS, TOP (DMNLESS)	CT (DMNLESS)	CT, TOP (DMNLESS)
4.45	0.8916	0.5891	0.8542	0.8516	0.9613	0.9551
4.75	0.8892	0.6289	0.8488	0.8463	0.9572	0.9517
5.25	0.8940	0.6636	0.8518	0.8493	0.9551	0.9500
5.75	0.8904	0.6881	0.8454	0.8429	0.9514	0.9467
6.25	0.8940	0.7082	0.8449	0.8424	0.9468	0.9423
6.75	0.8955	0.7113	0.8433	0.8408	0.9434	0.9390
7.25	0.8968	0.7147	0.8437	0.8413	0.9425	0.9381
7.75	0.8988	0.6665	0.8469	0.8443	0.9445	0.9394
8.25	0.8980	0.6760	0.8432	0.8407	0.9411	0.9362
8.75	0.8989	0.6791	0.8449	0.8424	0.9420	0.9371
9.25	0.8977	0.6860	0.8433	0.8408	0.9414	0.9366
9.75	0.9002	0.6936	0.8441	0.8416	0.9396	0.9349

CONFIDENTIAL

CONFIDENTIAL

APPENDIX 1 (Cont'd)

HOT - FIRING TEST DATA -- 12 PERCENT LENGTH AEROSPIKE NOZZLE
TEST NUMBER AC13, PAGE 1

CONFIDENTIAL

TIME (SECONDS)	LAMBDAP (DMNLESS)	PA (PSIA)	PC (PSIA)	PCS (PSIA)	PB (PSIA)	F (POUNDS)
4.45	348.07	0.8980	312.57	148.07	2.8567	7541.
4.75	289.94	1.0738	311.33	147.57	2.8787	7470.
5.25	236.84	1.3080	309.78	147.31	2.8902	7385.
5.75	202.56	1.5229	308.46	147.45	2.9004	7293.
6.25	178.80	1.7218	307.85	147.20	2.9347	7226.
6.75	160.22	1.9181	307.30	147.60	2.9832	7164.
7.25	145.11	2.1157	306.99	147.26	3.0881	7104.
7.75	136.29	2.2506	306.74	147.51	3.1934	7081.
8.25	124.18	2.4654	306.15	147.41	3.4254	7026.
8.75	117.29	2.6085	305.95	147.45	3.6025	7002.
9.25	112.37	2.7206	305.71	147.54	3.7552	6979.
9.75	107.50	2.8405	305.37	147.68	3.9451	6955.

TIME (SECONDS)	WS/WP (DMNLESS)	WS/WP, EFF. (DMNLESS)	WT (LBS/SEC)	MRP (DMNLESS)	MRS (DMNLESS)	IS (SECONDS)
4.45	0.0307	0.0219	28.1832	1.6740	0.1094	267.57
4.75	0.0308	0.0219	28.1236	1.6750	0.1096	265.61
5.25	0.0309	0.0218	28.0729	1.6625	0.1100	263.07
5.75	0.0308	0.0219	28.0179	1.6627	0.1103	260.30
6.25	0.0307	0.0219	28.1134	1.6634	0.1105	257.05
6.75	0.0306	0.0219	28.0249	1.6687	0.1107	255.64
7.25	0.0307	0.0219	27.9884	1.6647	0.1109	253.82
7.75	0.0306	0.0219	28.0319	1.6690	0.1110	252.60
8.25	0.0307	0.0219	27.9056	1.6782	0.1112	251.83
8.75	0.0306	0.0219	27.9570	1.6586	0.1113	250.44
9.25	0.0306	0.0219	27.9099	1.6637	0.1114	250.05
9.75	0.0307	0.0220	27.7495	1.6543	0.1115	250.63

CONFIDENTIAL

CONFIDENTIAL

APPENDIX 1 (Cont'd)

HOT - FIRING TEST DATA -- 12 PERCENT LENGTH AEROSPIKE NOZZLE
TEST NUMBER AC13, PAGE 2

CONFIDENTIAL

TIME (SECONDS)	A* (SQ. IN.)	EPSILON* (DMNLESS)	PB/PC (DMNLESS)	PB/PA (DMNLESS)	C*S (FT/SEC)	C*P (FT/SEC)
4.45	13.694	27.132	0.00914	3.181	3638.	5101.
4.75	13.733	27.055	0.00925	2.681	3619.	5107.
5.25	13.788	26.947	0.00933	2.210	3618.	5111.
5.75	13.832	26.861	0.00940	1.905	3634.	5115.
6.25	13.861	26.805	0.00953	1.704	3629.	5098.
6.75	13.884	26.760	0.00971	1.555	3656.	5113.
7.25	13.902	26.726	0.01006	1.460	3645.	5121.
7.75	13.914	26.703	0.01041	1.419	3661.	5113.
8.25	13.923	26.685	0.01119	1.389	3661.	5130.
8.75	13.931	26.670	0.01177	1.381	3666.	5120.
9.25	13.931	26.670	0.01228	1.380	3675.	5124.
9.75	13.931	26.670	0.01292	1.389	3683.	5149.

TIME (SECONDS)	NC*P (DMNLESS)	NC*S (DMNLESS)	NIS (DMNLESS)	NIS, TOP (DMNLESS)	CT (DMNLESS)	CT, TOP (DMNLESS)
4.45	0.8865	0.8412	0.8520	0.8460	0.9622	0.9543
4.75	0.8875	0.8369	0.8533	0.8473	0.9627	0.9547
5.25	0.8881	0.8365	0.8546	0.8485	0.9636	0.9555
5.75	0.8889	0.8401	0.8529	0.8469	0.9608	0.9528
6.25	0.8859	0.8390	0.8483	0.8423	0.9587	0.9508
6.75	0.8886	0.8452	0.8488	0.8428	0.9563	0.9485
7.25	0.8900	0.8425	0.8481	0.8420	0.9540	0.9461
7.75	0.8886	0.8463	0.8471	0.8411	0.9543	0.9465
8.25	0.8918	0.8461	0.8493	0.8432	0.9534	0.9455
8.75	0.8898	0.8473	0.8481	0.8421	0.9542	0.9464
9.25	0.8906	0.8493	0.8494	0.8434	0.9548	0.9470
9.75	0.8947	0.8512	0.8543	0.8482	0.9560	0.9481

CONFIDENTIAL

APPENDIX 1 (Cont'd)

HOT - FIRING TEST DATA — 12 PERCENT LENGTH AEROSPIKE NOZZLE

TEST NUMBER AC14, PAGE 1

CONFIDENTIAL

TIME (SECONDS)	LAMBDAP (DMNLESS)	PA (PSIA)	PC (PSIA)	PCS (PSIA)	PB (PSIA)	F (POUNDS)
4.45	313.28	0.9839	308.22	248.24	3.0998	7494.
4.75	269.86	1.1376	307.00	249.13	3.1043	7402.
5.25	219.51	1.3927	305.71	252.20	3.0982	7292.
5.75	190.06	1.6031	304.68	251.28	3.1433	7213.
6.25	172.86	1.7597	304.17	251.26	3.1602	7174.
6.75	151.72	2.0015	303.67	252.24	3.2943	7094.
7.25	142.95	2.1205	303.12	250.56	3.3707	7059.
7.75	133.29	2.2733	303.01	247.58	3.5522	7028.
8.25	124.01	2.4425	302.93	247.03	3.7295	6992.
8.75	115.85	2.6114	302.52	247.06	3.9434	6962.
9.25	109.44	2.7636	302.45	247.47	4.1354	6935.
9.75	104.23	2.9011	302.38	247.95	4.3155	6914.

TIME (SECONDS)	WS/WP (DMNLESS)	WS/WP, EFF (DMNLESS)	WT (LBS/SEC)	MRP (DMNLESS)	MRS (DMNLESS)	IS (SECONDS)
4.45	0.0501	0.0375	28.3275	1.7867	0.1174	264.54
4.75	0.0500	0.0377	28.2844	1.7822	0.1176	261.71
5.25	0.0494	0.0382	28.2603	1.7729	0.1181	258.02
5.75	0.0496	0.0381	28.2154	1.7736	0.1182	255.64
6.25	0.0497	0.0381	28.1967	1.7752	0.1181	254.41
6.75	0.0497	0.0382	28.2118	1.7663	0.1178	251.47
7.25	0.0499	0.0380	28.1749	1.7768	0.1178	250.53
7.75	0.0503	0.0376	28.1792	1.7917	0.1180	249.39
8.25	0.0503	0.0375	28.2212	1.7719	0.1180	247.75
8.75	0.0506	0.0376	28.0967	1.7823	0.1178	247.79
9.25	0.0505	0.0376	28.1344	1.7863	0.1177	246.50
9.75	0.0505	0.0377	28.0864	1.7812	0.1177	246.18

CONFIDENTIAL

CONFIDENTIAL

CONFIDENTIAL

APPENDIX 1 (Cont'd)

HOT - FIRING TEST DATA -- 12 PERCENT LENGTH AEROSPIKE NOZZLE
TEST NUMBER AC14, PAGE 2

CONFIDENTIAL

TIME (SECONDS)	A* (SQ. IN.)	EPSILON* (DMNLESS)	PB/PC (DMNLESS)	PB/PA (DMNLESS)	C*S (FT/SEC)	C*P (FT/SEC)
4.45	13.634	27.251	0.01006	3.151	3791.	5072.
4.75	13.661	27.197	0.01011	2.729	3820.	5069.
5.25	13.701	27.118	0.01013	2.225	3910.	5064.
5.75	13.736	27.049	0.01032	1.961	3891.	5068.
6.25	13.762	26.998	0.01039	1.796	3888.	5073.
6.75	13.780	26.962	0.01085	1.646	3901.	5069.
7.25	13.788	26.947	0.01112	1.590	3859.	5071.
7.75	13.788	26.947	0.01172	1.563	3788.	5070.
8.25	13.788	26.947	0.01231	1.527	3775.	5060.
8.75	13.788	26.947	0.01304	1.510	3770.	5078.
9.25	13.788	26.947	0.01367	1.496	3777.	5069.
9.75	13.788	26.947	0.01427	1.488	3788.	5077.

TIME (SECONDS)	NC*P (DMNLESS)	NC*S (DMNLESS)	NIS (DMNLESS)	NIS, TOP (DMNLESS)	CT (DMNLESS)	CT, TOP (DMNLESS)
4.45	0.8842	0.8681	0.8454	0.8359	0.9568	0.9454
4.75	0.8836	0.8747	0.8430	0.8336	0.9544	0.9434
5.25	0.8825	0.8949	0.8405	0.8312	0.9520	0.9420
5.75	0.8833	0.8906	0.8397	0.8304	0.9504	0.9401
6.25	0.8842	0.8899	0.8403	0.8309	0.9501	0.9398
6.75	0.8832	0.8930	0.8375	0.8282	0.9479	0.9377
7.25	0.8838	0.8835	0.8373	0.8279	0.9474	0.9367
7.75	0.8841	0.8674	0.8370	0.8275	0.9473	0.9359
8.25	0.8818	0.8644	0.8359	0.8265	0.9487	0.9372
8.75	0.8852	0.8632	0.8397	0.8301	0.9495	0.9377
9.25	0.8839	0.8649	0.8385	0.8290	0.9494	0.9378
9.75	0.8851	0.8674	0.8404	0.8308	0.9502	0.9387

CONFIDENTIAL

APPENDIX 1 (Cont'd)

HOT - FIRING TEST DATA -- 12 PERCENT LENGTH AEROSPIKE NOZZLE
TEST NUMBER AC15, PAGE 1

CONFIDENTIAL

TIME (SECONDS)	AMBOAP (DMNLESS)	PA (PSIA)	PC (PSIA)	PCS (PSIA)	PB (PSIA)	F (POUNDS)
4.45	107.57	2.8859	310.45	149.98	4.0970	6998.
4.75	91.38	3.3846	309.29	150.69	4.7658	6695.
5.25	78.72	3.9137	308.08	153.31	5.4477	6808.
5.75	71.99	4.2645	306.99	152.77	5.8186	6747.
6.25	[illegible].65	4.6010	306.68	152.26	6.2781	6691.
6.75	[illegible]43	4.9086	306.46	151.97	6.6638	6651.
7.25	[illegible].15	5.2654	306.14	151.58	7.1055	6581.
7.75	[illegible].52	5.6131	306.04	151.21	7.5479	6557.
8.25	5[illegible].40	5.9494	305.78	151.11	7.8806	6489.
8.75	48.86	6.2515	305.48	151.36	8.3672	6462.
9.25	46.88	6.5171	305.50	151.43	8.6271	6425.
9.75	45.26	6.7482	305.42	151.42	8.9006	6399.

TIME (SECONDS)	WS/WP (DMNLESS)	WS/WP, EFF (DMNLESS)	WT (LBS/SEC)	MRP (DMNLESS)	MRS (DMNLESS)	IS (SECONDS)
4.45	0.0309	0.0223	27.9357	1.6878	0.1130	250.50
4.75	0.0309	0.0225	27.7945	1.6883	0.1132	248.09
5.25	0.0302	0.0229	27.8079	1.6838	0.1135	244.83
5.75	0.0303	0.0228	27.7396	1.6881	0.1138	243.24
6.25	0.0304	0.0228	27.7245	1.6892	0.1139	241.32
6.75	0.0304	0.0227	27.7415	1.6814	0.1141	239.74
7.25	0.0305	0.0226	27.6579	1.6869	0.1142	237.95
7.75	0.0306	0.0225	27.6663	1.6873	0.1144	237.01
8.25	0.0305	0.0225	27.6852	1.6964	0.1145	234.39
8.75	0.0305	0.0225	27.6183	1.6827	0.1146	233.98
9.25	0.0305	0.0226	27.6568	1.6866	0.1146	232.32
9.75	0.0305	0.0226	27.5648	1.6774	0.1147	232.16

CONFIDENTIAL

APPENDIX 1 (Cont'd)

HOT - FIRING TEST DATA -- 12 PERCENT LENGTH AEROSPIKE NOZZLE
TEST NUMBER AC'5, PAGE 2

CONFIDENTIAL

TIME (SECONDS)	A* (SQ. IN.)	EPSILON* (DMNLESS)	PB/PC (DMNLESS)	PB/PA (DMNLESS)	C*S (FT/SEC)	C*P (FT/SEC)
4.45	13.705	27.110	0.01320	1.420	3692.	5119.
4.75	13.728	27.064	0.01541	1.408	3734.	5134.
5.25	13.763	26.996	0.01768	1.392	3885.	5121.
5.75	13.794	26.935	0.01895	1.364	3864.	5128.
6.25	13.806	26.911	0.02047	1.365	3842.	5130.
6.75	13.842	26.841	0.02174	1.358	3833.	5137.
7.25	13.865	26.795	0.02321	1.349	3817.	5157.
7.75	13.890	26.749	0.02466	1.345	3802.	5162.
8.25	13.912	26.706	0.02577	1.325	3801.	5162.
8.75	13.912	26.706	0.02739	1.338	3818.	5170.
9.25	13.912	26.706	0.02824	1.324	3824.	5163.
9.75	13.912	26.706	0.02914	1.319	3826.	5179.

TIME (SECONDS)	NC*P (DMNLESS)	NC*S (DMNLESS)	NIS (DMNLESS)	NIS, TOP (DMNLESS)	CT (DMNLESS)	CT, TOP (DMNLESS)
4.45	0.8900	0.8528	0.8526	0.8465	0.9589	0.9511
4.75	0.8926	0.8623	0.8541	0.8479	0.9576	0.9500
5.25	0.8902	0.8968	0.8523	0.8463	0.9572	0.9506
5.75	0.8915	0.8919	0.8525	0.8465	0.9563	0.9495
6.25	0.8920	0.8870	0.8510	0.8449	0.9542	0.9473
6.75	0.8930	0.8847	0.8502	0.8442	0.9523	0.9453
7.25	0.8966	0.8311	0.8438	0.8427	0.9470	0.9399
7.75	0.8975	0.8776	0.8501	0.8440	0.9476	0.9403
8.25	0.8977	0.8774	0.8448	0.8387	0.9416	0.9343
8.75	0.8988	0.8812	0.8476	0.8415	0.9435	0.9363
9.25	0.8976	0.8827	0.8447	0.8386	0.9414	0.9343
9.75	0.9003	0.8830	0.8471	0.8410	0.9414	0.9342

CONFIDENTIAL

APPENDIX 1 (Cont'd)

HOT - FIRING TEST DATA -- 12 PERCENT LENGTH AEROSPIKE NOZZLE
TEST NUMBER AC16, PAGE 1

CONFIDENTIAL

TIME (SECONDS)	LAMBDAP (DMNLESS)	PA (PSIA)	PC (PSIA)	PCS (PSIA)	PR (PSIA)	F (POUNDS)
4.45	105.28	2.9313	308.51	255.70	4.4585	6998.
4.75	86.85	3.5373	307.22	256.01	5.1628	6893.
5.25	74.39	4.1157	306.15	254.62	5.9116	6769.
5.75	67.37	4.5258	304.89	254.37	6.3598	6704.
6.25	61.51	4.9520	304.59	252.89	6.9136	6669.
6.75	56.88	5.3552	304.58	251.01	7.5532	6604.
7.25	53.18	5.7300	304.69	249.48	[illegible]	6570.
7.75	50.58	6.0127	304.15	247.48	8.4776	6518.
8.25	48.97	6.2139	304.27	246.85	8.7437	6491.
8.75	47.25	6.4298	303.83	246.82	9.0106	6467.
9.25	45.39	6.6928	303.80	247.25	9.3893	6436.
9.75	43.33	7.0035	303.49	247.09	9.7953	6400.

TIME (SECONDS)	WS/WP (DMNLESS)	WS/WP, EFF (DMNLESS)	WT (LBS/SEC)	MRP (DMNLESS)	MRS (DMNLESS)	IS (SECONDS)
4.45	0.0487	0.0384	28.3137	1.7169	0.1167	247.15
4.75	0.0488	0.0385	28.1731	1.7178	0.1170	244.68
5.25	0.0488	0.0383	28.2352	1.7088	0.1172	239.72
5.75	0.0491	0.0383	28.0799	1.7041	0.1175	238.74
6.25	[illegible]	0.0380	28.1667	1.7049	0.1176	236.76
6.75	0.0494	0.0376	28.1365	1.7103	0.1176	234.72
7.25	0.0498	0.0374	28.0508	1.7073	0.1175	234.23
7.75	0.0500	0.0371	28.1152	1.7125	0.1175	231.83
8.25	0.0502	0.0370	28.0670	1.6994	0.1174	231.25
8.75	0.0502	0.0371	28.0582	1.7134	0.1174	230.50
9.25	0.0502	0.0371	28.0093	1.7090	0.1174	229.78
9.75	0.0503	0.0371	27.9909	1.6998	0.1174	228.65

APPENDIX 1 (Cont'd)

CONFIDENTIAL

HOT - FIRING TEST DATA -- 12 PERCENT LENGTH AEROSPIKE NOZZLE
TEST NUMBER AC16, PAGE 2

CONFIDENTIAL

TIME (SECONDS)	A* (SQ. IN.)	EPSILON* (DMNLESS)	PB/PC (DMNLESS)	PB/PA (DMNLESS)	C*S (FT/SEC)	C*F (FT/SEC)
4.45	13.673	27.173	0.01445	1.521	4012.	5097.
4.75	13.708	27.104	0.01690	1.460	4028.	5113.
5.25	13.760	27.001	0.01931	1.436	3999.	5103.
5.75	13.805	26.913	0.02086	1.405	3909.	5128.
6.25	13.839	26.847	0.02270	1.396	3960.	5119.
6.75	13.863	26.801	0.02480	1.410	3913.	5135.
7.25	13.874	26.780	0.02651	1.410	3872.	5159.
7.75	13.874	26.780	0.02787	1.410	3819.	5139.
8.25	13.874	26.790	0.02874	1.407	3801.	5151.
8.75	13.874	26.780	0.02966	1.401	3800.	5145.
9.25	13.874	26.780	0.03091	1.403	3810.	5153.
9.75	13.874	26.780	0.03228	1.399	3806.	5157.

TIME (SECONDS)	NC*P (DMNLESS)	NC*S (DMNLESS)	NIS (DMNLESS)	NIS, TRP (DMNLESS)	CT (DMNLESS)	CT, TRP (DMNLESS)
4.45	0.8867	0.9185	0.8446	0.8353	0.9513	0.9421
4.75	0.8895	0.9220	0.8478	0.8384	0.9519	0.9427
5.25	0.8876	0.9154	0.8497	0.8315	0.9461	0.9368
5.75	0.8918	0.9154	0.8441	0.8347	0.9455	0.9360
6.25	0.8904	0.9066	0.8434	0.8349	0.9465	0.9367
6.75	0.8933	0.8958	0.8416	0.8327	0.9420	0.9316
7.25	0.8973	0.8865	0.8449	0.8354	0.9420	0.9310
7.75	0.8939	0.8745	0.8399	0.8304	0.9403	0.9289
8.25	0.8958	0.8766	0.8406	0.8311	0.9395	0.9278
8.75	0.8951	0.8702	0.8493	0.8307	0.9398	0.9282
9.25	0.8964	0.8726	0.8419	0.8314	0.9391	0.9274
9.75	0.8960	0.8717	0.8497	0.8311	0.9393	0.9276

CONFIDENTIAL

APPENDIX 1 (Cont'd)

HOT - FIRING TEST DATA -- 12 PERCENT LENGTH AEROSPIKE NOZZLE
TEST NUMBER AC17, PAGE 1

CONFIDENTIAL

TIME (SECONDS)	LAMBDAP (DMNLESS)	PA (PSIA)	PC (PSIA)	PCS (PSIA)	PB (PSIA)	F (POUNDS)
4.45	106.17	2.9152	309.51	140.77	4.1558	6967.
4.75	90.06	3.4223	308.20	144.04	4.6139	6860.
5.25	74.96	4.0979	307.17	144.42	5.6307	6716.
5.75	68.23	4.4879	306.20	145.07	6.1509	6653.
6.25	61.87	4.9411	305.72	144.92	6.6940	6578.
6.75	56.78	5.3858	305.82	145.39	7.2746	6517.
7.25	52.34	5.8411	305.71	145.89	7.8837	6462.
7.75	48.98	6.2324	305.24	146.07	8.3539	6412.
8.25	47.30	6.4575	305.45	145.70	8.6277	6400.
8.75	45.74	6.6728	305.23	145.89	8.8673	6372.
9.25	43.94	6.9388	304.91	146.08	9.1459	6330.
9.75	42.31	7.2043	304.80	146.04	9.4787	6311.

TIME (SECONDS)	WS/WP (DMNLESS)	WS/WP, EFF (DMNLESS)	WT (LBS/SEC)	MRP (DMNLESS)	MRS (DMNLESS)	IS (SECONDS)
4.45	0.0319	0.0211	27.9238	1.7285	0.0959	249.49
4.75	0.0312	0.0217	27.8365	1.7290	0.0953	246.44
5.25	0.0312	0.0217	27.7509	1.7207	0.0954	242.02
5.75	0.0309	0.0219	27.7634	1.7243	0.0954	239.63
6.25	0.0310	0.0219	27.7256	1.7251	0.0957	237.24
6.75	0.0308	0.0219	27.6917	1.7231	0.0956	235.33
7.25	0.0308	0.0220	27.6210	1.7299	0.0956	233.94
7.75	0.0306	0.0220	27.6616	1.7259	0.0956	231.80
8.25	0.0307	0.0220	27.6856	1.7357	0.0959	231.16
8.75	0.0306	0.0220	27.6695	1.7266	0.0959	230.28
9.25	0.0307	0.0221	27.5378	1.7366	0.0959	229.66
9.75	0.0307	0.0221	27.5184	1.7273	0.0960	229.35

CONFIDENTIAL

CONFIDENTIAL

CONFIDENTIAL

APPENDIX 1 (Cont'd)

HOT - FIRING TEST DATA -- 12 PERCENT LENGTH AEROSPIKE NOZZLE
TEST NUMBER AC17, PAGE 2

CONFIDENTIAL

TIME (SECONDS)	A* (SQ. IN.)	EPSILON* (DMNLESS)	PB/PC (DMNLESS)	PB/PA (DMNLESS)	C*S (FT/SEC)	C*P (FT/SEC)
4.45	13.638	27.243	0.01343	1.426	3372.	5084.
4.75	13.659	27.201	0.01497	1.348	3528.	5083.
5.25	13.690	27.139	0.01833	1.374	3555.	5093.
5.75	13.714	27.092	0.02009	1.371	3594.	5063.
6.25	13.730	27.060	0.02193	1.355	3594.	5088.
6.75	13.744	27.033	0.02379	1.351	3623.	5100.
7.25	13.755	27.011	0.02579	1.350	3654.	5115.
7.75	13.755	27.011	0.02737	1.340	3666.	5099.
8.25	13.755	27.011	0.02825	1.336	3651.	5098.
8.75	13.755	27.011	0.02905	1.329	3664.	5097.
9.25	13.755	27.011	0.03000	1.318	3676.	5117.
9.75	13.755	27.011	0.03110	1.316	3677.	5118.

TIME (SECONDS)	NC*P (DMNLESS)	NC*S (DMNLESS)	NIS (DMNLESS)	NIS, TOP (DMNLESS)	CT (DMNLESS)	CT, TOP (DMNLESS)
4.45	0.8848	0.7830	0.8488	0.8424	0.9620	0.9521
4.75	0.8846	0.8192	0.8482	0.8419	0.9605	0.9517
5.25	0.8861	0.8253	0.8449	0.8386	0.9549	0.9463
5.75	0.8844	0.8344	0.8427	0.8364	0.9540	0.9458
6.25	0.8853	0.8343	0.8410	0.8347	0.9512	0.9429
6.75	0.8874	0.8410	0.8404	0.8341	0.9481	0.9399
7.25	0.8902	0.8482	0.8412	0.8350	0.9460	0.9360
7.75	0.8873	0.8508	0.8386	0.8324	0.9459	0.9381
8.25	0.8874	0.8475	0.8388	0.8326	0.9462	0.9382
8.75	0.8871	0.8504	0.8384	0.8322	0.9460	0.9382
9.25	0.8907	0.8532	0.8398	0.8336	0.9438	0.9359
9.75	0.8908	0.8535	0.8412	0.8350	0.9453	0.9374

CONFIDENTIAL

APPENDIX 1 (Con't)

HOT - FIRING TEST DATA -- 12 PERCENT LENGTH AEROSPIKE NOZZLE

TEST NUMBER AC18, PAGE 1

CONFIDENTIAL

TIME (SECONDS)	LAMBDAP (DMNLESS)	PA (PSIA)	PC (PSIA)	PCS (PSIA)	PB (PSIA)	F (POUNDS)
4.45	315.38	0.9773	308.22	134.48	2.7843	7388.
4.75	270.25	1.1359	306.99	142.36	2.8139	7325.
5.25	228.11	1.3407	305.83	143.99	2.8228	7234.
5.75	195.98	1.5572	305.18	145.42	2.8106	7145.
6.25	173.56	1.7564	304.63	144.97	2.8540	7085.
6.75	155.03	1.9652	304.66	144.26	2.9480	7021.
7.25	142.37	2.1404	304.72	144.20	3.0696	6979.
7.75	129.79	2.3461	304.50	143.95	3.2319	6940.
8.25	117.83	2.5808	304.10	143.91	3.5517	6897.
8.75	114.37	2.6581	304.02	143.77	3.7044	6873.
9.25	105.27	2.8865	303.85	143.70	3.9823	6837.
9.75	99.11	3.0642	303.69	143.73	4.2133	6815.

TIME (SECONDS)	WS/WP (DMNLESS)	WS/WP, EFF (DMNLESS)	WT (LBS/SEC)	MRP (DMNLESS)	MRS (DMNLESS)	IS (SECONDS)
4.45	0.0329	0.0204	27.7278	1.7206	0.0979	266.46
4.75	0.0312	0.0216	27.5866	1.7258	0.0965	265.54
5.25	0.0308	0.0218	27.5786	1.7262	0.0963	262.31
5.75	0.0304	0.0221	27.4865	1.7124	0.0963	259.95
6.25	0.0305	0.0220	27.5224	1.7287	0.0965	257.42
6.75	0.0305	0.0219	27.5806	1.7206	0.0969	254.55
7.25	0.0306	0.0218	27.4483	1.7130	0.0971	254.26
7.75	0.0306	0.0218	27.4950	1.7322	0.0972	252.39
8.25	0.0306	0.0218	27.4838	1.7232	0.0974	250.94
8.75	0.0306	0.0218	27.4570	1.7281	0.0975	250.32
9.25	0.0306	0.0218	27.4019	1.7378	0.0976	249.51
9.75	0.0306	0.0218	27.4284	1.7329	0.0977	248.46

APPENDIX 1 (Con't)

HOT - FIRING TEST DATA -- 12 PERCENT LENGTH AEROSPIKE NOZZLE
TEST NUMBER AC18, PAGE 1

CONFIDENTIAL

TIME (SECONDS)	LAMBDAP (DMNLESS)	PA (PSIA)	PC (PSIA)	PCS (PSIA)	PB (PSIA)	F (POUNDS)
4.45	315.38	0.9773	303.22	134.48	2.7843	7386.
4.75	270.25	1.1359	306.99	142.36	2.8139	7325.
5.25	228.11	1.3407	305.83	143.99	2.8228	7234.
5.75	195.98	1.5572	305.18	145.42	2.8106	7145.
6.25	173.56	1.7564	304.83	144.97	2.8540	7085.
6.75	155.03	1.9652	304.66	144.26	2.9480	7021.
7.25	142.37	2.1404	304.72	144.20	3.0696	6979.
7.75	129.79	2.3461	304.50	143.95	3.2319	6940.
8.25	117.83	2.3808	304.10	143.91	3.5517	6897.
8.75	114.37	2.6581	304.02	143.77	3.7044	6873.
9.25	105.27	2.8865	303.85	143.70	3.9823	6837.
9.75	99.11	3.0642	303.69	143.73	4.2133	6815.

TIME (SECONDS)	WSAWP (DMNLESS)	WS/WP, EFF (DMNLESS)	WT (LBS/SEC)	HRP (DMNLESS)	HRS (DMNLESS)	IS (SECONDS)
4.45	0.0329	0.0204	27.7278	1.7206	0.0979	266.45
4.75	0.0312	0.0216	27.5866	1.7258	0.0965	265.54
5.25	0.0308	0.0218	27.5786	1.7262	0.0963	262.31
5.75	0.0304	0.0221	27.4865	1.7124	0.0963	259.95
6.25	0.0305	0.0220	27.5224	1.7287	0.0965	257.42
6.75	0.0305	0.0219	27.5806	1.7206	0.0969	254.55
7.25	0.0306	0.0218	27.4483	1.7130	0.0971	254.26
7.75	0.0306	0.0218	27.4950	1.7322	0.0972	252.39
8.25	0.0306	0.0218	27.4838	1.7232	0.0974	250.94
8.75	0.0306	0.0218	27.4570	1.7261	0.0975	250.32
9.25	0.0306	0.0218	27.4019	1.7378	0.0976	249.51
9.75	0.0306	0.0218	27.4284	1.7329	0.0977	248.46

CONFIDENTIAL

APPENDIX 1 (Con't)

HOT - FIRING TEST DATA -- 12 PERCENT LENGTH AEROSPIKE NOZZLE
TEST NUMBER AC18, PAGE 2

CONFIDENTIAL

TIME (SECONDS)	A* (SQ. IN.)	EPSILON* (DMNLESS)	PB/PC (DMNLESS)	PB/PA (DMNLESS)	C*S (FT/SEC)	C*P (FT/SEC)
4.45	13.608	27.303	0.00953	2.849	3159.	5091.
4.75	13.629	27.261	0.00917	2.477	3518.	5097.
5.25	13.660	27.199	0.00923	2.105	3611.	5088.
5.75	13.684	27.151	0.00921	1.805	3696.	5102.
6.25	13.700	27.120	0.00936	1.625	3679.	5095.
6.75	13.714	27.092	0.00968	1.500	3648.	5087.
7.25	13.725	27.070	0.01007	1.434	3651.	5117.
7.75	13.725	27.070	0.01061	1.378	3643.	5105.
8.25	13.725	27.070	0.01168	1.376	3645.	5100.
8.75	13.725	27.070	0.01218	1.394	3643.	5104.
9.25	13.725	27.070	0.01311	1.380	3642.	5111.
9.75	13.725	27.070	0.01387	1.375	3648.	5103.

TIME (SECONDS)	NC*P (DMNLESS)	NC*S (DMNLESS)	NIS (DMNLESS)	NIS, TOP (DMNLESS)	CT (DMNLESS)	CT, TOP (DMNLESS)
4.45	0.8858	0.7337	0.8510	0.8444	0.9647	0.9532
4.75	0.8869	0.8167	0.8542	0.8479	0.9649	0.9560
5.25	0.8854	0.8382	0.8512	0.8450	0.9625	0.9544
5.75	0.8875	0.8578	0.8513	0.8452	0.9600	0.9524
6.25	0.8867	0.8539	0.8483	0.8422	0.9575	0.9498
6.75	0.8851	0.8467	0.8449	0.8338	0.9555	0.9477
7.25	0.8902	0.8474	0.8487	0.8426	0.9545	0.9465
7.75	0.8885	0.8453	0.8468	0.8407	0.9542	0.9462
8.25	0.8874	0.8458	0.8476	0.8415	0.9562	0.9482
8.75	0.8882	0.8453	0.8471	0.8409	0.9548	0.9468
9.25	0.8896	0.8450	0.8489	0.8427	0.9551	0.9471
9.75	0.8883	0.8464	0.8491	0.8429	0.9569	0.9489

CONFIDENTIAL

APPENDIX 1 (Cont'd)

HOT - FIRING TEST DATA -- 12 PERCENT LENGTH AEROSPIKE NOZZLE
TEST NUMBER AC19, PAGE 1

CONFIDENTIAL

TIME (SECONDS)	LAMBDAP (DMNLESS)	PA (PSIA)	PC (PSIA)	PCS (PSIA)	PB (PSIA)	F (POUNDS)
4.45	320.35	0.9655	309.32	150.67	2.7751	7407.
4.75	271.20	1.1370	308.37	151.17	2.7821	7337.
5.25	224.11	1.3722	307.52	151.36	2.7928	7243.
5.75	189.06	1.6222	306.70	151.14	2.8071	7133.
6.25	169.00	1.8145	306.65	151.06	2.8579	7080.
6.75	152.98	2.0025	306.34	150.77	2.9386	7030.
7.25	136.71	2.2401	306.24	150.63	3.1404	6970.
7.75	133.02	2.2999	305.95	150.36	3.2262	6968.
8.25	123.84	2.4686	305.72	150.55	3.3953	6924.
8.75	114.20	2.6780	305.82	150.52	3.6829	6905.
9.25	110.25	2.7711	305.51	151.05	3.7760	6875.
9.75	105.38	2.8990	305.50	151.08	3.9836	6856.

111

TIME (SECONDS)	WS/WP (DMNLESS)	WS/WP, EFF (DMNLESS)	WT (LBS/SEC)	MRP (DMNLESS)	MRS (DMNLESS)	IS (SECONDS)
4.45	0.0296	0.0228	27.8235	1.745[illegible]	0.1742	266.22
4.75	0.0295	0.0229	27.7539	1.7459	0.1749	264.34
5.25	0.0294	0.0229	27.7110	1.7415	0.1757	261.37
5.75	0.0294	0.0229	27.7158	1.7374	0.1760	257.35
6.25	0.0294	0.0229	27.6728	1.7490	0.1765	255.85
6.75	0.0294	0.0228	27.6306	1.7414	0.1767	254.42
7.25	0.0295	0.0228	27.5765	1.7426	0.1770	252.74
7.75	0.0295	0.0228	27.6006	1.7524	0.1770	252.47
8.25	0.0294	0.0228	27.5840	1.7431	0.1774	251.01
8.75	0.0295	0.0228	27.5241	1.7524	0.1776	250.86
9.25	0.0292	0.0229	27.5846	1.7514	0.1783	249.24
9.75	0.0294	0.0229	27.4216	1.7424	0.1785	250.00

CONFIDENTIAL

CONFIDENTIAL

APPENDIX 1 (Cont'd)

HOT - FIRING TEST DATA -- 12 PERCENT LENGTH AEROSPIKE NOZZLE
TEST NUMBER AC19, PAGE 2

CONFIDENTIAL

TIME (SECONDS)	A* (SQ. IN.)	EPSILON* (DMNLESS)	PB/PC (DMNLESS)	PB/PA (DMNLESS)	C*S (FT/SEC)	C*P (FT/SEC)
4.45	13.565	27.390	0.00897	2.874	3889.	5056.
4.75	13.5[illegible]	27.349	0.00902	2.447	3922.	5063.
5.25	13.617	27.285	0.00908	2.035	3944.	5068.
5.75	13.640	27.239	0.00915	1.730	3941.	5062.
6.25	13.656	27.207	0.00932	1.575	3947.	5075.
6.75	13.670	27.179	0.00959	1.467	3938.	5083.
7.25	13.681	27.157	0.01025	1.402	3940.	5096.
7.75	13.681	27.157	0.01054	1.403	3928.	5086.
8.25	13.681	27.157	0.01111	1.375	3944.	5085.
8.75	13.681	27.157	0.01204	1.375	3946.	5098.
9.25	13.681	27.157	0.01236	1.363	3980.	5031.
9.75	13.681	27.157	0.01304	1.374	3984.	5112.

TIME (SECONDS)	NC*P (DMNLESS)	NC*S (DMNLESS)	NIS (DMNLESS)	NIS, TOP (DMNLESS)	CT (DMNLESS)	CT, TOP (DMNLESS)
4.45	0.8807	0.8859	0.8474	0.8419	0.9621	0.9560
4.75	0.8814	0.8932	0.8485	0.8431	0.9624	0.9565
5.25	0.8823	0.8981	0.8477	0.8422	0.9604	0.9546
5.75	0.8811	0.8973	0.8429	0.8375	0.9562	0.9504
6.25	0.8837	0.8985	0.8431	0.8376	0.9537	0.9478
6.75	0.8849	0.8966	0.8438	0.8383	0.9532	0.9473
7.25	0.8871	0.8969	0.8442	0.8387	0.9513	0.9453
7.75	0.8858	0.8944	0.8444	0.8389	0.9531	0.9471
8.25	0.8854	0.8978	0.8438	0.8383	0.9527	0.9468
8.75	0.8879	0.8982	0.8476	0.8420	0.9544	0.9484
9.25	0.8848	0.9058	0.8442	0.8387	0.9536	0.9479
9.75	0.8899	0.9067	0.8497	0.8441	0.9544	0.9486

APPENDIX 1 (Cont'd)

HOT - FIRING TEST DATA -- 12 PERCENT LENGTH AEROSPIKE NOZZLE
TEST NUMBER AC20, PAGE 1

CONFIDENTIAL

TIME (SECONDS)	LAMBDAP (DMNLESS)	PA (PSIA)	PC (PSIA)	PCS (PSIA)	PB (PSIA)	F (POUNDS)
4.45	106.24	2.9090	309.07	154.73	3.9972	6946.
4.75	90.59	3.4002	308.03	155.08	4.7145	6854.
5.25	77.13	3.9882	307.60	155.42	5.5303	6748.
5.75	70.28	4.3697	307.10	155.33	6.0049	6676.
6.25	65.86	4.6538	306.50	155.15	6.3537	6612.
6.75	61.72	4.9663	306.53	154.86	6.7670	6605.
7.25	58.99	5.1973	306.60	154.25	7.0271	6541.
7.75	55.25	5.5420	306.21	154.00	7.4960	6518.
8.25	51.49	5.9439	306.03	153.97	8.0303	6425.
8.75	48.28	6.3370	305.92	153.90	8.4052	6396.
9.25	45.63	6.7023	305.81	153.56	8.9372	6341.
9.75	43.76	6.9850	305.67	153.43	9.2592	6305.

TIME (SECONDS)	WS/WP (DMNLESS)	WS/WP, EFF (DMNLESS)	WT (LBS/SEC)	MRP (DMNLESS)	MRS (DMNLESS)	IS (SECONDS)
4.45	0.0296	0.0233	27.8531	1.7453	0.1725	249.38
4.75	0.0295	0.0234	27.8129	1.7409	0.1731	246.42
5.25	0.0295	0.0234	27.7176	1.7465	0.1740	243.47
5.75	0.0294	0.0234	27.7129	1.7419	0.1742	240.89
6.25	0.0294	0.0234	27.6900	1.7341	0.1745	238.77
6.75	0.0296	0.0234	27.6005	1.7453	0.1746	239.32
7.25	0.0296	0.0233	27.6171	1.7459	0.1744	236.66
7.75	0.0296	0.0233	27.6965	1.7453	0.1745	235.34
8.25	0.0296	0.0233	27.6274	1.7464	0.1747	232.56
8.75	0.0297	0.0233	27.5831	1.7418	0.1748	231.69
9.25	0.0298	0.0232	27.5095	1.7418	0.1748	230.51
9.75	0.0297	0.0232	27.5518	1.7463	0.1749	228.85

UNCLASSIFIED

CONFIDENTIAL

APPENDIX 1 (Cont'd)

HOT - FIRING TEST DATA -- 12 PERCENT LENGTH AEROSPIKE NOZZLE
TEST NUMBER AC20, PAGE 2

CONFIDENTIAL

TIME (SECONDS)	A* (SQ. IN.)	EPSILON* (DMNLESS)	PB/PC (DMNLESS)	PB/PA (DMNLESS)	C*S (FT/SEC)	C*P (FT/SEC)
4.45	13.609	27.301	0.01293	1.374	3988.	5068.
4.75	13.629	27.261	0.01531	1.387	4014.	5065.
5.25	13.652	27.215	0.01798	1.387	4045.	5083.
5.75	13.670	27.179	0.01955	1.374	4047.	5082.
6.25	13.683	27.153	0.02073	1.365	4045.	5082.
6.75	13.692	27.136	0.02208	1.363	4035.	5103.
7.25	13.697	27.126	0.02292	1.352	4006.	5103.
7.75	13.697	27.126	0.02448	1.353	3997.	5081.
8.25	13.697	27.126	0.02624	1.351	4000.	5091.
8.75	13.697	27.126	0.02747	1.326	3999.	5098.
9.25	13.697	27.126	0.02922	1.333	3984.	5110.
9.75	13.697	27.126	0.03029	1.326	3981.	5100.

111

TIME (SECONDS)	NC*P (DMNLESS)	NC*S (DMNLESS)	NIS (DMNLESS)	NIS, TOP (DMNLESS)	CT (DMNLESS)	CT, TOP (DMNLESS)
4.45	0.8823	0.9084	0.8471	0.8415	0.9595	0.9538
4.75	0.8817	0.9142	0.8467	0.8411	0.9596	0.9540
5.25	0.8851	0.9210	0.8466	0.8410	0.9557	0.9503
5.75	0.8848	0.9215	0.8439	0.8384	0.9530	0.9475
6.25	0.8845	0.9209	0.8411	0.8356	0.9501	0.9447
6.75	0.8864	0.9187	0.8474	0.8418	0.9531	0.9475
7.25	0.8885	0.9121	0.8419	0.8363	0.9471	0.9413
7.75	0.8847	0.9102	0.8413	0.8356	0.9503	0.9445
8.25	0.8865	0.9107	0.8366	0.8309	0.9431	0.9373
8.75	0.8875	0.9105	0.8391	0.8335	0.9449	0.9391
9.25	0.8897	0.9072	0.8386	0.8329	0.9421	0.9362
9.75	0.8880	0.9064	0.8357	0.8301	0.9407	0.9348

CONFIDENTIAL

UNCLASSIFIED

APPENDIX 1 (Cont'd)

HQT - FIRING TEST DATA -- 12 PERCENT LENGTH AEROSPIKE NOZZLE
TEST NUMBER AC21, PAGE 1

CONFIDENTIAL

TIME (SECONDS)	LAMBDAP (DMNLESS)	PA (PSIA)	PC (PSIA)	PCS (PSIA)	PB (PSIA)	F (POUNDS)
4.45	281.04	1.0981	308.60	153.72	2.8038	7367.
4.75	314.88	0.9777	307.85	153.04	2.8015	7401.
5.25	340.39	0.9011	306.74	153.11	2.7827	7404.
5.75	361.94	0.8467	306.47	153.28	2.7883	7425.
6.25	360.62	0.8489	306.12	153.20	2.7911	7419.
6.75	364.44	0.8394	305.90	152.98	2.8017	7418.
7.25	362.77	0.8445	306.36	153.05	2.8020	7432.
7.75	363.65	0.8413	305.94	152.85	2.8057	7423.
8.25	357.71	0.8560	306.20	152.58	2.8011	7425.
8.75	354.20	0.8624	305.47	152.32	2.7926	7399.
9.25	347.54	0.8794	305.62	152.01	2.7938	7388.
9.75	355.14	0.8604	305.57	151.65	2.7841	7399.

TIME (SECONDS)	WS/WP (DMNLESS)	WS/WP, EFF (DMNLESS)	WT (LBS/SEC)	MRP (DMNLESS)	MRS (DMNLESS)	IS (SECONDS)
4.45	0.0299	0.0231	27.8053	1.7164	0.1117	264.96
4.75	0.0301	0.0231	27.7175	1.7218	0.1119	247.03
5.25	0.0300	0.0231	27.7049	1.7131	0.1122	267.25
5.75	0.0300	0.0232	27.6053	1.7136	0.1125	268.98
6.25	0.0299	0.0232	27.6319	1.7150	0.1128	268.48
6.75	0.0299	0.0232	27.5893	1.7211	0.1130	268.89
7.25	0.0299	0.0231	27.5933	1.7127	0.1132	269.35
7.75	0.0299	0.0231	27.5735	1.7308	0.1133	269.21
8.25	0.0300	0.0231	27.5595	1.7231	0.1134	269.41
8.75	0.0300	0.0231	27.5364	1.7279	0.1135	268.72
9.25	0.0302	0.0230	27.4405	1.7331	0.1136	269.23
9.75	0.0301	0.0230	27.5425	1.7279	0.1136	268.62

APPENDIX 1 (Cont'd)

HOT - FIRING TEST DATA -- 12 PERCENT LENGTH AEROSPIKE NOZZLE
TEST NUMBER AC21, PAGE 2

CONFIDENTIAL

TIME (SECONDS)	A* (SQ. IN.)	EPSILON* (DMNLESS)	PB/PC (DMNLESS)	PB/PA (DMNLESS)	C*S (FT/SEC)	C*P (FT/SEC)
4.45	13.645	27.229	0.00909	2.553	3935.	5081.
4.75	13.656	27.207	0.00910	2.866	3932.	5090.
5.25	13.671	27.177	0.00907	3.088	3917.	5079.
5.75	13.681	27.157	0.00910	3.293	3937.	5097.
6.25	13.681	27.157	0.00912	3.288	3941.	5085.
6.75	13.681	27.157	0.00916	3.338	3936.	5090.
7.25	13.681	27.157	0.00915	3.318	3947.	5096.
7.75	13.681	27.157	0.00917	3.335	3941.	5093.
8.25	13.681	27.157	0.00915	3.272	3929.	5100.
8.75	13.681	27.157	0.00914	3.238	3919.	5093.
9.25	13.681	27.157	0.00914	3.177	3905.	5114.
9.75	13.681	27.157	0.00911	3.236	3889.	5094.

TIME (SECONDS)	NC*P (DMNLESS)	NC*S (DMNLESS)	NIS (DMNLESS)	NIS, TOP (DMNLESS)	CT (DMNLESS)	CT, TOP (DMNLESS)
4.45	0.8839	0.9087	0.8535	0.8447	0.9616	0.9556
4.75	0.8856	0.9012	0.8521	0.8462	0.9618	0.955[illegible]
5.25	0.8836	0.9046	0.8503	0.8441	0.9615	0.9554
5.75	0.8866	0.9090	0.8530	0.8471	0.9615	0.9554
6.25	0.8847	0.9099	0.8515	0.8456	0.9618	0.9558
6.75	0.8856	0.9088	0.8521	0.8462	0.9615	0.9555
7.25	0.8866	0.9112	0.8541	0.8482	0.9627	0.9567
7.75	0.8864	0.9099	0.8527	0.8469	0.9614	0.9554
8.25	0.8875	0.9071	0.8544	0.8485	0.9621	0.9561
8.75	0.8863	0.9049	0.8524	0.8465	0.9613	0.9551
9.25	0.8901	0.9017	0.8546	0.8485	0.9598	0.9535
9.75	0.8865	0.8979	0.8520	0.8461	0.9609	0.9545

CONFIDENTIAL

APPENDIX 1 (Cont'd)

HOT - FIRING TEST DATA -- 10 PERCENT LENGTH AEROSPIKE NOZZLE
TEST NUMBER AC21, PAGE 2

CONFIDENTIAL

TIME (SECONDS)	A* (SQ. IN.)	EPSILON* (DMNLESS)	PB/PC (DMNLESS)	PB/PA (DMNLESS)	C*S (FT/SEC)	C*P (FT/SEC)
4.45	13.645	27.229	0.00909	2.553	3935.	5081.
4.75	13.656	27.207	0.00910	2.866	3902.	5090.
5.25	13.671	27.177	0.00907	3.088	3917.	5079.
5.75	13.681	27.157	0.00910	3.293	3937.	5097.
6.25	13.681	27.157	0.00912	3.288	3941.	5085.
6.75	13.681	27.157	0.00916	3.338	3936.	5090.
7.25	13.681	27.157	0.00915	3.318	3947.	5096.
7.75	13.681	27.157	0.00917	3.335	3941.	5093.
8.25	13.681	27.157	0.00915	3.272	3929.	5100.
8.75	13.681	27.157	0.00914	3.238	3919.	5093.
9.25	13.681	27.157	0.00914	3.177	3905.	5114.
9.75	13.681	27.157	0.00911	3.236	3889.	5094.

TIME (SECONDS)	NC*P (DMNLESS)	NC*S (DMNLESS)	NIS (DMNLESS)	NIS, TOP (DMNLESS)	CT (DMNLESS)	CT, TOP (DMNLESS)
4.45	0.8839	0.9087	0.8505	0.8447	0.9616	0.9556
4.75	0.8856	0.9012	0.8521	0.8462	0.9618	0.9555
5.25	0.8836	0.9046	0.8500	0.8441	0.9615	0.9554
5.75	0.8866	0.9090	0.8530	0.8471	0.9615	0.9554
6.25	0.8847	0.9079	0.8515	0.8456	0.9618	0.9558
6.75	0.8856	0.9088	0.8521	0.8462	0.9615	0.9555
7.25	0.8856	0.9112	0.8541	0.8482	0.9627	0.9567
7.75	0.8864	0.9099	0.8527	0.8469	0.9614	0.9554
8.25	0.8875	0.9071	0.8544	0.8485	0.9622	0.9561
8.75	0.8863	0.9049	0.8524	0.8465	0.9613	0.9551
9.25	0.8901	0.9017	0.8546	0.8486	0.9598	0.9535
9.75	0.8865	0.8979	0.8520	0.8461	0.9608	0.9545

CONFIDENTIAL

APPENDIX 1 (Cont'd)

HOT - FIRING TEST DATA -- 12 PERCENT LENGTH AEROSPIKE NOZZLE
TEST NUMBER RD69, PAGE 1

CONFIDENTIAL

TIME (SECONDS)	LAMBDAP (DMNLESS)	PA (PSIA)	PC (PSIA)	PCS (PSIA)	PB (PSIA)	F (POUNDS)
0.50	29.27	13.7000	401.06	0.0	17.2005	6121.
1.00	29.04	13.7000	397.87	0.0	17.2083	6132.

TIME (SECONDS)	WS/WP (DMNLESS)	WS/WP, EFF (DMNLESS)	WT (LBS/SEC)	MRP (DMNLESS)	MRS (DMNLESS)	IS (SECONDS)
0.50	0.0	0.0	38.0076	1.7505	0.0	213.66
1.00	0.0	0.0	38.0355	1.7554	0.0	213.80

APPENDIX 1 (Cont'd)

HOT - FIRING TEST DATA — 12 PERCENT LENGTH AEROSPIKE NOZZLE
TEST NUMBER RD69, PAGE 2

CONFIDENTIAL

TIME (SECONDS)	A* (SQ. IN.)	EPSILON* (DMNLESS)	PB/PC (DMNLESS)	PB/PA (DMNLESS)	C*S (FT/SEC)	C*P (FT/SEC)
0.50	14.707	25.263	0.04289	1.256	0.	5042.
1.00	14.868	24.989	0.04325	1.256	0.	5053.

TIME (SECONDS)	NC*P (DMNLESS)	NC*S (DMNLESS)	NIS DMNLESS)	NIS, TOP (DMNLESS)	CT (DMNLESS)	CT, TOP (DMNLESS)
0.50	0.8770	0.0	0.8074	0.8074	0.9206	0.9206
1.00	0.8790	0.0	0.8086	0.8086	0.9198	0.9198

APPENDIX 1 (Cont'd)

HOT - FIRING TEST DATA -- 12 PERCENT LENGTH AEROSPIKE NOZZLE
TEST NUMBER RD71, PAGE 1

CONFIDENTIAL

TIME (SECONDS)	LAMBDAP (DMNLESS)	PA (PSIA)	PC (PSIA)	PCS (PSIA)	PB (PSIA)	F (POUNDS)
0.50	28.51	13.7200	391.09	0.0	17.1689	8033.
1.00	28.37	13.7200	389.26	0.0	17.1200	8040.
1.50	28.26	13.7200	387.72	0.0	17.1182	8044.
2.00	28.24	13.7200	387.44	0.0	17.1346	8064.
2.50	28.23	13.7200	387.38	0.0	17.1674	8079.

TIME (SECONDS)	WS/WP (DMNLESS)	WS/WP, EFF (DMNLESS)	WT (LBS/SEC)	MRP (DMNLESS)	MRS (DMNLESS)	IS (SECONDS)
0.50	0.0	0.0	38.2840	1.8202	0.0	209.82
1.00	0.0	0.0	38.2500	1.8233	0.0	210.19
1.50	0.0	0.0	38.2540	1.8223	0.0	210.29
2.00	0.0	0.0	38.2780	1.8212	0.0	210.67
2.50	0.0	0.0	38.3140	1.8222	0.0	210.66

CONFIDENTIAL

UNCLASSIFIED

APPENDIX 1 (Cont'd)

HOT - FIRING TEST DATA -- 12 PERCENT LENGTH AEROSPIKE NOZZLE
TEST NUMBER K071, PAGE 2

TIME (SECONDS)	A* (SQ. IN.)	EPSILON* (DMNLESS)	PB/PC (DMNLESS)	PB/PA (DMNLESS)	C*S (FT/SEC)	C*P (FT/SEC)
0.50	15.143	24.535	0.04390	1.251	0.	5024.
1.00	15.237	24.384	0.04398	1.248	0.	5036.
1.50	15.302	24.280	0.04414	1.248	0.	5038.
2.00	15.341	24.219	0.04422	1.249	0.	5043.
2.50	15.357	24.194	0.04432	1.251	0.	5043.

TIME (SECONDS)	NC*P (DMNLESS)	NC*S (DMNLESS)	NIS (DMNLESS)	NIS, TOP (DMNLESS)	CT (DMNLESS)	CT, TOP (DMNLESS)
0.50	0.8762	0.0	0.7948	0.7948	0.9071	0.9071
1.00	0.8785	0.0	0.7966	0.7966	0.9068	0.9068
1.50	0.8788	0.0	0.7974	0.7974	0.9074	0.9074
2.00	0.8796	0.0	0.7989	0.7989	0.9082	0.9082
2.50	0.8796	0.0	0.7996	0.7996	0.9091	0.9091

UNCLASSIFIED

APPENDIX 1 (Cont'd)

HOT - FIRING TEST DATA -- 12 PERCENT LENGTH AEROSPIKE NOZZLE
TEST NUMBER RD01, PAGE 1

CONFIDENTIAL

TIME (SECONDS)	LAMBDAP (DMNLESS)	PA (PSIA)	PC (PSIA)	PCS (PSIA)	PB (PSIA)	F (POUNDS)
0.50	28.85	13.8000	398.11	74.35	17.7936	8427.
1.00	28.74	13.8000	396.66	70.98	17.8173	8437.
1.50	28.69	13.8000	395.92	57.96	17.7963	8434.
2.00	28.69	13.8000	395.94	56.44	17.7591	8437.
2.50	28.66	13.8000	395.47	56.69	17.8025	8432.
3.00	28.68	13.8000	395.81	57.56	17.7383	8434.
3.45	28.67	13.8000	395.59	58.16	17.8808	8443.
4.30	28.67	13.8000	395.61	0.0	17.4643	8362.
4.70	28.66	13.8000	395.58	0.0	17.3815	8346.

TIME (SECONDS)	WS/WP (DMNLESS)	WS/WP, EFF (DMNLESS)	WT (LBS/SEC)	MRP (DMNLESS)	MRS (DMNLESS)	IS (SECONDS)
0.50	0.0157	0.0031	40.1488	1.7242	0.0533	209.88
1.00	0.0160	0.0030	40.0829	1.7202	0.0485	210.50
1.50	0.0162	0.0024	40.1042	1.7204	0.0474	210.30
2.00	0.0162	0.0024	40.0851	1.7244	0.0467	210.48
2.50	0.0163	0.0024	40.0285	1.7176	0.0454	210.64
3.00	0.0163	0.0024	40.0138	1.7243	0.0454	210.78
3.45	0.0163	0.0024	40.0082	1.7303	0.0457	211.02
4.30	0.0	0.0	39.2898	1.7303	0.0	212.84
4.70	0.0	0.0	39.2417	1.7280	0.0	212.69

APPENDIX 1 (Cont'd)

HOT - FIRING TEST DATA -- 12 PERCENT LENGTH AEROSPIKE NOZZLE
TEST NUMBER R001, PAGE 2

CONFIDENTIAL

UNCLASSIFIED CONFIDENTIAL

TIME (SECONDS)	A* (SQ. IN.)	EPSILON* (DMNLESS)	PB/PC (DMNLESS)	PB/PA (DMNLESS)	C*S (FT/SEC)	C*P (FT/SEC)
0.50	15.425	24.087	0.04470	1.289	997.	5047.
1.00	15.491	23.984	0.04492	1.291	941.	5060.
1.50	15.520	23.939	0.04495	1.290	757.	5058.
2.00	15.533	23.919	0.04485	1.287	738.	5065.
2.50	15.533	23.919	0.04502	1.290	738.	5066.
3.00	15.533	23.919	0.04482	1.285	748.	5073.
3.45	15.533	23.919	0.04520	1.296	757.	5071.
4.30	15.533	23.919	0.04415	1.266	0.	5081.
4.70	15.533	23.919	0.04394	1.260	0.	5087.

TIME (SECONDS)	NC*P (DMNLESS)	NC*S[1] (DMNLESS)	NIS[1] (DMNLESS)	NIS, TOP (DMNLESS)	CT[1] (DMNLESS)	CT, TOP (DMNLESS)
0.50	0.8772	—	—	0.7948	—	0.9061
1.00	0.8793	—	—	0.7975	—	0.9070
1.50	0.8791	—	—	0.7969	—	0.9066
2.00	0.8803	—	—	0.7976	—	0.9060
2.50	0.8805	—	—	0.7984	—	0.9068
3.00	0.8817	—	—	0.7987	—	0.9058
3.45	0.8815	—	—	0.7996	—	0.9071
4.30	0.8832	0.0	0.8065	0.8065	0.9131	0.9131
4.70	0.8842	0.0	0.8059	0.8059	0.9115	0.9115

[1]Theoretical Secondary Properties Outside the Range of Data Reduction Program.

UNCLASSIFIED CONFIDENTIAL

UNCLASSIFIED

APPENDIX 1 (Cont'd)

HOT - FIRING TEST DATA — 12 PERCENT LENGTH AEROSPIKE NOZZLE[1]
TEST NUMBER RDO2, PAGE 1

CONFIDENTIAL

TIME (SECONDS)	LAMBDAP (DMNLESS)	PA (PSIA)	PC (PSIA)	PCS (PSIA)	PB (PSIA)	F (POUNDS)
0.50	21.68	13.8400	300.12	0.0	15.6112	5936.
1.00	21.59	13.8400	298.77	0.0	15.6677	5938.
1.50	21.58	13.8400	298.68	0.0	15.7029	5958.
2.00	21.53	13.8400	298.01	0.0	15.6743	5951.
2.50	21.55	13.8400	298.23	0.0	15.6781	5961.
3.00	21.55	13.8400	298.28	0.0	15.7152	5961.
3.50	21.59	13.8400	298.79	164.03	16.0193	6012.
4.00	21.56	13.8400	298.43	149.86	15.9942	5997.
4.50	21.59	13.8400	298.82	147.82	15.9916	6000.
5.00	21.62	13.8400	299.20	148.00	15.9815	6001.
5.50	21.65	13.8400	299.70	147.88	15.9542	6004.
6.00	21.62	13.8400	299.22	148.10	15.9000	5982.
6.50	21.68	13.8400	299.99	147.89	15.9267	5998.
7.00	21.70	13.8400	300.38	147.86	15.9731	6003.

423

UNCLASSIFIED

TIME (SECONDS)	WS/WP (DMNLESS)	WS/WP, EFF (DMNLESS)	WT (LBS/SEC)	MRP (DMNLESS)	MRS (DMNLESS)	IS (SECONDS)
0.50	0.0	0.0	29.8268	1.6840	0.0	199.01
1.00	0.0	0.0	29.7894	1.6877	0.0	199.35
1.50	0.0	0.0	29.7872	1.6699	0.0	200.00
2.00	0.0	0.0	29.7506	1.6727	0.0	200.05
2.50	0.0	0.0	29.7742	1.6762	0.0	200.20
3.00	0.0	0.0	29.7900	1.6752	0.0	200.09
3.50	0.0102	0.0091	30.0543	1.6740	0.3029	200.04
4.00	0.0109	0.0083	29.9328	1.6722	0.2654	200.35
4.50	0.0110	0.0082	30.0190	1.6710	0.2599	199.89
5.00	0.0110	0.0082	29.9731	1.6793	0.2604	200.21
5.50	0.0110	0.0085	29.8696	1.6744	0.2617	200.99
6.00	0.0110	0.0082	29.8438	1.6788	0.2628	200.44
6.50	0.0110	0.0082	29.8717	1.6745	0.2628	200.79
7.00	0.0109	0.0082	29.8453	1.6891	0.2655	201.14

[1]Data for this test were obtained from 0.5-second Beckman data slices.

UNCLASSIFIED

APPENDIX 1 (Cont'd)

HOT - FIRING TEST DATA -- 12 PERCENT LENGTH AERUSPIKE NOZZLE
TEST NUMBER R002, PAGE 2

CONFIDENTIAL

TIME (SECONDS)	A* (SQ. IN.)	EPSILON* (DMNLESS)	PB/PC (DMNLESS)	PB/PA (DMNLESS)	C*S (FT/SEC)	C*P (FT/SEC)
0.50	15.357	24.194	0.05202	1.128	0.	5033.
1.00	15.413	24.106	0.05244	1.132	0.	5035.
1.50	15.441	24.062	0.05257	1.135	0.	5043.
2.00	15.474	24.011	0.05260	1.133	0.	5049.
2.50	15.478	24.004	0.05257	1.133	0.	5050.
3.00	15.465	24.025	0.05269	1.135	0.	5044.
3.50	15.436	24.067	0.05361	1.157	4518.	5050.
4.00	15.437	24.068	0.05359	1.156	3869.	5067.
4.50	15.424	24.088	0.05352	1.155	3768.	5056.
5.00	15.408	24.113	0.05341	1.155	3785.	5065.
5.50	15.396	24.132	0.05323	1.153	3906.	5087.
6.00	15.398	24.129	0.05314	1.149	3820.	5084.
6.50	15.379	24.159	0.05309	1.151	3809.	5086.
7.00	15.355	24.197	0.05318	1.154	3816.	5089.

TIME (SECONDS)	NC*P (DMNLESS)	NC*S[1] (DMNLESS)	NIS[1] (DMNLESS)	NIS, TOP (DMNLESS)	CT[1] (DMNLESS)	CT, TOP (DMNLESS)
0.50	0.8757	0.0	0.7809	0.7809	0.8918	0.8915
1.00	0.8762	0.0	0.7826	0.7826	0.8932	0.8932
1.50	0.8773	0.0	0.7855	0.7855	0.8954	0.8954
2.00	0.8783	0.0	0.7858	0.7858	0.8947	0.8947
2.50	0.8785	0.0	0.7863	0.7863	0.8950	0.8950
3.00	0.8774	0.0	0.7859	0.7859	0.8956	0.8956
3.50	0.8785	—	—	0.7855	—	0.8941
4.00	0.8815	—	—	0.7869	—	0.8926
4.50	0.8795	—	—	0.7849	—	0.8925
5.00	0.8812	—	—	0.7859	—	0.8919
5.50	0.8850	—	—	0.7889	—	0.8915
6.00	0.8845	—	—	0.7869	—	0.8897
6.50	0.8847	—	—	0.7880	—	0.8907
7.00	0.8855	—	—	0.7891	—	0.8911

[1] Theoretical Secondary Properties Outside the Range of Data Reduction Program.

UNCLASSIFIED

UNCLASSIFIED

APPENDIX 1 (Cont'd)

HOT - FIRING TEST DATA — 12 PERCENT LENGTH AEROSPIKE NOZZLE[1]
TEST NUMBER R003, PAGE 1

CONFIDENTIAL

TIME (SECONDS)	LAMBDAP (DMNLESS)	PA (PSIA)	PC (PSIA)	PCS (PSIA)	PB (PSIA)	F (POUNDS)
0.50	22.09	13.8000	304.81	0.0	15.4917	5952.
1.00	22.02	13.8000	303.84	0.0	15.5392	5971.
1.50	21.89	13.8000	302.11	0.0	15.4745	5948.
2.00	21.89	13.8000	302.12	0.0	15.5402	5964.
2.50	21.83	13.8000	301.32	0.0	15.4911	5946.
3.00	21.81	13.8000	301.01	0.0	15.4337	5935.
3.50	21.89	13.8000	302.11	274.00	15.8806	6025.
4.00	21.87	13.8000	301.76	257.47	15.7770	6006.
4.50	21.93	13.8000	302.62	254.76	15.8190	6020.
5.00	21.89	13.8000	302.05	254.02	15.8578	6004.
5.50	21.92	13.8000	302.56	255.49	15.7548	6006.
6.00	21.95	13.8000	302.90	254.47	15.7606	6006.
7.00	22.00	13.8000	303.66	0.0	15.4667	5966.
7.50	22.01	13.8000	303.79	0.0	15.4974	5959.

UNCLASSIFIED

TIME (SECONDS)	WS/WP (DMNLESS)	WS/WP, EFF (DMNLESS)	WT (LBS/SEC)	MRP (DMNLESS)	MRS (DMNLESS)	IS (SECONDS)
0.50	0.0	0.0	30.0442	1.7244	0.0	198.10
1.00	0.0	0.0	30.0065	1.7253	0.0	198.97
1.50	0.0	0.0	29.9394	1.7224	0.0	198.67
2.00	0.0	0.0	30.0012	1.7309	0.0	198.78
2.50	0.0	0.0	29.9271	1.7243	0.0	198.69
3.00	0.0	0.0	29.8844	1.7194	0.0	198.60
3.50	0.0190	0.0152	30.4703	1.7216	0.0950	197.73
4.00	0.0196	0.0143	30.4166	1.7220	0.0912	197.45
4.50	0.0196	0.0141	30.4868	1.7269	0.0922	197.46
5.00	0.0196	0.0141	30.4053	1.7264	0.0928	197.47
5.50	0.0196	0.0142	30.4130	1.7279	0.0915	197.49
6.00	0.0197	0.0141	30.3854	1.7222	0.0911	197.65
7.00	0.0	0.0	29.7629	1.7230	0.0	200.45
7.50	0.0	0.0	29.7301	1.7215	0.0	200.45

[1] Data for this test were obtained from 0.5-second Beckman data slices.

APPENDIX 1 (Cont'd)

HOT - FIRING TEST DATA -- 12 PERCENT LENGTH AERUSPIKE NOZZLE
TEST NUMBER RD03, PAGE 2

CONFIDENTIAL

TIME (SECONDS)	A* (SQ. IN.)	EPSILON* (DMNLESS)	PB/PC (DMNLESS)	PB/PA (DMNLESS)	C*S (FT/SEC)	C*P (FT/SEC)
0.50	15.115	24.581	0.05082	1.123	0.	4998.
1.00	15.182	24.472	0.05114	1.126	0.	5010.
1.50	15.248	24.366	0.05122	1.121	0.	5015.
2.00	15.256	24.354	0.05144	1.126	0.	5007.
2.50	15.280	24.315	0.05141	1.123	0.	5014.
3.00	15.293	24.295	0.05127	1 118	0.	5020.
3.50	15.264	24.341	0.05257	1.151	4030.	5026.
4.00	15.279	24.317	0.05228	1.143	3670.	5037.
4.50	15.249	24.365	0.05227	1.146	3632.	5030.
5.00	15.237	24.384	0.05250	1.149	3619.	5030.
5.50	15.246	24.370	0.05207	1.142	3639.	5040.
6.00	15.220	24.411	0.05210	1.144	3623.	5042.
7.00	15.205	24.435	0.05093	1.121	0.	5056.
7.50	15.178	24.479	0.05101	1.123	0.	5055.

TIME (SECONDS)	NC*P (DMNLESS)	NC*S (DMNLESS)	NIS (DMNLESS)	NIS, TOP (DMNLESS)	CT (DMNLESS)	CT, TOP (DMNLESS)
0.50	0.8703	0.0	0.7751	0.7751	0.8906	0.8906
1.00	0.8725	0.0	0.7788	0.7788	0.8926	0.8926
1.50	0.8733	0.0	0.7782	0.7782	0.8911	0.8911
2.00	0.8722	0.0	0.7786	0.7786	0.8927	0.8927
2.50	0.8732	0.0	0.7785	0.7785	0.8915	0.8915
3.00	0.8742	0.0	0.7783	0.7783	0.8903	0.8903
3.50	0.8752	0.9266	0.7780	0.7745	0.8882	0.8849
4.00	0.8772	0.8456	0.7772	0.7735	0.8865	0.8818
4.50	0.8760	0.8368	0.7769	0.7733	0.8875	0.8828
5.00	0.8760	0.8337	0.7771	0.7735	0.8877	0.8829
5.50	0.8779	0.8384	0.7770	0.7734	0.8857	0.8810
6.00	0.8780	0.8350	0.7776	0.7739	0.8863	0.8815
7.00	0.8804	0.0	0.7847	0.7847	0.8912	0.8912
7.50	0.8802	0.0	0.7846	0.7846	0.8915	0.8915

APPENDIX 1 (Cont'd)

HOT - FIRING TEST DATA -- 12 PERCENT LENGTH AEROSPIKE NOZZLE
TEST NUMBER RD05, PAGE 1

TIME (SECONDS)	LAMBDAP (DMNLESS)	PA (PSIA)	PC (PSIA)	PCS (PSIA)	PB (PSIA)	F (POUNDS)
0.50	23.02	13.7000	315.38	0.0	14.7595	5824.
1.00	22.94	13.7000	314.25	0.0	14.7660	5840.
1.38	22.93	13.7000	314.16	0.0	14.7627	5850.

TIME (SECONDS)	WS/WP (DMNLESS)	WS/WP, EFF (DMNLESS)	WT (LBS/SEC)	MRP (DMNLESS)	MRS (DMNLESS)	IS (SECONDS)
0.50	0.0	0.0	28.9664	1.7430	0.0	201.07
1.00	0.0	0.0	28.9294	1.7438	0.0	201.69
1.38	0.0	0.0	28.9543	1.7370	0.0	202.05

UNCLASSIFIED

APPENDIX 1 (Cont'd)

HOT - FIRING TEST DATA -- 12 PERCENT LENGTH AEROSPIKE NOZZLE
TEST NUMBER RD05, PAGE 2

CONFIDENTIAL

TIME (SECONDS)	A* (SQ. IN.)	EPSILON* (DMNLESS)	PB/PC (DMNLESS)	PB/PA (DMNLESS)	C*S (FT/SEC)	C*P (FT/SEC)
0.50	14.134	26.287	0.04680	1.077	0.	5023.
1.00	14.209	26.148	0.04699	1.078	0.	5039.
1.38	14.231	26.108	0.04699	1.078	0.	5041.

TIME (SECONDS)	NC*P (DMNLESS)	NC*S (DMNLESS)	NIS (DMNLESS)	NIS, TOP (DMNLESS)	CT (DMNLESS)	CT, TOP (DMNLESS)
0.50	0.8744	0.0	0.7822	0.7822	0.8946	0.8946
1.00	0.8771	0.0	0.7857	0.7857	0.8958	0.8958
1.38	0.8773	0.0	0.7865	0.7865	0.8965	0.8965

CONFIDENTIAL
UNCLASSIFIED

UNCLASSIFIED

APPENDIX 1 (Cont'd)

HOT - FIRING TEST DATA -- 12 PERCENT LENGTH AEROSPIKE NOZZLE
TEST NUMBER RD06, PAGE 1

CONFIDENTIAL

TIME (SECONDS)	LAMBDAP (DMNLESS)	PA (PSIA)	PC (PSIA)	PCS (PSIA)	PB (PSIA)	F (POUNDS)
0.50	23.65	13.7000	324.01	0.0	14.9164	5964.
1.00	23.51	13.7000	322.09	0.0	14.9039	5959.
1.50	23.49	13.7000	321.78	0.0	14.9209	5973.
2.00	23.50	13.7000	321.91	0.0	14.9292	5988.
2.50	23.44	13.7000	321.15	0.0	14.8738	5977.
3.00	23.42	13.7000	320.82	0.0	14.8656	5970.
3.50	23.47	13.7000	321.06	0.0	14.8535	5977.
4.00	23.48	13.7000	321.71	0.0	[illegible]	5991.
4.45	23.46	13.7000	321.45	0.0	14.8488	5982.
4.80	23.46	13.7000	321.40	0.0	14.8234	5982.

TIME (SECONDS)	WS/WP (DMNLESS)	WS/WP, EFF (DMNLESS)	WT (LBS/SEC)	MRP (DMNLESS)	MRS (DMNLESS)	IS (SECONDS)
0.50	0.0	0.0	29.3002	1.8371	0.0	203.55
1.00	0.0	0.0	29.2229	1.8446	0.0	203.92
1.50	0.0	0.0	29.2731	1.8457	0.0	204.56
2.00	0.0	0.0	29.2699	1.8394	0.0	204.58
2.50	0.0	0.0	29.2265	1.8345	0.0	204.51
3.00	0.0	0.0	29.2140	1.8345	0.0	204.35
3.50	0.0	0.0	29.2161	1.8363	0.0	204.57
4.00	0.0	0.0	29.2770	1.8388	0.0	204.62
4.45	0.0	0.0	29.2090	1.8419	0.0	204.79
4.80	0.0	0.0	29.2190	1.8445	0.0	204.72

UNCLASSIFIED

APPENDIX 1 (Cont'd)

HOT - FIRING TEST DATA — 12 PERCENT LENGTH AERUSPIKE NOZZLE
TEST NUMBER R006, PAGE 2

CONFIDENTIAL

TIME (SECONDS)	A* (SQ. IN.)	EPSILON* (DMNLESS)	PB/PC (DMNLESS)	PB/PA (DMNLESS)	C*S (FT/SEC)	C*P (FT/SEC)
0.50	13.984	26.569	0.04604	1.089	0.	5046.
1.00	14.063	26.420	0.04627	1.088	0.	5058.
1.50	14.095	26.360	0.04637	1.089	0.	5056.
2.00	14.111	26.330	0.04638	1.090	0.	5064.
2.50	14.142	26.272	0.04631	1.086	0.	5071.
3.00	14.142	26.272	0.04634	1.085	0.	5068.
3.50	14.142	26.272	0.04628	1.085	0.	5071.
4.00	14.142	26.272	0.04624	1.086	0.	5071.
4.45	14.142	26.272	0.04619	1.084	0.	5078.
4.80	14.142	26.272	0.04612	1.082	0.	5076.

TIME (SECONDS)	NC*P (DMNLESS)	NC*S (DMNLESS)	NIS (DMNLESS)	NIS, TOP (DMNLESS)	CT (DMNLESS)	CT, TOP (DMNLESS)
0.50	0.8815	0.0	0.7891	0.7891	0.8953	0.8953
1.00	0.8839	0.0	0.7912	0.7912	0.8952	0.8952
1.50	0.8836	0.0	0.7918	0.7918	0.8962	0.8962
2.00	0.8848	0.0	0.7938	0.7938	0.8972	0.8972
2.50	0.8857	0.0	0.7937	0.7937	0.8961	0.8961
3.00	0.8852	0.0	0.7932	0.7932	0.8961	0.8961
3.50	0.8859	0.0	0.7940	0.7940	0.8963	0.8963
4.00	0.8859	0.0	0.7940	0.7940	0.8962	0.8962
4.45	0.8874	0.0	0.7948	0.7948	0.8956	0.8956
4.80	0.8871	0.0	0.7945	0.7945	0.8956	0.8956

UNCLASSIFIED

APPENDIX 1 (Cont'd)

HOT - FIRING TEST DATA -- 12 PERCENT LENGTH AEROSPIKE NOZZLE
TEST NUMBER RD08, PAGE 1

CONFIDENTIAL

TIME (SECONDS)	LAMBDAP (DMNLESS)	PA (PSIA)	PC (PSIA)	PCS (PSIA)	PB (PSIA)	F (POUNDS)
0.50	22.76	13.8000	314.05	170.52	14.9661	5827.
1.00	22.59	13.8000	311.77	171.02	14.9659	5833.
1.50	22.56	13.8000	311.32	171.40	15.0288	5855.
1.95	22.50	13.8000	310.49	171.18	15.0278	5851.
2.35	22.51	13.8000	310.62	170.98	14.9908	5862.
3.72	22.49	13.8000	310.42	0.0	14.5701	5775.
4.32	22.49	13.8000	310.42	0.0	14.5236	5769.
4.82	22.56	13.8000	311.27	0.0	14.5585	5789.

TIME (SECONDS)	WS/WP (DMNLESS)	WS/WP, EFF (DMNLESS)	WT (LBS/SEC)	MRP (DMNLESS)	MRS (DMNLESS)	IS (SECONDS)
0.50	0.0322	0.0249	29.3466	1.8918	0.1656	198.43
1.00	0.0323	0.0250	29.2848	1.9055	0.1644	199.18
1.50	0.0324	0.0250	29.2765	1.8999	0.1637	199.98
1.95	0.0323	0.0250	29.2485	1.8965	0.1649	200.03
2.35	0.0321	0.0249	29.2642	1.9060	0.1660	200.31
3.72	0.0	0.0	28.3326	1.8997	0.0	203.84
4.32	0.0	0.0	28.3158	1.8998	0.0	203.75
4.82	0.0	0.0	28 3344	1.8985	0.0	204.30

UNCLASSIFIED

APPENDIX 1 (Cont'd)

HOT - FIRING TEST DATA -- 12 PERCENT LENGTH AEROSPIKE NOZZLE
TEST NUMBER RD08, PAGE 2

CONFIDENTIAL

TIME (SECONDS)	A* (SQ. IN.)	EPSILON* (DMNLESS)	PB/PC (DMNLESS)	PB/PA (DMNLESS)	C*S (FT/SEC)	C*P (FT/SEC)
0.50	13.849	26.828	0.04766	1.084	3870.	4993.
1.00	13.966	26.603	0.04800	1.084	3872.	5009.
1.50	14.005	26.529	0.04827	1.089	3877.	5018.
1.95	14.036	26.470	0.04840	1.089	3885.	5020.
2.35	14.045	26.454	0.04826	1.086	3897.	5022.
3.72	14.045	26.454	0.04694	1.056	0.	5022.
4.32	14.045	26.454	0.04679	1.052	0.	5025.
4.82	14.045	26.454	0.04677	1.055	0.	5036.

UNCLASSIFIED

CONFIDENTIAL
UNCLASSIFIED

TIME (SECONDS)	NC*P (DMNLESS)	NC*S (DMNLESS)	NIS (DMNLESS)	NIS, TOP (DMNLESS)	CT (DMNLESS)	CT, TOP (DMNLESS)
0.50	0.8748	0.8812	0.7793	0.7736	0.8807	0.8843
1.00	0.8785	0.8819	0.7832	0.7775	0.8915	0.8850
1.50	0.8797	0.8830	0.7865	0.7807	0.8939	0.8874
1.95	0.8799	0.8847	0.7869	0.7811	0.8941	0.8877
2.35	0.8807	0.8873	0.7880	0.7623	0.8946	0.8883
3.72	0.8805	0.0	0.7960	0.7960	0.9041	0.9041
4.32	0.8806	0.0	0.7956	0.7956	0.9034	0.9034
4.82	0.8828	0.0	0.7976	0.7976	0.9035	0.9035

UNCLASSIFIED

APPENDIX 1 (Cont'd)

HOT - FIRING TEST DATA -- 12 PERCENT LENGTH AEROSPIKE NOZZLE
TEST NUMBER RD09, PAGE 1

CONFIDENTIAL

TIME (SECONDS)	LAMBDAP (DMNLESS)	PA (PSIA)	PC (PSIA)	PCS (PSIA)	PB (PSIA)	F (POUNDS)
0.50	22.93	13.8000	316.44	288.63	15.5375	5975.
1.00	22.80	13.8000	314.57	288.23	15.5487	5968.
1.50	22.78	13.8000	314.41	288.21	15.5526	5991.
2.00	22.74	13.8000	313.75	287.95	15.5718	6000.
2.50	22.74	13.8000	313.80	288.61	15.5637	6006.
3.00	22.73	13.8000	313.71	288.97	15.5467	6008.
3.50	22.76	13.8000	314.04	289.17	15.5696	6016.
4.00	22.79	13.8000	314.46	289.66	15.5917	6028.
4.50	22.77	13.8000	314.19	289.22	15.5705	6021.
4.95	22.77	13.8000	314.27	290.09	15.5533	6020.
5.35	22.81	13.8000	314.72	289.62	15.5479	6031.
6.24	22.80	13.8000	314.64	0.0	14.6529	5886.
6.74	22.82	13.8000	314.92	0.0	14.5782	5881.
7.24	22.81	13.8000	314.73	0.0	14.5531	5872.
7.74	22.83	13.8000	315.01	0.0	14.5591	5876.

TIME (SECONDS)	WS/WP (DMNLESS)	WS/WP, EFF (DMNLESS)	WT (LBS/SEC)	MRP (DMNLESS)	MRS (DMNLESS)	IS (SECONDS)
0.50	0.0530	0.0416	30.1480	1.8620	0.1737	198.19
1.00	0.0532	0.0416	30.0228	1.8630	0.1734	198.77
1.50	0.0532	0.0415	30.0262	1.8612	0.1659	199.53
2.00	0.0530	0.0414	30.0165	1.8673	0.1628	199.89
2.50	0.0532	0.0415	30.0005	1.8594	0.1641	200.21
3.00	0.0530	0.0416	29.9999	1.8680	0.1627	200.26
3.50	0.0530	0.0415	30.0132	1.8642	0.1629	200.45
4.00	0.0530	0.0416	30.0166	1.8690	0.1622	200.81
4.50	0.0530	0.0415	29.9811	1.8678	0.1626	200.83
4.95	0.0530	0.0416	29.9900	1.8679	0.1621	200.74
5.35	0.0529	0.0415	30.0111	1.8714	0.1623	200.96
6.24	0.0	0.0	28.4425	1.8683	0.0	206.93
6.74	0.0	0.0	28.4207	1.8619	0.0	206.92
7.24	0.0	0.0	28.3669	1.8603	0.0	207.00
7.74	0.0	0.0	28.4514	1.8659	0.0	206.51

UNCLASSIFIED

APPENDIX 1 (Cont'd)

HOT - FIRING TEST DATA -- 12 PERCENT LENGTH AERUSPIKE NOZZLE
TEST NUMBER RD09, PAGE 2

TIME (SECONDS)	A* (SQ. IN.)	EPSILON* (DMNLESS)	PB/PC (DMNLESS)	PB/PA (DMNLESS)	C*S (FT/SEC)	C*P (FT/SEC)
0.50	13.923	26.685	0.04910	1.126	3950.	5025.
1.00	13.991	26.556	0.04943	1.127	3944.	5042.
1.50	14.036	26.470	0.04947	1.127	3946.	5054.
2.00	14.075	26.397	0.04963	1.128	3955.	5059.
2.50	14.085	26.378	0.04960	1.128	3954.	5067.
3.00	14.085	26.378	0.04956	1.127	3968.	5065.
3.50	14.085	26.378	0.04958	1.128	3973.	5047.
4.00	14.085	26.378	0.04958	1.130	3979.	5074.
4.50	14.085	26.378	0.04956	1.128	3979.	5075.
4.95	14.085	26.378	0.04949	1.127	3987.	5075.
5.35	14.085	26.378	0.04940	1.127	3989.	5078.
6.24	14.085	26.378	0.04657	1.062	0.	5088.
6.74	14.085	26.378	0.04629	1.056	0.	5096.
7.24	14.085	26.378	0.04624	1.055	0.	5103.
7.74	14.085	26.378	0.04622	1.055	0.	5092.

TIME (SECONDS)	NC*P (DMNLESS)	NC*S (DMNLESS)	NIS (DMNLESS)	NIS, TOP (DMNLESS)	CT (DMNLESS)	CT, TOP (DMNLESS)
0.50	0.8790	0.8911	0.7805	0.7716	0.8874	0.8778
1.00	0.8821	0.8898	0.7834	0.7744	0.8879	0.8780
1.50	0.8842	0.8916	0.7865	0.7774	0.8892	0.8792
2.00	0.8853	0.8941	0.7882	0.7791	0.8900	0.8801
2.50	0.8863	0.8937	0.7894	0.7802	0.8903	0.8803
3.00	0.8863	0.8971	0.7897	0.7805	0.8905	0.8806
3.50	0.8867	0.8983	0.7903	0.7812	0.8908	0.8810
4.00	0.8880	0.8995	0.7916	0.7825	0.8910	0.8812
4.50	0.8882	0.8995	0.7918	0.7826	0.8910	0.8812
4.95	0.8882	0.9014	0.7914	0.7823	0.8905	0.8807
5.35	0.8868	0.9018	0.7921	0.7830	0.8907	0.8809
6.24	0.8904	0.0	0.8063	0.8063	0.9055	0.9055
6.74	0.8916	0.0	0.8061	0.8061	0.9041	0.9041
7.24	0.8927	0.0	0.8064	0.8064	0.9034	0.9034
7.74	0.8911	0.0	0.8045	0.8045	0.9028	0.9028

APPENDIX 2

DATA REDUCTION PROCEDURES USED IN THE EXTERNAL FLOW INVESTIGATIONS

APPENDIX 2

DATA REDUCTION PROCEDURE USED IN THE EXTERNAL FLOW INVESTIGATION

(U) The basic data measured during each test are listed in Table 17 . The relations utilized to convert these data to parameters representative of still air and slipstream performance are discussed below.

(U) Average pressures acting across the forward face of the engine, the base of the missile body, and the engine base were obtained from the measured pressure and area data (see Figs. 116 and 212) by means of the following relation:

$$\overline{P} = \frac{F_P}{A} = \frac{\sum_i P_i A_i}{A} \qquad (1)$$

(U) These average pressures were used in conjunction with chamber pressure (corrected for gas velocity in the chamber) and cell pressure to form the ratios: $\overline{P}_B/P_c$, P_c/P_∞ , $P_c/\overline{P}_{B_v}$, and $\overline{P}_{B_v}/P_\infty$. Measured thrust was corrected for initial readings before each test. A thrust correction was also made for cases in which a pressure unbalance occurred between average engine and missile base pressure using the relation:

$$F_M = F_A + A_T \left(\overline{P}_{EF} - \overline{P}_{B_v}\right) \qquad (2)$$

(U) Specific impulse efficiency based on free stream conditions is defined as:

$$\eta_{I_s}\Big)_\infty = \frac{F_M + (\overline{P}_{B_v} - P_\infty)\, A_e}{(F_{id_p} + F_{id_s})\; P_c/P_\infty} \qquad (3)$$

TABLE 17

DATA MEASUREMENTS

Parameter	Location (Refer to Fig. 116)	Amplitude
Thrust, Axial	Facility	410
Primary Cha. Press.	P9	200
Primary Cha. Press.	P8	200
Primary Cha. Press.	P10	200
Secondary Cha. Press.	P3	200
Primary Inj. Press.	P2	225
Secondary Inj. Press.	P1	225
Nozzle Base Pressure	P4	Variable
Nozzle Base Pressure	P5	Variable
Nozzle Base Pressure	P6	Variable
Nozzle Base Pressure	P7	Variable
Nozzle Wall Pressure	P16	50
Nozzle Wall Pressure	P19	.5
Missile Base Pressure	P13	Variable
Missile Base Pressure	P14	Variable
Missile Base Pressure	P15	Variable
Missile Base Pressure	P26	Variable
Missile Skin Pressure	P27	Variable
Engine Face Pressure	P22	Variable
Engine Face Pressure	P12	Variable
Engine Face Pressure	P23	Variable
Engine Face Pressure	P24	Variable

TABLE 17
(Continued)
DATA MEASUREMENTS

Parameter	Location (Refer to Fig. 116)	Amplitude
Engine Face Pressure	P11	Variable
Engine Face Pressure	P25	Variable
Balance Pressure	P17	Variable
Balance Pressure	P18	Variable
Balance Pressure	P21	Variable
Balance Pressure	P28	Variable
Primary Cha. Temp.	T2	1400
Primary Cha. Temp.	T3	1400
Secondary Cha. Temp.	T1	1400
Base Temperature	T4	1400
Primary Flowmeter	Facility	2.460
Secondary Flowmeter	Facility	0.025
Peroxide Tank Pressure	Facility	300
Cell Press. (Static)	Facility	Variable
Cell Temperature	Facility	Variable
Cell Press. (Total)	Facility	Variable
Slot Pressure	P20	Variable

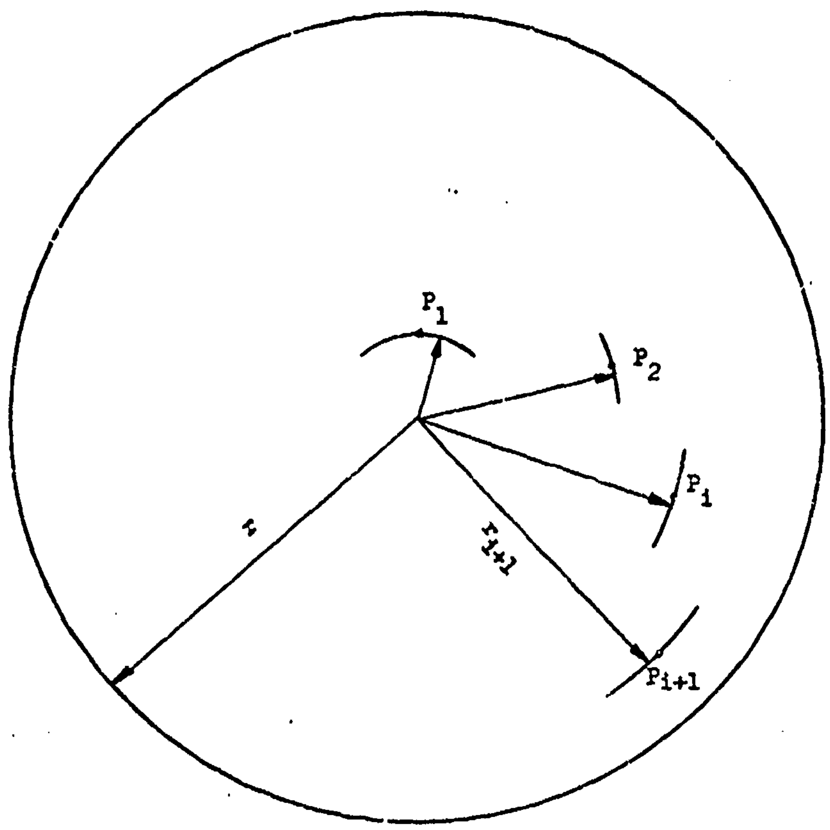

$$\overline{P} = \frac{\Sigma_i \; P_i \; A_i}{A}$$

$$A_i = \frac{\pi (r_{i+1} + r_i)^2 - \pi (r_{i-1} + r_i)^2}{4}$$

$$A = \pi r^2$$

Figure 212. Integrated-Average Pressure Method

(U) When referenced to the missile base pressure this relation becomes:

$$\Phi' = \frac{F_M}{\left(F_{id_p} + F_{id_s}\right)_{P_c/P_{B_v}}} \qquad (4)$$

(U) The quantities F_{id_p} and F_{id_s} are obtained from the following relation:

$$F_{id})_{P_c/P} = \left[\frac{\dot{W}\, C^*_{ic}}{g}\right] \; C_{f_{id}})_{P_c/P} \qquad (5)$$

where flowrate corresponds to the measured value for each test and the ideal thrust coefficient $C_{F_{id}}$ and characteristic velocity C* are obtained from computed ideal performance of the decomposition products of hydrogen peroxide at the correct concentration and inlet temperature. Thrust efficiency C_T is obtained from eqs (3) and (5) by correcting the ideal thrusts in these relations for the measured decomposition temperature of the primary and secondary gas flows which is essentially a characteristic velocity efficiency correction. This results in the following relations for thrust efficiency:

$$C_T)_\infty = \frac{F_M + (\bar{P}_{B_v} - P_\infty)\, A_e}{\left[\dfrac{\dot{W}_p C^*_p C_{F_{id_p}}}{g}\sqrt{\dfrac{T_c}{T_{id}}} + \dfrac{\dot{W}_s C^*_s C_{f_{id_s}}}{g}\sqrt{\dfrac{T_s}{T_{id}}}\right]_{P_c/P_\infty}} \qquad (6)$$

and

$$\Phi = \frac{F_M}{\left[\frac{\dot{W}_p C^*_p C_{F_{id_p}}}{g}\sqrt{\frac{T_c}{T_{id}}} + \frac{\dot{W}_s C^*_s C_{f_{id_s}}}{g}\sqrt{\frac{T_s}{T_{id}}}\right]_{P_c/P_{B_v}}} \qquad (7)$$

(U) Note that since $T_c \approx T_s$, this is essentially a topping cycle efficiency for the results in this program. Aerodynamic throat area was computed from measured chamber pressure, primary flowrate, and chamber temperature in conjunction with ideal properties as follows:

$$A^* = \frac{\dot{W}_p C^*_{id_p}}{P_c}\sqrt{\frac{T_c}{T_{id_p}}} \qquad (8)$$

and used to form the expansion area ratio, where:

$$\epsilon = A_e/A^* \qquad (9)$$

(U) The change in nozzle efficiency with the addition of secondary flow was computed from the measured change in base pressure as follows:

$$\Delta C_T = \left[\frac{C_T)_{\dot{W}_s=0} + \frac{\Delta P_B}{P_c}\frac{\epsilon_B}{C_{F_{id_p}}}}{1 + \frac{\dot{W}_s C^*_s C_{F_{id_s}}}{\dot{W}_p C^*_p C_{F_{id_p}}}}\right] - C_{T_{\dot{W}_s = 0}} \qquad (10)$$

(U) Mission parameters applicable to the trajectories in Figs. 100 and 101 are listed in Table 18. Pertinent performance and pressure data obtained using the above procedure are listed for each test in Appendix 3.

TABLE 18. MISSION PARAMETERS FOR TRAJECTORY ANALYSIS

CONFIDENTIAL

Designation	Vehicle Parameters		Booster Engine Parameters					
	No. of Stages	F/W	Feed System	Pro-pellants	ϵ	γ	P_c	$PR)_{des}$
I	1	1.29	Pump	LO_2/LH_2	80	1.25	1500	1063
II	2	1.29	Pump	LO_2/LH_2	80	1.25	1500	1065
III	2	1.29	Pump	LO_2/LH_2	80	1.25	1500	1063
IV	2	1.93	Pressure	Storable*	10	1.25	3[illegible]	91.4
V	1	1.25	Pump	Storable*	55	1.25	2000	885

*$N_2O_4/UDMH-N_2H_4$ (50-50)

APPENDIX 3

SLIPSTREAM TEST DATA

APPENDIX 3 SLIPSTREAM TEST DATA

DATA SUMMARY, TRANSONIC WIND TUNNEL

CONFIDENTIAL

Test	M_∞	P_c	T_c	$\dot{W}_P$	F_M	A^*	$\bar{P}_{E_F}$	$\bar{P}_{B_v}$	$\bar{P}_B$
3	0	193.8	1277	2.570	272.4	1.209	14.19	14.12	14.72
37	0	189.2	1287	2.531	368.5	1.244	1.24	1.24	1.53
38	0	185.9	1276	2.521	360.0	1.256	1.43	1.42	1.71
39	0	190.1	1290	2.556	365.3	1.249	1.62	1.62	2.05
42	0	190.9	1281	2.528	345.9	1.230	2.87	2.86	3.79
43	0	187.6	1285	2.518	387.7	1.243	0.55	0.55	1.42
46	0	192.1	1295	2.537	340.2	1.231	2.87	2.86	3.48
47	0	189.4	1295	2.540	354.4	1.247	1.63	1.62	1.45
48	0	190.1	1296	2.554	357.1	1.251	1.44	1.43	1.33
49	0	190.3	1297	2.544	370.7	1.245	0.94	0.93	0.97
52	0	196.2	1305	2.576	381.9	1.223	0.93	0.92	1.76
36	0.55	189.4	1289	2.531	362.8	1.244	1.29	1.27	1.59
18	0.90	182.1	1299	2.422	369.6	1.242	0.66	0.65	1.14
20	0.90	182.8	1296	2.441	350.3	1.246	1.44	1.41	1.57
21	0.90	190.8	1304	2.518	326.3	1.235	5.40	5.29	6.36
28	0.90	190.6	1284	2.527	351.1	1.234	2.52	2.45	3.14
29	0.90	190.1	1292	2.533	371.4	1.240	1.17	1.15	1.43
30	0.90	192.9	1285	2.591	380.3	1.250	1.09	1.07	1.40
22	1.20	188.3	1301	2.509	405.6	1.244	0.60	0.53	2.70
23	1.20	187.2	1303	2.506	395.9	1.251	0.34	0.30	1.32
31	1.20	192.0	1298	2.544	347.6	1.249	3.47	3.26	4.24
32	1.20	186.6	1286	2.505	389.6	1.236	0.45	0.41	1.35
33	1.20	188.2	1292	2.525	394.3	1.250	0.42	0.39	1.35
24	1.40	191.0	1302	2.553	405.4	1.249	0.26	0.23	1.33
25	1.40	189.1	1303	2.535	399.4	1.251	0.28	0.26	1.30
34	1.40	190.3	1288	2.543	405.3	1.244	0.52	0.48	2.20
35	1.40	188.6	1295	2.526	397.6	1.247	0.40	0.37	1.36

APPENDIX 3 SLIPSTREAM TEST DATA
(Continued)

DATA SUMMARY, TRANSONIC WIND TUNNEL

CONFIDENTIAL

Test	M_∞	P_c/P_∞	$\dot{W}_s/\dot{W}_p$	$\eta_{C^*_p}$	$\eta_{C^*_s}$	$\eta_{I_{s_\infty}}$	$\bar{\Phi}'$	C_{T_∞}	$\bar{\Phi}$
3	0	13.7	0.0073	0.972	0.945	0.852	0.852	0.892	0.892
37	0	153	0.0076	0.974	0.945	0.935	0.935	0.959	0.959
38	0	131	0.0075	0.971	0.945	0.925	0.925	0.952	0.952
39	0	118	0.0075	0.975	0.945	0.931	0.931	0.960	0.960
42	0	66	0.0075	0.975	0.945	0.927	0.927	0.949	0.949
43	0	361	0.0075	0.976	0.945	0.959	0.959	0.982	0.982
46	0	67	0	0.979	-	0.912	0.912	0.932	0.932
47	0	117	0	0.979	-	0.918	0.918	0.939	0.939
48	0	133	0	0.979	-	0.913	0.913	0.935	0.935
49	0	202	0	0.980	-	0.931	0.931	0.951	0.951
52	0	211	0.0170	0.982	0.945	0.930	0.930	0.950	0.950
36	0.55	132	0.0076	0.975	0.945	0.926	0.935	0.949	0.957
18	0.90	209	0.0076	0.978	0.945	0.947	0.953	0.968	0.974
20	0.90	106	0.0076	0.977	0.945	0.915	0.931	0.935	0.951
21	0.90	31.0	0.0077	0.979	0.945	0.859	0.917	0.876	0.936
28	0.90	67	0.0076	0.974	0.945	0.903	0.928	0.928	0.952
29	0.90	131	0.0076	0.976	0.945	0.925	0.939	0.947	0.968
30	0.90	142	0.0075	0.974	0.945	0.925	0.935	0.947	0.958
22	1.20	62	0.0076	0.978	0.945	0.866	1.001	0.903	1.022
23	1.20	216	0.0076	0.979	0.945	0.954	0.971	0.961	0.979
31	1.20	35.8	0.0076	0.977	0.945	0.783	0.931	0.800	0.952
32	1.20	114	0.0075	0.974	0.945	0.915	0.955	0.937	0.979
33	1.20	138	0.0075	0.976	0.945	0.930	0.956	0.979	0.952
24	1.40	311	0.0076	0.979	0.945	0.958	0.955	0.977	0.974
25	1.40	215	0.0076	0.979	0.945	0.948	0.952	0.968	0.972
34	1.40	66	0.0075	0.975	0.945	0.876	0.976	0.897	1.001
35	1.40	114	0.0075	0.977	0.945	0.924	0.961	0.945	0.984

Note: Ideal Decomposition Temperature was 1840 °R and 1831 °R for Tests 3 through 39 and Tests 42 through 52, respectively. Ideal Characteristic Velocity was 3068 ft/sec and 3061 ft/sec for Tests 3 through 39 and Tests 42 through 52, respectively.

APPENDIX 3 SLIPSTREAM TEST DATA
(Continued)
DATA SUMMARY, SUPERSONIC WIND TUNNEL

CONFIDENTIAL

Test	M_∞	P_c	T_c	$\dot{W}_P$	F_M	A^*	$\bar{F}_{E_F}$	$\bar{F}_{B_V}$	$\bar{F}_B$
14	0	187.1	1323	2.442	364.5	1.222	1.23	1.22	1.46
16	0	193.6	1329	2.530	387.0	1.229	0.85	0.84	1.44
17	0	195.3	1330	2.557	394.7	1.232	0.69	0.67	1.45
19	0	196.9	1326	2.523	325.5	1.204	6.07	6.05	7.34
20	0	193.6	1328	2.540	350.3	1.234	3.03	3.02	3.96
21	0	194.3	1324	2.535	362.4	1.225	2.19	2.19	2.87
22	0	196.7	1323	2.538	357.4	1.228	1.73	1.73	2.23
23	0	192.2	1326	2.523	366.9	1.234	1.51	1.51	1.68
38	0	193.0	1328	2.520	393.9	1.227	0.55	0.55	.43
27	2.2	193.1	1311	2.551	409.6	1.236	0.18	0.17	1.50
29	2.2	191.5	1316	2.526	407.7	1.236	0.15	0.14	1.46
31	2.2	191.6	1320	2.529	408.8	1.238	0.13	0.13	1.47
33	2.2	191.3	1314	2.533	407.5	1.240	0.12	0.12	1.47
35	1.8	193.0	1330	2.530	408.5	1.232	0.26	0.25	1.46
37	1.8	192.3	1333	2.524	407.3	1.236	0.23	0.22	1.45
41	1.8	193.0	1333	2.538	407.9	1.238	0.20	0.19	1.47
42	1.8	195.2	1341	2.549	411.9	1.232	0.17	0.17	1.46
43	1.8	192.5	1338	2.529	409.0	1.239	0.13	0.13	1.45

UNCLASSIFIED

APPENDIX 3 SLIPSTREAM TEST DATA
(Continued)

DATA SUMMARY, SUPERSONIC WIND TUNNEL

CONFIDENTIAL

Test	M_∞	P_c/P_∞	$\dot{W}_s/\dot{W}_p$	$\eta_{C^*_p}$	$\eta_{C^*_s}$	$\eta_{I_{s_\infty}}$	Φ'	C_{T_∞}	Φ
14	0	154	0.0083	0.972	0.872	0.942	0.944	0.971	0.973
16	0	220	0.0082	0.974	0.874	0.949	0.950	0.976	0.977
17	0	284	0.0082	0.974	0.875	0.949	0.949	0.976	0.975
19	0	32.5	0.0083	0.973	0.873	0.907	0.908	0.934	0.935
20	0	64.0	0.0082	0.974	0.873	0.919	0.920	0.946	0.946
21	0	88.6	0.0085	0.973	0.873	0.932	0.932	0.960	0.960
22	0	112	0.0085	0.972	0.872	0.931	0.931	0.960	0.950
23	0	127	0.0084	0.973	0.870	0.929	0.929	0.956	0.957
38	0	337	0.0084	0.974	0.864	0.952	0.9[illegible]	0.979	[illegible]
27	2.2	223	0.0083	0.970	0.865	0.946	0.944	0.979	0.976
29	2.2	313	0.0082	0.971	0.864	0.954	0.945	0.985	0.976
31	2.2	397	0.0082	0.972	0.862	0.950	0.938	0.980	0.968
33	2.2	467	0.0083	0.970	0.861	0.949	0.937	0.981	0.968
35	1.8	110	0.0083	0.974	0.866	0.919	0.959	0.945	0.986
37	1.8	158	0.0083	0.975	0.865	0.943	0.956	0.969	0.982
41	1.8	224	0.0084	0.975	0.865	0.948	0.948	0.974	0.974
42	1.8	322	0.0083	0.977	0.866	0.957	0.950	0.981	0.974
43	1.8	469	0.0083	0.977	0.864	0.955	0.944	0.980	0.968

Note: For these tests Ideal Decomposition Temperature was 1890 °R, and Ideal Characteristic Velocity was 3110 ft/sec.

UNCLASSIFIED

APPENDIX 4

DATA REDUCTION AND ANALYSIS PROCEDURE
FOR TVC PROGRAM

APPENDIX 4

DATA REDUCTION AND ANALYSIS PROCEDURE FOR TVC PROGRAM

(U) The basic parameters measured during each test are listed in Table 19. The measurements were used to compute nozzle performance with and without TVC, and side forces and total control moments generated during TVC operation. The methods by which these parameters were determined in this test program are discussed in the following paragraphs.

BASIC ENGINE PERFORMANCE

(U) Nozzle performance was computed as it was for the 12-percent length nozzle. Heat loss and propellant impurity corrections were obtained from the theoretical data presented previously after computing the heat loss and propellant water content as follows:

$$Q/Q_{th} = \frac{\dot{W}_{H_2O}\ (\Delta T_{H_2O}) + (450)}{(\dot{W}_p)\ (205.1)}$$

$$\text{Percent } H_2O = \frac{(\text{Percent } H_2O \text{ in oxidizer})(MR_p) + (\text{Percent } H_2O \text{ in fuel})}{1 + (MR_p)}$$

(U) The constants in the heat loss relation were adjusted from those obtained for the 12-percent length nozzle to account for the revised hardware geometry and operating conditions. Specific impulse corrections, $\Delta I_{s_{H.L.}}$ and $\Delta I_{s_{H_2O}}$, and the characteristic velocity corrections, $\eta_{C^*_{H.L.}}$ and

TABLE 19
TVC ENGINE MEASURED PARAMETERS

PARAMETER	SYMBOL	LOCATION	NOMINAL VALUE	INSTRUMENT RANGE
Force, pounds				
Axial	F_A	Facility	5600	0-10,000
Fore Yaw	F_{YF}	Facility	0-10	0-1000
Fore Pitch	F_{PF}	Facility	0-10	0-1000
Aft Yaw	F_{YA}	Facility	0-100	0-1000
Aft Pitch	F_{PA}	Facility	0-10	0-1000
Roll	F_R	Facility	0-20	0-1000
Primary Chamber Pressure, Psia	PC-1	P3	200	0-300
	PC-2	P4	200	0-300
	PC-3	P5	200	0-300
Primary Injection Pressure, Psia				
Oxidizer	POJ	P1	330	0-500
Fuel	PFJ	P2	360	0-500
Secondary Chamber Pressure, Psia	PCG-1	P8	100	0-100
	PCG-2	P9	100	0-100
	PCG-3	P10	100	0-100
Secondary Injection Pressure, Psia				
Oxidizer	POJG	P6	145	0-500
Fuel	PFJG	P7	150	0-500
Oxidizer	POJG-1	Facility	200	0-500
Fuel	PFJG-1	Facility	175	0-500
Base Pressure, Psia	PB1	P22	1	0-25
	PB2	P23	1	0-25
	PB3	P24	1	0-25
	PB4	P29	1	0-25

TABLE 19
TVC ENGINE MEASURED PARAMETERS

PARAMETER	SYMBOL	LOCATION	NOMINAL VALUE	INSTRUMENT RANGE
Force, pounds				
Axial	F_A	Facility	5600	0-10,000
Fore Yaw	F_{YP}	Facility	0-10	0-1000
Fore Pitch	F_{PP}	Facility	0-10	0-1000
Aft Yaw	F_{YA}	Facility	0-100	0-1000
Aft Pitch	F_{PA}	Facility	0-10	0-1000
Roll	F_R	Facility	0-20	0-1000
Primary Chamber Pressure, Psia	PC-1	P3	200	0-300
	PC-2	P4	200	0-300
	PC-3	P5	200	0-300
Primary Injection Pressure, Psia				
Oxidizer	POJ	P1	330	0-500
Fuel	PFJ	P2	360	0-500
Secondary Chamber Pressure, Psia	PCG-1	P8	100	0-100
	PCG-2	P9	100	0-100
	PCG-3	P10	100	0-100
Secondary Injection Pressure, Psia				
Oxidizer	POJG	P6	145	0-500
Fuel	PFJG	P7	150	0-500
Oxidizer	POJG-1	Facility	200	0-500
Fuel	PFJG-1	Facility	175	0-500
Base Pressure, Psia	PB1	P22	1	0-25
	PB2	P23	1	0-25
	PB3	P24	1	0-25
	PB4	P29	1	0-25

TABLE 19

(Continued)

PARAMETER	SYMBOL	LOCATION	NOMINAL VALUE	INSTRUMENT RANGE
Nozzle Skirt Pressure, Psia	PNS-1	P25	3	0-25
	PNS-2	P26	3	0-25
	PNS-3	P27	3	0-25
	PNS-4	P28	3	0-25
Outer Nozzle Pressure, Psia	PN-1	P15	Ambient	0-25
	PN-2	P16	Ambient	0-25
	PN-3	P17	Ambient	0-25
	PN-4	P18	Abmient	0-25
	PN-5	P19	Ambient	0-25
Secondary Chamber Temperature, F	TCG-1	T3	1600	0-2000
	TCG-2	T4	1600	0-2000
Water Temperature, F				
Inlet	TWI	Facility	Ambient	0-150
Outlet	TWO	Facility	160	0-250
Primary Flow, lb/sec				
Oxidizer	WOP	Facility	12.5	0-23
Fuel	WFP	Facility	7.5	0-8
Secondary Flow, lb/sec				
Oxidizer	WOS	Facility	0.03	System ΔP
Fuel	WFS	Facility	0.30	System ΔP
TVC Flow, lb/sec	WTVC	Facility	0-6	0-6
Coolant Water Flow, lb/sec	WCW	Facility	60	0-120
Primary Tank Pressure				
Oxidizer	PTOP	Facility	-	-
Fuel	PTFP	Facility	-	-

TABLE 19
(Continued)

PARAMETER	SYMBOL	LOCATION	NOMINAL VALUE	INSTRUMENT RANGE
Secondary Tank Pressure				
Oxidizer	PTOS	Facility	-	-
Fuel	PTFS	Facility	-	-
TVC Tank Pressure				
TVC Purge Pressure (Line), Psia	PPLT	Facility	Variable	0-500
Primary Line Temp., F				
Oxidizer	TLOP	Facility	Ambient	0-60
Fuel	TLFP	Facility	Ambient	0-60
Secondary Line Temp, F				
Oxidizer	TLOS	Facility	Ambient	0-60
Fuel	TLFS	Facility	Ambient	0-60
TVC Line Temp., F		Facility	Ambient	0-60
Water Pressure (Inner), Psia				
Inlet	PWII	Inlet Tee	730	0-1500
Outlet	PWOI	Outlet Tee	160	0-1000
Water Pressure (Outer) Psia				
Inlet	PWIO	Inlet Tee	520	0-1500
Outlet	PWOO	Outlet Tee	220	0-1000
Cell Pressure, Psia	P_a	Facility	0.7	0-15

$\eta C^*_{H_2O}$, are given as functions of $\tilde{Q}$ and percent H_2O in a previous section. Values of these factors applied to each test are given in Table 20. Specific impulse efficiency was obtained from

$$\eta_{I_s} = \frac{F_{A_c}}{F_{opt_p} + F_{opt_s}}$$

where

F_{A_c} = measured axial thrust corrected for impurities and heat loss

$= F_A + (\Delta I_{s_{H.L.}})\ \dot{W}_p$

$F_{opt_p} = (I_{s_{opt_p}} - \Delta I_{s_{H_2O}})\ \dot{W}_p$

$F_{opt_s} = I_{s_{opt_s}}\ \dot{W}_s$ (Or $I_{s_{opt_p}}\ \dot{W}_s$ for topping cycle specific impulse efficiency)

where $I_{s_{opt}}$ = theoretical shifting equilibrium specific impulse at P_c/P_a (Fig. 213 and 214).

(U) The thrust and efficiency data in Tables 13 and 14 are measured values corrected to $P_a = 0.7$ psia. Characteristic velocity (C*) efficiency is defined as:

$$\eta_{C^*_p} = \frac{P_c A^*_p g_c}{C^*_{th_p}\ \dot{W}_p\ \eta_{C^*_{H.L.}}\ \eta_{C^*_{H_2O}}}$$

$$\eta_{C^*_s} = \frac{P_{c_s} A^*_s g_c}{C^*_{th_s}\ \dot{W}_s}$$

TABLE 20

HEAT LOSS FACTORS APPLIED TO MEASURED TVC DATA*

CONFIDENTIAL

Test	$\eta_{C^*_{H.L.}}$	$\Delta I_{s_{H.L.}}$ (Sec)
1**	0.990	6.0
BA01	0.991	5.7
BA02	0.991	5.6
BA03	0.990	6.0
BA04	0.990	6.0
BA05	0.990	6.0
BB06	0.990	5.9
BB07	0.991	5.6
BB08	0.991	5.8
BB09	0.991	5.6
BB10	0.991	5.5
BB11	0.991	5.6
BC12	0.991	5.6
BC13	0.991	5.9
BC14	0.991	5.9
BC15	0.991	5.9
BC16	0.991	5.9
BC17	0.991	5.9
BC18	0.990	6.0
BD19	0.990	6.5
BD20	0.990	6.3
BD21	0.990	6.7

*$\eta_{C^*_{H_2O}} = 1.000$; $\Delta I_{s_{H_2O}} = 0.0$ Sec.

**Rocketdyne Sea-Level Checkout Test. Factors were assumed.

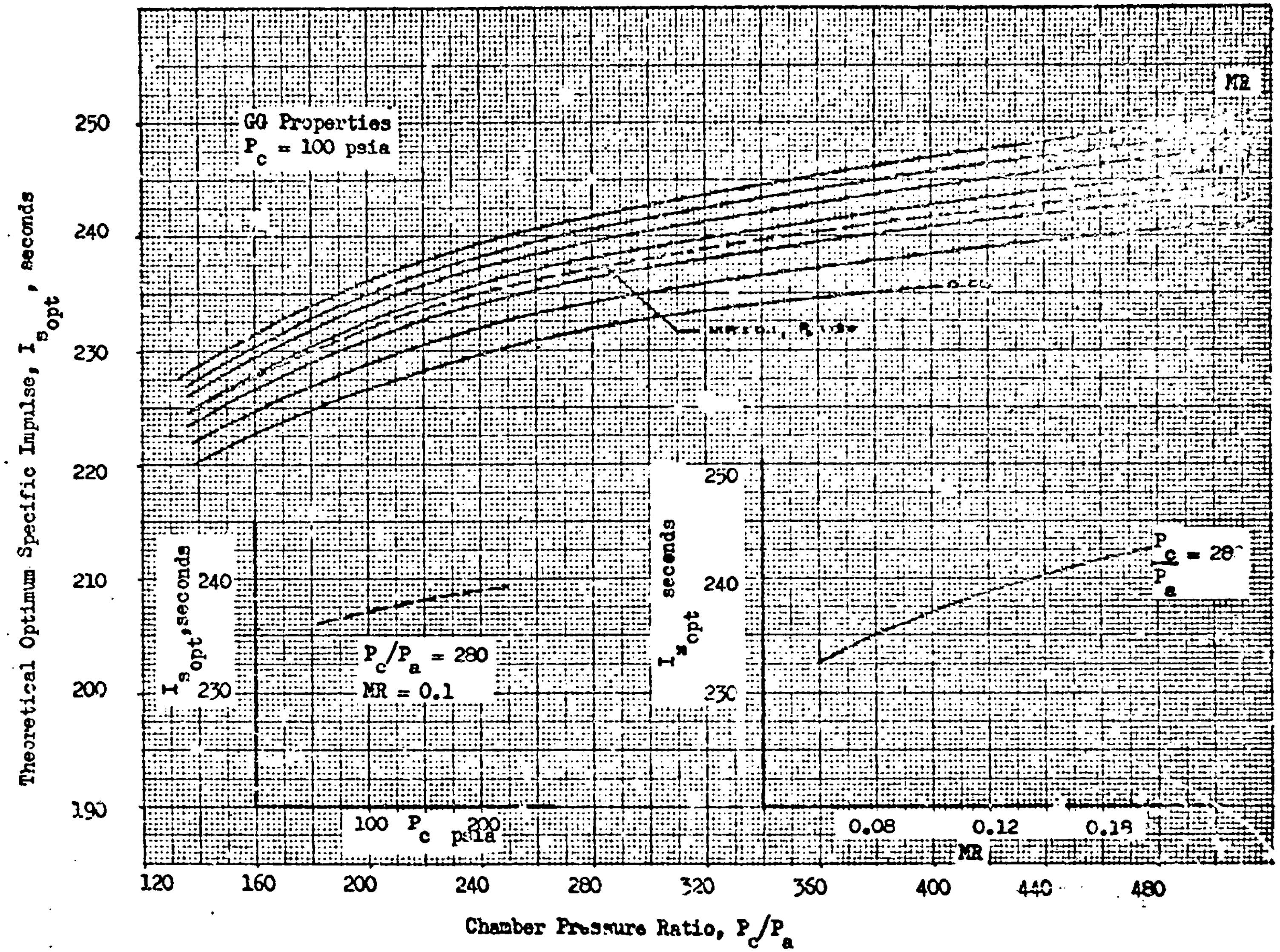

Figure 213. Gas Generator Theoretical Specific Impulse

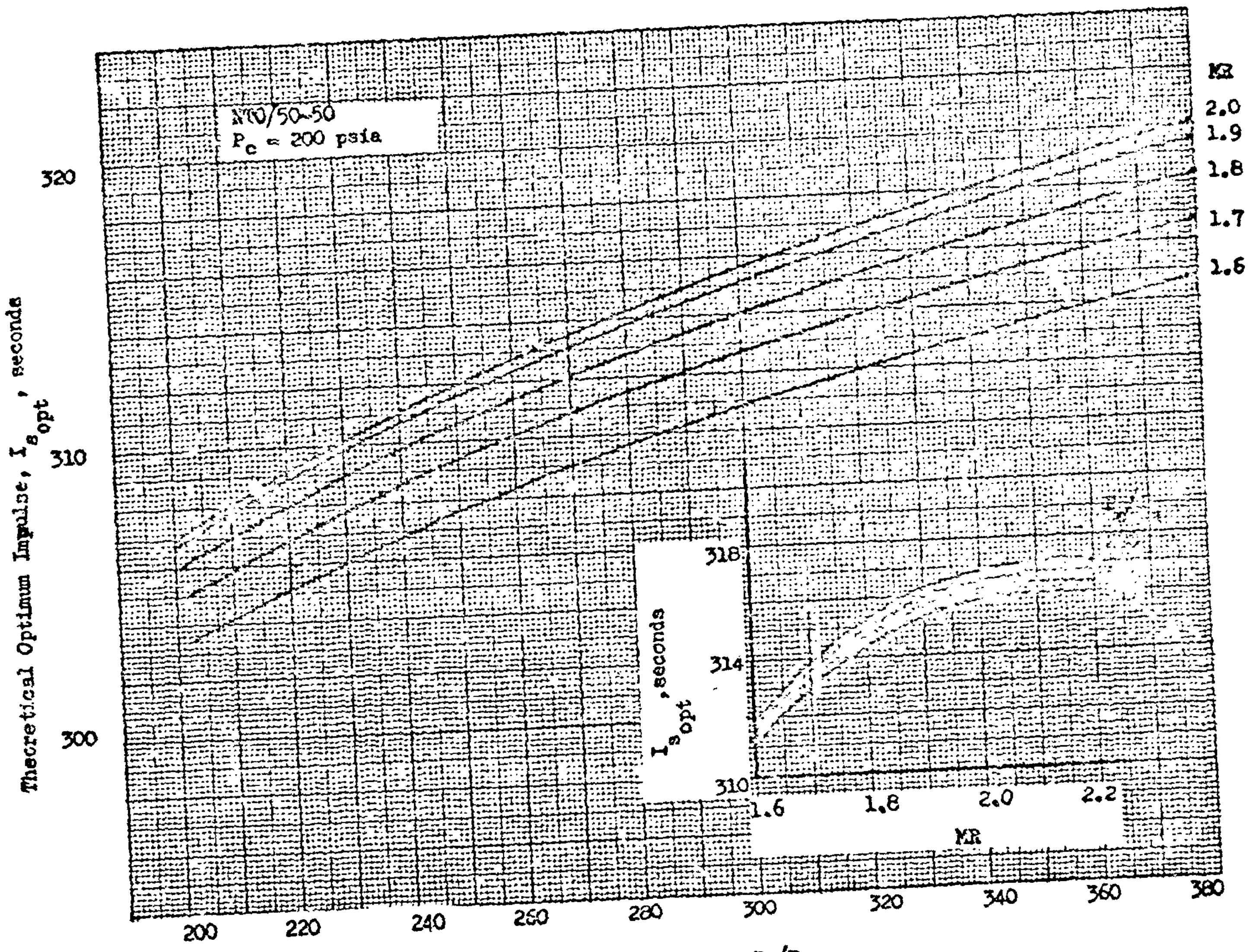

Figure 214. Main Engine Theoretical Specific Impulse

where

C^*_{th} = Theoretical shifting equilibrium characteristic velocity (Fig. 215 and 216)

P_c = PC-3/0.998)

$A^*_p = 1.0135\ C_D\ A_{p\ meas.}$

where C_D is the theoretical throat discharge coefficient (= .9893).

$A^*_s = (0.85)\ A_{s\ Meas.}$

(U) As indicated, the primary throat area was increased by a factor of 1.35 percent to account for the change in throat area during this test up to the time at which all reference data were computed. This correction was obtained in the same manner as for the 12-percent length engine but was constant throughout the TVC testing. The nozzle thrust efficiency exclusive of combustion chamber effects and combustion efficiency was obtained from:

$$C_T = \frac{F_{A_c}}{F_{opt_p} \eta C^*_p + F_{opt_s} \eta C^*_s}$$

Topping cycle thrust efficiency was obtained from:

$$C_{T_{top}} = \frac{F_{A_c}}{F_{th_p} \eta C^*_p + I_{s_{opt_p}} \dot{w}_s \eta C^*_p}$$

LITVC PERFORMANCE

(U) The unbalanced forces generated during liquid injection TVC were corrected for initial thrust misalignment (determined from average force data obtained during the 0.5-second period prior to signalling for TVC flow), and used to compute induced forces and control moments about a reference axis in the throat plane as follows:

$$F_{YF} = F_{YF})_{TVC} - F_{YF})_{ref}$$

$$F_{YA} = F_{YA})_{TVC} - F_{YA})_{ref}$$

$$F_s = F_Y = F_{YA} + F_{YF}$$

$$M_T = M_Y = (F_{YA})\ d_1 + (F_{YF})\ d_2$$

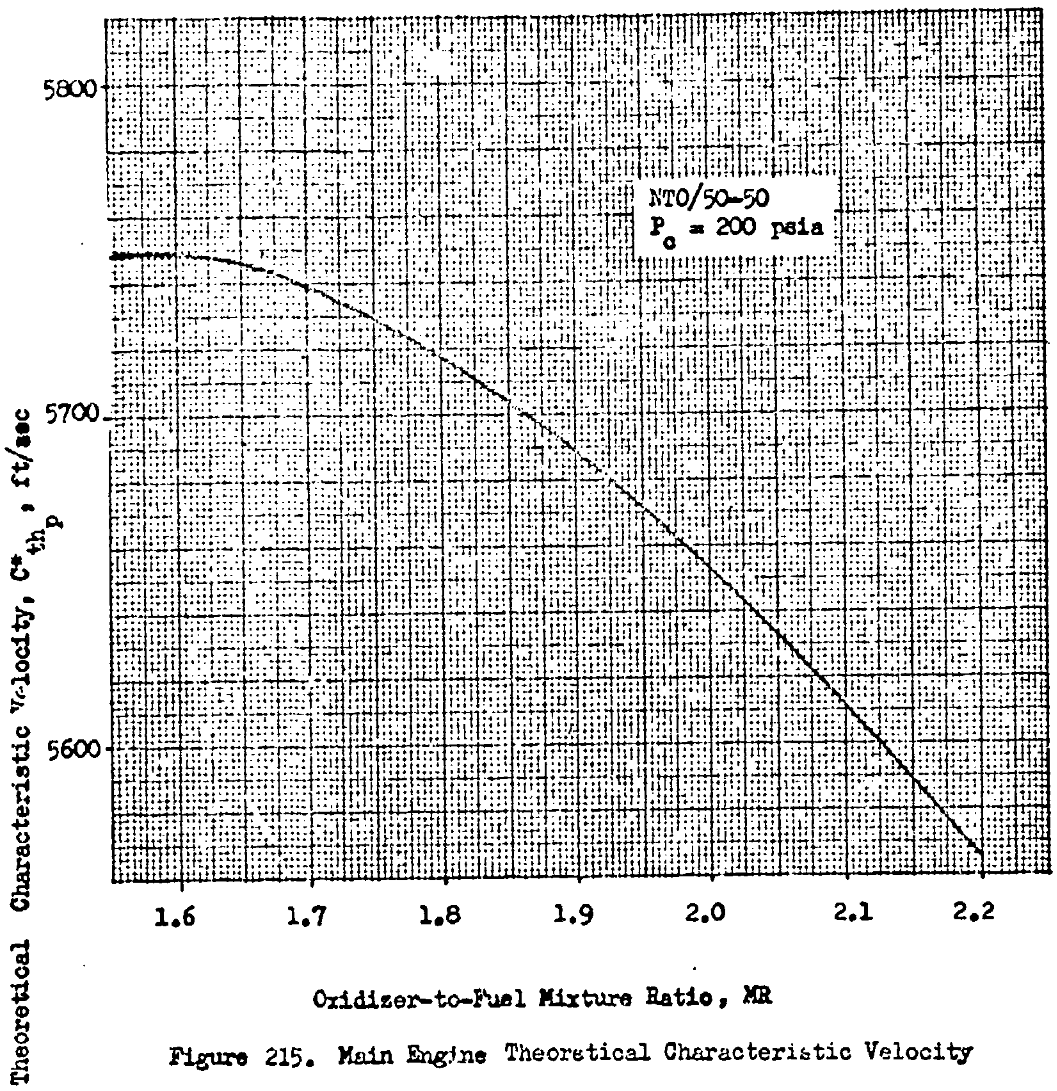

Figure 215. Main Engine Theoretical Characteristic Velocity

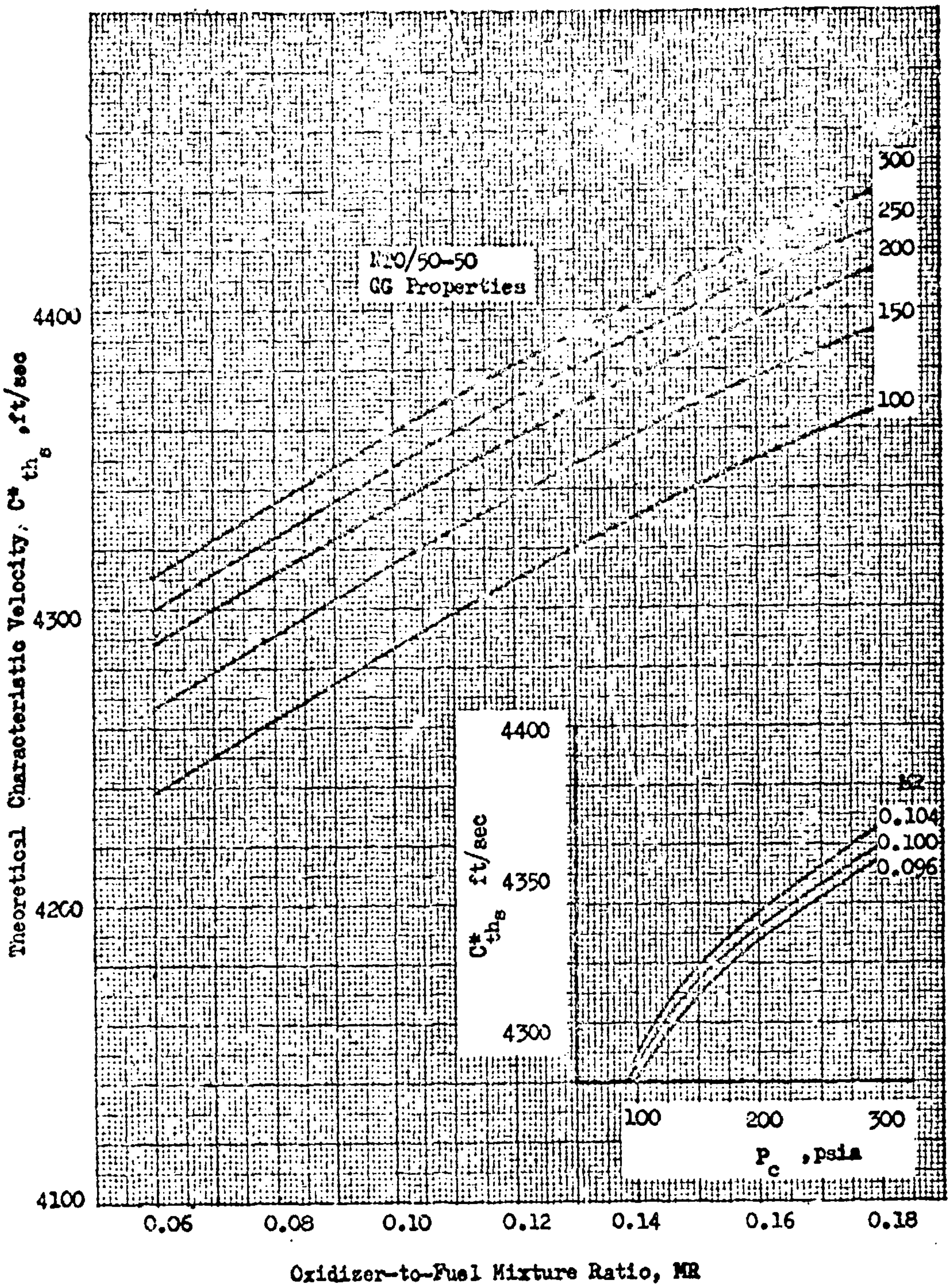

Figure 216. Gas Generator Theoretical Characteristic Velocity

(U) The dimensionless moment about an arbitrary axis a distance h from the reference plane (nondimensionalized in terms of the reference thrust without TVC and the distance, h) was found from:

$$\frac{M}{F_v h} = \frac{F_s}{F_v} + \frac{M_T}{F_v r_e} \frac{r_e}{h}$$

$$= \frac{F_s}{F_v} + \frac{F_{oc}}{F_v} \frac{r_e}{h}$$

where the dimensionless axial thrust and axial thrust displacement were combined to form a new quantity designated as the dimensionless off-center force. This quantity may be interpreted as a fictitious force aligned in the axial direction (i.e., parallel to the engine centerline) which produces a moment about the reference axis that is equivalent to the moments produced by the secondary injection system as shown schematically in Fig. 217. Thus,

$$\frac{F_{oc}}{F_v} = \frac{M_T}{F_v r_e}$$

(U) The off-center force is a fictitious quantity in that it contributes nothing to the axial thrust of the nozzle even though it has been defined above as a force vector acting in the axial direction. However, representing the TVC effectiveness in this fashion enables a more convenient comparison of injection methods since only two quantities, F_s and F_{oc}, are needed to establish a control moment for a given geometry; also, nozzle performance and TVC effectiveness comparisons can be examined separately.

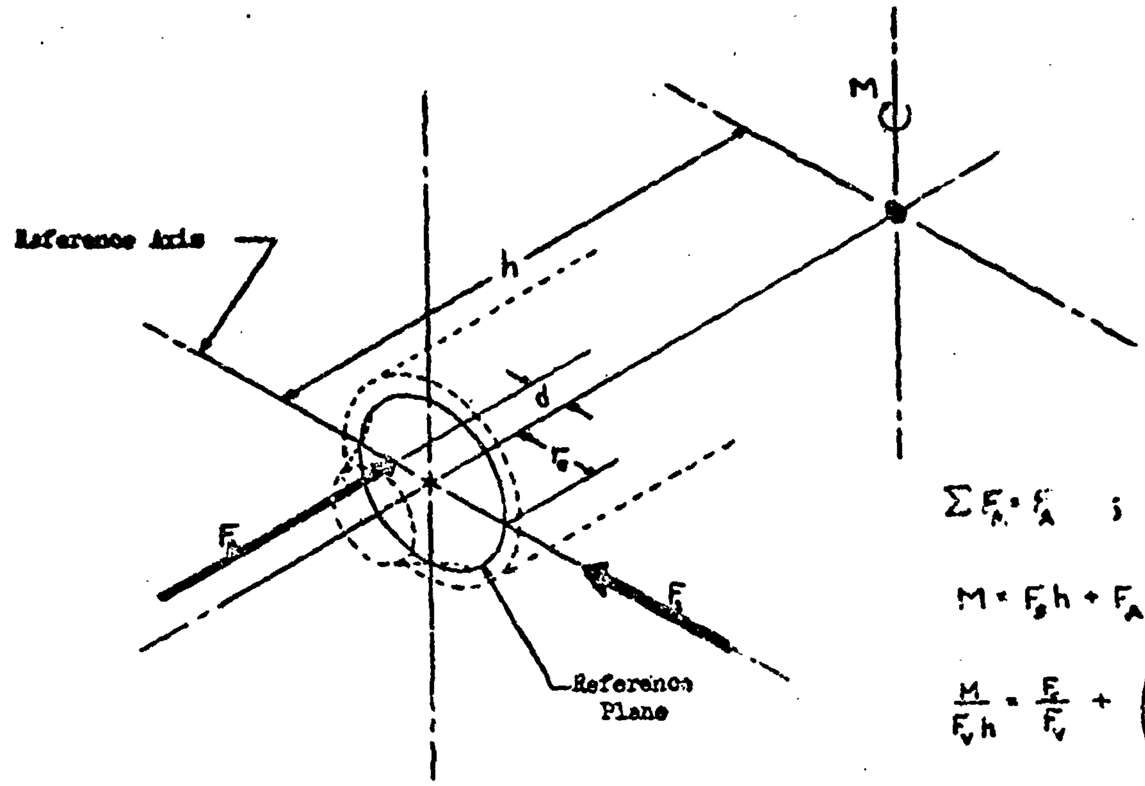

$$\sum F_A = F_A \quad ; \quad \sum F_s = F_s$$

$$M = F_s h + F_A d$$

$$\frac{M}{F_v h} = \frac{F_s}{F_v} + \left(\frac{F_A}{F_v}\right)\left(\frac{d}{r_e}\right)\left(\frac{r_e}{h}\right)$$

a) Actual force representation

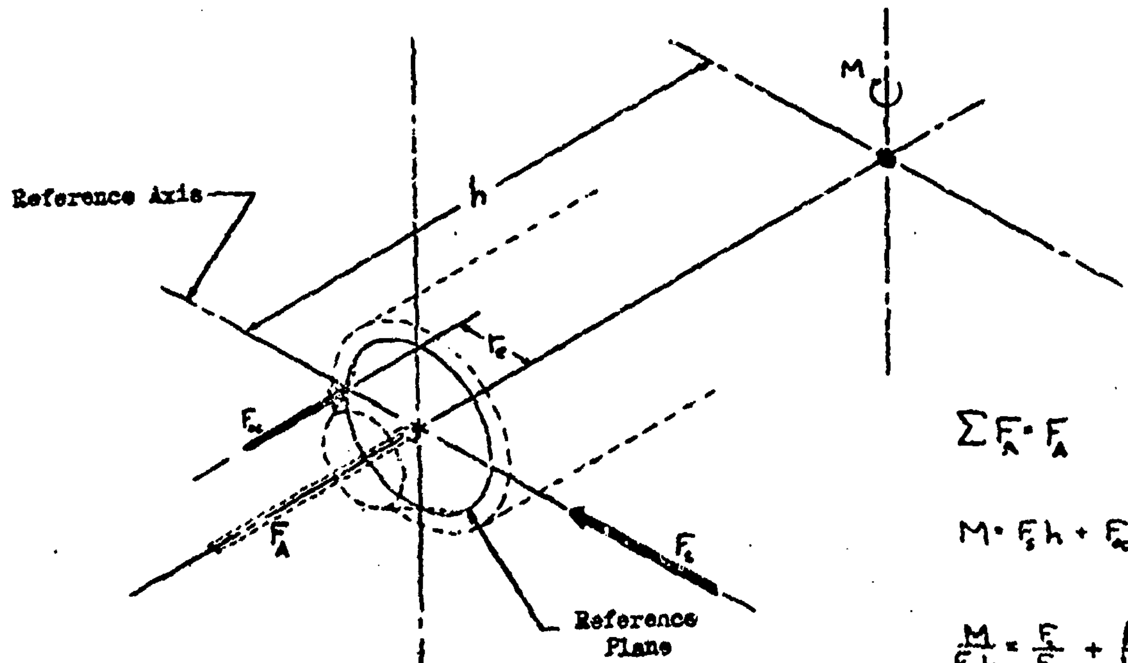

$$\sum F_A = F_A \quad ; \quad \sum F_s = F_s$$

$$M = F_s h + F_{Ac} r_e$$

$$\frac{M}{F_v h} = \frac{F_s}{F_v} + \left(\frac{F_{Ac}}{F_v}\right)\left(\frac{r_e}{h}\right)$$

b) Off-center force representation

Figure 217. Unbalanced Forces with Secondary Injection TVC

(U) Engine performance during TVC was represented in terms of the change in engine specific impulse with a change in TVC flowrate. This quantity was computed from:

$$\Delta I_s = 1 - \left(\frac{1 + (\Delta F_A / F_v)}{1 + \dot{W}_{TVC}/\dot{W}_p} \right)$$

where:

$$\Delta F_A = F_m)_{TVC} - F_m)_{REF}$$

and represents the change in engine thrust (vacuum) during TVC.

(U) A commonly used representation of the moment produced under various injection SITVC conditions is the equivalent gimbal angle which is defined as the angle to which the engine would have to be gimbaled about the reference plane to produce a moment about the vehicle center of gravity which is equivalent to the moment generated by fluid injection. This equivalence is illustrated in the sketch below.

$M_{gimbal} = M_{SITVC}$

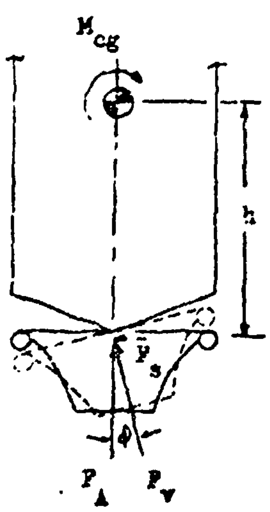

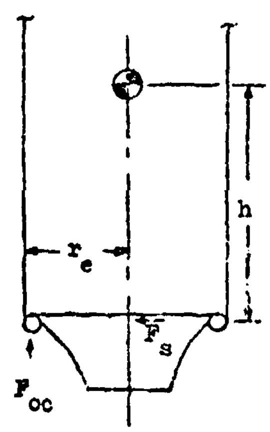

(U) For the gimbaled engine:

$$\sin \phi = \frac{F_s}{F_v} = \frac{F_s h}{F_v h} = \frac{M_{cg.}}{F_v h}$$

or

$$\phi = \text{Arcsin} \left[\frac{M_{cg.}}{F_v h} \right]$$

(U) Thus, for the fluid injection system:

$$\phi = \text{arcsin} \left[\frac{M_{cg.}}{F_v h} \right] = \text{arcsin} \left[\frac{F_s}{F_v} \quad \frac{F_{oc}}{F_v} \quad \frac{r_e}{h} \right]$$

(U) The quantities: F_Y, M_Y, ϕ, F_s, F_{oc}, F_A, $\dot{W}_{TVC}$, were computed from the data obtained during the last 0.5-second time interval during each test, and were used to form the basis for present ng and comparing nozzle performance during TVC, and the TVC effectiveness of the various injection techniques. Comparisons were made in terms of quantities designed to characterize various specific aspects of fluid injection operation. The effectiveness with which the SITVC system generates side thrust if often represented in terms of a side thrust amplification factor defined as:

$$K_s = \frac{I_{s_s}}{I_{s_v}} = \frac{F_s/F_v}{\dot{W}_{TVC}/\dot{W}_e}$$

(U) A similar quantity can be used to represent the off-center thrust efficiency and is defined as:

$$K_M = \frac{F_{oc}/F_v}{\dot{W}_{TVC}/\dot{W}_e}$$

(U) For the aerospike, the total efficiency of the system must reflect the influence of both forces so that the control moment efficiency becomes:

$$\bar{K} = K_\varepsilon + K_M \left[\frac{r_e}{h}\right]$$

(U). Of interest in the design of engine systems utilizing LITVC is the location of the resultant induced force vector along the contour. If it is assumed that flow interference effects are negligible and that injectant momentum is small compared to the induced pressure force so that discrete forces normal to the nozzle wall are produced downstream of each port, the effective location of the induced force vector can be ascertained from the test data and the nozzle geometry (Fig. 218) by considering the following:

1) $F_s = f_s \left[1 \quad 2 \sum_{k=1}^{\frac{n-1}{2}} \cos k\Psi \right]$

2) $f_A = f_s \tan \alpha$

3) f_s is constrained to lie on the curve $x = f(x)$ where x and $f(x)$ are the coordinates of the nozzle contour.

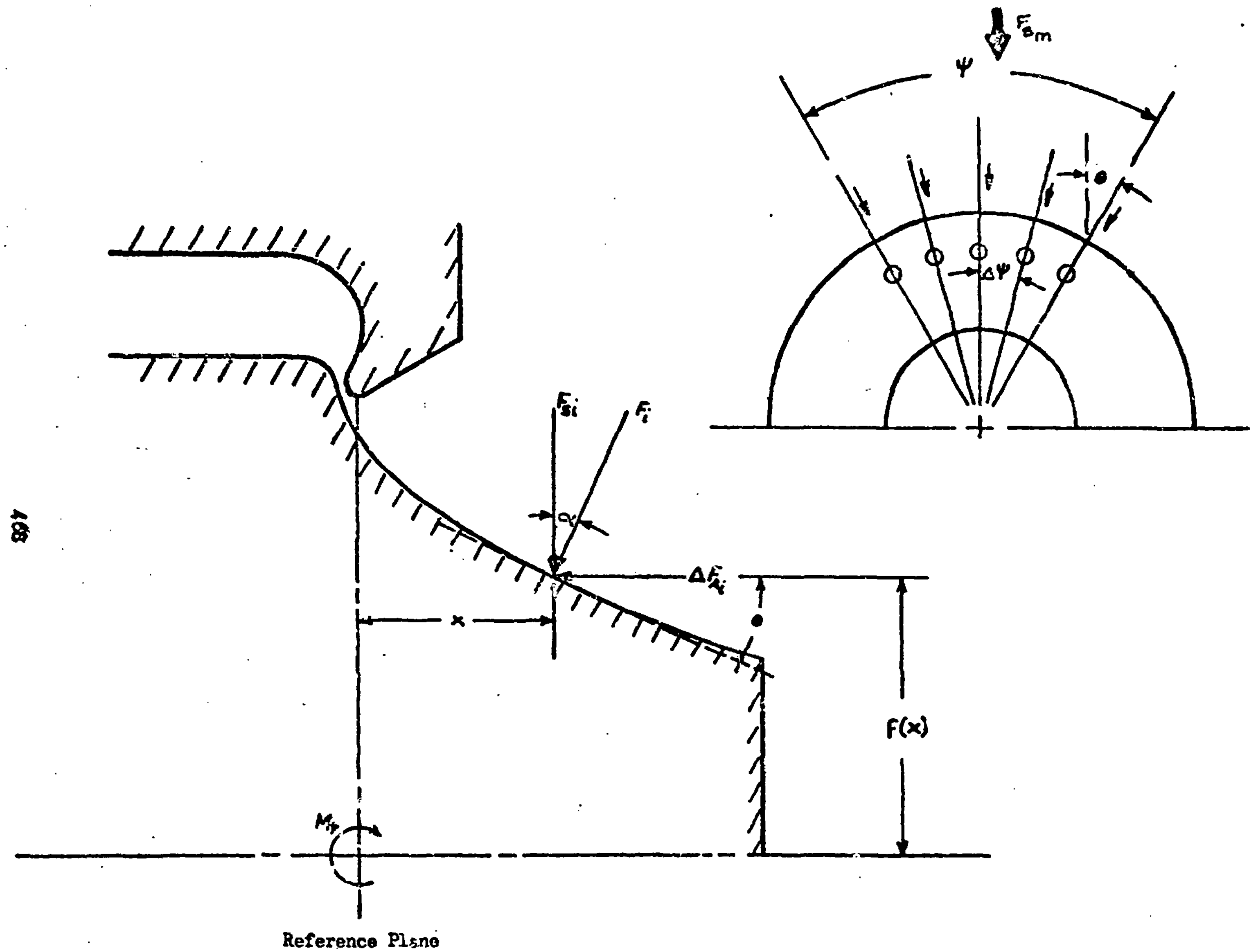

Figure 218. Location of the Induced Force Vector

(U) Thus:

$$M_T = F_s\left[1 + 2\sum_{k=1}^{\frac{n-1}{2}} \cos k\psi\right] x - (\Delta F_s)\ f(x)\left[1 + 2\sum_{k=1}^{\frac{n-1}{2}} \cos k\psi\right]$$

or

$$x = \frac{M_T}{F_{s_m}} + f(x)\tan\alpha$$

(U) Since $f(x)\tan\alpha$ is known, the quantity x can be obtained through an iterative solution of the above equation using the measured values of F_s and M_T. Unless flow interference effects are severe, the above relation remains qualitatively correct even if these phenomena do occur.

REFERENCES[1]

1. Dahm, T. J., The Development of an Analogy to Blast Wave Theory for the Prediction of Interaction Forces Associated with Gaseous Secondary Injection into a Supersonic Stream, Vidya Corp., Vidya Technical Note 9166, TN-3, May 1964.

* 2. Final Report, Aerodynamic Nozzle Study, Vol. 1, Rocketdyne, A Division of North American Aviation, Inc., R-6582, July 1966. Confidential

3. Hsia, H. S. and Karamcheti, K., Shocks Induced by Secondary Fluid Injection, Journal of Spacecraft and Rockets, Vol. 2, Number 1, Jan-Feb. 1965.

4. Zukoski, E. E., and Spaid, F. W., Secondary Injection of Gases Into a Supersonic Flow, AIAA Journal, Vol. 2, Number 10, October 1964.

5. Newton, J. F., Jr., and Spaid, F. W., Experiments on the Interaction of Secondary Injectants and Rocket Exhaust for Thrust Vector Control, Technical Report No. 32-303, Jet Propulsion Laboratory, Feb. 1962.

6. Sukari, A., On the Propagation and Structure of the Blast Wave-I, Journal of the Physical Sciences of Japan, Vol. 8, Number 5, Sept.-Oct. 1953.

7. Lees, L. and Kubota, T., Inviscid Hypersonic Flow Over Blunt Nosed Slender Bodies, Journal of the Aeronautical Sciences, Vol. 24, No. 3, 1957.

* 8. Design Criteria for Hot Gas Secondary Injection Thrust Vector Control of Solid Propellant Rocket Motors, Thiocol Chemical Corporation, Wasatch Division, TW93-2-65, Vol. I, Book I, Feb. 1965. Confidential

---

1. Classified material (all Confidential, Group 4) from asterisked documents has been reproduced in this report.

9. Zimmerman, C. A., et al., Secondary Injection Thrust Vector Control, Lockheed Missiles and Space Co., AD 617 689, April 1965.

* 10. Hair, L. M., and Baumgartner, A. T., An Empirical Model of Secondary Injection Thrust Vector Control, Lockheed Missiles and Space Co., LMSC/HREC A710184, Oct. 1964. Confidential.

* 11. Fox, J. J., et al., Thrust Vector Control by Reactive Liquid Secondary Injection, Bulletin of the 18th Meeting, JANAF-ARPA-NASA, Solid Propellant Group, Vol. III, June 1962, pp. 61-177. Confidential.

12. LeCount, R. L., et al, An Analysis of the Effects of Injection Parameters on the Thrust Vector Control Performance of the Lance Missile, Lockheed Missiles and Space Company, LMSC-664523, May 1965. Confidential

13. Green, C. J. and McCullough, F., Liquid Injection Thrust Vector Control, AIAA Journal, Vol. I, No. 3, pp. 573-578, March 1963.

* 14. Pauckert, R., High Area Ratio N zle Study, Rocketdyne, A Division of North American Aviation, Inc., [illegible]. Confidential.

* 15. Interim Report, Aerodynamic Nozzle Study, Vol. II, Rocketdyne, A Division of North American Aviation, Inc., R-6273, 1965. Confidential.

* 16. Parametric Study of the Lance Booster Engine Liquid Injection TVC System, Rocketdyne, A Division of North American Aviation, Inc., RR-66-21. Confidential.

17. Erickson, L. H. and Bell, H. S., Optimum Design Investigation of Secondary Injection Thrust Vector Control Systems, Thiocol Chemical Corporation, AFSC-TR-61-1, TW-965-12-61, March 1962. Confidential.

18. Sengel, R., and Wu, J. M., Thrust Vector Control by Liquid Injection into Rocket Nozzles, Journal of Spacecraft and Rockets, Vol. I, Number 5, September-October, 1964.

19. LeCount, R. L., et al., Analysis of the Physical and Chemical Aspects of Fluid Injection Thrust Vector Control, Lockheed Missiles and Space Corporation, LMSC A-24-65-1, TM-55-12-6, May 1965.

20. Test Facilities Handbook, Arnold Engineering Development Center, Arnold Air Force Station, Tennessee, November 1966.

* 21. Interim Report, Aerodynamic Nozzle Study, Vol. III - Slipstream Studies, Rocketdyne, A Division of North American Aviation, Inc., R-6273, 1965. Confid.

22. Salmi, R. J., Preliminary Investigation of Methods to Increase Base Pressure of Plug Nozzles at Mach 0.9, NACA RM E56 J05, 1956.

23. Korst, H. H., et al., A Theory for Base Pressures in Transonic and Supersonic Flow, University of Illinois, METN392-2, OSR-TN-55-89, May 1962.

24. Rabone, G.R., Low Angle Plug Nozzle Performance Characteristics, presented to the AIAA, Second Propulsion Joint Specialist Conference, Colorado Springs, Colorado, June 13-17, 1966, AIAA Paper No. 66-664.

* 25. Davidson, D. L., Performance Evaluation of a Rocketdyne Aerodynamic Spike Nozzle Configuration, Rocket Test Facility, Arnold Engineering Development Center, Arnold Air Force Station, Tennessee, AEDC-TR-67-8, March 1967. Confidential.

26. Smith, R. E., and Runyan, R. B., Performance Evaluation of an Aerodynamic Spike Nozzle Engine with Liquid (N_2O_4) Injection TVC, Rocket Test Facility, Arnold Engineering Development Center, Arnold Air Force Station, Tennessee, AEDC-TR-67-1[illegible] 1967. Confidential.